UNIVERSITY OF CRETE
SCHOOL OF SCIENCES AND ENGINEERING
DEPARTMENT OF CHEMISTRY

Doctoral Thesis

DEVELOPMENT OF NOVEL COORDINATION POLYMERS

IOANNIS SPANOPOULOS

Thesis Supervisor: Prof. Pantelis Trikalitis

HERAKLION 2015

UNIVERSITY OF CRETE
SCHOOL OF SCIENCES AND ENGINEERING
DEPARTMENT OF CHEMISTRY

Doctoral Thesis

DEVELOPMENT OF NOVEL COORDINATION POLYMERS

IOANNIS SPANOPOULOS

Thesis Supervisor: Prof. Pantelis Trikalitis

HERAKLION 2015

THESIS COMMITTEE

Dr. Pantelis N. Trikalitis (Supervisor)
Professor, Department of Chemistry, University of Crete

Dr. Georgios E. Froudakis
Professor, Department of Chemistry, University of Crete

Dr. Constantinos J. Milios
Assistant Professor, Department of Chemistry, University of Crete

Dr. Georgios E. Vassilikogiannakis
Professor, Department of Chemistry, University of Crete

Dr. Manolis Stratakis
Professor, Department of Chemistry, University of Crete

Dr. Thedoros A. Steriotis
Research Director, Institute of Physical Chemistry, NCSR "Demokritos"

Dr. Georgia Charalambopoulou
Senior Researcher, Institute of Nuclear Technology and Radiation Protection,
NCSR "Demokritos"

“For the things we have to learn before we can do, we learn by doing them”

Aristotle

Acknowledgements

Curriculum Vitae

Ioannis Spanopoulos, M.Sc

Personal information	• Date of birth: 18/09/1984 • Nationality: Greek • Family status: Single • Military service: Fulfilled • Email: ioaspan@chemistry.uoc.gr

Education

- 10/2010 – 09/2015: **PhD Candidate,** Department of Chemistry, University of Crete. **Project:** Synthesis, Characterization and Gas-Sorption Studies of Novel Porous Coordination Polymers.

- 9/2007 – 7/2009: **MSc Environmental Chemistry and Technology,** Department of Chemistry, National and Kapodistrian University of Athens. **MSc Thesis:** "Development, optimization and validation of a method for the simultaneous determination of 23 VOCs in samples of surface and tap water, with HS-SPME, GC-MS".

- 9/2002 – 8/2007: **BSc in Chemistry**, Department of Chemistry, National and Kapodistrian University of Athens.

Research experience

- 10/2010 – 09/2015: **PhD Candidate,** Department of Chemistry, University of Crete, under the supervision of *Prof. Pantelis N. Trikalitis.* a) Synthesis and characterization of new functionalized organic ligands, b) synthesis of new, highly porous, open framework coordination polymers (or metal-organic frameworks, MOFs), c) structural characterization using advanced methodologies and instrumentation and d) advanced gas-sorption studies using various gases at different temperatures.

- 2012: Assistant in undergraduate Analytical Chemistry laboratory teaching Atomic Absorption Spectroscopy (AAS), theory and practice.

- 2011: Assistant in undergraduate Inorganic Chemistry laboratory.

- 8/2009 - 5/2010: Private in Hellenic Armed Forces, with specialty **Chemical Engineering.**

- 9/2007 – 7/2009: **MSc Environmental Chemistry and Technology,** Department of Chemistry, National and Kapodistrian University of Athens, under the supervision of *Prof. Michael Scoullos*. Development, optimization and validation of a new methodology for the simultaneous determination of 23 volatile organic compounds present in either surface or tap water, using advanced solid phase micro-extraction technique (SPME) and analysis with mass-spectrometry techniques (GC-MS).

- 7/2008 - 7/2009: Water quality control in Athens Water Supply and

Sewage Company (EYDAP SA).

Publications

1. **MOF Crystal Chemistry Paving the Way to Gas Storage Needs: Aluminum Based soc-MOF for CH$_4$, O$_2$ and CO$_2$ Storage,** D. Alezi, Y. Belmabkhout, M. Suetin, P. M. Bhatt, L. J. Weselinski, V. Solovyeva, K. Adil, I. Spanopoulos, P. N. Trikalitis, A. Emwas, M. Eddaoudi, *J. Am. Chem. Soc.*, **2015**, 137 (41), 13308-13318.

2. **A Microporous Co^{2+} Metal Organic Framework with Single-Crystal to Single-Crystal Transformation Properties and High CO$_2$ Uptake,** E. E. Moushi, A. Kourtellaris, I. Spanopoulos, M. J. Manos, G. S. Papaefstathiou, P. N. Trikalitis, A. J. Tasiopoulos, *Cryst. Growth Des.,* **2015**, 15, 185-193.

3. **Enhanced gas-sorption properties of a high surface area, ultramicroporous magnesium formate,** I. Spanopoulos, I. Bratsos, Ch. Tampaxis, A. Kourtellaris, A. Tasiopoulos, G. Charalambopoulou, T. A. Steriotis, P. N. Trikalitis, *CrystEngComm.*, **2015**, 17, 532-539.

4. **Understanding the adsorption mechanism of noble gases Kr and Xe in CPO-27-Ni, CPO-27-Mg, and ZIF-8,** O. V. Magdysyuk, F. Adams, H.-P. Liermann, I. Spanopoulos, P. N. Trikalitis, M. Hirscher, R. E. Morris, M. J. Duncan, L. J. McCormick and R. E. Dinnebier, *Phys. Chem. Chem. Phys.*, **2014**, 16, 23908-23914.

5. **A "turn-on"–turning-to-ratiometric sensor for zinc(II) ions in aqueous media,** G. K. Tsikalas, P. Lazarou, E. Klontzas, S. A. Pergantis, I. Spanopoulos, P. N. Trikalitis, G. E. Froudakis, H. E. Katerinopoulos, *RSC Adv.,* **2014**, 4, 693-696.

6. **Drastic Enhancement of the CO$_2$ Adsorption Properties in Sulfone-Functionalized Zr- and Hf-UiO-67 MOFs with Hierarchical Mesopores,** P. Xydias, I. Spanopoulos, E. Klontzas, G. E. Froudakis, P. N. Trikalitis, *Inorg. Chem.,* **2014**, 53 (2), 679-681.

7. **A Straight Forward Route for the Development of Metal−Organic Frameworks Functionalized with Aromatic −OH Groups: Synthesis, Characterization, and Gas (N$_2$, Ar, H$_2$, CO$_2$, CH$_4$, NH$_3$) Sorption Properties**, I. Spanopoulos, P. Xydias, C. D. Malliakas, P. N. Trikalitis, *Inorg. Chem.*, **2013**, 52 (2), 855-862.

<table>
<tr><td>**Conference Presentations**</td><td>

1. **Israel-Greece Joint Meeting on Nanotechnology and Bionanoscience,** October 20 - 23, 2014, The David Lopatie Conference Center, Weizmann Institute of Science, Israel. "Expanded tbo Metal Organic Frameworks for Methane Storage" Ioannis D. Spanopoulos, Constantinos M. Tsangarakis and Pantelis N. Trikalitis (**Oral & Poster presentation**).

2. **MOF-2014: 4th International Conference on Metal-Organic Frameworks and Open Framework Compounds.** September 28, 2014 – October 01, 2014, Kobe, Japan. "Expanded tbo Metal Organic Frameworks for Methane Storage" Ioannis D. Spanopoulos, Constantinos M. Tsangarakis and Pantelis N. Trikalitis (**Oral presentation**).

3. **30th Panhellenic Conference on Solid-State Physics and Materials Science,** September 21-24, 2014, Heraklion, Crete, ''Enhanced Gas-sorption Properties of a High Surface Area, Ultramicroporous Magnesium Formate''. Ioannis Spanopoulos and Pantelis N. Trikalitis (**Poster presentation**).

4. **International Symposium on Advance Nanoporous and Nanostructured Materials,** September 03-04, 2014, Heraklion, Greece.

5. **6th Panhellenic Symposium on Porous Materials,** September 9-10, 2013, Kavala Institute of Technology, Greece. "Mix-Metal synthesis of hydroxyl functionalized IRMOF-8: Characterization and Gas Sorption Properties". Ioannis D. Spanopoulos, Pantelis N. Trikalitis (**Oral presentation, award for best presentation**).

6. **MOF-2012: 3rd International Conference on Metal-Organic Frameworks and Open Framework Compounds.** September 16, 2012 - September 19, 2012, John McIntyre Conference Centre, Edinburgh. "A Straight Forward Route for the Development of Hydroxyl Functionalized Metal-Organic Frameworks" Ioannis D. Spanopoulos, Pantelis A. Xydias and Pantelis N. Trikalitis (**Poster presentation**).

7. **Summer School on micro- and nano- Structural Characterization of Materials focused on Electron Microscopy,** July 11-15, 2012, Thessaloniki, Greece.

8. **5th Panhellenic Symposium on Porous Materials,** June 30th – July 1st, Univeristy of Crete, Heraklion, Greece. "Synthesis, Characterization and Gas-Sorption Studies of Hydroxyl Functionalized MOFs". Ioannis Spanopoulos and Pantelis N. Trikalitis (**Oral presentation**).

</td></tr>
</table>

Abbreviations

ACN	Acetonitrile
BET	Brunauer–Emmett–Teller
bis-pyr	1,2-bis(4-pyridyl)ethane
CAU	Christian-Albrechts-University of Kiel
CDCl$_3$	Deuterated chloroform
CH$_2$Cl$_2$	Dichloromethane
CHCl$_3$	Chloroform
DEF	N,N-Diethylformamide
DMA	N,N-Dimethylacetamide
DMAP	4-Dimethylaminopyridine
DMF	N,N-Dimethylformamide
DMSO	Dimethyl sulfoxide
D$_2$O	Deuterium oxide
dobdc	2,5-dihydroxyterephthalic acid
DUT	Dresden University of Technology
EDS	Energy-dispersive X-ray spectroscopy
EtOH	Ethanol
H$_2$BDC	Terephthalic acid
H$_2$BPDC	Biphenyl-4,4′-dicarboxylic acid
H$_2$NDC	2,6-Naphthalenedicarboxylic acid
H$_3$BTB	1,3,5-Tris(4-carboxyphenyl)benzene
H$_3$BTC	Trimesic acid
H$_3$BTE	4,4′,4″-[benzene-1,3,5-triyl-tris (ethyne-2,1-diyl)]tribenzoate
H$_4$BTTB	1,2,4,5-tetrakis(4-carboxyphenyl)benzene
HKUST	Hong Kong University of Science and Technology
H$_3$TATAB	4,4′,4″-s-triazine-1,3,5-triyltri-p-aminobenzoic acid
H$_4$TBAPy	1,3,6,8-tetrakis(p-benzoicacid) pyrene
H$_2$TPDC	p-terphenyl-dicarboxylic acid

IAST	Ideal Adsorbed Solution Theory
IRMOF	Isoreticular metal organic framework
IUPAC	International Union of Pure and Applied Chemistry
MeOH	Methanol
MIL	Materials Institute Lavoisier
min	Minute
MOF	Metal Organic Framework
NLDFT	Non-Local Density Functional Theory
NMP	N-methyl-2-pyrrolidone
NMR	Nuclear magnetic resonance
NOTT	University of Nottingham
NU	Northwestern University
PCN	Porous Coordination Network
PCP	Porous Coordination Polymer
pxrd	Powder X-ray diffraction
SBU	Secondary building unit
SEM	Scanning electron microscopy
SNU	Seoul National University
TGA	Thermogravimetric analysis
THF	Tetrahydrofuran
UiO	University of Oslo
UMCM	University of Michigan Crystalline Material
UTSA	University of Texas at San Antonio
XRD	X-ray diffraction
ZIF	Zeolitic imidazolate frameworks

Περίληψη

Τα πολυμερή συναρμογής ή μεταλλο-οργανικά στερεά (Metal Organic Frameworks) αποτελούν μία νέα κατηγορία κρυσταλλικών υλικών που αποτελούνται από δύο μέρη, ένα οργανικό και ένα ανόργανο. Αυτή ακριβώς η διττή τους φύση μπορεί να οδηγήσει στο σχηματισμό καινοτόμων υλικών με πολύ σημαντικές ιδιότητες και πιθανές σύγχρονες εφαρμογές, όπως είναι η αποθήκευση και ο διαχωρισμός αερίων.

Ο σκοπός της παρούσας διατριβής ήταν η ανάπτυξη καινοτόμων MOFs τροποποιημένα με κατάλληλες λειτουργικές ομάδες ικανές για την σημαντική βελτίωση της προσρόφησης ή/και του διαχωρισμού σημαντικών αερίων όπως CO_2, CH_4, H_2, Kr και Xe. Για την επιλογή της κατάλληλης λειτουργικής ομάδας λάβαμε υπ' όψιν την ύπαρξη οξινοβασικών αλληλεπιδράσεων ή αλληλεπιδράσεων διπόλου-διπόλου μεταξύ του υλικού και των προσροφούμενων αερίων. Αυτό μπορεί να γίνει με τη χρήση λειτουργικών ομάδων όπως αρωματικά υδροξύλια (όξινες ομάδες -OH), σουλφωνικές ομάδες ($-SO_3H$), σουφλόνο ομάδες ($-SO_2$), νίτρο ομάδες ($-NO_2$) και άμινο ομάδες ($-NH_2$) μεταξύ άλλων. Για την ανάπτυξη των νέων MOFs, σε πρώτο στάδιο συντέθηκαν οι επιθυμητοί υποκαταστάτες με διαφορετική τοπολογία σύνδεσης. Συγκεκριμένα, συντέθηκαν 77 οργανικοί υποκαταστάτες οι οποίοι χρησιμοποιήθηκαν για τη σύνθεση περισσότερων από 90 νέων MOFs. Τα περισσότερα από αυτά έδειξαν πολύ ενδιαφέρουσες προσροφητικές ιδιότητες.

Πιο συγκεκριμένα, επιτεύχθηκε η σύνθεση υλικών με δομή tbo τα οποία εμφανίζουν πολύ μεγάλη ικανότητα προσρόφησης CH_4 σε θερμοκρασία δωματίου και υψηλές πιέσεις. Αυτά τα υλικά κατατάσσονται ανάμεσα στα 5 καλύτερα υλικά τύπου MOF για αποθήκευση CH_4 σε θερμοκρασία δωματίου και υψηλές πιέσεις. Ακολούθως συντέθηκε ένας οργανικός υποκαταστάτης ο οποίος είναι τροποποιημένος με $PdCl_2$ και χρησιμοποιήθηκε για την σύνθεση ενός υλικού το οποίο εμφανίζει πολύ μεγάλη ικανότητα αποθήκευσης CO_2 σε θερμοκρασία δωματίου και πίεση 1 ατμόσφαιρας. Αυτό το υλικό συγκαταλέγεται ανάμεσα στα 10 καλύτερα υλικά τύπου MOF για αποθήκευση CO_2 σε θερμοκρασία δωματίου και πίεση 1 ατμόσφαιρας. Παράλληλα ένα άλλο υλικό με δομή NbO που αποτελείται από ένα τροποποιημένο υποκαταστάτη με σουφλονικές ομάδες ($-SO_3H$), εμφανίζει πολύ μεγάλη ικανότητα διαχωρισμού των δύο ευγενών αερίων Xe και Kr. Η τιμή της εκλεκτικότητας του διαχωρισμού Xe/Kr βρίσκεται ανάμεσα στις 5 καλύτερες για υλικά τύπου MOF, σε θερμοκρασία δωματίου. Επιπλέον, χρησιμοποιώντας ένα οργανικό υποκαταστάτη τροποποιημένο με αμιδικές ομάδες (-NH-CO) επετεύχθη η σύνθεση ενός υλικού με δομή fcu (τύπου UiO) το οποίο έχει το μεγαλύτερο όγκο πόρων από όλα τα υλικά αυτού του τύπου μέχρι τώρα. Ομοίως, κάνοντας χρήση ενός οργανικού υποκαταστάτη τροποποιημένου με μεθόξυ ομάδες ($-OCH_3$) συντέθηκε ένα υλικό τύπου UiO-67 το οποίο εμφανίζει μία πολύ μεγάλη τιμή ενθαλπίας προσρόφησης μεθανίου. Η τιμή αυτή είναι η δεύτερη υψηλότερη που έχει καταγραφεί για υλικά τύπου MOF.

Τα ευρήματα της παρούσας διατριβής βελτιώνουν την κατανόηση της σχέσης μεταξύ της δομής και των προσροφητικών ιδιοτήτων των MOFs, για τα αέρια που μελετήθηκαν και με τον τρόπο αυτό ανοίγουν νέους ορίζοντες για την ανάπτυξη υλικών που θα μπορούν να χρησιμοποιηθούν σε πραγματικές εφαρμογές. Ο στόχος αυτός απαιτεί επιπλέον εμβάθυνση σε θέματα σταθερότητας και αναγέννησης των MOFs, τα οποία με την σειρά τους απαιτούν έλεγχο των ιδιοτήτων του υλικού σε πραγματικές συνθήκες, όπως για παράδειγμα πραγματικά μίγματα αερίων τα οποία συνήθως περιέχουν H_2O. Η ύπαρξη του τελευταίου αποτελεί σε πολλές περιπτώσεις ανασταλτικό παράγοντα λόγω της περιορισμένης υδροθερμικής σταθερότητας πολλών MOFs.

Λέξεις κλειδιά: Μέταλλο οργανικά στερεά, πορώδες, προσρόφηση αερίων, ειδική επιφάνεια, ενθαλπία προσρόφησης, διαχωρισμός αερίων, αποθήκευση αερίων, εκλεκτικότητα.

Abstract

Metal Organic Frameworks (MOFs) is a novel class of crystalline hybrid nanomaterials comprised of both an organic and an inorganic part. This hybrid nature of MOFs can give rise to a plethora of unique properties and therefore MOFs are considered important candidates for numerous applications, including gas storage and gas separation.

The objective of this thesis was the development of novel porous MOFs that would exhibit enhanced gas sorption properties and could be used in important industrial applications. These applications include CO_2, CH_4 and H_2 storage as well as CO_2/CH_4, CO_2/N_2 and Xe/Kr separation. This could be achieved by the use of organic ligands functionalized with polar, acidic or basic side groups that can enhance the interaction of the framework with gas molecules through dipole-induced dipole, or acid-base interactions. For that purpose more than 77 new tailor made organic linkers were exploited for the synthesis of more than 90 novel MOFs. So far successful activation, and evaluation of the gas sorption properties, was possible for less than the half of these materials. Nonetheless important structural characteristics and improved gas sorption properties were observed for most of them.

In particular, utilization of expanded rectangular linkers resulted in the synthesis of new tbo-MOFs exhibiting a very high methane uptake at ambient temperature and high pressures. These materials are among the five best MOF candidates for CH_4 storage in terms of total gravimetric uptake and gravimetric working capacity.

Another tailor made organic linker bearing $PdCl_2$ entities was used for the synthesis of a material exhibiting a notable CO_2 uptake at 298 K and 1 bar. This material is among the ten best MOF candidates for CO_2 storage under mild conditions.

An NbO type of MOF based on an organic linker functionalized with sulfonic groups ($-SO_3H$) was synthesized, that exhibits a very high selectivity for the separation of Xe over Kr at RT. This value is among the five highest reported for MOFs, rendering this material a promising candidate for the separation of Xe over Kr.

Using an elongated amide functionalized organic linker, it was possible to synthesize a UiO type of MOF with the largest unit cell and pore volume reported to date. Similarly, the use of a methoxy functionalized organic linker for the synthesis of a UiO-67 analogue revealed an impressive isosteric heat of methane adsorption with a value of 24.3 kJ mol^{-1}, the second highest reported in the family of MOFs.

The important results of the present thesis provide new directions towards the development of functional MOFs that could find real applications in the field of gas storage/separation.

Key words: MOFs, porosity, gas sorption, surface area, heat of adsortpion, selectivity, gas separation, gas storage.

Table of Contents

PART A

Chapter 1: Introduction

1.1 Coordination Polymers or Metal Organic Frameworks

Coordination Polymers (CPs) or Metal Organic Frameworks (MOFs) are a novel class of crystalline nanomaterials comprised of both an organic and an inorganic part. The inorganic part can be a single metal ion or a metal cluster, and the organic part can be any organic linker able to coordinate to a metal ion. [1] Combination of those components can give rise to 1-dimension (1-D), 2-dimension (2-D) or 3-dimension (3-D) structures. The uniqueness of their nature stems from the fact that both their components can be adjusted and modified. The inorganic part can be acquired from different metal ions or metal clusters with variable connectivity and topology, while the organic part can be any tailor made organic linker, carrying various functional groups, with tunable size and geometry. This hybrid architecture opens the possibility to design and synthesize a plethora of new materials, each one with unique structure and properties.

The first coordination polymer, the synthetic pigment widely known as Prussian Blue (Preußisch blau) has been in use since the early 1700s. [2] However its structure was determined much later, by X-ray diffraction in 1977 to reveal a mixed-valent Fe(II)/Fe(III) 3-D network with Fe(II)-carbon distances of 1.92 Å and Fe(III)-nitrogen distances of 2.03 Å (Figure 1.1). [3]
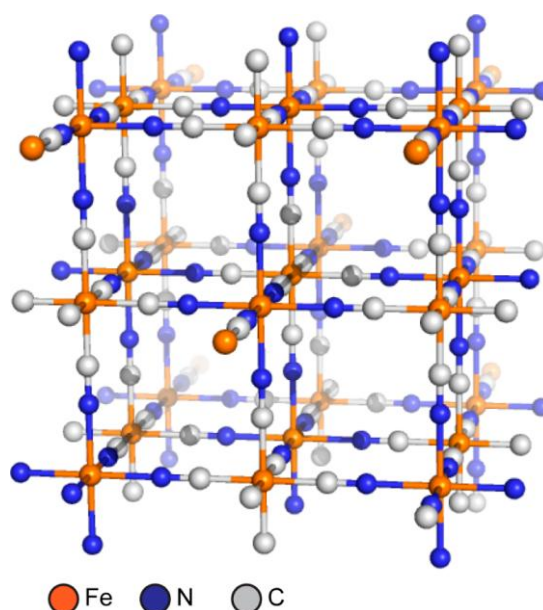

Fe   N   C

Figure 1.1. Structure of Prussian Blue. Octahedral nodes of Fe(II) and Fe(III) ions are bridged by cyanide ligands to generate a cubic 3D network. [4]

Evidently it was only until the beginning of 1990s that those materials drove the interest of the scientific community, due their promising extraordinary properties, such as porosity, along with optical, magnetic, electrical, and catalytic properties, that could result in the application of MOFs into numerous fields. The first application of MOFs on gas adsorption was reported from Kondo and co-workers, who synthesized a material with chemical formula $M_2(4,4'\text{-bpy})_3(NO_3)_4 xH_2O$ constructed from Co^{2+} ions bridged by 4,4-bipyridine ligands forming a 3D porous network.[5] A few years later Li and co-workers synthesized one of the most famous and studied MOF that exhibited very high porosity: MOF-5 (or IRMOF-1) with chemical formula $Zn_4O(BDC)_3 \times (DMF)_8$ and a Langmuir specific surface area of 2900 $m^2 g^{-1}$.[6]
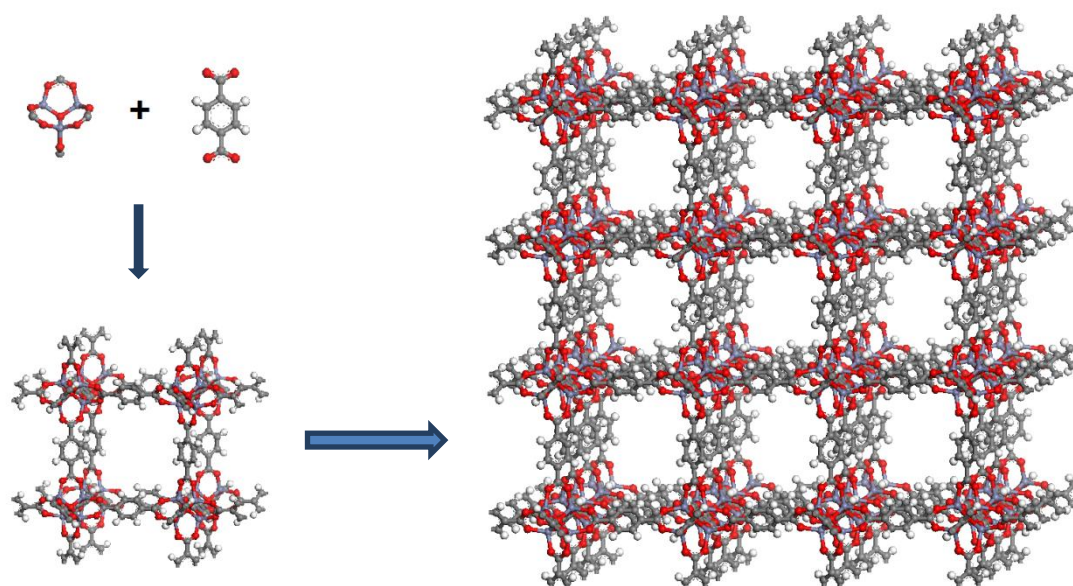

Figure 1.2. Synthesis of MOF-5. Reaction of Zn^{2+} ions with terepthalic acid leads to the formation of a 3-D cubic network.

Metal Organic Frameworks can be easily synthesized by a wide range of synthetic procedures. The most commonly used is the solvothermal method, where a solvent, or a mixture of solvents (polar, non polar, protic, aprotic), including water, is used to dissolve the starting materials, (organic linkers and metal salts) followed by heating the reaction solution to a wide temperature range from 25 ^{0}C to as high as 250 ^{0}C.[7] Additionally other synthetic methods can be utilized in MOF synthesis, such as microwave heating,[8] sonication assisted synthesis,[9] or mechanochemical procedures.[10] It is worth mentioning that to date there are several MOFs that are produced in an industrial scale for research and development purposes and for every day applications.[11]

Careful and meticulous adjustment of the reaction conditions can result to high quality crystalline materials exhibiting properties without precedent in comparison to other porous solids, (zeolites, carbons, alloys, polymers and silicate solids). So far there have been synthesized MOFs that exhibit: ultrahigh specific surface areas, 7140 $m^2 g^{-1}$ (BET), for NU-110,[12] ultralow crystal density 0.126 g cm^{-3}

for MOF-399,[13] 98 Å pore aperture for IRMOF-74-XI,[14] very high values in terms of CO_2 uptake with 350 $cm^3 cm^{-3}$ (total uptake), at 30 bar and 298 K, for NU-111,[15] in terms of H_2 uptake with a value of 167 mg g^{-1} (total), at 70 bar and 77 K, for MOF-210,[16] in terms of CH_4 uptake with a value of 230 cm^3 cm^{-3} (total), at 35 bar and 298 K, for Ni-MOF-74,[17] high proton conductivity (98% relative humidity, 25°C) with a value of 8×10^{-3} S cm^{-1} for $(NH_4)_2(ADP)[Zn_2(oxalate)_3]\cdot 3H_2O$,[18] high charge mobility values of 0.2 $cm^2 V^{-1} \cdot s^{-1}$ for $Zn_2(TTFTB)$,[19] and high Lithium storage capacity (after 60 cycles) with a value of 560 mAh g^{-1} for $Zn_3(HCOO)_6$.[20]

Accordingly the applications of MOFs can be equally impressive and numerous. Metal Organic Frameworks can be efficiently used in fields as: gas storage (Figure 1.3.1) [21], gas separation, (Figure 1.3.2),[22] catalysis,[23] nonlinear optics[24] and ferroelectricity,[25] energy conversion[26] and storage,[27] chemical sensing,[28] bio-imaging (Figure 1.3.4) [29] and drug delivery (Figure 1.3.3).[30]
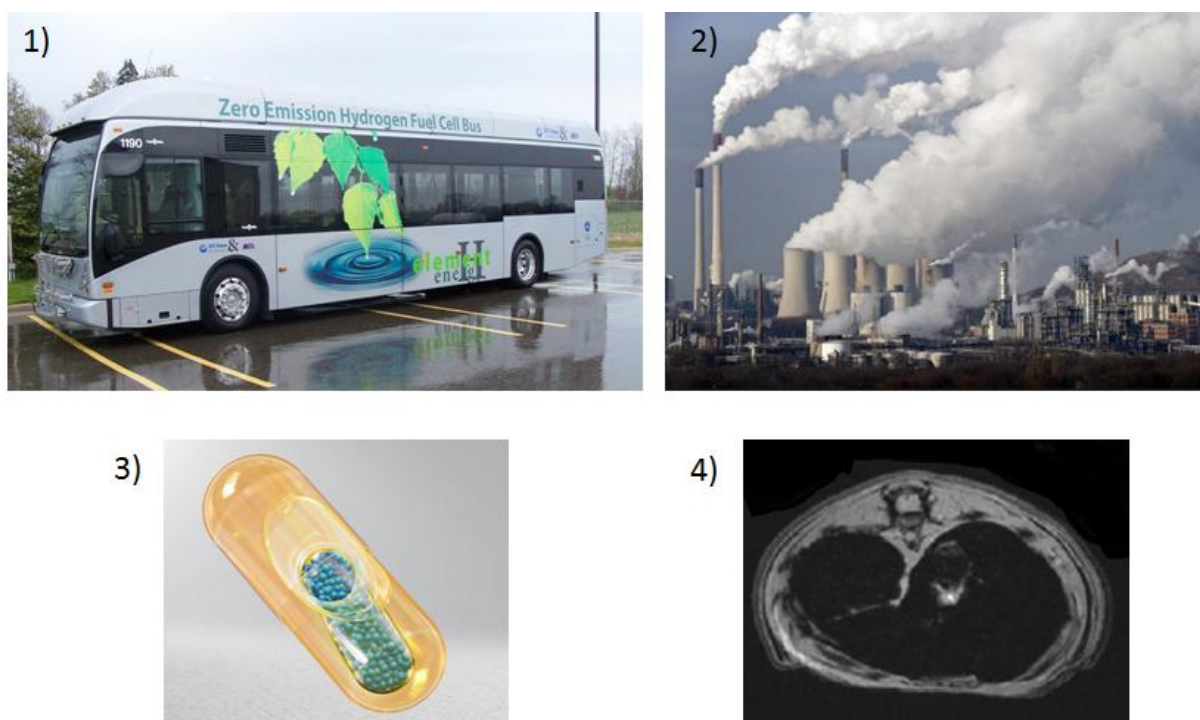

Figure 1.3. Applications of Metal Organic Frameworks: 1) gas storage, a hydrogen fuel cell bus. Addition of a small amount of a MOF inside the hydrogen storage tank can increase significantly the hydrogen storage tank capacity .[31] 2) gas separation, some MOFs are able to selectively adsorb and remove large amounts of CO_2 from a flue gas stream,[32] 3) drug delivery, some MOFs can act as drug delivery nanocarriers,[33] 4) bioimaging, a small quantity of MOF nanoparticles can act as contrast agents for magnetic resonance imaging (MRI).[34]

1.2 Inorganic building units and organic linkers for MOF synthesis

The two essential components in a MOF synthesis are the metal ions and the organic ligands. The organic linkers act as Lewis bases, donating a lone pair of electrons and the metal ions act as Lewis acids accepting the lone pair of electrons thus forming a coordination bond.[35] In the reaction mixture the organic linker can coordinate either to a single metal ion (both act as primary building units), or to a metal cluster that is formed in situ, through self assembly, containing multiple metal ions. In this case the organic linkers can coordinate to more than one metal ions, usually by bridging two of them in the metal cluster (secondary building units SBUs). One of the major advantages of the formation of secondary building units, through self assembly, is that an SBU can link more organic linkers than a single metal ion, resulting in highly porous and robust frameworks.[36] For instance bio-MOF-100 contains a large SBU consisting of eight Zn^{2+} cations interconnected by four adeninates and two μ-oxo groups that are bridged by 12 organic linkers. This combination of metal clusters and organic linkers resulted to the formation of a highly porous material with the second largest MOF pore volume reported to date 4.3 cm^3 g^{-1}.[37] Additionally, the zirconium fcu type MOFs, first synthesized in the University of Oslo, are composed of a $Zr_6O_4(OH)_4$-$(CO_2)_{12}$ cluster bridged by 12 organic linkers forming a very robust and air stable framework.[38] Figure 1.4 shows some representative metal clusters.

A great variety of metal ions can be utilized in MOF synthesis. Some of the most common metal ions used are divalent transition metal cations (Zn^{2+}, Cu^{2+}, Co^{2+}, Ni^{2+}, Mn^{2+}, Cd^{2+}), along with alkaline earth metals (Mg^{2+}, Ca^{2+}) and p block metal ions, (Al^{3+}, Ga^{3+}, In^{3+}). Especially Zn^{2+} ions can be efficiently utilized for the synthesis of high quality single crystals, due to their labile nature.[39] Zn^{2+} is a soft transition metal ion with d^{10} electron configuration and it exhibits no ligand field stabilization energy when forming coordination bonds with incoming ligands. Additionally low-oxidation state metals form less stable coordination bonds with harder bases like the oxygen donors of carboxylate ligands. Therefore the coordination bonds between the organic linkers and the metal ions are not strong enough and can be displaced many times during crystallization process. However, this results to lower chemical stability of the resulting MOF, since the organic linkers can be easily replaced by water molecules or other nucleophilic moieties.[40] This problem can be surpassed by the use of high valence hard metal ions, such as Al^{3+}, Cr^{3+}, Fe^{3+}, and Zr^{4+}. An increased charge density will decrease lability and ligand substitution simply by increasing the electrostatic interaction between the metal ions and the organic ligands. In this way thermal and chemical stable MOFs can be synthesized.[41,42]

The organic part of a MOF can vary significantly as well. There is a huge variety of organic linkers of numerous geometries and sizes. Apparently the organic linkers must have specific functional groups to be able to coordinate to the metal ions. Carboxylic acids,[43] phosphonic acids,[44] phosphonates,[45] N-heterocyclics,[46] and cyanides[47] represent some of the most viewed linkers used for the synthesis of coordination polymers.
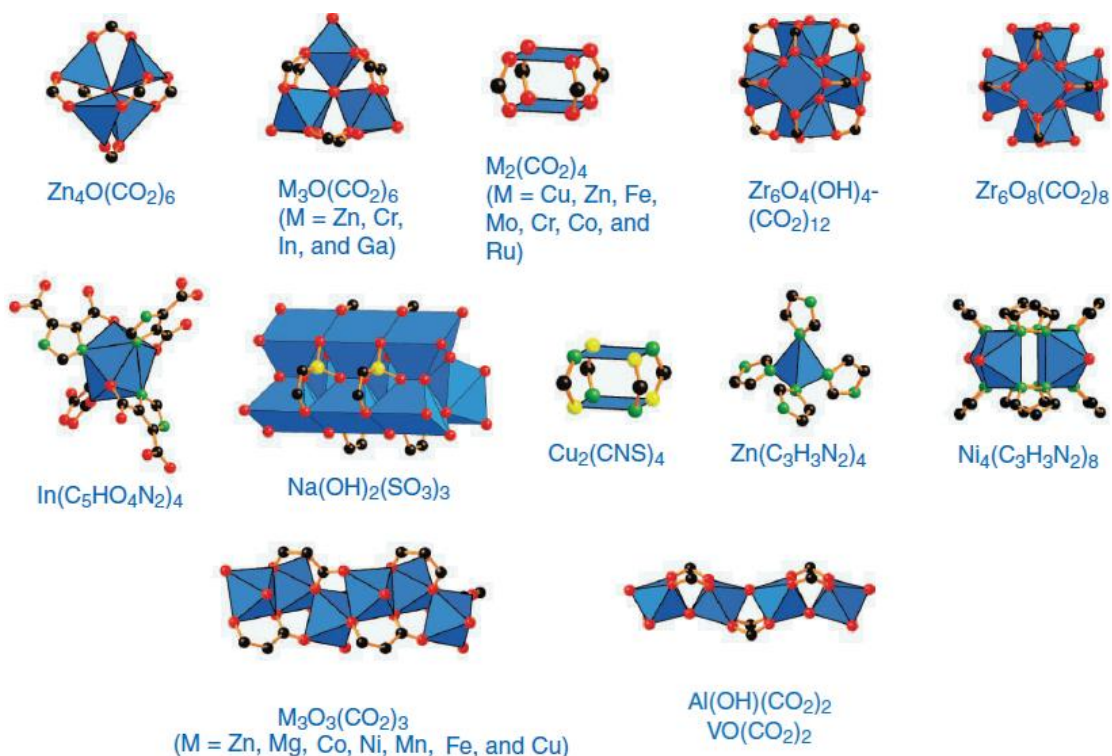
Figure 1.4. Inorganic secondary building units (SBUs). Color code: black, C; red, O; green, N; yellow, S; purple, P; light green, Cl; blue polyhedra, metal ions.[48]

The organic ligand is the heart of the framework, since it can alter and affect dramatically the properties of the material. For instance it can give flexibility, as in the case of MIL-88.[49] The framework consists of a trimeric $Cr_3O(H_2O)_2(OH)^{6+}$ SBU linked together by linear dicarboxylate linkers, terepthalic acid, 2,6-napthalen-dicarboxylic acid and 4,4-biphenyldicarboxylic acid. The volume of the unit cell increases from 1135 Å^3 for the evacuated material, to 2090 Å^3 for the methanol filled material, and to 2110 Å^3 when the framework adsorbs water. A rigid polyaromatic linker can offer robustness to the framework as in the case of MOF-200, where the use of a trigonal organic linker made up of 7 aromatic rings gave rise to a highly porous material exhibiting a specific surface area of 4530 m^2 g^{-1} (BET).[50] Furthermore, a functionalized organic linker with polar groups can enhance the gas sorption properties of the resulting material, as we have shown in the case of the sulfone-functionalized analogue of UiO-67 (Zr), using the ligand 4,4′-dibenzoic acid-2,2′-sulfone (H$_2$bbs). The incorporation of the polar sulfone groups increased 122% the CO_2 uptake at 1 bar and 273 K in comparison to the parent non-functionalized material.[51] Another important effect of the modification of the organic linker is the synthesis of hydrophobic, thus water stable, MOFs. As in the case of a series of NbO-type Cu(II)-based MOFs functionalized with different alkoxy substitutions. The analogue with the hexamethyl alkoxy functionality exhibited exceptional hydrophobic properties.[52]
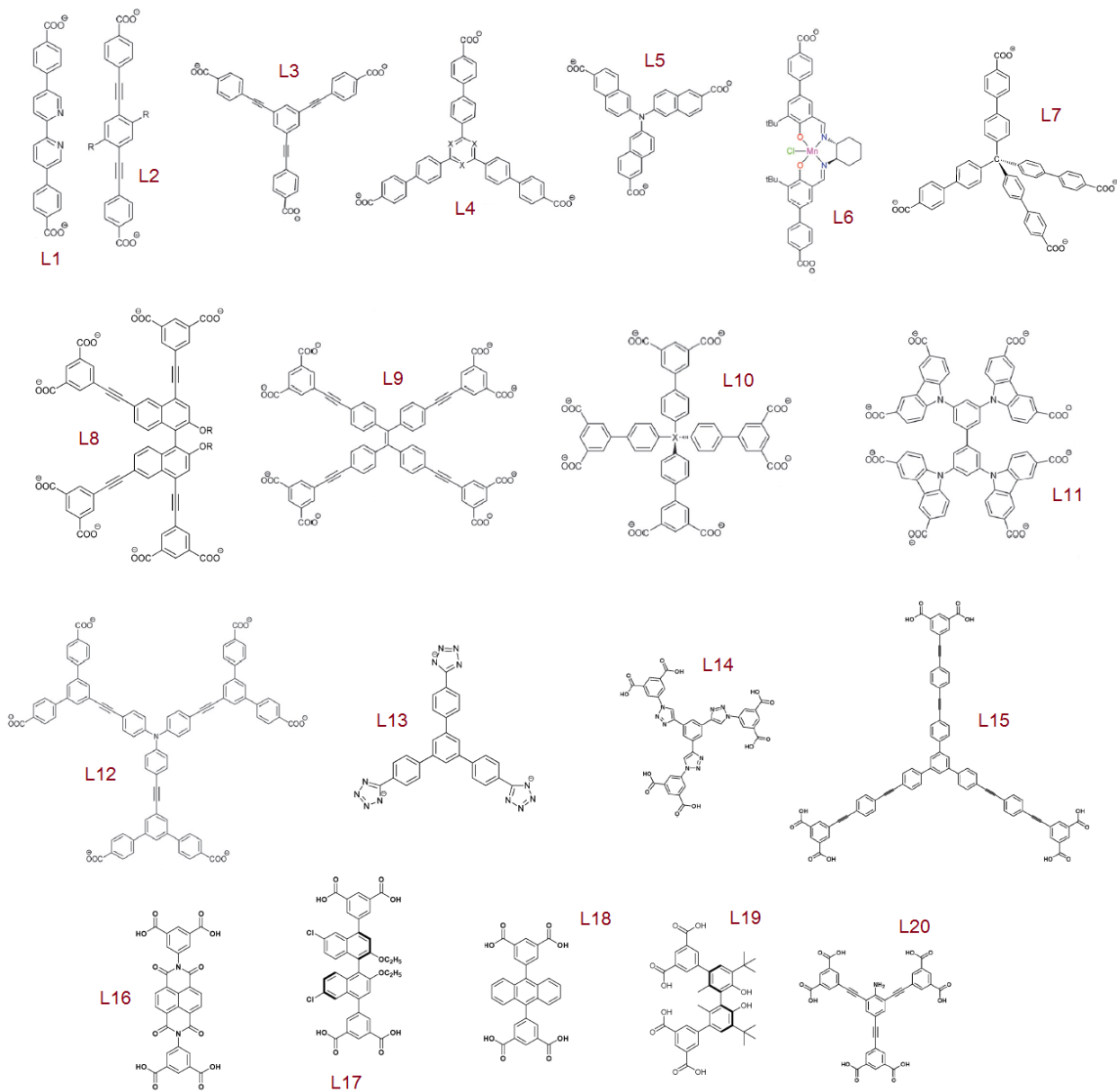
Figure 1.5. Some representative organic linkers used in MOF synthesis: L1[53], L2[54], L3[50], L4[55], L5[56], L6[57], L7[58], L8[59], L9[60], L10[61], L11[62], L12[63], L13[64], L14[65], L15[12], L16[66], L17[67], L18[68], L19[69], L20[70].

Chapter 2: <u>Applications of Metal Organic Frameworks</u>

<u>2.1 Gas separation</u>

Metal Organic Frameworks can be efficiently used for the selective separation of various gases. This can be accomplished through careful selection of organic linkers and SBUs that can result to either a porous framework with specific pore size distribution, or to a framework carrying functional groups that enhance its interaction with specific molecules. In the first case the material can act as a molecular sieve enabling the entrance of those molecules that have kinetic diameter less than the dimensions of the pore windows of the framework, while at the same time it excludes molecules that are of greater size (sieving and/or kinetic separation effect). In the second case, the pore walls are decorated with functional groups (polar, basic, acidic) that highly enhance the interaction of the framework only with certain molecules, that can be adsorbed in large amounts from the material while other molecules with lower or no affinity will not be adsorbed and thus remain in the gas phase.

One of the most significant industrial gas separations is the selective capture of CO_2 from post-combustion stationary and mobile sources, such as a flue gas stream. In this case a material that can selectively adsorb CO_2 from the rich N_2 stream of flue gases can be utilized. Additionally the selective capture of CO_2 is essential to other industrial applications. When cryogenic distillation or pressure swing adsorption is used for the separation of nitrogen and oxygen, air must be free of CO_2 because it can freeze and block the pipelines during the liquefaction process,[71] or it can be adsorbed to the adsorbents used for the oxygen production by pressure swing adsorption procedure, rendering them inactive.[72] Furthermore alkaline fuel cells require a supply of oxygen and hydrogen without CO_2 because even trace amounts of CO_2 can provoke the degradation of the electrolyte.[73] It is of paramount importance to remove CO_2 in confined spaces so that people would not suffocate from the excess amount of CO_2 that they exhale during breathing process and is accumulated around them. Thus in submarines, and space aviation MOFs can be efficiently used for the selective removal of trace amounts of CO_2.[74]

Of equal value is the removal of CO_2 in processes such as Natural Gas Purification or Landfill Gas Separation. In this case CO_2 must be separated from CH_4 stream to produce natural gas of high quality. When present, CO_2 reduces the energy content of natural gas and induces pipeline corrosion.[75]

Recently the Eddaoudi group synthesized a very important MOF that can selectively adsorb CO_2 in trace amounts and in very low pressure regions.[76] SIFSIX-3-Cu, is a MOF consisting of pyrazine/copper(II) two-dimensional periodic 4^4 square grids pillared by silicon hexafluoride anions. This results to a framework with 3.5 Å pore diameter that can selectively adsorb CO_2, in the presence of CH_4 and N_2. Its calculated IAST selectivity CO_2/N_2 is more than 25000, since it has narrower pores than the kinetic diameter of the aforementioned gas molecules, accompanied by strong polarizing sites that enhance significantly the interaction of the framework with CO_2. This stems from the fact that

CO_2 has a significant quadrapole moment and higher polarizability than CH_4 and N_2.[77,78] Its high selectivity can be envisaged by the highest uptake ever reported for MOFs without unsaturated metal centers or exposed amino functionalities at pressures of CO_2 below 38 torr (0.05 bar).
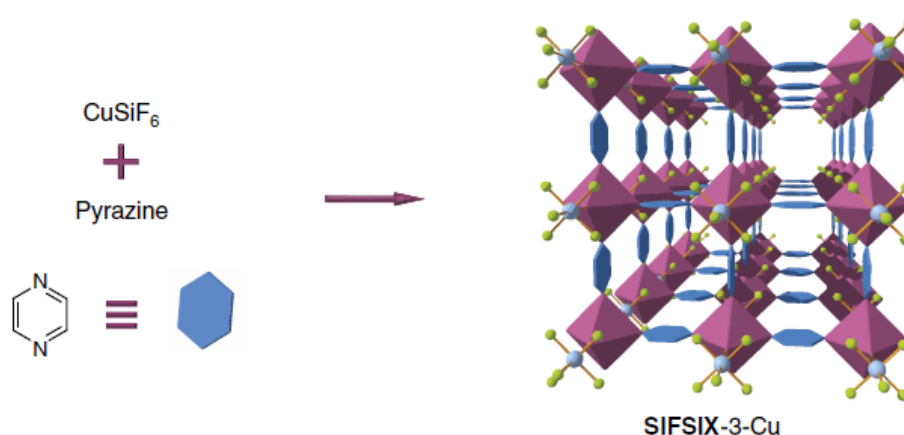

Figure 2.1. The structure of SIFSIX-3-Cu. Colour code: pyrazine (pyz, blue polygon), Cu (purple polyhedra), Si (light blue spheres), F (light green spheres). All guest molecules are omitted for clarity.[76]

Another important yet not widely known industrial process is the separation of noble gases Xe and Kr. Those gases are used in plenty applications including medicine and lighting.[79, 80] They are present in the atmosphere in trace amounts, (1.14 ppm Kr, 0.086 ppm Xe) rendering their extraction and separation extremely difficult. They are produced through cryogenic distillation, a high energy demanding and costly process. MOFs have attracted great attention in this industrial application too, since they can exhibit both high adsorption capacities for the two gas molecules, but most importantly they can separate them more efficiently than any other porous material, (zeolites and carbons).[81] To date the best MOF for the selective separation of Xe towards Kr is referenced to be MOF-74-Co. This material is synthesized from the reaction of $Co(NO_3)_2 \cdot 6H_2O$ with the organic linker dobdc, (2,5-dihydroxyterephthalic acid) forming a 3-D network with 1-D hexagonal channels of 11 Å in diameter. It exhibits a selectivity value Xe/Kr of 10.37.[82] Metal Organic Frameworks can also be used for the selective capture and separation of saturated, unsaturated, and aromatic hydrocarbons. All hydrocarbons are produced from petroleum and natural gas through various processes, including fractional distillation, cryogenic distillation, and catalytic cracking. Most of these processes are very costly and demand huge amounts of energy.[83] For instance, the compound MAMS-1, $Ni_8(5\text{-bbdc})_6(\mu_3\text{-}$ $OH)_4$, (bbdc^{2-} = 5-tert-butyl-1,3-benzenedicarboxylate) can also separate methane/ethane or ethane/ propane mixtures based on gate-opening phenomena. As the temperature increases the gates of MAMS-1 open linearly, giving rise to a unique molecular sieve with an adjustable mesh that can separate any two gas molecules with kinetic diameters in the range of 2.9 to 5.0 Å. Allowing in this

Table 2.1. Physical parameters of selected molecules, relevant to gas separation procedures.[84]

molecule	kinetic diameter (Å)	polarizability (10^{-25} cm^{-3})	dipole moment (10^{-19} esu^{-1} cm^{-1})	quadrapole moment (10^{-27} esu^{-1} cm^{-1})
H_2O	2.64	14.5	18.5	-
H_2	2.89	8.04	0	6.62
CO_2	3.30	29.1	0	43
Ar	3.54	16.41	0	0
Kr	3.60	24.8	0	0
N_2	3.64	17.4	0	15.2
CH_4	3.76	26	0	0
Xe	3.96	40.4	0	0

way the separation of methane and ethane from propane and butane, or the separation of methane from ethane, propane, and butane.[85] In other respects, Fe$_2$(dobdc) with soft, high-spin Fe^{2+} cation sites exposed on its surface, has an excellent performance for the separation of ethane/ethylene. This softer character, as compared to the Mg^{2+} MOF-74 analogue, results in an increased interaction of the metal center with the π electron cloud of the olefins. Enhancing in this way the selectivity for ethylene over ethane, which increases from 7 in Mg$_2$(dobdc) to 18 in Fe$_2$(dobdc). In breakthrough experiments, Fe$_2$(dobdc) is capable of separating an equimolar mixture of ethane and ethylene at 1 bar and 318 K into 99% and 99.5% pure components, respectively. Neutron powder diffraction experiments confirm that the unsaturated metal cation is the strongest adsorption site, and ethylene adsorbs via the side-on binding mode (Figure 2.2).[86]
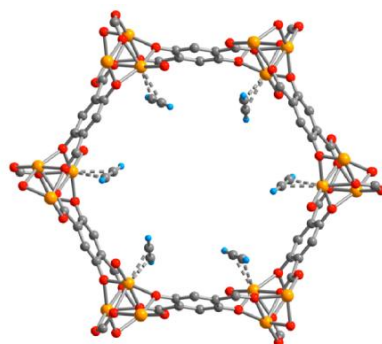
Figure 2.2. Structure of acetylene bound to the open Fe^{2+} sites in Fe$_2$(dobdc), where orange, red, gray, and blue spheres represent Fe, O, C, and D atoms, respectively.[86]

Moreover, industrial separation of the BTEX mixture (benzene, toluene, ethylbenzene, and the three xylene isomers) is highly important as each of the above compounds can be used for the production of numerous petrochemicals, but is also complex and highly energy demanding. A particular MOF has been found to behave impressively for the efficient separation of this complex mixture. MIL-53(Fe), is a material constructed from chains of trans-linked $[FeO_4(OH,F)]_6$ octahedral units, cross-linked by terephthalate ligands giving rise to a 3D net with one-dimensional channels.[87] In a variety of experiments, xylene isomers have been found to behave differently in the pores of the framework. The material has a substantially higher uptake of o-xylene isomer compared to the other isomers, although m-xylene exhibits the highest heat of adsorption. Crystal structures of MIL-53(Fe) loaded with xylenes show similar behavior between o- and m-xylenes, with π-π interactions between the xylenes and the organic linker, yet this interaction is not found in p-xylene. To simulate better the separation of C_8-alkylaromatics with the industrial one, Millange and coworkers, packed a liquid chromatography column with activated MIL-53(Fe). Once the column becomes more and more saturated with the gas mixture, the compound with the less interaction with the framework will elute first and the compound with the highest affinity for the framework will displace the less preferred compound out of the pores back into the effluent stream and elute last. The exact mechanism for the separation of the xylene isomers is not yet clear and it seems that is a combination of thermodynamic and kinetic factors. Nonetheless this method resulted to the efficient separation of the gas BTEX mixture (Figure 2.3).
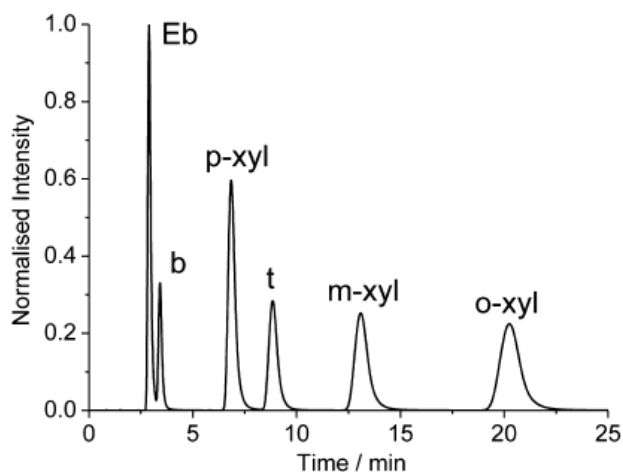
Figure 2.3. Chromatogram of the BTEX mixture passed through a column filled with activated MIL-53(Fe) at 323 K.[87]

2.2 Air Purification of Toxic Chemicals

In World War I man observed the first use of chemical weapons. Chlorine gas was used at Ypres, Belgium, rising from that time anxiety and fear for all those who could come in close proximity with this chemical. After World War II, G-type nerve agents were mass produced, and in the early 1950s V-type nerve agents were discovered in the United Kingdom. In particular, VX [O-ethyl S-(2-

(diisopropylamino)ethyl) methylphosphonothioate] was found to be one of the most lethal substances known and was produced by several nations in large quantities.[88] Apart from that, the extended use of chemicals in industry can result to an increased risk of an accidental release. One of the most world known and lethal chemical incident in recent history was the accidental release of methyl isocyanate, an extremely toxic compound used as an intermediate in pesticide production, from a chemical plant in Bhopal, India, in 1984, being responsible for almost 4000 deaths. Thus the efficient removal of harmful gas from air is of utmost importance. MOFs due to their versatile nature can find application in a wide variety of removal from harmful gasses from air.

The removal of sulfur mustard gas (HD), bis(2-chloroethyl) sulfide, as well as the HD simulant 2-chloroethyl ethyl sulfide (CEES) using the porous material HKUST-1, $Cu_3(C_9H_3O_6)_2$, was investigated by Roy et al.[89] The toxicant molecules get physisorbed in the pores of the MOF and then they undergo a hydrolysis reaction with the formation of an intermediate sulfonium ion. The rate constant and half-life for HD removal were found to be 0.020 min^{-1} and 34.65 min, respectively, while CEES was removed more quickly, with a rate constant and half-life of 0.043 min^{-1} and 16.11 min, respectively. HKUST-1 degraded more than 70% HD and 91% CEES in 40 min. The same group has also performed studies using again HKUST-1 for the degradation of sarin (GB) and its simulants with and without coadsorbed water. The toxic gas molecules are adsorbed to the material, and then a reaction with the chemisorbed water molecules takes place resulting in the formation of the hydrolysis products, the corresponding phosphoric acids. This reaction was found to be dependent on the nucleophilic substitution mechanism, vapor pressure and molecular diameter of the toxic molecules.[90]
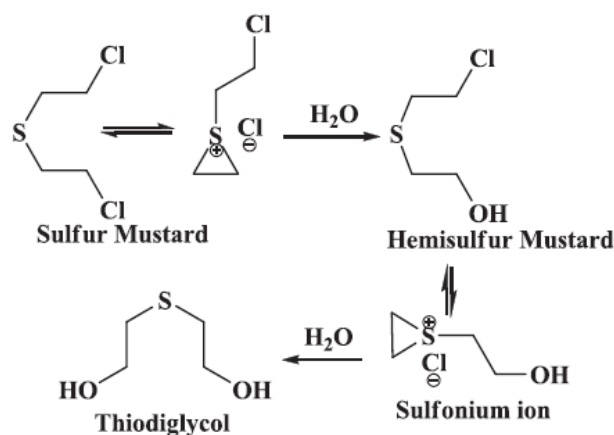
Figure 2.4. Degradation mechanism of HD in HKUST-1.[89]

Another deadly gas molecule is carbon monoxide (CO), a colorless and odorless gas. Carbon monoxide is produced from the burning of fossil fuels, iron smelting, as well as natural processes. It is estimated that approximately 5 billion metric tons of carbon monoxide are produced from photochemical reaction in the troposphere, while volcanoes and forest fires are other natural sources of carbon monoxide.[91] The Centers for Disease Control and Prevention estimates that approximately 500 persons die from non-fire-related carbon monoxide exposure annually.[92] That's because exposures at

100 ppm or greater can be dangerous to human health. Carbon monoxide can bind strongly and preferably to the heme of hemoglobin taking the place of oxygen, thus hindering the transfer of O_2 to the tissues through the blood stream, causing in this way hypoxia. The affinity of hemoglobin for carbon monoxide is 210 times greater than for oxygen, as a result of the stronger bond that it is created between the CO and the Fe^{2+} ion of the heme. CO can form apart from the σ bond that can create with the metal ion another π bond, due to π-back bonding phenomena. A pair of π bonds arises from overlap of filled d-orbitals on the metal with a pair of π-antibonding orbitals projecting from the carbon of the CO.[93] Whereas O_2 can form only a σ bond with the metal ion. Zou et al. synthesized a material, Cu(mipt), (mipt = 5-methylisophthalate), which consists of paddle-wheel Cu_2 clusters that are interconnected by bent mipt linkers to form a two-dimensional (2D) net. The framework is decorated with Lewis acid coordination sites on the interior walls that can be easily accessed from the incoming gas molecules. Activation of the MOF by heating in air at 250 ^{0}C, can give rise to a material that exhibits an impressive 100% catalytic conversion of CO to CO_2 at 200 ^{0}C, in the presence of O_2.[94]

2.3 Gas storage

The hybrid nature of MOFs has bestowed upon them exceptional properties. One of the major and most studied properties is the porosity of numerous MOFs. A porous material is a material containing a large number of voids, (cavities, channels, interstices) which are deeper than they are wide (otherwise these are considered as surface irregularities). IUPAC classifies three pore size regimes: microporous, with pore diameter smaller than 2 nm, mesoporous with pore diameter between 2 and 50 nm, and macroporous with pore diameter larger than 50 nm. The porosity of MOFs can be evaluated through calculation of the specific surface area and pore volume, with means that will be presented in Chapter 3.2.

To date MOFs exhibit the highest values in terms of pore volume and specific surface area in comparison to all other porous materials. NU-110 is a metal organic framework with chemical formula $[Cu_3(L^{6-}{}_{(109)}(H_2O)_3]_n$, synthesized by the solvothermal reaction of Cu^{2+} metal ions and a trigonal hexacarboxylate (H_6L) organic linker. The resulting framework nodes consist of Cu_2 units coordinated by the carboxylates of L^{6-} in a paddlewheel fashion, giving rise to a (3,24)-paddlewheel connected MOF with rht-topology.[95] This material exhibits world record values in terms of ultrahigh specific surface area, with 7140 m^2 g^{-1} (BET), and a record value of 4.4 cm^3 g^{-1} for pore volume.[12] These impressive attributes render MOFs unique candidates for gas storage applications.
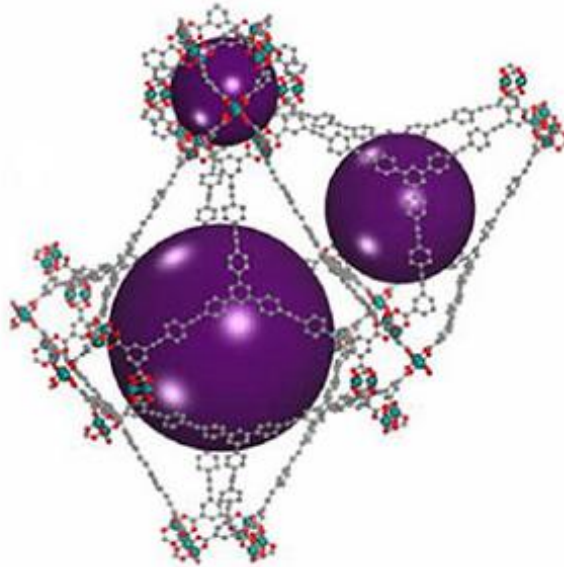
Figure 2.5. Single-crystal X-ray structure of NU-110 showing the different cages in NU-110. Carbon = gray; oxygen = red; copper = teal. Purple spheres represent the empty space.[12]

2.3.1 Hydrogen storage

The climate is changing, the average temperature of the planet is rising and one of the major responsible for that is the huge amounts of CO_2 that are emitted to the atmosphere. Those emissions come mostly from the burning of fossil fuels. Even if all the CO_2 emissions on the earth will stop now, there will still be an average increase of 1 ^0C of the temperature of the planet until the end of the century (Figure 2.6). [96] Thus, the use of environmental friendly fuels is of utmost importance. One of the best and most promising potential solutions to replace fossil fuels for the production of energy and for transportation is the use of hydrogen.
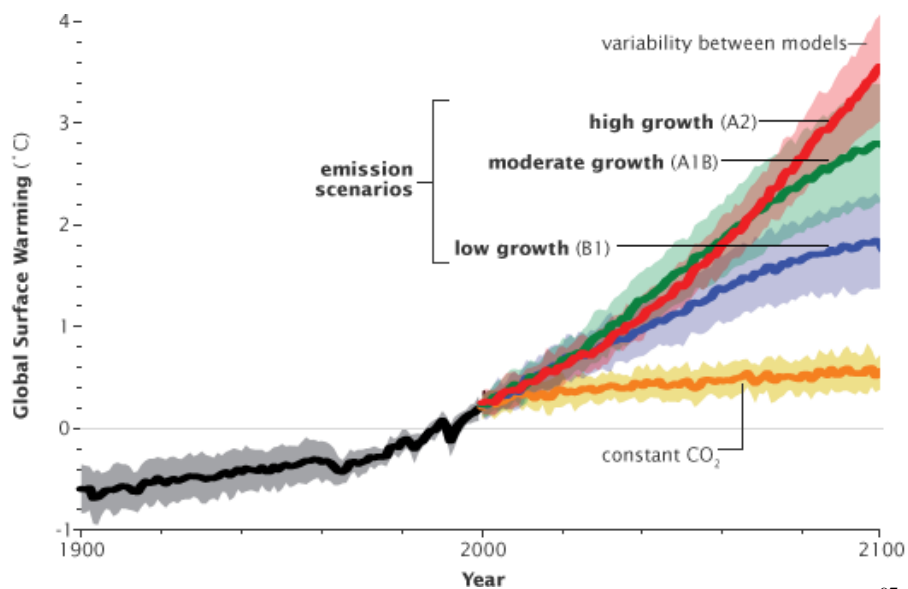
Figure 2.6. Projection of the global surface warming, best case and worst case scenario.[97]

28

Hydrogen is a clean and renewable energy resource and it poses an ideal energy carrier for a variety of fuel cell applications including stationary, mobile and portable power applications. It has a higher gravimetric energy density than gasoline, (123 MJ kg^{-1}) for hydrogen and (47.2 MJ kg kg^{-1}) for gasoline, and when it burns it produces only pure water as a product. Nonetheless the efficient use of H_2 as a power source, especially in automobile industry comes with significant limitations. Hydrogen is stored at the moment using two strategies, compressed gas using very high pressures, because it has a very low density (0.09 kg m^{-3}), and liquefied hydrogen, using cryogenic temperatures because it has a very low boiling point (20 K).[98] All these facts result in heavy and bulky storage tanks. Apart from that, there are also serious safety risks deriving from these storage conditions. The boil off losses due to the high volatility of the hydrogen molecule and the high energy density of liquid hydrogen poses a serious threat for public safety.[99] Therefore the need for an effective, safe and affordable hydrogen storage method using appropriate media is highly desirable.

There are many materials that have been tested and used for the improvement of hydrogen storage processes, such as metal hydrides,[100] complex hydrides,[101] chemical hydrides,[102] carbohydrates,[103] clathrates,[104] inorganic nanotubes,[105] and sorbents such as carbon materials,[106] and metal-organic frameworks (MOFs).[107] Those candidates can be divided into three categories based on the relative strength of the interaction of the storage media with hydrogen molecules, which in return determines the kinetics and the thermodynamics of the hydrogen uptake and release: "physisorption materials", "on-board reversible hydrides", and "off-board regenerable hydrides".[108] When it comes to hydrides the bond between the hydrogen and those materials is very strong, covalent bonding, resulting in chemisorption, with enthalpies of adsorption of more than 70 kJ mol^{-1}.[109] On the other hand the bond formed in the case of physisorption materials is weak and is attributed only to van der Waals interactions, with enthalpies of adsorption of about 3-9 kJ mol^{-1}.[110] Metal hydride materials offer the advantage that can store a large amount of hydrogen at ambient conditions, but they require a large amount of energy to release and capture the hydrogen molecules, hindering in this way the reversibility of the refueling process. On the other hand, materials such as MOFs, where hydrogen is physisorbed on the material, may have lower adsorption capacities under ambient conditions but they offer a fully reversible medium for hydrogen storage, that it needs no additional energy to capture and release hydrogen. Additionally MOFs exhibit very high specific surface areas, in this way they can store large amounts of hydrogen under very high pressures and low temperatures. The U.S. Department of Energy (DOE) has set up the targets for on-board H_2 storage systems, the 2017 H_2 storage targets are 5.5 wt % in gravimetric capacity, 40 g L^{-1} of volumetric capacity at an operating temperature of -40 to -60 ^{0}C under a maximum delivery pressure of 100 atm.[111] To date none of the aforementioned class of materials satisfies the DOE targets. Nonetheless MOFs have achieved great values in terms of hydrogen storage, cryogenic conditions (e.g. 77 K) and at high pressures.

PCN-12 is a porous 3D framework with chemical formula [Cu$_6$(C$_s$-mdip)$_2$(C$_{2v}$-mdip)-(H$_2$O)$_6$]·3DMA·6H$_2$O, synthesized by the reaction of the '*bent*' organic linker 5,5'-methylene-di-

isophthalate (mdip) and Cu^{2+} ions. A paddlewheel Cu_2 SBU is formed, occupying the 12 vertices of a cuboctahedron while 24 isophthalate moieties reside at the 24 edges. Each square face is connected to another square face of a neighboring cuboctahedron through four organic linkers and every cuboctahedron connects to six others in three orthogonal directions to form a 3D net. At the 12 corners of the cuboctahedron, there are 12 open copper-coordination sites pointing toward the center of the cage. PCN-12 exhibits a record-high hydrogen uptake, among MOFs, of 3.05 wt% at 77 K and 1 atm. [112] This high hydrogen uptake of the resulting material can be ascribed to the formation of 12 metal SBUs, each one containing 2 open metal sites, that can interact with the incoming adsorbed gas molecules, through partial charge–induced dipole interactions.[113] This high number of open metal, charge density sites along with the close orientation of those unsaturated metal sites resulted to a material exhibiting such a high hydrogen uptake at ambient conditions.

On the other hand, MOF-210 a material synthesized from the solvothermal reaction of Zn^{2+} ions and two organic linkers, biphenyl-4,4′-dicarboxylic acid and 4,4′,4″-(benzene-1,3,5-triyl-tris(ethyne-2,1-diyl))tribenzoic acid, exhibits an ultrahigh specific surface area of 6240 m^2 g^{-1} (BET), followed by a record total gravimetric H_2 capacity of 176 mg g^{-1}, 14.96 wt%, and a total volumetric capacity of 44 g L^{-1} at 77 K and 80 bar. Both these values surpass the DOE targets but at cryogenic temperatures. This impressive H_2 uptake is attributed to the ultra high specific surface area and very high pore volume of this material.[16]

2.3.2 Carbon dioxide storage

The numerous consequences from the extended use of fossil fuels followed by the huge amounts of CO_2 that are emitted to the atmosphere (more than 30 Gt per year)[114] have attracted the interest of the scientific community for many years. Some of the most prominent are the thickening of the ozone layer and the increase of the average temperature of the planet. Those two alone can adversely affect the quality and the future of our life. The combination of those two factors can force the melting of the gigantic glaciers and ice sheets of the poles, resulting to the increase of the sea level. All these are not mere imagination but feasible scenario that we will witness until the end of this century.[115] Yet the predictions are more and more alarming since there is projected an increase to the average CO_2 emissions from the use of fossil fuels, especially from the developing countries.[116] One solution could be the replacement of fossil fuels with other environmental friendly energy sources, such as sunlight, wind, tides and geothermal heat. But this scenario cannot be efficiently used since it would require a large amount of economic resources and most importantly, time. Another more practical, efficient and already implemented method to decrease the amount of CO_2 that is emitted to the atmosphere, is its selective capture from the emission sources. Current capture technologies involve the use of aqueous

amine solutions, but this method has the drawback of the high energy regeneration cost of the adsorptive medium.[117]

Global Mean Sea Level (GMSL) – 1880 to 2012
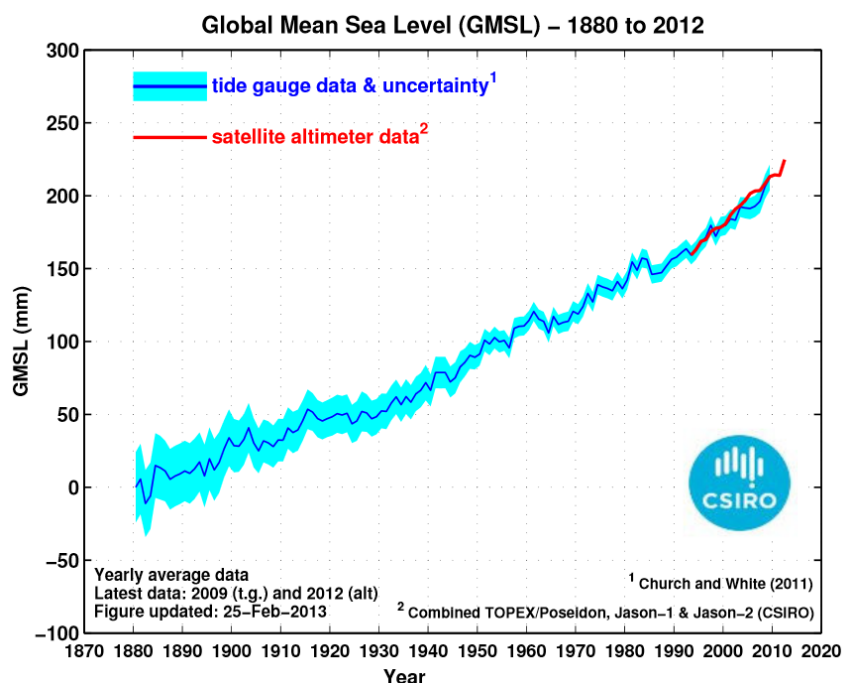
Figure 2.8. Estimation of changes in global averaged sea level, those since 1993 are estimated from satellite altimeter data (red) and those since 1880 by combining in situ sea level data from coastal tide gauges and the spatial patterns of variability determined from satellite altimeter data (blue).[118]

Metal organic frameworks can be again of great value for this significant application. With their tunable functionalization and porosity it is possible to synthesize materials that can adsorb, store and release easily large amounts of CO_2. Mg-MOF-74, is a material with chemical formula $Mg_2(dobdc)(H_2O)_2$, synthesized by the reaction of Mg^{2+} ions with the organic linker 2,5-dihydroxyterephthalic acid (dobdc). This reaction results to a 3D network with 1-D hexagonal channels and pores of 1.1 nm in diameter, decorated by a large number of open metal sites. This is the best MOF candidate to adsorb CO_2 at ambient conditions with an impressive uptake of 35.2 wt% CO_2 at 298 K and 1 bar.[119] It has been found that the relatively high ionic character of the Mg-O bond facilitates a greater degree of polarization and thus a higher adsorption capacity for CO_2 through partial charge-induce dipole interactions.[120] At high pressures, 50 bar and 298 K, again a familiar MOF from the previous section, MOF-210 has the highest total gravimetric CO_2 uptake of 74.2 wt%.[16]
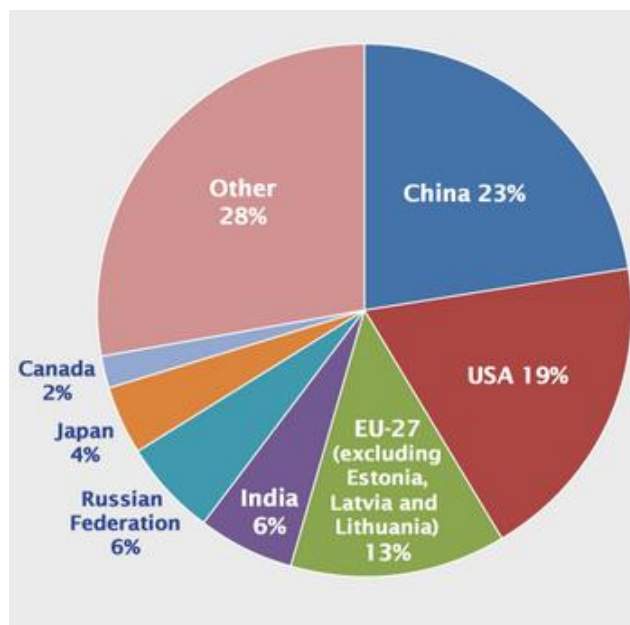
Figure 2.7. 2010 Global CO_2 Emissions from Fossil Fuel Combustion and some Industrial Processes (million metric tons of CO_2).[121]

2.3.3 Methane storage

Along with the ever increasing demand and consumption of fossil fuels around the world, for the production of energy and for mobile transportation, comes the ever increasing emission of CO_2 to the atmosphere contributing to numerous environmental problems and health issues.[122] Scientists around the world are striving to find viable solutions for the alleviation of those environmental phenomena. The use of cleaner energy carriers or renewable energy sources has attracted much interest and research as a potential solution. One of the most efficient alternative energy sources is natural gas. Natural gas, consisting of almost 95% CH_4, is a good candidate for replacing gasoline in mobile transportation and coal in stationary power plants, since it can cover the same energy demands with much less release of CO, CO_2, NO_x, SO_2, PMs (Particulate Matter) pollutants.[123] Furthermore natural gas is abundant since many countries of the world have huge natural gas reserves, (Figure 2.9). Additionally natural gas is in many countries much cheaper than gasoline and diesel. Unfortunately natural gas has a very low volumetric energy density at ambient temperatures and pressures in comparison to gasoline, 0.04 MJ L^{-1} compared to 32.4 MJ L^{-1}.[124] This means that larger amounts of natural gas must be used to produce the same energy output. To overcome this drawback an increase to the volumetric energy density of natural gas is needed. This can be achieved either by applying very high pressures (Compressed Natural Gas) or by applying cryogenic temperatures (Liquefied Natural Gas) to liquefy it. When it comes to stationary applications those two methods can be efficiently used. But when it comes to mobile transportation, then the use of natural gas as an alternative fuel is still
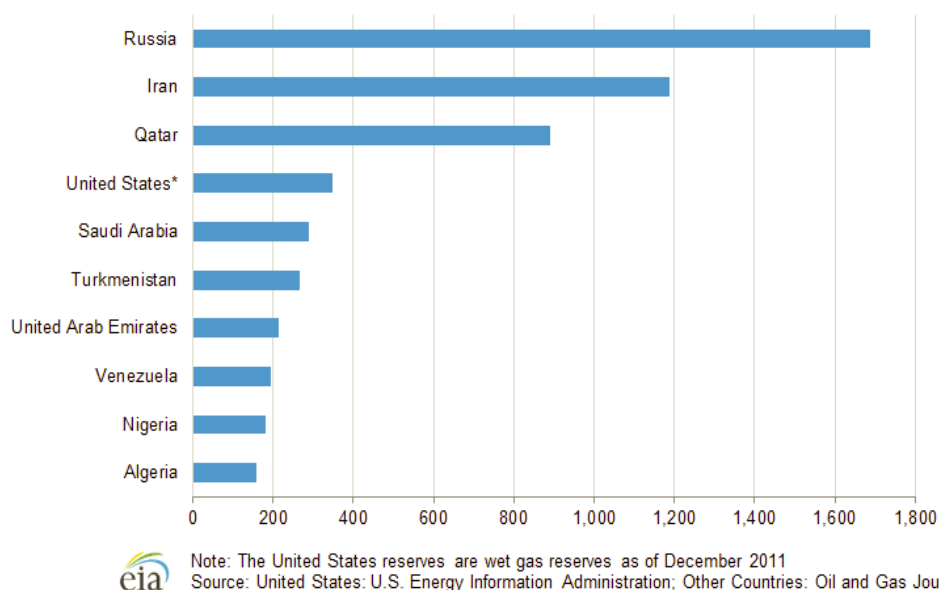
Figure 2.9. Largest proven natural gas reserves countries. Those values are in trillion of cubic feet.[125]

deficient, due to cost limitations in its storage and delivery. The solution can come from the use of a different storage media, a porous material that can adsorb natural gas, (Adsorbed Natural Gas). In this way the gravimetric and volumetric capacity of a storage tank is increased by the addition of an adsorbent that can adsorb and desorb natural gas, (methane) at ambient temperatures and moderate pressures. For this purpose the US Department of Energy (DOE) has set CH_4 storage targets for absorbents at 350 $cm^3_{(STP)}$ $cm^{-3}_{adsorbent}$ (v/v) and 0.5 g_{CH4} $g^{-1}_{adsorbent}$ (699 $cm^3_{(STP)}g^{-1}$), at 35 bar and 298 K.[126] If a 25% loss in volumetric capacity due to packing an adsorbent inside a fuel tank is taken into account, then the target of 350 cm^3 cm^{-3} comes to a value of 263 cm^3 cm^{-3}. Additionally there is another important parameter for the evaluation of a material towards methane storage for mobile applications, called working capacity (or deliverable capacity). It represents the actual usable amount of methane that is delivered to the engine, and it is the difference between the uptakes of the desorption operational pressure (5 bar) and the adsorption operational pressure.

Metal Organic Frameworks with their custom made porosity and functionalization, draw the attention towards these significant applications. Very recently, HKUST-1, a MOF with tbo topology,[127] formed by Cu_2 square paddlewheel units linked by H_3BTC linkers was reported to be the best MOF for methane storage in terms of total volumetric methane uptake, 267 cm^3 (STP) cm^{-3} at 298 K and 65 bar.[128] Since that time it was observed a sudden increase in the number of MOF materials tested for methane storage. To date the best MOF material for volumetric methane storage at 35 bar and 298 K, is a MOF, Ni-MOF-74, Ni_2(dhtp), with a total methane uptake of 230 cm^3 cm^{-3}.[129] The existence of a large number of open metal sites enhanced the affinity of the framework with the methane molecules through Coulomb interactions, resulting in such a high uptake.[130] HKUST-1 has the best total volumetric value at 65 bar, meeting the DOE target if the packing loss is ignored at 65 bar. This stems from the fact that this material has apart from the open copper sites additional strong

methane binding sites.[131] This factor along with the higher surface area in comparison to Ni-MOF-74 results to a higher methane uptake at 65 bar. Recently MOF-519, $Al_8(OH)_8(BTB)_4(H_2BTB)_4$, synthesized by the reaction of Al^{3+} ions and the 4,4,4-benzene-1,3,5-tryil-tribenzoic acid organic linker, exhibits 279 cm^3 cm^{-3} total methane uptake at 80 bar and 298 K, and a volumetric working capacity between 5 bar and 65 bar of 230 cm^3 cm^{-3}, these are the best values to date for porous materials in terms of volumetric total methane uptake and working capacity. This material has higher surface area and higher crystal density than HKUST-1, but since that it does not have open aluminum sites, this record high methane uptake is attributed to the fact that the average pore diameter of MOF-519 is of optimal size to confine methane molecules in the pores, maximizing the interaction of methane molecules with the framework, and with each other through van der Waals interactions.[132] Nonetheless, the DOE targets are yet to be satisfied from any porous material.

2.4 Energy conversion

The population of the planet is increasing dramatically and along with it the demand for more energy.[133] The current energy production technologies are based on the use of fossil fuels and to a much lower extend to the use of renewable energy sources, (solar, wind, tides). The use of fossil fuels has impaired significantly the quality of our life as we are witnessing adverse environmental problems and various health issues.[134] Combined with the fact that the natural reserves of fossil fuels are diminishing,[135] new and cleaner energy sources must be therefore utilized and developed in due time to cover the global energy demands. One potential solution is the conversion of chemical energy to electricity. For instance, molecular hydrogen or even methanol and ethanol can be used in fuel cell devices for the production of electricity.[136] Fuel cells are defined as electrochemical conversion devices which can generate electric current, and are composed of three parts. A fuel component such as hydrogen, natural gas, methanol etc., an oxidant such as oxygen, air or hydrogen peroxide, and an electrolyte that allows charges to move between the two sides of the fuel cells.[137] The efficiency of the fuel cell depends mostly on the nature of the electrolyte. An electrolyte with high proton conductivity, that is low resistance, where the protons can move fast and easily across the electrolyte, is of supreme value. Equally important is the chemical and thermal resistance of this media. One of the most studied and exploited proton-conducting materials in PEMFCs is Nafion, a polymer which is composed of perfluorovinyl ether groups terminated with sulfonate groups onto a tetrafluoroethylene backbone. This material has a very good value of proton conductivity (σ) of 10^{-2} S cm^{-1} but it works efficiently only in the presence of water and at temperatures lower than 80 ^{0}C.[138] Therefore in order to acquire these values of proton conduction and even higher, in anhydrous conditions and at elevated temperatures, over 100 ^{0}C, where many industrial applications take place, the use of a different material is needed.[139] Metal organic Frameworks with their tailor made architecture offer a unique

platform to design materials that can exhibit very high values of anhydrous proton conductivities at elevated temperatures. MIL-101 is a mesoporous 3-D MOF synthesized from the hydrothermal reaction of terephthalic acid (H_2BDC) with $Cr(NO_3)_3 \cdot 9H_2O$, HF, and H_2O. Its structure consists of Cr_3O trimers that are linked with the organic linkers, to form supertetrahedra, that are linked together through the vertexes, resulting in an augmented zeolitic structure (MTN type). Treatment of this MOF with strong acids H_2SO_4 and H_3PO_4 followed by drying at elevated temperatures, gave rise to the following solid products $H_2SO_4@MIL$-101 and $H_3PO_4@MIL$-101. These materials, achieved σ values of 1×10^{-2} S cm^{-1} and $\sigma = 3 \times 10^{-3}$ S cm^{-1} respectively, at 150 °C and 0.13% RH. The trace amount of water molecules were the proton carriers. These values can be compared with that of Nafion, are the highest reported for MOFs and among the best for proton-conducting materials.[140] For comparison purposes, another MOF must be mentioned. An oxalate-based MOF, $\{[(Me_2NH_2)_3$-$(SO_4)]_2[Zn_2(ox)_3]\}n$, is composed of a 3-D anionic framework, $[Zn_2(ox)_3]^{2-}$, built from zinc cations bridged by oxalate units. In the pores of the framework reside dimethyl ammonium (DMA) cations and sulphate anions which are bound to each other by electrostatic interactions. Under humid conditions (98% RH), this material exhibits conductivity values of 4.2×10^{-2} S cm^{-1} at 25 °C, which is the highest value reported to date for a MOF. In this case again the proton carriers are water molecules.[141]
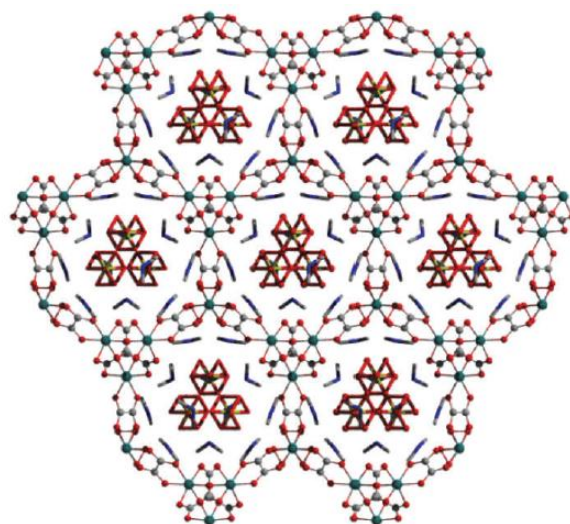
Figure 2.10. Crystal structure of $\{[(Me_2NH_2)_3$-$(SO_4)]_2[Zn_2(ox)_3]\}n$ with DMA cations and disordered sulphate anions in the pores of the framework. Colour code: Zn green, O red, N blue, C gray, S yellow.[139]

2.5 Asymmetric Catalysis

Catalytic processes are of utmost importance in many industrial applications. Since it is possible to synthesize novel chemical compounds, in minimum reaction time and of high quality and yield.[142] Zeolites, which are porous aluminum silicate materials, have been used extensively in numerous catalytic processes. The importance of their industrial utilization is evident from the annual production of Zeolites, which comes to a few million tonnes per year.[143] But zeolites, cannot be used in specific catalytic procedures, such as asymmetric catalysis, for the production of enantiopure compounds.[144] Metal Organic Frameworks, due to their hybrid nature can be efficiently used in the field of asymmetric catalysis. On the one hand it is possible to design and synthesize a chiral catalyst (MOF) with the exact pore aperture to accommodate the reacting species, and on the other hand it is possible to incorporate the desired functional groups to serve as catalytic center. Wu and coworkers, synthesized a homochiral MOF for a highly enantioselective heterogeneous asymmetric catalytic reaction. Reaction of Cd^{2+} ions with the chiral bridging ligand (*R*)-6,6'-dichloro-2,2'-dihydroxy- 1,1'-binaphthyl-4,4'-bipyridine, BINOL (L), gave rise to a 3-D framework, with chemical formula $[Cd_3Cl_6L_3]\cdot4DMF\cdot6MeOH\cdot3H_2O$. This MOF was post synthetic modified with $Ti(O^iPr)_4$. Ti-$(O^iPr)_4$ can react with the chiral dihydroxy groups in BINOL or its analogues to afford Lewis acidic (BINOLate)$Ti(O^iPr)_2$ compounds which are active catalysts for the addition of $ZnEt_2$ to aromatic aldehydes to afford chiral secondary alcohols.[145] Therefore the resulting material could efficiently catalyze asymmetric diethylzinc addition to aromatic aldehydes with complete conversion (99%) and enantiomeric excess (ee) up to 94%.[146]
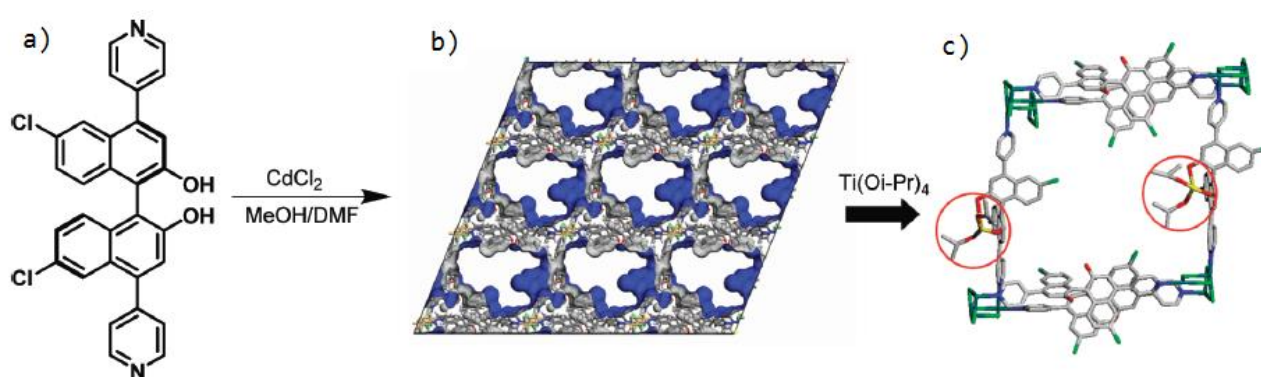
Figure 2.11. a) the organic linker BINOL, b) Connolly surface of the resulting MOF showing the large 1D chiral channels, and c) schematic representation of the active (BINOL)$Ti(O^iPr)_2$ catalytic sites (marked by a red circle) in the open channels of the framework.[147]

2.6 Drug delivery

  Pharmaceutical industries spend hundreds of millions of dollars annually for the development of new drugs.[148] Apparently the synthesis of a therapeutic agent that has the desired high selectivity for a specific damaged cell tissue (cancer therapy) is of utmost importance. But the efficient delivery of that drug to the desired target is of equal significance. For that purpose a variety of methods is used. One of them is the use of carriers, which are molecules that exhibit specific properties. Drug carriers must be non-toxic and biocompatible,[149] able to stabilize the drug through encapsulation or surface attachment,[150] target a specific cell population,[151] and be able to control the release of the drug molecules.[152] Most of the existing carrier materials (liposomes, inorganic zeolites, ordered porous silica)[153,154,155] show either very low drug loading (usually less than 5 wt% of the transported drug versus the carrier material), or exhibit rapid release of the drug molecule, and poor biocompatibility.[156] Metal organic frameworks can play an important role as drug nanocarriers, offering significant advantages. It is possible in this case to design the exact components of the drug carrier, and the desired porosity. Therefore Horcajada et al. synthesized biocompatible MOFs for drug delivery of anticancer and retroviral drugs.[34] MIL-88A and MIL-100 (MIL = Materials of Institut Lavoisier) are two 3-D MOFs synthesized from Fe^{3+} ions and the organic linkers fumaric acid and trimesic acid. In the case of MIL-88A, the degradation products, iron and fumaric acid, are endogenous. This means that those two components are naturally found in the human body. Iron is an element that is part of many proteins and enzymes,[157] while fumarate is an intermediate of the citric acid cycle, a metabolic pathway, during which energy in the form of adenosine triphosphate (ATP) is generated from the catabolism of carbohydrates, fats and proteins.[158] Additionally they exhibit low toxicity values, $LD_{50}(Fe) = 30$ g kg^{-1}, LD_{50}(fumaric acid) $= 10.7$ g kg^{-1}, (LD_{50}, oral lethal dose, is the dose required to kill half the members of a tested population after a specified test duration). Furthermore the organic linker trimesic acid exhibits low toxicity as well, LD_{50}(trimesic acid) $= 8.4$ g kg^{-1}.[159] The next step was the incorporation of the desired drug to the MOF. In this case the amphiphilic antitumoural drug busulfan (Bu) was chosen. On the one hand, this is a small molecule, and can fit easily to a microporous material, such as MIL-88A, while on the other it is a very important drug molecule, widely used in combination with high-dose chemotherapy treatments, for leukemia, especially in pediatrics, because it represents a good alternative to total-body irradiation.[160] But this molecule possesses a poor stability in aqueous solution and an important hepatic toxicity because of its microcrystallization in the hepatic microvenous system.[161] Therefore the use of a suitable drug carrier to transport and protect the drug until it reaches the target cells is of unique importance. For MIL-100 an enormous Bu loading was observed, 25 wt%, which is 5 times higher than the best drug delivery nanocarrier for Bu.[162] and 8 wt% for MIL-88A, lower than MIL-100 but yet higher than the other Bu drug delivery candidates. The advantages of this method are many. First the drug is protected from decomposition from body fluids, secondly it is possible to deliver large amounts of the desired drug

with minimum amount of drug nanocarierrs, and last but not least the drug doses are diminished. Therefore the time of the treatment of the patient is reduced.
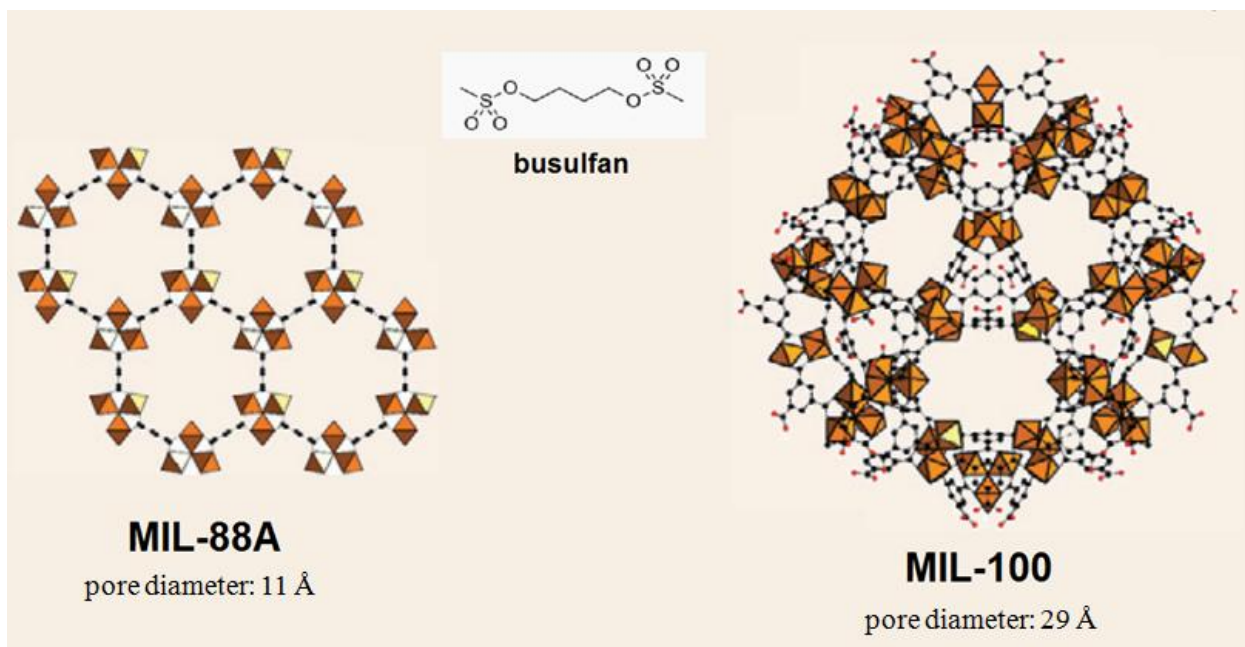
Figure 2.12. The structures of MIL-88A, MIL-100 and the drug molecule busulfan. Metal octahedra, oxygen and carbon atoms are in orange, red, and black, respectively.[34]

Chapter 3: <u>Characterization of Metal Organic Frameworks</u>

All MOFs were extensively characterized with the following modern techniques and methods:
i) powder and single crystal X-ray diffractometry ii) gas sorption measurements for porosity determination (surface area, pore volume and pore size distribution) and gas uptake of MOFs, iii) NMR (Nuclear Magnetic Resonance) spectroscopy was used to monitor the removal of residual solvents before MOF activation and to give insight to the exact composition of mixed linker MOFs, iv) Thermogravimetric analysis (TGA) analysis was used for the evaluation of the thermal stability of MOFs, v) Energy dispersive X-ray spectroscopy (EDS) was used for elemental analysis and vi) Scanning electron microscopy (SEM) was used to gain information about the particle morphology of the materials.

Given the particular importance of the X-ray diffraction techniques as well as the gas sorption measurements, more details are provided below.

3.1 X-ray diffraction

3.1.1 Introduction

One major characteristic of MOFs is their high crystallinity. Actually in many cases it is possible to synthesize large single crystals. The advantage of this fact is that a crystalline material is easier to be characterized, as one can gather information about its exact composition, and crystal structure. A most important characterization technique of crystalline solids is X-ray diffraction. By using powder X-ray diffraction it is possible to evaluate the crystallinity of a material, its uniform phase, and record a unique diffraction pattern that is the fingerprint of any crystalline solid. By using single crystal X-ray diffraction it is possible to find the exact crystal structure of a crystalline material, that is the arrangement of atoms in space and their distances.

3.1.2 Crystals and diffraction of X-rays

When a beam of light hits a slit with diameter close to the wavelength of the beam, then the slit act as secondary light source re-radiating light in all directions. This phenomenon is called diffraction. When there are several slits close enough, then the diffracted beams from each point source interact with other. When the adjacent beams are in phase, constructive interference occurs and the beams have maximum light intensity. When the beams are not in phase constructive interference occurs and the beams disappear.[163]

X-rays are electromagnetic radiation of wavelength ~1 Å, that is a value close to the inter-atomic distance. They are produced when high energy charged particles collide with matter. In this case a beam of electrons produced by the heating of a filament, is accelerated through high voltage, to a

metal target (anode). The most common element used as an anode in powder X-ray diffraction experiments is Copper and the most common used in the case of single crystal X-ray diffraction is Molybdenum. The electrons that strike the anode ionize some of the metal's inner shell electrons. Then an electron from the outer shell jumps to cover the position of the ionized electron, emitting characteristic X-rays.[164]

A crystal is a highly ordered structure that can be envisaged by the repetition of a small unit, called unit cell, that has all the structural and symmetry information to build-up the macroscopic structure. Translation of the unit cell to the three directions gives rise to a periodic framework.

Therefore when X-rays interact with a crystal, the atoms of the crystal, whose distance is comparable to the wavelength of the X-ray beam, can act as secondary point sources and diffract the X-rays. The diffraction of a crystal is described by the Bragg Law. According to Braggs' approach a crystalline solid is built up in layers or planes. Each of these planes is constructed by connecting at least three different lattice points together and, because of the periodicity of the lattice, there will be a family (series) of parallel planes passing through every lattice point. The orientation of any of these families of planes is described with a Miller Index of the form (hkl). Those values are determined from the intersection points of the planes with a unit cell of a/h, b/k and c/l. Thus the Miller indices are the reciprocal of these intercepts.

The incoming waves are scattered from the lattice planes separated by the interplanar distance d. When the scattered waves are in phase, then they interfere constructively, when they are out of phase they interfere destructively. The path difference between two waves undergoing interference is equal by a value of $2d\sin\theta$, where θ is the scattering angle.
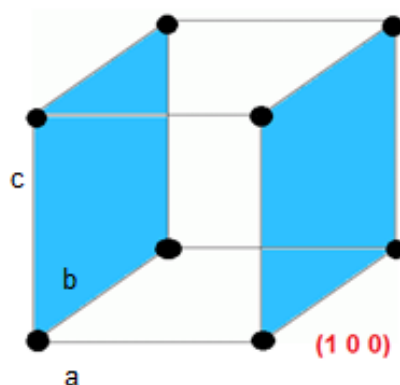
Figure 3.1. The (100) lattice planes of a cubic unit cell.
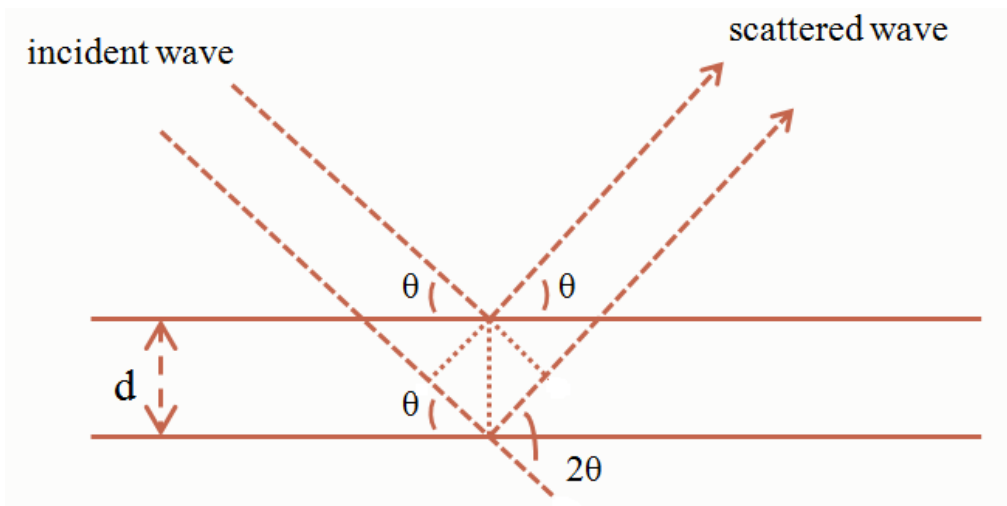
Figure 3.2. Geometrical illustration of the Braggs' law. The lower beam travels an extra length of $2d\sin\theta$. Constructive interference occurs when this length is equal to an integer multiple of the wavelength of the radiation.

This condition leads to Braggs' law, $2d\sin\theta = n\lambda$, where n is a positive integer expressing the order of the diffracted beam, and λ is the wavelength of the incident wave. When this condition is satisfied constructive interference occurs and diffraction is observed. A diffraction pattern is obtained by measuring the intensity of scattered waves as a function of scattering angle.[165] The actual result of the diffraction is the formation of a regular array of diffraction spots. Those spots constitute the reciprocal lattice and each spot represents a diffracted beam from a set of crystal planes (hkl). The reciprocal lattice is constructed to help us explain the phenomenon of diffraction.

In a real lattice the interplanar distance d can be connected with the unit cell parameters in a manner as we see in Figure 3.3. There is a shaded plane (hkl) in a Cartesian coordinate system that
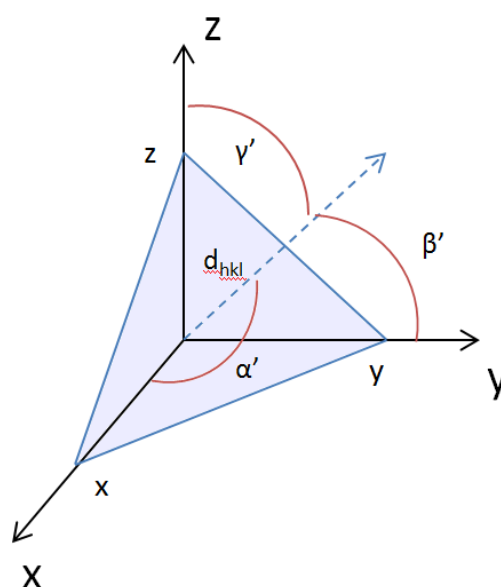
Figure 3.3. Relationship of lattice plane spacings and the unit cell parameters, a, b, c and α, β, γ.

41

intercepts the three axes at x, y, and z. The blue arrow indicates the normal direction of the plane. The angles between the x, y, and z axes to the normal are α', β', and γ', respectively. The d_{hkl} is the perpendicular distance from the origin along the normal direction to the plane. It is clear that

$$d_{hkl} = x \cos α' = y \cos β' = z \cos γ' \qquad (3.1)$$

If we use the direction cosines type:

$$\cos^2 α' + \cos^2 β' + \cos^2 γ' = 1 \qquad (3.2)$$

then :

$$d_{hkl} = \frac{1}{\sqrt{\frac{1}{x^2} + \frac{1}{y^2} + \frac{1}{z^2}}} \qquad (3.3)$$

Formation of the reciprocal lattice: If there is a real space unit cell with real lattice basis vectors a,b and c, then the reciprocal lattice vectors are defined as follows:

$$a^* = \frac{b \ x \ c}{V} \qquad (3.4)$$

$$b^* = \frac{a \ x \ c}{V} \qquad (3.5)$$

$$c^* = \frac{b \ x \ a}{V} \qquad (3.6)$$

V = a (b x c), the volume of the unit cell. The reciprocal interplanar distance can be expressed

$$d_{hkl}^* = ha^* + kb^* + lc^* \qquad (3.7)$$

$$a^* x \ a = 1, \quad b^* x \ b = 1, \quad c^* x \ c = 1 \qquad (3.8)$$

The reciprocal d spacing is related with the real d spacing :

$$d^* = \frac{k}{d} \qquad k, constant \qquad (3.9)$$

Imagine a direct monoclinic unit cell with its two real unit cell axes a and c, Figure 3.4. The reciprocal lattice aces a* and c* lie perpendicular to the end faces of the direct cell. Then the

reciprocal lattice points are spaced $a^* = 1/d_{100}$ and $c^* = 1/d_{001}$ on the reciprocal aces. If we extend the lattice to the three directions we have the reciprocal lattice points.[166]

1)

2)

3)

4)
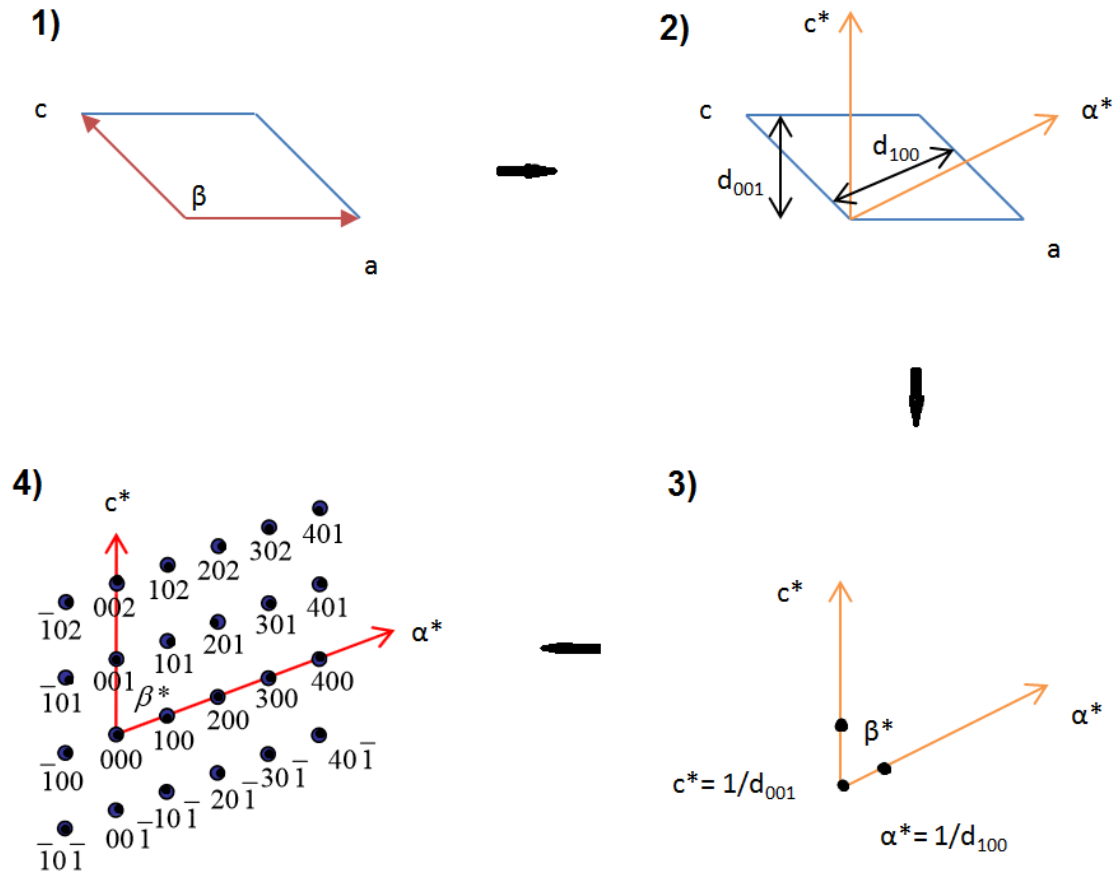
Figure 3.4. Construction of a reciprocal lattice. Black dots represent the reciprocal lattice points.
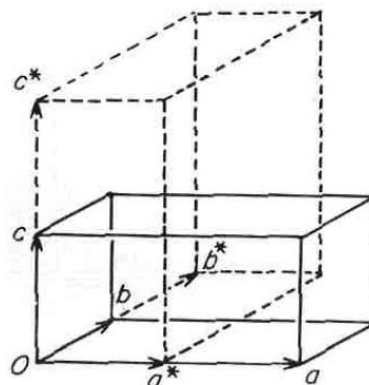
Figure 3.5. Relationship of a real unit cell a, b, c and its reciprocal unit cell a*, b*, c*.

3.2 Gas adsorption studies

One of the most important characteristic of MOFs is their porous nature. This inherent property can be evaluated and quantified by means of gas adsorption studies. In this way it is possible to measure the gas uptake of a porous material for a specific gas molecule, and/or calculate a series of physical parameters such as the specific surface area, the pore volume and the pore size distribution. These measurements can be carried out at various temperatures and pressures, and by different apparatuses. The most commonly used are the volumetric and gravimetric techniques.

The volumetric technique is based on an introduction of a known mass (m_s) of an adsorbent into a sample cell of calibrated volume (V_t), followed by evacuation of the sample at elevated temperatures under high vacuum. Consequently the sample is set to the desired temperature and a measured dose of gas (n) is introduced to the sample cell. Adsorption of the gas by the sample occurs and the pressure in the confined volume falls until the adsorbate and the remaining gas in the sample container are in equilibrium. After equilibrium, the temperature (T) and pressure (P) are measured and the specific excess amount adsorbed (n_e) is defined by a mass balance:

$$n_e = \frac{n_t - V_d \, \rho_g}{m_s} \qquad\qquad 3.10$$

where V_d is the helium dead space of the sample cell, ρ_g (T,P) is the density of the bulk gas (mol/m^3) obtained from an equation of state and $n_t = \sum_j(\Delta n_j)$ is the total amount of gas in the sample cell. At sufficiently low pressure, the density of the bulk gas phase is given by the perfect gas law (ρ_g=P/RT). The helium dead space (V_d) is obtained from a calibration with helium gas at ambient temperature (T) and pressure (P) before starting the experiment.

The gravimetric technique is based on the introduction of a mass (m_s) of solid adsorbent into a bucket attached to a microbalance. The sample is evacuated at elevated temperatures usually under high vacuum or inert gas flow, then the experimental sample temperature is fixed and gas is admitted to the sample cell. After adsorption is complete, at equilibrium, the temperature (T) and pressure (P) are measured and the adsorption is determined from the weight of the bucket containing the solid and adsorbed gas. The Gibbs excess amount adsorbed is:

$$n_e = \frac{\Delta m}{M m_s} + \rho_g \, u_{sk} \qquad\qquad 3.11$$

Where M is the molecular weight of the gas. The second term ($\rho_g \, u_{sk}$) is a buoyancy correction. Depending on the gas density, a certain amount of force due to the gas pressure acts upward on the

object. Since the solid is weighed while immersed in a gas, a buoyancy correction equal to the weight of bulk gas displaced is added to the weight registered by the microbalance.[167]

By using either technique, an adsorption isotherm can be recorded. Adsorption isotherms are classified by IUPAC in six types (see figure 3.6).[168] The horizontal axis is the relative pressure (P/P$_0$) which is the equilibrium pressure divided by the saturation pressure. The vertical axis represents the adsorption amount, and is commonly expressed as V/cm^3(STP)g^{-1}. The shape of sorption isotherms is determined by a combination of gas-solid and gas-gas interactions. The reversible Type I isotherm is characteristic of microporous materials in which the rapid rise at low pressures corresponds to monolayer adsorption, followed by a plateau because of the filling of the micropores. The reversible Type II and III isotherms are typical for non-porous or macroporous adsorbents. At point B the monolayer coverage is complete and multilayer adsorption begins. Type IV isotherms are characteristic of mesoporous materials. In this case a capillary condensation and a hysteresis loop are observed. Type V is an uncommon isotherm related to the Type III isotherm where the adsorbent-adsorbate interaction is weak. Type VI isotherm is typical of stepwise multilayer adsorption on a uniform nonporous surface.
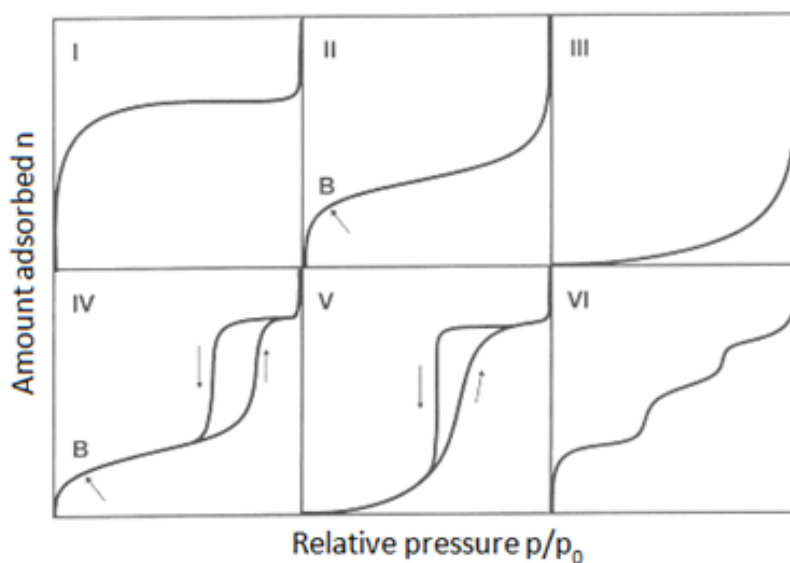
Figure 3.6. The six types of adsorption isotherms as classified by IUPAC.

Usually, for the determination of the specific surface area two methods are used. The Langmuir and the BET (Brunauer, Emmett and Teller) method. The Langmuir equation is mostly applied for microporous materials, having a type I isotherm and has the following form:

$$\frac{P}{W} = \frac{1}{KW_m} + \frac{P}{W_m} \qquad\qquad 3.12$$

where P is the adsorbate equilibrium pressure, and W and W_m are the adsorbed weight and monolayer weights respectively. A plot of P/W versus P should give a straight line with a slope of value of $1/W_m$. The calculated surface area can be derived from the equation:

$$S_t = N_m A_x = \frac{W_m N A_x}{M} \qquad 3.13$$

where, A_x is the cross-sectional are of the adsorbate, M is the adsorbate molecular weight and N is the Avogadro's number.

The BET has the following form:

$$\frac{1}{W[\frac{P_0}{P} - 1]} = \frac{1}{CW_m} + \frac{C-1}{CW_m} \left(\frac{P}{P_0}\right) \qquad 3.14$$

P is the partial vapour pressure of adsorbate gas in equilibrium with the surface, P_0 is the saturated pressure of adsorbate gas, and C is a dimensionless constant that is related to the enthalpy of adsorption of the adsorbate gas on the powder sample. A plot of $1/W[P_0/P]$ versus P/P_0 will yield a straight line usually in the range $0.05 \leq P/P_0 \leq 0.35$. The slope s and the intercept i of a BET plot are:

$$s = \frac{C-1}{W_m C} \qquad 3.15$$

$$i = \frac{1}{W_m C} \qquad 3.16$$

Therefore the weight adsorbed in the monolayer W_m is:

$$W_m = \frac{1}{s+i} \qquad 3.17$$

And the resulting equation for C constant is:

$$C = \frac{s}{i} + 1 \qquad 3.18$$

The surface area then can be calculated from the following equation:

$$S_t = \frac{W_m N A_x}{M} \qquad 3.19$$

where, A_x is the cross-sectional area of the adsorbate, M is the adsorbate molecular weight and N is the Avogadro's number.[169]

There are many different methods and theories in terms of deducing pore size distributions. They are divided to two categories. One the one hand there are the classical approaches, which are based on

macroscopic thermodynamic assumptions, such as the Polanyi,[170] Dubinin,[171] and Horvarth-Kawazoe[172] methods. The disadvantage of these methods lies on the diminished accuracy of such thermodynamic, macroscopic approaches, because of the assumption that the fluid that resides into the pores has similar thermophysical properties as the bulk fluid. On the other hand there are the microscopic approaches which are based on statistical mechanics in order to describe the sorption and phase behavior of fluids inside a porous material. Those methods include the Density Functional Theory,[173] Monte Carlo simulation and Molecular Dynamics method.[174] The advantage of those techniques lies on the fact that they are able to correlate and elucidate better the interactions of the gas molecules with the porous media.

Therefore for the determination of the pore size distribution of a porous material, from an adsorption isotherm with the Non Local Density Functional Theory (NLDFT), a set of isotherms are calculated, for a set of pore sizes, in a given pressure range. Adsorption isotherms in model pores are determined based on the intermolecular potentials of the fluid-fluid and solid-fluid interactions. Those isotherms constitute the kernel, which will be correlated with the experimental ones. The calculation of the pore size distribution derives as a solution from the Generalized Adsorption Isotherm (GAI):

$$\text{N}\left(\frac{\text{P}}{\text{P}_0}\right) = \int_{W_{min}}^{W_{max}} N(\frac{P}{P_0}, W) f(W) dW \qquad 3.20$$

Where $N(P/P_0)$ = experimental adsorption isotherm data, W = pore width, $N(P/P_0,W)$ = kernel of theoretical isotherms in pores of different widths, and f(W) = pore size distribution function.[175]

Another important piece of information that can be derived from an adsorption isotherm is the total pore volume of the porous material. Total pore volume can be quantified from the amount of vapor adsorbed at a relative temperature close to unity, assuming that pores are filled with liquid adsorbate. The liquid molar volume adsorbed at this relative pressure (P/P_0) (either measured or interpolated) is calculated by converting the adsorbed gas volume to liquid molar volume using the density of the adsorbate at the recording temperature:

$$\text{V}_\text{p} = \frac{W_0}{\rho_{liq}} \qquad 3.21$$

where W_0 is the saturated adsorption amount obtained from either BET or Langmuir plots, ρ_{liquid} is the density of pure liquid absorbates.[176]

Chapter 4: <u>Scope and objectives of this thesis</u>

Undoubtedly MOFs pose a unique platform for the development of novel materials that can be efficiently used for numerous applications both in industry and in our everyday life. Their versatile hybrid nature, the simple synthetic procedures, the efficient characterization techniques, and their plentiful physicochemical properties that accompany them, render those crystalline solids an exciting and unrivaled accomplishment in the field of materials science.

As it was clear from Chapter 2, MOFs can have impressive properties and can be therefore utilized in a wide range of applications. Actually they have a strong potential to replace efficiently the materials that are currently used in some of these processes. However, in other applications, such as gas storage, their properties although impressive enough are yet far from the target values that have been set by the US Department of Energy. Particularly in terms of hydrogen and methane storage for on-board applications, and in terms of carbon dioxide storage, for post or pre combustion capture.

Therefore the synthesis of novel porous materials with improved gas sorption properties, towards each of these (H_2, CH_4, CO_2) target gas molecules, is of utmost importance. Through years of research it has been found that the gas uptake of a MOF can be enhanced in various ways.

A material with ultra high surface area can have a very high hydrogen uptake under high pressures and low temperatures. These values can be further increased by the existence of open (unsaturated) metal sites and the incorporation of metal ions or metal nanoparticles into the pores of the framework.[177] Similarly under high pressures and low temperatures, a very high surface area will result in a high CO_2 uptake. But at ambient temperatures and pressures a porous material must have specific structural characteristics that can enhance significantly the interaction of the framework with CO_2 molecules. This can be accomplished either by the existence of open metal sites inside the pores of the framework or by the incorporation of strong polarizing functional groups, such as amines ($-CH_2-NH_2$), ($-NH_2$), hydroxyl ($-OH$), sulfonic ($-SO_3H$), sulfone ($-SO_2$) and carboxy ($-COOH$) groups.[178] Concerning the enhancement of the methane uptake of a porous material several factors must be taken into account. A framework consisting of narrow pores able to accommodate one or two methane molecules, decorated with open metal sites and/or polar functional groups can give rise to materials with very high methane capacities. At the same time a high gravimetric surface area can result to a high gravimetric methane capacity, while a high volumetric surface area can result to a high volumetric methane uptake.[179] Both are considered important and should be maximized. Some examples of the nature of interactions of these gas molecules with open metal sites and polar functional groups are reported in Chapter 2.

The objective of this thesis was the development of novel porous materials that would exhibit remarkable gas sorption properties and could be used in the aforementioned important industrial applications. This could be achieved by the implementation of all the above critical parameters in MOF synthesis. This includes the design of suitable functionalized organic ligands that will be used for the targeted synthesis of MOFs with specific structure. For that purpose more than 77 tailor made

organic linkers were synthesized and used for the synthesis of more than 90 new MOFs each one exhibiting impressive properties.

References

1 He Y., Li B., O'Keeffe M., Chen B., *Chem. Soc. Rev.,* **2014**, 43, 5618-5656.

2 Dunbar K. R., Heintz R. A., Chemistry of Transition Metal Cyanide Compounds: Modern Perspectives, in Progress in Inorganic Chemistry, Volume 45, John Wiley & Sons, Inc., Hoboken, NJ, USA, **1996**, pp. 283-391.

3 Buser H. J., Schwarzenbach D., Petter W., Ludi A., *Inorg. Chem.*, **1977**, 16, 2704-2710.

4 Cook T. R., Zheng Y., Stang P. J., *Chem. Rev.*, **2013**, 113, 734-777.

5 Kondo M., Yoshitomi T., Seki K., Matsuzaka H., Kitagawa S., *Angew. Chem. In. Ed.,* **1997**, 36, 1725-1727.

6 Li H., Eddaoudi M., O'Keeffe M., Yaghi O. M., *Nature,* **1999**, 402, 276-279.

7 Sun Y.-X., Sun W.-Y., *Chin. Chem. Lett.,* **2014**, 25, 823-828.

8 Klinowski J., Paz F. A., Silva P., Rocha J., *Dalton Trans.,* **2011**, 40, 321-330.

9 Jung D.W., Yang D. A., Kim J., Ahn W. S., *Dalton Trans.,* **2010**, 39, 2883-2887.

10 Klimakow M., Klobes P., Thuenemann A. F., Rademann K., Emmerling F., *Chem. Mater.,* **2010**, 22, 5216-5221.

11 Jacoby M., *Chem. Eng. News*, **2013**, 91, 34-35.

12 Farha O. K., Eryazici I., Jeong N., Hauser B. G., Wilmer C. E., Sarjeant A. A., Snurr R. Q., Nguyen S. T., Yazaydın A. Ö., Hupp J. T., *J. Am. Chem. Soc.,* **2012**, 134, 15016-15021.

13 Furukawa H., Go Y. B., Ko N., Park Y. K., Uribe-Romo F. J., Kim J., O'Keeffe M., Yaghi O. M., *Inorg. Chem.,* **2011**, 50, 9147-9152.

14 Deng H., Grunder S., Cordova K. E., Valente C., Furukawa H., Hmadeh M., Gándara F., Whalley A. C., Liu Z., Asahina S., Kazumori H., O'Keeffe M., Terasaki O., Stoddart F., Yaghi O. M., *Science* **2012,** 336, 1018-1023.

15 Peng Y., Srinivas G., Wilmer C. E., Eryazici I., Snurr R. Q., Hupp J. T., Yildirim T., Farha O. K., *Chem. Commun.,* **2013**, 49, 2992-2994.

16 Furukawa H., Ko N., Go Y. B., Aratani N., Choi S. B., Choi E., Yazaydin A. Ö., Snurr R. Q., O'Keeffe M., Kim J., Yaghi1 O. M., *Science,* **2010,** 329, 424-428.

17 Gándara F., Furukawa H., Lee S., Yaghi O. M., *J. Am. Chem. Soc.,* **2014**, 136, 5271-5274.

18 Sadakiyo M., Yamada T., Kitagawa H., *J. Am. Chem. Soc.*, **2009,** 131, 9906-9907.

19 Narayan T. C., Miyakai T., Seki S., Dincă M., *J. Am. Chem. Soc.,* **2012,** 134, 12932-12935.

20 Saravanan K., Nagarathinam M., Balaya P., Vittal J. J., *J. Mater. Chem.,* **2010,** 20, 8329-8335.

21 McDonald T. M., Lee W. R., Mason J. A., Wiers B. M., Hong C. S., Long J. R., *J. Am. Chem. Soc.,* **2012**, 134, 7056-7065.

22 Li J., Fu H. R., Zhang J., Zheng L., Tao J., *Inorg. Chem.*, **2015**, 54, 3093-3095.

23 Dybtsev D. N., Nuzhdin A. L., Chun H., Bryliakov K. P., Talsi E. P., Fedin V. P., Kim K., *Angew. Chem., Int. Ed.*, **2006**, 45, 916-920.

24 Cui H., Wang Z., Takahashi K., Okano Y., Kobayashi H., Kobayashi A., *J. Am. Chem. Soc.*, **2006**, 128, 15074-15075.

25 Evans O. R., Lin W., *Acc. Chem. Res.,* **2002**, 35, 511-522.

26 Kent C. A., Liu D., Ma L., Papanikolas J. M., Meyer T. J., Lin W., *J. Am. Chem. Soc.,* **2011,** 133, 12940-12943.

27 Wiers B. M., Foo M. L., Balsara N. P., Long J. R., *J. Am. Chem. Soc.,* **2011**, 133, 14522-14525.

28 Chen B., Wang L., Xiao Y., Fronczek F. R., Xue M., Cui Y., Qian G., *Angew. Chem., Int. Ed.*, **2009**, 48, 500-503.

29 Taylor K. M. L., Rieter W. J., Lin W., *J. Am. Chem. Soc.,* **2008**, 130, 14358-14359.

30 Taylor-Pashow K. M. L., Rocca J. D., Xie Z., Tran S., Lin W., *J. Am. Chem. Soc.*, **2009**, 131, 14261-14263.

31 http://www.mlive.com/news/flint/index.ssf/2012/05/mta_opens_alternative_fuel_fac.html

32 http://www.airbetter.org/category/air-pollution/

33 http://www.ezpak.net/pages/ezfolio2.html

[34] Horcajada P., Chalati T., Serre C., Gillet B., Sebrie C., Baati T., Eubank J. F., Heurtaux D., Clayette P., Kreuz C., Chang J., Hwang Y. K., Marsaud V., Bories P., Cynober L., Gil S., Férey G., Couvreur P., Gref R., *Nat. Mater.,* **2010**, 9, 172-178.

[35] Dan Z., Timmons D. J., Yuan, D., Zhou H. C., *Acc. Chem. Res.,* **2011**, 44, 123-133.

[36] Eddaoudi M., Moler D. B., Li H., Chen B., Reineke T. M., O'Keeffe M., Yaghi O. M., *Acc. Chem. Res.,* **2001**, 34, 319-330.

[37] An J., Farha O. K., Hupp J. T., Pohl E., Yeh J. I., Rosi N. L., *Nat.Commun.,* **2012**, 604,1-6.

[38] Kandiah M., Nilsen M. H., Usseglio S., Jakobsen S., Olsbye U., Tilset M., Larabi C., Quadrelli E. A., Bonino F., Lillerud K. P., *Chem. Mater.,* **2010**, 22, 6632-6640.

[39] Wei Z., Lu W., Jiang H., Zhou H., *Inorg. Chem.,* **2013**, 52, 1164-1166.

[40] Bosch M., Zhang M., Zhou H., *Adv. Chem.,* **2014**, 2014, 1-8.

[41] Katie A. C. Matzger A. J., *Langmuir*, **2010**, 26, 17198-17202.

[42] Ferey G., Mellot-Draznieks C., Serre C., Millange F., Dutour J., Surblé S., Margiolaki I., *Science*, **2005**, 309, 2040-2042.

[43] Cao W., Li Y., Wang L., Liao S., *J. Phys. Chem. C,* **2011**, 115, 13829-13836.

[44] Plabst M., Bein T., *Inorg.Chem.,* **2009**, 48, 4331-4341.

[45] Shimizu G. K. H., Vaidhyanathan R., Taylor J. M., *Chem. Soc. Rev.,* **2009**, 38, 1430-1449.

[46] Wang B., Côté A. P., Furukawa H., O'Keeffe M., Yaghi O. M., *Nature*, **2008**, 453, 207-211

[47] Etaiw S. El-din H., El-din A.S. B., El-bendary M. M., *Z. Anorg. Allg. Chem.,* **2013,** 639, 810-816.

[48] Furukawa H., Cordova K. E., O'Keeffe M., Yaghi O. M., *Science,* **2013,** 341, 1230444

[49] Mellot-Draznieks C., Serre C., Surble S., Audebrand N., Ferey G., *J. Am. Chem. Soc.,* **2005**, 127, 16273-16278.

[50] Song L., Zhang J., Sun L., Xu F., Li F., Zhang H., Si X., Jiao C., Li Z., Liu S., Liu Y., Zhou H., Sun D., Du Y., Cao Z., Gabelica Z., *Energy Environ. Sci.,* **2012**, 5, 7508-7520.

[51] Xydias P., Spanopoulos I., Klontzas E., Froudakis E. G., Trikalitis N. P., *Inorg. Chem.,* **2014**, 53, 679-681.

[52] Makal T. A., Wang X., Zhou H-C., *Cryst. Growth Des.,* **2013**, 13, 4760-4768.

[53] Wang C., Wang J.-L., Lin W., *J. Am. Chem. Soc.,* **2012**, 134, 19895-19908.

[54] Schaate A., Roy P., Preuse T., Lohmeier S. J, Godt A., Behrens P., *Chem.-Eur. J.,* **2011**, 17, 9320-9325.

[55] Furukawa H., Go Y. B., Ko N., Park Y. K., Uribe-Romo F. J., Kim J., O'Keeffe M., Yaghi O. M., *Inorg. Chem.,* **2011**, 50, 9147-9152.

[56] Choi M.-H., Park H. J., Hong D. H, Suh M. P., *Chem.–Eur. J.,* **2013**, 19, 17432-17438.

[57] Song F., Wang C., Falkowski J. M., Ma L., Lin W., *J. Am. Chem. Soc.,* **2010**, 132, 15390-15398.

[58] Zhang M., Chen Y.-P., Bosch M., Gentle T., Wang K., Feng D., Wang Z. U., Zhou H.-C., *Angew. Chem., Int. Ed.,* **2014**, 53, 815-818.

[59] Mihalcik D. J., Zhang T., Ma L., Lin W., *Inorg. Chem.,* **2012**, 51, 2503-2508.

[60] Shustova N. B., Cozzolino A. F., Dinca M., *J. Am. Chem. Soc.,* **2012**, 134, 19596-19599.

[61] Tan C., Yang S., Champness N. R., Lin X., Blake A. J., Lewis W., Schroder M., *Chem. Commun.,* **2011**, 47, 4487-4489.

[62] Lu W., Yuan D., Makal T. A., Li J.-R., Zhou H.-C., *Angew. Chem., Int. Ed.,* **2012**, 51, 1580-1584.

[63] Eubank J. F., Nouar F., Luebke R., Cairns A. J., Wojtas L., Alkordi M., Bousquet T., Hight M. R., Eckert J., Embs J. P, Georgiev P. A, Eddaoudi M., *Angew. Chem., Int. Ed.,* **2012**, 51, 10099-10103.

[64] Dinca M., Dailly A., Liu Y., Brown C. M., Neumann D. A., Long J. R., *J. Am. Chem. Soc.,* **2006**, 128, 16876-16883.

[65] Wang X.-J., Li P.-Z, Chen Y., Zhang Q., Zhang H., Chan X. X., Ganguly R., Li Y., Jiang J., Zhao Y., *Sci. Rep.,* **2013**, 3, 1149.

[66] Han L., Qin L., Xu L., Zhou Y., Sun J., Zou X., *Chem. Commun.,* **2013**, 49, 406-408.

[67] He Y., Xiang S., Zhang Z., Xiong S., Wu C., Zhou W., Yildirim T., Krishna R., Chen B., *J. Mater. Chem. A*, **2013**, 1, 2543-2551.

[68] Ma S., Sun D., Simmons J. M., Collier C. D., Yuan D., Zhou H.-C., *J. Am. Chem. Soc.,* **2008**,130 1012-1016.

[69] Peng Y., Gong T., Cui Y., *Chem. Commun.,* **2013**, 49, 8253-8255.

[70] Yan Y., Blake A. J., Lewis W., Barnett S. A., Dailly A., Champness N. R., Schroder M., *Chem. – Eur. J.,* **2011**, 17, 11162-11170.

[71] Rege S. U., Yang R. T., Buzanowski M. A., *Chem. Eng. Sci.,* **2000**, 55, 4827-4838.

[72] Santos J. C., Magalhaes F. D., Mendes A., *Ind. Eng. Chem. Res.*, **2008**, 47, 6197-6203.

[73] Kordesch K., Hacker V., Gsellmann J., Cifrain M., Faleschini G., Enzinger P., Fankhauser R., Ortner M., Muhr M., Aronson R. R., *J. Power Sources,* **2000**, 86, 162-165.

[74] Mattox E. M., Knox J. C., Bardot D. M., *Acta Astronaut.,* **2013**, 86, 39-46.

[75] Cavenati S., Grande C. A., Rodrigues A. E., Energy Fuels, **2006**, 20, 2648-2659.

[76] Shekhah O., Belmabkhout Y., Chen Z., Guillerm V., Cairns A., Adil K., Eddaoudi M., *Nat. Commun.,* **2014**, 5, 4228, 1-7.

[77] Lide D. R., CRC Handbook of Chemistry and Physics, CRC Press: Boca Raton, FL, **2004**.

[78] Yamposkii Y., Pinnau I., Freeman B. D., Materials Science of Membranes for Gas and Vapor Separation, John Wiley & Sons Ltd.: West Sussex, England, **2006**.

[79] Holstraeter T. F., Georgieff M., Foehr K. J., Klingler W., Uhl M. E., Walker T., Koester S., Groen G., Adolph O., *Anesthesiology*, **2011**, 115, 398-407.

[80] Cullen S. C., Gross E. G., *Science,* **1951**, 113, 580-582.

[81] Banerjee D., Cairns A. J., Liu J., Motkuri R. K., Nune S. K., Fernandez C. A., Krishna R., Strachan D. M., Thallapally P. K., *Acc. Chem. Res.,* **2015**, 48, 211-219.

[82] Perry J. J., Teich-McGoldrick S. L., Meek S. T., Greathouse J. A., Haranczyk M., Allendorf M. D., *J. Phys. Chem. C*, **2014**, 118, 11685-11698.

[83] Moulijn J. A., Makkee M., Diepen A., Chemical Process Technology, Wiley, New York, **2001**.

[84] Li J., Kuppler R. J., Zhou H., *Chem. Soc. Rev.,* **2009**, 38, 1477-1504.

[85] Ma S., Sun D., Wang X.-S., Zhou H.-C., *Angew. Chem. Int. Ed.,* **2007**, 46, 2458 -2462.

[86] Bloch E. D., Queen W. L., Krishna R., Zadrozny J. M., Brown C. M., Long J. R., *Science,* **2012**, 335, 1606-1610.

[87] El Osta, R., Carlin-Sinclair A., Guillou N., Walton R. I., Vermoortele F., Maes M., de Vos D., Millange F., *Chem. Mater.,* **2012**, 24, 2781-2791.

[88] DeCoste J. B., Peterson G. W., *Chem. Rev.*, **2014**, 114, 5695-5727.

[89] Roy A., Srivastava A. K., Singh B., Mahato T. H., Shah D., Halve A. K., *Micropor. Mesopor. Mater.*, **2012**, 162, 207-212.

[90] Roy A., Srivastava A. K., Singh B., Shah D., Mahato T. H., Srivastava A., *Dalton Trans.,* **2012**, 41, 12346-12348.

[91] Weinstock B., Niki H., *Science,* **1972**, 176, 290-292.

[92] Vajani M., Annest J. L., Ballesteros M., Gilchrist J., Stock A., *Morbidity Mortality Wkly Rep.,* **2005**, 54, 36-39.

[93] Miessler G. L., Tarr D. A., Inorganic Chemistry, 2nd Edition, Prentice Hall, Upper Saddle River, NJ, **1999**, pp. 338.

[94] Zou R.-Q., Sakurai H., Han S., Zhong R.-Q., Xu Q., *J. Am. Chem. Soc.,* **2007**, 129, 8402-8403.

[95] Nouar F., Eubank J. F., Bousquet T., Wojtas L., Zaworotko M. J., Eddaoudi M., *J. Am. Chem. Soc.,* **2008**, 130, 1833-1835.

[96] Le Quéré C., Peters G. P., Andres R. J., Andrew R. M., Boden T. A., Ciais P., Friedlingstein P., Houghton R. A., Marland G., Moriarty R., Sitch S., Tans P., Arneth A., Arvanitis A. D., Bakker C. E., Bopp L., Canadell J. G., Chini L. P., Doney S. C., Harper A., Harris I., House J. I., Jain A. K., Jones S. D., Kato E., Keeling R. F., Klein Goldewijk K., Körtzinger A., Koven C., Lefèvre N., Maignan F., Omar A., Ono T., Park G.-H., Pfeil B., Poulter B., Raupach M. R., Regnier P., Rödenbeck C., Saito S., Schwinger J., Segschneider J., Stocker B. D., Takahashi T., Tilbrook B., van Heuven S., Viovy N., Wanninkhof R., Wiltshire A., Zaehle S., *Earth Syst. Sci. Data,* **2014**, 6, 235-263.

[97] http://earthobservatory.nasa.gov/Features/GlobalWarming/page5.php

[98] Eberle U., Müller B., Von Helmolt R., *Energy Environ. Sci.*, **2012**, 5, 8780-8798.

[99] Schlapbach L., Züttel A, *Nature,* **2001,** 414, 353-358.

[100] Sakintuna B., Lamari-Darkrimb F., Hirscher M., *Int. J. Hydrogen Energy,* **2007**, 32, 1121-1140.

[101] Schuth F., Bogdanovic B., Felderhoff M., *Chem. Commun.,* **2004**, 2249-2258.

[102] Hugle T., Hartl M., Lentz D., *Chem.-Eur. J.,* **2011**, 17, 10184-102207.

[103] Zhang Y.-H. P., *Int. J. Hydrogen Energy,* **2010**, 35, 10334-10342.

[104] Struzhkin V. V., Militzer B., Mao W. L., Mao H.-k., Hemley R. J., *Chem. Rev.,* **2007**, 107, 4133-4151.

[105] Chen J., Wu F., *Appl. Phys. A: Mater. Sci. Process.,* **2004**, 78, 989-994.

[106] Cheng H.-M., Yang Q.-H., Liu C., *Carbon,* **2001**, 39, 1447-1454.

[107] Kim J., Yeo S., Jeon J., Kwak S., *Micropor. Mesopor. Mater.*, **2015**, 202, 8-15.

[108] Suh M., Park H., Prasad T., Lim D., *Chem. Rev.*, **2012**, 112, 782-835.

[109] Hoang T. K. A, Antonelli D. M., *Adv. Mater.,* **2009**, 21, 1787-1800.

[110] Berg A. W. C., Arean C. O., *Chem. Commun.,* **2008**, 668-681.

[111] Long J., Head-Gordon M., FY **2014** Annual Progress Report, IV-73, DOE Hydrogen and Fuel Cells Program.

[112] Wang X., Ma S., Forster P.M., Yuan D., Eckert J., López J.J., Murphy B.J., Parise J. B., Zhou H., *Angew. Chem. Int. Ed.,* **2008**, 47, 7263-7266.

[113] Lochan R. C., Head-Gordon M., *Phys. Chem. Chem. Phys.*, **2006**, 8, 1357-1370.

[114] International Energy Agency (IEA): http://www.iea.org/index_info.asp?id=1959, 2011.

[115] Qin T. F. D., Plattner G.-K., Tignor M., Allen S. K., Boschung J., Nauels A., Xia Y., Bex V., Midgley P. M., IPCC, **2013**, Climate Change 2013: The Physical Science Basis. Contribution of Working Group I to the Fifth Assessment Report of the Intergovernmental Panel on Climate Change Stocker, Cambridge University Press, Cambridge, United Kingdom and New York, NY, USA.

[116] Olivier J.G.J. (PBL), Janssens-Maenhout G. (IES-JRC), Muntean M. (IES-JRC), Peters J.A.H.W., (PBL),Trends in global CO_2 emissions: 2013 Report, **2013**, PBL Netherlands Environmental Assessment Agency, The Hague.

[117] Haszeldine R. S., *Science,* **2009**, 325, 1644-1645.

[118] http://www.cmar.csiro.au/sealevel/

[119] Millward A. R., Yaghi O. M., *J. Am. Chem. Soc.,* **2005**, 127, 17998-17999.

[120] Yazaydin A. O., Snurr R. Q., Park T. H., Koh K., Liu J., LeVan M. D, Benin A. I., Jakubczak P., Lanuza M., Galloway D. B., Low J. L., Willis R. R., *J. Am. Chem. Soc.,* **2009**, 131, 18198-18199.

[121] Boden T. Andres B., World's countries ranked by **2010** total fossil-fuel CO_2 emissions, Carbon Dioxide Information Analysis Center Oak Ridge National Laboratory, http://cdiac.ornl.gov/trends/emis/top2010.tot

[122] Li L. S., Xu Q., *Energy Environ. Sci.,* **2013**, 6, 1656-1683.

[123] Lozanao-Castello D., Alcaniz-Monge J., de la Casa-Lillo M. A., Cazorla- Amoros D., Linares-Solano A., *Fuel*, **2002**, 81, 1777-1803.

[124] Alternative Fuels Data Center-Fuel Properties Comparison, **2013**, http://www.afdc.energy.gov/fuels/fuel_comparison_ chart.pdf.

[125] http://www.eia.gov/countries/cab.cfm?fips=rs

[126] Methane Opportunities for Vehicular Energy, Advanced Research Project Agency-Energy, U.S. Dept. of Energy, Funding Opportunity no. DE-FOA-0000672, **2012**.

[127] O'Keeffe M., Peskov M. A., Ramsden S. J., Yaghi O. M., *Acc. Chem. Res.,* **2008**, 41, 1782-1789.

[128] Peng Y., Krungleviciute V., Eryazici I., Hupp T. J., Farha K. O., Yildirim T., *J. Am. Chem. Soc.,* **2013**, 135, 11887-11894.

[129] Mason J. A., Veenstra M., Long J. R., *Chem. Sci.,* **2014**, 5, 32-51.

[130] Wu H., Zhou W., Yildirim T., *J. Am. Chem. Soc.,* **2009**, 131, 4995-5000.

[131] Wu H., Simmons J. M., Liu Y., Brown C. M., Wang X.-S., Ma S., Peterson V. K., Southon P. D., Kepert C. J., Zhou H.-C., Yildirim T., Zhou W., *Chem.-Eur. J.,* **2010**, 16, 5205-5214.

[132] Gándara F., Furukawa H., Lee S., Yaghi O. M., *J. Am. Chem. Soc.,* **2014**, 136, 5271-5274.

[133] U.S. Department of Energy, U.S. Energy Information Administration: International Energy Outlook **2013** (Report: DOE/EIA-0484(2013).

[134] Dorian J. P., Franssen H.T., Simbeck D.R., *Energy Policy,* **2006**, 34, 1984-1991.

[135] Shafiee S., Topal E., *Energy Policy*, **2009**, 37, 181-189.

[136] Crabtree G.W., Dresselhaus M. S., *MRS Bull.,* **2008**, 33, 421-428.

[137] Hamrock S., Yandrasits M., *Polym. Rev.,* **2006**, 46, 219-244.

[138] Paddison S. J., *Annu. Rev. Mater. Res.,* **2003**, 33, 289-319.

[139] Peighambardoust S. J., Rowshanzamir S., Amjadi M., *Int. J. Hydrogen Energy,* **2010**, 35, 9349-9384.

[140] Ponomareva V. G., Kovalenko K. A., Chupakhin A. P., Dybtsev D. N., Shutova E. S., Fedin V. P., *J. Am. Chem. Soc.,* **2012**, 134, 15640-15643.

[141] Nagarkar S. S., Unni S. M., Sharma A., Kurungot S., Ghosh S. K., *Angew. Chem., Int. Ed.,* **2014**, 53, 2638-2642.

[142] Mc Morn P., Hutchings G. J., *Chem. Soc. Rev.,* **2004**, 33, 108-122.

[143] Corma A., *Chem. Rev.,* **1997**, 97, 2373-2420.

[144] Anderson M. W., Terasaki O., Ohsuna T., Philippou A., MacKay S. P., Ferreira A., Rocha J., Lidin S., *Nature,* **1994**, 367, 347-351.

[145] Lee S. J., Hu A., Lin W., *J. Am. Chem. Soc.,* **2002**, 124, 12948-12949.

[146] Wu C. D., Hu A., Zhang L., Lin W., *J. Am. Chem. Soc.,* **2005**, 127, 8940-8941.

[147] Kim K., Banerjee M., Yoon M., Das S., *Top. Curr. Chem.,* **2010**, 293, 115-153.

[148] http://www.pfizer.com/system/files/presentation/2014_Pfizer_Financial_Report.pdf

[149] Gref R., Minamitake Y., Peracchia M.T., Trubetskoy V., Torchilin V., Langer R., *Science,* **1994**, 263, 1600-1603.

[150] Samad A., Sultana Y., Aqil M., *Curr. Drug Delivery,* **2007**, 4, 297-305.

[151] Kong G., Braun R. D., Dewhirst M. W., *Cancer Res.,* **2000**, 60, 4440-4445.

[152] Trewyn B. G., Slowing I. I., Giri S., Chen H.-T., Lin V. S. Y., *Acc. Chem. Res.,* **2007**, 40, 846-853.

[153] Arruebo M., Fernandez-Pacheco R., Irusta S., Arbiol J., Ibarra M. R., Santamaría J., *Nanotechnology*, **2006**, 17, 4057-4064.

[154] He Q., Shi J., *J. Mater. Chem.,* **2011**, 21, 5845-5855.

[155] Petros R. A., DeSimone J. M., *Nat. Rev. Drug Discovery*, **2010**, 9, 615-627.

[156] Levy M. H., Wheelock E. F., *J. Immunol.,* **1975**, 115, 41-48.

[157] Yuan Y., Tam M. F., Simplaceanu V., Ho C., *Chem. Rev.*, **2015**, 115, 1702-1724.

[158] Johnson J. F., Allan D., Vance C. P., *Plant Physiol.,* **1994**, 104, 657-665.

[159] a) Sheftel V. O., Indirect Food Additives and Polymers: Migration and Toxicology, Lewis Publishers, **2000**, pp 148-154. b)<http://www.chem.unep.ch/irptc/sids/OECDSIDS/100-21-0.pdf> (2008). c).<http://www.chemicalland21.com/specialtychem/perchem/TRIMESIC%20ACID.htm> (2008). d) < http://www.sciencelab.com/msds.php?msdsId=9927173>.

[160] Vassal G., Gouyette A., Hartmann O., Pico J. L., Lemerle J., *Cancer Chemother. Pharmacol.,* **1989**, 24, 386-390.

[161] Baron F., Deprez M., Beguin Y., *Haematologica*, **1997**, 82, 718-725.

[162] Layre A., Gref R., Richard J., Requier D., Couvreur P., Nanoparticules polymeriques composites FR 04 07569, **2004**.

[163] West A. R., Basic Solid State chemistry, John Wiley & Sons, **1999**, pp. 130-133.

[164] Putnis, A., Introduction to Mineral Sciences. Cambridge, UK: Cambridge University Press, **1992**, Chapter 3, pp. 41-80.

[165] Eby G.N., Principles of Environmental Geochemistry. Brooks/Cole-Thomson Learning, **2004**, pp. 212-214.

[166] Tilley R. J. D., Crystals and Crystal Structures, John Wiley & Sons, Hoboken, NJ, **2006**, pp. 17-35.

[167] Myers A. L., Monson P. A., *Adsorption*, **2014**, 20, 591-622.

[168] IUPAC Recommendations, *Pure Appl. Chem.*, **1994**, 66, 1739-1758.

[169] Lowell S., Shields J. E., Thomas M. A., Thommes M., Characterization of Porous Solids and Powders: Surface Area, Pore Size and Density, Springer Science & Business Media, **2004**, Chapter 5.

[170] Polanyi M., *Verh. Dtsch. Phys. Ges.,* **1914**, 16, 1012-1016.

[171] Dubinin M. M., Astakhov V. A., *Adv. Chem. Ser.,* **1970**, 102, 69.

[172] Horvath G., Kawazoe K., *J. Chem. Eng. Japan,* **1983**, 16, 470-475.

[173] Kowalczyka P., Terzykb A. P., Gaudenb P.A., Leboda R., Szmechtig-Gauden E., Rychlicki G., Ryu Z., Rong H., *Carbon,* **2003**, 41, 1113-1125.

[174] López-Ramón M. V., Jagiełło J., Bandosz T. J., Seaton N. A., *Langmuir*, **1997**, 13, 4435-4445.

[175] Neimark A.V., Ravikovitch P. I., Grün M., Schüth F., Unger K. K., *J. Colloid Interface Sci.,* **1998**, 207, 159-169.

[176] Yang W., Davies A. J., Lin X., Suyetin M., Matsuda R., Blake A. J., Wilson C., Lewis W., Parker J.E., Tang C.C., George M.W., Hubberstey P., Kitagawa S., Sakamoto H., Bichoutskaia E., Champness N. R., Yang S., Schröder M., *Chem. Sci.,* **2012**, 3, 2993-2999.

[177] Suh M. P., Park H. J., Prasad T. K., Lim D.-W., *Chem. Rev.*, **2012**, 112, 782-835.

[178] Sumida K., Rogow D. L., Mason J. A., McDonald T. M., Bloch E. D., Herm Z. R., Bae T.-H., Long J. R., *Chem. Rev.*, **2012**, 112, 724-781.

[179] Wilmer C. E., Leaf M., Lee C. Y., Farha O. K., Hauser B. G., Hupp J. T., Snurr R. Q., *Nat. Chem.*, **2012**, 4, 83-89.

Chapter 5: <u>Results and discussion</u>

  Taking into account all the critical parameters (Chapter 4) that can affect the gas sorption properties of a porous material we designed and synthesized all the following linkers that were used for the synthesis of MOFs with different structures and topologies. Most of them (90%) are novel, unique ligands that were synthesized for the first time. The idea behind the design and synthesis of each linker is presented in detail in the following sub Chapters.
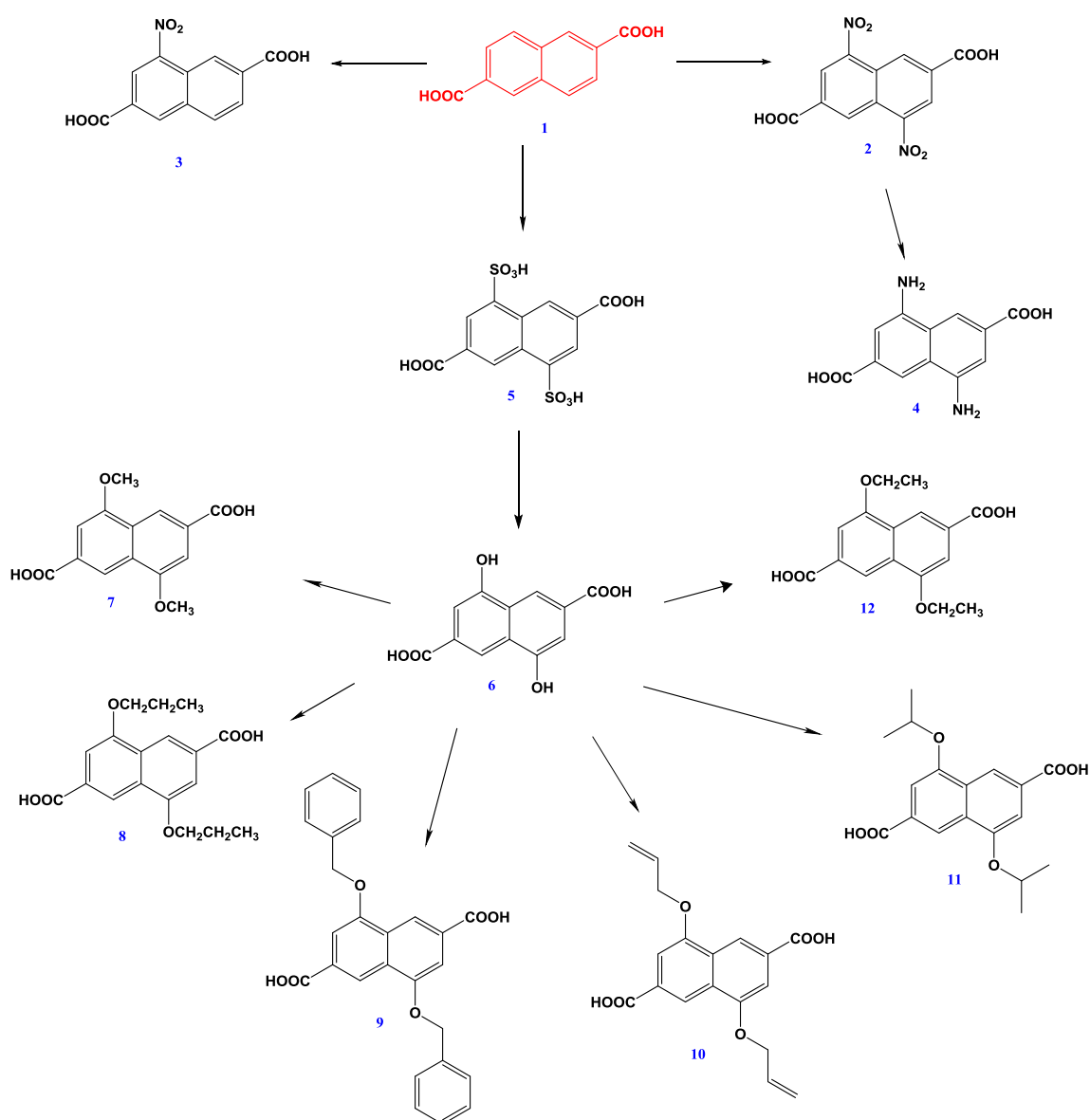
<u>Figure 5.1.</u> Organic linkers based on the commercially available 2,6-naphthalenedicarboxylic acid, (H$_2$NDC).
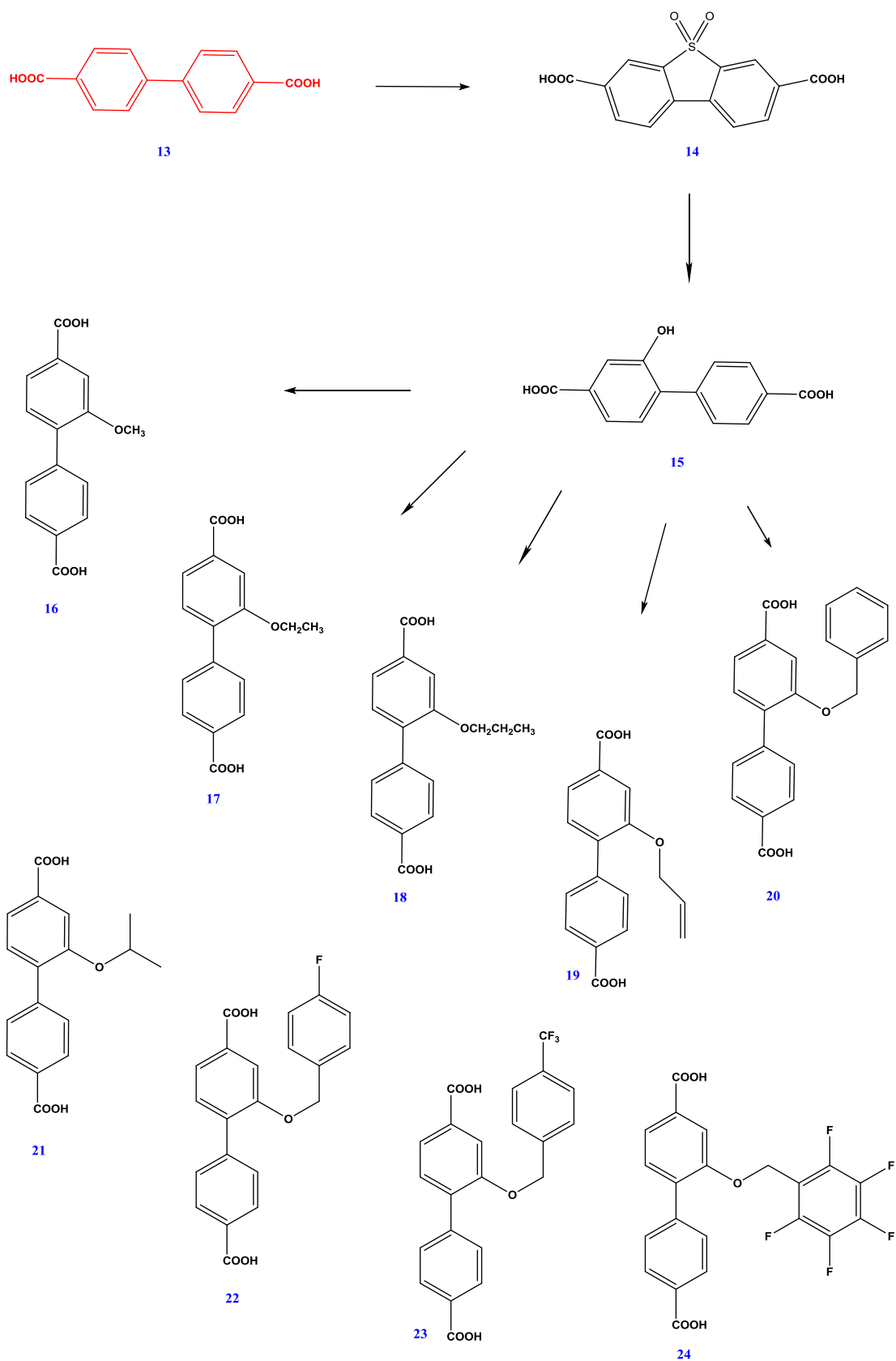
Figure 5.2. Organic linkers based on the commercially available biphenyl-4,4′-dicarboxylic acid, (H$_2$BPDC).
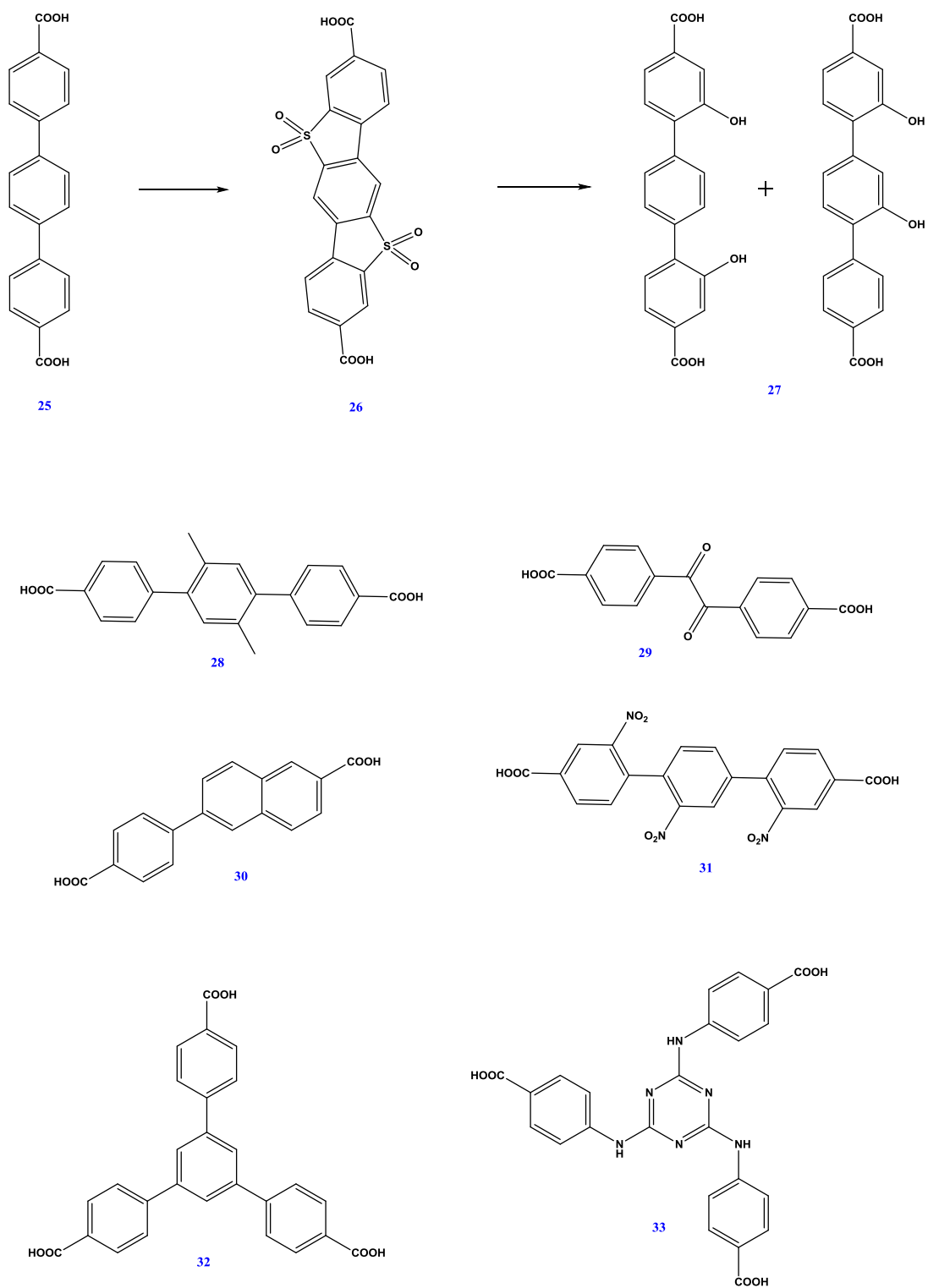
Figure 5.3. Linear and trigonal organic linkers.
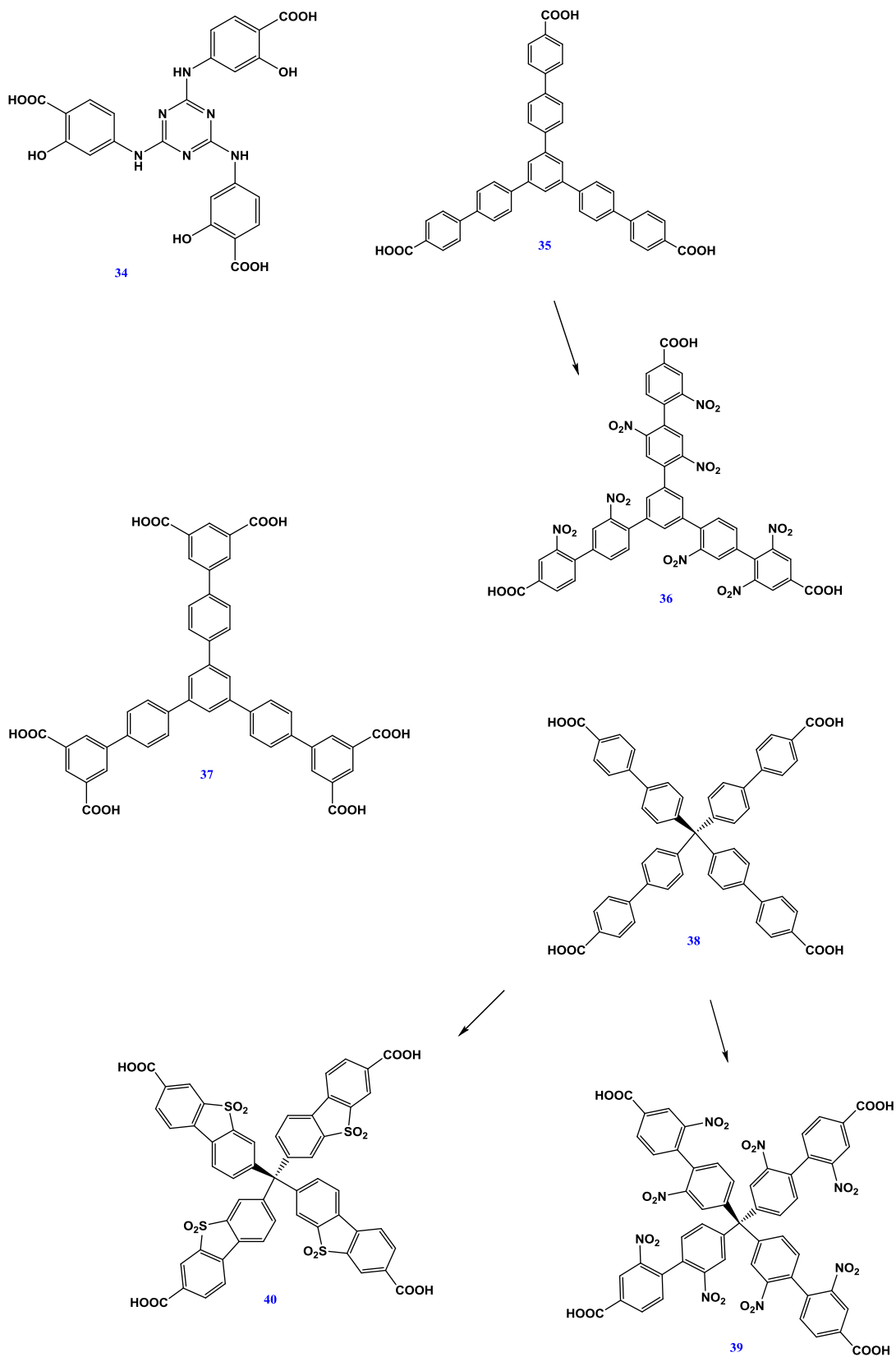
Figure 5.4. Trigonal and tetrahedral linkers.
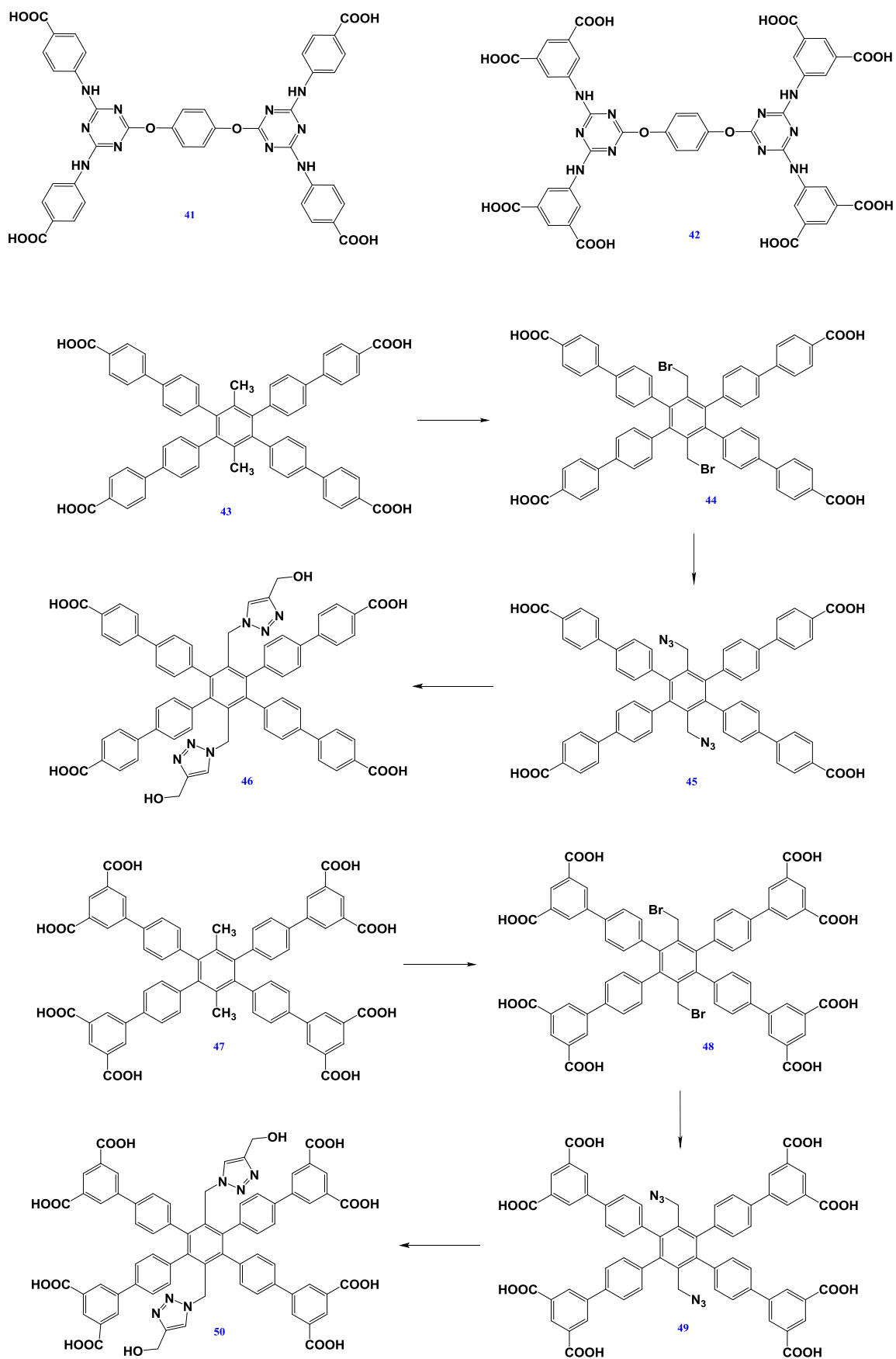
Figure 5.5. Rectangular organic linkers. Linkers 41 and 42 are represented as rectangular for clarity purposes.
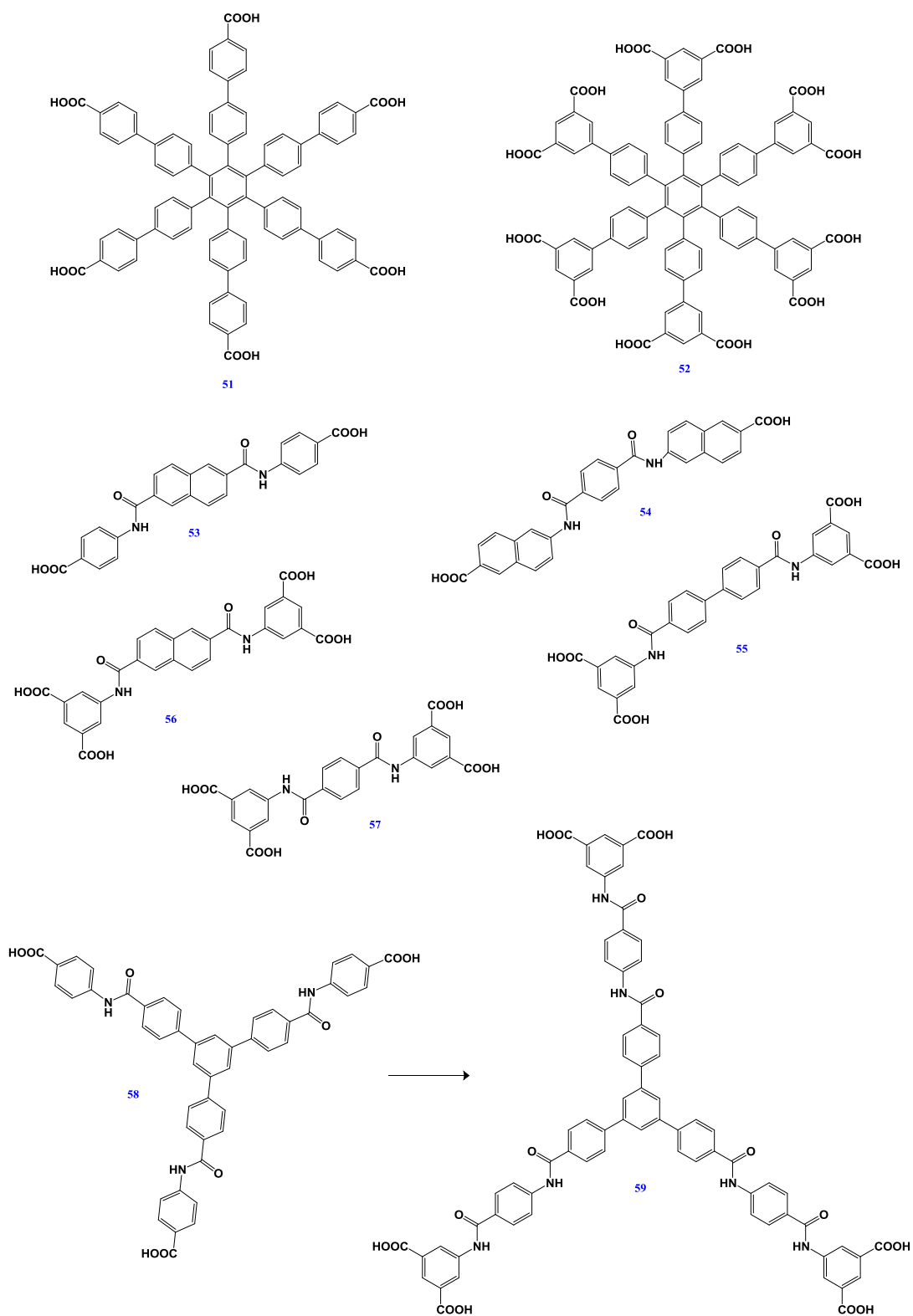
Figure 5.6. Dendritic, linear and expanded organic linkers functionalized with amide groups.
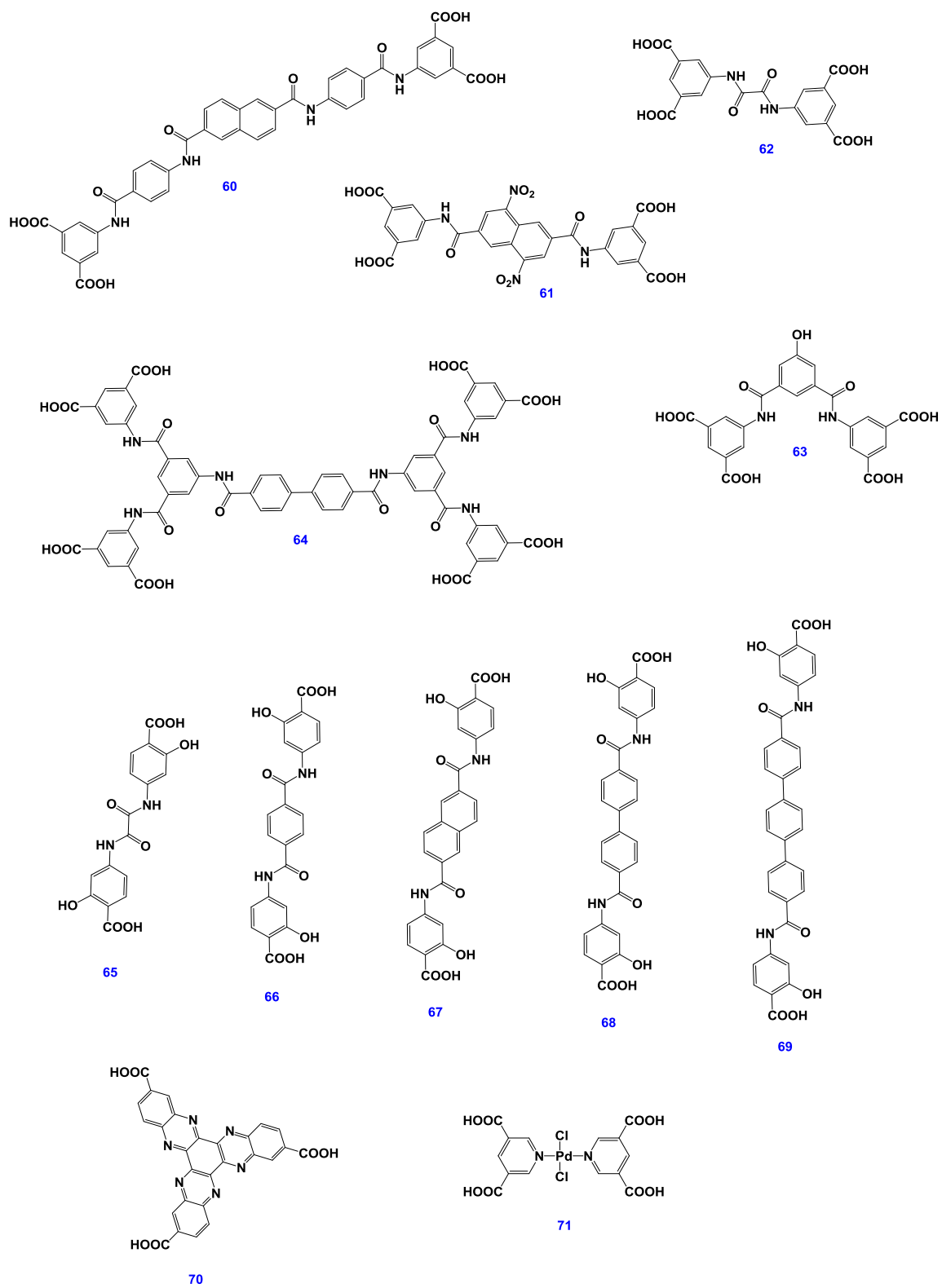
Figure 5.7. Bent, linear and expanded organic linkers functionalized with amide groups.
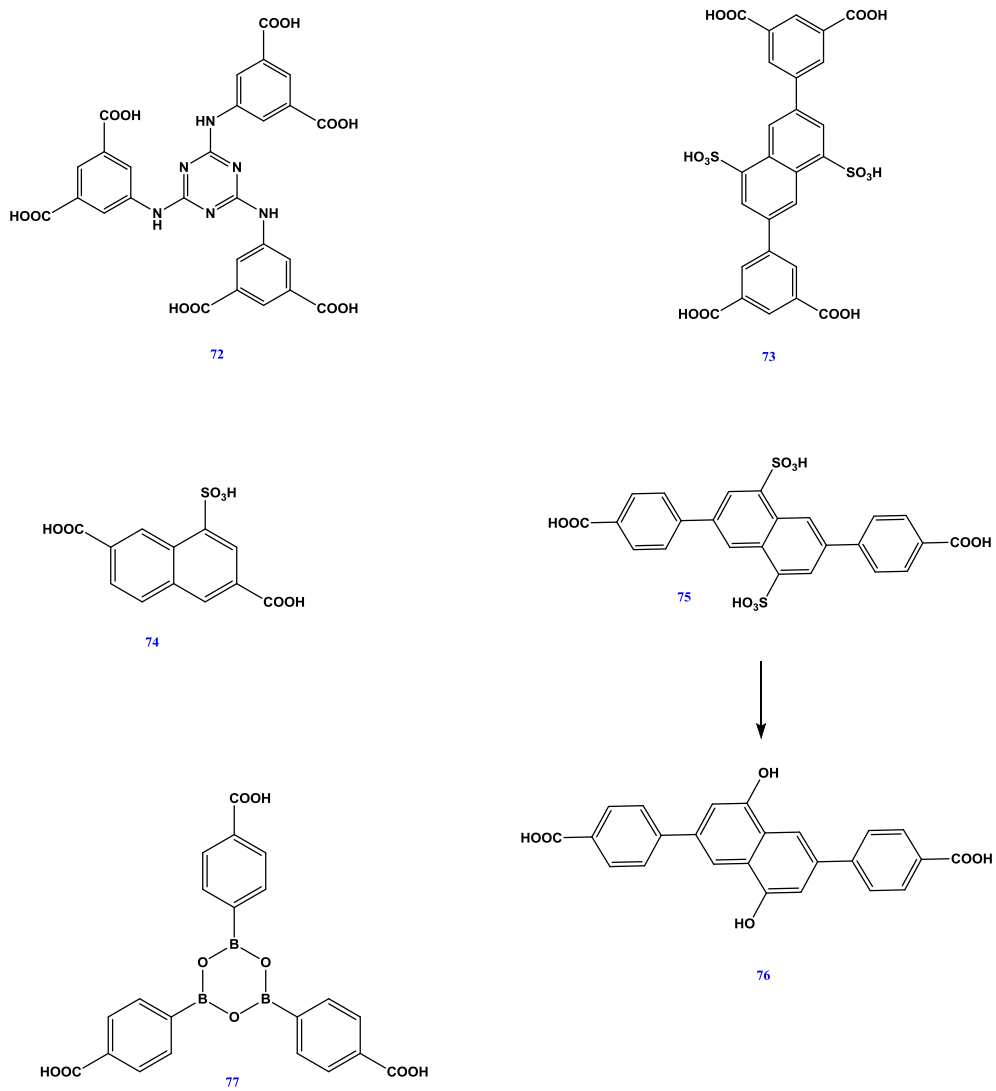
Figure 5.8. Linear and trigonal functionalized organic linkers.

5.1 Syntheses of MOFs based on Zr^{4+} metal clusters.

  We describe below the syntheses, characterization and extensive gas-sorption properties of a series of Zr-based MOFs using different organic linkers of various topologies, some of them functionalized with different functional groups ($-SO_3H$, $-OH$, $-NH_2$, $-NO_2$, $-OR$).

  The goal of this work was the synthesis of fcu MOFs, with face cencterd cubic topology, analogous to the UiO family of solids, first synthesized by the University of Oslo. The SBU of this type of MOFs consists of six Zr^{4+} ions, where each zirconium atom is eight-coordinated forming a square-antiprismatic coordination with eight oxygen atoms. Four oxygen atoms are supplied by the carboxylates of the organic linkers and four oxygen atoms come from μ_3-O and μ_3-OH groups. Each SBU is twelve connected by the organic linkers and each organic linker bridges two SBUs, resulting to an overall framework formula $Zr_6O_4(OH)_4(L)_6$, L = organic ligand.[1] A most important characteristic of these type of MOFs is their high chemical and thermal stability. This is attributed to the inherent structural characteristics of this material. On the one hand lies the very high connectivity of the metal cluster and on the other hand lies the very strong coordination bond between the carboxylate groups of the organic linkers and the metal ions (see Chapter 1). Therefore these materials pose a very promising platform to synthesize new moisture stable functionalized MOFs, with possible interesting gas sorption properties. Indeed by utilizing different linear organic linkers a whole family of isoreticular MOFs can be synthesized.[2] Noticeably all the UiO type MOFs share a unique diffraction pattern. The only difference observed is the shift of the pattern to lower or higher 2θ degrees depending on the MOF's unit cell.
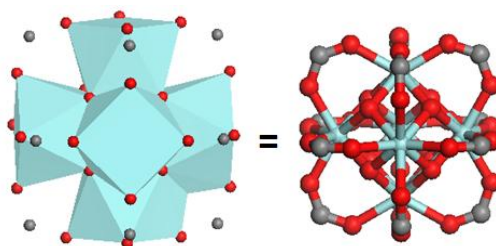
Figure 5.9. Two representations of the twelve connected SBU, the blue polyhedra represent the zirconium atoms. Turquoise spheres: Zr, gray: C, red: O.

  The first group of UiO type MOFs that we studied is based on the synthesis of functionalized linear organic linkers based on the commercially available 2,6-naphthalenedicarboxylic acid, (H_2NDC). By using various synthetic pathways (see Appendix D) we managed to incorporate polar, acidic and basic groups on this linker. Therefore the organic linkers 1, 2, 4, 5, 6, 74 were used for the targeted synthesis of nine materials, eight with fcu topology and one with bcu (body centered cubic). Those materials were characterized using powder X-ray diffraction studies (pxrd). From these materials it was possible to activate only six of them in order to evaluate their gas sorption properties.

Below it is reported for each material the structural characterization and the results of the gas sorption studies. Following this, there is a comparison of the gas sorption properties of all the aforementioned materials.

The first material that it was examined, is based on the non functionalized linker H_2NDC, and it was synthesized as a reference (blank) for comparison purposes. It must be mentioned that this MOF is already synthesized by another group.[3] In our case the material was characterized using powder X-ray diffraction analysis. The diffraction pattern was compared with the calculated one from the single crystal structure data. Apparently a highly crystalline material, with fcu topology was synthesized, as it was expected. Noticeably the synthetic methodology that was used is different than the published procedures. Furthermore it was observed that an increase in the amount of modulator (acetic acid) resulted to the formation of a different phase, a material with a 6 connected SBU, instead of 12, as it was shown recently in the literature.[4] Modulators are chemical entities that can support the formation of the desired cluster, by coordination to the metal ions and can be replaced during synthesis, by the organic linkers. Incomplete replacement by the organic linkers can result to a material with missing linker defects and subsequently larger pores and different properties than the defect-free material.[5]

Compound $Zr_6O_4(OH)_4(NDC)_6$ forms a 3-D fcu framework, exhibiting two types of pores. An octahedral cage with diameter 9.3 Å and a tetrahedral cage with 7.5 Å in diameter, taking into account the van der Waals radii. The two types of pores are connected through triangular windows.
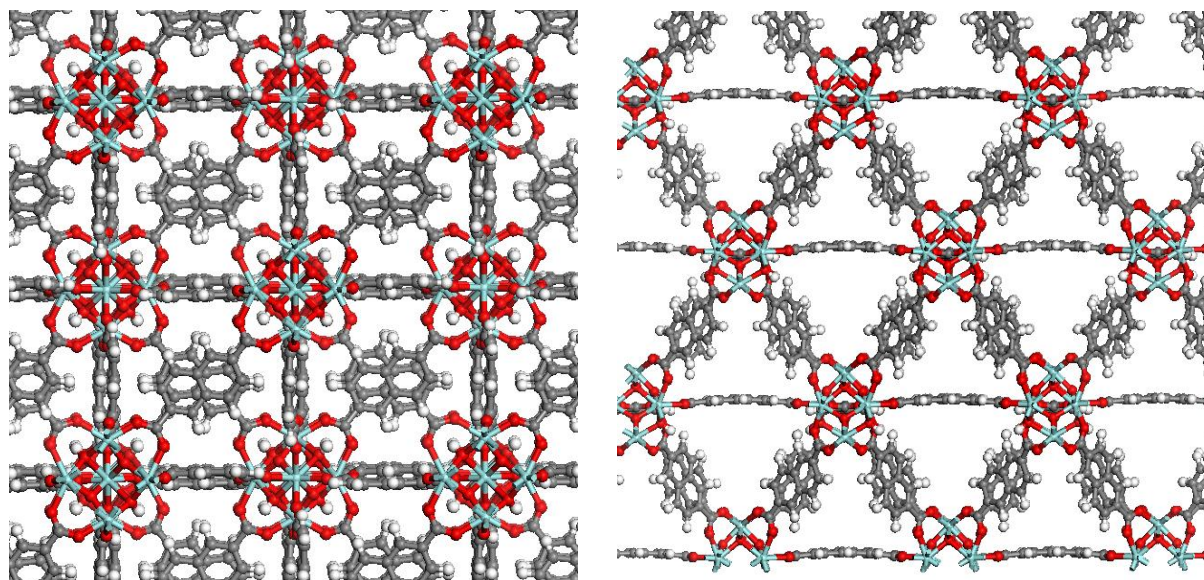
<u>Figure 5.10.</u> Left: Part of the 3-D crystal structure looking down the b axis, Right: the triangular windows, looking along the [110] direction. Turquoise spheres: Zr, gray: C, red: O.

Argon adsorption measurements at 87 K revealed a fully reversible pseudo Langmuir isotherm. The calculated surface area from the Argon isotherm was found to be 1451 $m^2 g^{-1}$ (BET) and the total pore volume 0.66 $cm^3 g^{-1}$ at P/P_0 0.99, a little higher than the expected one from the crystal structure, 0.60 $cm^3 g^{-1}$. The calculation of the specific surface area was performed using consistency criteria[6] for this

material and all the following. ^{1}H NMR measurements after acid digestion of the activated sample, revealed a very low percentage of acetate ions (ratio of organic linker to acetate 1:38). Additionally, pore size distribution analysis showed only sharp peaks at the micropore region in fully agreement with the crystallographic data. These facts state that this material contains no defects, that is the SBU is twelve connected with organic linkers.

In order to evaluate its gas sorption properties we performed CO_2, H_2, and CH_4 sorption measurements. It must be mentioned that we provide for the first time extensive gas sorption properties on UiO type MOFs based on the H_2NDC organic linker. At 77 K and 1 bar $Zr_6O_4(OH)_4(NDC)_6$ adsorbs 1.6 wt% H_2 with a calculated isosteric heat of adsorption (Q_{st}) value of 7.48 kJ mol^{-1}, which are very high values for low surface area MOFs and can be well compared to materials with open metal sites.[7] The isosteric heat of adsorption (Q_{st}) stands for the average binding energy of an adsorbing molecule at a specific surface coverage and is a parameter indicative of the affinity of a surface with the adsorbing molecules.[8] The term isosteric means that this parameter has been calculated using the isosteric method, where a series of isotherms are measured at different temperatures. Adsorption is a spontaneous exothermic phenomenon, therefore the higher the heat of adsorption is, the higher the energy that is released by the adsorption of a gas molecule on the surface of the framework.[9]

CO_2 measurements revealed an impressive uptake of 4.18 mmol g^{-1} at 273 K and 1 bar, while at 298 K and 1 bar the uptake reaches a value of 3.06 mmol g^{-1}, these findings are among the highest reported for UiO type MOFs.[10] The calculated Q_{st}^0 for CO_2 was found to be 26.26 kJ mol^{-1} with a small decline during CO_2 loading. This decline is observed in many other cases in this thesis and can be explained as follows: the first gas molecules that approach the framework will be attracted by the strongest adsorption (binding) sites, depending on the geometric and chemical features of the pore surface, such as narrow cavities, exposed metal cation sites or strong polarizing functional groups. When those sites are occupied by the first gas molecules, the next incoming gas molecules will interact with sites with lower binding energy and so on, resulting to a decrease to the isosteric heat of adsorption. However there is another case in which the enthalpy of adsorption remains constant with increasing surface coverage. This behavior is attributed to the fact that all the binding sites occupied at the examined coverage, are of equal binding energy. Therefore all the incoming gas molecules interact in the same way with the framework at the specific surface coverage.[11]

We have also performed CH_4 adsorption measurements at 273 K and 298 K at 1 bar. $Zr_6O_4(OH)_4(NDC)_6$ adsorbs at 273 K and 1 bar 1.03 mmol g^{-1} of CH_4. We calculated the isosteric heat of adsorption and found a value of $Q_{st}^0 = 19.18$ kJ mol^{-1} using the virial equation, which is a very high value for MOFs without open metal sites, and among the UiO family of solids. Those findings prompted us to perform high pressure CH_4 measurements to evaluate $Zr_6O_4(OH)_4(NDC)_6$ towards methane storage. Indeed at 303 K and 26 bar the excess uptake reaches a value of 1.85 mmol g^{-1}. Additionally the CO_2/CH_4 selectivity was calculated using IAST for a 5/95 molar mixture at 273 K

and 298 K giving rise to a value of 8 and 6.4 respectively. Those values can be well compared with materials with open metal sites and are among the highest for the UiO family of MOFs.[12]

The second material was based on the linker 5, ($H_2NDC-2SO_3H$). The as synthesized MOF was characterized using pxrd analysis. The resulting material exhibits a pxrd pattern identical to the DUT-53 (Hf), which is a bcu type MOF with an 8 connected SBU instead of a 12 connected one for the fcu type, UiO MOFs. The formation of a bcu zirconium MOF can be obtained by the addition of excess amount of modulator (acetic acid or benzoic acid) that occupy the linker positions on the metal cluster. Many attempts to synthesize the 12 connected analogue were made, using lower equivalents of modulator, but all resulted to amorphous materials. Evidently the existence of the two bulky sulfonic groups ($-SO_3H$) leads to the formation of the bcu material due to steric effects. Because in the case of the fcu analogue the two side groups would be too close to each other. ^{1}H NMR measurements after acid digestion of the activated sample, revealed the presence of acetate ions in a 1:1 ratio with $H_2NDC-2SO_3H$. Therefore the resulting charged balanced chemical formula of the material is $Zr_6O_6(OH)_2(NDC-2SO_3H)_{2.5}(CH_3COO)_5$.

There have been made several attempts to activate the resulting material using acetone and other low boiling solvents, but all resulted to framework collapse upon solvent removal, since prior to activation the DMF solvent molecules were fully exchanged with the examined activation solvent as it was verified by NMR spectroscopy. The existence of the acidic pendant sulfonic groups was expected to increase significantly the interaction of the framework with CO_2, due to acid-base interactions.
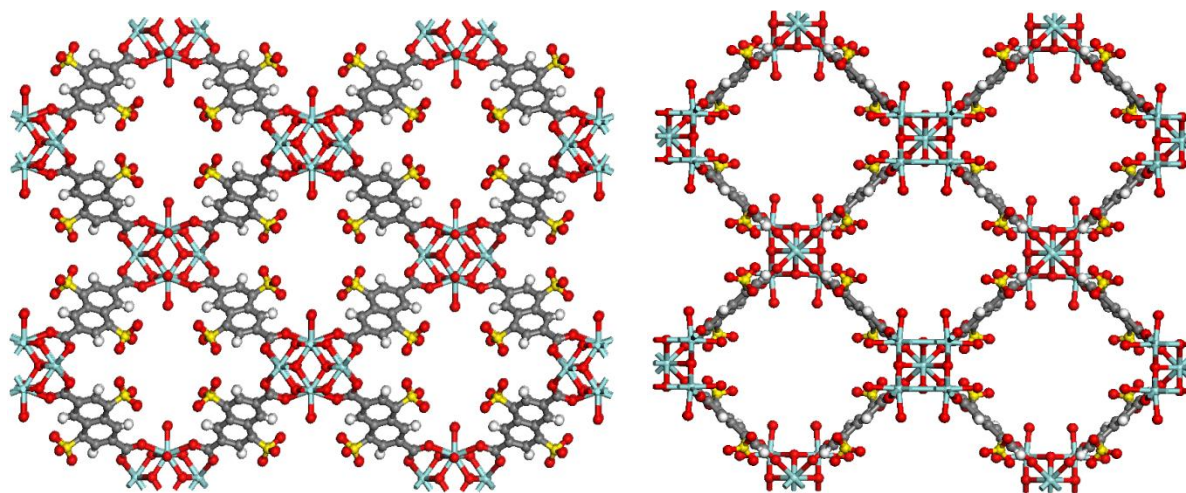
Figure 5.11. Left: Part of the 3-D crystal structure looking down the b axis, Right: Part of the 3-D crystal structure looking down the c axis. Turquoise spheres: Zr, gray: C, yellow: S, red: O, white: H. Solvent and acetate molecules are omitted for clarity.

The third material that was synthesized is based on linker 74 ($H_2NDC-SO_3H$). The resulting material was characterized using pxrd measurements. This synthetic procedure revealed an fcu MOF with a 12 connected SBU, as it is clear from the pxrd pattern, compared to the non-functionalized Zr-NDC analogue. Noticeably the existence of only one sulfonic functional group can result to the formation of a 12 connected SBU in contrast to the double sulfonic functionalized analogue, where only the

material with an 8 connected SBU can be synthesized. Interestingly this compound is air stable after two weeks in air which is something that was observed for the first time compared to all functionalized UiO type MOFs that were synthesized in this thesis. The reasons for this fact are not clear yet, and possible additional measurements will give insight to the explanation of this phenomenon. TGA analysis will reveal if the SBU is twelve connected with organic linkers and the framework is defect free. NMR measurements will reveal the existence of dimethylammonium counter anions, charge balancing the deprotonated sulfonic groups. In the first case a twelve connected with organic linkers SBU offers stability towards hydrolysis from the moisture of the air. On the other hand the existence of dimethylammonium ions inside the pores of the framework will block the incoming water molecules from reaching the SBU and start to decompose the framework.

The fourth material that was synthesized is based on linker 4 ($H_2NDC-2NH_2$). The resulting material was characterized using pxrd measurements. This synthetic procedure revealed an fcu MOF with a 12 connected SBU as it was clear from the characteristic pxrd pattern. There have been made only one attempt to activate this material, using acetone to exchange the DMF solvent molecules followed by acetone removal under vacuum, but apparently the material collapsed upon solvent removal. In this case the existence of the basic pendant amine groups was expected to increase significantly the interaction of the framework with CO_2, due to base-acid interactions. This stems from the fact that CO_2, can act both as a Lewis acid and a Lewis base.

The fifth material that was synthesized is based on linker 6 ($H_2NDC-2OH$). The resulting material was characterized using pxrd measurements. This synthetic procedure revealed an fcu MOF with a 12 connected SBU as it is clear from the pxrd pattern. Noticeably increasing the amount of acetic acid from 0.5 mL to 2 mL the bcu analogue was synthesized with an 8 connected SBU. After the successful characterization the evaluation of its gas sorption properties took place. The activation protocol can be found in Appendix B, and is the same for all MOFs based on Zr^{4+} SBUs. In this case the existence of the polar pendant hydroxyl groups was expected to increase the interaction of the framework with CO_2, due to dipole-induced dipole interactions.

Argon adsorption measurements at 87 K revealed a reversible pseudo Langmuir isotherm, with a small hysteresis step at P/P_0 0.45 and a step at P/P_0 0.02 which is an indication of existence of mesopores defects in the structure, that it is not microporous as it was expected to be.

The calculated surface area from the Argon isotherm was found to be 863 $m^2 g^{-1}$ (BET) and the total pore volume 0.43 $cm^3 g^{-1}$. ^1H NMR measurements after acid digestion of the activated sample, revealed the presence of acetate ions in a 1:1 ratio with $H_2NDC-2OH$. Therefore the resulting charged balanced chemical formula of the material is $Zr_6O_4(OH)_4(NDC-2OH)_3(CH_3COO)_6$. This means that the resulting material exhibits the fcu topology but at the same time it has a six connected SBU. The large number of the missing linkers resulted to the formation of mesopores in the structure as it was verified from pore size distribution analysis. Pore size distribution analysis using NLDFT, revealed

not only the presence of microporous at 6.4 Å, but an additional large broad peak at 20 Å, indicative of mesopores structures.

In order to evaluate its gas sorption properties we performed CO_2, H_2, and CH_4 sorption measurements. At 77 K and 1 bar $Zr_6O_4(OH)_4(NDC-2OH)_3(CH_3COO)_6$ adsorbs 0.97 wt% H_2 with a calculated Q_{st} value of 7.59 kJ mol^{-1}, with a sharp decline during H_2 loading. Those are typical values for low surface area MOFs without open metal sites.[13] CO_2 measurements revealed an uptake of 2.8 mmol g^{-1} at 273 K and 1 bar, while at 298 K and 1 bar the uptake reaches a value of 1.8 mmol g^{-1}, these findings are indicative for UiO type MOFs.[14] The calculated Q_{st}^0 for CO_2 was found to be as high as 30.07 kJ mol^{-1} with a sharp decline during CO_2 loading. This value is among the highest reported for UiO type MOFs. We have also performed CH_4 adsorption measurements at 273 K and 298 K at 1 bar. $Zr_6O_4(OH)_4(NDC-2OH)_3(CH_3COO)_6$ adsorbs at 273 K and 1 bar 0.71 mmol g^{-1} of CH_4. We calculated the isosteric heat of adsorption and found a value of $Q_{st}^0 = 18.94$ kJ mol^{-1}, which is a very high value for MOFs without open metal sites, and among the UiO family of solids. The high isosteric heat of adsorption for CO_2 prompted us to calculate the CO_2/CH_4 selectivity. It was calculated using IAST for a 5/95 molar mixture at 273 K and 298 K giving rise to impressive values of 11.5 and 8 respectively. Those values are among the highest reported within the UiO family of MOFs, and for materials without open metal sites.[15]

The sixth material that was synthesized is based on linker 2 ($H_2NDC-2NO_2$). Our synthetic methodology resulted to the formation of a highly crystalline new functionalized UiO type MOF with overall framework formula $Zr_6O_4(OH)_4(NDC-2NO_2)_{4.2}(CH_3COO)_{3.6}$ as it was verified by pxrd and ^1H NMR measurements. In this case the existence of the polar pendant nitro groups was expected to increase the interaction of the framework with CO_2, due to dipole-induced dipole interactions.

Argon adsorption measurements at 87 K revealed a fully reversible pseudo Langmuir isotherm, with a small step at P/P_0 0.02 which is an indication of existence of defects in the structure, that it is not totally microporous as it was expected to be. This stems from the fact that its pxrd pattern is identical to the crystalline microporous material Zr-NDC. These defects can originate from the missing linkers of the twelve connected SBU. Therefore the SBU could not be twelve connected but it is possible that some linkers are replaced either by acetate molecules or hydroxyl ions (-OH), leading to the formation of larger cavities, and thus defects in the crystal structure. The existence of the acetate molecules can be verified by ^1H NMR spectroscopy and the missing linker defects by TGA analysis. That is something we have observed and published recently.[16] TGA analysis of the activated material can give insight to the actual number of linkers that are connected to the SBU. Performing a TGA measurement under air or oxygen flow will oxidize all the organic part to CO_2, while the inorganic part will become ZrO_2. Pxrd measurements of this bright white solid will verify the formation of pure zirconia. If the theoretical weight loss of the organic part of the framework is identical to the experimental then the SBU is twelve connected by organic linkers. Therefore the framework formula would be $Zr_6O_4(OH)_4(L)_6$, and the framework is defect free.

The calculated surface area from the Argon isotherm was found to be 1273 $m^2 g^{-1}$ (BET) and the total pore volume 0.56 $cm^3 g^{-1}$. ^{1}H NMR measurements after acid digestion of the activated sample, revealed the presence of acetate ions in a 3.6:8.4 ratio with $H_2NDC-2NO_2$. Therefore the resulting charged balanced chemical formula of the material is $Zr_6O_4(OH)_4(NDC-2NO_2)_{4.2}(CH_3COO)_{3.6}$. To validate this result a blank measurement was performed, by dissolving glacial acetic acid in DMSO-d$_6$, followed by the addition of 1 drop of HF 40%. ^{1}H NMR measurements showed a sharp singlet at 1.90 ppm, if the solvent is locked at 2.50 ppm, indicative of the protons of the methyl group of acetic acid (CH_3COOH). Furthermore another blank experiment was performed in case the deuterated solvent is D_2O, that is base digestion instead of acid digestion. Glacial acetic acid was dissolved in D_2O, followed by the addition of 1 drop of NaOH 5N. ^{1}H NMR measurements showed a sharp singlet at 1.83 ppm, if the solvent is locked at 4.70 ppm, indicative of the protons of the methyl group of the acetate ion (CH_3COO^-). Pore size distribution revealed that the incorporation of the nitro groups diminished the pore space, from 9.3 Å and 7.5 Å for the non-functionalized analogue to 6.44 Å and 5.52 Å. However lack of data points in the micropore region didn't made possible the verification of the existence of mesopores from pore size distribution analysis.

In order to evaluate its gas sorption properties we performed CO_2, H_2, and CH_4 sorption measurements. At 77 K and 1 bar $Zr_6O_4(OH)_4(NDC-2NO_2)_{4.2}(CH_3COO)_{3.6}$ adsorbs 1.61 wt% H_2 with a calculated Q_{st} value of 7.64 kJ mol^{-1}, which are high values for low surface area MOFs without open metal sites.[17] CO_2 measurements revealed an impressive uptake of 4.64 mmol g^{-1} at 273 K and 1 bar, while at 298 K and 1 bar the uptake reaches a value of 2.85 mmol g^{-1}. At 195 K and 1 bar the material adsorbs an amount of 10.5 mmol g^{-1}. These findings are among the highest reported for UiO type MOFs.[18] The calculated Q_{st}^0 for CO_2 was found to be 26.6 kJ mol^{-1} remaining constant during CO_2 loading, which is a very desirable value. We have also performed CH_4 adsorption measurements at 273 K and 298 K at 1 bar. $Zr_6O_4(OH)_4(NDC-2NO_2)_{4.2}(CH_3COO)_{3.6}$ adsorbs at 273 K and 1 bar 1.16 mmol g^{-1} of CH_4. We calculated the isosteric heat of adsorption and found a value of $Q_{st}^0 = 17.67$ kJ mol^{-1} using the virial equation, remaining constant during methane loading, which is a very high value for MOFs without open metal sites, and among the UiO family of solids.[19] Additionally the CO_2/CH_4 selectivity was calculated using IAST for a 5/95 molar mixture at 273 K and 298 K giving rise to a value of 8 and 6 respectively. Those values can be well compared with materials with open metal sites and are among the highest for the UiO family of MOFs.[20]

At this point, we observed that the incorporation of the side functional groups did not increase significantly the gas uptake of the aforementioned materials. For that reason we used a mixed linker method to determine if the there is an optimum ratio among the linkers where the gas uptake is maximized. This synthetic methodology includes the use of the non functionalized linker H_2NDC and the functionalized linker $H_2NDC-2NO_2$. Three materials with different ratios of linkers were synthesized and characterized.

The first one of the three materials is a highly crystalline new functionalized UiO type MOF with overall framework formula $Zr_6O_4(OH)_4(NDC)_{4.4}(NDC\text{-}2NO_2)_{1.6}$ as it was verified by pxrd measurements and ^{1}H NMR measurements. An important question was whether this material is a single phase or a mixture of the two MOFs each one having only one ligand. To distinguish between these two cases the pxrd pattern is not informative because the two materials form the same structure. A solution to this important problem is to determine the pore size distribution from accurate Ar adsorption isotherms, performing a detailed microporous analysis. In the case of formation of only one phase, the pore size should be between the two ends (NDC and $NDC\text{-}NO_2$). Indeed, this is the case as we present in detail below.

After the efficient characterization of the material the evaluation of its gas sorption properties took place. Argon adsorption measurements at 87 K revealed a fully reversible pseudo Langmuir isotherm. ^{1}H NMR measurements, after acid digestion of the activated sample, revealed complete absence of acetate ions. Additionally, pore size distribution analysis showed not only sharp peaks at the micropore region but also a very small broad peak at 21 Å. Therefore it is possible that this material might contains a small amount of defects. That is the missing linkers of the cluster, can be replaced either by hydroxyl (-OH) or chloride groups (-Cl) to charge balance the framework.[21] However in this synthesis there was no HCl acid as a modulator used, but only acetic acid. EDS measurements can verify the absence or existence of Cl^- ions. In the case of absence the missing linkers can be replaced only by (-OH) groups. This can be verified by IR measurements, where it would be possible to see the O-H stretching region and compare it with a defect free material, containing only the inner μ_3-OH groups.

The calculated surface area from the Argon isotherm was found to be 1548 $m^2\,g^{-1}$ (BET) and the total pore volume 0.67 $cm^3\,g^{-1}$.

In order to evaluate its gas sorption properties we performed CO_2, H_2, and CH_4 sorption measurements. At 77 K and 1 bar $Zr_6O_4(OH)_4(NDC)_{4.4}(NDC\text{-}2NO_2)_{1.6}$ adsorbs 1.9 wt% H_2 with a calculated Q_{st} value of 7.69 $kJ\,mol^{-1}$, which are high values for low surface area MOFs and can be well compared to MOFs with open metal sites.[22] CO_2 measurements revealed an impressive uptake of 5.3 mmol g^{-1} at 273 K and 1 bar, while at 298 K and 1 bar the uptake reaches a value of 3.08 mmol g^{-1}, these findings are among the highest reported for UiO type MOFs.[23] The calculated Q_{st}^0 for CO_2 was found to be 25.78 $kJ\,mol^{-1}$ with a small decline during CO_2 loading. We have also performed CH_4 adsorption measurements at 112 K, 273 K and 298 K at 1 bar. $Zr_6O_4(OH)_4(NDC)_{4.4}(NDC\text{-}2NO_2)_{1.6}$ adsorbs at 112 K and 1 bar 15.15 mmol g^{-1} (339 $cm^3\,cm^{-3}$), while at 273 K and 1 bar it adsorbs 1.2 mmol g^{-1} of CH_4. We calculated the isosteric heat of adsorption and found a value of $Q_{st}^0 = 17$ $kJ\,mol^{-1}$, which is a very high value for MOFs without open metal sites, and among the UiO family of solids.[24] Additionally the CO_2/CH_4 selectivity was calculated using IAST for a 5/95 molar mixture at 273 K and 298 K giving rise to a value of 7.5 and 5.8 respectively. Those values can be well compared with materials without open metal sites and are among the highest for the UiO family of MOFs.[25]

The second one of the three materials is a highly crystalline new functionalized UiO type MOF with overall framework formula $Zr_6O_4(OH)_4(NDC)_{3.4}(NDC-2NO_2)_{2.3}(CH_3COO)_{0.6}$ as it was verified by pxrd measurements and ^1H NMR measurements.

After the efficient characterization of the material the evaluation of its gas sorption properties took place. Argon adsorption measurements at 87 K revealed a fully reversible pseudo Langmuir isotherm, with a small step at P/P_0 0.02 which is an indication of possible existence of defects in the structure, that it is not microporous as it was expected to be.

The calculated surface area from the Argon isotherm was found to be 1420 $m^2\,g^{-1}$ (BET) and the total pore volume 0.61 $cm^3\ g^{-1}$. ^1H NMR measurements after acid digestion of the activated sample, revealed the presence of acetate ions in a 1:7.6:11.4 ratio with $H_2NDC-2NO_2$ and H_2NDC respectively. Therefore the resulting charged balanced chemical formula of the material is $Zr_6O_4(OH)_4(NDC)_{3.4}(NDC-2NO_2)_{2.3}(CH_3COO)_{0.6}$. Pore size distribution revealed only the presence of microporous of 6.4 Å and 8.8 Å. Consequently the replacement of the organic linkers by acetate ions might have led to the formation of defects to the structure but not in the mesopore region, as it is obvious from pore size distribution analysis.

In order to evaluate its gas sorption properties we performed CO_2, H_2, and CH_4 sorption measurements. At 77 K and 1 bar $Zr_6O_4(OH)_4(NDC)_{3.4}(NDC-2NO_2)_{2.3}(CH_3COO)_{0.6}$ adsorbs 1.9 wt% H_2 with a calculated Q_{st} value of 7.66 kJ mol^{-1}, which are high values for low surface area MOFs without open metal sites.[26] CO_2 measurements revealed an impressive uptake of 13.26 mmol g^{-1} (297 $cm^3\ g^{-1}$) at 195 K, 5.7 mmol g^{-1} at 273 K and 1 bar, while at 298 K and 1 bar the uptake reaches a value of 3.3 mmol g^{-1}, these findings are among the highest reported for UiO type MOFs.[27] The calculated Q_{st}^0 for CO_2 was found to be 26.59 kJ mol^{-1} with a small decline during CO_2 loading. We have also performed CH_4 adsorption measurements at 112 K, 273 K and 298 K at 1 bar. $Zr_6O_4(OH)_4(NDC)_{3.4}(NDC-2NO_2)_{2.3}(CH_3COO)_{0.6}$ adsorbs at 112 K and 1 bar 13.66 mmol g^{-1} (306 cm^3 g^{-1}), while at 273 K and 1 bar it adsorbs 1.34 mmol g^{-1} of CH_4. We calculated the isosteric heat of adsorption and found a value of $Q_{st}^0 = 17.58$ kJ mol^{-1} remaining constant during methane loading, which is a very high value for MOFs without open metal sites, and among the UiO family of solids.[28] Additionally the CO_2/CH_4 selectivity was calculated using IAST for a 5/95 molar mixture at 273 K, 283 K and 298 K giving rise to a value of 8.2, 7.2 and 6.3 respectively. Those values can be well compared with materials with open metal sites and are among the highest for the UiO family of MOFs.[29]

The third one of the three materials is a highly crystalline new functionalized UiO type MOF with overall framework formula $Zr_6O_4(OH)_4(NDC)_2(NDC-2NO_2)_{2.8}(CH_3COO)_{2.4}$ as it was verified by pxrd measurements and ^1H NMR measurements.

Our synthetic methodology resulted to the formation of a highly crystalline new functionalized UiO type MOF with overall framework formula $Zr_6O_4(OH)_4(NDC)_2(NDC-2NO_2)_{2.8}(CH_3COO)_{2.4}$ as it was verified by pxrd measurements.

After the efficient characterization of the material the evaluation of its gas sorption properties took place. Nitrogen adsorption measurements at 77 K revealed a fully reversible pseudo Langmuir isotherm, with a small step at P/P_0 0.02 which is an indication of possible existence of defects in the structure, that it is not microporous as it was expected to be.

The calculated surface area from the Nitrogen isotherm was found to be 1283 m^2 g^{-1} (BET) and the total pore volume 0.57 cm^3 g^{-1}. ^1H NMR measurements after acid digestion of the activated sample, revealed the presence of acetate ions in a 1:2.4:1.7 ratio with $H_2NDC-2NO_2$ and H_2NDC respectively. Therefore the resulting charged balanced chemical formula of the material is $Zr_6O_4(OH)_4(NDC)_2(NDC-2NO_2)_{2.8}(CH_3COO)_{2.4}$. It was not possible to perform mircopore measurements, and determine the pore size distribution. This analysis could provide valuable information for the existence of mesopores in the structure. Consequently the replacement of the organic linkers by acetate ions might have led to the formation of defects to the structure.

In order to evaluate its gas sorption properties we performed CO_2, H_2, and CH_4 sorption measurements. At 77 K and 1 bar $Zr_6O_4(OH)_4(NDC)_2(NDC-2NO_2)_{2.8}(CH_3COO)_{2.4}$ adsorbs 1.67 wt% H_2 with a calculated Q_{st} value of 7.6 kJ mol^{-1}, which are high values for low surface area MOFs and can be well compared to MOFs with open metal sites.[30] CO_2 measurements revealed an uptake of 5 mmol g^{-1} at 273 K and 1 bar, while at 298 K and 1 bar the uptake reaches a value of 3.1 mmol g^{-1}, these findings are among the highest reported for UiO type MOFs.[31] The calculated Q_{st}^0 for CO_2 was found to be 25.65 kJ mol^{-1} with a small decline during CO_2 loading. We have also performed CH_4 adsorption measurements at 273 K and 298 K at 1 bar. $Zr_6O_4(OH)_4(NDC)_2(NDC-2NO_2)_{2.8}(CH_3COO)_{2.4}$ adsorbs at 273 K and 1 bar 1.4 mmol g^{-1}. We calculated the isosteric heat of adsorption and found an amazingly high value of Q_{st}^0 = 22.9 kJ mol^{-1} using the virial and the Clausius clapeyron equation, remaining constant during methane loading. This is the third highest reported value among MOFs, if the material $Zr_6O_4(OH)_4(BPDC-OCH_3)_{4.85}(CH_3COO)_{2.3}$ (see below) takes the second place with a value of 24.3 kJ mol^{-1} and the material SNU-50' holds the first place with a value of 26.8 kJ mol^{-1}.[32] Those findings prompted us to perform high pressure CH_4 measurements to evaluate $Zr_6O_4(OH)_4(NDC)_2(NDC-2NO_2)_{2.8}(CH_3COO)_{2.4}$ towards methane storage. Indeed at 298 K and 100 bar the total gravimetric uptake reaches a value of 177 cm^3 g^{-1}, while the total volumetric uptake was found to be 166 cm^3 cm^{-3}. The volumetric working capacity was estimated to be (between 65 bar and 5 bar) 99 cm^3 cm^{-3} which is a moderate value among MOFs. This is attributed to the very high isosteric heat of adsorption, which causes more methane to be left inside the storage tank at 5 bar (desorption pressure). Additionally the CO_2/CH_4 selectivity was calculated using IAST for a 5/95 molar mixture at 273 K and 298 K giving rise to a value of 6.6 and 6 respectively. Those values are indicative of MOFs without open metal sites and among the highest reported in the UiO family of MOFs.[33]

Comparison of functionalized Zr-MOFs based on H_2NDC

In this case the robust nature of the UiO family of solids was taken advantage for the synthesis and characterization of different functionalized MOFs based on the functionalized linker H_2NDC. The use of this linker in the UiO family of materials is limited and there are no reports whatsoever of the gas sorption properties of materials based on its functionalized analogues. Nine new functionalized UiO type MOFs have been successfully synthesized and extensive gas sorption properties at 1 bar are presented for six of them. (For clarity purposes the chemical formula of each material is simplified).

These materials exhibit moderate surface areas, ranging from 863 $m^2\,g^{-1}$ for the Zr-NDC-2OH material to 1548 $m^2\,g^{-1}$ (BET) for the Zr-NDC/NDC-2NO_2(2.8:1). As it was expected the introduction of functional groups increases the density of the resulting material resulting to a lower gravimetric surface area, in comparison to the parent non-functionalized material. However in the case of Zr-NDC/NDC-2NO_2(2.8:1) the calculated surface area is higher than the Zr-NDC analogue, while the pore volume is almost identical. This difference can be attributed to the existence of defects (missing linkers) in the functionalized material, as it was observed in the pore size distribution analysis.

In all cases the introduction of functional groups increases the gas uptake compared to the non-functionalized analogue, however at the same time reduces the accessible surface area. In our quest to enhance further the gas uptake of the functionalized materials we tested a mix linker strategy. In this case three different ratios among the linkers NDC and NDC-2NO_2 was used for the synthesis of a mix linker material Zr-NDC/NDC-2NO_2. The results of this experiment were impressive. For a certain ratio between the two linkers the amount of CO_2 and H_2 was maximized by 24% and 17% respectively compared to the fully functionalized material (see figures 5.13 and 5.14). The origin of the observed maximum is due to the fact that as the number of functional groups is increasing (increasing in this way the uptake), the available pore space is reduced (lowering the overall uptake). The maximum uptake was observed for a ratio of NDC:NDC-2NO_2 1.5:1. Apparently, this is the maximum synergistic effect between accessible surface area and number of functional groups.

In terms of CO_2 uptake at 273 K and 1 bar the best material was found to be the Zr-NDC/NDC-2NO_2(1.5:1) with a very high uptake of 20.1 wt% while in terms of CO_2 isosteric heat of adsorption the Zr-NDC-2OH material exhibited an impressive value of 30.1 kJ mol^{-1}. This is attributed to dipole-induce dipole interaction between the –OH groups and CO_2. But due to its almost half surface area compared to the Zr-NDC/NDC-2NO_2(1.5:1) material, its CO_2 uptake was a lot lower.

In terms of H_2 uptake at 77 K and 1 bar the best material is again Zr-NDC/NDC-2NO_2(1.5:1) with a very high value of 1.9 wt%, while in terms of H_2 isosteric heat of adsorption the four nitro functionalized materials exhibited very similar values of 7.65 kJ mol^{-1}. Apparently their bulky size compared to the hydroxyl groups confined the H_2 molecules inside the pores of the framework maximizing the interaction of the hydrogen molecules with the pore walls and between them. The shape of the H_2 isotherms (figure 5.13) depicts also the difference in the value of isosteric heat of

adsorption among those materials. The material with the highest Q_{st} value exhibits the steeper isotherm compared to the non-functionalized material with the lowest Q_{st}. This stems from the fact that at low pressures the material with the strongest binding sites can adsorb more gas molecules, due to their higher affinity for the framework compared to a material with sites with lower binding energy. In this second case only the increase of the pressure can drive the molecules inside the pores of the framework.[34]

In terms of CH_4 uptake at 273 K and 1 bar the best material is Zr-NDC/NDC-2NO$_2$(0.7:1) with an uptake of 1.43 mmol g^{-1}. This is in accordance to the very high value of isosteric heat of adsorption towards methane that this material exhibits, with an amazing value of 22.9 kJ mol^{-1} remaining constant during methane loading.
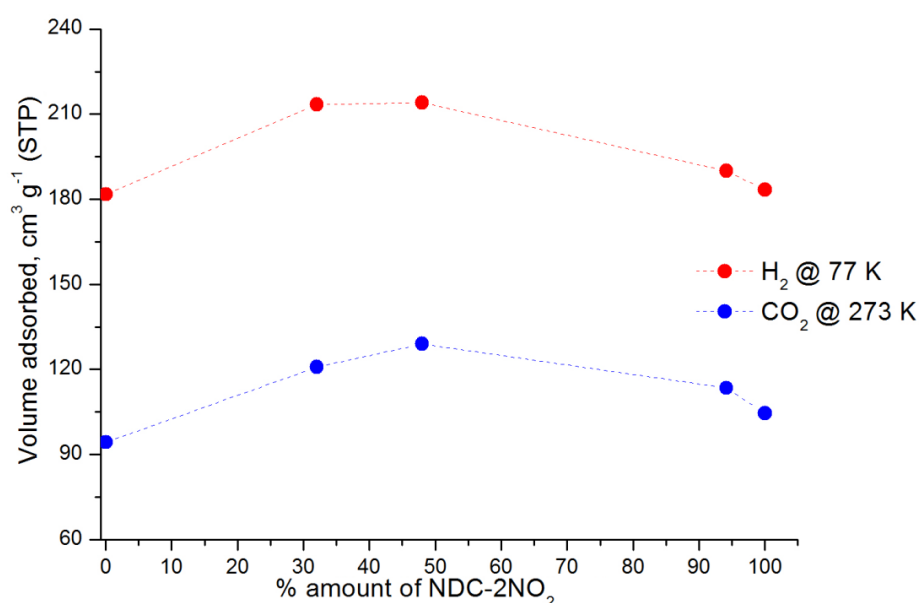
Figure 5.12. Distribution between the amount of gas adsorbed and the % of H$_2$NDC-2NO$_2$ substitution of compound Zr$_6$O$_4$(OH)$_4$(NDC-2NO$_2$)$_6$. For CO_2 and H_2 the compound with 48% ligand substitution exhibits the highest uptake.

Table 5.1. CO_2, CH_4, H_2 uptake and specific surface areas for the five examined materials in the mix linker strategy experiment.

% NDC-2NO$_2$	CO$_2$ uptake 273 K (cm^3 g^{-1})	H$_2$ uptake 77 K (cm^3 g^{-1})	CH$_4$ uptake 273 K (cm^3 g^{-1})	S.A BET (m^2 g^{-1})
100%	104	183	26	1273
94%	113	190	**32**	1283
48%	**128**	**214**	30	1420
32%	121	213	27	**1548**
0%	94	182	23	1451

Table 5.2. Comparison of selected gas sorption properties for six new UiO compounds based on the H$_2$NDC linker.

Organic linker	S. A BET (m^2 g^{-1})	CO$_2$ uptake 273 K (cm^3 g^{-1})	CO$_2$ Q$_{st}^0$ (kJ mol^{-1})	CH$_4$ uptake 112 K (cm^3 g^{-1})	CH$_4$ Q$_{st}^0$ (kJ mol^{-1})	H$_2$ uptake 77 K (cm^3 g^{-1})	H$_2$ Q$_{st}^0$ (kJ mol^{-1})
NDC-2NO$_2$	1273	104.5	26.6	288	17.67	183	7.64
NDC/NDC-2NO$_2$ (0.7:1)	1283	112.4	25.6	-	**22.9**	190	7.60
NDC/NDC-2NO$_2$ (1.5:1)	1420	**128**	26.6	306	17.58	**214**	7.66
NDC/NDC-2NO$_2$ (2.8:1)	**1548**	120	25.8	339	17	213	**7.69**
NDC	1451	93.6	26.3	-	19.18	182	7.48
NDC-2OH	863	63.0	**30.1**	-	18.94	110	7.59
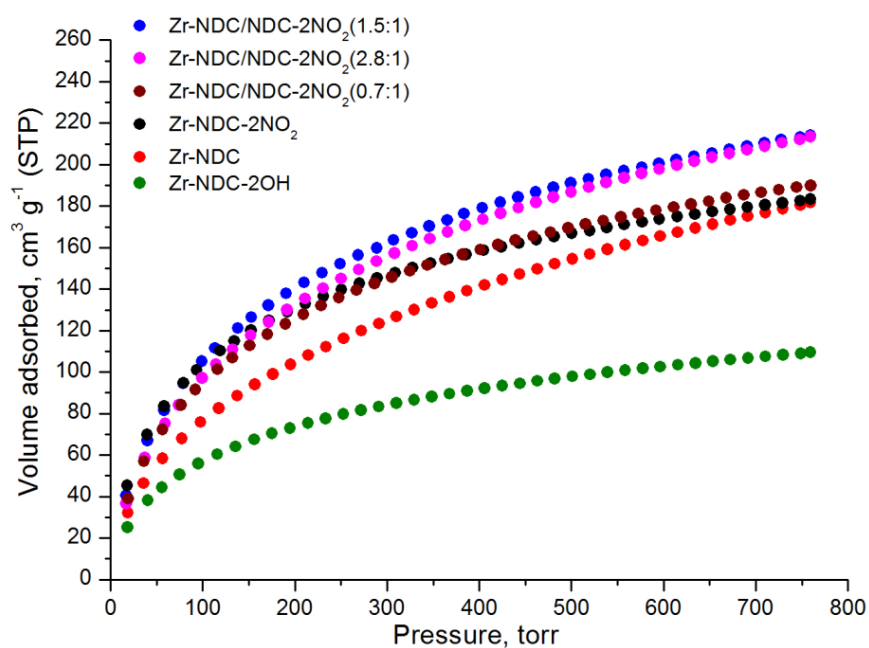
Figure 5.13. Hydrogen adsorption isotherms recorded at 77 K and 1 bar.

76
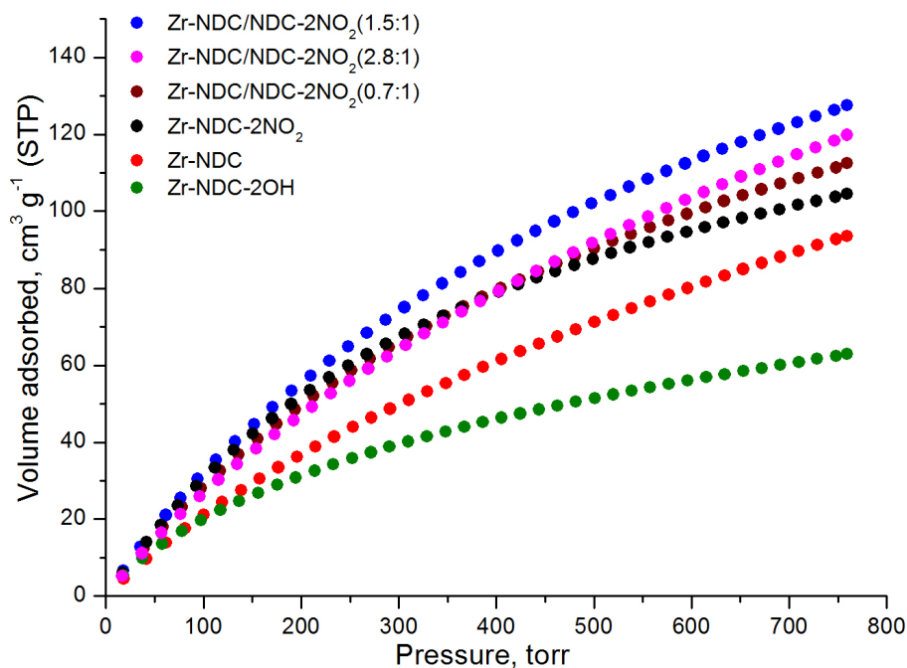
Figure 5.14. CO_2 adsorption isotherms recorded at 273 K and 1 bar.

Taking into account those results we tried to find a way to increase further the accessible surface area utilizing the same fcu topology. For this purpose we have designed and synthesized various functionalized organic linkers based on the commercially available biphenyl-4,4′-dicarboxylic acid (H_2BPDC). The longer length of this linker compared to the H_2NDC, can give rise to materials with higher surface areas. Therefore it is described below the synthesis, characterization and extensive gas-sorption properties of a series of functionalized UiO-67 type MOFs. Following this, there is a comparison of the gas sorption properties of the aforementioned materials.

The first material that it was examined, is based on the non functionalized linker H_2BPDC, and it was synthesized as a reference (blank) for comparison purposes. The resulting material was characterized using pxrd measurements. This synthetic procedure revealed an fcu MOF with a 12 connected SBU, as it is clear from the pxrd pattern, isostructural to the UiO-67 analogue. ^{1}H NMR measurements after acid digestion of the activated sample, revealed the presence of acetate ions in a 1:3.6 ratio with H_2BPDC. Therefore the resulting charged balanced chemical formula of the material is $Zr_6O_4(OH)_4(BPDC)_{4.7}(CH_3COO)_{2.6}$.

After the efficient characterization of the material the evaluation of its gas sorption properties took place. Argon adsorption measurements at 87 K revealed a reversible Langmuir isotherm, indicative of microporous materials. The calculated surface area from the Argon isotherm was found to be 2126 m^2 g^{-1} (BET) and the total pore volume 0.85 cm^3 g^{-1} close to the calculated one from the crystal structure 0.91 cm^3 g^{-1}.

In order to evaluate its gas sorption properties we performed CO_2, H_2, and CH_4 sorption measurements. At 77 K and 1 bar $Zr_6O_4(OH)_4(BPDC)_{4.7}(CH_3COO)_{2.6}$ adsorbs 1.51 wt% H_2 with a calculated Q_{st} value of 7.9 kJ mol^{-1} with a sharp decline during H_2 loading. The uptake has a typical

value for MOFs without open metal sites, while the high isoteric heat of adsorption is among the highest reported for UiO type MOFs.[35] CO_2 measurements revealed an uptake of 2.9 mmol g^{-1} at 273 K and 1 bar, while at 298 K and 1 bar the uptake reaches a value of 1.64 mmol g^{-1}, these findings are indicative for non-functionalized MOFs without open metal sites.[36] The calculated Q_{st}^0 for CO_2 was found to be 25.95 kJ mol^{-1} with a small decline during CO_2 loading. We have also performed CH_4 adsorption measurements at 112 K, 273 K and 298 K at 1 bar. $Zr_6O_4(OH)_4(BPDC)_{4.7}(CH_3COO)_{2.6}$ adsorbs at 112 K and 1 bar an impressive amount of 26.8 mmol g^{-1} (600 cm^3 g^{-1}, 448 cm^3 cm^{-3}), while at 273 K and 1 bar it adsorbs 0.9 mmol g^{-1} of CH_4. We calculated the isoteric heat of adsorption and found a value of Q_{st}^0 = 19.9 kJ mol^{-1} remaining constant during methane loading, which is a very high value for MOFs without open metal sites, and among the UiO family of solids.[37] High pressure measurements will reveal if this material could be used efficiently for methane storage applications. Additionally the CO_2/CH_4 selectivity was calculated using IAST for a 5/95 molar mixture at 273 K and 298 K giving rise to a value of 6.3 and 4.9 respectively. Those values can be well compared with materials without open metal sites and polar functional groups.[38]

The second material that was synthesized is based on linker 16 (H_2BPDC-OCH$_3$). The resulting material was characterized using pxrd measurements. This synthetic procedure revealed an fcu MOF with a 12 connected SBU, as it is clear from the pxrd pattern, compared to the non-functionalized UiO-67 analogue. ^{1}H NMR measurements after acid digestion of the activated sample, revealed the presence of acetate ions in a 1:4.2 ratio with H_2BPDC-OCH$_3$. Therefore the resulting charged balanced chemical formula of the material is $Zr_6O_4(OH)_4(BPDC-OCH_3)_{4.85}(CH_3COO)_{2.3}$.

After the efficient characterization of the material the evaluation of its gas sorption properties took place. Argon adsorption measurements at 87 K revealed a reversible Langmuir isotherm, indicative of microporous materials. The calculated surface area from the Argon isotherm was found to be 1895 m^2 g^{-1} (BET) and the total pore volume 0.70 cm^3 g^{-1}. The existence of the side methoxy groups diminishes the pore space as it is obvious from the pore size distribution analysis, there is a decline from 16 Å and 12 Å to 12 Å and 7.7 Å.

In order to evaluate its gas sorption properties we performed CO_2, H_2, and CH_4 sorption measurements. At 77 K and 1 bar $Zr_6O_4(OH)_4(BPDC-OCH_3)_{4.85}(CH_3COO)_{2.3}$ adsorbs 1.66 wt% H_2 with a calculated Q_{st} value of 7.6 kJ mol^{-1} with a sharp decline during H_2 loading, values which can be well compared to MOFs with open metal sites.[39] CO_2 measurements revealed an impressive uptake of 4.19 mmol g^{-1} at 273 K and 1 bar, while at 298 K and 1 bar the uptake reaches a value of 2.1 mmol g^{-1}, these findings are among the highest reported for UiO type MOFs.[40] The calculated Q_{st}^0 for CO_2 was found to be 27.59 kJ mol^{-1} with a small decline during CO_2 loading. We have also performed CH_4 adsorption measurements at 112 K, 273 K and 298 K at 1 bar. $Zr_6O_4(OH)_4(BPDC-OCH_3)_{4.85}(CH_3COO)_{2.3}$ adsorbs at 112 K and 1 bar an impressive amount of 22.24 mmol g^{-1} (498 cm^3 g^{-1}, 398 cm^3 cm^{-3}), while at 273 K and 1 bar it adsorbs 1.35 mmol g^{-1} of CH_4. We calculated the isoteric heat of adsorption and found an impressive value of Q_{st}^0 = 24.33 kJ mol^{-1} remaining constant

during methane loading, which is the second highest recorded for MOFs.[41] High pressure measurements will reveal if this material could be used efficiently for methane storage applications. Additionally the CO_2/CH_4 selectivity was calculated using IAST for a 5/95 molar mixture at 273 K and 298 K giving rise to a value of 5.5 and 5 respectively. Those moderate values are attributed to the higher affinity of the framework for CH_4 towards CO_2.[42]

The third material that was synthesized is based on linker 17 (H_2BPDC-OEt). The resulting material was characterized using pxrd measurements. This synthetic procedure revealed an fcu MOF with a 12 connected SBU, as it is clear from the pxrd pattern, compared to the non-functionalized UiO-67 analogue. ^{1}H NMR measurements after acid digestion of the activated sample, revealed the presence of acetate ions in a 1:2.5 ratio with H_2BPDC-OEt. Therefore the resulting charged balanced chemical formula of the material is $Zr_6O_4(OH)_4(BPDC\text{-}OEt)_{4.3}(CH_3COO)_{3.4}$. The material will be activated shortly.

The fourth material that was synthesized is based on linker 18 (H_2BPDC-OPr). The resulting material was characterized using pxrd measurements. This synthetic procedure revealed an fcu MOF with a 12 connected SBU, as it is clear from the pxrd pattern, isostructural to the non-functionalized UiO-67 analogue. ^{1}H NMR measurements after acid digestion of the activated sample, revealed a very small mount of acetate ions, a 1:56 ratio with H_2BPDC-OPr. Therefore the resulting charged balanced chemical formula of the material is $Zr_6O_4(OH)_4(BPDC\text{-}OPr)_6$.

After the efficient characterization of the material the evaluation of its gas sorption properties took place. Argon adsorption measurements at 87 K revealed a reversible Langmuir isotherm, indicative of microporous materials. The calculated surface area from the Argon isotherm was found to be 1706 m^2 g^{-1} (BET) and the total pore volume 0.63 cm^3 g^{-1}.

In order to evaluate its gas sorption properties we performed CO_2, H_2, and CH_4 sorption measurements. At 77 K and 1 bar $Zr_6O_4(OH)_4(BPDC\text{-}OPr)_6$ adsorbs 1.7 wt% H_2 with a calculated Q_{st} value of 7.72 kJ mol^{-1} with a sharp decline during H_2 loading, which can be well compared to MOFs with open metal sites.[43] CO_2 measurements revealed an impressive uptake of 3.8 mmol g^{-1} at 273 K and 1 bar, while at 298 K and 1 bar the uptake reaches a value of 2.1 mmol g^{-1}. The calculated Q_{st}^0 for CO_2 was found to be 28 kJ mol^{-1} with a small decline during CO_2 loading, these findings are among the highest reported for UiO type MOFs.[44] We have also performed CH_4 adsorption measurements at 112 K, 273 K and 298 K at 1 bar. $Zr_6O_4(OH)_4(BPDC\text{-}OPr)_6$ adsorbs at 112 K and 1 bar an impressive amount of 18.58 mmol g^{-1} (416 cm^3 g^{-1}, 353 cm^3 cm^{-3}), while at 273 K and 1 bar it adsorbs 1.07 mmol g^{-1} of CH_4. We calculated the isosteric heat of adsorption and found a high value of $Q_{st}^0 = 18.56$ kJ mol^{-1} remaining constant during methane loading, which is among the highest recorded for MOFs.[45] High pressure measurements will reveal if this material could be used efficiently for methane storage applications. Additionally the CO_2/CH_4 selectivity was calculated using IAST for a 5/95 molar mixture at 273 K and 298 K giving rise to a value of 8 and 6 respectively. Those values can be well

compared with materials with open metal sites and are among the highest for the UiO family of MOFs.[46]

The fifth material that was synthesized is based on linker 19 (H$_2$BPDC-OAllyl). The resulting material was characterized using pxrd measurements. This synthetic procedure revealed an fcu MOF with a 12 connected SBU, as it is clear from the pxrd pattern, isostructural to the non-functionalized UiO-67 analogue. ^{1}H NMR measurements after acid digestion of the activated sample, revealed the presence of acetate ions in a 1:5 ratio with H$_2$BPDC-OAllyl. Therefore the resulting charged balanced chemical formula of the material is Zr$_6$O$_4$(OH)$_4$(BPDC-OAllyl)$_5$(CH$_3$COO)$_2$.

After the efficient characterization of the material the evaluation of its gas sorption properties took place. Nitrogen adsorption measurements at 77 K revealed a reversible Langmuir isotherm, indicative of microporous materials. The calculated surface area from the Nitrogen isotherm was found to be 1622 m^2 g^{-1} (BET) and the total pore volume 0.64 cm^3 g^{-1}.

In order to evaluate its gas sorption properties we performed CO$_2$, H$_2$, and CH$_4$ sorption measurements. At 77 K and 1 bar Zr$_6$O$_4$(OH)$_4$(BPDC-OAllyl)$_5$(CH$_3$COO)$_2$ adsorbs 1.43 wt% H$_2$ with a calculated Q$_{st}$ value of 7.56 kJ mol^{-1} with a sharp decline during H$_2$ loading, which are typical values for MOFs without open metal sites.[47] CO$_2$ measurements revealed a high uptake of 3.4 mmol g^{-1} at 273 K and 1 bar, while at 298 K and 1 bar the uptake reaches a value of 1.95 mmol g^{-1}. The calculated Q$_{st}^0$ for CO$_2$ was found to be 25.77 kJ mol^{-1} with a small decline during CO$_2$ loading, these findings are among the highest reported for UiO type MOFs.[48] We have also performed CH$_4$ adsorption measurements at 273 K and 298 K at 1 bar. Zr$_6$O$_4$(OH)$_4$(BPDC-OAllyl)$_5$(CH$_3$COO)$_2$ adsorbs at 273 K and 1 bar it adsorbs 0.95 mmol g^{-1} of CH$_4$. We calculated the isosteric heat of adsorption and found an impressive value of Q$_{st}^0$ = 21.52 kJ mol^{-1} remaining constant during methane loading, which is among the highest recorded for MOFs.[49] High pressure measurements will reveal if this material could be used efficiently for methane storage applications. Additionally the CO$_2$/CH$_4$ selectivity was calculated using IAST for a 5/95 molar mixture at 273 K and 298 K giving rise to a value of 6.4 and 5.6 respectively. Those values can be well compared with materials without open metal sites.[50]

The sixth material that was synthesized is based on linker 20 (H$_2$BPDC-OPh). The resulting material was characterized using pxrd measurements. This synthetic procedure revealed an fcu MOF with a 12 connected SBU, as it is clear from the pxrd pattern, isostructural to the non-functionalized UiO-67 analogue. ^{1}H NMR measurements after acid digestion of the activated sample, revealed the presence of acetate ions in a 1:12.5 ratio with H$_2$BPDC-OPh. Therefore the resulting charged balanced chemical formula of the material is Zr$_6$O$_4$(OH)$_4$(BPDC-OPh)$_{5.5}$(CH$_3$COO)$_{0.9}$.

After the efficient characterization of the material the evaluation of its gas sorption properties took place. Argon adsorption measurements at 87 K revealed a type I isotherm, indicative of microporous materials. The calculated surface area from the Argon isotherm was found to be 1272 m^2 g^{-1} (BET) and the total pore volume 0.50 cm^3 g^{-1}.

In order to evaluate its gas sorption properties we performed CO_2, H_2, and CH_4 sorption measurements. At 77 K and 1 bar $Zr_6O_4(OH)_4(BPDC-OPh)_{5.5}(CH_3COO)_{0.9}$ adsorbs 1.31 wt% H_2 with a calculated Q_{st} value of 7.54 kJ mol^{-1} with a sharp decline during H_2 loading, which are typical values for MOFs without open metal sites.[51] CO_2 measurements revealed an impressive uptake of 3.7 mmol g^{-1} at 273 K and 1 bar, which is a high value among the UiO family of MOFs.[52] We have also performed CH_4 adsorption measurements at 112 K and 1 bar. $Zr_6O_4(OH)_4(BPDC-OPh)_6$ adsorbs at 112 K and 1 bar an impressive amount of 14.65 mmol g^{-1} (328 cm^3 g^{-1}, 278 cm^3 cm^{-3}). High pressure measurements will reveal if this material could be used efficiently for methane storage applications.

The seventh material that was synthesized is based on linker 21 ($H_2BPDC-OisoPr$). The resulting material was characterized using pxrd measurements. This synthetic procedure revealed an fcu MOF with a 12 connected SBU, as it is clear from the pxrd pattern, isostructural to the non-functionalized UiO-67 analogue. ^{1}H NMR measurements after acid digestion of the activated sample, revealed the presence of acetate ions in a 1:9 ratio with $H_2BPDC-OisoPr$. Therefore the resulting charged balanced chemical formula of the material is $Zr_6O_4(OH)_4(BPDC-OisoPr)_{5.4}(CH_3COO)_{1.2}$.

After the efficient characterization of the material the evaluation of its gas sorption properties took place. Argon adsorption measurements at 87 K revealed a reversible Langmuir isotherm, indicative of microporous materials. The calculated surface area from the Argon isotherm was found to be 1497 m^2 g^{-1} (BET) and the total pore volume 0.55 cm^3 g^{-1}.

In order to evaluate its gas sorption properties we performed CO2, H2, and CH4 sorption measurements. At 77 K and 1 bar Zr6O4(OH)4(BPDC-OisoPr)5.4(CH3COO)1.2 adsorbs 1.54 wt% H2 with a calculated Qst value of 7.66 kJ mol-1 with a sharp decline during H2 loading, values which can be well compared to MOFs with open metal sites.[53] CO2 measurements revealed an impressive uptake of 3.5 mmol g^{-1} at 273 K and 1 bar, while at 298 K and 1 bar the uptake reaches a value of 2.1 mmol g^{-1}. The calculated Q_{st}^0 for CO_2 was found to be 27.79 kJ mol^{-1} with a small decline during CO_2 loading, these findings are among the highest reported for UiO type MOFs.[54] We have also performed CH_4 adsorption measurements at 112 K and 1 bar. $Zr_6O_4(OH)_4(BPDC-OisoPr)_{5.4}(CH_3COO)_{1.2}$ adsorbs at 112 K and 1 bar an impressive amount of 17 mmol g^{-1} (381 cm^3 g^{-1}, 324 cm^3 cm^{-3}). However those values can be achieved at RT only under very high pressures. Therefore high pressure measurements will reveal if this material could be used efficiently for methane storage applications.

The eighth material that was synthesized is based on linker 22 ($H_2BPDC-Obenzyl-F$). The resulting material was characterized using pxrd measurements. This synthetic procedure revealed an fcu MOF with a 12 connected SBU, as it is clear from the pxrd pattern, isostructural to the non-functionalized UiO-67 analogue. ^{1}H NMR measurements after acid digestion of the activated sample, revealed the presence of acetate ions in a 1:2.5 ratio with H_2BPDC- Obenzyl-F. Therefore the resulting charged balanced chemical formula of the material is $Zr_6O_4(OH)_4(BPDC-Obenzyl-F)_{4.3}(CH_3COO)_{3.4}$.

After the efficient characterization of the material the evaluation of its gas sorption properties took place. Argon adsorption measurements at 87 K revealed a reversible Langmuir isotherm, indicative of

microporous materials. The calculated surface area from the Argon isotherm was found to be 1175 m^2 g^{-1} (BET) and the total pore volume 0.47 $cm^3 g^{-1}$.

In order to evaluate its gas sorption properties we performed CO_2, H_2, and CH_4 sorption measurements. At 77 K and 1 bar $Zr_6O_4(OH)_4(BPDC\text{-}Obenzyl\text{-}F)_{4.3}(CH_3COO)_{3.4}$ adsorbs 1.2 wt% H_2 with a calculated Q_{st} value of 7.76 kJ mol^{-1} with a sharp decline during H_2 loading. The low uptake is indicative for low surface area MOFs without open metal sites, while the high isosteric heat of adsorption is among the highest in the UiO family of MOFs and can be well compared to materials with open metal sites.[55] CO_2 measurements revealed an impressive uptake of 3.17 mmol g^{-1} at 273 K and 1 bar, while at 298 K and 1 bar the uptake reaches a value of 1.75 mmol g^{-1}. The calculated Q_{st}^0 for CO_2 was found to be 27.59 kJ mol^{-1} with a small decline during CO_2 loading, these findings are among the highest reported for UiO type MOFs.[56] We have also performed CH_4 adsorption measurements at 112 K, 273 K and 298 K at 1 bar. $Zr_6O_4(OH)_4(BPDC\text{-}Obenzyl\text{-}F)_{4.3}(CH_3COO)_{3.4}$ adsorbs at 112 K and 1 bar an impressive amount of 14.07 mmol g^{-1} (315 $cm^3 g^{-1}$), while at 273 K and 1 bar it adsorbs 0.86 mmol g^{-1} of CH_4. We calculated the isosteric heat of adsorption and found a high value of $Q_{st}^0 = 19$ kJ mol^{-1} remaining constant during methane loading, which is among the highest recorded for MOFs, including the UiO type of MOFs.[57] High pressure measurements will reveal if this material could be used efficiently for methane storage applications. Additionally the CO_2/CH_4 selectivity was calculated using IAST for a 5/95 molar mixture at 273 K and 298 K giving rise to a value of 7.2 and 5.7 respectively. Those values can be well compared with materials with open metal sites and are among the highest in the UiO family of MOFs.[58]

The ninth material that was synthesized is based on linker 24 ($H_2BPDC\text{-}Obenzyl\text{-}5F$). The resulting material was characterized using pxrd measurements. This synthetic procedure revealed an fcu MOF with a 12 connected SBU, as it is clear from the pxrd pattern, isostructural to the non-functionalized UiO-67 analogue. However its gas sorption properties aren't evaluated yet.

Comparison of functionalized Zr-MOFs based on H_2BPDC

The robust nature of the UiO-67 (Zr-biphenyl) along with its high specific surface area, were taken advantage for the synthesis and characterization of different modified MOFs based on the functionalized linker H_2BPDC. The use of this linker in the UiO family of materials is well studied but we present here novel functionalities and evaluate their performance in terms of gas adsorption. For that purpose eight new functionalized UiO-67 MOFs have been successfully synthesized and extensive gas sorption properties at 1 bar are presented for six of them. (For clarity purposes the chemical formula of each material is simplified).

These materials exhibit surface areas ranging from 1175 $m^2 g^{-1}$ for the Zr-BPDC-ObenzylF material to 1895 $m^2 g^{-1}$ (BET) for the Zr-BPDC-OMe. For comparison purposes a non-functionalized UiO-67 analogue was synthesized under identical conditions. As it was expected the introduction of functional

groups decreases the available pore space resulting in materials with lower gravimetric surface area, in comparison to the parent non-functionalized material. Furthermore a previously published by us UiO-67 functionalized material, the Zr-BPDC-SO$_2$ is added to the comparison list as a reference.

In terms of CO$_2$ uptake at 273 K and 1 bar the best of the new materials was found to be the Zr-BPDC-OMe with an uptake of 15.6 wt%, lower than the Zr-BPDC-SO$_2$ with an uptake of 17.5 wt%. This difference is ascribed to the highly polar nature of the –SO$_2$ groups compared to the –OCH$_3$ groups.[59] When it comes to CO$_2$ isosteric heat of adsorption the Zr-BPDC-OPr material exhibited an impressive value of 29.1 kJ mol^{-1}. It is possible that the long side propyl chains may confine the CO$_2$ molecules inside the pores of the framework resulting in enhanced interaction between the molecules and between the molecules and the framework. However its uptake was lower than the Zr-BPDC-OMe analogue. This is attributed to the fact that the Zr-BPDC-OPr material has a lower surface area. Apparently the incorporation of the pendant polar groups increased the interaction of the framework with CO$_2$ substantially, taking into account the fact that the non functionalized material with similar surface area with Zr-BPDC-OMe, has a lot lower uptake.

In terms of H$_2$ uptake at 77 K and 1 bar the best material is Zr-BPDC-OPr with a high value of 1.7 wt%, while in terms of H$_2$ isosteric heat of adsorption the highest value was found to be 7.6 kJ mol^{-1} for the Zr-BPDC-ObenzylF compound. In this case the large bulky side group may confine significantly the hydrogen molecules inside the pores of the framework resulting in enhanced interaction between the molecules and between the molecules and the framework. However due to its very low surface area compared to the other materials it exhibited a lower H$_2$ uptake. Apparently in this case the surface area determines the maximum uptake and not the existence of functional groups. That's because the non functionalized material has a little lower H$_2$ uptake than the functionalized materials with similar surface area.

In terms of CH$_4$ uptake at 273 K and 1 bar the best material is Zr-BPDC-OMe with an uptake of 1.35 mmol g^{-1}. This is in accordance to the very high value of isosteric heat of adsorption towards methane, 24.3 kJ mol^{-1}, which remains constant during methane loading. It must be mentioned at this point that the gas uptake of a material is determined by a combination of factors. Apart from the surface area and the existence of functional groups and open metal sites, the most important parameter seems to be the packing of the gas molecules inside the pores of the framework. The interaction of the gas molecules with each other and their optimum "packing" can maximize the gas uptake of a material. However that is something that can be verified only by means of theoretical calculations and it is well established in the literature.[60]

Table 5.3. Comparison of selected gas sorption properties for eight UiO-67 compounds based on different functionalized organic linkers.

Organic linker	S. A BET ($m^2\ g^{-1}$)	CO_2 uptake 273 K ($cm^3\ g^{-1}$)	CO_2 Q_{st} ($kJ\ mol^{-1}$)	CH_4 uptake 112 K ($cm^3\ g^{-1}$)	CH_4 Q_{st} ($kJ\ mol^{-1}$)	H_2 uptake 77 K ($cm^3\ g^{-1}$)	H_2 Q_{st} ($kJ\ mol^{-1}$)
BPDC-ObenzylF	1175	71	27.5	315	19	137	**7.6**
BPDC-Obenzyl	1272	84	-	328	-	149	7.2
BPDC-SO$_2$	1442	**108**	26.5	-	14.5	165	7.2
BPDC-OisoPr	1497	78	27.5	381	-	169	7.3
BPDC-OAllyl	1622	76	25.5	-	21.4	163	7.2
BPDC-OPr	1706	66	**29.1**	416	18.6	**193**	7.3
BPDC-OMe	1895	94	27.5	498	**24.3**	189	7.3
BPDC	**2126**	68	25.9	**600**	19.9	172	7.5
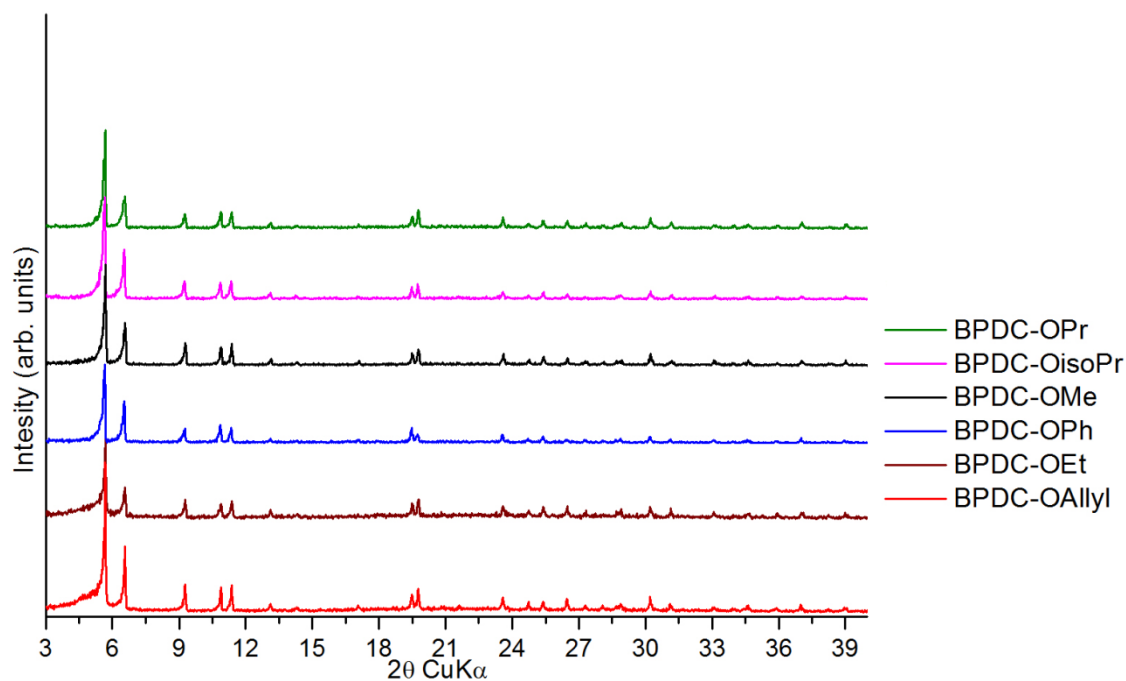
Figure 5.15. Comparison of experimental pxrd patterns for six functionalized UiO-67 analogues.
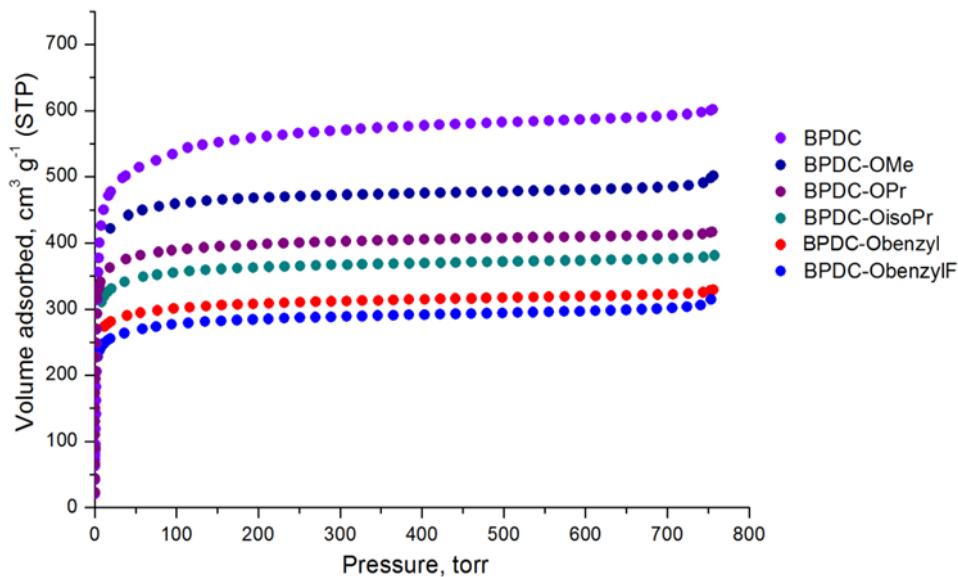
Figure 5.16. CH_4 adsorption isotherms recorded at 112 K and 1 bar.
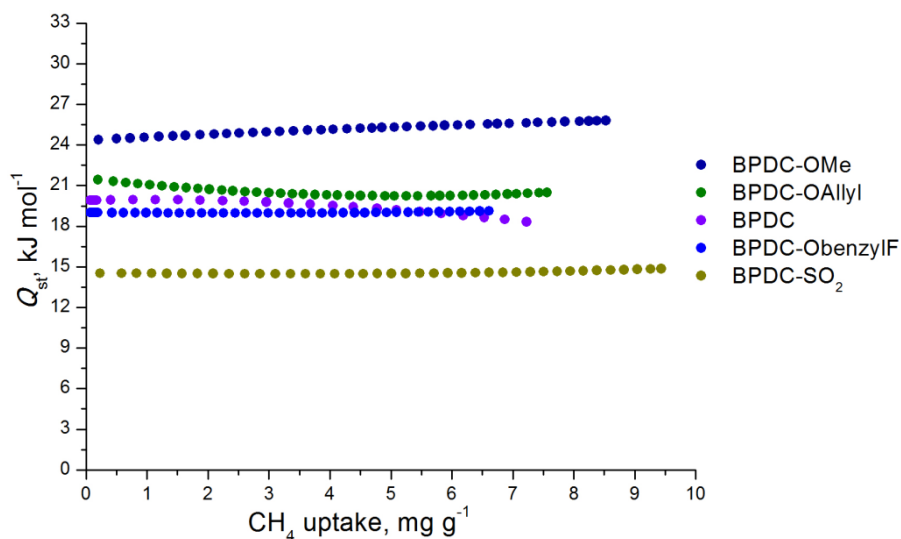
Figure 5.17. CH_4 isosteric heats of adsorption as a function of surface coverage.
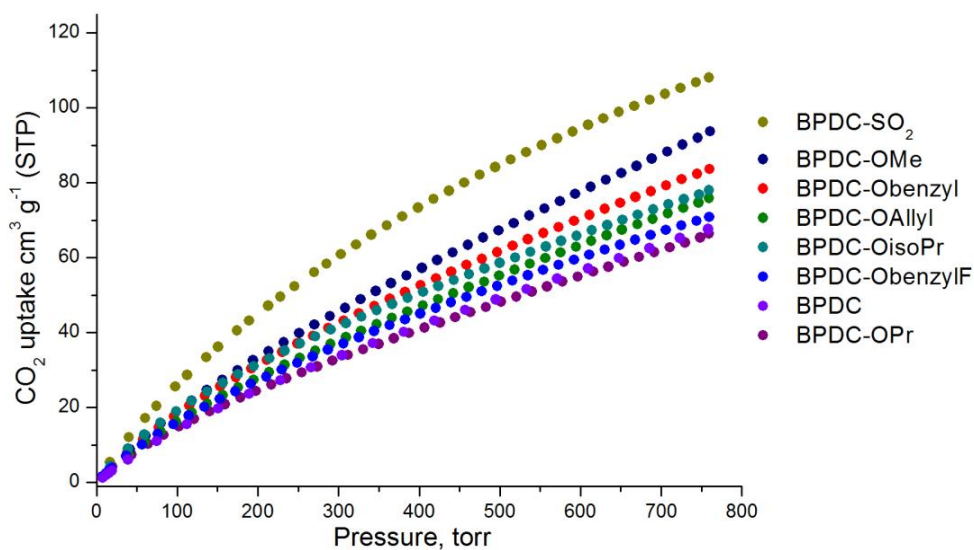
Figure 5.18. CO_2 adsorption isotherms recorded at 273 K and 1 bar.
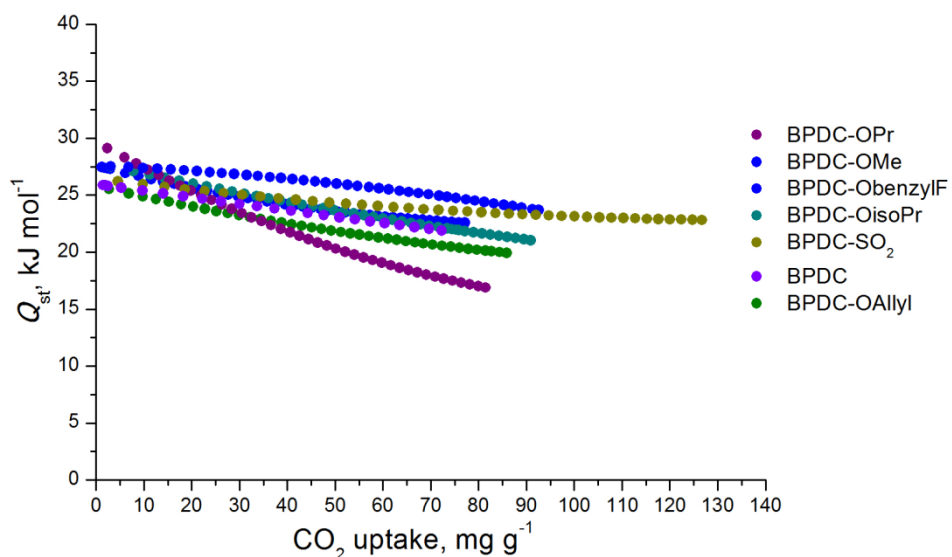
Figure 5.19. CO_2 isosteric heats of adsorption as a function of surface coverage.
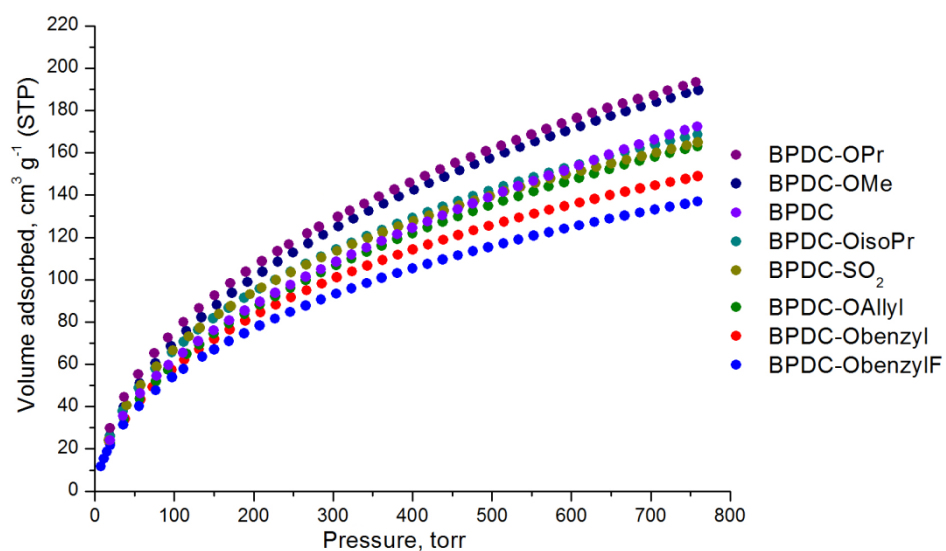
Figure 5.20. Hydrogen adsorption isotherms recorded at 77 K and 1 bar.
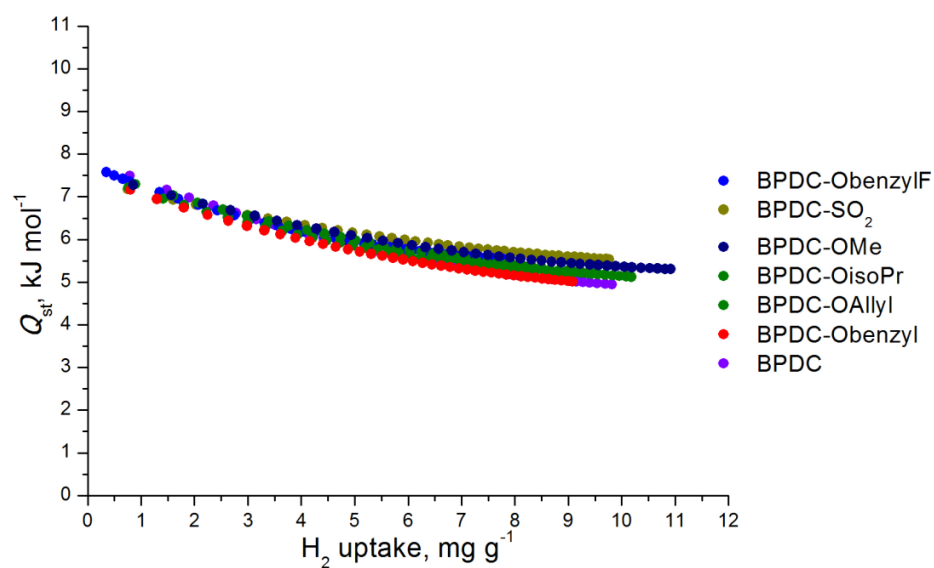
Figure 5.21. H_2 isosteric heats of adsorption as a function of surface coverage.

Taking a step further, we wanted to increase even more the accessible surface area. This could be possible by using longer organic linkers than the H_2BPDC, that was used for the synthesis of UiO-67 materials. For this purpose we synthesized two functionalized organic linkers based on p-terphenyl-4,4″-dicarboxylic acid (H_2TPDC). An increased surface area along with the existence of more functional groups per linker could result to a material with enhanced gas sorption properties.

The first material that was synthesized is based on linker 31 ($H_2TPDC-3NO_2$). This material was characterized using pxrd measurements. This synthetic procedure revealed an fcu MOF with a 12 connected SBU, isostructural to UiO-68 as it is clear from the pxrd pattern. Noticeably increasing the amount of acetic acid from 0.5 mL to 2 mL the bcu analogue with an 8 connected SBU was synthesized. ^1H NMR measurements after acid digestion of the activated sample, revealed only traces of acetate ions. Therefore the resulting charged balanced chemical formula of the material is $Zr_6O_4(OH)_4(TPDC-3NO_2)_6$.

After the efficient characterization of the material the evaluation of its gas sorption properties took place. Argon adsorption measurements at 87 K revealed a fully reversible pseudo Langmuir isotherm. The calculated surface area from the Argon isotherm was found to be 3448 $m^2 g^{-1}$ (BET) and the total pore volume 1.11 $cm^3 g^{-1}$. Pore size distribution revealed that the incorporation of the nitro groups diminished the pore space, from 25 Å and 7 Å for the non-functionalized analogue to 18 Å and 6.2 Å, taking into account the van der Waals radii. Furthermore it is clear from the pore size distribution that there is no indication of formation of mesopores. In accordance to NMR analysis. Therefore the SBU of the material is 12 connected with organic linkers.

In order to evaluate its gas sorption properties CO_2, H_2, and CH_4 sorption measurements were performed. At 77 K and 1 bar $Zr_6O_4(OH)_4(TPDC-3NO_2)_6$ adsorbs 1.39 wt% H_2 with a calculated Q_{st} value of 6.99 kJ mol^{-1} with a sharp decline during H_2 loading. This low uptake is indicative for high surface area MOFs without open metal sites.[61] CO_2 measurements revealed an impressive uptake of 25.33 mmol g^{-1} (567 $cm^3 g^{-1}$) at 195 K and 1 bar, 4.14 mmol g^{-1} at 273 K and 1 bar, while at 298 K and 1 bar the uptake reaches a value of 2.56 mmol g^{-1}. These findings are among the highest reported for UiO type MOFs and higher than the functionalized UiO-68 analogues.[62] The calculated Q_{st}^0 for CO_2 was found to be 23 kJ mol^{-1} with a sharp decline during CO_2 loading. We have also performed CH_4 adsorption measurements at 273 K and 298 K at 1 bar. $Zr_6O_4(OH)_4(TPDC-3NO_2)_6$ adsorbs at 273 K and 1 bar it adsorbs 1 mmol g^{-1} of CH_4. We calculated the isosteric heat of adsorption and found a high value of $Q_{st}^0 = 15.21$ kJ mol^{-1} with a small decline during methane loading, which is among the highest values reported for MOFs, including the UiO type of MOFs.[63] Additionally the CO_2/CH_4 selectivity was calculated using IAST for a 5/95 molar mixture at 273 K and 298 K giving rise to a value of 7.1 and 5.8 respectively. Those values can be well compared with materials with open metal sites and are among the highest for the UiO family of MOFs.[64]

The second material that was synthesized is based on linker 27 ($H_2TPDC-2OH$). The resulting material was characterized using pxrd measurements. This synthetic procedure revealed an fcu MOF

with a 12 connected SBU, isostructural to UiO-68 as it is clear from the pxrd pattern. UiO-68 is an fcu MOF synthesized from Zr^{4+} ions and the organic linker p-terphenyl dicarboxylic acid (H_2TPDC). Noticeably increasing the amount of the modulator, acetic acid, from 0.5 mL to 2 mL the bcu analogue with an 8 connected SBU was synthesized. However its gas sorption properties aren't evaluated yet.

The third material that was synthesized is based on linker 26 (H_2TPDC-2SO_2). The resulting material was characterized using pxrd measurements. Although it was possible to acquire single crystals the crystal structure of this material using single crystal XRD measurements couldn't be determined. The resulting MOF was highly crystalline and it was compared to all three UiO type MOFs exhibiting different SBU connectivity (12, 8, 6). Apparently the pxrd pattern doesn't look similar to any of the three different UiO type MOFs. Therefore its crystal structure can only be determined by means of single crystal XRD.

Apparently the significant increase in the surface area followed by the existence of pendant polar functional groups didn't improve the gas sorption properties of those materials. This is evident by the fact that the functionalized Zr-NDC analogues with the same functional groups (-NO_2) and 50% less accessible surface area outperform the nitro functionalized UiO-68 analogue. Evidently the gas sorption properties of those functionalized fcu materials can be maximized only by the existence of narrow pores that are decorated with polar functional groups and confine the gas molecules. In this way the interaction of the targeted gas molecules with the framework is enhanced both by the presence of the polar groups and from the overlallaping potentials of the walls of the framework.

After those results we tried alternative combinations of critical parameters that affect the gas sorption properties of a porous material. In this case we utilized a different functional group, the amide group (-NH-CO-) that was found to interact strongly with CO_2.[65] Therefore new linear organic linkers were synthesized each one carrying two amide groups and two hydroxyl groups. Those linkers were employed again for the synthesis of fcu type MOFs, due to their inherent stability.

The first material that was synthesized is based on linker 66 (H_2L). This material was characterized using pxrd measurements. This synthetic procedure revealed an fcu MOF with a 12 connected SBU, isoreticular to UiO type MOFs. The longer size of H_2L in comparison to H_2TPDC results to a larger unit cell than UiO-68 as it is clear from the pxrd pattern. A shift of the pxrd pattern to lower 2θ angles, therefore higher values of d spacing, is indicative of a larger unit cell.

The second material that was synthesized is based on linker 67 (H_2L). The resulting material was characterized using pxrd measurements. This synthetic procedure revealed an fcu MOF with a 12 connected SBU, isoreticular to UiO type MOFs. The longer size of H_2L in comparison to H_2TPDC and H_2TPHN linear organic linkers results to a larger unit cell than both UiO-68 and mpt-MOF[66] as it is clear from the pxrd pattern. A shift of the pxrd pattern to lower 2θ angles, therefore higher values of d spacing, is indicative of a larger unit cell. These findings prove that this new MOF exhibits the larger unit cell and pore volume reported so far among the UiO family of MOFs. Noticeably the use of this longer organic linker didn't result to the formation of the interpenetrated PIZOF analogues.[67]
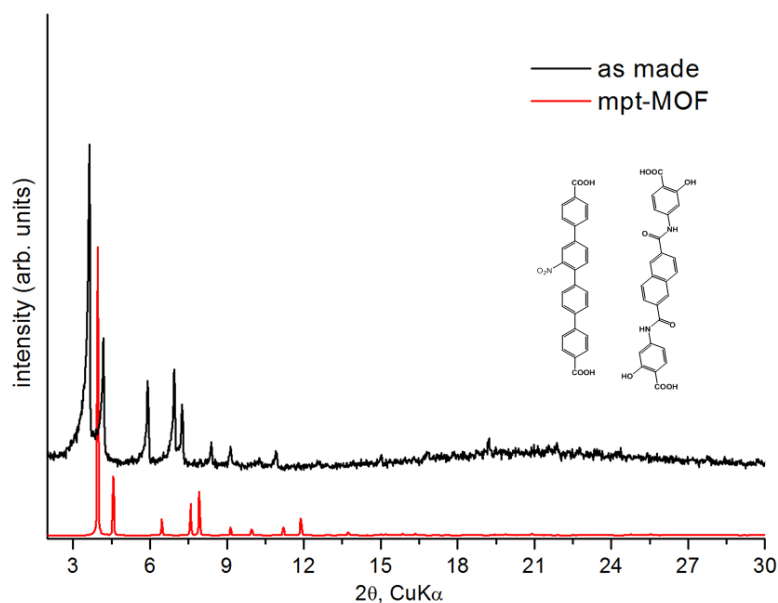
<u>Figure 5.22.</u> Experimental pxrd pattern for the compound $Zr_6O_4(OH)_4(L)_6$ compared to the calculated mpt-MOF pxrd pattern. Inset figure shows the two organic linkers, to the right is the amide functionalized one and to the left the linker of the mpt-MOF compound.

As it was reported earlier the Zr^{4+} SBUs can exhibit different connectivities (6, 8, 12). This means that by altering the connectivity a new material with specific topology can be synthesized. For this reason we wanted to see if the formation of a different network other than the fcu, can give rise to highly porous materials with interesting gas sorption properties. These new topologies could offer the advantage of the formation of cavities with various shape and size, otherwise inaccessible in the fcu topology. We have therefore synthesized the trigonal tritopic organic linker 32 (H_3BTB) that would be used for the synthesis of robust and moisture stable MOFs.

Solvothermal reaction of Zr^{4+} ions with the organic linker 32 resulted to the synthesis of a highly crystalline material. The material was characterized using pxrd measurements. Due to the absence of single crystals we tried to find the potential crystal structure by taking into account the possible combinations of Zr^{4+} SBUs with a tritopic organic linker. So far they are recorded only four possible binodal edge-transitive nets, the *the*, the *pyr*, the *spn* and the *ttt* net.[68] The first one results from the combination of a tritopic organic linker and an eight connected SBU, that is a (3,8) connectivity. The following two result from the combination of a tritopic organic linker and a six connected SBU, that is a (3,6) connectivity. The third one results from the combination of a tritopic organic linker and a twelve connected SBU, that is a (3,12) connectivity. By comparing the as synthesized pattern of the examined material with the calculated patterns of three compounds exhibiting the the-a, the spn-a and the ttt-a net a conclusive result could not be obtained.
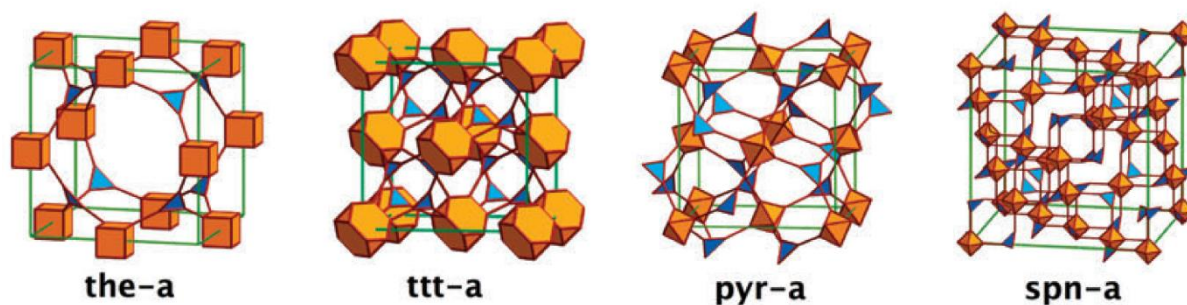
Figure 5.23. The (3,8) connected the-a, the (3,12) ttt-a and the (3,6) pyr-a and spn-a edge-transitive nets in augmented form.[69]

Nonetheless, during our attempts to activate this material and evaluate its gas sorption properties, Wang and coworkers published a work based on the same organic linker and the same metal ion.[70] Single crystal XRD measurements revealed that they have synthesized an interpenetrated material with chemical formula $Zr_6(\mu_3\text{-}O)_4(\mu_3\text{-}OH)_4(OH)_6(H_2O)_6(BTB)_2$. A $Zr_6(\mu_3\text{-}O)_4(\mu_3\text{-}OH)_4$ octahedral core is connected by six carboxylate groups from six BTB ligands in the ac plane, and each BTB ligand is connected to three $Zr_6(\mu_3\text{-}O)_4(\mu_3\text{-}OH)_4$ octahedral cores to give rise to a 2D framework. However the parallel 2D layers of one set are displaced with each other and interpenetrate perpendicularly with another set of parallel 2D nets to generate a 3D open framework with 3,6-connected kgd topology and 1D square channels. Comparison of the calculated pxrd pattern of this compound and experimental pxrd pattern of the compound based on linker 32 verified that those materials are isostructural. Therefore our synthetic methodology lead to the synthesis of the compound $Zr_6(\mu_3\text{-}O)_4(\mu_3\text{-}OH)_4(OH)_6(H_2O)_6(BTB)_2$.
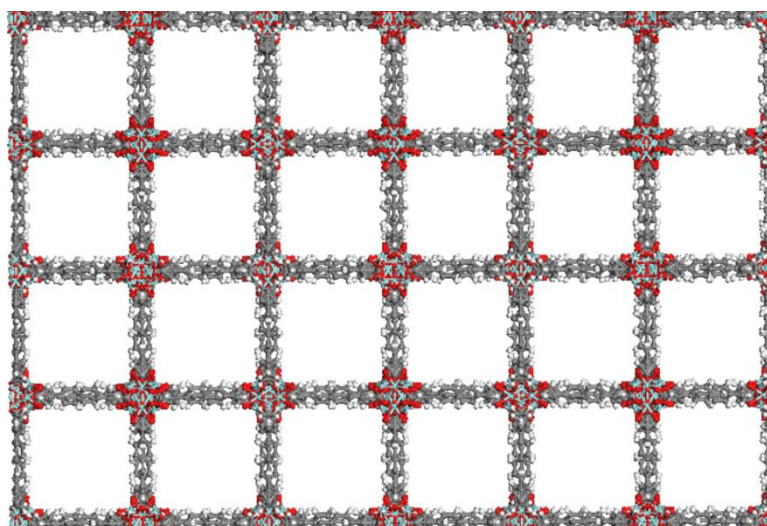
Figure 5.24. Part of the 3-D crystal structure looking down the c axis. The one 2-D net is vertical and the other identical 2-D net is horizontal. Turquoise spheres: Zr, gray: C, red: O, white: H.

Continuing our quest to target the synthesis of specific networks with trigonal linkers we synthesized the expanded tritopic trigonal linker 36 functionalized with eight nitro groups. Solvothermal reaction of Zr^{4+} ions with the organic linker 36 resulted to the synthesis of a highly crystalline material. The resulting material was characterized using pxrd measurements. Due to the absence of single crystals the potential crystal structure could be predicted by taking into account the possible combinations of Zr^{4+} SBUs with a tritopic organic linker. We compared again the experimental pxrd pattern with the calculated patterns of known edge-transitive nets, the *the*, the *pyr*, the *spn* and the *ttt* net. However in this case the experimental pxrd pattern doesn't look similar to any of those calculated ones. Furthermore it is likely that an interpenetrated compound might have been synthesized as it was observed with the previous material. Yet again the two patterns look similar but they are not identical. Therefore only if a single crystal is acquired would be possible to determine the structure of this MOF.
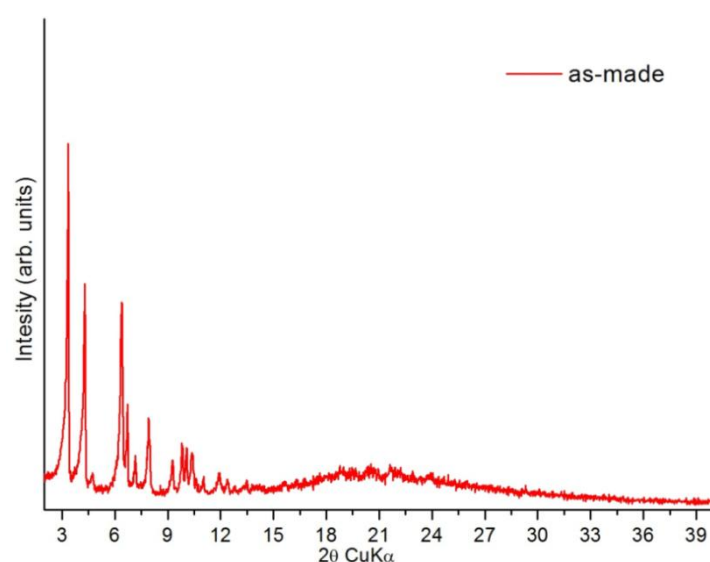
Figure 5.25. Experimental pxrd pattern for compound 6.22.1.

Another promising net that offers the possibility to construct highly porous and robust frameworks based again on Zr^{4+} SBUs is the *flu* network. Recently Zhang et al. reported the synthesis of a highly porous non-interpenetrated material PCN-521 with the fluorite (*flu*) topology.[71] This MOF is synthesized from the non-functionalized organic linker 4',4'',4''',4''''-methanetetrayltetrabiphenyl-4-carboxylate, (H_4MTBC) and an 8 connected Zr_6O_8 SBU. Each SBU connects to eight organic linkers and each organic linker connects to four SBUs, resulting to a 4,8-connected net with the fluorite (*flu*) topology.[72] The framework exhibits two types of large cavities one tetrahedral and one octahedral. However its gas sorption properties were not evaluated. It is possible therefore that the use of the same functionalized linker could result again to the formation of material with the same topology. Additionally the presence of large number of polar functional groups per linker could result to a porous material with enhanced gas sorption properties. We have therefore synthesized the nitro functionalized linker H_4MTBC-8NO_2, bearing eight functional groups per linker.

Our synthetic procedure revealed a MOF isostructural to PCN-521. Comparison of experimental and calculated from the single crystal structure pxrd patterns verified the successful synthesis of the nitro functionalized PCN-521 analogue as a pure product. However its gas sorption properties haven't been evaluated yet.
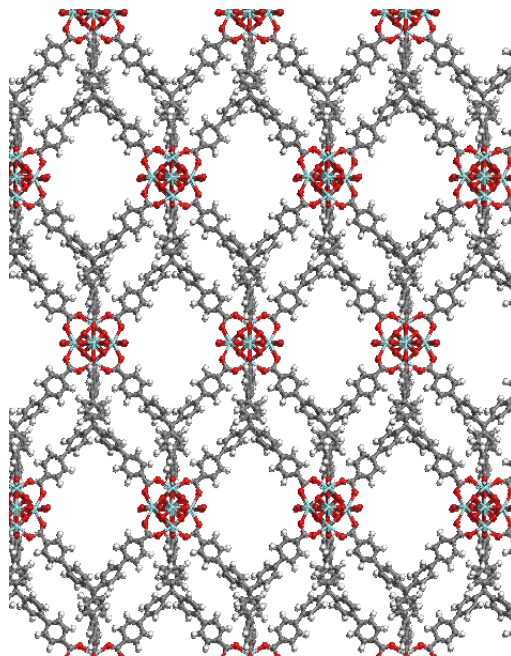
Figure 5.26. Part of the 3-D crystal structure of PCN-521 looking down the a axis. Turquoise spheres: Zr, gray: C, red: O, white: H. Solvent molecules are omitted for clarity.

Furthermore we have synthesized the same organic linker bearing pendant sulfone groups. Those polar groups are expected to increase substantially the interaction of specific gas molecules (e.g. CO_2) with the framework. Two different synthetic procedures were utilized for the successful synthesis of a highly crystalline material. Comparison of experimental and calculated from the single crystal structure pxrd patterns verified the successful synthesis of the sulfone functionalized PCN-521 analogue as a pure product. This material is also isostructural to the nitro functionalized PCN-521 compound. However its gas sorption properties haven't been evaluated yet.

Interestingly combination of a Zr^{4+} SBU and a tetratopic organic linker can give rise to different type of frameworks each one with unique structural characteristics. Taking into account the possible combinations of Zr^{4+} SBUs with a tetratopic organic linker it was found that there are only three possible structures. The first one results from the combination of a tetratopic organic linker and a twelve connected SBU, that is a (4,12) connectivity. The second one results from the combination of a tetratopic organic linker and an eight connected SBU, that is a (4,8) connectivity. And the third one results from the combination of a tetratopic organic linker and a six connected SBU, that is a (4,6) connectivity. In the first case an *ftw* or a *shp* topology is formed. The *ftw* topology is observed in materials NU-1100[73] and MOF-525[74], while the *shp* topology is observed in compound PCN-223.[75] In the second case a kagome like lattice is formed with *csq-a* topology. This topology is observed in the

92

materials NU-1000,[76] PCN-222[77] and MOF-545.[75] In the last case a net with *she-a* topology is formed as in the case of material PCN-224.[78] In all these examples the organic part was a tetragonal porphyrin except for NU-1000 where the organic part is the pseudo tetragonal linker H_4TBAPy. Of those structures a most promising one in terms of high porosity and post modification is the csq net found in NU-1000. This material has already been extensively studied and poses a versatile structure that can exhibit apart from the high accessible surface area, open metal Zr^{4+} sites.[79] Taking all these into account we have designed and synthesized the expanded rectangular tetratopic organic linker 43.

Solvothermal reaction of this linker with Zr^{4+} ions resulted to the formation of a highly crystalline material. The resulting material was characterized using pxrd measurements. Although this synthetic procedure allowed the formation of single crystals, the structure of this material couldn't be determined through single crystal XRD measurements. However in this case it was possible to compare the experimental pxrd pattern with some calculated patterns from known crystal structures containing tetragonal or rectangular organic linkers and Zr^{4+} metal ions. The comparison revealed that its pxrd pattern is similar to compound NU-1000. Therefore it exhibits a kagome type of lattice with two kinds of 1-D channels, one hexagonal and one triangular. However due to the slightly shorter distance among the carboxylate groups in our linker compared to the H_4TBAPy, it is expected that both the hexagonal and the triangular channels would be a little smaller. Although there are similarities between the calculated pxrd pattern of MOF-525 and the examined material, the structure of MOF-525 was excluded, because in this case the net must be composed of a tetragonal linker. That is the distances of the four carboxylate groups must be identical. Something that is not feasible in our case.

There have been many attempts to activate this material using low boiling solvents, but so far it was not possible to evaluate its gas sorption properties.
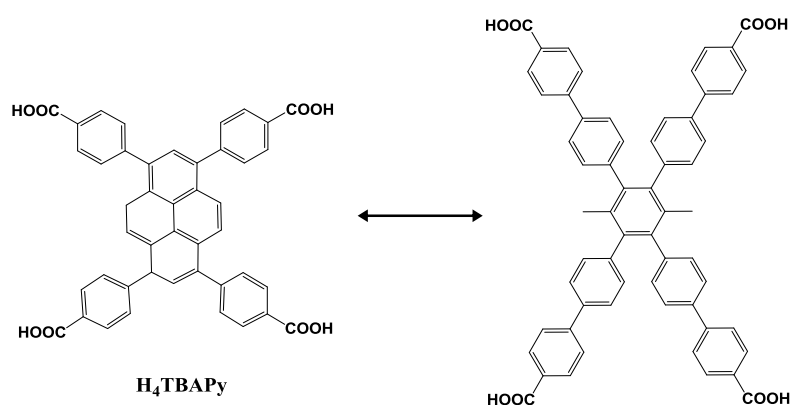
Figure 5.27. Right: the H_4TBAPy organic linker of compound NU-1000. Left: the expanded organic linker 43.
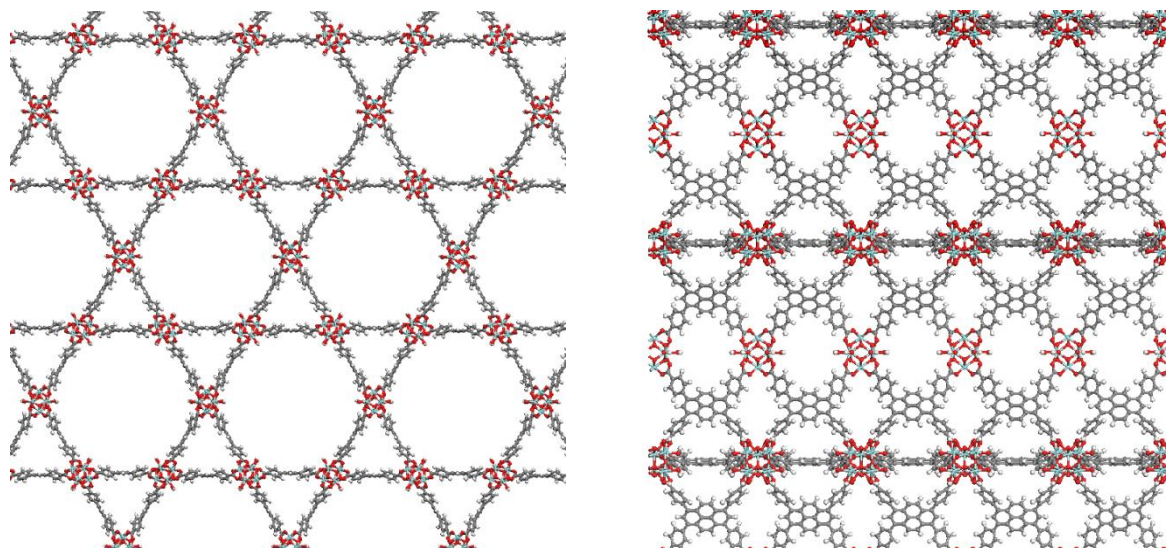
Figure 5.28. Left: the two types of channels in NU-1000, Right: part of the 3-D crystal structure of NU-1000 looking down the a axis. Turquoise spheres: Zr, gray: C, red: O, white: H. Solvent molecules are omitted for clarity.
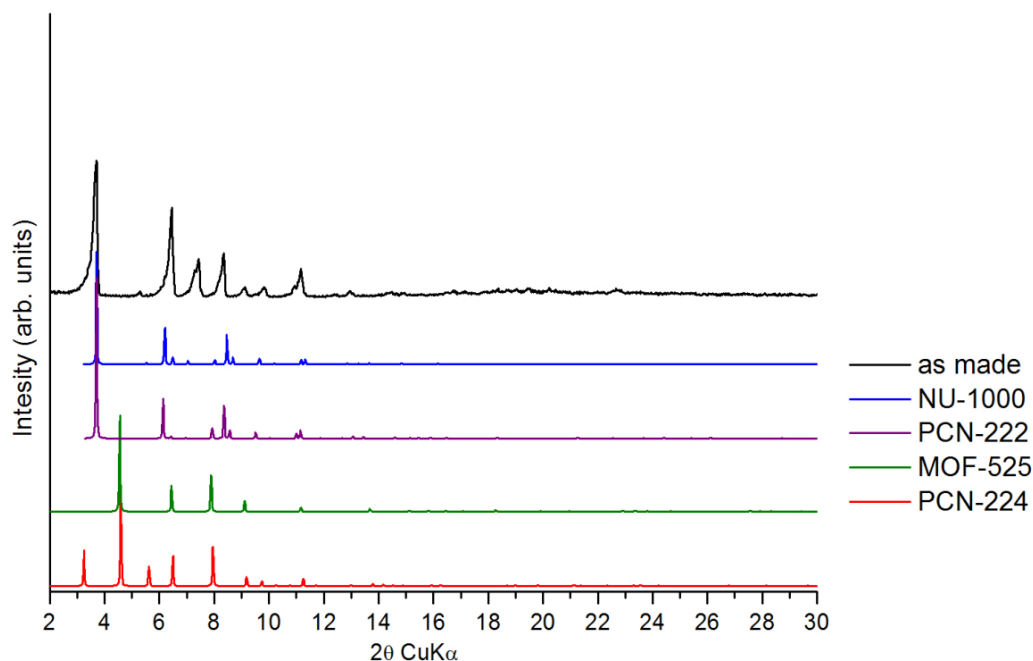
Figure 5.29. Comparison of experimental pxrd pattern of the examined compound and calculated patterns of compounds NU-1000, PCN-222, MOF-525 and PCN-224.

After the synthesis of linkers with various shapes and sizes and their successful implementation in MOF synthesis, we designed the exotic hexatopic organic linker 51. The idea behind the design and synthesis of this linker was the formation of a functionalized organic linker, bearing a graphene type core. This could be possible by a close up reaction of the six central benzene rings (see figure 5.30).[80] The fusion of the central benzene rings would create a small graphene core made from 13 benzene rings, while the existence of the terminal carboxy groups would allow both the coordination of metal ions and the easy dissolution of the linker into a polar solvent (e.g. DMF). The resulting linker could be used for the syntheses of MOFs bearing a graphene functionality. This functionalization was

94

expected to bestow upon the resulting material interesting properties,[81] and lay the path for the synthesis of a new family of graphene type MOFs. However this close up reaction could be made only with the iodo compound, and not with the bromine or chloro compound (see Appendix D). Therefore it was not possible to synthesize the organic linker bearing the graphene core. So the resulting hexacarboxylate linker was used for the synthesis of MOFs, as it could lead to potential unknown topologies and frameworks with interesting gas sorption properties.
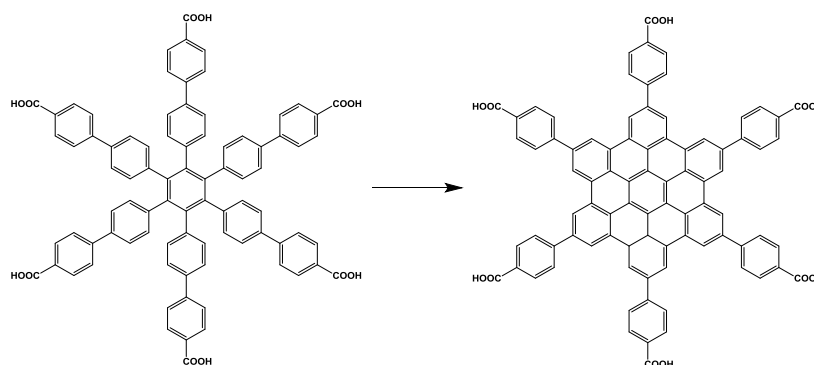
Figure 5.30. Close up reaction of the benzene rings for the formation of a graphene core.
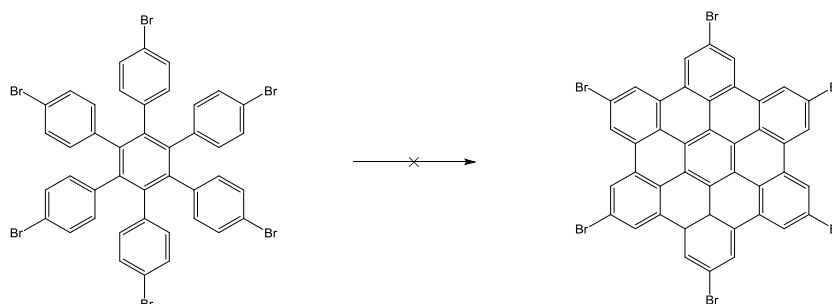
Figure 5.31. Under the examined experimental conditions it was not possible to acquire the desired product.

If it is taken into account that the previous material based on linker 43 has a kegome structure, then the use of a linker with six arms instead of four could possibly create the same network and the two central arms would reside freely into the pores of the framework without metal coordination. In this way the existence of acidic pendant carboxylic acid groups would increase the interaction of the framework with specific gas molecules. Therefore solvothermal reaction of linker 51 with Zr^{4+} ions resulted to the formation of small cubic single crystals. Although this synthetic procedure allowed the formation of single crystals, the structure of this material couldn't be determined through single crystal XRD measurements. So the resulting material was characterized using pxrd measurements.

Apparently comparison of the experimental pxrd patterns of this compound and the previous one strongly suggests that those materials are isostructural. There have been made efforts to activate this material including acetone exchange of the DMF molecules. However the determination of the exact crystal structure through single crystal XRD measurements could provide information about the total

pore volume and surface area of the aforementioned material. Otherwise it could not be possible to find out if an activation procedure can give access to the total accessible pore volume of the MOF without framework collapse.
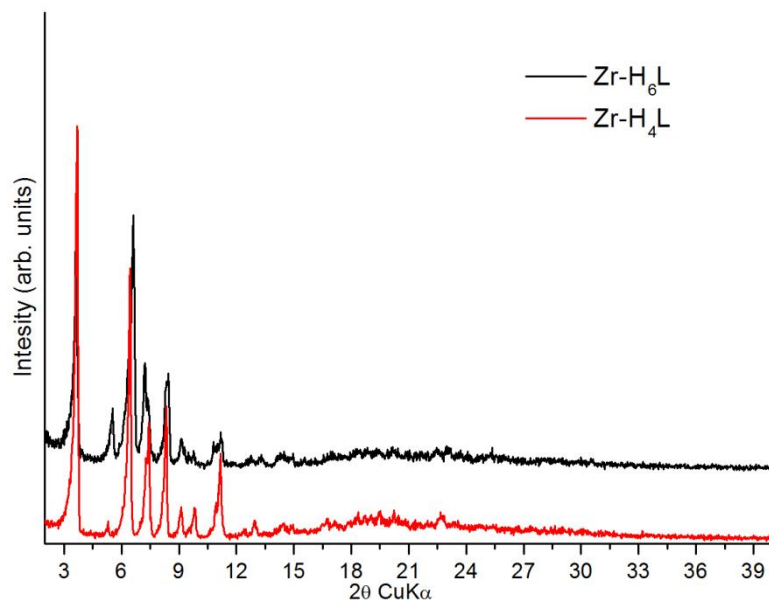
Figure 5.32. Comparison of experimental pxrd patterns for compounds Zr-H_6L and Zr-H_4L.

5.2 Syntheses of functionalized IRMOFs

Another important family of MOFs is the IRMOFs. Those materials are composed of linear ditopic carboxylate organic linkers and an octahedral [Zn_4O] SBU.[82] The main characteristic is their tunable porosity, since by increasing the length of the organic linker the surface area of the material can be substantially increased. Additionally they offer uniform cubic pores, again with tunable pore size. Yet a most important characteristic is the fact that the organic linkers can be functionalized with pendant functional groups that point into the pores enhancing in this way the interaction of the framework with specific gas molecules (e.g. CO_2, CH_4, H_2).[83]

Taking these into account we used the functionalized organic linkers 2, 3, 5, 6, based on H_2NDC for the synthesis of functionalized IRMOF-8 analogues. In this case the large number of functional groups per organic linker (24 groups per cubic pore), along with the high porosity of the material is expected to increase significant the gas uptake of specific gas molecules.

The first material that was synthesized is the IRMOF-8-2OH, which was synthesized using the H_2NDC-2OH linker. Solvothermal reaction with Zn^{2+} ions resulted to the formation of large dark orange cubic crystals. The large single crystals made possible the determination of the structure of this MOF. Through single crystal X-ray difractometry the structure was solved revealing the hydroxyl-IRMOF-8 analogue. It crystallizes in the cubic system (space group Fm$\bar{3}$m), isostructural to the non functionalized IRMOF-8, with a unit cell parameter a = 30.174(4) Å. This is a non-interpenetrated

structure based on the pseudo-octahedral $Zn_4O(-CO_2)_6$ secondary building unit (SBU). It is build up by four tetrahedral Zn^{2+} ions linked together by an O^{2-} ion. Each SBU is linked to six organic linkers and each organic linker connects two SBUs, resulting to an overall framework formula $Zn_4O(NDC-2NO_2)_3$. The structure consists of cubic interconnected 1-D channels. Powder X-ray diffraction analysis verified the formation of a pure phase as the calculated and experimental powder pattern are identical.
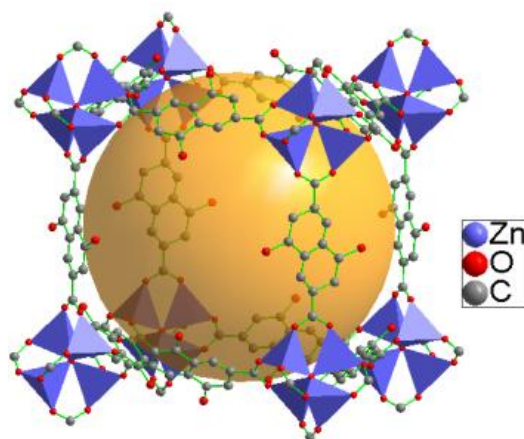
Figure 5.33. Part of the cubic framework of IRMOF-8-2OH as determined from single-crystal X-ray diffraction data. For clarity, only one orientation of the disordered NDC-2OH ligands is shown. The orange sphere indicates pore space. Hydrogen atoms are omitted for clarity.

Nitrogen adsorption measurements at 77 K revealed a calculated specific surface area of 1927 m^2 g^{-1} (BET). This value is almost the half than the calculated from the crystal structure 4352 m^2 g^{-1}. This can be attributed to partial collapse of the framework during activation process. Hydrogen adsorption measurements showed an uptake of 0.95 wt% at 1 bar and 77 K, while the calculated H_2 Q_{st} value at zero coverage was found to be 5.2 kJ mol^{-1}. CO_2 measurements were performed at 298 K and 273 K at 1 bar. An uptake of 2.5 mmol g^{-1} was recorded at 273 K while the calculated isosteric heat of adsorption was found to be 12.5 kJ mol^{-1}. CH_4 adsorption measurements were also performed at 273 K and 298 K at 1 bar. At 273 K an uptake of 0.4 mmol g^{-1} was recorded. The calculated CO_2/CH_4 selectivity at zero coverage, using the IAST model, at 298 K/273 K was 9.6/13.6. These selectivity values are among the highest reported for MOFs based on $Zn_4O(-CO_2)_6$ SBUs.[84]

The second material that was synthesized is the IRMOF-8-NO$_2$, which was synthesized using the $H_2NDC-NO_2$ linker. Solvothermal reaction with Zn^{2+} ions resulted to the formation of large yellow cubic crystals. The resulting crystalline material is isostructural to the non-functionalized IRMOF-8, a 3- D cubic non interpenetrated structure. This was verified by the comparison of the experimental and the calculated pxrd pattern that were identical. It must be mentioned that IRMOF-NO$_2$ decomposes rapidly upon exposure to air. However its gas sorption properties are not evaluated yet.

The third material that was synthesized is the IRMOF-8-2SO$_3$H, which was synthesized using the $H_2NDC-2SO_3H$ linker. Solvothermal reaction with Zn^{2+} ions resulted to the formation of colourless

plate crystals. We must mention at this point that after 10 hours at 85 ^{0}C colourless plate like crystals are formed. That is a different crystalline material other than IRMOF-8 as it is evident from its pxrd pattern. However when these crystals remain inside the mother liquid, at 85 ^{0}C for 6 days, they are all transformed to small cubes which are identified as the IRMOF-8-SO$_3$H analogue, as it is evident from its pxrd pattern. Because of the very small crystal size single crystal structure determination using single XRD was not possible. Therefore the calculated pattern from the IRMOF-8-2OH crystal structure was used to verify the phase purity of the new material. Indeed the experimental pattern matches the calculated one from the crystal structure. Unfortunately it was not possible to determine the structure of the plate like crystals using single crystal X-ray diffraction. The gas sorption properties of the resulting material are not evaluated yet.

The fourth material that was synthesized is the interpenetrated IRMOF-8-2NO$_2$, which was synthesized using the H$_2$NDC-2NO$_2$ linker. In this case it was not possible to synthesize the non interpenetrated analogue. Solvothermal reaction with Zn^{2+} ions resulted to the formation of large dark red crystals. The large single crystals made possible the determination of the structure of this MOF. Through single crystal X-ray difractometry the structure was solved revealing a cubic 3-D framework (see figure 5.34). We provide for the first time direct structural evidence of the existence of an interpenetrated IRMOF-8 analogue. The material crystallizes in the cubic system (space group $Fd\bar{3}m$), with a unit cell parameter a = 30.1552 Å. This is a doubly interpenetrated structure based on the octahedral Zn$_4$O(-CO$_2$)$_6$ secondary building unit (SBU). Powder X-ray diffraction analysis verified the formation of a pure phase as the calculated and experimental powder pattern are identical. Noticeably the pxrd pattern of this material is totally different than the non-interpenetrated IRMOF-8 analogue, in contrast to what is reported in the literature.[85]
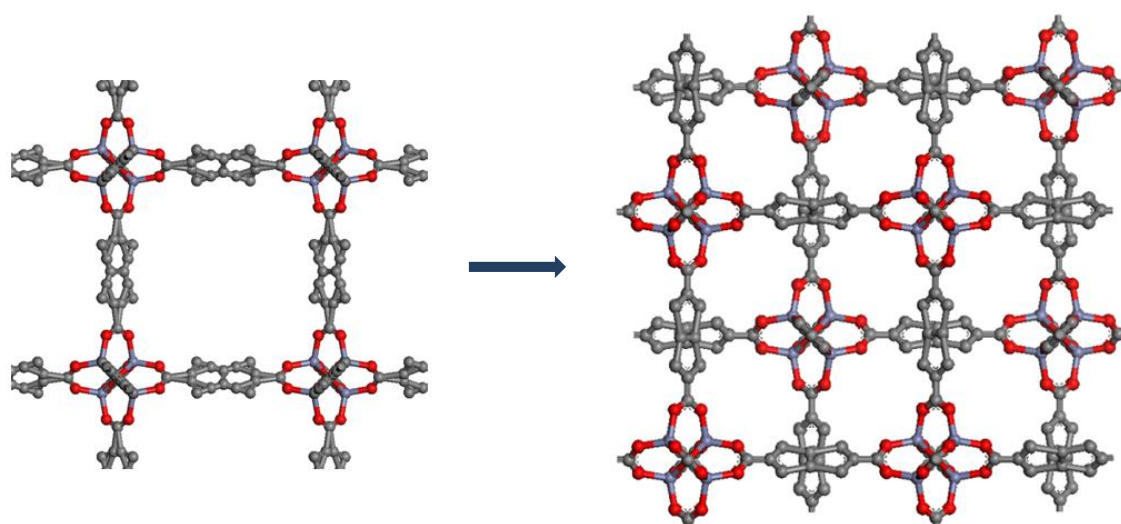
Figure 5.34. Left: the non interpenetrated structure of IRMOF-8. Right: Part of the 3-D interpenetrated crystal structure of compound IRMOF-8-2NO$_2$. The organic linker is disordered. Purple spheres: Zn, gray: C, red: O. Solvent molecules, hydrogen and nitrogen atoms are omitted for clarity.
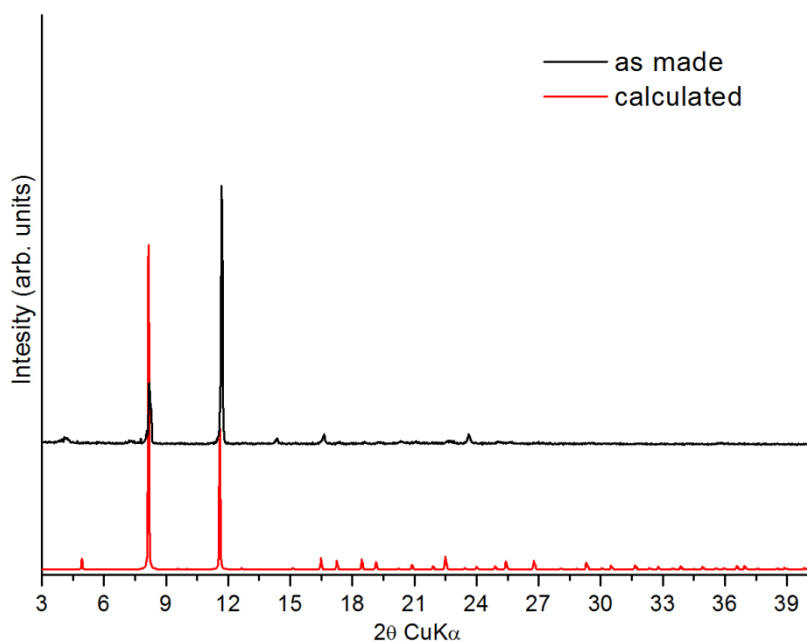
<u>Figure 5.35.</u> Comparison of experimental and calculated pxrd patterns for interpenetrated IRMOF-8-2NO$_2$.

Moving a step forward we wanted to examine the effect of the replacement or substitution of Zn^{2+} ions with other metal ions to the gas sorption properties of those materials. Although this type of framework does not contain open metal sites yet there are strong binding sites close to the metal cluster.[86] Therefore the use of a different metal ion is expected to affect the interaction of the framework with the gas molecules. Initially we tried to synthesize an IRMOF-8 analogue with an SBU containing only one type of metal ion other than Zn^{2+}.

A solvothermal reaction between Co^{2+} ions and the linker H$_2$NDC-2OH, resulted to the formation of large dark blue crystals. The large single crystals made possible the determination of the structure of this MOF. Through single crystal X-ray difractometry the structure was solved revealing the hydroxyl-IRMOF-8 analogue with cobalt. It crystallizes in the cubic system (space group Fm$\bar{3}$m), isostructural to IRMOF-8 (Zn), with a unit cell parameter a = 30.167(4) Å. This unit cell parameter is lower than the zinc analogue, because the size of the tetrahedral Co^{2+} ion is smaller than the Zn^{2+} ion. The blue colour of the crystals was indicative of tetrahedral cobalt, as it was expected from the crystal structure. This material was highly hydroscopic and decomposed rapidly in air, changing colour from deep blue to pink. So the measurement of a good quality X-ray powder pattern was difficult. Notably it was the first time that an IRMOF-8 analogue with cobalt was synthesized and characterized. There have been made numerous attempts to activate this material, including SCD CO$_2$ as well as exchange with various low boiling solvents such as CH$_2$Cl$_2$ and CHCl$_3$. In all cases it was not possible to remove the solvents without structural collapse.
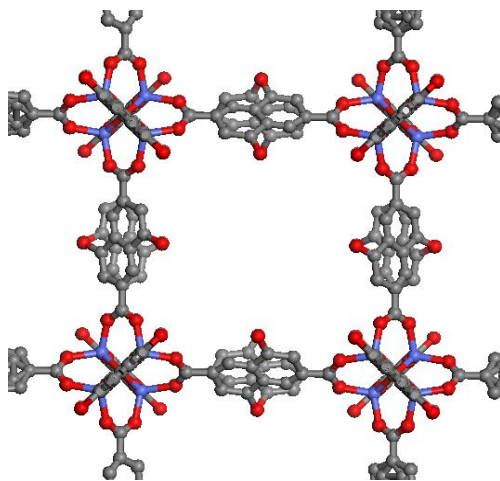
Figure 5.36. Part of the cubic framework of IRMOF-8-2OH (Co) as determined from single-crystal X-ray diffraction data. The organic linker is disordered. Blue spheres: Co, gray: C, red: O. Solvent molecules and hydrogen atoms are omitted for clarity.
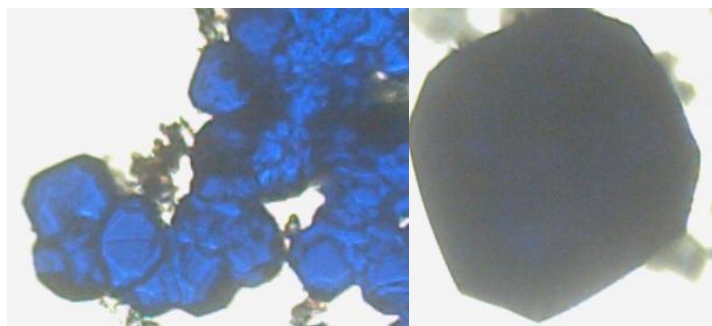
Figure 5.37. Uniform blue single crystals of IRMOF-8-2OH (Co).

Although many attempts were made to synthesize an IRMOF-8 analogue containing only one type of metal ion, other than Co^{2+} and Zn^{2+}, it was not possible to accomplice it. Therefore a different synthetic methodology was tried using a mix metal synthesis for the partial substitution rather than the total replacement of Zn^{2+}. Five novel mix metal IRMOF-8-2OH analogues were successfully synthesized and characterized. All materials are isostructural to the parent material containing only zinc. The Zn-Mn, analogue contained Zn^{2+} ions and Mn^{2+} ions in a ratio 1:3. The same ratio was found for the Zn-Cd and Zn-Mg analogues. That is a 25% zinc substitution on the $[Zn_4O]$ cluster was accomplished. The Zn-Co analogue contained Zn^{2+} ions and Co^{2+} ions in ratio 1:4. The same counts for the Zn-Ni analogue. In this case a 20% zinc substitution on the $[Zn_4O]$ cluster was acquired. The Zn^{2+}/M^{2+} ratio was verified through EDS measurements and the successful incorporation of the M^{2+} ions in the structure was verified through single crystal X-ray diffraction analysis. The different size of each M^{2+} ion resulted to a different unit cell for each of the five new materials. Furthermore the size of those analogues followed a rational trend and they were analogous to the size of the M^{2+} ion (see figure 5.38). The Zn-Mg, crystallizes in the cubic space group, Fm-3m, with unit cell parameter a = 30.145 Å, The Zn-Mn analogue, crystallizes in the cubic space group, Fm-3m, with unit cell parameter

a = 30.185 Å, the Zn-Co, crystallizes in the cubic space group, Fm-3m, with unit cell parameter a = 30.185 Å, the Zn-Ni, crystallizes in the cubic space group, Fm-3m, with unit cell parameter a = 30.163 Å, and the Zn-Cd, crystallizes in the cubic space group, Fm-3m, with unit cell parameter a = 30.328 Å.

In order to evaluate the gas option properties of those new MOFs a successful activation procedure was required. All materials were activated using supercritical CO_2. Gas sorption results are summarized in Appendix A.
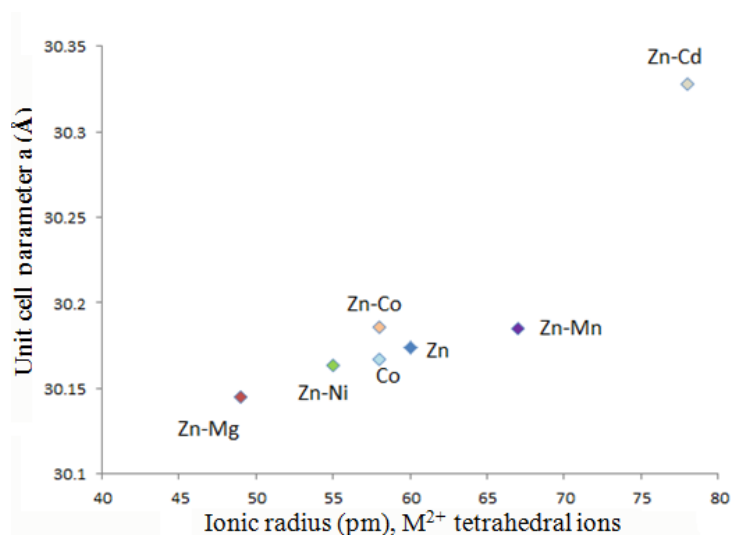
Figure 5.38. This graph shows the relationship between the ionic radius of the metal ions and the unit cell parameter a. The material containing the metal ion with the smaller ionic radius exhibits a lower unit cell parameter in comparison to the material containing larger metal ions.[87]

Evidently this methodology enabled the synthesis of new MOFs that exhibited enhanced gas sorption properties than the parent non-functionalized material, that is the IRMOF-8-2OH containing only Zn^{2+} ions. The Zn-Co analogue revealed an improved CO_2 and CH_4 uptake of all the functionalized analogues including the parent material. At 273 K it adsorbed an amount of 3.25 mmol g^{-1} of CO_2 and 0.83 mmol g^{-1} of CH_4. The Zn-Ni analogue exhibited an improved H_2 uptake at 77 K with a value of 9.72 mmol g^{-1}. This value is the highest of all analogues, including the parent material and the Zn-Ni MOF-5 analogue.[88] Furthermore the Zn-Mg analogue exhibited improved isosteric heat of hydrogen adsorption with a value of 5.95 kJ mol^{-1}. Whereas the Zn-Ni analogue exhibited an improved CO_2 isosteric heat of adsorption with a value of 25.77 kJ mol^{-1} outperforming all analogues. However in all cases the accessible surface area was still lower than the expected one from the crystal structure.

Another well known and studied IRMOF is the IRMOF-10 material. This compound is isostructural to IRMOF-8 but in this case the organic linker is the H_2BPDC. Due to the increased length of this linker compared to H_2NDC the resulting material exhibits even higher surface area, and larger pore size. For this purpose the functionalized organic linkers 16, 17, 20 and 23 were utilized for the synthesis of a series of functionalized IRMOF-10 analogues. All materials were characterized using pxrd measurements. They were all highly crystalline and isostructural to the parent non functionalized IRMOF-10 analogue. It must be mentioned that increasing the metal: ligand ratio from 1:1 to 3:1

under the same synthetic conditions the interpenetrated IRMOF-9 analogue was synthesized. The gas sorption properties of those materials are not evaluated yet.
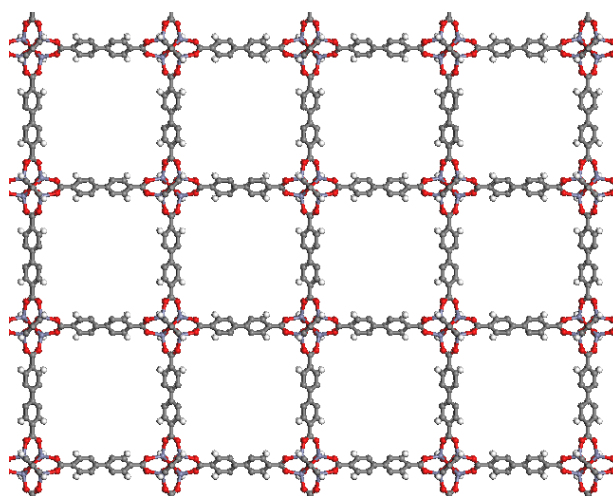
<u>Figure 5.39.</u> Part of the 3-D structure of compound IRMOF-10. Purple spheres: Zn, gray: C, red: O, white: H. Solvent molecules are omitted for clarity.

5.3 Syntheses of MOFs based on combination of organic ligands

   One of the most prominent methods for the synthesis of ultra high porous materials is the use of more than one organic linkers, usually a trigonal tritopic and a linear ditopic one. For instance MOF-210 and MOF-205 are two materials, containing different types of linkers, both exhibiting ultra high surface areas (6240 m^2 g^{-1} and 4460 m^2 g^{-1} respectively). [89] This inherent property of ultra high surface area is ideal for gas storage applications at high pressures. The higher the gravimetric surface area the higher the gravimetric uptake. Being aware of all these, we targeted the synthesis of highly porous MOFs using a combination of linkers.

   The fisrt material that was synthesized is based on the reaction of linkers 32 (H$_3$BTB) and 6 (H$_2$NDC-2OH) with Zn^{2+} ions. This lead to the formation of large dark orange truncated octahedral crystals. The large single crystals made possible the determination of the structure of this MOF. Through single crystal X-ray difractometry the structure was solved revealing the MOF-205-2OH analogue. It crystallizes in the cubic system (space group $P m \overline{3} n$) with a unit cell parameter a = 30.367(4) Å. The framework is made of $Zn_4O(-CO_2)_6$ SBUs connected through four BTB and two NDC-2OH ligands having an overall formula $Zn_4O[(NDC-2OH)(BTB)_{4/3}]$. As shown in figure 1b, this type of connectivity results in a quite remarkable three-dimensional structure that contains large cavities of approximately 25 Å in diameter, in the form of dodecahedral mesopore cages formed by twelve $[Zn_4O]^{6+}$ units, eight BTB ligands and four NDC-2OH ligands. These mesopore cages are connected together by smaller micropores. Powder X-ray diffraction analysis verified the formation of a pure phase as the calculated and experimental powder patterns are identical.
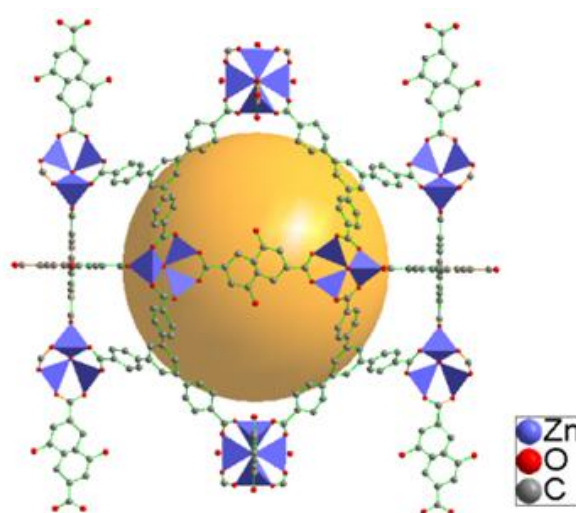
<u>Figure 5.40.</u> Part of the cubic framework of MOF-205-2OH as determined from single-crystal X-ray diffraction data.

Activation of this material was possible through exchange with absolute ethanol for 4 days, 4 times per day, followed by exchange with supercritical CO_2. A remarkable maximum nitrogen uptake of 1363 cm^3 g^{-1} was recorded, corresponding to a total pore volume of 2.01 cm^3 g^{-1}. These values are very close to those reported for the non-functionalized analogues DUT-6[90] (1380 cm^3 g^{-1}/2.02 cm^3 g^{-1}) and MOF-205 (1410 cm^3 g^{-1}/2.16 cm^3 g^{-1}), indicating that -OH groups in MOF-205-2OH do not reduce the accessible space. Careful BET calculations using consistency criteria revealed an ultrahigh surface area (SA_{BET}) of 4354 m^2 g^{-1}, in excellent agreement with the accessible surface area (4671 m^2 g^{-1}) calculated from the crystal structure[91], indicating that MOF-205-2OH is structurally intact after pore evacuation. The latter is also confirmed by pxrd where a high degree of crystallinity is retained after removal of the guest molecules. The nitrogen adsorption isotherm shows a distinct condensation step in the relative pressure range P/P_o 0.04 - 0.14 suggesting the presence of small mesopores, in full agreement with the crystallographic data.

In addition, accurate high resolution micropore analysis using Ar at 87 K allowed us to calculate the pore size distribution, total pore volume and surface area in MOF-205-2OH using Non-Local Density Functional Theory (NLDFT). Accordingly, after a successful fitting of the isotherm data using a suitable NLDFT kernel, the pore size distribution curve shows three distinct peaks centered at 24 Å, 17 Å and 13 Å, in agreement with the crystallographic analysis. Also important, the NLDFT calculated surface area is 4543 m^2 g^{-1}, in excellent agreement with the corresponding BET value.

Hydrogen adsorption measurements showed an uptake of 1.4 wt% at 1 bar and 77 K, which is higher than the non-functionalized MOF-205 analogue, while the calculated H_2 Q_{st} value at zero coverage was found to be 4.6 kJ mol^{-1}. Due to its ultrahigh surface area, MOF-205-2OH shows a remarkable saturation uptake of 1083 cm^3 g^{-1} (214 wt%) at 1 bar and 195 K which represents one of highest reported values, rendering this solid potentially very interesting for CO_2 storage. The corresponding S-shaped isotherm captures the presence of micro- and mesopores, as indicated by the distinct step at

~380 torr. Interestingly, the desorption branch of the isotherm shows a hysteresis which is not typical for non-flexible MOFs and could be related to the presence of -OH groups. The CO_2 isotherms recorded at 298 K and 273 K revealed a Q_{st} value at zero coverage of 16.0 kJ mol^{-1} which is higher than UMCM-1 a non-functionalized analogue.[92] Our strategy of incorporating pendant hydroxyl groups indeed increased the H_2, and CO_2 isosteric heat of adsorption in comparison to the non-functionalized analogues. Finally, the combination of ultrahigh surface area and -OH groups in MOF-205-2OH prompted us to investigate how this solid performs and compares with other MOFs in ammonia adsorption at room temperature. The NH_3 uptake for MOF-205-2OH at 1 bar is 16.4 mol kg^{-1} which, to the best of our knowledge, represents a record value in both MOF and COF family of porous solids. For example, recently COF-10 was reported to be the best performing material having an uptake of 15 mol kg^{-1} at 298 K and 1bar.[93] Compared with DUT-6 (MOF-205) which shows a lower maximum uptake (12 mol kg^{-1}), MOF-205-2OH shows a significant higher uptake at the low pressure region, with the first data point to be 4.7 mol kg^{-1} at 0.76 torr (versus 0.8 mol kg^{-1} at 0.76 torr) indicating a stronger binding, presumably due to the acid-base interaction between the -OH groups and NH_3 molecules. However, as in the case of all reported MOFs based on late, first row transition metal cations[94], ammonia adsorption is not fully reversible in both MOF-205-2OH and DUT-6 (MOF-205) and the framework did not hold its integrity as pxrd measurements showed. More information about IRMOF-8-2OH and MOF-205-2OH can be found in our published work.[95]

The second material that was synthesized is based on the reaction of linkers 33 (H_3TATAB) and H_2BDC with Zn^{2+} ions. The use of the tritopic H_3TATAB linker instead of H_3BTB, was preferred because the existence of the triazine core and the amino groups is expected to increase the interaction of the resulting framework with polar, or polarizable gas molecules. The resulting large single crystals made possible the determination of the structure of this MOF. Through single crystal X-ray diffractometry using synchrotron radiation, the structure was solved revealing a 3-D framework. It crystallizes in the hexagonal system (space group $P6_3$), with unit cell parameters a = b = 43.099998 Å, c = 18.392 Å, $\alpha = \beta = 90^0$, $\gamma = 120^0$. This is a non-interpenetrated structure based on the octahedral $Zn_4O(-CO_2)_6$ secondary building unit (SBU). The SBU is build up by four tetrahedral Zn^{2+} ions linked together by an O^{2-} ion. Each SBU is linked to six organic linkers, four H_3TATAB occupying the axial and two adjacent equatorial positions of the octahedral cluster and two H_2BDC linkers occupying the other two equatorial positions. Each H_2BDC organic linker connects two SBUs, and each H_3TATAB linker connects three SBUs resulting to an overall framework formula $Zn_4O(BDC)(TATAB)_{4/3}$. This linker placement results to a material containing both micro and meso pores. The cage-like micro pores have dimensions of 24 x 18 Å without taking into account the van der Waals radii. Six microporous cages assemble to form a mesoporous 1-D hexagonal channel of 32 Å in diameter, including the van der Waals radii. The estimated crystal density is 0.39 g cm^{-3}. The material has the same structure with UMCM-1 but due to the presence of the H_3TATAB linker instead of H_3BTB it

loses its mirror plane and crystallizes in a lower symmetry space group.[96] Pxrd measurements confirmed the formation of a phase pure compound as calculated and as made patterns are identical.
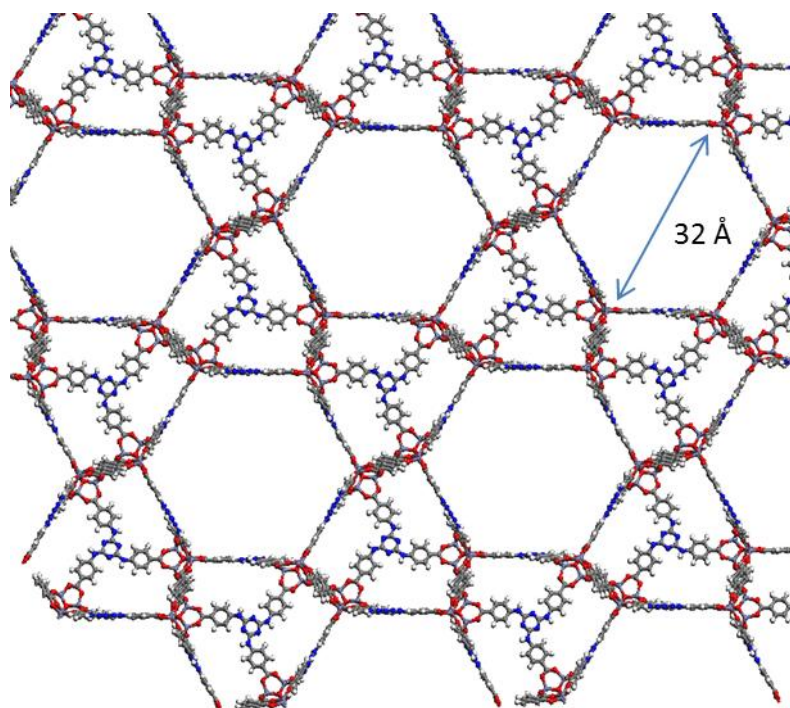
Figure 5.41. Part of the of the structure of compound $Zn_4O(BDC)(TATAB)_{4/3}$ looking down the c axis. The hexagonal mesopores are 32 Å in diameter. Purple spheres: Zn, gray: C, red: O, blue: N, white: H. Solvent molecules are omitted for clarity.
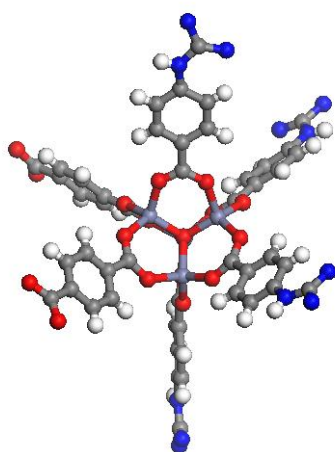
Figure 5.42. The connectivity of the [Zn_4O] cluster. The axial positions of the cluster and two of the equatorial positions are occupied by the H_3TATAB organic linker, while the two remaining cis equatorial positions of the octahedral cluster are occupied by the H_2BDC linker. Purple spheres: Zn, gray: C, red: O, blue: N, white: H.

  After the efficient characterization of the material the evaluation of its gas sorption properties took place. The activated material is highly air sensitive and the pxrd pattern of the evacuated material showed complete loss of crystallinity.

Argon adsorption measurements at 87 K revealed a reversible pseudo type IV isotherm, indicative of mesoporous materials. There is a distinct condensation step at a relative pressure $P/P_o \sim 0.28$ suggesting the presence of mesopores, in full agreement with the crystallographic data. The calculated surface area from the Argon isotherm, assuming monolayer coverage up to the first plateau, was found to be 2375 $m^2\,g^{-1}$ (BET) and the total solvent-accessible volume was found to be 82%, using the PLATON software[97] and the estimated crystal density is 0.36 g cm^{-3}. The experimental total pore volume was found to be 1.23 $cm^3\,g^{-1}$ a lot lower than the calculated one from the crystal structure 2.24 $cm^3\,g^{-1}$. Pore size distribution analysis reveals that there is a narrow distribution of micropores centered at about 13.7 Å and a narrow distribution of mesopores centered at about 32 Å, which is in excellent agreement with the theoretical results from the single crystal data.

Although it wasn't possible to get access to the total pore volume of this material, in order to evaluate its gas sorption properties we performed CO_2, H_2, and CH_4 sorption measurements. CO_2 measurements revealed an impressive uptake of 11.6 mmol g^{-1} at 195 K and 1 bar. We have also performed CH_4 adsorption measurements at 112 K, 273 K and 298 K at 1 bar. $Zn_4O(BDC)(TATAB)_{4/3}$ adsorbs at 112 K and 1 bar an enormous amount of 32.83 mmol g^{-1} (735 $cm^3\,g^{-1}$, 287 $cm^3\,cm^{-3}$, 0.525 g g^{-1}), those values can achieved at RT only under very high pressures. While at 273 K and 1 bar it adsorbs 0.9 mmol g^{-1} of CH_4. We calculated the isosteric heat of adsorption and found a high value of $Q_{st}^0 = 21.95$ kJ mol^{-1} remaining constant during methane loading, which is among the highest recorded for MOFs.[98] High pressure measurements will reveal if this material could be used efficiently for methane storage applications.

The third material that was synthesized is based on the reaction of linkers 33 (H_3TATAB) and 2 (H_2NDC-2NO_2) with Zn^{2+} ions. The resulting large single crystals made possible the determination of the structure of this MOF. Through single crystal X-ray difractometry using synchrotron radiation, the structure was solved revealing a neutral 3-D framework. It crystallizes in the hexagonal system (space group $P6_3$), with unit cell parameters a = b = 43.747002 Å, c = 54.653 Å, $\alpha = \beta = 90^0$, $\gamma = 120^0$. This is a non-interpenetrated structure based on the octahedral $Zn_4O(-CO_2)_6$ secondary building unit (SBU). The SBU is build up by four tetrahedral Zn^{2+} ions linked together by an O^{2-} ion. Each SBU is linked to six organic linkers, four H_3TATAB occupying the equatorial positions of the octahedral cluster and two H_2BDC linkers occupying the two axial positions. Each H_2NDC-2NO_2 organic linker connects two SBUs, and each H_3TATAB linker connects three SBUs resulting to an overall framework formula $Zn_4O(NDC-2NO_2)(TATAB)_{4/3}$. This linker placement results to a material containing two types of large adjacent cages. The first one exhibits dimensions 27 x 19 Å and the second one 36 x 30 Å without taking into account the van der Waals radii. The estimated crystal density is 0.36 g cm^{-3} and the total solvent-accessible volume was found to be 85%, using the PLATON software. Those two factors indicate that this material is highly porous and poses a very promising candidate for gas storage applications. This structure is similar but not identical to MOF-210 a material that is also synthesized from a trigonal (H_3BTE) and a linear (H_2BPDC) organic linker. Comparing this compound with the

previous one and MOF-210 we observe that combination of the same topology and ratio of linkers can result to different networks. This stems from the fact that the position of the linkers on the metal cluster is different in each case. The linear linkers in this compound occupy the axial positions, in the previous one they occupy two cis equatorial positions, while in MOF-210 they occupy one axial and one equatorial position in cis arrangement. Pxrd measurements confirmed the formation of a phase pure compound as calculated and as made patterns are identical. The evaluation of its gas sorption properties is yet to be accomplished since a proper activation procedure is required.
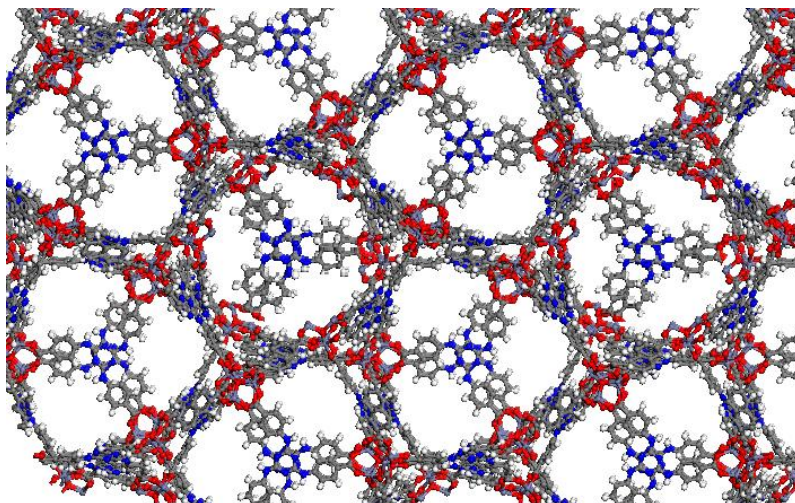
Figure 5.43. Part of the of the structure of compound $Zn_4O(NDC-2NO_2)(TATAB)_{4/3}$ looking down the c axis. Purple spheres: Zn, gray: C, red: O, blue: N, white: H. Solvent molecules are omitted for clarity.
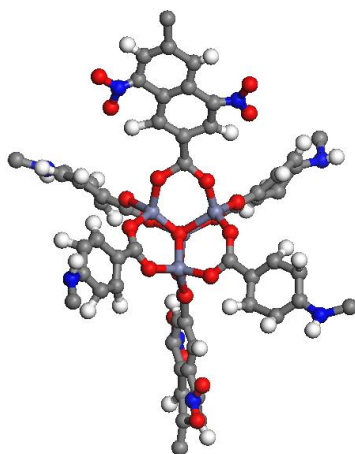
Figure 5.44. The connectivity of the [Zn_4O] cluster. The equatorial positions of the cluster are occupied by the H_3TATAB organic linker, while the two axial positions of the octahedral cluster are occupied by the $H_2NDC-2NO_2$ linker. Purple spheres: Zn, gray: C, red: O, blue: N, white: H.

Following this, it were synthesized three more mix linker analogues based on H_3TATAB and linear functionalized linkers 8 ($H_2NDC-2OPr$), 9 ($H_2NDC-2OPh$) and 10 ($H_2NDC-2OAllyl$). Pxrd measurements revealed that all materials are isotructural and highly crystalline. However there have been made no attempts yet to activate those materials.

5.4 Syntheses of tbo-MOFs

Until recently,[99] HKUST-1, a MOF with *tbo* topology,[100] was reported to be the best material for CH_4 storage showing a total volumetric uptake of 267 cm^3 (STP) cm^{-3} at 298 K and 65 bar with a corresponding working capacity (5-65 bar) of 190 cm^3 (STP) cm^{-3}.[101] However, these values are still lower than the new DOE target of 350 cm^3 (STP) cm^{-3} at 35 bar and 298 K and therefore it is natural to consider that expanded tbo-MOFs with higher gravimetric and volumetric surface area will result in higher CH_4 uptake.

This topology can be acquired either by the use of a trigonal tritopic organic linker, or by the use of a rectangular octatopic linker. Eddaoudi et al., were the first to design and synthesize this new family of isoreticular MOFs with *tbo* topology by using quadrangular (octatopic) organic ligands instead of trigonal (tritopic) ones as in the case of HKUST-1.[102] The use of quadrangular organic ligands offers the advantages of modulation of porosity and functionalization of the resulting material but most important it prevents self-interpenetration as it is observed in the case of MOF-388.[103] In this way it is possible to efficiently utilize extended organic ligands and synthesize tailor made materials with specific pore size and volume. Additionally this topology allows the formation of open metal sites, uncoordinated metal sites, that are easily accessible to the incoming gas molecules. Their existence is one of the most critical parameters to increase substantially the interaction of the framework with specific gas molecules.[104]

It is important to note that the *tbo* topology requires an isophthalate-based octatopic organic linker (four isophthalate groups) with specific geometrical constrains which limits the choice of suitable organic linkers.[105] To overcome these limitations, the use of flexible octatopic linkers was proven to be a successful strategy. However, this flexibility could be at the expense of framework stability due to the increased strain energy of the ligand. It is therefore challenging to identify and synthesize new, rigid octatopic linkers suitable for the formation of expanded tbo-MOFs.

With these considerations in mind we designed and synthesized the rigid octatopic organic linker 47 (H_8L). In addition, the presence of the two methyl-groups attached at the central phenyl ring is favorable because i) will increase the electron density of this ring which expected to increase the CH_4 interaction at this site and in turn, will increase the total CH_4 storage capacity and ii) will decrease the relatively large size of the central cavity of the structure, keeping in this way the overall porosity at the micropore region.

Solvothermal reaction of linker 47 with Zn^{2+} ions resulted to the formation of single crystals. Using single crystal XRD the structure of this MOF was determined. This material (Zn-tbo) crystallizes in the orthorombic space group *Fmmm*, with unit cell parameters a = 25.920 Å, b = 28.560 Å, c = 40.270 Å, $\alpha = \beta = \gamma = 90^0$. The 4-connected quadrangular ligand serves as a pillar between the sql layers that link the 4-connected $Zn_2(O_2CR)_4$ paddlewheel clusters. The topology of the resultant 3D network corresponds to the expected tbo, that is, Zn-tbo can be considered as a tbo-MOF analogous to the

prototypical MOF, HKUST-1. The framework consists of three types of open cages. Truncated cuboctahedra having diameters of 17.781 and 20.802 Å, truncated cubes and truncated tetrahedra with 12.521 Å (height) and 10.220 Å (width).
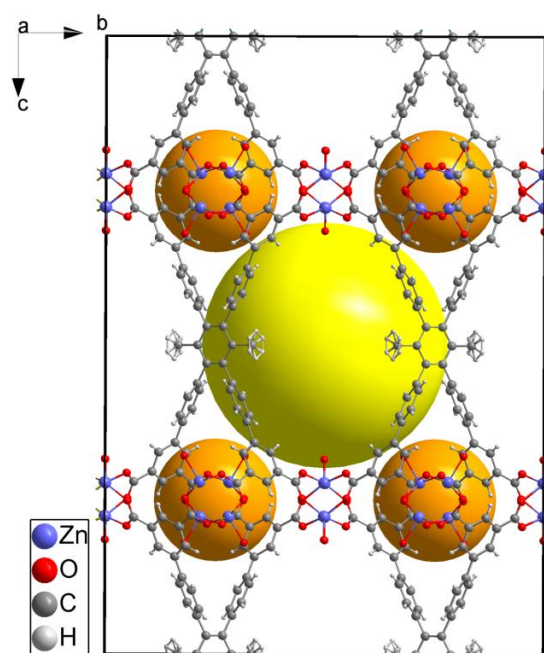
Figure 5.45. Part of the 3-D crystal structure of compound Zn-tbo looking down the a axis. Orange and yellow spheres represent empty space. Solvent molecules are omitted for clarity.

Similarly, two more tbo-MOFs were synthesized using $Co(NO_3)_2 \cdot 6H_2O$ and $Cu(NO_3)_2 \cdot 3H_2O$ as a metal source. The resulting materials Cu-tbo, Co-tbo, were characterized using powder X-ray diffraction measurements, all materials are highly crystalline and isostructural to the zinc analogue. However it was possible to synthesize single crystals only in the case of zinc and cobalt analogues. The Cu-tbo analogue was synthesized as microcrystalline solid. Nonetheless we utilized a methodology, used in the literature before for the acquisition of large single crystals. The method included the exchange of a metal ion from a single crystal and its replacement with another metal ion, with similar size and charge.[106] Therefore we placed the large single crystals of Zn-tbo into a solution of 0.06 M $Cu(NO_3)_2 \cdot 3H_2O$, and replaced the solution with fresh one, once per day for 4 days. The initial pale brown crystals turned light blue, they were washed thoroughly with DMF and the structure was determined using synchrotron radiation. The resulting material was the Cu-tbo analogue as it was expected. The total replacement of Zn^{2+} ions was verified using EDS measurements. The Cu-tbo analogue crystallizes in the orthorombic space group *Fmmm*, with unit cell parameters a = 25.6163 Å, b = 28.1575 Å, c = 40.5487 Å, $\alpha = \beta = \gamma = 90^0$. This unit cell is smaller than the Zn-tbo analogue, since the Cu^{2+} ion has a smaller ionic radius than the Zn^{2+} ion. Of the three tbo analogues it was possible to activate only the Cu-tbo analogue. For the gas sorption measurements it was used the microcrystalline solid and not the metal exchanged large single crystals.

Argon sorption measurements confirmed the permanent porosity of Cu-tbo, giving a fully reversible type-I isotherm characteristic of microporous materials. The BET (Langmuir) surface area of Cu-tbo, was estimated to be 3971 m^2 g^{-1} (4123 m^2 g^{-1}), which is almost double than that of prototypical HKUST-1 (1977 m^2 g^{-1}). The calculated geometric surface area from the Duren software[90] is 3972 m^2g^{-1} identical to the experimental one, and the calculated volumetric surface area is as high as 2452 m^2 cm^{-3}. The calculated total free volume from the argon isotherm was estimated to be 1.12 cm^3 g^{-1} and the total solvent-accessible volume was found to be 72%, using the PLATON software. Pore size distribution analysis reveals that there is a narrow distribution of micropores centered at about 8 Å, 11 Å and 16 Å, which are in excellent agreement with the theoretical results from the single crystal data.

In order to evaluate its gas sorption properties we performed CO_2, H_2, and CH_4 sorption measurements. At 77 K and 1 bar Cu-tbo adsorbs an impressive 2.3 wt% H_2 with a calculated Q_{st} value of 6.28 kJ mol^{-1}, which are among the highest reported values for high surface area MOFs with open metal sites.[107] CO_2 measurements revealed a high uptake of 6.63 mmol g^{-1} (22.6 wt%) at 273 K and 1 bar, while at 298 K and 1 bar the uptake reaches a value of 3.6 mmol g^{-1} (13.6 wt%), these findings are among the highest reported for high surface area MOFs.[108] The calculated Q_{st}^0 for CO_2 was found to be 24.51 kJ mol^{-1} remaining constant during CO_2 loading. Additionally the CO_2/CH_4 selectivity was calculated using IAST for a 5/95 molar mixture at 273 K and 298 K giving rise to a value of 5.2 and 4.2 respectively. Those very low values are indicative for the low affinity of the framework for CO_2 and the higher affinity for CH_4. This is evident by taking into account the resulting high isosteric heat of methane adsorption and the low isosteric heat of carbon dioxide adsorption.

In order to determine the maximum methane uptake that this material can adsorb we performed methane adsorption measurements at 112 K and 1 bar. Cu-tbo was found to adsorb 691 cm^3 (STP) g^{-1}, (411 cm^3 (STP) cm^{-3}). This value surpasses the DOE target but at 298 K is achievable only under very high pressures. Additional measurements at 273 K, 283 K and 298 K and 1 bar were performed. From which the calculated isosteric heat of adsorption at zero coverage, was found to be $Q_{st}^0 = 20.4$ kJ mol^{-1} using the virial equation, and 21.7 kJ mol^{-1} with the Clausius clapeyron equation, remaining constant during methane loading. This value is higher than HKUST-1 and among the highest reported for MOFs (see table 6.6). Compared to HKUST-1, Cu-tbo has the same unsaturated copper sites as strong methane binding sites and another strong binding site is located on the four windows of each octahedral cage.[109] Additionally in Cu-tbo the methyl groups of the organic linker protrude into the porous of the framework creating a window of 8 Å (without taking into account the wan der Waals radii) which is found to be optimum for the accommodation of two methane molecules, enhancing in this way the methane uptake, through $CH_4 \cdots CH_4$ and methane-framework interactions.[110] Kim et al.[111] have shown that methane molecules can interact with the phenyl rings of an organic linker through $\pi \cdots H–C$ interactions. Thus the existence in our case of 9 phenyl rings per linker can have a significant impact on the interaction of methane molecules with the framework due to the increased number of those weak binding sites.

High pressure methane measurements can evaluate this material's performance as methane storage candidate. Measurements up to 85 bar at 298 K and 273 K were carried out. In terms of total gravimetric methane uptake at 85 bar and 273 K, Cu-tbo adsorbs a significant amount of 0.309 g (STP) g^{-1}, while at 85 bar and 298 K Cu-tbo adsorbs 0.266 g (STP) g^{-1}. At this point it is mentioned that an important parameter for the evaluation of a material towards methane storage for mobile applications, called working capacity (or deliverable capacity) must be determined. It represents the actual usable amount of methane that is delivered to the engine, and it is the difference between the uptakes of the desorption operational pressure (5 bar) and the adsorption operational pressure.
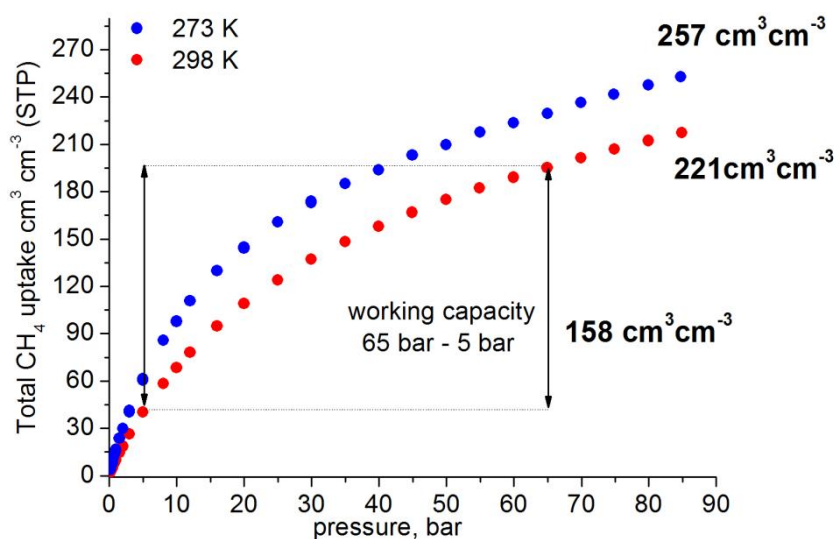
Figure 5.46. Total volumetric CH$_4$ adsorption isotherms of Cu-tbo at 273 K and 298 K, the black arrows indicate the working capacity (65 bar – 5 bar) at 298 K.

Thus the working capacity (80 bar - 5 bar) at 298 K, of Cu-tbo is 0.210 g (STP) g^{-1}. This value surpasses 2 of the best MOFs for methane storage, HKUST-1 with a working capacity of 0.162 g (STP) g^{-1} and MOF-519 with a value of 0.172 g (STP) g^{-1}, and places Cu-tbo among the best materials for methane storage under those conditions (see Appendix A). In terms of total volumetric methane uptake at 85 bar and 273 K, Cu-tbo adsorbs 257 cm^3 (STP) cm^{-3}, while at 85 bar and 298 K Cu-tbo adsorbs 221 cm^3 (STP) cm^{-3}. Those are remarkable values for high surface area MOFs, including MOF-5, PCN-66 and PCN-68[112] and second best reported for tbo-MOFs. Interestingly, although high enough, these values are lower than those recorded for the HKUST-1 prototype, 267 cm^3 (STP) cm^{-3}, at 80 bar and 298 K. It seems that even if we managed to increase substantially the volumetric surface area and the isosteric heat of adsorption, the highest crystal density of HKUST-1, 0.881 g cm^{-3}, in comparison to the lower mass per unit volume of Cu-tbo 0.585 g cm^{-3}, contributes to a higher total volumetric methane uptake for the HKUST-1.

Additionally, the calculated volumetric working capacity (80 bar - 5 bar) at 298 K, of Cu-tbo is 175 cm^3 (STP) cm^{-3} and between 65 bar and 5 bar this value is 158 cm^3 (STP) cm^{-3}. This value surpasses Ni-MOF-74 (129 cm^3 (STP) cm^{-3}), and can be well compared with some of the best methane storage

111

candidates PCN-14 (157 cm^3 (STP) cm^{-3}) and NU-1100 (160 cm^3 (STP) cm^{-3}). Nonetheless, these values are lower than those for the HKUST-1, 190 cm^3 (STP) cm^{-3} between 65 bar and 5 bar and 200 cm^3 (STP) cm^{-3} between 80 bar and 5 bar. This is attributed to the fact that Cu-tbo has higher methane uptake at 5 bar, due to the higher isosteric heat of adsorption, and lower total methane uptake at high pressures, resulting in lower working capacity.
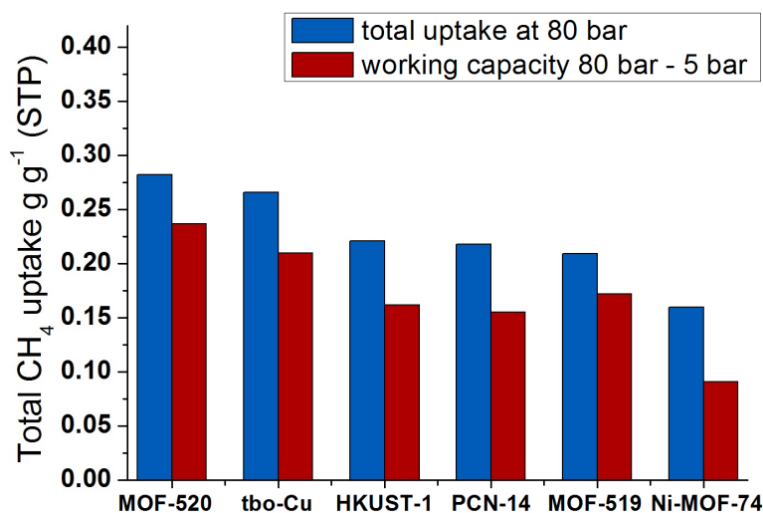
Figure 5.47. Comparison of Cu-tbo with some of the best methane storage candidates in terms of total gravimetric CH$_4$ uptake at 80 bar and 298 K and gravimetric working capacity between 80 bar and 5 bar at 298 K.
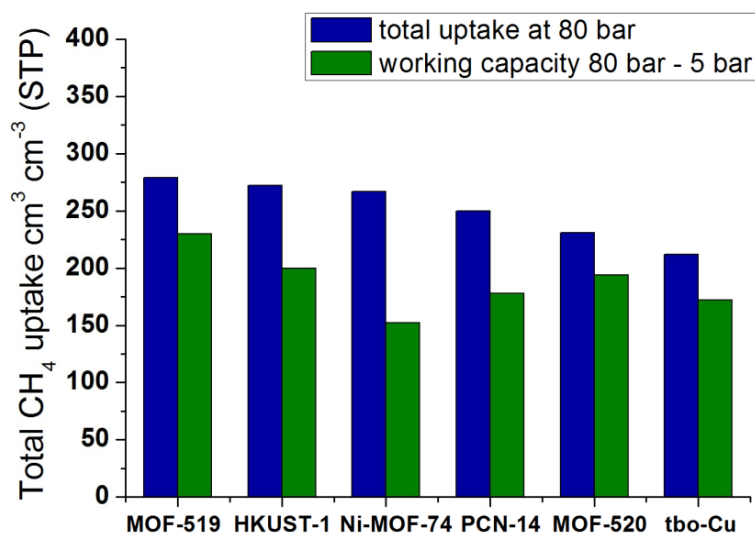
Figure 5.48. Comparison of Cu-tbo with some of the best methane storage candidates in terms of total volumetric CH$_4$ uptake at 80 bar and 298 K and volumetric working capacity between 80 bar and 5 bar at 298 K.

Although the Cu-tbo material performed well in terms of volumetric methane storage, yet the target of 350 cm^3 cm^{-3} couldn't be reached. However it is possible that modification of linker 47 could result to a different functionalized material with enhanced volumetric methane uptake. For this reason we designed and synthesized a modified version of linker 47, linker 48. To the methyl groups (-CH_3) were added pendant bromide (-CH_2-Br) groups. Apparently this modification would have two repercussions to the resulting tbo-MOF. An increase to the crystal density of the material and a diminish of the pore space from the side functional groups. This would result to an increased interaction of the gas molecules with the framework due to closer position of the opposite overlapping potentials of the pore walls.

Solvothermal reaction of linker 48 with Cu^{2+} ions resulted to the formation of microstalline material Cu-tbo-Br. This material was characterized using pxrd measurements. The synthetic procedure revealed a tbo-MOF isostructural with the previous tbo compounds as it is clear from the pxrd pattern. Because of the small size of the crystals it was not possible to solve the structure through singe crystal X-ray diffraction.

After the efficient characterization of the material the evaluation of its gas sorption properties took place. Argon adsorption measurements at 87 K revealed a fully reversible Langmuir isotherm. The calculated surface area from the Argon isotherm was found to be 2587 m^2 g^{-1} (BET) and the total pore volume 0.92 cm^3 g^{-1}, a little lower than the crystallographic value of 1.16 cm^3 g^{-1}. This is an indication that the material was not successfully evacuated, as it was not possible to gain access to its full accessible pore volume. This might be a result of partial structural damage during the activation process. As the complete DMF removal was validated by ^{1}H NMR measurements of the evacuated sample. Furthermore the higher crystal density (0.674 g cm^{-3}) of Cu-tbo-Br in comparison to the Cu-tbo (0.595 g cm^{-3}) leads to a lower gravimetric surface area.

In order to evaluate its gas sorption properties we performed CO_2, H_2, and CH_4 sorption measurements. At 77 K and 1 bar Cu-tbo-Br adsorbs a value of 2.02 wt% (232 cm^3 g^{-1}) H_2 with a calculated Q_{st} value of 6.1kJ mol^{-1}, which are typical values for high surface area MOFs with open metal sites.[113] CO_2 measurements revealed a high uptake of 5.5 mmol g^{-1} (19.6 wt%) at 273 K and 1 bar, while at 298 K and 1 bar the uptake reaches a value of 3.1 mmol g^{-1} (11.9 wt%), these are high values and can be well compared to high surface area MOFs with open metal sites.[114] The calculated Q_{st}^0 for CO_2 was found to be 22.85 kJ mol^{-1} remaining constant during CO_2 loading. Additionally the CO_2/CH_4 selectivity was calculated using IAST for a 5/95 molar mixture at 273 K and 298 K giving rise to a value of 5.5 and 4.2 respectively. Those very low values are indicative of the low affinity of the framework for CO_2 and the higher affinity for CH_4.

Methane adsorption measurements were performed at various temperatures, at 112 K and 1 bar Cu-tbo-Br adsorbs 573 cm^3 (STP) g^{-1}, (386 cm^3 (STP) cm^{-3}). This value surpasses the DOE target but at 298 K is achievable only under very high pressures. From the adsorption data at 273 K, 283 K and 298 K the isosteric heat of adsorption at zero coverage was calculated, it was found to be Q_{st}^0 = 18.3 kJ

mol^{-1}, remaining constant during methane loading. This value is lower than the initial Cu-tbo analogue, revealing that the incorporation of the bromine groups didn't enhance the interaction of the framework with the methane molecules although the pore space was diminished. Apparently in the case of Cu-tbo there are other phenomena that play a major role in the high affinity of the framework with the methane molecules, possibly a better "packing" of the molecules inside the pores of the framework. In this case only theoretical calculations can give better insight to this phenomenon.

Following this high pressure methane measurements up to 100 bar and 298 K were carried out. In terms of total gravimetric methane uptake at 100 bar and 298 K, Cu-tbo-Br adsorbs an amount of 0.239 g (STP) g^{-1}. A value lower than the Cu-tbo compound due its significant lower gravimetric surface area. In terms of total volumetric methane uptake at 100 bar and 298 K, Cu-tbo-Br adsorbs an amount of 235 cm^3 (STP) cm^{-3}, while this value at 85 bar is 215 cm^3 (STP) cm^{-3}. This value is very close to the Cu-tbo compound (221 cm^3 (STP) cm^{-3}). This stems from the fact that although the Cu-tbo-Br compound has a lot lower gravimetric surface area than Cu-tbo, its higher crystal density results to high volumetric uptake. The calculated gravimetric working capacity (65 bar - 5 bar) at 298 K, of Cu-tbo-Br is 0.160 g (STP) g^{-1}, while the volumetric working capacity (65 bar - 5 bar) at 298 K has an impressive value of 155 cm^3 (STP) cm^{-3}. This value is almost identical to compound Cu-tbo (158 cm^3 (STP) cm^{-3}). This stems from the fact that the two materials have similar total uptake at 65 bar, but the Cu-tbo-Br analogue has lower uptake at 5 bar. This is attributed to its lower Q_{st}^0 compared to Cu-tbo compound. Although it was not possible to improve significantly the methane uptake of this tbo-MOF compared to the initial Cu-tbo, yet these values, in terms of methane storage, can be well compared with some of the best methane storage candidates (see tables 6.6, 6.7, Appendix A).
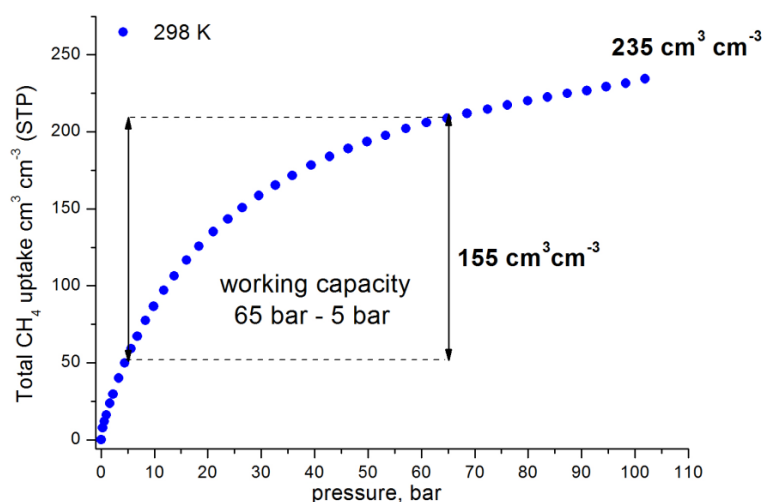
Figure 5.49. Total volumetric CH$_4$ adsorption isotherm of Cu-tbo-Br at 298 K, the black arrows indicate the working capacity (65 bar – 5 bar).

The high surface area, the existence of open metal sites along with the narrow pores that the pendant functional groups create, prompt us to perform Xe and Kr gas sorption measurements at various temperatures. At 180 K and 1 bar Cu-tbo-Br adsorbs 14.2 mmol g^{-1} Kr (318 cm^3 g^{-1}), while at 292 K it adsorbs 1.02 mmol g^{-1} (23 cm^3 g^{-1}). The calculated Q_{st}^0 was found to be 18.41 kJ mol^{-1}. Additionally

the Xe uptake at 1 bar and 240 K was found to be 11.8 mmol g^{-1} (264 cm^3 g^{-1}), while at 292 K it adsorbs 4 mmol g^{-1} (90.6 cm^3 g^{-1}). The calculated Q_{st}^0 was found to be 23.5 kJ mol^{-1} with a slight decline during Xe loading. Those values are among the highest reported for MOFs rendering this material a potential candidate for the storage of Xe and Kr.[115] Furthermore those results prompted us to calculate the selectivities of Xe/Kr. Indeed using the IAST method, for a 5/95 molar mixture at 273 K and 292 K, the selectivity was found to be almost identical for both temperatures with a value of 6.3. Ultimately those values can be well compared with some of the best MOF candidates for the separation of Xe from Kr.[116]

Taking a step further we functionalized linker 47 with a different functional group. The methyl groups were modified with the polar azide group (R-N=N^+=N^-) giving rise to linker 49. In this case again the resulting tbo-MOF would have higher crystal density and diminished more space than the initial Cu-tbo analogue. Furthermore the longer size and the polar character of the azide group compared to the bromide groups is expected to increase further the interaction of the gas molecules with the framework.

Solvothermal reaction of linker 49 with Cu^{2+} ions resulted to the formation of microcrystalline material Cu-tbo-N_3. This material was characterized using pxrd measurements. The synthetic procedure revealed a tbo-MOF isostructural with the previous tbo compounds as it is clear from the pxrd pattern. Because of the small size of the crystals it was not possible to solve the structure through singe crystal X-ray diffraction.

After the efficient characterization of the material the evaluation of its gas sorption properties took place. Argon adsorption measurements at 87 K revealed a fully reversible Langmuir isotherm. The calculated surface area from the Argon isotherm was found to be 2278 m^2 g^{-1} (BET) and the total pore volume 0.86 cm^3 g^{-1}, significantly lower than the crystallographic value of 1.20 cm^3 g^{-1}. This is an indication that the material was not successfully evacuated, as it was not possible to gain access to its full accessible pore volume. This might be a result of partial structural damage during the activation process. As the complete DMF removal was validated by ^{1}H NMR measurements of the evacuated sample. Furthermore the higher crystal density (0.636 g cm^{-3}) of Cu-tbo-N_3 in comparison to the Cu-tbo (0.595 g cm^{-3}) leads to a lower gravimetric surface area.

In order to evaluate its gas sorption properties we performed CO_2, H_2, and CH_4 sorption measurements. At 77 K and 1 bar Cu-tbo-N_3 adsorbs a value of 2.02 wt% (232 cm^3 g^{-1}) H_2 with a calculated Q_{st} value of 6.27 kJ mol^{-1}, which are high values for moderate surface area MOFs with open metal sites.[117] The hydrogen uptake is the same to the Cu-tbo-Br compound which has higher surface area. Additionally the isosteric heat of adsorption of Cu-tbo-N_3 is higher than the Cu-tbo-Br compound. Therefore indeed the replacement of the bulky bromide groups with the longer polar azide groups resulted to a stronger interaction with hydrogen molecules, resulting to an improved hydrogen uptake for the Cu-tbo-N_3 compound. CO_2 measurements revealed a high uptake of 5.2 mmol g^{-1} (18.5 wt%) at 273 K and 1 bar, while at 298 K and 1 bar the uptake reaches a value of 3.2 mmol g^{-1} (12.4

wt%), these are high values and can be well compared to moderate surface area MOFs with open metal sites.[118] The calculated Q_{st}^0 for CO_2 was found to be 21.55 kJ mol^{-1} remaining constant during CO_2 loading. The CO_2 uptake values are similar to the Cu-tbo-Br compound, while the Q_{st}^0 is lower than the Cu-tbo-Br compound. Therefore the incorporation of the polar azide groups didn't enhance the affinity of the framework towards CO_2.

Methane adsorption measurements were performed at various temperatures, at 112 K and 1 bar Cu-tbo-N_3 adsorbs 535 cm^3 (STP) g^{-1}, (340 cm^3 (STP) cm^{-3}). This value surpasses the DOE target but at 298 K is achievable only under very high pressures. From the adsorption data at 273 K and 298 K the isosteric heat of adsorption at zero coverage was calculated, it was found to be Q_{st}^0 = 15.99 kJ mol^{-1}, remaining constant during methane loading. Although this value is among the highest reported for MOFs (see table 6.6), is lower than the initial Cu-tbo and the Cu-tbo-Br analogues, revealing that the incorporation of the azide groups didn't enhance the interaction of the framework with the methane molecules although the pore space was diminished. Nonetheless high pressure measurements will reveal whether this material could be used as a potential methane storage candidate. This material exhibits lower Q_{st}^0 than the previous two tbo compounds, therefore a higher working capacity is expected to be achieved. The fact that the Cu-tbo-N_3 analogue exhibits lower values for isosteric heat of adsorption for CH_4 and CO_2 than the other tbo analogues, might be attributed to the fact that the longer azide group hinders the close packing of the adsorbed gas molecules. In this way the energy that the system could gain from their interaction is minimized. Additionally the CO_2/CH_4 selectivity was calculated using IAST for a 5/95 molar mixture at 273 K and 298 K giving rise to a value of 6.2 and 4.8 respectively. Those low values are indicative of the low affinity of the framework for CO_2 and the higher affinity for CH_4, taking into account the high isosteric heat of methane adsorption and the low isosteric heat of carbon dioxide adsorption.

After those results we tried a different functional group to modify linker 47. The use of a bulky triazole moiety coupled with an aliphatic terminal hydroxyl group bound to the methyl groups resulted to the synthesis of linker 50. This modification was expected to improve the volumetric methane uptake of the resulting tbo-MOF. This could be feasible by an increase in the crystal density of the material, by the diminishing of the pore space caused from the side functional groups and by the increased interaction of the gas molecules with the basic triazole and acidic hydroxyl groups.[119]

Solvothermal reaction of linker 50 with Cu^{2+} ions resulted to the formation of the microcrystalline material Cu-tbo-triazol. The resulting material was characterized using pxrd measurements. The synthetic procedure revealed a tbo-MOF isostructural with the previous tbo compounds as it was clear from the pxrd pattern. Apparently the incorporation of the longer and bulky triazole group did not hinder the formation of a tbo analogue. Because of the small size of the crystals it was not possible to solve the structure through singe crystal X-ray diffraction.

There have been many efforts towards the activation of this material, including the use of various low boiling solvents such as methanol and CH_2Cl_2. The material was stable during solvent exchange as

verified by pxrd measurements. Complete DMF removal was verified using ^{1}H NMR spectroscopy. However during solvent removal under vacuum the material possibly collapsed. This was justified first from the color of the activated material that did not turned purple as it was expected and second it exhibited no accessible surface area. This was verified from nitrogen adsorption measurements at 77 K. A mixed linker methodology was tested for the synthesis of a compound containing both linker 50 and 47 in 1:1 ratio. The resulting material was isostructural with all other tbo-MOFs. However again during solvent removal under vacuum the material did not turned its color into purple and exhibited no nitrogen uptake at 77 K. Additionally another tbo-MOF was synthesized using linkers 50 and 47 in ratio 0.3:1. This material was successfully activated and its gas sorption properties will be evaluated soon.

Continuing our pursuit of functionalized tbo-MOFs, we used the symmetric functionalized organic linker 52 for the synthesis of a tbo compound. The idea behind the synthesis of this linker was the design of a linker that could form a tbo network (see above) while at the same time the two central arms of the linker could be free inside the pores of the framework. In this way there would be pendant acidic groups inside the pores, four from each linker. These polar acidic groups would increase the interaction of the framework with specific gas molecules as it was found by Belmabkhout et al.[120] They have synthesized a hexatopic organic linker ($H_{12}L2$) with twelve carboxylates that was used for the synthesis of a tbo type MOF (tbo-MOF-3). In this case four of the six arms of the linker were used to construct the network, while the two central remaining arms freely pointed into the generated cavities with no metal coordination. Similarly we have designed a rectangular linker, H_8L (linker 50), that was used for the successful synthesis of a tbo-MOF (Cu-tbo-triazole). This organic linker was composed of four arms carrying isopthalate moieties and two arms carrying triazole moieties functionalized with hydroxyl groups. Linker 50 and linker 52 exhibit the same length across the one axis so one would expect that an isostructural tbo-MOF could be formed by the solvothermal reaction of linker 52 with a M^{2+} ion. Solvothermal reaction of linker 52 and Zn^{2+} ions resulted to the formation of small colorless single crystals. Although this synthetic procedure allowed the formation of single crystals, the structure of this material couldn't be determined through single crystal XRD measurements. The resulting material was characterized using pxrd measurements. The experimental pxrd pattern was compared with all other tbo type MOFs based on similar organic linkers, Cu-tbo-triazol and tbo-MOF-3. Apparently there is no resemblance among the three pxrd patterns, so the structure of this new compound can only be verified by means of single crystal XRD measurements.

H$_{12}$L2   linker 52   linker 50
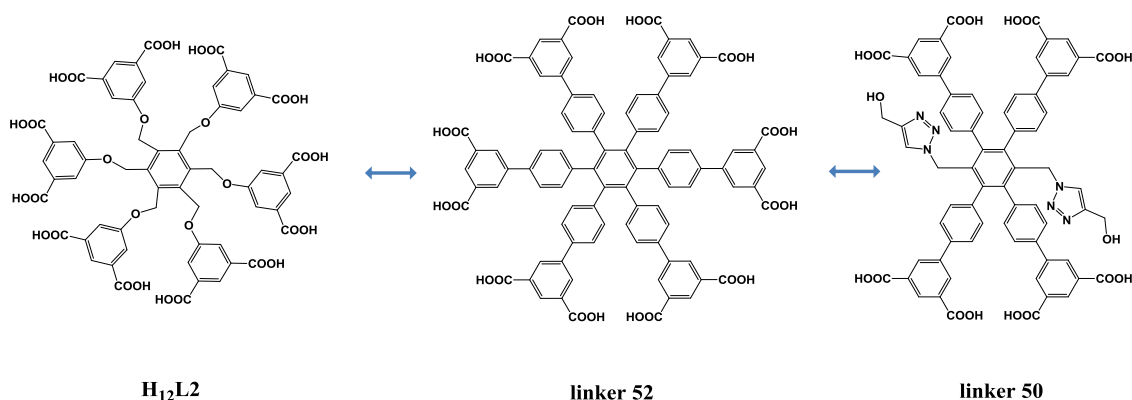
Figure 5.50. Left: the organic linker H$_{12}$L2 used for the synthesis of tbo-MOF-3, middle: the organic linker 52, right: the rectangular linker 50 used for the synthesis of a tbo-MOF.

5.5 Syntheses of functionalized NbO-MOFs

Another versatile family of MOFs is the NbO type MOFs that exhibit the niobium oxide topology. This network can be assembled by the combination of a linear linker with terminal isopthalate groups on each end and a Cu^{2+} paddlewheel SBU. This topology has a few major characteristics. By modifying the length of the organic linker it is possible to tune the porosity of the resulting material and by using a functionalized organic linker it is possible to incorporate pendant functional groups inside the pores of the material. Additionally there are open metal sites that lie on the axial positions of the SBUs. Therefore those MOFs are a very promising platform for the synthesis of functionalized porous materials with enhanced gas sorption properties.[121]

For that purpose we designed and synthesized a variety of linear linkers, each one with different length and different functional groups.

The first material that was synthesized is based on the reaction of linker 73 with Cu^{2+} ions. This solvothermal reaction resulted to the formation of small green crystals. The resulting material was characterized using pxrd measurements. This synthetic procedure revealed an NbO type MOF isostructural with NOTT-103 compound.[122] The structure contains a Cu$_2$(O$_2$CR)$_4$ paddlewheel SBU. Each SBU contains two Cu^{2+} ions that exhibit square pyramidal geometry, with each Cu^{2+} coordinated to four oxygen atoms of four carboxylates and one axial DMF molecule. The SBUs are bridged by four organic ligands, and each organic linker bridges four SBUs, resulting to a 3-D framework with overall framework formula Cu$_2$L1 (L1 = linker 73).The SBU can be viewed as a square planar 4 connected node and the organic linkers can also be viewed as square-planar 4-connected nodes since the four carboxylate groups on the isophthalate in all ligands lie in the same plane. This combination of nodes gives rise to an NbO type network. There are two types of cages in the structure, one elongated octahedron and one spherical adjacent to each other connected by two different windows.

This material was stable in air for at least 6 days and at various solvents including acetone and methanol. However, as it was verified from pxrd measurements, it was not possible to evaluate its gas sorption properties. Apparently the material collapsed upon solvent removal under vacuum.
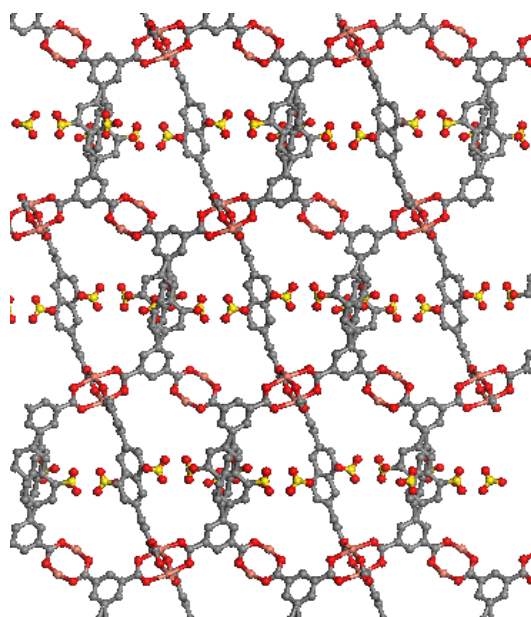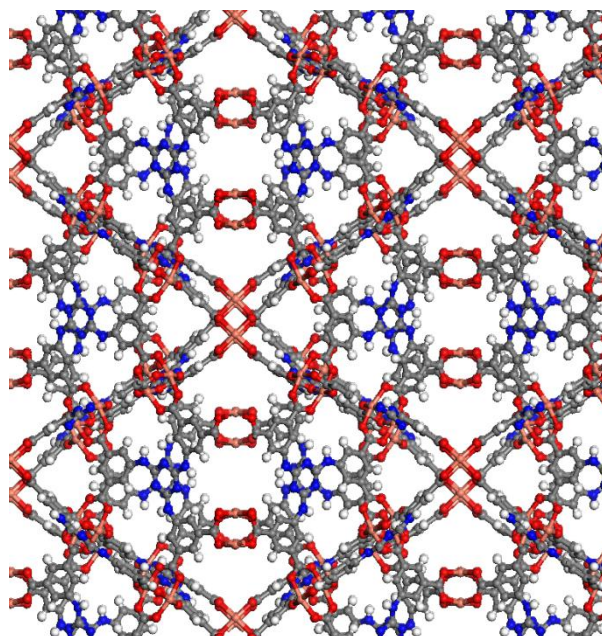
<u>Figure 5.51.</u> Part of the 3-D crystal structure of compound Cu_2L1, looking down the b axis. Orange spheres: Cu, gray: C, red: O, yellow: S. Solvent molecules and hydrogen atoms are omitted for clarity.

The fact that the material consisting of 100% functionalized organic linker collapsed upon solvent removal, prompted us to find an alternative way to evaluate its gas sorption properties. It is possible that partial substitution of the functionalized linker with the non-functionalized one could result to a more robust framework judging by the fact that the NOTT-103 compound containing only the non-functionalized organic linker is stable upon solvent removal. Therefore we used a mixed linker strategy for the synthesis of a new MOF, utilizing the functionalized ligand 73 (L1) and its non functionalized parent linker (L2). The resulting material was characterized using pxrd measurements. This synthetic procedure revealed again an NbO type MOF isostructural with NOTT-103 compound and compound Cu_2L1. Apparently although the as made material is air stable for many days the evacuated material decomposes rapidly upon exposure to air as it is obvious from the pxrd measurements. This might be attributed to the fact that the open metal sites are now accessible to the water molecules present in the air, which due to their high concentration decompose immediately the paddlewheel cluster. This fact is amplified due to the presence of Cu^{2+} ions, which have a high affinity for water molecules.[123]

After the efficient characterization of the material the evaluation of its gas sorption properties took place. ^{1}H NMR measurements of the DMF washed material in D_2O solvent confirmed the absence of dimethyl ammonium ions, providing in this way evidence that the two sulfonic groups are protonated. Additionally ^{1}H NMR measurements of the acetone exchanged material in DMSO-d_6 solvent confirmed the complete removal of residual DMF from the pores of the framework. With this measurement it was also possible to determine the exact ratio of the two organic linkers of the material. The initial ratio that was used in the synthesis was 1:2, that is excess for the non-functionalized linker (L2), while the final ratio was found to be 1:1.6. So the resulting framework

formula is $Cu_2L1_{0.4}L2_{0.6}$. Apparently the system used more of the functionalized organic linker to construct the resulting framework.

Argon adsorption measurements at 87 K revealed a fully reversible Langmuir isotherm. The calculated surface area from the Argon isotherm was found to be 1587 $m^2 g^{-1}$ (BET) and the total pore volume 0.61 $cm^3 g^{-1}$. Pore size distribution analysis revealed that the pore space is diminished by the introduction of the functional groups, from 15.5 Å to 11.07 Å.

CO_2 and CH_4 gas sorption measurements were performed. CO_2 measurements revealed an impressive uptake of 5.6 mmol g^{-1} at 273 K and 1 bar, while at 298 K and 1 bar the uptake reaches a value of 3.2 mmol g^{-1}. Those values are typical for low surface area MOFs with open metal sites and functional groups.[124] The calculated Q_{st}^0 for CO_2 was found to be 24.1 kJ mol^{-1} with a small decline during CO_2 loading. We have also performed CH_4 adsorption measurements at 112 K, 273 K, and 298 K at 1 bar. $Cu_2L1_{0.4}L2_{0.6}$ adsorbs at 112 K and 1 bar 17 mmol g^{-1} (380 $cm^3 g^{-1}$) while at 273 K it adsorbs 1.34 mmol g^{-1}. The calculated Q_{st}^0 for CH_4 was found to be 19.72 kJ mol^{-1} remaining constant during CH_4 loading. This value is among the highest reported for MOFs. Although this material has a low gravimetric surface area, its high crystal density (0.987 g cm^{-3} for the non-functionalized NOTT-103) leads to a high volumetric surface area, and therefore to a high volumetric methane uptake. Consequently high pressure methane measurements could reveal whether this material is a promising candidate for methane storage applications.

The narrow pores along with the existence of open metal sites and polar functional groups prompt us to perform Xe and Kr gas sorption measurements at various temperatures. At 180 K and 1 bar $Cu_2L1_{0.4}L2_{0.6}$ adsorbs 11.5 mmol g^{-1} Kr (258 $cm^3 g^{-1}$), while at 292 K it adsorbs 0.9 mmol g^{-1} (19.6 $cm^3 g^{-1}$). The calculated Q_{st}^0 was found to be 18.57 kJ mol^{-1}. Additionally the Xe uptake at 1 bar and 240 K was found to be 8.9 mmol g^{-1} (200 $cm^3 g^{-1}$), while at 292 K it adsorbs 3.8 mmol g^{-1} (85.3 $cm^3 g^{-1}$). The calculated Q_{st}^0 was found to be 25 kJ mol^{-1} with a slight decline during Xe loading. Those values are among the highest reported for MOFs rendering this material a potential candidate for the storage of Xe and Kr.[125] Furthermore those results prompted us to calculate the selectivities of Xe/Kr. Indeed using the IAST method, for a 5/95 molar mixture at 273 K and 292 K, the selectivity was found to be almost identical for both temperatures with a value of 6.9. Unequivocally those values can be well compared with some of the best MOF candidates for the separation of Xe from Kr,[126] rendering $Cu_2L1_{0.4}L2_{0.6}$ a potential candidate for the efficient separation of Xe over Kr.

Bearing in mind the impact of this functional group in gas sorption properties we used a linker of almost the same length but with different functional groups.

The second material that was synthesized is based on the reaction of linker 57 with Cu^{2+} ions. This solvothermal reaction resulted to the formation of small light blue crystals. The large single crystals made possible the determination of the structure of this MOF. Through single crystal X-ray diffractometry the structure was solved revealing a neutral non interpenetrated 3-D NbO type of framework. It crystallizes in the hexagonal system (space group *R-3m*) with unit cell parameters a = b

= 18.7576 Å, c = 52.2075 Å, α = β = 90^0, γ = 120^0. The framework is made of paddlewheel Cu$_2$(O$_2$CR)$_4$ SBUs connected through four linkers (H$_4$L), and each organic linker connects four SBUs resulting to an overall framework formula Cu$_2$L. There are two types of cages in the structure, one elongated octahedron and one spherical adjacent to each other connected by two different windows. The material is highly porous and the total solvent-accessible volume was found to be 71 %, using the PLATON software. However its porosity wasn't evaluated by means of gas adsorption because of lack of a suitable activation procedure. Many methods have been tested, including the use of low boiling solvents, such as acetone, CH$_2$Cl$_2$, and supercritical CO$_2$. Apparently the material collapsed upon solvent removal under vacuum. Since the structural integrity before solvent removal was verified by pxrd measurements. The formation of a pure phase was verified using pxrd measurements. Experimental and calculated from the single crystal structure patterns are identical. It must be mentioned at this point that during our attempts to activate this material Zheng and coworkers published the same structure based on the same organic linker.[127]
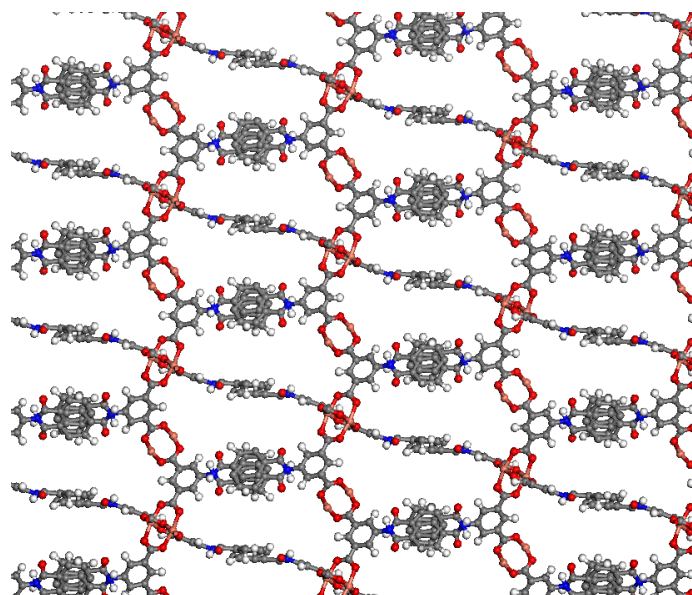
Figure 5.52. Part of the 3-D crystal structure of compound Cu$_2$L, looking down the a axis. Orange spheres: Cu, gray: C, red: O, white: H, blue: N. Solvent molecules are omitted for clarity. The central benzene ring is disordered.

After those results we synthesized two more elongated organic linkers functionalized with amide groups that were expected to form highly porous materials. Of course a suitable activation procedure would allow the successful evaluation of their gas sorption properties.

The third material that was synthesized is based on the reaction of linker 56 with Cu^{2+} ions. This solvothermal reaction resulted to the formation of small light blue crystals.The large single crystals made possible the determination of the structure of this MOF. Through single crystal X-ray diffractometry using synchrotron radiation the structure was solved revealing a neutral non interpenetrated 3-D NbO type of framework. It crystallizes in the trigonal system (space group *P3$_1$21*) with unit cell parameters a = b = 18.840 Å, c = 57.860 Å, α = β = 90^0, γ = 120^0. This material is

isostructural to previous compound based on the shorter organic linker 57. The framework is made of paddlewheel $Cu_2(O_2CR)_4$ SBUs connected through four linkers (H_4L), and each organic linker connects four SBUs resulting to an overall framework formula Cu_2L. There are two types of cages in the structure, one elongated octahedron and one spherical adjacent to each other connected by two different windows. This structure can be viewed as analogues to the NOTT-103 framework. So far it was not possible to evaluate its gas sorption properties because of lack of a suitable activation procedure. Many methods have been tested, including the use of low boiling solvents, such as acetone, CH_2Cl_2, and supercritical CO_2. Apparently the material collapsed upon solvent removal under vacuum. Since the structural integrity before solvent removal was verified by pxrd measurements. The formation of a pure phase was verified using pxrd measurements, as experimental and calculated from the single crystal structure patterns are identical.

The fourth material that was synthesized is based on the reaction of linker 55 with Cu^{2+} ions. This solvothermal reaction resulted to the formation of small light blue crystals. The resulting material was characterized using pxrd measurements. This synthetic procedure revealed a highly crystalline material. Although this synthetic procedure allowed the formation of single crystals, the structure of this material couldn't be determined through single crystal XRD measurements. Comparison of experimental pxrd patterns of previous NbO compounds proved that an expanded NbO analogue is synthesized, as the two patterns are identical. The longer size of linker 55 in comparison to linker 56 results to a larger unit cell as it is clear from the pxrd pattern. A shift of the pxrd pattern to lower 2θ angles, therefore higher values of d spacing, is indicative of a larger unit cell. This is a non interpenetrated structure and it is expected to be highly porous.

Indeed the existence of polar functional groups can improve the interaction of the framework with gas molecules. But the interaction of specific gas molecules with the open metal sites is much stronger. Therefore maximizing the density/number of open metal sites inside a porous material is expected to increase substantially the interaction of this media with the targeted gas molecules.[128] This can be achieved by assembling an NbO network using an organic linker with relative small length in order to have high density of open metal sites, due to the existence of Cu^{2+} SBUs. At this point a highly desirable property would be the existence of more open metal sites in the framework. This can be achieved by using organic linkers that are functionalized with open metal sites.

Taking into account all these parameters we designed and synthesized the organic linker 71. The idea behind the synthesis of this linker was the design of a linker bearing a $PdCl_2$ moiety that is already part of the ligand and it is not post synthetically attached to the linker after the formation of a framework. In this case it is definite that all the linkers of the framework bear this functionality, whereas a post synthetic modification of a non-functionalized linker would provide uncertain results about the percentage of the linker modification. Furthermore the synthesis of linkers bearing heavy metal atoms would give rise to porous materials with high crystal density, this property bestows upon the material high volumetric surface area and capacity. Those two are very desirable properties for gas storage

applications. Additionally in this case the Pd^{2+} atom has the axial (or opposite equatorial) positions uncoordinated, therefore reaction of this linker with metal ions can lead to the synthesis of materials already functionalized with open metal sites. Noticeably this moiety was former introduced in a covalent framework resulting to very high hydrogen uptake at ambient temperature.[129] Therefore this strategy is expected to improve significantly the gas uptake of the resulting porous materials.

  Solvothermal reaction of linker 71 with Cu^{2+} ions resulted to the formation of small light blue cubic crystals.The single crystals made possible the determination of the structure of this MOF. Through single crystal X-ray difractometry, using synchrotron radiation, the structure was solved revealing a 3-D NbO type of framework (see figure 5.53). It crystallizes in the hexagonal system (space group *R-3m*), with unit cell parameters a = b = 18.899 Å, c = 31.690001 Å, $\alpha = \beta = 90^0$, $\gamma = 120^0$. This is a non-interpenetrated neutral structure with an overall framework formula $Cu_2[Pd(PDC)Cl_2]$. The structure contains a $Cu_2(O_2CR)_4$ paddlewheel SBU. Each SBU contains two Cu^{2+} ions that exhibit square pyramidal geometry, with each Cu^{2+} coordinated to four oxygen atoms of four carboxylates and one axial DMF molecule. The SBUs are bridged by four organic ligands, and each organic linker bridges four SBUs. The resulting framework contains one type of open cage, forming a truncated cube having a diameter of 11.1 Å, taking into account the van der Waals radii. All cages are connected through a narrow 1-D channel with a diameter of 4.3 Å that runs down the c axis of the framework.
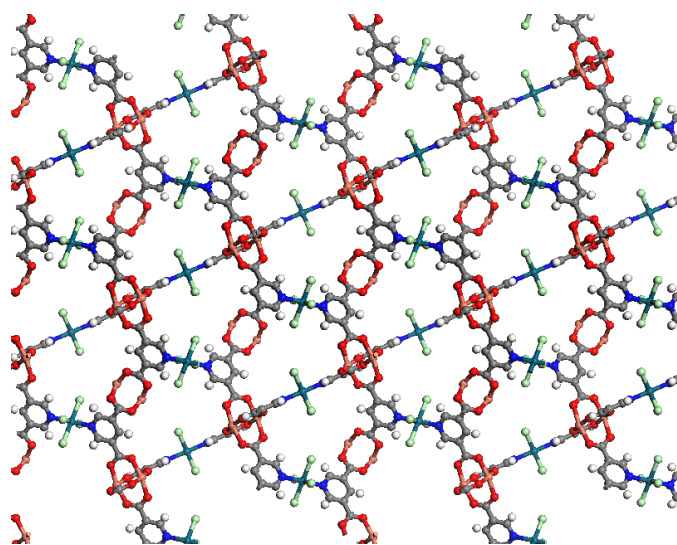
Figure 5.53. Part of the 3-D crystal structure of compound $Cu_2[Pd(PDC)Cl_2]$, looking down the a axis. The two types of cavities are perpendicular to the layers of the structure. Orange spheres: Cu, gray: C, red: O, white: H, blue: N, green: Cl. Solvent molecules are omitted for clarity.

  Powder X-ray diffraction analysis verified the formation of a pure phase. The solvent accessible volume was calculated by the PLATON software and found to be 61%. After the successful characterization of the material a suitable activation procedure would allow the evaluation of its gas sorption properties. Therefore the as made material was washed with DMF four times per day for 2 days and then the sample was soaked in methanol over a period of 4 days, replenishing the methanol 4

times per day. The methanol suspended sample was transferred inside a pre-weighted sample cell and the methanol was removed under reduced pressure. Finally, the sample was activated under dynamic vacuum at 60 °C for 12 hours and until the outgas rate was less than 2 mTorr/min.

Nitrogen sorption measurements confirmed the permanent porosity of $Cu_2[Pd(PDC)Cl_2]$, giving a fully reversible type I isotherm indicative of microporous materials, in full agreement with the crystallographic data. The calculated BET surface area was estimated to be 1588 m^2 g^{-1} and the total pore volume was found to be 0.62 cm^3 g^{-1}.

In order to evaluate its gas sorption properties we performed CO_2, H_2, and CH_4 sorption measurements. At 77 K and 1 bar $Cu_2[Pd(PDC)Cl_2]$ adsorbs a very high amount of 2 wt% H_2. Those values are very high for low surface area MOFs, and can be well compared to high surface area MOFs with open metal sites.[130] CO_2 measurements revealed an impressive uptake of 9 mmol g^{-1} (28.4 wt%, 197 cm^3 cm^{-3}) at 273 K and 1 bar, while at 298 K and 1 bar the uptake reaches a value of 5.6 mmol g^{-1} (19.7 wt%, 121 cm^3 cm^{-3}). Those values place $Cu_2[Pd(PDC)Cl_2]$ among the ten best candidates for CO_2 storage at RT and 1 bar.[131] The calculated Q_{st}^0 for CO_2 was found to be 23.4 kJ mol^{-1} remaining constant during CO_2 loading. We have also performed CH_4 adsorption measurements at 273 K, 288 K, 293 K and 298 K at 1 bar. $Cu_2[Pd(PDC)Cl_2]$ adsorbs at 273 K and 1 bar 1.6 mmol g^{-1} while at 298 K it adsorbs 0.9 mmol g^{-1}. The high CO_2 uptake of this material prompted us to determine the calculated selectivity values for the separation of CO_2/CH_4 and CO_2/N_2. The CO_2/CH_4 selectivity was calculated using IAST for a 5/95 molar mixture at 273 K and 298 K giving rise to a value of 8.5 and 8 respectively. These are high values and are indicative for MOFs with open metal sites.[132] Additionally we calculated the CO_2/N_2 selectivity for a 5/95 molar mixture at 273 K and 298 K and some very impressive values were revealed, 38 and 33 respectively. Those are very high values and can be compared with some of the best materials for the separation of CO_2 from N_2.[133] Those results verified our initial hypothesis that a material synthesized by this metalated organic linker was expected to have improved gas sorption properties.

5.6 Syntheses of functionalized etb-MOFs

   A well studied family of MOFs is the *etb* type MOFs, or MOF-74 analogues. The organic part of these MOFs is composed of linear organic linkers, bearing at each end a carboxy (-COOH) and a hydroxyl group (-OH) in ortho position. The inorganic part is a 1-D $M_3O_3(CO_2)_3$ chain. Combination of those two leads to the formation of a structure with 1-D hexagonal channels. This diverse MOF platform exhibits some important characteristics that are exceptional. On the one hand it is possible to tune the porosity by using organic linkers with variable size. Furthermore the use of functionalized organic linkers can give rise to functionalized analogues with interesting properties. On the other hand lay the existence of a large number of open metal sites per hexagonal ring.[134]

   Taking all these into account we have synthesized a series of functionalized organic linkers to target this topology. These linkers are functionalized with two amide groups and exhibit different sizes. The use of a longer organic linker compared to MOF-74 analogues based on H_2BDC and H_2BPDC[135] organic linkers would result to higher gravimetric surface areas as it was shown by Deng et al.[136] Additionally the incorporation of twelve amide groups per hexagonal ring, along with the six open metal sites is expected to increase substantially the interaction of the framework with specific gas molecules (e.g. CO_2, CH_4).[137]

   Solvothermal reaction of linker 66 with Zn^{2+} ions resulted to the formation of a crystalline material. However due to the lack of single crystals its structure could be determined. Therefore its structure was constructed in order to acquire the calculated pxrd pattern and compare it to the experimental one. This comparison would verify the hypothesis that and an expanded MOF-74 analogue was formed.

   The MOF crystallizes in the hexagonal system (space group *R-3*), with unit cell parameters a = b = 53.337 Å, c = 6.306 Å, $\alpha = \beta = 90^0$, $\gamma = 120^0$. This is a non-interpenetrated neutral structure with an overall framework formula Zn_2L. The structure is composed of infinite $Zn_3O_3(CO_2)_3$ chains, where each metal ion has an octahedral geometry and is coordinated to three carboxyl, two hydroxyl groups, and a coordinated solvent molecule.
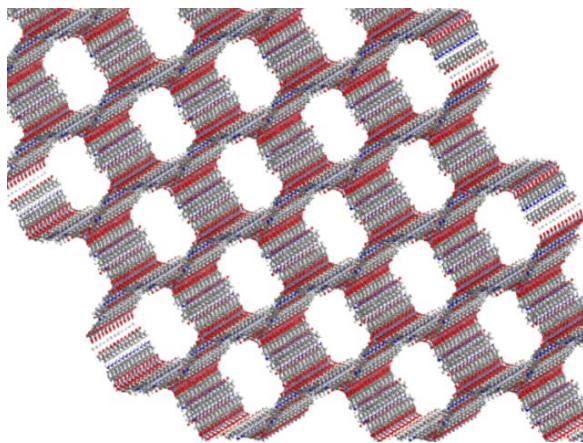
Figure 5.54. Part of the 3-D crystal structure of compound Zn_2L, looking slightly off the c axis. Purple spheres: Zn, gray: C, red: O, white: H, blue: N. Solvent molecules are omitted for clarity.

The resulting framework contains one type of 1-D hexagonal channels of 34 Å in diameter, without taking into account the van der Waals radii. The estimated crystal density is 0.54 g cm^{-3}. The formation of a phase pure and highly crystalline material was verified as experimental and calculated pxrd patterns are identical. There have been many attempts to activate this material but it was not possible so far to evaluate its gas sorption properties. Further attempts are ongoing using flow of supercritical CO_2.
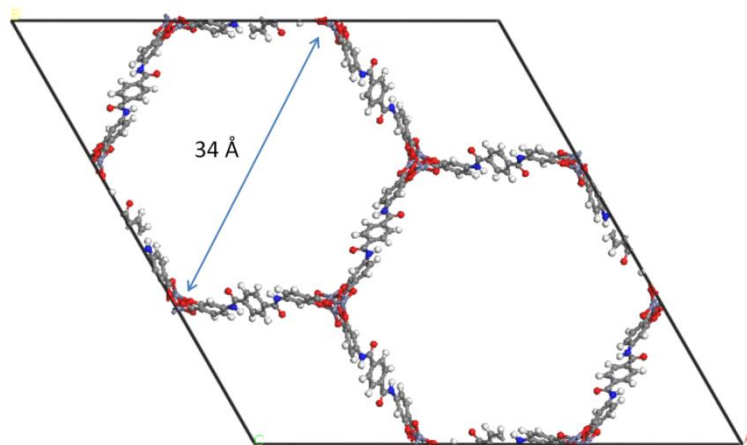
Figure 5.55. The unit cell of compound Zn$_2$L looking down the c axis. Purple spheres: Zn, gray: C, red: O, white: H, blue: N. Solvent molecules are omitted for clarity.

The next material was based on the longer linker 67. Solvothermal reaction with Zn^{2+} ions resulted to the formation of a crystalline material. The resulting material was characterized using pxrd measurements. Comparing the pxrd patterns of this compound and the previous one compound is obvious that we have synthesized an expanded MOF-74 analogue, with a larger unit cell. That is clear from the shift of the pxrd pattern to lower 2θ angles due to the longer length of linker 67.

This linker was also used for the synthesis of the Mg^{2+}, Mn^{2+} and Co^{2+} analogues. The resulting materials were characterized using pxrd measurements. All materials are highly crystalline and isostructural.
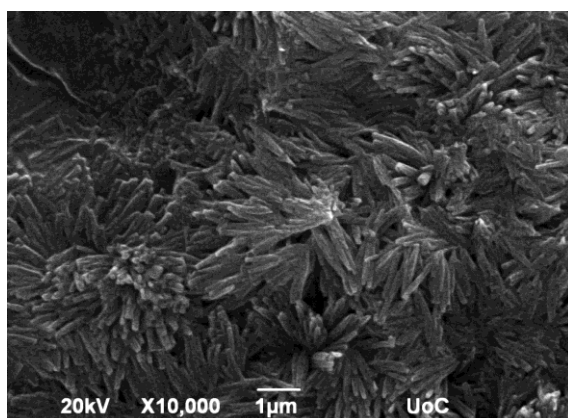
Figure 5.56. Representative SEM image of the as synthesized Mg$_2$L material.
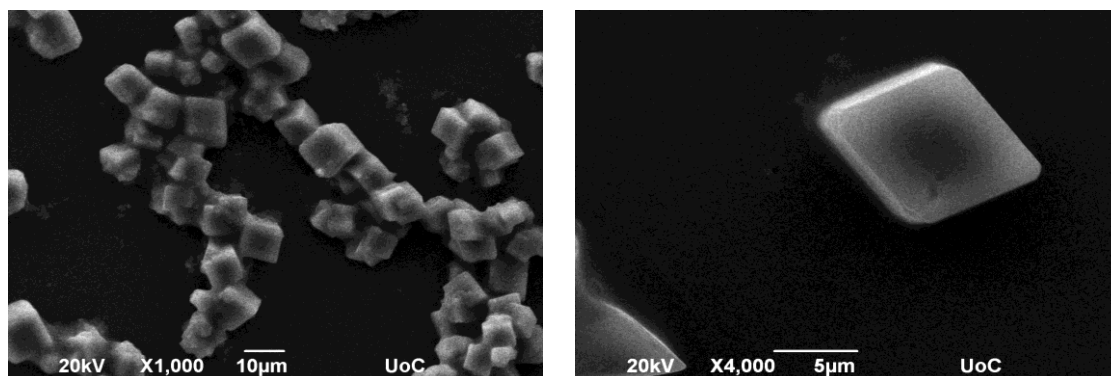
Figure 5.57. Representative SEM images of the as synthesized Mn$_2$L material. The material consists of very small crystal cubes.

Following this we used the longer organic linker 68 to access, after successful activation, even higher gravimetric surface area.

Solvothermal reaction with Zn^{2+} ions resulted to the formation of a crystalline material. The resulting material was characterized using pxrd measurements. The structure of this MOF was constructed in order to acquire the calculated pxrd pattern and compare it to the experimental one. This comparison could verify the hypothesis that and an expanded MOF-74 analogue was formed.

The MOF crystallizes in the trigonal system (space group *P3*), with unit cell parameters a = b = 69.819 Å, c = 6.7297 Å, α = β = 90^0, γ = 120^0. This is a non-interpenetrated neutral structure with an overall framework formula Zn$_2$L. The structure is composed of infinite Zn$_3$O$_3$(CO$_2$)$_3$ chains, where each metal ion has an octahedral geometry and is coordinated to three carboxyl, two hydroxyl groups, and a coordinated solvent molecule. The resulting framework contains one type of 1-D hexagonal channels of 44 Å in diameter, without taking into account the van der Waals radii. The estimated crystal density is 0.34 g cm^{-3}. The formation of a phase pure material was verified as experimental and calculated pxrd patterns are identical. This linker was also used for the synthesis of the Mg^{2+} analogue. The resulting material was characterized using pxrd measurements. It is highly crystalline and isostructural to the Zn^{2+} analogue.
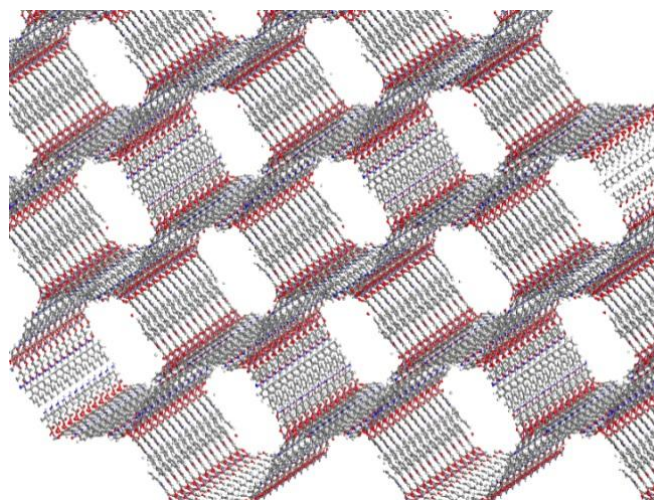
Figure 5.58. Part of the 3-D crystal structure of compound Zn$_2$L, looking slightly off the c axis. Purple spheres: Zn, gray: C, red: O, white: H, blue: N. Solvent molecules are omitted for clarity.
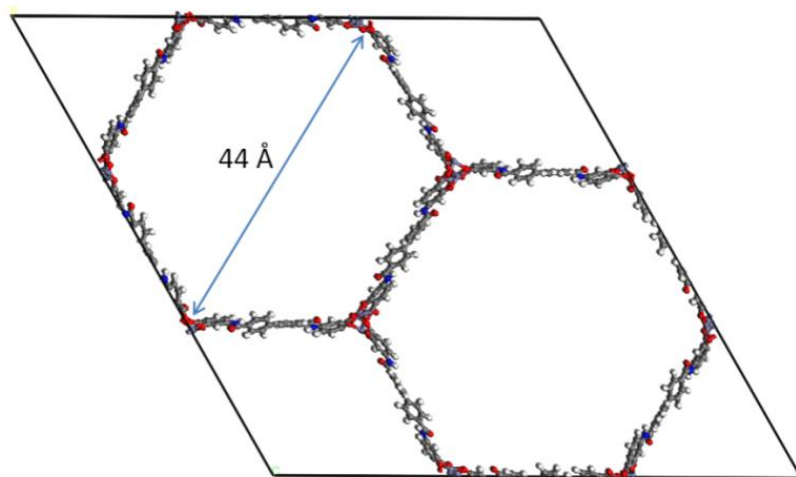
<u>Figure 5.59.</u> The unit cell of compound Zn_2L looking down the c axis. Purple spheres: Zn, gray: C, red: O, white: H, blue: N. Solvent molecules are omitted for clarity.

Nonetheless this interesting structure can be synthesized by a different combination of organic and inorganic parts. It is possible by using a trigonal tritopic linker and Al^{3+} ions to construct the same framework, as it was observed in the case of CAU-4.[138] The use of Al^{3+} ions is expected to construct highly robust and air stable MOFs. However this material contains no open metal sites, which is a significant drawback compared to the MOF-74 analogues, in terms of gas sorption properties. To overcome this deficiency, we have designed and synthesized the trigonal tritopic linker 58, which is functionalized with three amide groups. The large number of amide groups (six) per hexagonal ring is expected to compensate for the absence of open metal sites, giving rise to robust materials with enhanced gas sorption properties.

Solvothermal reaction of linker 58 with Al^{3+} ions resulted to the formation of a highly crystalline material. The resulting material was characterized using pxrd measurements. The lack of single crystals prompted us to construct the crystal structure using molecular simulations.

The construction of the theoretical periodic model was based on the periodic model of the CAU-4 structure. At first, the molecular model of the proposed organic linker was optimized by performing first principles calculations. The prediction of the geometry was based on the Density Functional Theory (DFT) method and the RI-PBE/def2-TZVP[139] computational model was used during calculations. Very tight convergence criteria were used for both the self consistent field procedure (10^{-8} au) and the gradient (10^{-4} au). The corresponding auxiliary basis sets were used for the Resolution of Identity (RI) [140]approximation. During the optimization of the geometry, symmetry restrictions were applied in order to keep the carboxylate groups which are connected to the Al atoms in a geometry similar with that in CAU-4. The calculation was performed with the Turbomole[141] quantum chemistry package. Afterwards, the periodic model of the new Al-MOF was constructed. In order to build it, we removed the organic linkers of the CAU-4 and we replaced them with the new organic linker. At the same time, we altered the dimensions of the a, b, c axes (the angles of the cell were kept fixed) and the positions of the Al and O atoms in order to achieve that the new organic linker will fit in the position

of the replaced organic linker of the CAU-4. Then, we performed a molecular mechanics calculation for the periodic cell in order to equilibrate the position of the atoms and the dimensions of the periodic cell. The symmetry of the periodic cell was P1 during the calculation. The calculation was performed with a modified version of the UFF[142] forcefield especially for MOF structures, as implemented in the GULP[143] program.

The unit cell parameters were found to be as follows: a = 27.7027 Å, b = 27.7033 Å, c = 11.4602 Å, $\alpha = 93.7278^0$, $\beta = 90.5615^0$, $\gamma = 120.3821^0$. This is a non-interpenetrated mesoporous structure with an overall framework formula Al(L). The resulting framework is based on single [AlO$_6$] octahedra, which are connected via bridging carboxylate groups. Thus, an infinite 1-D chain of bridged octahedra is formed. Each Al^{3+} ion is connected to six organic linkers and each organic linker is connected to six Al^{3+} ions. The tritopic linker connects these octahedra to form a honeycomb framework with one-dimensional channels. These channels exhibit a diameter of 25 Å, taking the van-der-Waals radii of the framework atoms into account. Powder X-ray diffraction analysis verified the formation of a pure phase as the calculated and experimental powder pattern are identical.
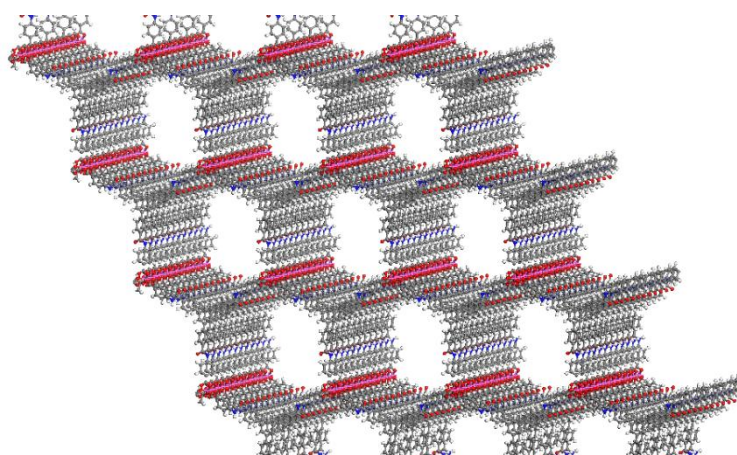
Figure 5.60. The 1-D honeycomb channels of the crystal structure. Pink spheres: Al, gray: C, red: O, white: H, blue: N. Solvent molecules are omitted for clarity.
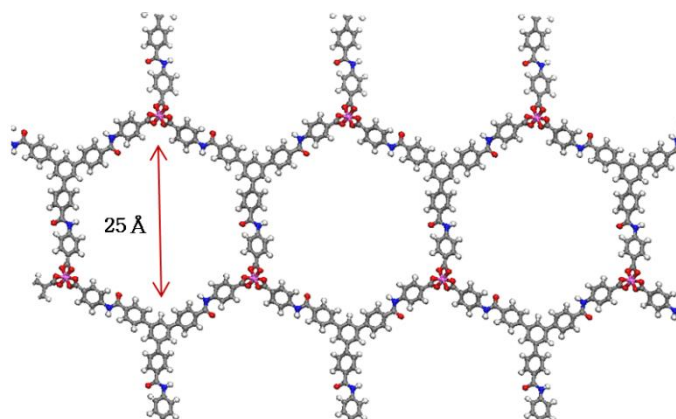
Figure 5.61. Part of the 3-D mesoporous crystal structure of compound Al(L), looking down the c axis. Pink spheres: Al, gray: C, red: O, white: H, blue: N. Solvent molecules are omitted for clarity.

After the successful characterization of the material a suitable activation procedure would allow the evaluation of its gas sorption properties.

Argon sorption measurements confirmed the permanent porosity of Al(L), giving a fully reversible isotherm with a distinct condensation step in the relative pressure range P/P_o 0.04 - 0.15 suggesting the presence of small mesopores, in full agreement with the crystallographic data. The calculated BET surface area of Al(L), assuming monolayer coverage of Ar up to the first step, was estimated to be 1617 m^2 g^{-1}. Accordingly, isotherm data were fitted using a suitable NLDFT kernel and the pore size distribution curve revealed a distinct peak centered at 25 Å, in agreement with the crystallographic analysis. However the presence of a small step at relative pressure 4 x 10^{-2} P/P_0, could not be fitted well with any of the NLDFT kernels used, resulting to the presence of two additional peaks centered at 10 Å and 12 Å, that are not expected from the crystal structure. The void volume calculated by using the crystal structure data from PLATON software had a value of 66%. While the calculated total pore volume from the argon isotherm was estimated to be 0.95 cm^3 g^{-1} very close to the calculated one from the crystal structure 0.99 cm^3 g^{-1}.

In order to evaluate its gas sorption properties we performed CO_2, H_2, and CH_4 sorption measurements. At 77 K and 1 bar Al(L) adsorbs 1.1 wt% H_2 with a calculated Q_{st} value of 5.89 kJ mol^{-1}. These are typical values for mesoporous MOFs without open metal sites.[144] CO_2 measurements revealed an uptake of 2.19 mmol g^{-1} at 273 K and 1 bar, 1.25 mmol g^{-1} at 298 K and 1 bar while at 195 K and 1 bar the uptake reaches a value of 23.45 mmol g^{-1}. The CO_2 uptake at 273 K and 1 bar although it exhibits a moderate value it can be well compared to other mesoporous MOFs without open metal sites.[145]

The calculated Q_{st}^0 for CO_2 was found to be 22.85 kJ mol^{-1} with a sharp decline during CO_2 loading. We have also performed CH_4 adsorption measurements at 273 K, 298 K and 112 K at 1 bar. Impressively Al(L) adsorbs at 112 K and 1 bar 570 cm^3 g^{-1} which is a high value for a mesoporous MOF with low surface area. We calculated the isosteric heat of adsorption and found a value of Q_{st}^0 = 21.7 kJ mol^{-1} using the virial equation, and 21.3 kJ mol^{-1} with the Clausius clapeyron equation, which is among the highest values reported for MOFs, but most important this value remains constant during methane loading.[146] Those findings prompted us to perform high pressure CH_4 measurements to evaluate Al(L) towards methane storage. Indeed at 298 K and 100 bar the total gravimetric uptake reaches a value of 356 cm^3 g^{-1}, while the total volumetric uptake was found to be 192 cm^3 cm^{-3}. The volumetric working capacity was estimated to be (between 65 bar and 5 bar) 133 cm^3 cm^{-3} which is a very promising value for a mesoporous MOF and can be well correlated with some of the best methane storage candidates (see table 6.6 and 6.7). Although this material has no open metal sites, the existence of six polar amide groups per hexagonal ring may be responsible for this high methane uptake, by increasing substantially the interaction of the framework with the methane molecules. This assumption can also be supported by the fact that this material contains only mesopores (25 Å), therefore the methane molecules are not so confined in order to maximize the $CH_4 \cdots CH_4$ interactions

as it was observed in the case of UTSA-20.[147] Consequently this high methane uptake can only be explained by the existence of the large number of amide groups that protrude into the 1-D channels. Nonetheless only theoretical calculations can give truly insight for the interpretation of this high methane uptake of this mesoporous structure. The CO_2/CH_4 selectivity was calculated using IAST for a 5/95 molar mixture at 273 K and 298 K giving rise to a value of 3.7 and 3.2 respectively. Those very low values are indicative of the lower affinity of the framework for CO_2 towards CH_4, as it was also observed from the low isosteric heat of adsorption for CO_2 and the very high isosteric heat of adsorption for CH_4.

5.7 Syntheses of rht-MOFs

A most prominent family of MOFs is the one exhibiting the *rht* type of framework. This material consists of trigonal hexacarboxylate ligands, bearing three isophthalate moieties that coordinate to 24 square paddlewheel $M_2(COO)_4$ units, forming a cuboctahedron cluster. It is possible that by adjusting the size of the organic linker the porosity of the resulting material can be tuned.[148] Additionally the existence of a very high density of open metal sites renders those materials promising candidates for gas storage and separation applications. Furthermore by using a functionalized organic linker it would be possible to enhance further the gas sorption properties of the resulting material. This is something that was observed in the case of Cu-TDPAT, a material with remarkable gas sorption properties. [149]

Taking all these into account we synthesized the same organic linker H_6TDPAT, linker 72, for the synthesis of isostructural compounds but with different metal ions. To be more specific it was expected that replacement of Cu^{2+} ions with Co^{2+} ions will improve the interaction of the framework with H_2 as it was observed in the case of SNU-15, a material with open Co^{2+} sites, that exhibits the highest H_2 isosteric heat of adsorption among MOFs so far.[150]

Solvothermal reaction of linker 72 with Co^{2+} ions resulted to the formation of single crystals. The resulting material was characterized using pxrd measurements. This synthetic procedure revealed a highly crystalline material. Although this synthetic procedure allowed the formation of single crystals, the structure of this material couldn't be determined through single crystal XRD measurements. We compared the experimental pxrd pattern with all other materials based on the same organic linker. This synthetic procedure revealed an rht type MOF isostructural with Cu-TDPAT compound. This rht type of framework consists of $Cu_2(O_2CR)_4$ paddlewheel units that form cuboctahedral SBBs (supramolecular building blocks), which are connected by 24 organic linkers, and each organic linker connects 3 SBBs, resulting to a (3,24)-connected rht-type of network with framework formula Cu_3L. This net contains three types of cages, a cuboctahedron, a truncated tetrahedron and a truncated octahedron.

Comparison of the calculated Cu-TDPAT pxrd pattern and our experimental one verified that we have successfully synthesized the Co-TDPAT analogue. However due to the smaller ionic radius of

the five-coordinated (CuO$_5$) Cu^{2+} ions, square pyramidal geometry, compared with the five-coordinated Co^{2+} ions,[84] the experimental pxrd pattern of Co-TDPAT is shifted to lower 2θ values. That is the unit cell in Co-TDPAT is larger than Cu-TDPAT. However there have been no attempts to activate this material yet.

Figure 5.62. Part of the 3-D crystal structure of compound Cu-TDPAT, looking down the a axis. Orange spheres: Cu, gray: C, red: O, white: H, blue: N. Solvent molecules are omitted for clarity.

Taking a step further we wanted to see if it was possible to synthesize the same material with Mg^{2+} ions. This modification would result to a lighter material with higher gravimetric surface area than the Cu^{2+} analogue, and due to the harder nature of the Mg^{2+} ions one would expect to enhance more the interactions of the framework with specific gas molecules (e.g. CO$_2$).

Solvothermal reaction of linker 72 with Mg^{2+} ions resulted to the formation of single crystals. The large single crystals made possible the determination of the structure of this MOF. Through single crystal X-ray difractometry, using synchrotron radiation, the structure was solved revealing a 3-D framework (see figure 5.63). It crystallizes in the cubic system (space group *F432*), with unit cell parameters a = b = c = 39.980 Å, α = β = γ = 90^0. The structure contains a single molecule Mg^{2+} SBU. Each Mg^{2+} ion exhibits an octahedral geometry. It is bridged monodentate by four organic linkers on the equatorial positions, while the axial positions are occupied by solvent molecules. Each organic linker bridges six metal ions, resulting to an overall framework formula Mg$_3$L$_2$. The framework is charged balanced due to the fact that half of the carboxylate groups are protonated. Therefore the organic linker is coordinated to three metal ions by its carbonyl group and to the other three metal ions by its deprotonated alcoxy group of the carboxylate. This was verified by the difference of the bond lengths between the Mg^{2+} ion and the surrounding oxygen atoms. Two opposite equatorial Mg-O bonds lie in a distance of 2.037 Å while the two other equatorial Mg-O bonds exhibit a distance of

2.059 Å. At the same time the two axial Mg-O bonds lie at a distance of 2.116, indicative of bond length between an Mg^{2+} ion and a carbonyl group of a solvent DMF molecule.[151] Furthermore if all the linkers were deprotonated then there would be a need for six positive charges to charge balance the framework, possibly in the form of dimethylammonium ions. However ^{1}H NMR measurements verified their absence. This net contains three types of adjacent cages, a cuboctahedron, a truncated tetrahedron and a truncated octahedron. Noticeably this structure is the same with the previous compound containing Co^{2+} ions, but in this case the framework is composed of single node SBUs, instead of paddle wheel SBUs. A careful comparison of the two structures reveals that the two opposite Mg^{2+} ions in the case of Mg_3L_2, have replaced two opposite paddle wheel SBUs of Co_3L, resulting to the same structure. The distance between opposite Mg^{2+} ions is 7.2 Å, while the distance between opposite paddle wheel SBUs is 5.4 Å, including the van der Waals radii. That is why the same rht net is formed. Amazingly it the first time that this phenomenon is observed in MOF synthesis. Powder X-ray diffraction analysis verified the formation of a pure phase. The estimated crystal density is 0.529 g cm^{-3} and the total solvent-accessible volume was found to be 69%, using the PLATON software. Therefore this material is highly porous and a suitable activation procedure will allow access to its gas sorption properties. The existence of the triazine core, the amino groups, along with the open Mg^{2+} sites are expected to enhance significantly the interaction of the framework with specific gas molecules.
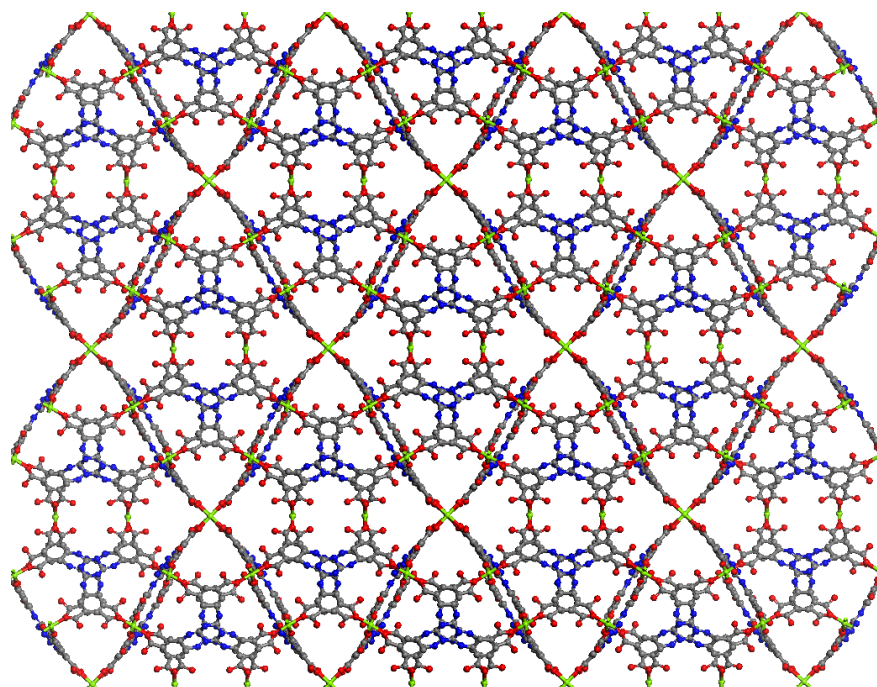
Figure 5.63. Part of the 3-D crystal structure of compound Mg_3L_2, looking along the [110] direction. Green spheres: Mg, gray: C, red: O, white: H, blue: N. Solvent molecules are omitted for clarity.

5.8 Syntheses of MOFs based on a sulfone functionalized organic ligand with tetrahedral linking topology

This functionalized tetrahedral organic linker was used for the successful synthesis of the PCN-521-4SO$_2$ analogue. However it is possible that reaction with other metal ions could result to materials with unknown topologies and potential interesting gas sorption properties.

Solvothermal reaction of linker 40 with Cu^{2+} ions resulted to the formation of large green single crystals. The large single crystals made possible the determination of the structure of this MOF. Through single crystal X-ray difractometry using synchrotron radiation the structure was solved revealing a neutral non interpenetrated 3-D framework. It crystallizes in the tetragonal system (space group $P4_2/ncm$) with unit cell parameters a = b = 25.230 Å, c = 34.891998 Å, $\alpha = \beta = \gamma = 90^0$. The framework is made of paddlewheel Cu$_2$(O$_2$CR)$_4$ SBUs connected through four H$_4$L, and each organic linker connects four SBUs resulting to an overall framework formula Cu$_2$L. The framework consists of two types of 1-D interconnecting channels, one cubic with a diameter of 17.4 Å, and one hexagonal with dimensions 34.9 Å x 15.2 Å, without taking into account the van der Waals radii. The material is highly porous and the total solvent-accessible volume was found to be 84 %, using the PLATON software. Therefore the existence of the open metal sites along with the strong polarizing pendant sulfone groups is expected to increase substantially the interaction of the framework with specific gas molecules. However its porosity wasn't evaluated by means of gas adsorption because of lack of a suitable activation procedure. Many methods have been tested, including the use of low boiling solvents, such as acetone, THF, CH$_2$Cl$_2$, and supercritical CO$_2$. Apparently the material collapsed upon solvent removal under vacuum. Since the structural integrity before solvent removal was verified by pxrd measurements. The formation of a pure phase was verified using pxrd measurements. Experimental and calculated from the single crystal structure patterns are identical.
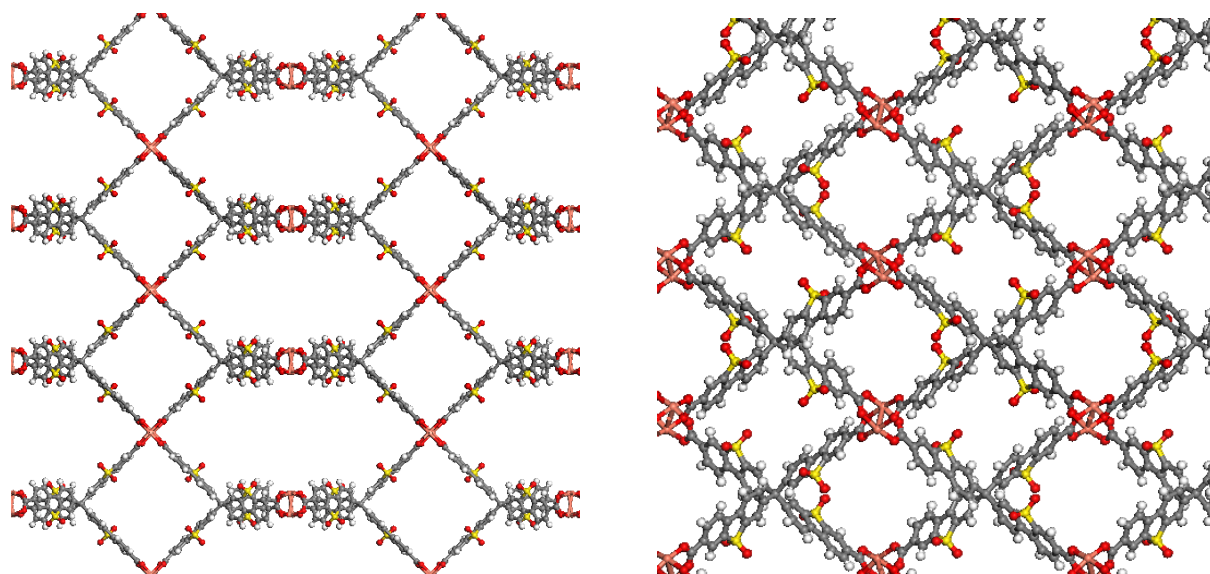
Figure 5.64. Left: Part of the 3-D crystal structure looking along the [110] direction. Right: Part of the 3-D crystal structure looking down the a axis. Orange spheres: Cu, gray: C, yellow: S, red: O, white: H. Solvent molecules are omitted for clarity.

After those promising results we tested a different metal ion. Solvothermal reaction of linker 40 with Mg^{2+} ions resulted to the formation of single crystals. The large single crystals made possible the determination of the structure of this MOF. Through single crystal X-ray difractometry using synchrotron radiation the structure was solved revealing an anionic non interpenetrated 3-D framework. It crystallizes in the monoclinic system (space group *C2/m*) with unit cell parameters a = 32.924 Å, b = 35.819 Å, c = 25.594 Å, $\alpha = 90^0$, $\beta = 105.457^0$ $\gamma = 90^0$. The framework is made of trimer $[Mg_3O_2]^{2+}$ SBUs connected through eight H_4L, and each organic linker connects four SBUs. The four side linkers are coordinated monodentate to the SBU. If these side linkers are protonated, then the framework is charged balanced by two dimethyl ammonium ions, resulting to an overall framework formula $Mg_3O_2L_2(Me_2NH_2)_2$. The number of dimethyl ammonium cations can be verified by ^1H NMR spectroscopy. The framework consists of one type of octahedral cavities that are interconnected through two types of cubic channels. The first one exhibits a diameter of 11.7 Å and the second one a diameter of 18 Å, without taking into account the van der Waals radii. Therefore the existence of the open metal sites along with the strong polarizing pendant sulfone groups is expected to increase substantially the interaction of the framework with specific gas molecules.

It was not possible to evaluate its gas sorption properties by means of gas adsorption because of lack of a suitable activation procedure. Many methods have been tested, including the use of low boiling solvents, such as acetone, CH_2Cl_2, and supercritical CO_2. Apparently the material collapsed upon solvent removal under vacuum. Since the structural integrity before solvent removal was verified by pxrd measurements. The formation of a pure phase was verified using pxrd measurements.
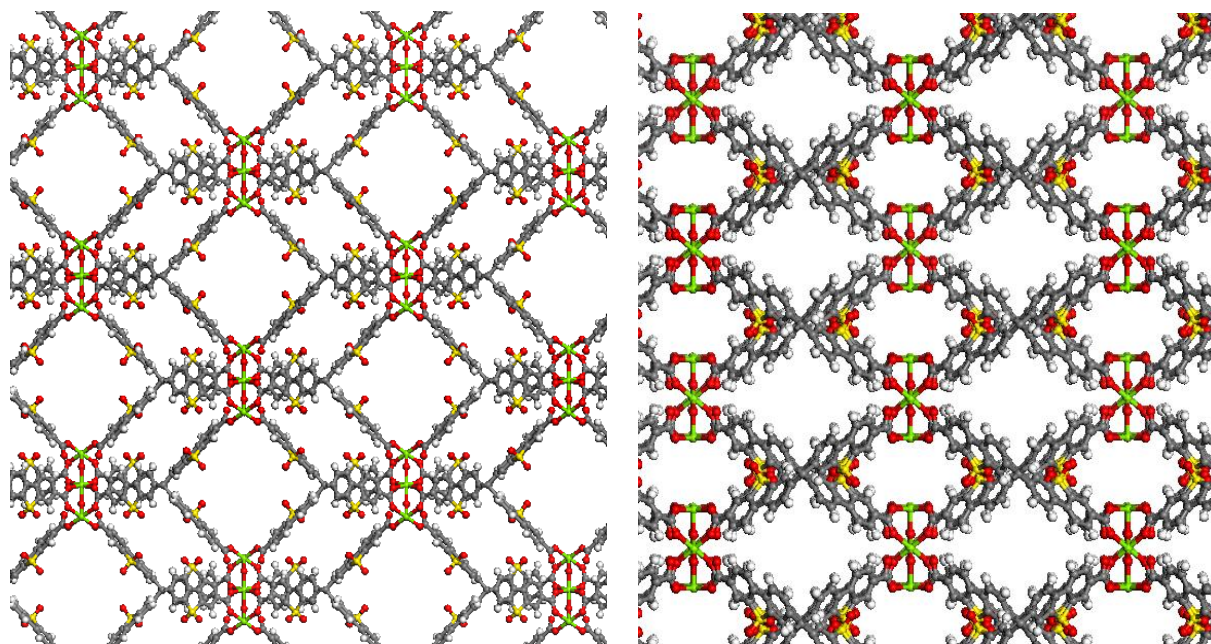
Figure 5.65. Left: Part of the 3-D crystal structure looking along the [101] direction. Right: Part of the 3-D crystal structure looking down the a axis. Green spheres: Mg, gray: C, yellow: S, red: O, white: H. Solvent and dimethyl ammonium molecules are omitted for clarity.

5.9 Synthesis of a MOF based on a nitro functionalized organic ligand with tetrahedral linking topology

After the successful utilization of the sulfone functionalized linker 40, we used the nitro functionalized one, linker 39 to assemble the same networks and study the effect of the nitro groups to the gas sorption properties of those novel materials.

Solvothermal reaction of linker 39 with Cu^{2+} ions resulted to the formation of large green single crystals. The resulting material was characterized using pxrd measurements. Its pxrd pattern was compared to the calculated pattern of the previous sulfone analogue. Apparently the two materials are isostructural as it was expected. The framework is made of paddlewheel $Cu_2(O_2CR)_4$ SBUs connected through four H_4L, and each organic linker connects four SBUs resulting to an overall framework formula Cu_2L. The framework consists of two types of 1-D interconnecting channels, one cubic with a diameter of 17.4 Å, and one hexagonal with dimensions 35 Å x 15 Å, without taking into account the van der Waals radii. Therefore the existence of the open metal sites along with the large number of pendant nitro groups (8 per linker) is expected to increase substantially the interaction of the framework with specific gas molecules. A suitable activation method could open the way to evaluate its gas sorption properties.
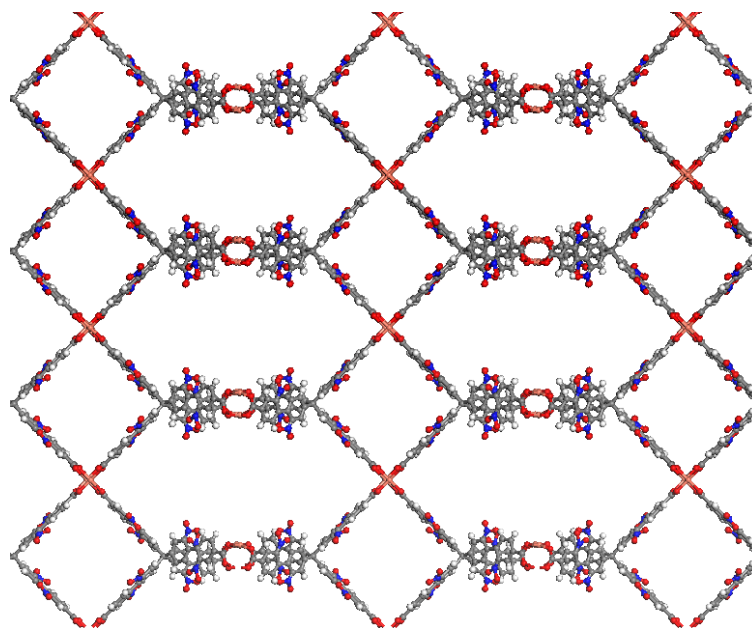
Figure 5.66. Part of the 3-D crystal structure looking along the [110] direction. Orange spheres: Cu, gray: C, blue: N, red: O, white: H. Solvent molecules are omitted for clarity.

5.10 Syntheses of MOFs based on a novel nanosized, polyaromatic hexatopic organic ligand

The idea behind the synthesis of this linker is reported in section 5.1, where it was used for the successful synthesis of MOFs based on Zr^{4+} SBUs. This procedure resulted to a highly crystalline material, however its structure couldn't be determined. After these results we wanted to see if reaction with different metal ions could result to porous materials with novel topologies and possible important gas sorption properties.

Solvothermal reaction of linker 51 with Co^{2+} ions resulted to the formation of blue plate like crystals. The large single crystals made possible the determination of the structure of this MOF. Through single crystal X-ray difractometry the structure was solved revealing a 2-D framework consisting of 2 layers (see figure 5.68). It crystallizes in the monoclinic system (space group *C2/m*) with unit cell parameters a = 30.8383 Å, b = 23.8297 Å, c = 21.3148 Å, $\alpha = 90^0$, $\beta = 101.531^0$, $\gamma = 90^0$. The framework is cationic and it is charged balanced by the presence of two Cl^- ions that are bound to the Co^{2+} ions on the SBUs. The $Co_2(RCOO)_3Cl(DMF)_3$ SBU is formed by a tetrahedral Co and an octahedral Co. The tetrahedral Co is connected to three organic linkers and to a Cl^- ion. The octahedral Co is connected to three organic linkers and to three solvent molecules. The overall framework formula is $Co_4(L)Cl_2(DMF)_3$. The framework exhibits two kinds of cavities that are perpendicular to the layers of the structure. The first one is formed by adjacent organic linkers and has a size of 9.4 Å and the other one lies between the adjacent SBS and has a size of 8.3 Å, without taking into account the van der Waals radii. The distance between the two layers is not uniform but ranges from 2.9 Å to 5.3 Å. Although this was a 2-D structure, the presence of so many aromatic rings and the open metal Co sites prompt us to activate this material and evaluate its gas sorption properties. Activation using low boiling solvents (CH_2Cl_2, $CHCl_3$) to exchange the DMF molecules and then remove the solvent molecules under vacuum resulted to framework collapse. Therefore activation with supercritical CO_2 was utilized.
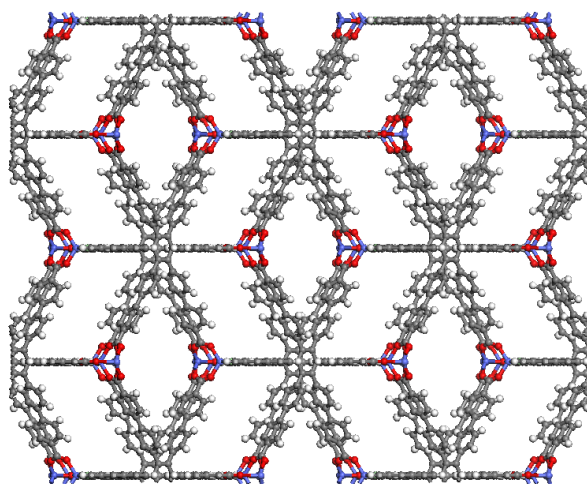
<u>Figure 5.67.</u> Part of the 2-D crystal structure of compound $Co_4(L)Cl_2(DMF)_3$, looking down the c axis. The two types of cavities are perpendicular to the layers of the structure. Blue spheres: Co, gray: C, red: O, white: H. Solvent molecules are omitted for clarity.
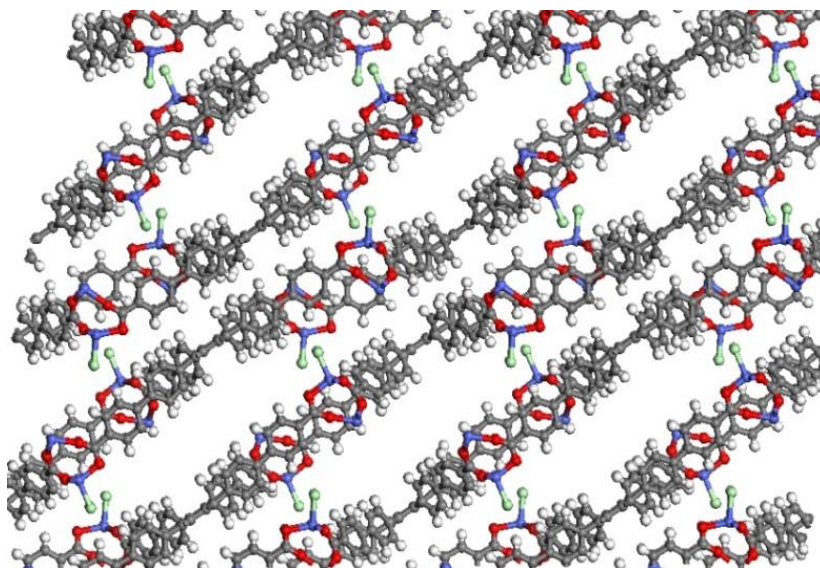
<u>Figure 5.68.</u> The 2 layers of the structure. Blue spheres: Co, gray: C, red: O, green: Cl, white: H. Solvent molecules are omitted for clarity.

Argon sorption measurements confirmed the permanent porosity of $Co_4(L)Cl_2(DMF)_3$, giving a reversible pseudo type I isotherm. The calculated BET surface area of $Co_4(L)Cl_2(DMF)_3$, was estimated to be 1299 m^2 g^{-1}. The void volume calculated by using the crystal structure data from PLATON software had a value of 63%. While the calculated total pore volume from the argon isotherm was estimated to be 0.74 cm^3 g^{-1}, a little lower than the calculated one from the crystal structure 0.88 cm^3 g^{-1}. Accordingly, isotherm data were fitted using a suitable NLDFT kernel and the pore size distribution curve revealed a distinct peak centered at 9.6 Å, in agreement with the crystallographic analysis.

In order to evaluate its gas sorption properties we performed CO_2, H_2, and CH_4 sorption measurements. At 77 K and 1 bar $Co_4(L)Cl_2(DMF)_3$ adsorbs a high uptake of 1.9 wt% H_2 with a calculated Q_{st} value of 5.2 kJ mol^{-1}. These are high values for medium surface area MOFs with open metal sites.[152] CO_2 measurements revealed an uptake of 14.56 mmol g^{-1} at 195 K and 1 bar, 4.8 mmol g^{-1} (17.4 wt%) at 273 K and 1 bar, while at 298 K and 1 bar the uptake reaches a value of 2.53 mmol g^{-1}. These values are high and can be well compared to materials with similar surface areas and open metal sites.[153] The calculated CO_2 isosteric heat of adsorption exhibited a moderate value for MOFs with open metal sites, of 20 kJ mol^{-1}. This may be ascribed to the fact that due to nature of this 2-D structure, the CO_2 molecules either cannot reach the open metal sites at all, or even they come to close proximity they lay in a way that the maximum interaction among the gas molecules and the open metal sites cannot be established. We have also performed CH_4 adsorption measurements at 273 K, 298 K and 112 K at 1 bar. At 273 K $Co_4(L)Cl_2(DMF)_3$ adsorbs 1.15 mmol g^{-1} while at 195 K this value becomes 7.19 mmol g^{-1}. We calculated the isosteric heat of adsorption and found a value of $Q_{st}^0 = 24$ kJ mol^{-1} using the virial equation, which is a very high value indicative for materials with open metal sites and among the highest recorded for MOFs, but it drops significantly during methane loading.[154]

This behavior might also be a result of the packing of the methane molecules between the 2-D layers and close to the open metal sites that maximize their interaction resulting to such a high value for the isosteric heat of adsorption. High pressure methane measurements will reveal if this material can be efficiently characterized as a methane storage candidate. Additionally the CO_2/CH_4 selectivity was calculated using IAST for a 5/95 molar mixture at 273 K and 298 K giving rise to a value of 4.6 and 5 respectively. Those low values are indicative of the lower affinity of the framework for CO_2 towards CH_4, as it was observed from the very low isosteric heat of adsorption for CO_2 and the very high isosteric heat of adsorption for CH_4.

After those encouraging results we used a trivalent metal ion, to possible access different topologies. Solvothermal reaction of linker 51 with In^{3+} ions resulted to the formation of large brown block crystals. The large single crystals made possible the determination of the structure of this MOF. Through single crystal X-ray difractometry, using synchrotron radiation, the structure was solved revealing a 3-D framework (see figure 5.70). It crystallizes in the tetragonal system (space group *P42/ncm*), with unit cell parameters a = b = 27.8633 Å, c = 48.9497 Å $\alpha = \beta = \gamma = 90^0$. The structure contains a single molecule In^{3+} SBU, which is connected to three different hexatopic linkers via chelating carboxylate groups, and each linker is connected to six different In^{3+} cations. Notably, the coordination sphere of In^{3+} is completed by one chelating acetate anion. These anions are formed in-situ from the decomposition of the solvent DMA used in the synthesis. Therefore, this is an anionic framework and charge balance considerations imply the presence of dimethylammonium counterions $((CH_3)_2NH_2^+)$. The later is the product of a partial decomposition of the DMA solvent and cannot be located due to its highly disorder nature.[155] Based on the above, the overall charge balanced framework formula is $[In_2(L)(CH_3COO)_2]((CH_3)_2NH_2)_2$. ^{1}H NMR spectroscopy verified the presence of the acetate and the dimethylammonium ions in the expected ratio. The framework consists of three types of cross linked 1-D channels. One hexagonal with a diameter of 11.5 Å, one hexagonal with a diameter of 14 Å and one cubic with a diameter of 13 Å, without taking into account the van der Waals radii. The formation of a pure phase was verified using pxrd measurements, as experimental and calculated from the single crystal structure patterns are identical.
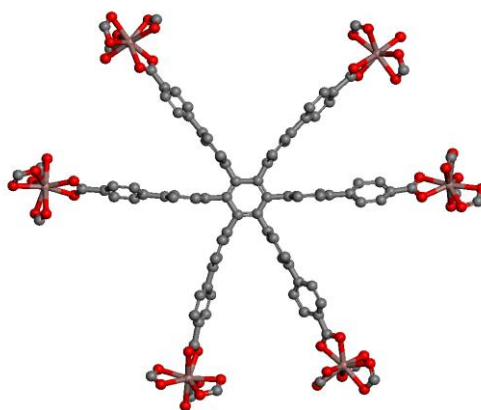
Figure 5.69. The connectivity of the organic linker. Each arm of the linker connects bidentate to one In^{3+} ion. Beige spheres: In, gray: C, red: O. Hydrogen atoms are omitted for clarity.
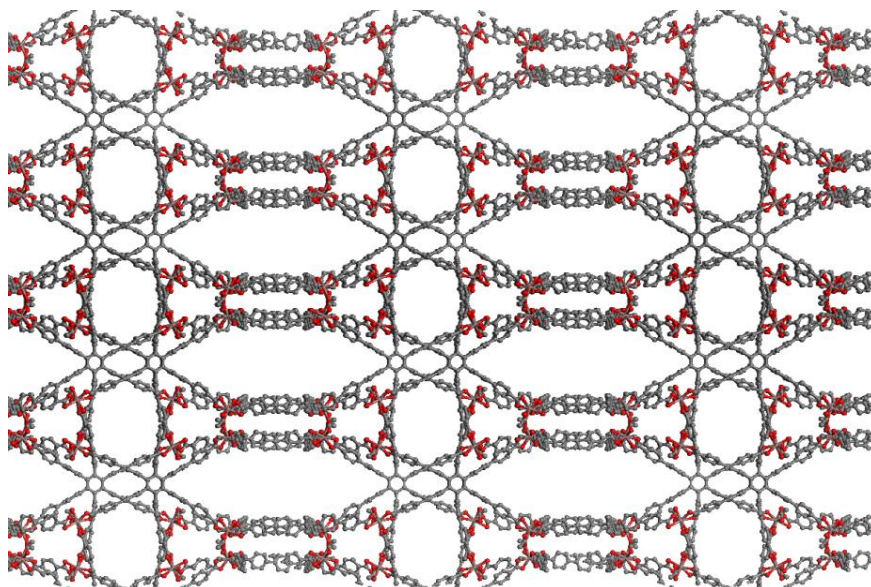
<u>Figure 5.70.</u> Part of the 3-D crystal structure of compound $[In_2(L)(CH_3COO)_2]((CH_3)_2NH_2)_2$ looking along the [110] direction. Beige spheres: In, gray: C, red: O. Solvent and dimethylammonium molecules and hydrogen atoms are omitted for clarity.

5.11 Syntheses of MOFs based on a nanosized rectangular organic ligand

The idea behind the synthesis of this linker is reported in section 5.1, where it was used for the successful synthesis of MOFs based on Zr^{4+} SBUs. This procedure resulted to a highly crystalline material. After these results we wanted to see if reaction with different metal ions could result to porous materials with novel topologies and possible important gas sorption properties.

The use of Al^{3+} in MOF synthesis results usually in robust and air stable MOFs, two highly desired properties. There are many MOFs based on Al^{3+} ions, one of them is MIL-120, with chemical formula $Al_4(OH)_8[C_{10}O_8H_2]_3$. This material is based on the organic linker pyromellitic acid and Al^{3+} ions. It consists of infinite 1-D chains of aluminum centers in octahedral coordination connected to each other through the pyromellitate linker. There are $AlO_2(OH)_4$ octahedra linked to each other via a common edge consisting of two μ_2-hydroxo groups. Taking a closer look at the structure, the organic linker can be viewed as a small tetragonal that links the aluminum chains. Therefore the use of an expanded rectangular linker could result to the same structure followed by an increase to the distance between the chains, resulting to a significant increase to the accessible surface area.

Solvothermal reaction of linker 43 with Al^{3+} ions resulted to the formation of a crystalline material. This material was characterized using pxrd measurements. Comparison of the two patterns, MIL-120 and this new compound took place. However there was no similarity among them. Evidently there can be no certainty for the exact crystal structure of this new MOF unless its crystal structure is solved by means of single crystal XRD.

140
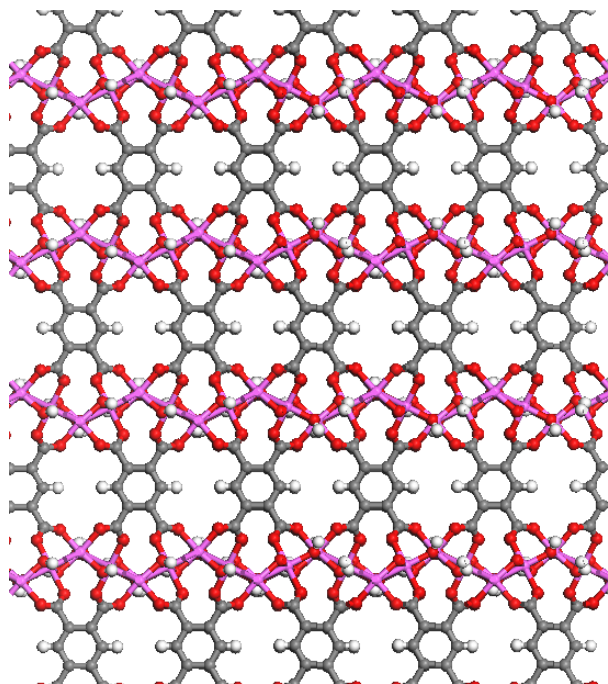
Figure 5.71. Part of the 3-D crystal structure of MIL-120 looking along the [102] direction. Pink spheres: Al, gray: C, red: O, white: H. Solvent molecules are omitted for clarity.

In a similar manner, there have been reported in the literature compounds based on renctangular linkers but with shorter dimensions than linker 43. Therefore replacement of a smaller linker with linker 43 could result to the formation of the same structure accompanied by an increase to the porosity of the new material. So far it is reported in the literature only a smaller similar non-functionalized tetragonal linker (H_4BTTB). Yet, there are only five different materials based only on this linker.[156]
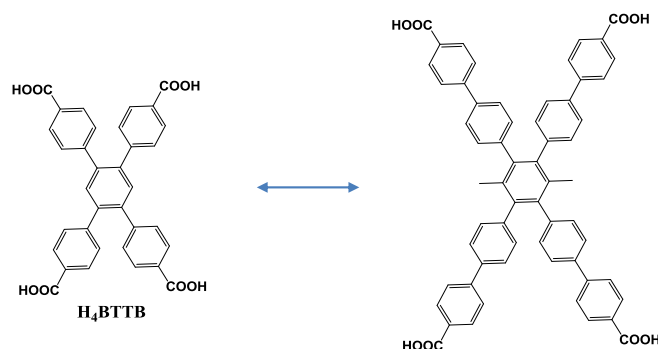
Figure 5.72. Left: the organic linker H_4BTTB, right: the expanded rectangular linker 43.

Solvothermal reaction of linker 43 with Ni^{2+} ions resulted to the formation of a highly crystalline material. The resulting material was characterized using pxrd measurements. Although this synthetic procedure allowed the formation of single crystals, the structure of this material couldn't be determined through single crystal XRD measurements. Therefore the as made pxrd pattern of this new material was compared to the calculated patterns of all compounds based on the smaller linker

H$_4$BTTB, taking into account the unit cell expansion due to presence of our elongated organic linker. Apparently the as made material looks similar with the compound NiL (ref. 156c), a two-dimensional grid layer, where each organic linker binds monodentate to a single Ni^{2+} ion, and each metal ion binds four organic linkers. Nonetheless there is no certainty for the exact crystal structure of this new compound unless its crystal structure is solved by means of single crystal XRD measurements.

Following those results we used this novel linker for the synthesis of new porous materials with various metal ions. For that purpose linker 43 was used for the solvothermal reaction with Zn^{2+}, Mg^{2+}, Cu^{2+}, In^{3+}, Pr^{3+} and La^{3+}. Our meticulously developed synthetic conditions resulted in all cases to the formation of single crystals. However it was not possible to solve none of those structures using single crystal XRD measurements. This could shed light to the possible novel topologies created by the utilization of this new linker.

5.12 Synthesis of a MOF based on an elongated organic ligand functionalized with sulfonic (-SO$_3$H) groups

It was reported in section 5.1 and 5.2 that the use of a linear ditopic carboxylate organic linker could be efficiently used for the synthesis of an fcu MOF, or an IRMOF based on the choice of the metal ion. For that purpose we have designed and synthesized the expanded linear organic linker 75, functionalized with pendant sulfonic groups. This linker was expected to form highly porous MOFs functionalized with the highly acidic sulfonic groups, that could result to increased interaction of the framework with specific molecules (e.g. CO$_2$). Indeed this linker was used for the successful synthesis of an expanded fcu type MOF by another member of our group.

We tried to synthesize the IRMOF analogue with Zn^{2+} metal ions, but so far it was not possible to acquire it. After those efforts we utilized this linker in MOF synthesis with different metal ions, other than Zn^{2+}. This could possibly lead to highly porous functionalized crystalline materials. Their structure determination could give insight to the nature and behavior of this linker under specific synthetic reaction conditions. Allowing us to understand why it is not possible to synthesize the IRMOF analogue.

Solvothermal reaction of linker 75 with Mg^{2+} ions resulted to the formation of a highly crystalline material. The large single crystals made possible the determination of the structure of this MOF. Through single crystal X-ray difractometry using synchrotron radiation the structure was solved revealing a neutral 3-D framework. It crystallizes in the trigonal system (space group *P-3c1*) with unit cell parameters a = b = 17.4229 Å, c = 30.2905 Å, α = β = 90^0, γ = 120^0. The framework is made of a very rare Mg$_3$O(CO$_2$)$_6$ SBU connected through six linkers (H$_4$L), and each organic linker connects two SBUs. The metal trimers contain three [MgO$_5$(H$_2$O)] octahedra sharing one central μ$_3$-oxo anion. In each octahedron, the apical position is occupied by a terminal water molecule. To our knowledge there is only one publication based on this Mg$_3$O(CO$_2$)$_6$ SBU.[157] However in our case there is another metal cluster with formula Mg$_2$(SO$_3$)$_3$, based on two octahedral Mg^{2+} ions which are bridged by three

sulfonic molecules from different organic linkers. Each Mg^{2+} ion is connected to three oxygen atoms from three sulfonic groups and three solvent molecules. Taking both the aforementioned SBUs into account the resulting framework is anionic and is charged balanced by a dimethylammonium $(Me_2NH_3^+)$ cation. The overall framework formula is $Mg_{4.5}(H_2O)_3OL_{1.5}(Me_2NH_2)$. If the coordinating solvent molecules are removed 1-D cubic channels are revealed exhibiting a diameter of 13 Å, without taking into account the van der Waals radii. Powder X-ray diffraction analysis verified the formation of a pure phase, as the experimental and calculated patterns are identical. Apparently the sulfonic groups can coordinate to the metal ions hindering in this way the formation of some specific topologies (e.g. IRMOF).
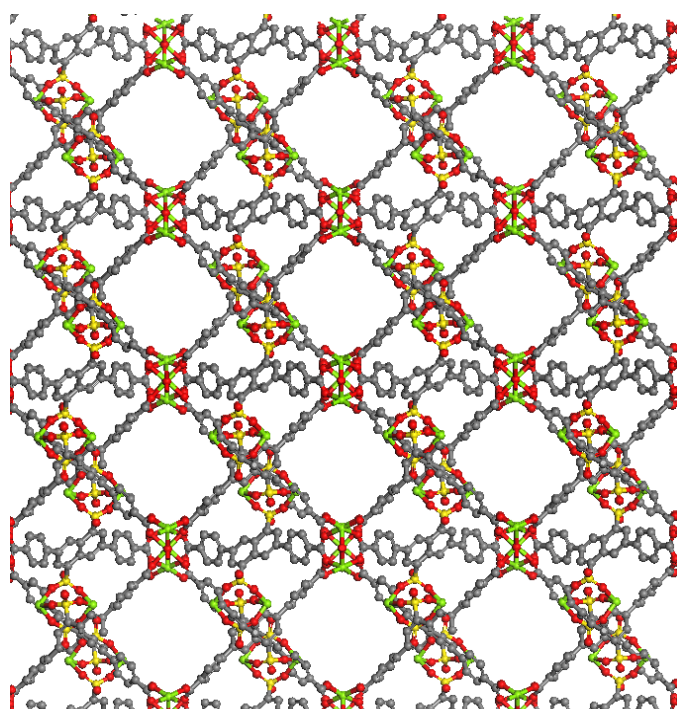
Figure 5.73. Part of the 3-D crystal structure of compound $Mg_{4.5}(H_2O)_3OL_{1.5}(Me_2NH_2)$, looking structure looking along the [110] direction. Green spheres: Mg, gray: C, red: O, yellow: S. Solvent molecules and hydrogen atoms are omitted for clarity.
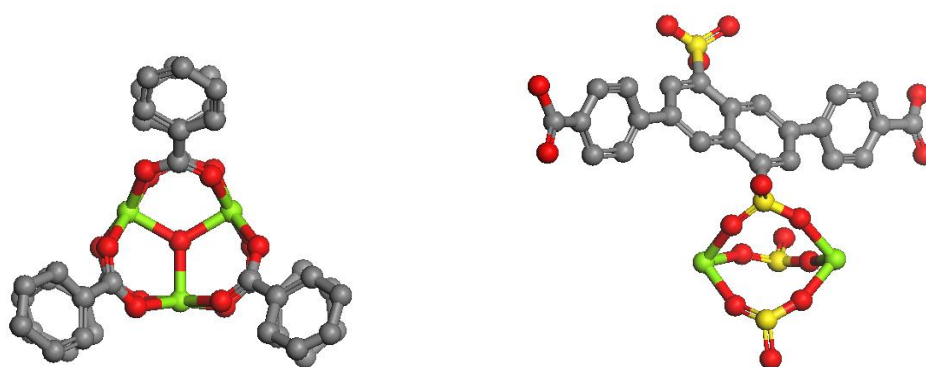
Figure 5.74. Left: the $Mg_3O(CO_2)_6$ SBU of compound $Mg_{4.5}(H_2O)_3OL_{1.5}(Me_2NH_2)$. Right: the $Mg_2(SO_3)_3$ SBU. Green spheres: Mg, gray: C, red: O, yellow: S. Solvent molecules and hydrogen atoms are omitted for clarity.

5.13 Synthesis of a MOF based on an organic ligand functionalized with sulfonic (-SO₃H) groups

It was reported in section 5.1 and 5.2 the use of linker 5, for the synthesis of a bcu MOF and an IRMOF-8 analogue. However this linker bearing two sulfonic groups could be used for the synthesis of MOFs with different topologies and potential interesting properties.

Solvothermal reaction of linker 5 with In^{3+} ions resulted to the formation of a highly crystalline material. The large single crystals made possible the determination of the structure of this MOF. Through single crystal X-ray difractometry the structure was solved revealing an anionic 3-D chiral framework (see figure 5.75). It crystallizes in the tetragonal system (space group $P4_32_12$), with unit cell parameters a = b = 25.6612 Å, c = 11.8105 Å, α = β = γ = 90⁰. This is a non-interpenetrated structure with an overall framework formula $In(NDC-2SO_3H)_2(Me_2NH_2)$. The structure contains a single molecule In(III) SBU. These mononuclear nodes are bridged by four organic ligands. Each In(III) is 8-coordinate through binding to O centres from four chelating carboxylate groups to form a tetrahedral 4-connected node and each organic linker bridges two In(III) nodes. The resulting framework contains two types of 1-D helical nanotube-like channels, one is right-handed and the other one is left-handed. Both channels exhibit a uniform dimension of 10 Å. The charge of the framework is balanced by a dimethylammonium ($Me_2NH_2^+$) cation that resides into the pores, one for every In(III) node. The counter-cation $Me_2NH_2^+$ is generated via decomposition of the DMF solvent.[158] ¹H NMR spectroscopy was used to verify the existence of the dimethylammonium ions. Noticeably, in the presence of DMSO-d₆ the peak of the six protons of the $Me_2NH_2^+$ lie inside the peak of the DMSO-d₆ solvent at 2.5 ppm.[159] Therefore the use of a different deuterated NMR solvent is needed. For that purpose MOF crystals were dissolved in D₂O using 1 drop of NaOH 5N. ¹H NMR measurements revealed the presence of Me_2NH at 2.15 ppm. Obviously in the environment of a strong base the dimethylammonium ion ($Me_2NH_2^+$) becomes dimethylamine (Me_2NH). To validate this result a blank measurement was performed, by dissolving dimethylammonium chloride in D₂O, followed by the addition of 1 drop of NaOH 5N. ¹H NMR measurements showed a sharp singlet at 2.15 ppm, if the solvent is locked at 4.70 ppm, indicative of Me_2NH. Powder X-ray diffraction analysis verified the formation of a pure phase. There have been made several attempts to activate this material, using low boiling solvents. It is possible that the existence of the dimethylammonium cations in the pores result to framework collapse upon solvent removal. Nonetheless this material could be used for anhydrous proton conduction applications. That stems from the fact that the existence of the dimethylammonium cations inside the porous of this material can act as proton carriers. The proton transfer can take place among the sulfonic groups and the dimethylammonium cations, without the use of water molecules, or other moieties, as proton carriers.[160] Therefore the proton conduction of this material using ac impedance measurements will be tested soon.
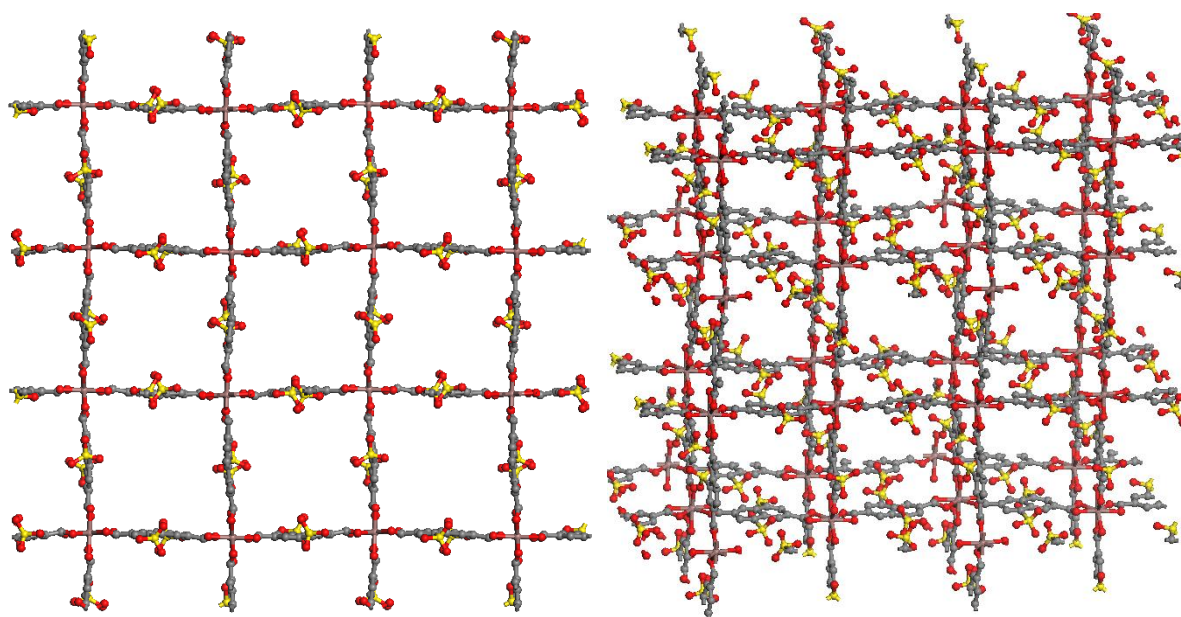
Figure 5.75. Left: the of 1-D helical nanotube-like channels. Right: Part of the 3-D crystal structure of compound In(NDC-2SO$_3$H)$_2$(Me$_2$NH$_2$) looking slightly off the c axis. Beige spheres: In, gray: C, red: O, yellow: S. Solvent and dimethylammonium molecules are omitted for clarity.
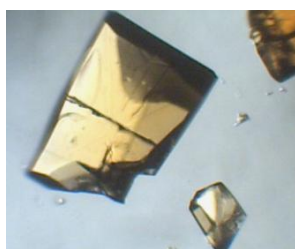
Figure 5.76. Optical microscope picture of In(NDC-2SO$_3$H)$_2$(Me$_2$NH$_2$) crystals.

5.14 Synthesis of a MOF based on an organic ligand functionalized with aromatic hydroxyl (-OH) groups.

It was reported in section 5.2 the use of linker 6 for the synthesis of an IRMOF-8 analogue. During our quest to acquire this type of framework we stumbled upon the formation of a 2-D structure. This material was based on a Zn$_2$(O$_2$CR)$_4$ paddlewheel SBU bridging four organic linkers. A well known and tested method for the transformation of a 2-D material to a 3-D material, is the use of a linear linker that acts as a bridge for the two layers. This linker serves as a pillar among the two 2-D layers, connecting the axial positions of opposite metal clusters, leading to the formation of a 3-D structure.[161] Some common ligands used in this linker insertion, are the 4,4'-bipyridine, 1,2-bis(4-pyridyl)ethane, and 1,2-bis(4-pyridyl)ethylene.

Taking all these into account we targeted the synthesis of pillared MOFs, composed of the H$_2$NDC-2OH linker and a pillared linker of choice.

Solvothermal reaction of linker 6, with Zn^{2+} ions and 1,2-bis(4-pyridyl)ethane resulted to the formation of a highly crystalline material. The large single crystals made possible the determination of

145

the structure of this MOF. Through single crystal X-ray difractometry the structure was solved revealing an impressive 3-D framework. It crystallizes in the monoclinic system (space group $P2_1$) with unit cell parameters a = 12.3709 Å, b = 17.206 Å, c = 18.3069 Å, $\alpha = 90^0$, $\beta = 102.198^0$, $\gamma = 90^0$. The framework is made a 2-D array of layers that are connected through a bridge of two 1,2-bis(4-pyridyl)ethane molecules and one free Zn^{2+} ion. The network constitutes of a square paddlewheel $Zn_2(O_2CR)_4$ SBUs connected through four NDC-2OH ligands and two1,2-bis(4-pyridyl)ethane molecules having an overall formula $Zn_2(NDC-2OH)(NO_3)_2(bis-pyr)(DMF)_3$. The Zn^{2+} ions exhibit square pyramidal geometry, with each Zn^{2+} coordinated to four oxygen atoms of four carboxylates and one axial 1,2-bis(4-pyridyl)ethane molecule. The axial molecule binds from the one side to the SBU and from the other side to a free Zn^{2+} ion. This free Zn^{2+} ion bridges the SBUs through the 1,2-bis(4-pyridyl)ethane molecules resulting to a 3-D network. The framework is neutral and it is charged balanced by the presence of nitrate ions inside the porous, two for each free Zn^{2+} ion. Surprisingly the two 1,2-bis(4-pyridyl)ethane molecules do not bridge two adjacent layers, the first and the second for instance, but through the free Zn^{2+} ion, they connect the first and the third layer. This material was almost non-porous, with only a 15% of solvent accessible volume, calculated by the PLATON software.
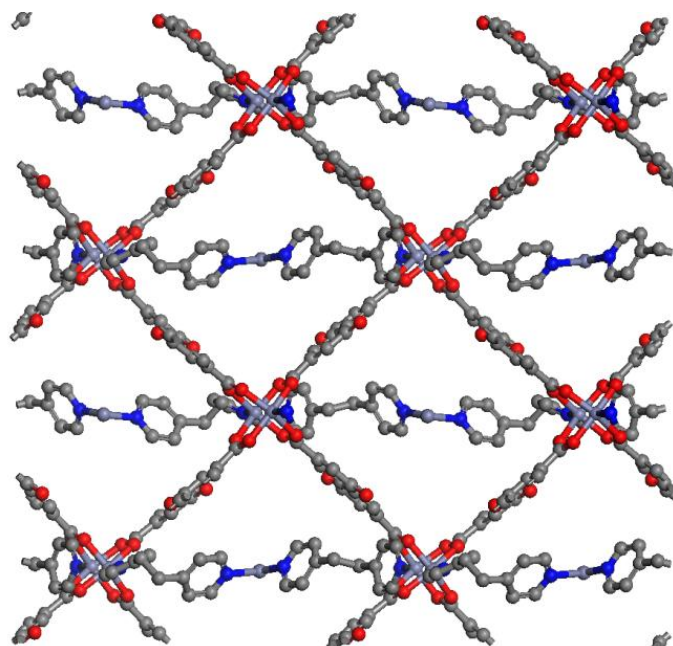
Figure 5.77. Part of the of the structure of compound $Zn_2(NDC-2OH)(NO_3)_2(bis-pyr)(DMF)_3$ looking down the a axis. Purple spheres: Zn, gray: C, red: O, blue: N. Hydrogen atoms, solvent and nitrate molecules are omitted for clarity.

Chapter 6: <u>Conclusions and outlook</u>

The objective of this thesis was the meticulous design of novel organic linkers and their successful implementation for the synthesis of new porous materials that could exhibit improved gas sorption properties. Through methodical research and planning we focused on the targeted synthesis of more than 75 new tailor made organic linkers, that were used for the development of more than 90 novel Metal Organic Frameworks each one exhibiting unique properties.

For the synthesis of the organic linkers novel, simple synthetic routes were utilized that could result to pure products with minimum reaction times and very high yields. Indeed the majority of the organic reactions performed in this thesis exhibited very high yields (>80%) and were composed of minimum reaction steps, in most cases less than 3. Some of the reactions that were already used for the synthesis of linkers utilized in MOF synthesis had to be optimized or totally remodeled in order to lead to the new desired product. Noticeably a whole new database based on unique organic linkers was assembled. This database contains linkers with numerous functional groups, the majority of which are presented for the first time in the MOF literature. Apart from the functional groups these organic linkers were favored with versatile geometries, shapes and sizes (linear, trigonal, tetrahedral, rectangular, bent, dendritic).

The next step was the use of these magnificent linkers for the synthesis of new porous MOFs. Although it may sound simple, the crystallization process is a very delicate procedure and demands very careful selection of reagents and reaction parameters (type and quantity of solvent, reaction time and temperature, ratios of reactants, co-solvents). Nonetheless after uncountable reactions it was possible to optimize the reaction parameters for the synthesis of each desired type of MOF. It was found that every metal ion has some unique reaction parameters in order to produce a highly crystalline material, in most cases in single crystal form. All the linkers were tested for the synthesis of new crystalline materials, but it was not possible in all cases to aquire one. For some linkers actually it was almost impossible to be dissolved in most common reaction solvents including DMF, DMA, DEF and NMF. This problem was overpassed by the use of NMP solvent, but only the formation of amorphous materials was observed.

At this point a most significant scientific quality criterion and one of the tenets of the scientific method must be mentioned. That is reproducibility.[162] This term stands for the ability of an entire experiment to be replicated, either by the same researcher or by someone else.[163] Through meticulous and precise work during the syntheses of new materials in this thesis the reproducibility was almost 100%. However in some cases, less than a hand full, reproducibility problems did occur. By examining thoroughly all the reaction parameters, the quality and the condition of the starting materials reproducibility problems were eventually surpassed. Apparently in all these cases the parameter that was hindering the repetition of the synthesis of the initial crystalline material was the same. During the synthesis of the organic linkers, the last step was the washing of the linker with a solvent, water in most cases, to remove impurities, unreacted species, inorganic salts and excess strong acids that were used for the protonation and precipitation of the final solid.

Incomplete removal of the strong acids results in solids that are highly acidic and can alter dramatically the exact adjusted acid concentration of the initial reaction, resulting to various synthetic results except for the desired one. Therefore by washing the organic linkers, every time that a new batch was synthesized, with the same amount of solvent resulted to the solution of the aforementioned problem.

After the successful synthesis of a crystalline material its efficient characterization is of utmost importance. That is the point that the formation of single crystals, especially in dimensions that could be distinguished with an optical microscope, is invaluable. That's because in this way the crystal structure of the MOF can be precisely determined by means of single crystal X-ray diffraction. The knowledge of the structure can open the way for the understanding, evaluation and prediction of the possible interesting properties of a material. However the acquisition of large single crystals doesn't always make possible the determination of the structure of the material, usually due to bad diffraction quality of the crystals. They may look shiny and well shaped from outside, but from the inside the crystal structure may contain defects or being disorder that "break" the periodicity of the crystal hindering in this way the single diffraction analysis. Unfortunately that was something that we experienced in many of our samples, hiding in this way potential very interesting structures that could be evaluated and lead to important properties.

Following characterization, the material has to be activated, that is the trapped reaction solvents inside the framework must be removed, in order to evaluate its gas sorption properties. The activation procedure is one the most critical and delicate procedures without which the material cannot be exploited further. During this thesis, many activation protocols were tested but most importantly novel activation procedures were developed for the activation of a porous material. The activation protocols that were used for the exchange of the reaction solvents were many and varied. The simplest one included the use of low boiling solvents ($CHCl_3$, CH_2Cl_2, EtOH, MeOH, acetone) either only one at a time or even two different solvents in succession. However some materials had to be activated using a combination of methods, such as initial exchange with a low boiling solvent followed by supercritical drying with CO_2. All of the materials that were activated successfully in this work followed either the first or the second way. Nevertheless there were many cases that successful activation without framework collapse was not possible. In this case different activation protocols were used, including freeze drying with benzene and the use of soxhlet extraction, both of which lead to unsatisfactory results. Noticeably each MOF has its own unique activation procedure. Satisfyingly we were able to develop new and efficient activation protocols for almost half of the MOFs that were synthesized during this thesis.

The final and most intriguing part in a MOF's "life" is the evaluation of its properties, in our case its gas sorption properties. Fortunately in our laboratory we are equipped with two volumetric instruments for sorption analysis, which along with the help of a cryocooler can offer precise and extensive gas sorption measurements at 1 bar and various temperatures using a great variety of adsorbents, including N_2, Ar, CO_2, CH_4, H_2, NH_3, Xe and Kr. From these gas sorption measurements one can deduce precious information concerning the usage of a material in significant industrial applications, such as gas storage and gas separation.

Unambiguously some of the MOFs that were evaluated towards gas sorption applications proved to be quite promising. To be more precise, it was possible to synthesize new tbo type MOFs exhibiting a very high methane uptake at ambient temperature (298 K) and high pressures. These results place up to date these materials among the 5 best MOF candidates for methane storage in terms of total gravimetric uptake and gravimetric working capacity. Additionally another tailor made organic linker bearing $PdCl_2$ entities was used for the efficient synthesis of a material exhibiting a notable CO_2 uptake at 298 K and 1 bar. This material is among the 10 best MOF candidates for CO_2 storage under mild conditions. Furthermore an NbO type of MOF based on a functionalized organic linker was successfully synthesized, that exhibits a very high selectivity for the separation of Xe over Kr at RT. This value is among the 5 highest reported for MOFs, rendering this material a promising candidate for the separation of Xe over Kr. Similarly, the use of a methoxy functionalized organic linker for the synthesis of a UiO-67 analogue revealed an impressive isosteric heat of methane adsorption, the second highest reported in the family of MOFs. Moreover using an elongated amide functionalized organic linker, it was possible to synthesize a UiO type of MOF with the largest unit cell and pore volume reported to date. Apart from these noteworthy gas sorption properties, some materials revealed interesting structural characteristics and novel type of nets that were observed for the first time in the MOF family.

It must be mentioned that many of the materials that was not possible to be activated, are expected to reveal exceptional gas sorption properties. This stems from the fact that the aforementioned MOFs, contain either a large number of polar functional groups in combination with narrow cavities, or they exhibit ultra high specific surface areas along with a large number of polar functional groups and/without open metal sites. Therefore a new suitable activation protocol must be implemented. The solution to this problem may be the use of supercritical drying with flow of CO_2 instead of static CO_2, a method which was found to activate efficiently most types of porous networks.[164]

Finally after all these synthetic procedures, characterization techniques, activation methods and gas sorption properties a huge amount of knowledge and experience has been amassed. All this expertise that has been acquired will now be used for the design of new linkers, and consequently MOFs that could meet and surpass the challenging US DOE targets in terms of gas storage or exhibit a lot higher selectivity values for gas separation processes.

References

[1] Kandiah M., Nilsen M. H., Usseglio S., Jakobsen S., Olsbye U., Tilset M., Larabi C., Quadrelli E. A., Bonino F., Lillerud K. P., *Chem. Mater.,* **2010**, 22, 6632-6640.

[2] Cavka J. H., Jakobsen S., Olsbye U., Guillou N., Lamberti C., Bordiga S., Lillerud K. P., *J. Am. Chem. Soc.,* **2008**, 130, 13850-13851.

[3] Zhang W., Huang H., Liu D., Yang Q., Xiao Y., Ma Q., Zhong C., *Micropor. Mesopor. Mater.*, **2013**, 171, 118-124.

[4] Bon V., Senkovska I., Weiss M. S., Kaskel S., *Cryst. Eng. Comm.,* **2013**, 15, 9572-9577.

[5] Wu H., Chua Y. S., Krungleviciute V., Tyagi M., Chen P., Yildirim T, Zhou W., *J. Am. Chem. Soc.,* **2013**, 135, 10525-10532.

[6] Moellmer J., Celer E. B., Luebke R., Cairns A. J., Staudt R., Eddaoudi M., Thommes M., *Micropor. Mesopor. Mater.*, **2010**, 129, 345-353.

[7] Zhao D., Yuan D., Yakovenko A., Zhou H.-C., *Chem. Commun.,* **2010**, 46, 4196-4198.

[8] A) Sumida K., Rogow D. L., Mason J. A., McDonald T. M., Bloch E. D., Herm Z. R., Bae T.-H., Long J. R., *Chem. Rev.,* **2012**, 112, 724-781 B) Sircar S., *Ind. Eng. Chem. Res.,* **1992**, 31, 1813-1819.

[9] Myers A. L., *AIChE J.,* **2002**, 48, 145-160.

[10] Biswas S., Voort P. V. D., *Eur. J. Inorg. Chem*., **2013**, 2154-2160.

[11] Mason J. A., Veenstra M., Long J. R., *Chem. Sci.,* **2014**, 5, 32-51.

[12] Biswas S., Zhang J., Li Z., Liu Y.-Y., Grzywa M., Sun L., Volkmerc D., Voort P. V. D., *Dalton Trans.,* **2013**, 42, 4730-4737.

[13] Dinca M., Yu A. F., Long J. R., *J. Am. Chem. Soc.,* **2006**, 128, 8904-8913.

[14] Abida H. R., Tianb H., Anga H.-M., Tadea M. O., Buckleyb C. E., Wang S., *Chem. Eng. J.,* **2012**, 187, 415-420.

[15] Yang Q., Wiersum A. D., Llewellyn P. L., Guillerm V., Serred C., Maurin G., *Chem. Commun.,* **2011**, 47, 9603-9605.

[16] P. Xydias, Spanopoulos I., Klontzas E., Froudakis G. E., Trikalitis P. N., *Inorg. Chem.,* **2014**, 53, 679-681.

[17] Rowsell J.L.C., Yaghi O.M, *J. Am. Chem. Soc.,* **2006**, 128, 1304-1315.

[18] Zhang W., Huang H., Zhong C., Liu D., *Phys. Chem. Chem. Phys*., **2012**, 14, 2317-2325.

[19] Wang Y., Tan C., Sun Z., Xue Z., Zhu Q., Shen C., Wen Y., Hu S., Wang Y., Sheng T., Wu, X., *Chem. Eur. J.,* **2014**, 20, 1341-1348.

[20] Xiang Z. H., Peng X., Cheng X., Li X. J., Cao D. P., *J. Phys. Chem. C,* **2011**, 115, 19864-19871.

[21] Katz M. J., Brown Z. J., Colo Y. J., Siu P. W., Scheidt K. A., Snurr R. Q., Hupp J. T., Farha O. K., *Chem. Commun.,* **2013**, 49, 9449-9451.

[22] D. Sun, S. Ma, Y. Ke, D.J. Collins, H.-. Zhou, *J. Am. Chem. Soc.,* **2006**, 128, 3896-3897.

[23] Jasuja H., Walton K. S., *J. Phys. Chem. C,* **2013**, 117, 7062-7068.

[24] Tan C., Yang S., Champness N. R., Lin X., Blake A. J., Lewis W., Schroder M., *Chem. Commun.,* **2011**, 47, 4487-4489.

[25] Hamon L., Llewellyn P. L., Devic T., Ghoufi A., Clet G., Guillerm V., Pirngruber G. D., Maurin G., Serre C., Driver G., Beek W., Jolimaıtre E., Vimont A., Daturi M., Ferey G., *J. Am. Chem. Soc.,* **2009**, 131, 17490-17499.

[26] Lee J. Y., Pan L., Kelly S. P., Jagiello J., Emge T. J, Li J., *Adv. Mater.,* **2005**, 17, 2703-2706.

[27] Lau C. H., Babarao R., Hill M. R., *Chem. Commun.,* **2013**, 49, 3634-3636.

[28] Seki K., Mori W., *J. Phys. Chem. B,* **2002**, 106, 1380-1385.

[29] Zhang Z., Gao W.-Y., Wojtas L., Ma S., Eddaoudi M., Zaworotko M. J., *Angew. Chem. Int. Ed*., **2012**, 51, 9330-9334.

[30] Lee Y., Moon H. R., Cheon K., Suh M. P., *Angew. Chem. Int. Ed*., **2008**, 47, 7741-7745.

[31] Huang Y., Qin W., Li Z., Li Y., *Dalton Trans.,* **2012**, 41, 9283-9285.

[32] Prasad T. K., Hong D. H., Suh M. P., *Chem. Eur. J.,* **2010**, 16, 14043-14050.

[33] Biswas S., Zhang J., Li Z., YLiu.-Y., Grzywa M., Sun L., Volkmerc D., Voort P. V. D., *Dalton Trans.,* **2013**, 42, 4730-4737.

[34] Bloch E. D., Queen W. L., Krishna R., Zadrozny J. M., Brown C. M., Long J. R., *Science,* **2012**, 335, 1606-1610.

[35] Perles J., Iglesias M., Martın-Luengo M.-A., Monge M. A., Ruiz-Valero C., Snejko N., *Chem. Mater.,* **2005**, 17, 5837-5842.

[36] Abid H. R., Pham G. H., Ang H.-M., Tade M. O., Wang S., *J. Colloid Interface Sci.,* **2012**, 366, 120-124.

[37] Zhao X., Wang X., Wang S., Dou J., Cui P., Chen Z., Sun D., Wang X., Sun D., *Cryst. Growth Des.,* **2012**, 12, 2736-2739.

[38] Bae Y. S., Farha O. K., Hupp J. T., Snurr R. Q., *J. Mater. Chem.,* **2009**, 19, 2131-2134.

[39] Jia J., Lin X., Wilson C., Blake A. J., Champness N. R., Hubberstey P., Walker G., Cussen E. J., Schroder M., *Chem. Commun.,* **2007**, 43, 840-842.

[40] Jasuja H., Zang J., Sholl D. S., Walton K. S., *J. Phys. Chem. C,* **2012**, 116, 23526-23532.

[41] He Y., Zhou W., Qiand G., Chen B., *Chem. Soc. Rev.,* **2014**, 43, 5657-5678.

[42] Hamon L., Jolimaitre E., Pirngruber G. D., *Ind. Eng. Chem. Res.,* **2010**, 49, 7497-7503.

[43] Park T., Cychosz K. A., Wong-Foy A. G., Dailly A., Matzger A. J., *Chem. Commun.,* **2011**, 47, 1452-1454.

[44] Biswas S., Voort P.V. D., *Eur. J. Inorg. Chem.,* **2013**, 2154-2160.

[45] Llewellyn P. L., Bourrelly S., Serre C., Vimont A., Daturi M., Hamon L., Weireld G. D., Chang J.-S., Hong D.-Y., Hwang Y. K., Jhung S. H., Ferey G., *Langmuir,* **2008**, 24, 7245-7250.

[46] Yang Q., Wiersum A. D., Llewellyn P. L., Guillerm V., Serre C., Maurin G., *Chem. Commun.,* **2011**, 47, 9603-9605.

[47] Park K. S., Ni Z., Cote A. P., Choi J. Y., Huang R., Uribe-Romo F. J., Chae H. K., O'Keeffe M., Yaghi O. M., *Proc. Natl. Acad. Sci.,* **2006**, 103, 10186-10191.

[48] Foo M. L., Horike S., Fukushima T., Hijikata Y., Kubota Y., Takataf M., Kitagawa S., *Dalton Trans.,* **2012**, 41, 13791-13794.

[49] Wu H., Zhou W., Yildirim T., *J. Am. Chem. Soc.,* **2009**, 131, 4995-5000.

[50] Saha D., Bao Z. B., Jia F., Deng S. G., *Environ. Sci. Technol.* **2010**, 44, 1820-1826.

[51] Rowsell J. L. C., Millward A. R., Park K. S., Yaghi O. M., *J. Am. Chem. Soc.,* **2004**, 126, 5666-5667.

[52] Abid H. R., Ang H. M., Wang S., *Nanoscale,* **2012**, 4, 3089-3094.

[53] Kim T. K., Suh M. P., *Chem. Commun.,* **2011**, 47, 4258-4260.

[54] Nik O. G., Chen X. Y., Kaliaguine S., *J. Membr. Sci.,* **2012**, 413, 48-61.

[55] Zhou H.-C., Ma S. Q., Sun D. F., Ambrogio M., Fillinger J. A., Parkin S., *J. Am. Chem. Soc.,* **2007**, 129, 1858-1859.

[56] Zhang W., Huang H., Zhong C., Liu D., *Phys. Chem. Chem. Phys.,* **2012**, 14, 2317-2325.

[57] Wiersum A. D., Soubeyrand-Lenoir E., Yang Q., Moulin B., Guillerm V., Yahia M. B., Bourrelly S., Vimont A., Miller S., Vagner C., Daturi M., Clet G., Serre C., Maurin G., Llewellyn P. L., *Chem. Asian J.,* **2011**, 6, 3270-3280.

[58] Abida H. R., Shang J., Wang H.-M. A. S., *Int. J. Smart Nano Mat.,* **2013**, 4, 72-82.

[59] Wang B., Huang H., Lv X.-L., Xie Y., Li M., Li J.-R.*, Inorg. Chem.,* **2014**, 53, 9254-9259.

[60] A) Hulvey Z., Vlaisavljevich B., Mason J. A., Tsivion E., Dougherty T. P., Bloch E. D., Head-Gordon M., Smit B., Long J. R., Brown C. M. *J. Am. Chem. Soc.,* **2015**, 137, 10816-10825, B) Wilmer C. E., Leaf M.,. Lee C. Y., Farha O. K., Hauser B. G., Hupp J. T., Snurr R. Q., *Nat. Chem.,* **2012**, 4, 83-89.

[61] Yan Y., Yang S., Blake A. J., Lewis W., Poirier E., Barnett S. A., Champness, N. R., Schroder M., *Chem. Commun.,* **2011**, 47, 9995-9997.

[62] Jiang H.-L., Feng D., Liu T.-F., Li J.-R., Zhou H.-C., *J. Am. Chem. Soc.,* **2012**, 134, 14690-14693.

[63] Li L., Tang S., Wang C., Lv X., Jiang M., Wu H., Zhao X., *Chem. Commun.,* **2014**, 50, 2304-2307.

[64] Hong D. H., Suh M. P., *Chem. Eur. J.,* **2014**, 20, 426-434.

[65] Duan J., Yang Z., Bai J., B. Zheng, Lia Y., Li S., *Chem. Commun.,* **2012**, 48, 3058-3060.

[66] Manna K., Zhang T., Greene F. X., Lin W., *J. Am. Chem. Soc.,* **2015**, 137, 2665-2673.

[67] Schaate A., Roy P., Preuße T., Lohmeier S. J., Godt A., Behrens P., *Chem. Eur. J.,* **2011**, 17, 9320-9325.

[68] Delgado-Friedrichs O., O'Keeffe M., Yaghi O. M., *Acta Cryst.,* **2006**, A62, 350-355.

[69] Delgado-Friedrichs O., O'Keeffe M., Yaghi O. M., *Phys. Chem. Chem. Phys.,* **2007**, 9, 1035-1043.

[70] Wang R., Wang Z., Xu Y., Dai F., Zhang L., Sun D.*, Inorg. Chem.*, **2014**, 53, 7086-7088.

[71] Zhang M., Chen Y.-P., Bosch M., Gentle T., Wang K., Feng D., Wang Z. U., Zhou H.-C., *Angew. Chem. Int. Ed.,* **2014**, 53, 815-818.

[72] Chun H., Kim D., Dybtsev D. N., Kim K., *Angew. Chem.,* **2004**, 116, 989-992.

[73] Gutov O. V., Bury W., Gomez-Gualdron D. A., Krungleviciute V., Fairen-Jimenez D., Mondloch J. E., Sarjeant A. A., Al-Juaid S. S., Snurr R. Q., Hupp J. T., Yildirim T., Farha O. K., *Chem. Eur. J.,* **2014**, 20, 12389-12393.

[74] W. Morris, B. Volosskiy, S. Demir, F. Gándara, McGrier P. L., H. Furukawa, D. Cascio, Stoddart F., Yaghi O. M., *Inorg. Chem.,* **2012**, 51, 6443-6445.

[75] Feng D., Gu Z.-Y., Chen Y.-P., Park J., Wei Z., Sun Y., Bosch M., Yuan S., Zhou H.-C., *J. Am. Chem. Soc.*, **2014**, 136, 17714-17717.

[76] Mondloch J. E., Bury W., Fairen-Jimenez D., Kwon S., DeMarco E. J., Weston M. H., Sarjeant A. A., Nguyen S. T., Stair P. C., Snurr R. Q., Farha O. K., Hupp J. T., *J. Am. Chem. Soc.*, **2013**, 135, 10294-10297.

[77] Feng D., Gu Z.-Y., Li J.-R., Jiang H.-L., Wei Z., Zhou H.-C., *Angew. Chem. Int. Ed.,* **2012**, 51, 10307-10310.

[78] Feng D., Chung W.-C., Wei Z., Gu Z.-Y., Jiang H.-L., Chen Y.-P., Darensbourg D. J., Zhou H.-C., *J. Am. Chem. Soc.,* **2013**, 135, 17105-17110.

[79] Mondloch J. E., Katz M. J., Isley W. C. III, Ghosh P., Liao P., Bury W., Wagner G. W., Hall M. G., DeCoste J. B., Peterson G. W., Snurr R. Q., Cramer C. J., Hupp J. T., Farha O. K., *Nature Mater.*, **2015**, 14, 512-516.

[80] Wu J., Watson M. D., Mullen K., *Angew. Chem. Int. Ed.,* **2003**, 42, 5329-5333.

[81] Zhu Y., Murali S., Cai W., Li X., Suk J. W., Potts J. R., Ruoff R. S., *Adv. Mater.,* **2010**, 22, 3906-3924.

[82] Rowsell J. L.C., Yaghi O. M., *Micropor. Mesopor. Mater.*, **2004**, 73, 3-14.

[83] Deng H., Doonan C. J., Furukawa H., Ferreira R. B., Towne J., Knobler C. B., Wang B., Yaghi O. M., *Science*, **2010**, 327, 846-850.

[84] Zhang Z., Xiang S., Hong K., Das M. C., Arman H. D., Garcia M., Mondal J. U., Thomas K. M., Chen B., *Inorg. Chem.,* **2012**, 51, 4947-4953.

[85] Yao Q., Su J., Cheung O., Liu Q., Hedin N., Zou X., *J. Mater. Chem.,* **2012**, 22, 10345-10351.

[86] Rowsell J. L. C., Eckert J., Yaghi O. M., *J. Am. Chem. Soc.*, **2005**, 127, 14904-14910.

[87] Shannon R. D., *Acta Cryst.,* **1976**, A32, 751-767.

[88] Li H., Shi W., Zhao K., Li H., Bing Y., Cheng P., *Inorg. Chem.,* **2012**, 51, 9200-9207.

[89] Furukawa H., Ko N., Go Y. B., Aratani N., Choi S. B., Choi E., Yazaydin A. Ö., Snurr R. Q., O'Keeffe M., Kim J., Yaghi O. M., *Science,* **2010,** 329, 424-428.

[90] Klein N., Senkovska I., Gedrich K., Stoeck U., Henschel A., Mueller U., Kaskel S., *Angew. Chem. Int. Ed.*, **2009**, 48, 9954-9957.

[91] Duren T., Millange F., Ferey G., Walton K. S., Snurr R. Q., *J. Phys. Chem. C,* **2007**, 111, 15350-15356.

[92] Koh K., Wong-Foy A. G., Matzger A. J., *Angew. Chem. Int. Ed.,* **2008**, 47, 677-680.

[93] Doonan C. J., Tranchemontagne D. J., Glover T. G., Hunt J. R., Yaghi O. M., *Nat. Chem.,* **2010**, 2, 235-238.

[94] Petit C., Mendoza B., Bandosz T. J., *Langmuir,* **2010**, 26, 15302-15309.

[95] Spanopoulos I., Xydias P., Malliakas D. C., Trikalitis N. P., *Inorg. Chem.*, **2013**, 52, 855-862.

[96] Koh K., Wong-Foy A. G., Matzger A. J., *Angew. Chem. Int. Ed.,* **2008**, 47, 677-680

[97] Spek A. L., PLATON, Utrecht University, The Netherlands, **2003**.

[98] Gong Y.-N., Meng M., Zhong D.-C., Huang Y.-L., Jiang L., Lu T.-B., *Chem. Commun.,* **2012**, 48, 12002-12004.

[99] Gandara F., Furukawa H., Lee S., Yaghi O. M., *J. Am. Chem. Soc.,* **2014**, 136, 5271-5274.

[100] O'Keeffe M., Peskov M. A., Ramsden S. J., Yaghi O. M., *Acc. Chem. Res.,* **2008**, 41, 1782-1789.

[101] Peng Y., Krungleviciute V., Eryazici I., Hupp J. T., Farha O. K., Yildirim T., *J. Am. Chem. Soc,.* **2013**, 135, 11887-11894.

[102] Eubank J. F., Mouttaki H., Cairns A. J., Belmabkhout Y., Wojtas L., Luebke R., Alkordi M., Eddaoudi M., *J. Am. Chem. Soc.,* **2011**, 133, 14204-14207.

[103] Furukawa H., Go Y. B., Ko N., Park Y. K., Uribe-Romo F. J., Kim J., O'Keeffe M., Yaghi O. M., *Inorg. Chem.,* **2011**, 50, 9147-9152.

[104] Karra J. R., Walton K. S., *Langmuir*, **2008**, 24, 8620-8626.

[105] Shustova N. B., Cozzolino A. F., Dinca M., *J. Am. Chem. Soc,.* **2012**, 134, 19596-19599.

[106] Wang X.-J., Li P.-Z., Liu L., Zhang Q., Borah P., Wong J. D., Chan X. X., Rakesh G., Li Y., Zhao Y., *Chem. Commun.,* **2012**, 48, 10286-10288.

[107] Yan Y., Blake A.J., Lewis W., Barnett S. A., Dailly A., Champness N. R, Schröder M., *Chem. Eur. J.,* **2011**, 17, 11162-11170.

[108] Tan C., Yang S., Champness N. R., Lin X., Blake A. J., Lewis W., Schroder M., *Chem. Commun.,* **2011**, 47, 4487-4489.

[109] Wu H., Simmons J. M., Liu Y., Brown C. M., Wang X.-S., Ma S., Peterson V. K., Southon P. D., Kepert C. J., Zhou H.-C., Yildirim T., Zhou W., *Chem. Eur. J.,* **2010**, 16, 5205-5214.

[110] Tran L. D., Feldblyum J. I., Wong-Foy A. G., Matzger A. J., *Langmuir*, **2015**, 31, 2211-2217.

[111] Kim H., Samsonenko D. G., Das S., Kim G.-H., Lee H.-S., Dybtsev D. N., Berdonosova E. A., Kim K., *Chem. Asian J.,* **2009**, 4, 886-891.

[112] Yuan D., Zhao D., Sun D., Zhou H.-C., *Angew. Chem. Int. Ed.,* **2010**, 49, 5357-5361.

[113] Wong-Foy A. G., Lebel O., Matzger A. J., *J. Am. Chem. Soc.,* **2007**, 129, 15740-15741.

[114] Kim J., Yang S., Choi S. B., Sim J., Kim J., Ahn W., *J. Mater. Chem.,* **2011**, 21, 3070-3076.

[115] A) Wang H., Yao K., Zhang Z., Jagiello J., Gong Q., Hanb Y., Li J., *Chem. Sci.,* **2014**, 5, 620-624 B) Magdysyuk O. V., Adams F., Liermann H.-P., Spanopoulos I., Trikalitis P. N., Hirscher M., Morris R. E., Duncan M. J., McCormicke L. J., Dinnebier R. E., *Phys. Chem. Chem. Phys.,* **2014**, 16, 23908-23914.

[116] Perry J. J., Teich-McGoldrick S. L., Meek S. T., Greathouse J. A., Haranczyk M., Allendorf M. D., *J. Phys. Chem. C,* **2014**, 118, 11685-11698.

[117] Zhao D., Yuan D., Yakovenko A., Zhou H.-C, *Chem. Commun.,* **2010**, 46, 4196-4198.

[118] Caskey S. R., Wong-Foy A. G., Matzger A. J., *J. Am. Chem. Soc.,* **2008**, 130, 10870-10871.

[119] An J., Geib S. J, Rosi N. L., *J. Am. Chem. Soc.,* **2010**, 132, 38-39.

[120] Belmabkhout Y., Mouttaki H., Eubank J. F., Guillerm V., Eddaoudi M., *RSC Adv.*, **2014**, 4, 63855-63859.

[121] Yan Y., Yang S., Blake A. J., Schröder M., *Acc. Chem. Res.*, **2014**, 47, 296-307.

[122] Lin X., Telepeni I., Blake A. J., Dailly A. Brown C. M., Simmons J. M., Zoppi M., Walker G. S., Thomas K. M., Mays T. J., Hubberstey P., Champness N. R, Schroder M., *J. Am. Chem. Soc.,* **2009**, 131, 2159-2171.

[123] Tan K., Nijem N., Canepa P., Gong Q., Li J., Thonhauser T., Chabal Y. J, *Chem. Mater.*, **2012**, 24, 3153-3167.

[124] Luebke R., Eubank J. F., Cairns A. J., Belmabkhout Y., Wojtas L., Eddaoudi M., *Chem. Commun.,* **2012**, 48, 1455-1457.

[125] A) Thallapally P. K., Grateb J. W., Motkuria R. K., *Chem. Commun.,* **2012**, 48, 347-349 B) Meek S. T., Teich-McGoldrick S. L., Perry J. J., Greathouse J. A., Allendorf M. D., *J. Phys. Chem. C,* **2012**, 116, 19765-19772.

[126] Ryan P., Farha O. K., Broadbelt L. J., Snurr R. Q., *AIChE J.,* **2011**, 57, 1759-1766.

[127] Zheng B., Liu H., Wang Z., Yu X., Yia P., Bai J., *Cryst. Eng. Comm.,* **2013**, 15, 3517-3520.

[128] Yazaydın A. Ö., Snurr R. Q., Park T., Koh K., Liu J., LeVan M. D., Benin A. I., Jakubczak P., Lanuza M., Galloway D. B., Low J. J., Willis R. R*., J. Am. Chem. Soc.*, **2009**, 131, 18198-18199.

[129] Mendoza-Cortes J. L., Goddard W. A., Furukawa H., Yaghi O. M., *J. Phys. Chem. Lett.,* **2012**, 3, 2671-2675.

[130] Yan Y., Telepeni I., Yang S., Lin X., Kockelmann W., Dailly A., Blake A. J., Lewis W., Walker G. S., Allan D. R., Barnett S. A., Champness N. R., Schroder M., *J. Am. Chem. Soc.,* **2010**, 132, 4092-4094.

[131] Zhang Z., Yao Z.-Z., Xiang S., Chen B., *Energy Environ. Sci.,* **2014**, 7, 2868-2899.

[132] Park J., Li J.-R., Chen Y.-P., Yu J., Yakovenko A. A., Wang Z. U., Sun L.-B., Balbuenab P. B., Zhou H.-C., *Chem. Commun.,* **2012**, 48, 9995-9997.

[133] Dietzel P. D. C., Besikiotis V., Blom R., *J. Mater. Chem.,* **2009**, 19, 7362-7370.

[134] Caskey S. R., Wong-Foy A. G., Matzger A. J., *J. Am. Chem. Soc.,* **2008**, 130, 10870-10871.

[135] McDonald T. M., Lee W. R., Mason J. A., Wiers B. M., Hong C. S., Long J. R., *J. Am. Chem. Soc.,* **2012**, 134, 7056-7065.

[136] Deng H., Grunder S., Cordova K. E., Valente C., Furukawa H., Hmadeh M., Gándara F., Whalley A. C., Liu Z., Asahina S., Kazumori H., O'Keeffe M., Terasaki O., Stoddart J. F., Yaghi O. M., *Science,* **2012**, 336, 1018-1023.

[137] Duan J., Yang Z., Bai J., B. Zheng, Lia Y., Li S., *Chem. Commun.,* **2012**, 48, 3058-3060.

[138] Reinsch H., Krüger M., Wack J., Senker J., Salles F., Maurin G., Stock N., *Micropor. Mesopor. Mater.*, **2012**, 157, 50-55.

[139] Weigend F., Ahlrichs R., *Phys. Chem. Chem. Phys.*, **2005**, 7, 3297-3305.

[140] Weigend F., Häser M., *Theor. Chem. Acc.,* **1997**, 97, 331-340.

[141] Ahlrichs R., Bar M., Haser M., Horn H., Kolmel C., *Chem. Phys. Lett.,* **1989**, 162, 165-169.

[142] Rappe A. K., Casewit C. J., Colwell K. S., Goddard W. A., Skiff W. M., *J. Am. Chem. Soc.,* **1992**, 114, 10024-10035.

[143] Gale J. D., *JCS Faraday Trans.,* **1997**, 93, 629-637.

[144] Fang Q.-R., Zhu G.-S., Jin Z., Ji Y.-Y., Ye J.-W., Xue M., Yang H., Wang Y., Qiu S.-L, *Angew. Chem.,* **2007**, 119, 6758-6762.

[145] Mu B., Schoenecker P. M., Walton K. S.*, J. Phys. Chem. C*, **2010**, 114, 6464-6471.

[146] Llewellyn P. L., Bourrelly S., Serre C., Vimont A., Daturi M., Hamon L., De Weireld G., Chang J.-S., Hong D.-Y., Hwang Y. K., Jhung S. H., Férey G., *Langmuir*, **2008**, 24, 7245-7250.

[147] Guo Z., Wu H., Srinivas G., Zhou Y., Xiang S., Chen Z., Yang Y., Zhou W., O'Keeffe M., Chen B., *Angew. Chem., Int. Ed.,* **2011**, 50, 3178-3181.

[148] Nouar F., Eubank J. F., Bousquet T., Wojtas L., Zaworotko M. J., Eddaoudi M., *J. Am. Chem. Soc.,* **2008**, 130, 1833-1835.

[149] Li B., Zhang Z., Li Y., Yao K., Zhu Y., Deng Z., Yang F., Zhou X., Li G., Wu H., Nijem N., Chabal Y. J., Lai Z., Han Y., Shi Z., Feng S., Li J., *Angew. Chem. Int. Ed.,* **2012**, 51, 1412-1415.

[150] Cheon Y. E., Suh M. P., *Chem. Commun.*, **2009**, 45, 2296-2298.

[151] Senkovska I., Kaskel S., *Eur. J. Inorg. Chem.,* **2006**, 4564-4569.

[152] Sun D., Ma S., Simmons J. M., Li J.-R., Yuan D., Zhou H.-C., *Chem. Commun.,* **2010**, 46, 1329-1331.

[153] Wu S., Ma L., Long L.-S., Zheng L.-S., Lin W., *Inorg. Chem.*, **2009**, 48, 2436-2442.

[154] Noro S.-i., Kitaura R., Kondo M., Kitagawa S., Ishii T., Matsuzaka H., Yamashita M., *J. Am. Chem. Soc.,* **2002**, 124, 2568-2583.

[155] Hao X.-R., Wang X.-L., Su Z.-M., Shao K.-Z., Zhao Y.-H., Lana Y.-Q., Fu Y.-M., *Dalton Trans.,* **2009**, 8562-8566.

[156] A) Ibarra I. A., Bayliss P. A., Pérez E., Yang S., Blake A. J., Nowell H., Allan D. R., Poliakoff M., Schröder M., *Green Chem.,* **2012**, 14, 117-122 B) Farha O. K., Mulfort K. L., Hupp J. T., *Inorg. Chem.,* **2008**, 47, 10223-10225 C) Karra J. R., Huang Y.-G., Walton K. S., *Cryst. Growth Des.,* **2013**, 13, 1075-1081.

[157] Zhai Q., Lin Q., Wu T., Zheng S.-T., Bu X., Feng P., *Dalton Trans.,* **2012**, 41, 2866-2868.

[157] Muzart J., *Tetrahedron,* **2009**, 65, 8313-8323.

[159] Lin Z.J., Liu T.-F., Huang Y.-B., Jian L., Cao R., *Chem. Eur. J.,* **2012**, 18 , 7896-7902.

[160] Ramaswamy P., Wong N. E., Shimizu G. K. H.*, Chem. Soc. Rev.,* **2014**, 43, 5913-5932.

[161] Deria P., Mondloch J. E., Karagiaridi O., Bury W., Hupp J. T., Farha O. K., *Chem. Soc. Rev.,* **2014**, 43 ,5896-5912.

[162] Marcus E., *Cell*, **2014**, 159, 965-966.

[163] Camilli A., *Infect. Immun.,* **2010**, 78, 4972-4975.

[164] Liu B., Wong-Foy A. G., Matzger A. J., *Chem. Commun.,* **2013**, 49, 1419-1421.

APPENDIX A

Synthesis, characterization of MOFs and gas sorption measurements

6.1 Zr-MOF synthesis based on organic linker 1
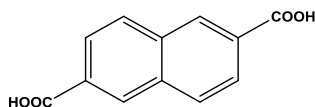
6.1.1 Synthesis of compound $Zr_6O_4(OH)_4(NDC)_6$

An amount of 0.025 g (0.11 mmol) of H_2NDC and 0.027 g (0.11 mmol) of $ZrCl_4$ were dissolved in a 20 mL glass scintillation vial containing 10 mL DMF and 0.25 mL of glacial acetic acid. The vial was placed in an oven, heated up to 120 ^0C with 0.06 ^0C/min and then held at 120 ^0C for 24 h. After that time a white powder was deposited. Yield: 45 % based on H_2NDC.

After the efficient characterization of the material the evaluation of its gas sorption properties took place. Successful activation was possible as follows: as-made sample was washed with DMF four times per day for 2 days and then the sample was soaked in acetone over a period of 4 days, replenishing the acetone 4 times per day. The sample was transferred to a pre weighted sample cell and acetone was removed under reduced pressure. Finally, the sample was activated under dynamic vacuum at 100 °C for 12 hours and until the outgas rate was less than 2 mTorr/min.
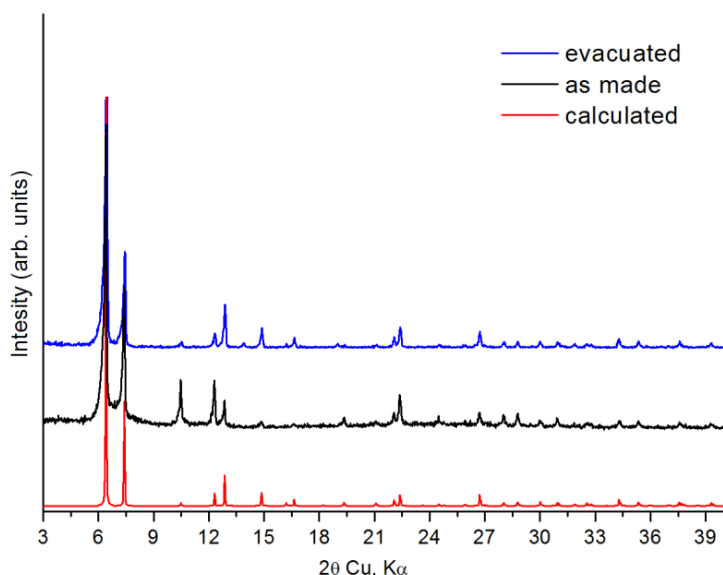
Figure 6.3. Comparison of experimental, calculated and evacuated pxrd patterns for the compound $Zr_6O_4(OH)_4(NDC)_6$.
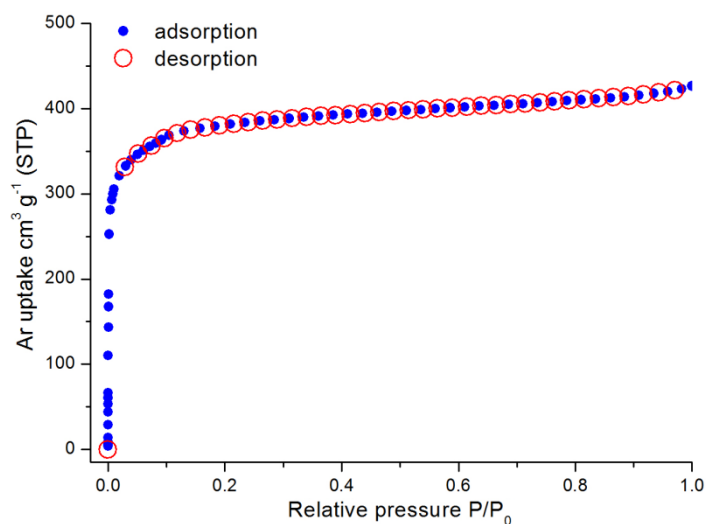
Figure 6.4. Argon sorption isotherm of $Zr_6O_4(OH)_4(NDC)_6$ at 87 K.
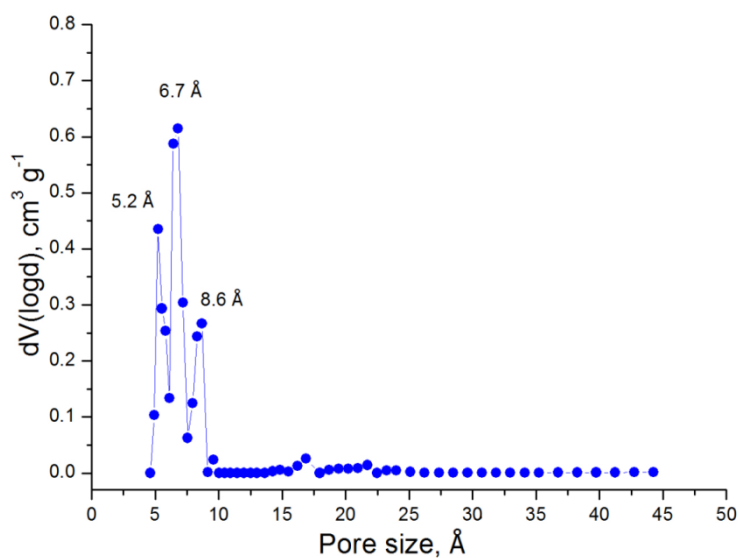
Figure 6.5. Pore size distribution in $Zr_6O_4(OH)_4(NDC)_6$ calculated from NLDFT analysis.
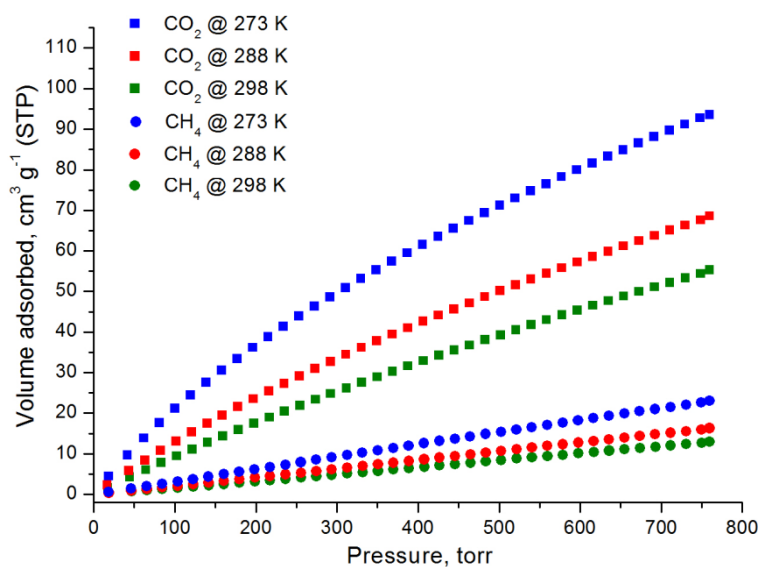
Figure 6.6. CO_2 and CH_4 adsorption isotherms of $Zr_6O_4(OH)_4(NDC)_6$ at 273 K, 288 K and 298 K.

156
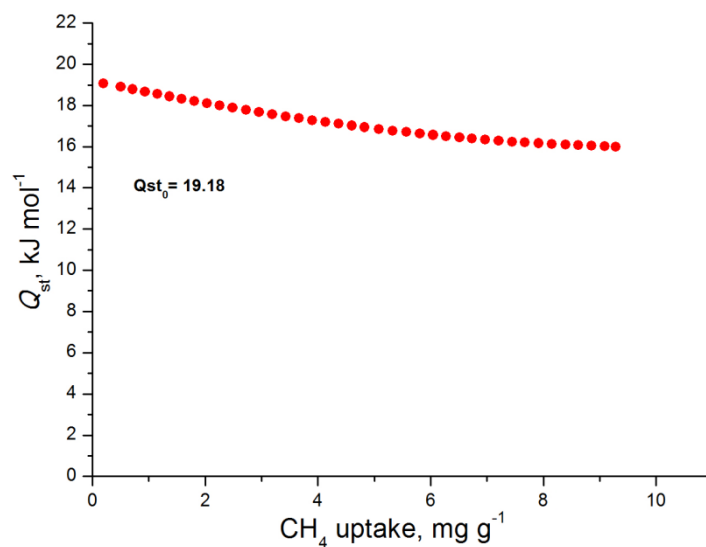
Figure 6.7. CH_4 isosteric heat of adsorption in $Zr_6O_4(OH)_4(NDC)_6$ as a function of surface coverage.
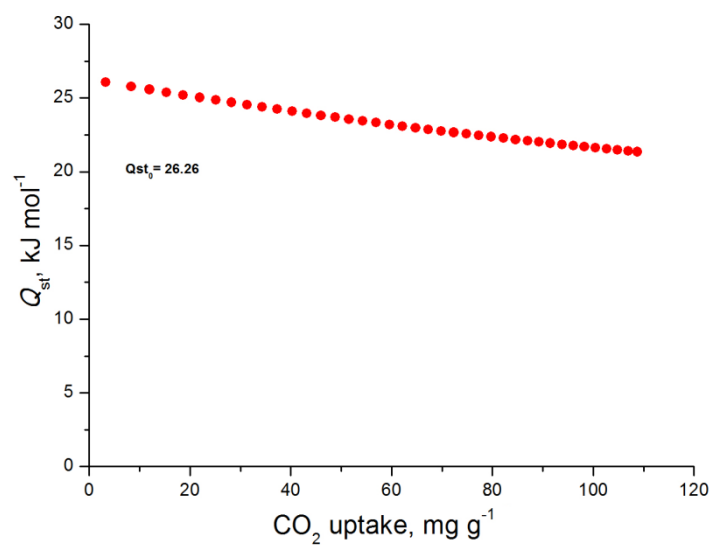
Figure 6.8. CO_2 isosteric heat of adsorption in $Zr_6O_4(OH)_4(NDC)_6$ as a function of surface coverage.
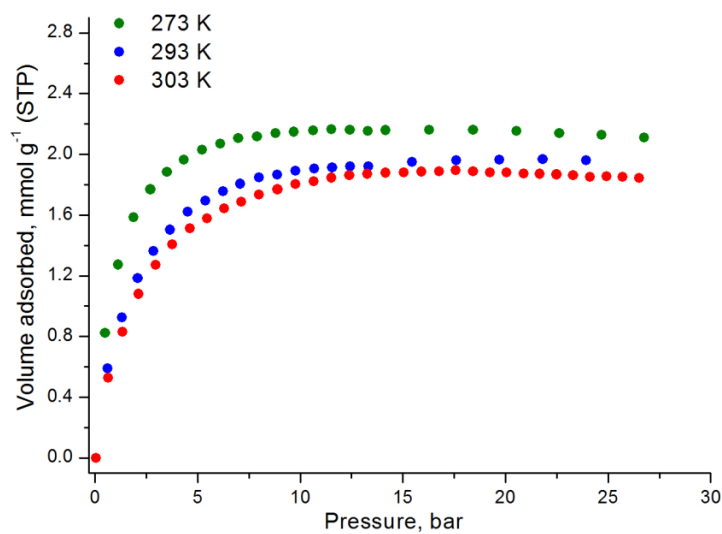
Figure 6.9. High pressure CH_4 adsorption isotherms of $Zr_6O_4(OH)_4(NDC)_6$ at 273 K, 293 K and 303 K.
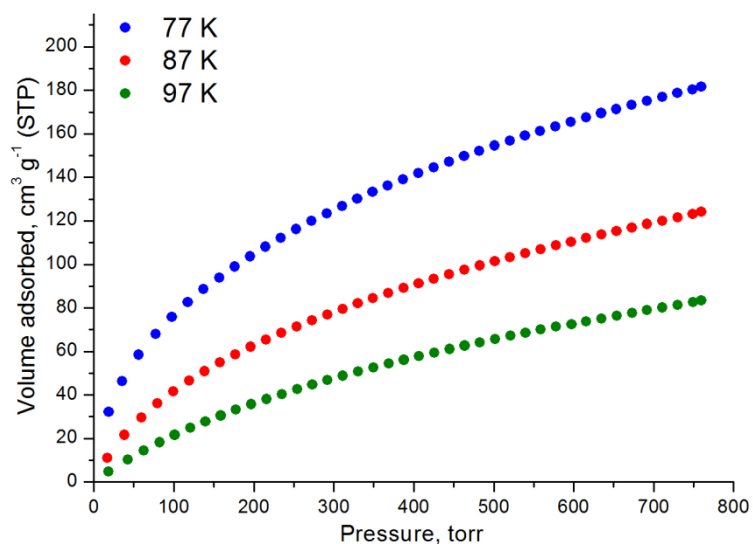
Figure 6.10. H_2 adsorption isotherms of $Zr_6O_4(OH)_4(NDC)_6$ at 77 K, 87 K and 97 K.
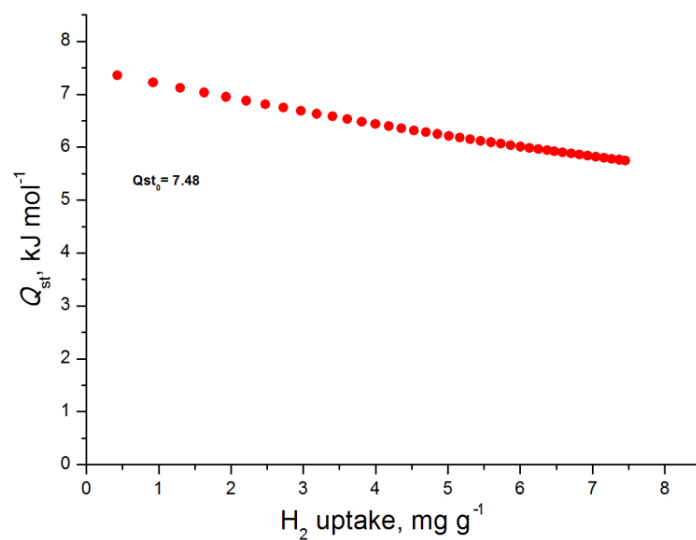
Figure 6.11. H_2 isosteric heat of adsorption in $Zr_6O_4(OH)_4(NDC)_6$ as a function of surface coverage.
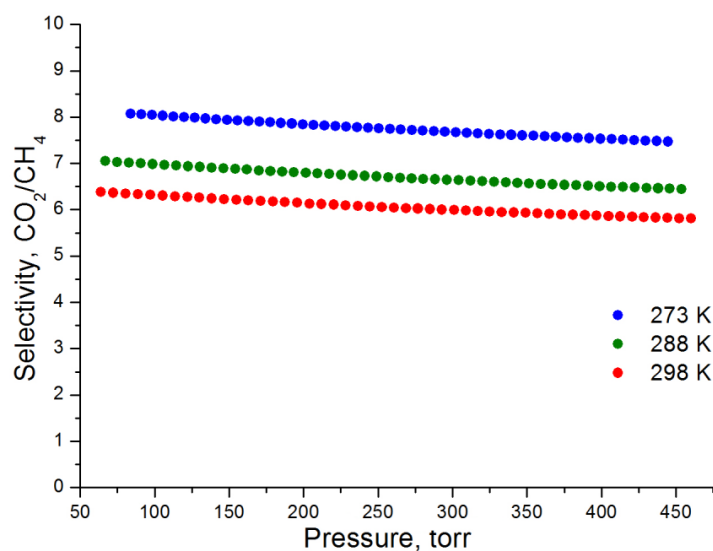
Figure 6.12. Selectivities of CO_2 over CH_4 at 273 K, 288 K and 298 K for $Zr_6O_4(OH)_4(NDC)_6$ as predicted by IAST for a 5/95 CO_2/CH_4 molar mixture.

6.2 Zr-MOF synthesis based on organic linker 74
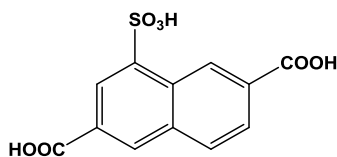
6.2.1 Synthesis of compound $Zr_6O_4(OH)_4(NDC\text{-}SO_3H)_6$

An amount of 0.020 g (0.07 mmol) of $H_2NDC\text{-}SO_3H$ and 0.016 g (0.07 mmol) of $ZrCl_4$ were dissolved in a 20 mL glass scintillation vial containing 10 mL DMF and 1 mL of glacial acetic acid. The vial was placed in an oven, heated up to 120 ^0C with 0.06 ^0C/ min and then held at 120 ^0C for 24 h. After that time an off white powder was deposited. Yield: 12 % based on $H_2NDC\text{-}SO_3H$.
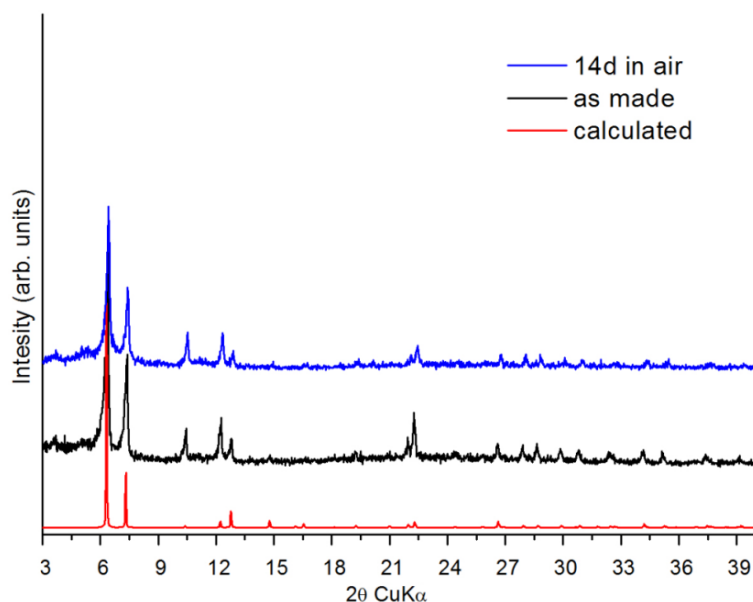
Figure 6.13. Comparison of experimental, 14 days exposure in air and calculated pxrd patterns for the compound $Zr_6O_4(OH)_4(NDC\text{-}SO_3H)_6$.

6.3 Zr-MOF syntheses based on organic linker 2
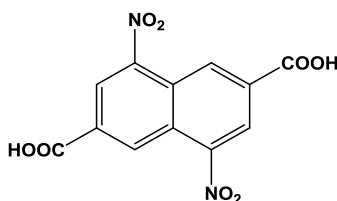
6.3.1 Synthesis of compound $Zr_6O_4(OH)_4(NDC\text{-}2NO_2)_{4.2}(CH_3COO)_{3.6}$

An amount of 0.040 g (0.13 mmol) of $H_2NDC\text{-}2NO_2$ and 0.032 g (0.13 mmol) of $ZrCl_4$ were dissolved in a 20 mL glass scintillation vial containing 13 mL DMF and 2 mL of glacial acetic acid.

159

The vial was placed in an oven, heated up to 120 ^{0}C with 0.06 ^{0}C/min and then held at 120 ^{0}C for 24 h. After that time an orange powder was deposited. Yield: 45 % based on H$_2$NDC-2NO$_2$.

After the efficient characterization of the material the evaluation of its gas sorption properties took place. Successful activation was possible as follows: as-made sample was washed with DMF four times per day for 2 days and then the sample was soaked in acetone over a period of 4 days, replenishing the acetone 4 times per day. The sample was transferred to a pre weighted sample cell and acetone was removed under reduced pressure. Finally, the sample was activated under dynamic vacuum at 100 °C for 12 hours and until the outgas rate was less than 2 mTorr/min.
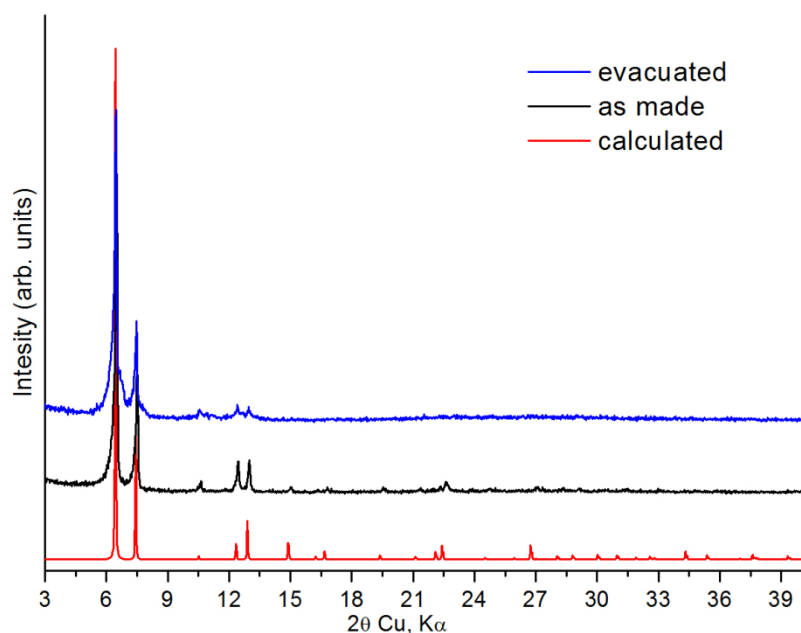
Figure 6.14. Comparison of experimental, evacuated and calculated pxrd patterns for the materials Zr$_6$O$_4$(OH)$_4$(NDC-2NO$_2$)$_{4.2}$(CH$_3$COO)$_{3.6}$ and Zr$_6$O$_4$(OH)$_4$(NDC)$_6$ respectively.
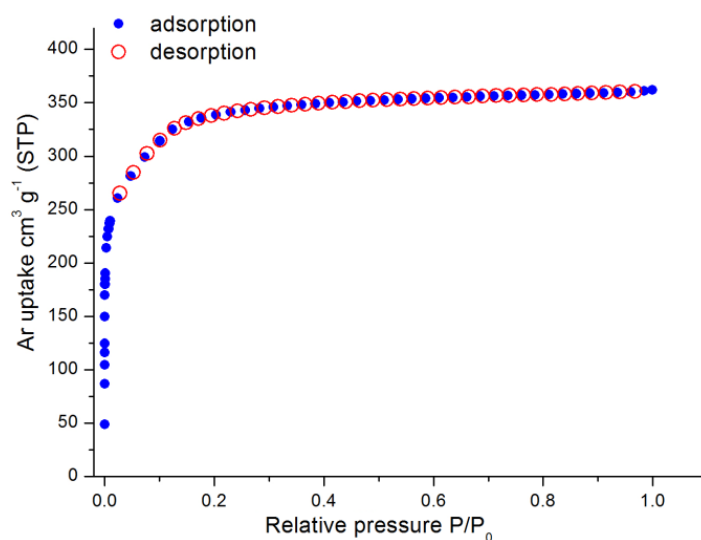
Figure 6.15. Argon sorption isotherm of Zr$_6$O$_4$(OH)$_4$(NDC-2NO$_2$)$_{4.2}$(CH$_3$COO)$_{3.6}$ at 87 K.
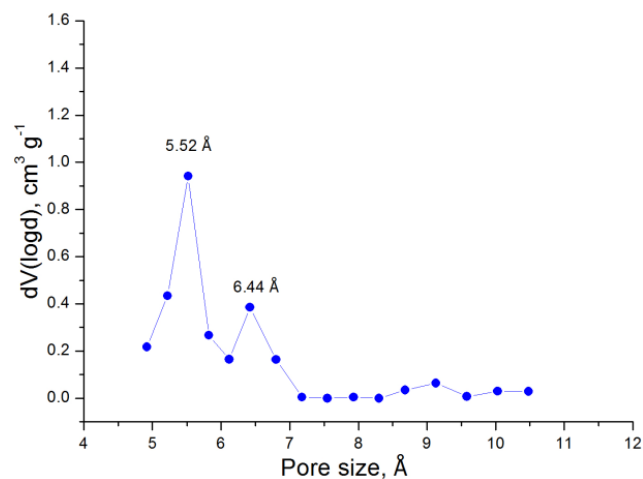
Figure 6.16. Pore size distribution in $Zr_6O_4(OH)_4(NDC-2NO_2)_{4.2}(CH_3COO)_{3.6}$ calculated from NLDFT analysis.
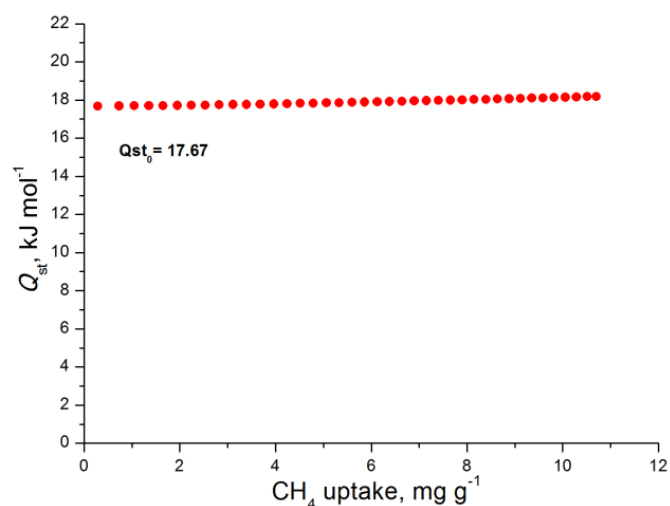
Figure 6.17. CH_4 isosteric heat of adsorption in $Zr_6O_4(OH)_4(NDC-2NO_2)_{4.2}(CH_3COO)_{3.6}$ as a function of surface coverage.
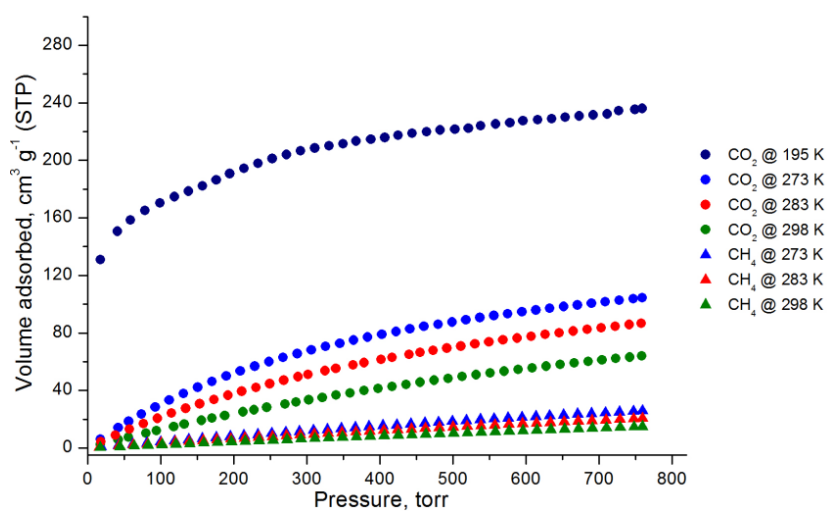
Figure 6.18. CO_2 adsorption isotherms of $Zr_6O_4(OH)_4(NDC-2NO_2)_{4.2}(CH_3COO)_{3.6}$ at 195 K, 273 K, 283 K, 298 K and CH_4 adsorption isotherms at 273 K, 283 K and 298 K.
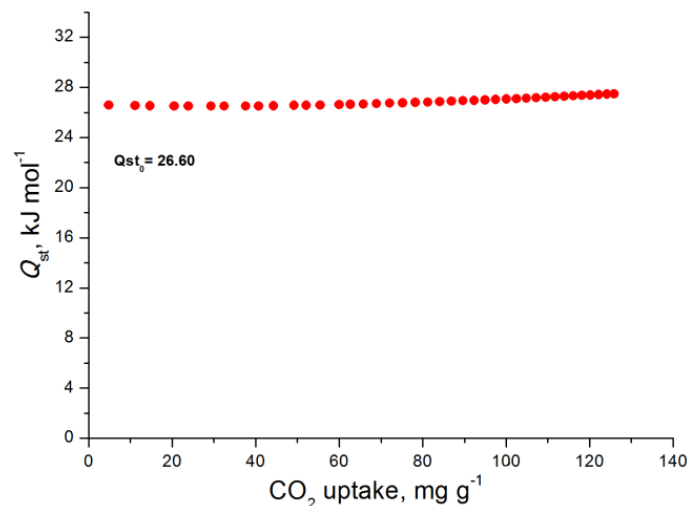
Figure 6.19. CO_2 isosteric heat of adsorption in $Zr_6O_4(OH)_4(NDC-2NO_2)_{4.2}(CH_3COO)_{3.6}$ as a function of surface coverage.
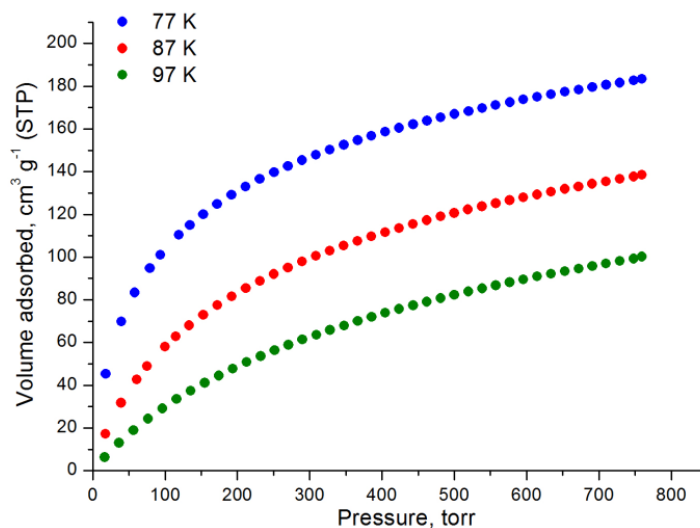
Figure 6.20. H_2 adsorption isotherms of $Zr_6O_4(OH)_4(NDC-2NO_2)_{4.2}(CH_3COO)_{3.6}$ at 77 K, 87 K and 97 K.
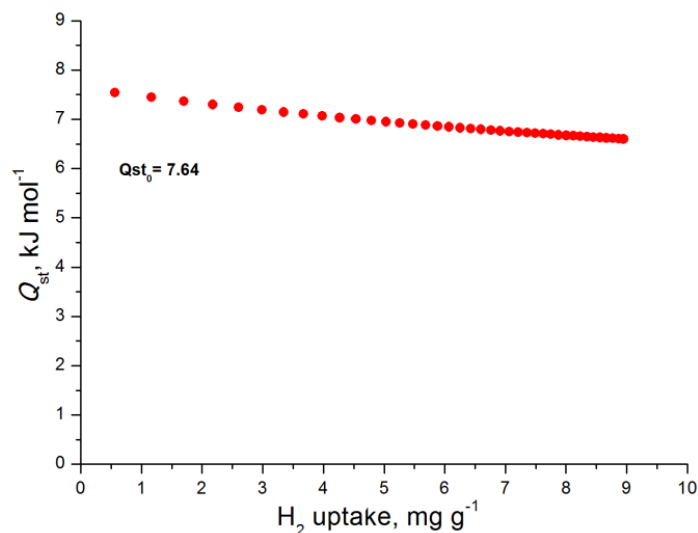
Figure 6.21. H_2 isosteric heat of adsorption in $Zr_6O_4(OH)_4(NDC-2NO_2)_{4.2}(CH_3COO)_{3.6}$ as a function of surface coverage.

162
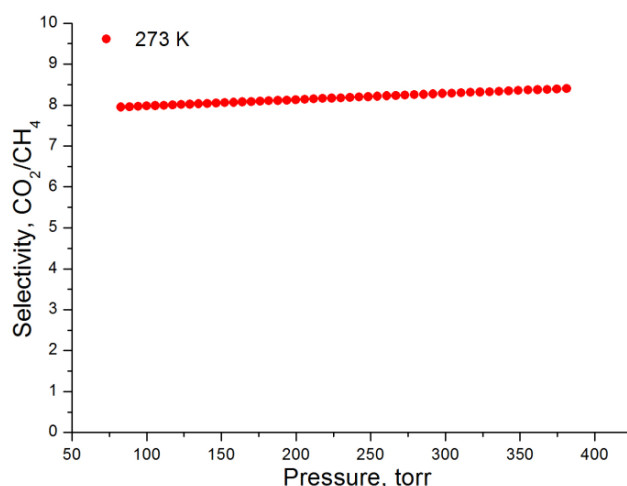
Figure 6.22. Selectivity of CO_2 over CH_4 at 273 K for $Zr_6O_4(OH)_4(NDC\text{-}2NO_2)_{4.2}(CH_3COO)_{3.6}$ as predicted by IAST for a 5/95 CO_2/CH_4 molar mixture.
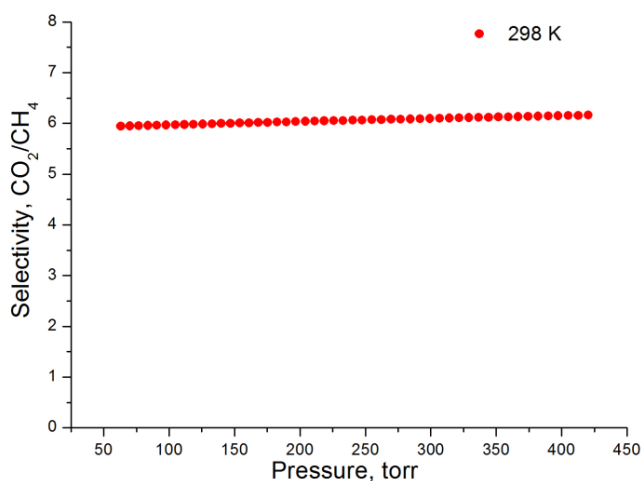
Figure 6.23. Selectivity of CO_2 over CH_4 at 298 K for $Zr_6O_4(OH)_4(NDC\text{-}2NO_2)_{4.2}(CH_3COO)_{3.6}$ as predicted by IAST for a 5/95 CO_2/CH_4 molar mixture.

6.3.2 Synthesis of compound $Zr_6O_4(OH)_4(NDC)_{4.4}(NDC\text{-}2NO_2)_{1.6}$

An amount of 0.009 g (0.003 mmol) of $H_2NDC\text{-}2NO_2$, 0.020 g (0.09 mmol) H_2NDC and 0.022 g (0.09 mmol) of $ZrCl_4$ were dissolved in a 20 mL glass scintillation vial containing 10 mL DMF and 2 mL of glacial acetic acid. The vial was placed in an oven, heated up to 120 ^{0}C with 0.06 ^{0}C/min and then held at 120 ^{0}C for 24 h. After that time an orange powder was deposited. Yield: 45 % based on $H_2NDC\text{-}2NO_2$.
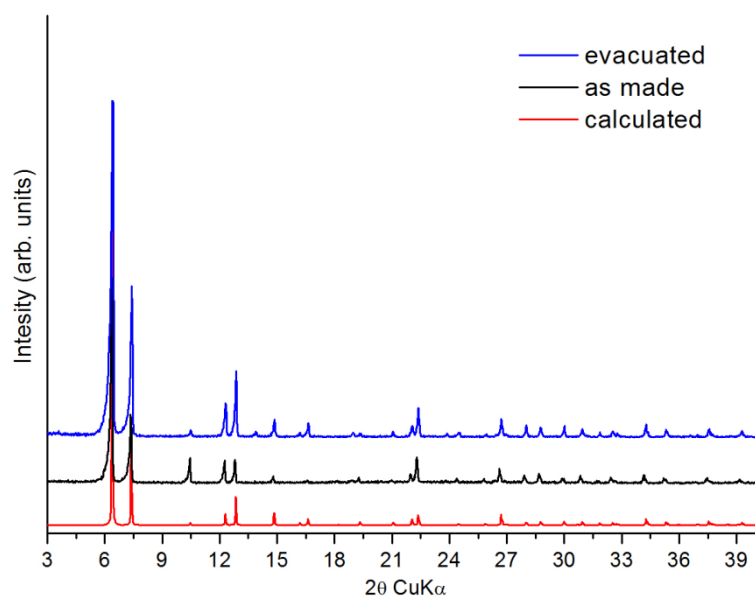
Figure 6.24. Comparison of experimental, calculated and evacuated pxrd patterns for the materials $Zr_6O_4(OH)_4(NDC)_{4.4}(NDC-2NO_2)_{1.6}$ and $Zr_6O_4(OH)_4(NDC)_6$ respectively.
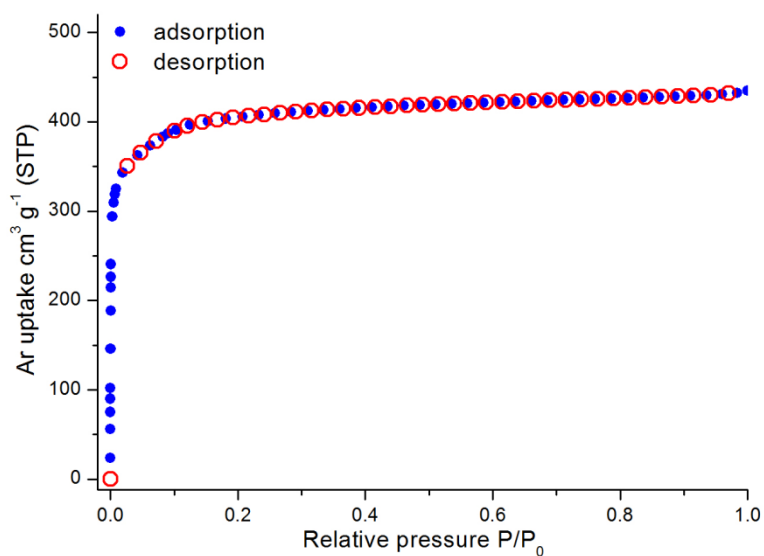
Figure 6.25. Argon sorption isotherm of $Zr_6O_4(OH)_4(NDC)_{4.4}(NDC-2NO_2)_{1.6}$ at 87 K.
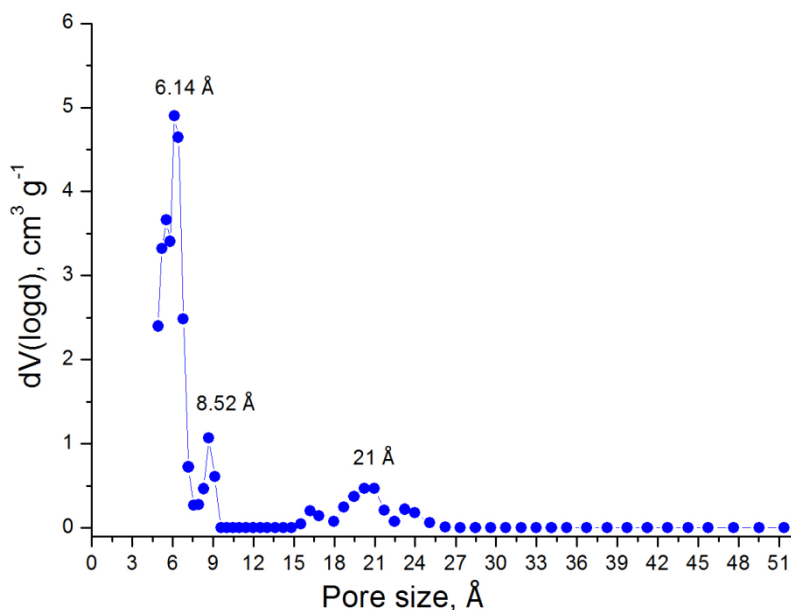
Figure 6.26. Pore size distribution in $Zr_6O_4(OH)_4(NDC)_{4.4}(NDC-2NO_2)_{1.6}$ calculated from NLDFT analysis.

After the efficient characterization of the material the evaluation of its gas sorption properties took place. Successful activation was possible as follows: as-made sample was washed with DMF four times per day for 2 days and then the sample was soaked in acetone over a period of 4 days, replenishing the acetone 4 times per day. The sample was transferred to a pre weighted sample cell and acetone was removed under reduced pressure. Finally, the sample was activated under dynamic vacuum at 100 °C for 12 hours and until the outgas rate was less than 2 mTorr/min.
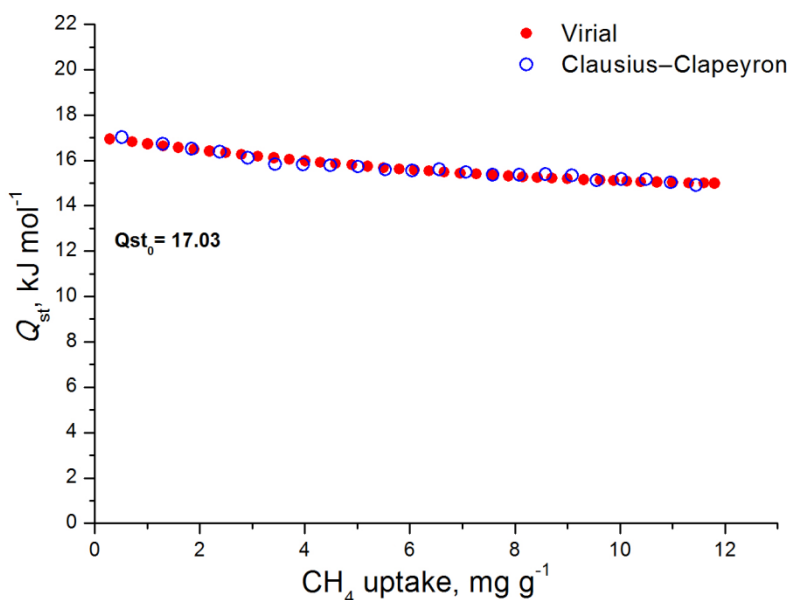
Figure 6.27. CH_4 isosteric heat of adsorption in $Zr_6O_4(OH)_4(NDC)_{4.4}(NDC-2NO_2)_{1.6}$ as a function of surface coverage.
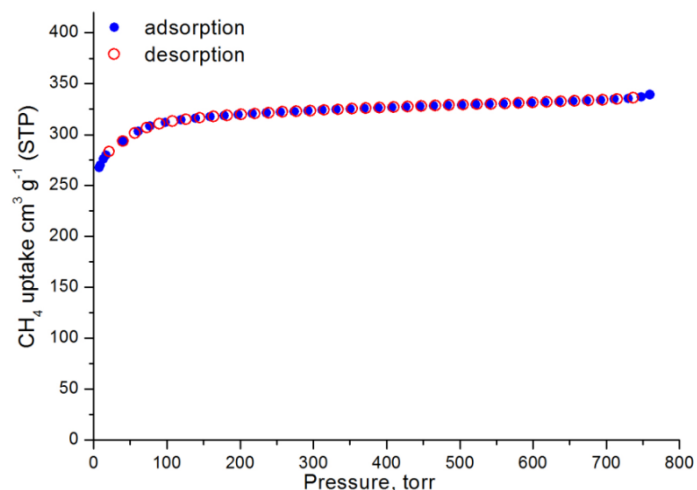
Figure 6.28. CH_4 sorption isotherm of $Zr_6O_4(OH)_4(NDC)_{4.4}(NDC\text{-}2NO_2)_{1.6}$ at 112 K.
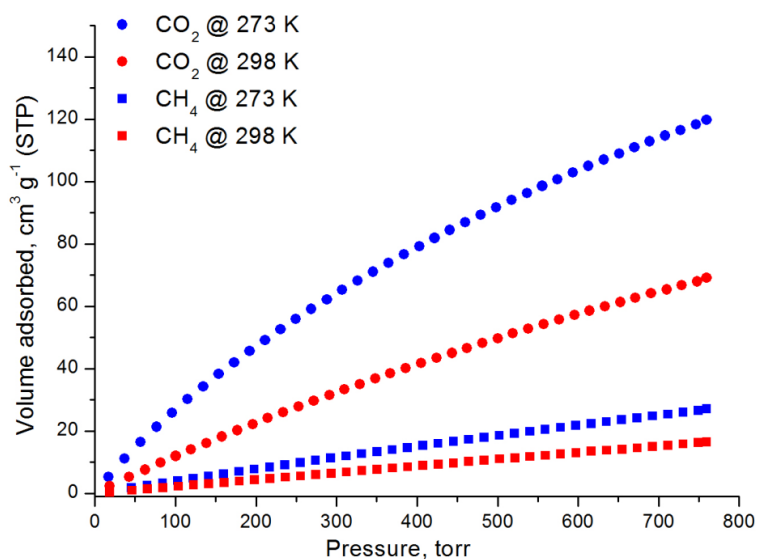
Figure 6.29. CO_2 and CH_4 adsorption isotherms of $Zr_6O_4(OH)_4(NDC)_{4.4}(NDC\text{-}2NO_2)_{1.6}$ at 273 K and 298 K.
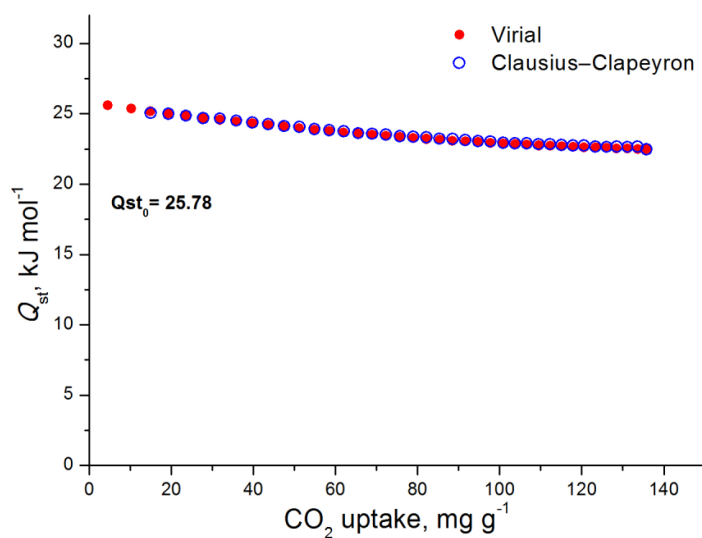
Figure 6.30. CO_2 isosteric heat of adsorption in $Zr_6O_4(OH)_4(NDC)_{4.4}(NDC\text{-}2NO_2)_{1.6}$ as a function of surface coverage.
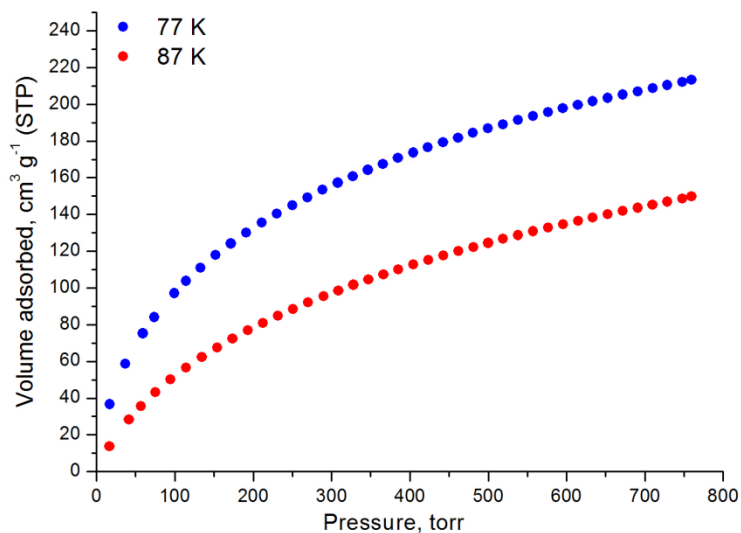
Figure 6.31. Hydrogen adsorption isotherms of $Zr_6O_4(OH)_4(NDC)_{4.4}(NDC-2NO_2)_{1.6}$ at 77 K and 87 K.
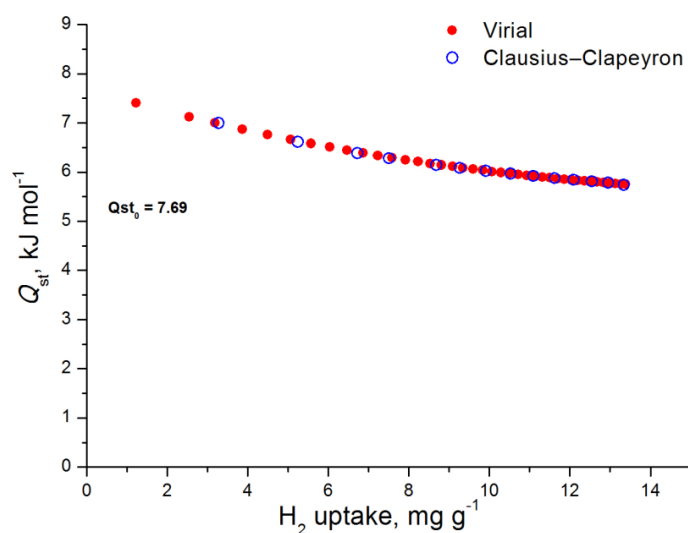
Figure 6.32. H_2 isosteric heat of adsorption in $Zr_6O_4(OH)_4(NDC)_{4.4}(NDC-2NO_2)_{1.6}$ as a function of surface coverage.
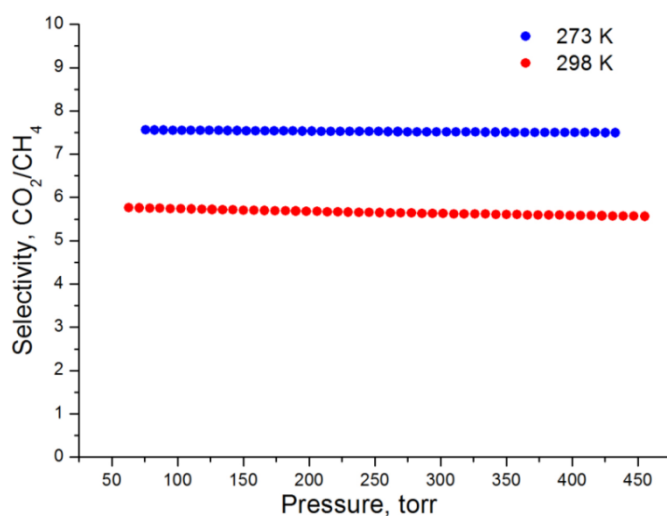
Figure 6.33. Selectivities of CO_2 over CH_4 at 298 K and 273 K for $Zr_6O_4(OH)_4(NDC)_{4.4}(NDC-2NO_2)_{1.6}$ as predicted by IAST for a 5/95 CO_2/CH_4 molar mixture.

167

6.3.3 Synthesis of compound $Zr_6O_4(OH)_4(NDC)_{3.4}(NDC-2NO_2)_{2.3}(CH_3COO)_{0.6}$

An amount of 0.014 g (0.045 mmol) of $H_2NDC-2NO_2$, 0.020 g (0.09 mmol) H_2NDC and 0.022 g (0.09 mmol) of $ZrCl_4$ were dissolved in a 20 mL glass scintillation vial containing 10 mL DMF and 2 mL of glacial acetic acid. The vial was placed in an oven, heated up to 120 ^0C with 0.06 ^0C/min and then held at 120 ^0C for 24 h. After that time an orange powder was deposited. Yield: 45 % based on $H_2NDC-2NO_2$.
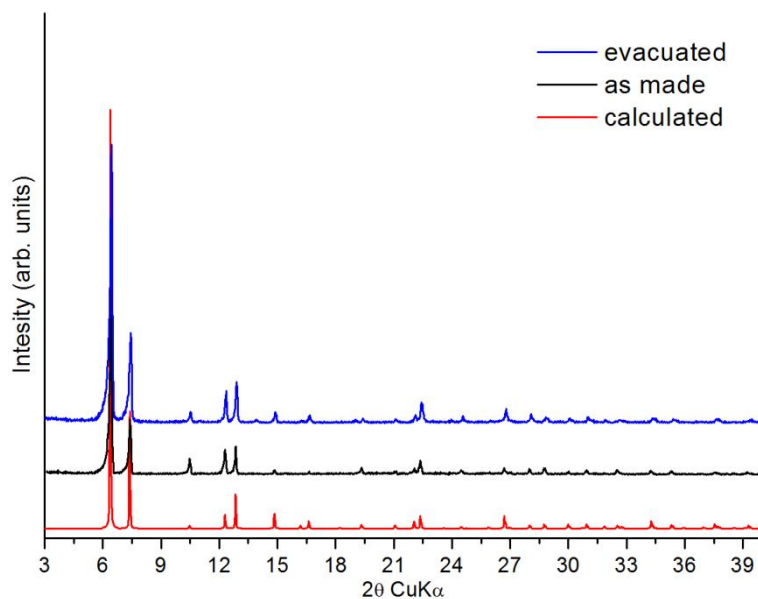
Figure 6.34. Comparison of experimental, calculated and evacuated pxrd patterns for the materials $Zr_6O_4(OH)_4(NDC)_{3.4}(NDC-2NO_2)_{2.3}(CH_3COO)_{0.6}$ and $Zr_6O_4(OH)_4(NDC)_6$ respectively.

After the efficient characterization of the material the evaluation of its gas sorption properties took place. Successful activation was possible as follows: as-made sample was washed with DMF four times per day for 2 days and then the sample was soaked in acetone over a period of 4 days, replenishing the acetone 4 times per day. The sample was transferred to a pre weighted sample cell and acetone was removed under reduced pressure. Finally, the sample was activated under dynamic vacuum at 100 °C for 12 hours and until the outgas rate was less than 2 mTorr/min.

168
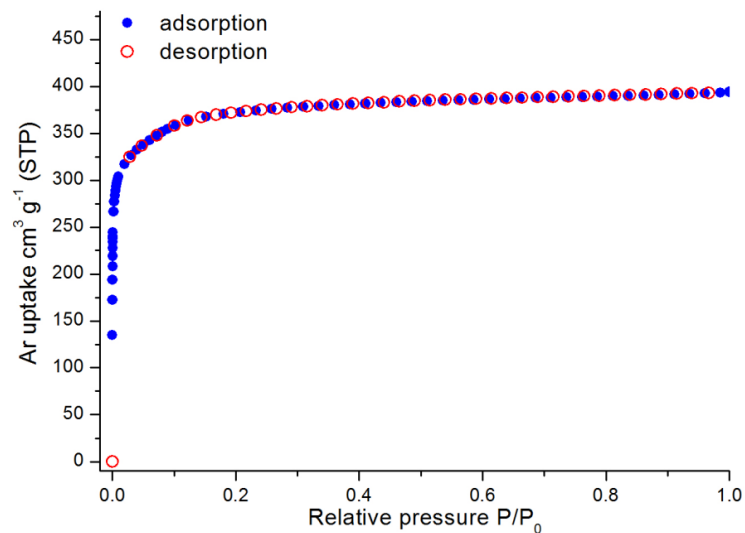
Figure 6.35. Argon sorption isotherm of $Zr_6O_4(OH)_4(NDC)_{3.4}(NDC-2NO_2)_{2.3}(CH_3COO)_{0.6}$ at 87 K.
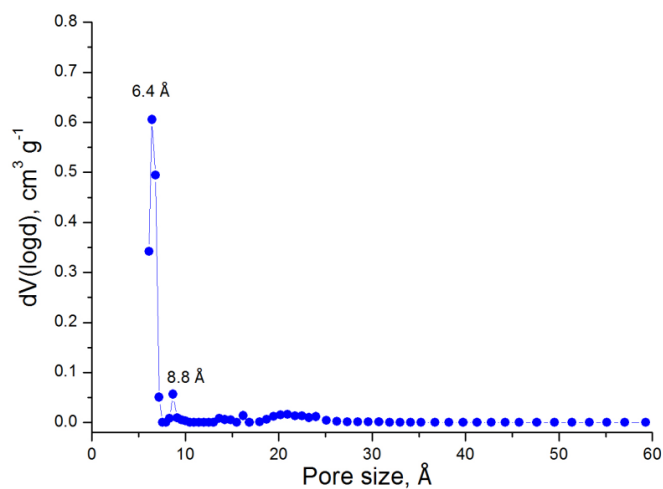
Figure 6.36. Pore size distribution in $Zr_6O_4(OH)_4(NDC)_{3.4}(NDC-2NO_2)_{2.3}(CH_3COO)_{0.6}$ calculated from NLDFT analysis.
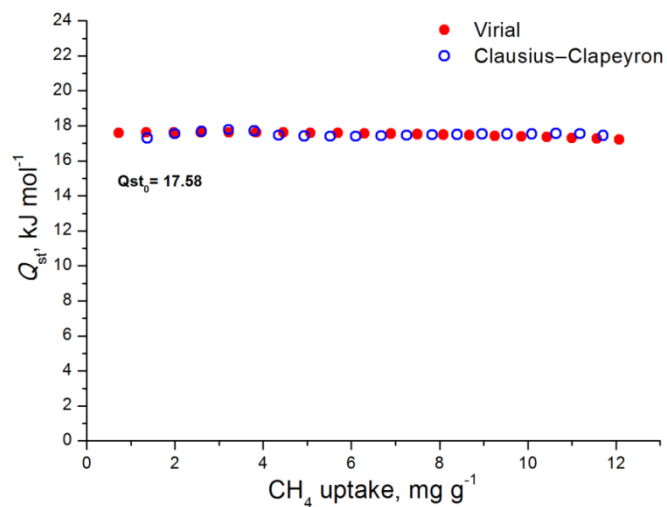
Figure 6.37. CH$_4$ isosteric heat of adsorption in $Zr_6O_4(OH)_4(NDC)_{3.4}(NDC-2NO_2)_{2.3}(CH_3COO)_{0.6}$ as a function of surface coverage.
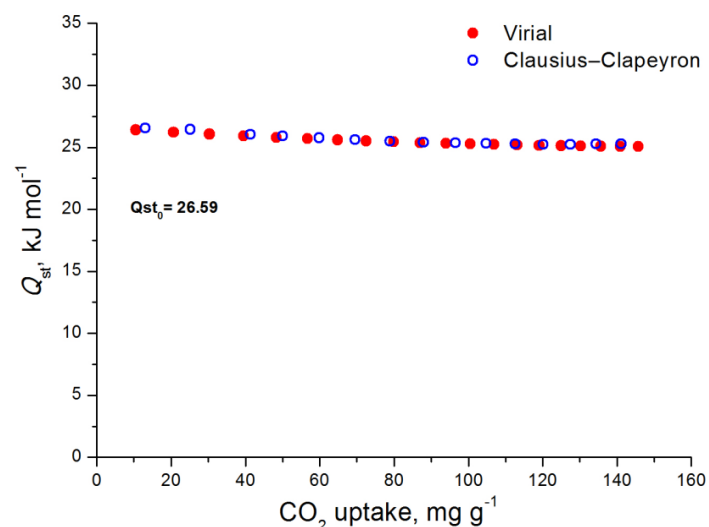
Figure 6.38. CO_2 isosteric heat of adsorption in $Zr_6O_4(OH)_4(NDC)_{3.4}(NDC\text{-}2NO_2)_{2.3}(CH_3COO)_{0.6}$ as a function of surface coverage.
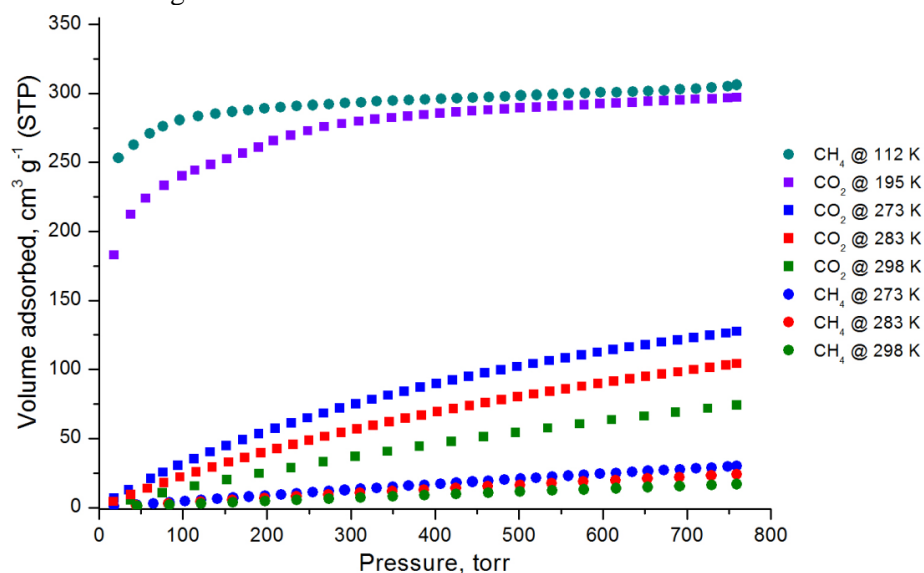
Figure 6.39. CO_2 adsorption isotherms of $Zr_6O_4(OH)_4(NDC)_{3.4}(NDC\text{-}2NO_2)_{2.3}(CH_3COO)_{0.6}$ at 195 K, 273 K, 283 K, 298 K and CH_4 adsorption isotherms at 112 K, 273 K, 283 K and 298 K.
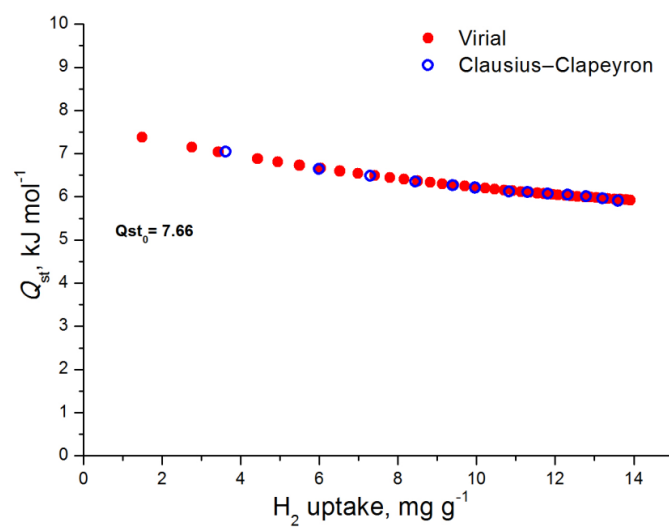
Figure 6.40. H_2 isosteric heat of adsorption in $Zr_6O_4(OH)_4(NDC)_{3.4}(NDC\text{-}2NO_2)_{2.3}(CH_3COO)_{0.6}$ as a function of surface coverage.
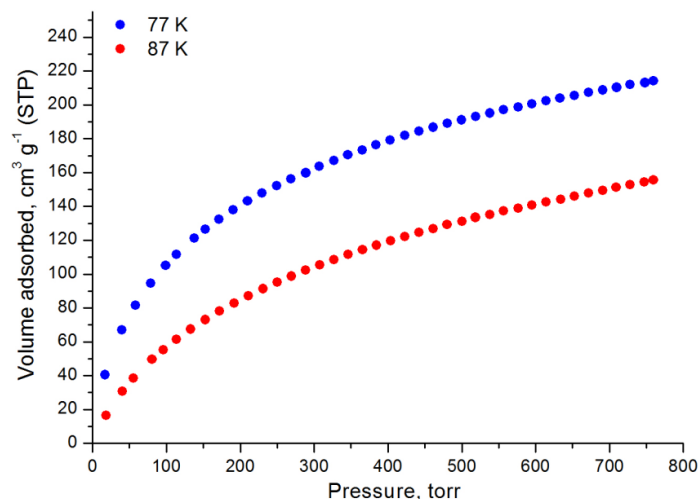
Figure 6.41. H$_2$ adsorption isotherms of Zr$_6$O$_4$(OH)$_4$(NDC)$_{3.4}$(NDC-2NO$_2$)$_{2.3}$(CH$_3$COO)$_{0.6}$ at 77 K and 87 K.
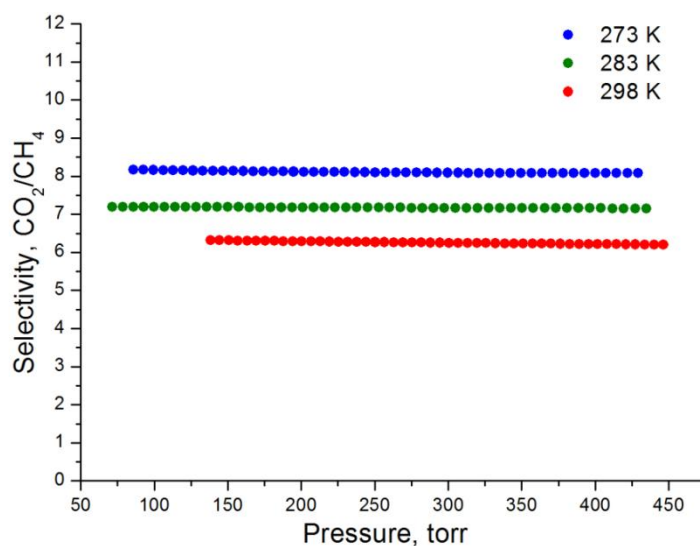
Figure 6.42. Selectivity of CO$_2$ over CH$_4$ at 273 K, 283 K and 298 K for Zr$_6$O$_4$(OH)$_4$(NDC)$_{3.4}$(NDC-2NO$_2$)$_{2.3}$(CH$_3$COO)$_{0.6}$ as predicted by IAST for a 5/95 CO$_2$/CH$_4$ molar mixture.

6.3.4 Synthesis of compound Zr$_6$O$_4$(OH)$_4$(NDC)$_2$(NDC-2NO$_2$)$_{2.8}$(CH$_3$COO)$_{2.4}$

An amount of 0.042 g (0.14 mmol) of H$_2$NDC-2NO$_2$, 0.015 g (0.07 mmol) H$_2$NDC and 0.016 g (0.07 mmol) of ZrCl$_4$ were dissolved in a 20 mL glass scintillation vial containing 10 mL DMF and 2 mL of glacial acetic acid. The vial was placed in an oven, heated up to 120 ^{0}C with 0.06 ^{0}C/min and then held at 120 ^{0}C for 24 h. After that time an orange powder was deposited. Yield: 45 % based on H$_2$NDC-2NO$_2$.
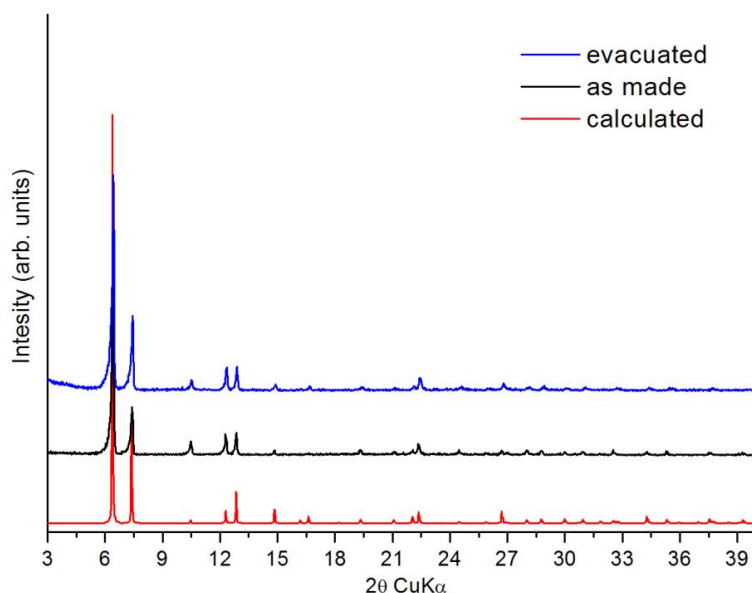
Figure 6.43. Comparison of experimental, calculated and evacuated pxrd patterns for the materials $Zr_6O_4(OH)_4(NDC)_2(NDC\text{-}2NO_2)_{2.8}(CH_3COO)_{2.4}$ and $Zr_6O_4(OH)_4(NDC)_6$ respectively.

After the efficient characterization of the material the evaluation of its gas sorption properties took place. Successful activation was possible as follows: as-made sample was washed with DMF four times per day for 2 days and then the sample was soaked in acetone over a period of 4 days, replenishing the acetone 4 times per day. The sample was transferred to a pre weighted sample cell and acetone was removed under reduced pressure. Finally, the sample was activated under dynamic vacuum at 100 °C for 12 hours and until the outgas rate was less than 2 mTorr/min.
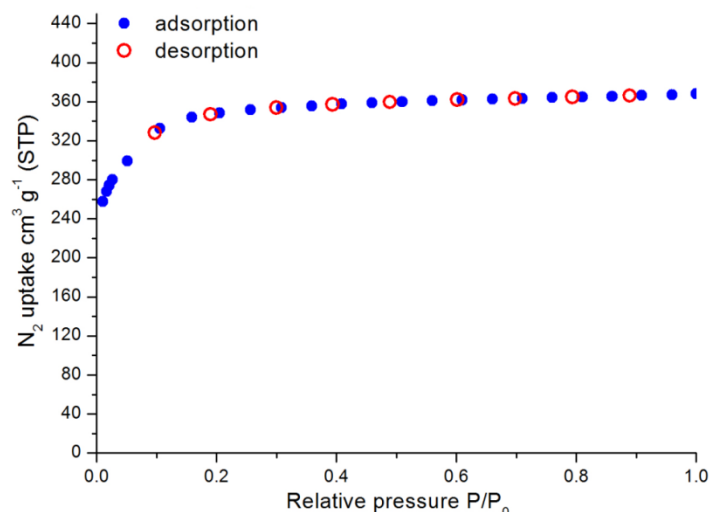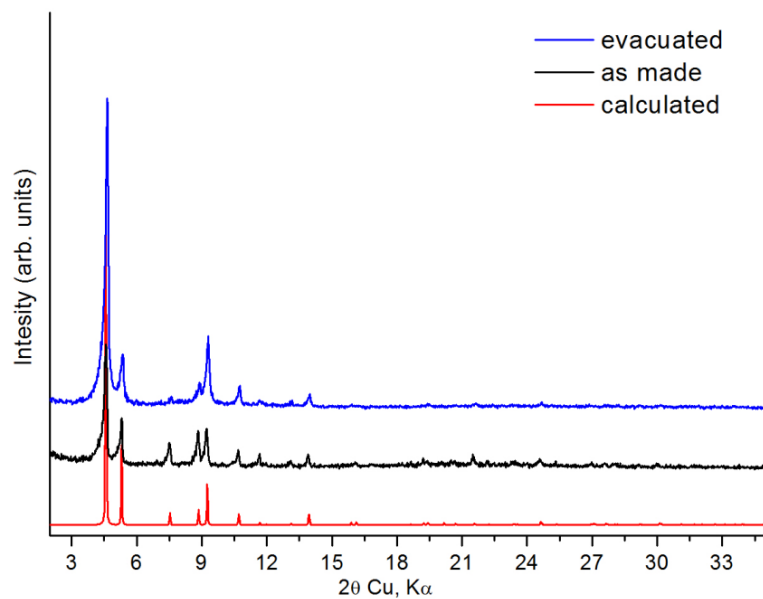

Figure 6.44. Nitrogen sorption isotherm of $Zr_6O_4(OH)_4(NDC)_2(NDC\text{-}2NO_2)_{2.8}(CH_3COO)_{2.4}$ at 77 K.

172
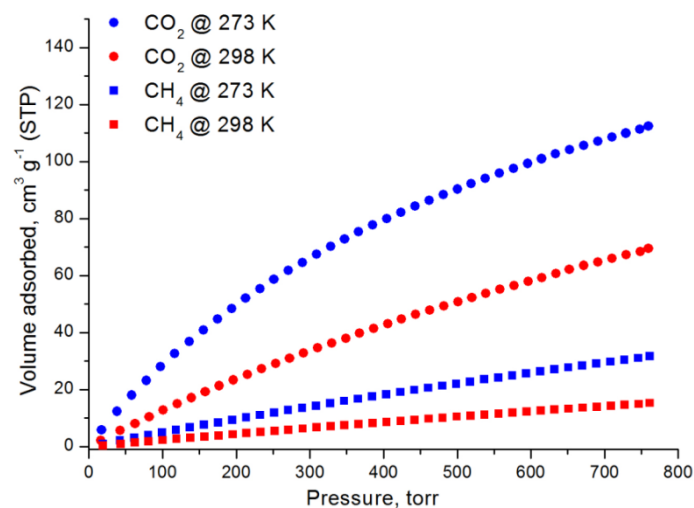
Figure 6.45. CO$_2$ and CH$_4$ adsorption isotherms of Zr$_6$O$_4$(OH)$_4$(NDC)$_2$(NDC-2NO$_2$)$_{2.8}$(CH$_3$COO)$_{2.4}$ at 273 K and 298 K.
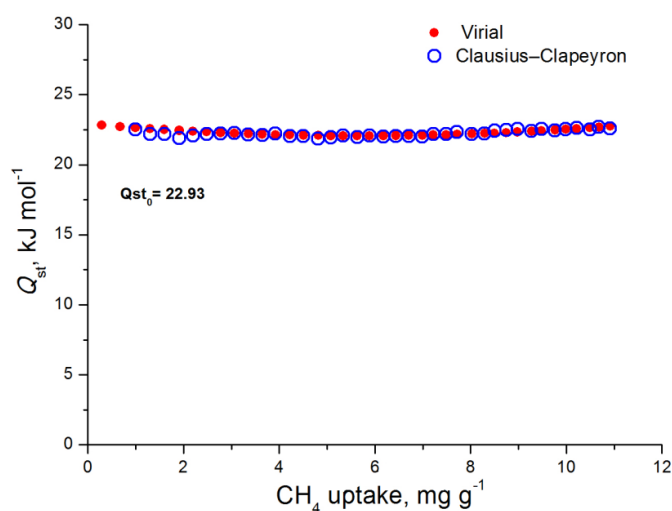
Figure 6.46. CH$_4$ isosteric heat of adsorption in Zr$_6$O$_4$(OH)$_4$(NDC)$_2$(NDC-2NO$_2$)$_{2.8}$(CH$_3$COO)$_{2.4}$ as a function of surface coverage.
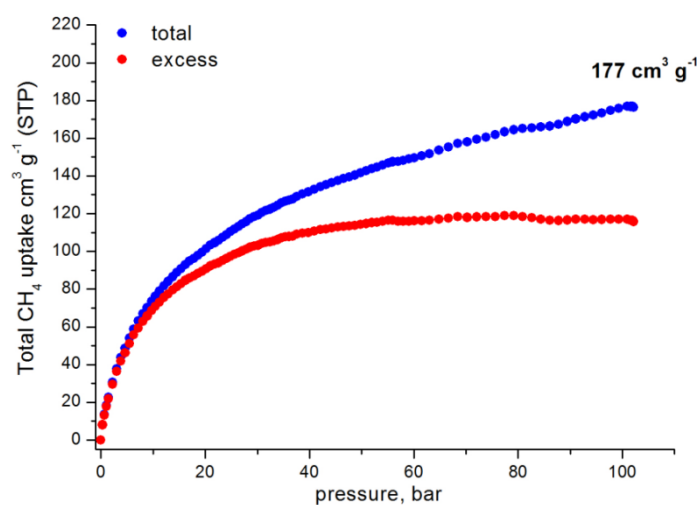
Figure 6.47. Total and excess gravimetric CH$_4$ adsorption isotherms of Zr$_6$O$_4$(OH)$_4$(NDC)$_2$(NDC-2NO$_2$)$_{2.8}$(CH$_3$COO)$_{2.4}$ at 298 K.
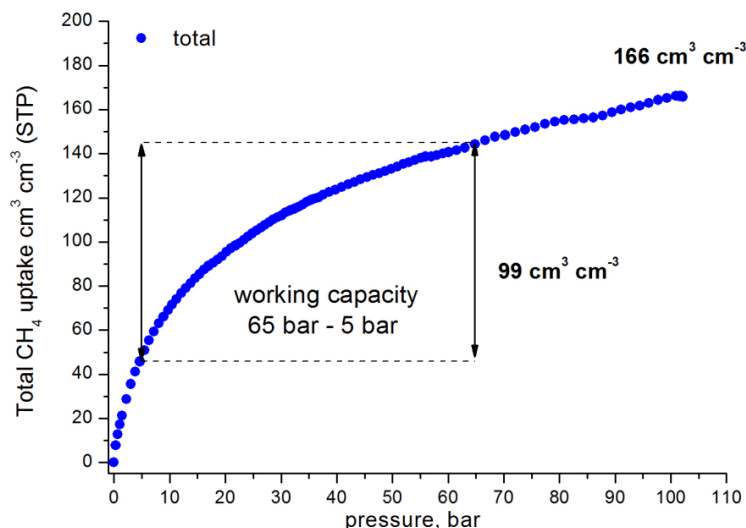
Figure 6.48. Total volumetric CH_4 adsorption isotherm of $Zr_6O_4(OH)_4(NDC)_2(NDC-2NO_2)_{2.8}(CH_3COO)_{2.4}$ at 298 K, the black arrows indicate the working capacity (65 bar – 5 bar).
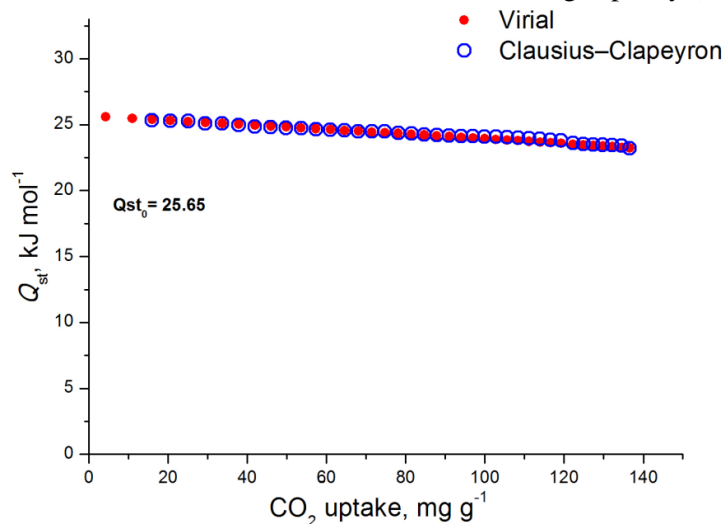
Figure 6.49. CO_2 isosteric heat of adsorption in $Zr_6O_4(OH)_4(NDC)_2(NDC-2NO_2)_{2.8}(CH_3COO)_{2.4}$ as a function of surface coverage.
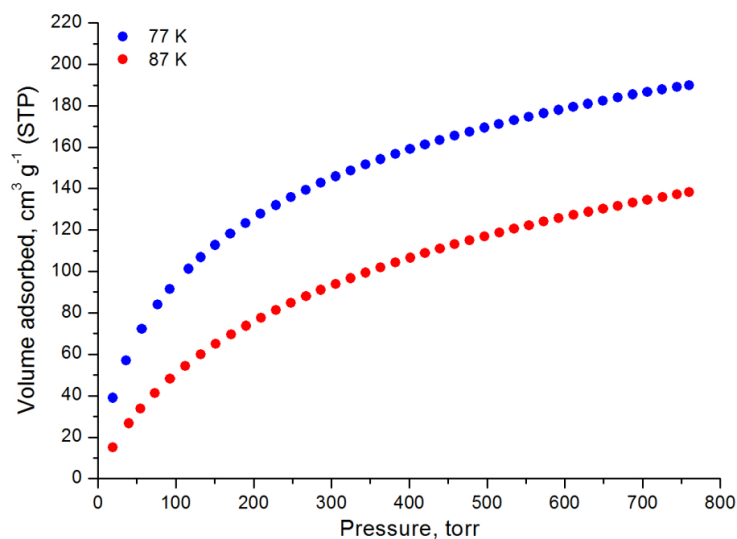
Figure 6.50. Hydrogen adsorption isotherms of $Zr_6O_4(OH)_4(NDC)_2(NDC-2NO_2)_{2.8}(CH_3COO)_{2.4}$ at 77 K and 87 K.

174
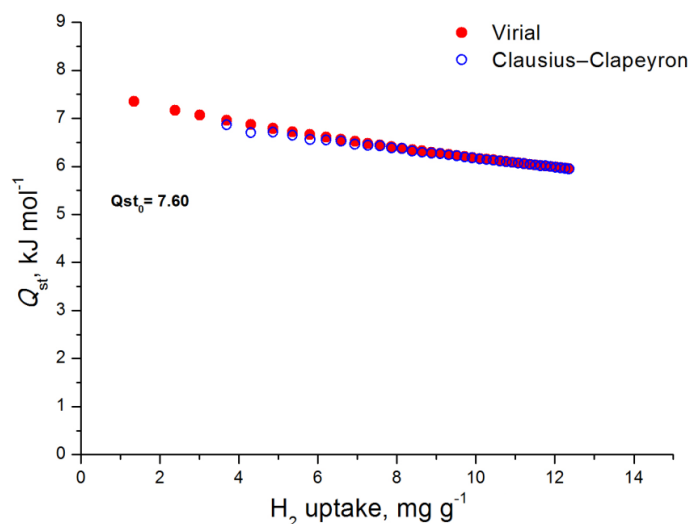
Figure 6.51. H$_2$ isosteric heat of adsorption in Zr$_6$O$_4$(OH)$_4$(NDC)$_2$(NDC-2NO$_2$)$_{2.8}$(CH$_3$COO)$_{2.4}$ as a function of surface coverage.
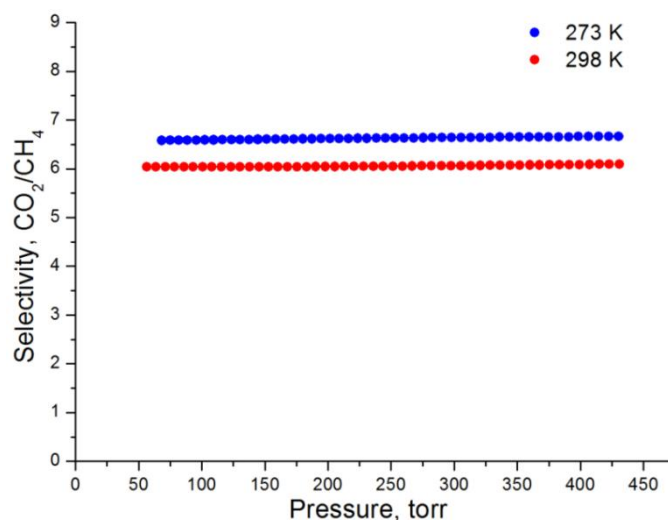
Figure 6.52. Selectivities of CO$_2$ over CH$_4$ at 298 K and 273 K for Zr$_6$O$_4$(OH)$_4$(NDC)$_2$(NDC-2NO$_2$)$_{2.8}$(CH$_3$COO)$_{2.4}$ as predicted by IAST for a 5/95 CO$_2$/CH$_4$ molar mixture.

6.4 Zr-MOF synthesis based on organic linker 4
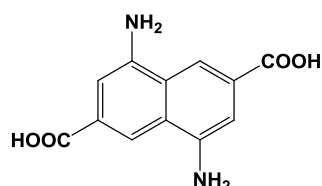
6.4.1 Synthesis of compound Zr$_6$O$_4$(OH)$_4$(NDC-2NH$_2$)$_6$

An amount of 0.020 g (0.08 mmol) of H$_2$NDC-2NH$_2$ and 0.057 g (0.24 mmol) of ZrCl$_4$ were dissolved in a 20 mL glass scintillation vial containing 10 mL DMF and 2 mL of glacial acetic acid. The vial was placed in an oven, heated up to 120 ^{0}C with 0.06 ^{0}C/min and then held at 120 ^{0}C for 24 h. Yield: 41 % based on H$_2$NDC-2NH$_2$.
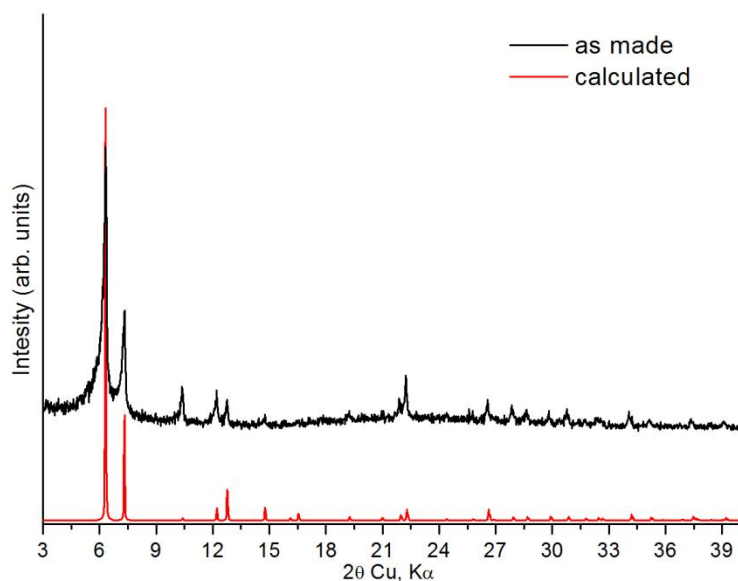
Figure 6.53. Comparison of experimental and calculated pxrd patterns for $Zr_6O_4(OH)_4(NDC-2NH_2)_6$.

6.5 Zr-MOF synthesis based on organic linker 5
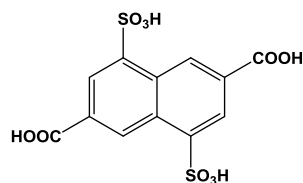
6.5.1 Synthesis of compound $Zr_6O_6(OH)_2(NDC-2SO_3H)_{2.5}(CH_3COO)_5$

An amount of 0.030 g (0.08 mmol) of $H_2NDC-2SO_3H$ and 0.059 g (0.24 mmol) of $ZrCl_4$ were dissolved in a 20 mL glass scintillation vial containing 13 mL DMF and 2 mL of glacial acetic acid. The vial was placed in an oven, heated up to 120 ^{0}C with 0.06 ^{0}C/min and then held at 120 ^{0}C for 24 h. After that time white powder was deposited. Yield: 40 % based on $H_2NDC-2SO_3H$.
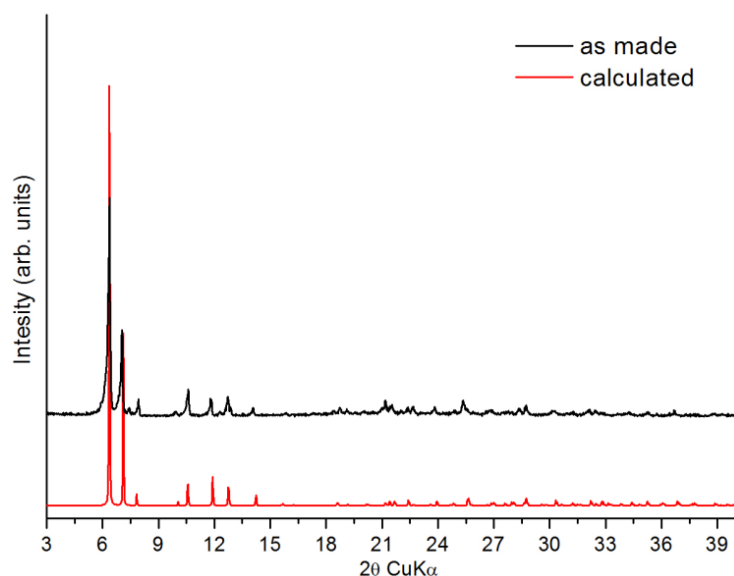
Figure 6.55. Comparison of experimental and calculated pxrd patterns for $Zr_6O_6(OH)_2(NDC-2SO_3H)_4(CH_3COO)_2$ and DUT-53 (Hf).

6.6 Zr-MOF syntheses based on organic linker 6
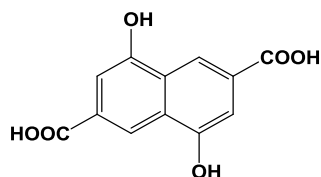
6.6.1 Synthesis of compound $Zr_6O_4(OH)_4(NDC-2OH)_3(CH_3COO)_6$

An amount of 0.025 g (0.10 mmol) of $H_2NDC-2OH$ and 0.024 g (0.10 mmol) of $ZrCl_4$ were dissolved in a 20 mL glass scintillation vial containing 10 mL DMF and 0.5 mL of glacial acetic acid. The vial was placed in an oven, heated up to 120 ^{0}C with 0.06 ^{0}C/min and then held at 120 ^{0}C for 24 h. Yield: 41 % based on $H_2NDC-2OH$.

After the efficient characterization of the material the evaluation of its gas sorption properties took place. Successful activation was possible as follows: as-made sample was washed with DMF four times per day for 2 days and then the sample was soaked in acetone over a period of 4 days, replenishing the acetone 4 times per day. The sample was transferred to a pre weighted sample cell and acetone was removed under reduced pressure. Finally, the sample was activated under dynamic vacuum at 100 °C for 12 hours and until the outgas rate was less than 2 mTorr/min.

177
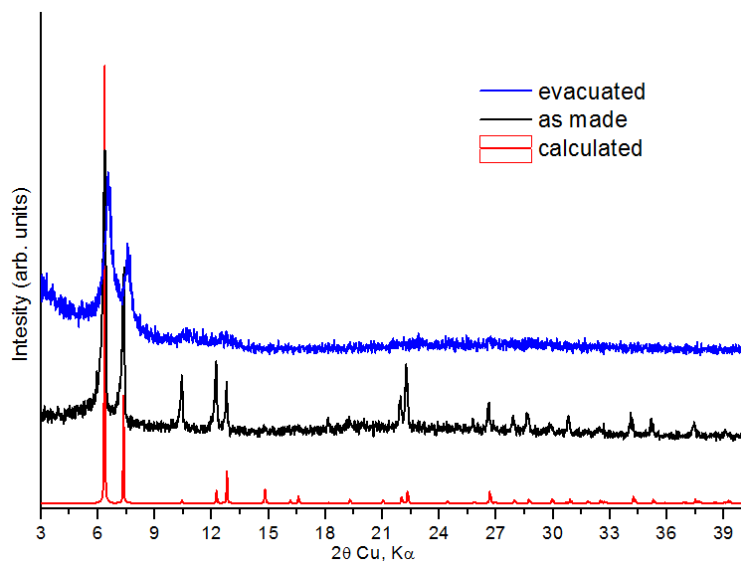
Figure 6.56. Comparison of experimental and calculated pxrd patterns for $Zr_6O_4(OH)_4$(NDC-2OH)$_3$(CH$_3$COO)$_6$.
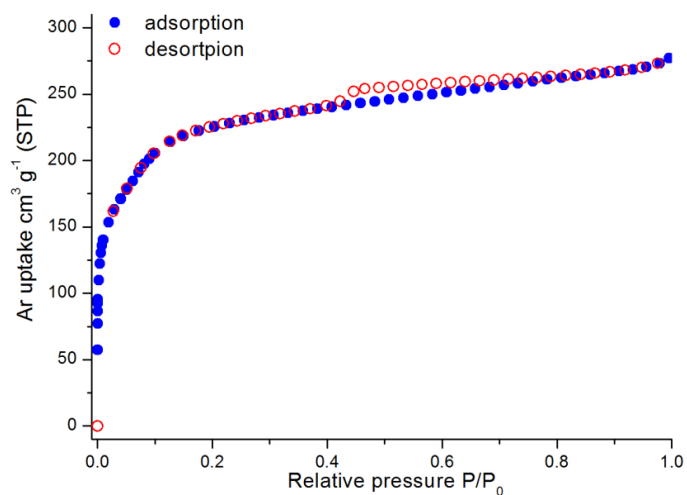
Figure 6.57. Argon sorption isotherm of $Zr_6O_4(OH)_4$(NDC-2OH)$_3$(CH$_3$COO)$_6$ at 87 K.
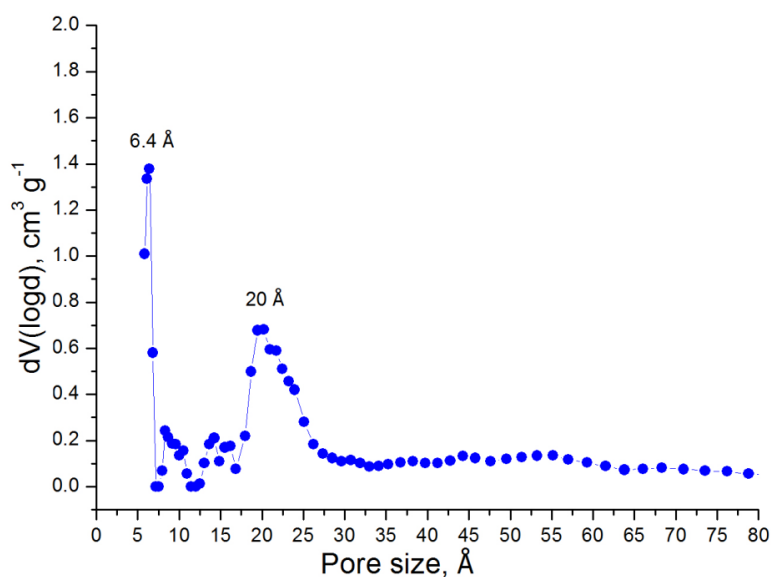
Figure 6.58. Pore size distribution in $Zr_6O_4(OH)_4$(NDC-2OH)$_3$(CH$_3$COO)$_6$ calculated from NLDFT analysis.
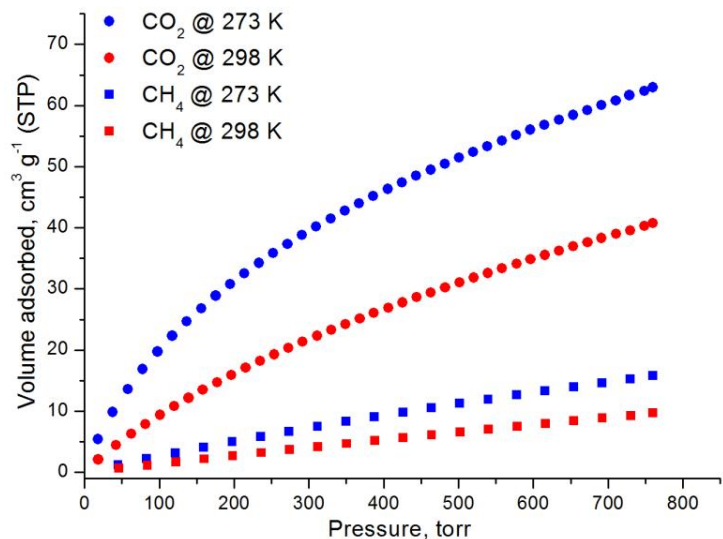
Figure 6.59. CO_2 and CH_4 adsorption isotherms of $Zr_6O_4(OH)_4(NDC-2OH)_3(CH_3COO)_6$ at 273 K and 298 K.
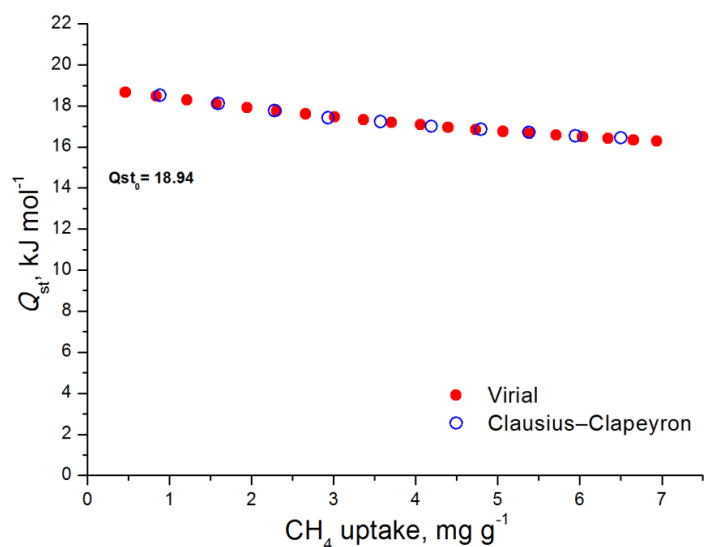
Figure 6.60. CH_4 isosteric heat of adsorption as a function of surface coverage.
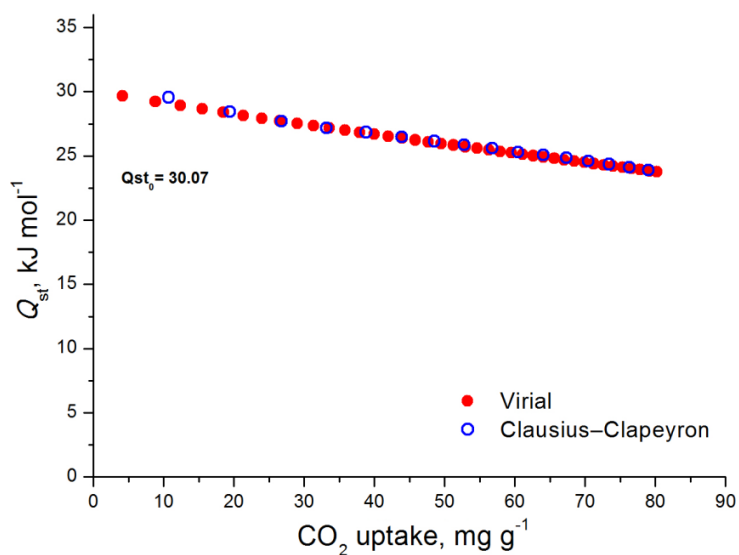
Figure 6.61. CO_2 isosteric heat of adsorption as a function of surface coverage.
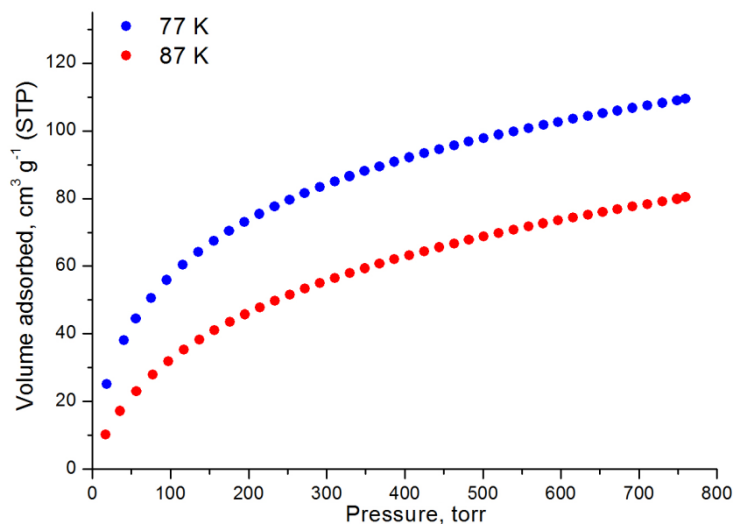
Figure 6.62. Hydrogen adsorption isotherms of $Zr_6O_4(OH)_4(NDC\text{-}2OH)_3(CH_3COO)_6$ at 77 K and 87 K.
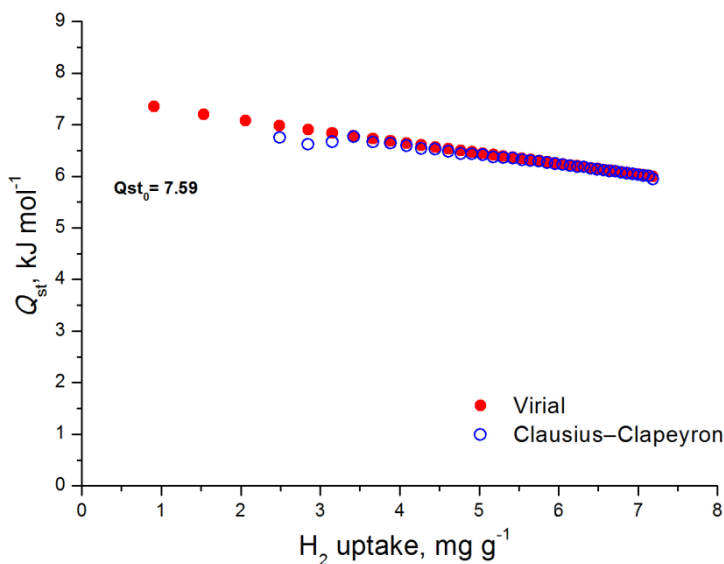
Figure 6.63. H_2 isosteric heat of adsorption as a function of surface coverage.
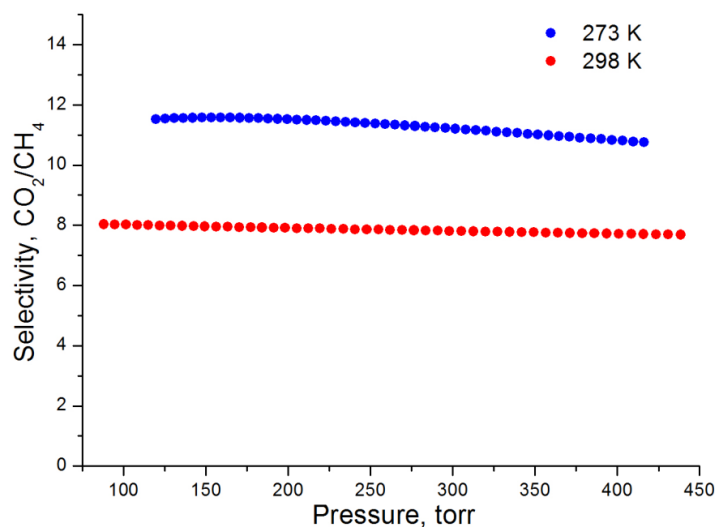
Figure 6.64. Selectivities of CO_2 over CH_4 at 273 K and 298 K for $Zr_6O_4(OH)_4(NDC\text{-}2OH)_3(CH_3COO)_6$ as predicted by IAST for a 5/95 CO_2/CH_4 molar mixture.

6.7 Zr-MOF synthesis based on organic linker 13
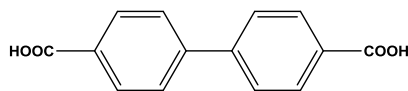
6.7.1 Synthesis of compound $Zr_6O_4(OH)_4(BPDC)_{4.7}(CH_3COO)_{2.6}$

An amount of 0.025 g (0.10 mmol) of H_2BPDC and 0.024 g (0.10 mmol) of $ZrCl_4$ were dissolved in a 20 mL glass scintillation vial containing 10 mL DMF and 1 mL of glacial acetic acid. The vial was placed in an oven, heated up to 120 ^0C with 0.06 ^0C/ min and then held at 120 ^0C for 24 h. After that time a white powder was deposited. Yield: 10 % based on H_2BPDC.

After the efficient characterization of the material the evaluation of its gas sorption properties took place. Successful activation was possible as follows: as-made sample was washed with DMF four times per day for 2 days and then the sample was soaked in acetone over a period of 4 days, replenishing the acetone 4 times per day. The sample was transferred to a pre weighted sample cell and acetone was removed under reduced pressure. Finally, the sample was activated under dynamic vacuum at 120 °C for 12 hours and until the outgas rate was less than 2 mTorr/min.
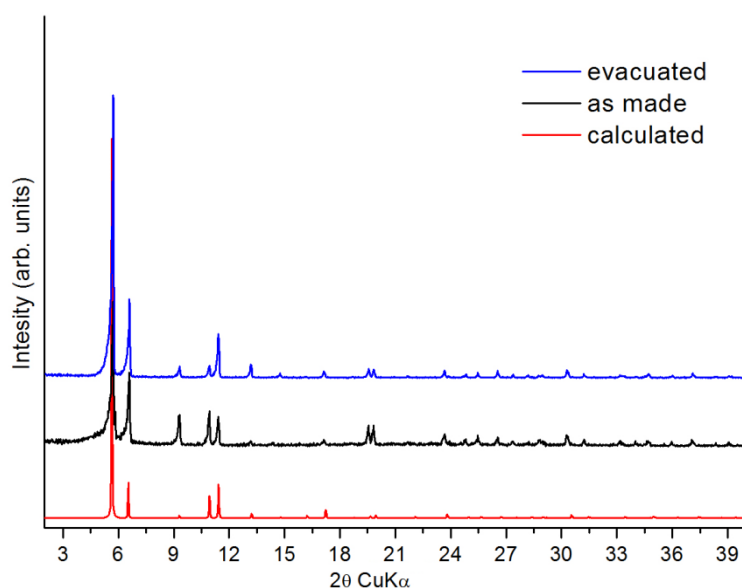
Figure 6.68. Comparison of experimental, evacuated and calculated pxrd patterns for $Zr_6O_4(OH)_4(BPDC)_{4.7}(CH_3COO)_{2.6}$.
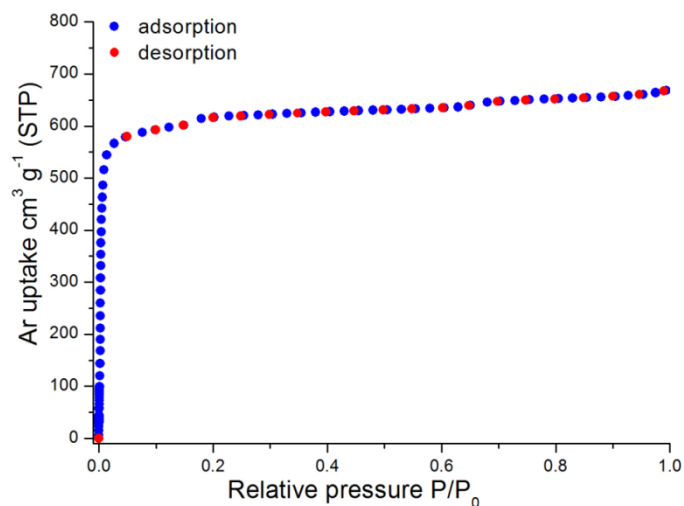
Figure 6.69. Argon sorption isotherm of $Zr_6O_4(OH)_4(BPDC)_{4.7}(CH_3COO)_{2.6}$ at 87 K.
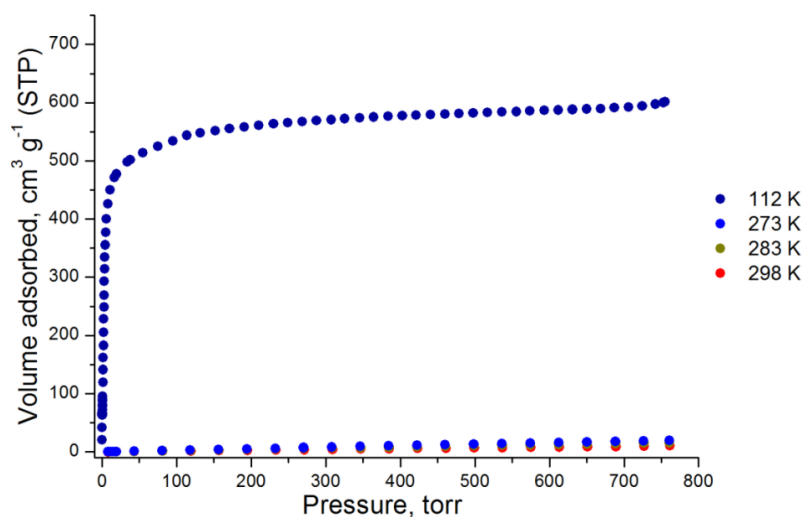
Figure 6.70. CH$_4$ adsorption isotherms of $Zr_6O_4(OH)_4(BPDC)_{4.7}(CH_3COO)_{2.6}$ at 112 K, 273 K, 283 K and 298 K.
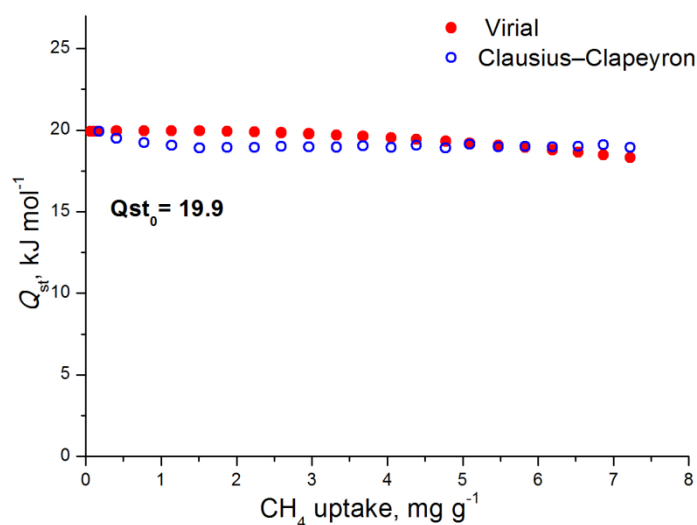
Figure 6.71. CH$_4$ isosteric heat of adsorption in $Zr_6O_4(OH)_4(BPDC)_{4.7}(CH_3COO)_{2.6}$ as a function of surface coverage.
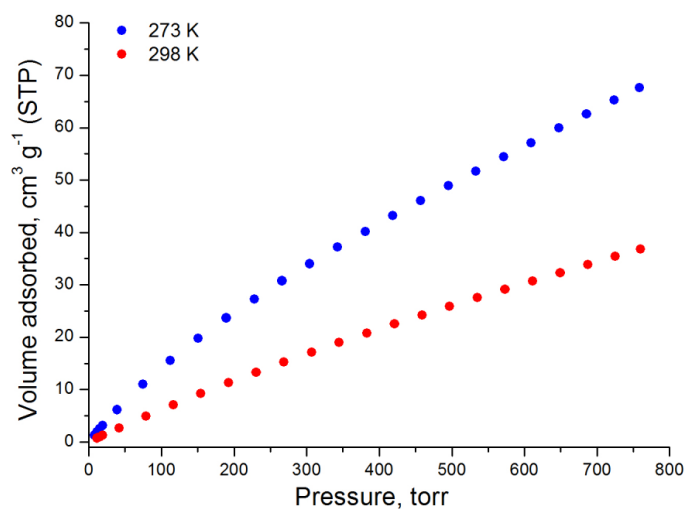
Figure 6.72. CO_2 adsorption isotherms of $Zr_6O_4(OH)_4(BPDC)_{4.7}(CH_3COO)_{2.6}$ at 273 K and 298 K.
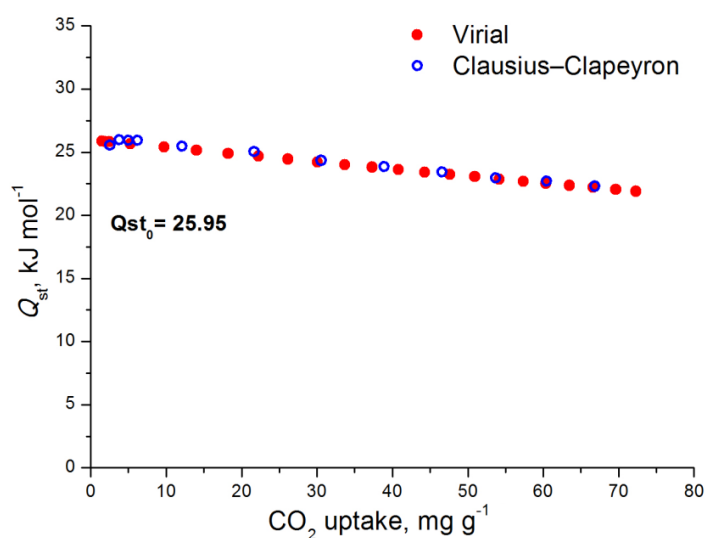
Figure 6.73. CO_2 isoteric heat of adsorption in $Zr_6O_4(OH)_4(BPDC)_{4.7}(CH_3COO)_{2.6}$ as a function of surface coverage.
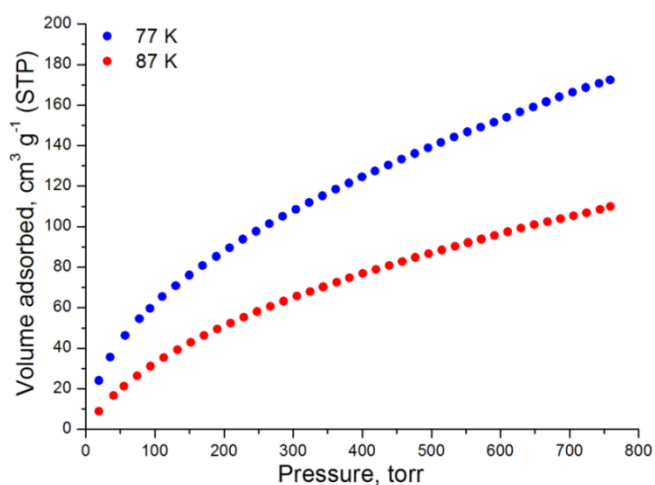
Figure 6.74. Hydrogen adsorption isotherms of $Zr_6O_4(OH)_4(BPDC)_{4.7}(CH_3COO)_{2.6}$ at 77 K and 87 K.
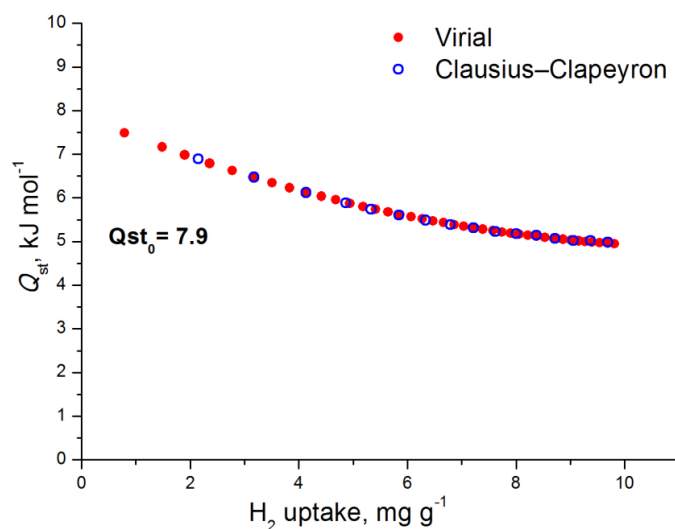
Figure 6.75. H_2 isosteric heat of adsorption in $Zr_6O_4(OH)_4(BPDC)_{4.7}(CH_3COO)_{2.6}$ as a function of surface coverage.
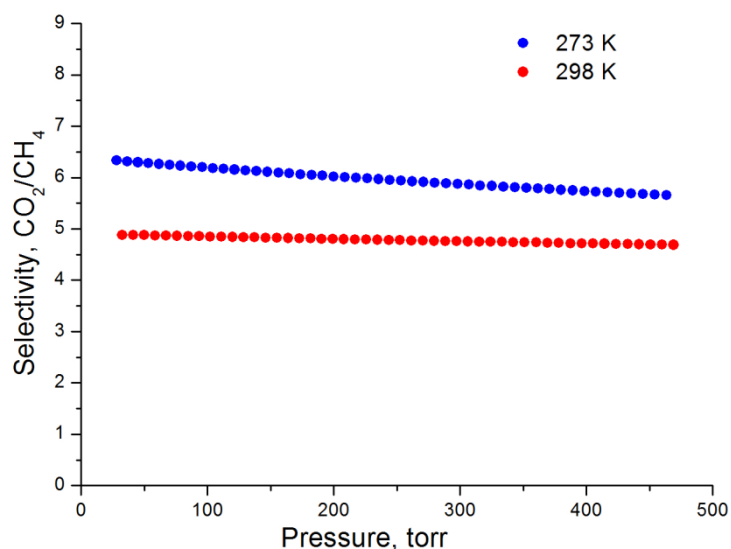
Figure 6.76. Selectivities of CO_2 over CH_4 at 298 K and 273 K for $Zr_6O_4(OH)_4(BPDC)_{4.7}(CH_3COO)_{2.6}$ as predicted by IAST for a 5/95 CO_2/CH_4 molar mixture.

6.8 Zr-MOF synthesis based on organic linker 16
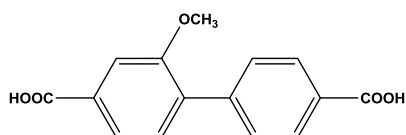
6.8.1 Synthesis of compound $Zr_6O_4(OH)_4(BPDC-OCH_3)_{4.85}(CH_3COO)_{2.3}$

An amount of 0.030 g (0.11 mmol) of $H_2BPDC-OCH_3$ and 0.026 g (0.11 mmol) of $ZrCl_4$ were dissolved in a 20 mL glass scintillation vial containing 10 mL DMF and 1 mL of glacial acetic acid. The vial was placed in an oven, heated up to 120 ^0C with 0.06 ^0C/ min and then held at 120 ^0C for 24 h. After that time a white powder was deposited. Yield: 10 % based on $H_2BPDC-OCH_3$.

After the efficient characterization of the material the evaluation of its gas sorption properties took place. Successful activation was possible as follows: as-made sample was washed with DMF four times per day for 2 days and then the sample was soaked in acetone over a period of 4 days, replenishing the acetone 4 times per day. The sample was transferred to a pre weighted sample cell and acetone was removed under reduced pressure. Finally, the sample was activated under dynamic vacuum at 120 °C for 12 hours and until the outgas rate was less than 2 mTorr/min.
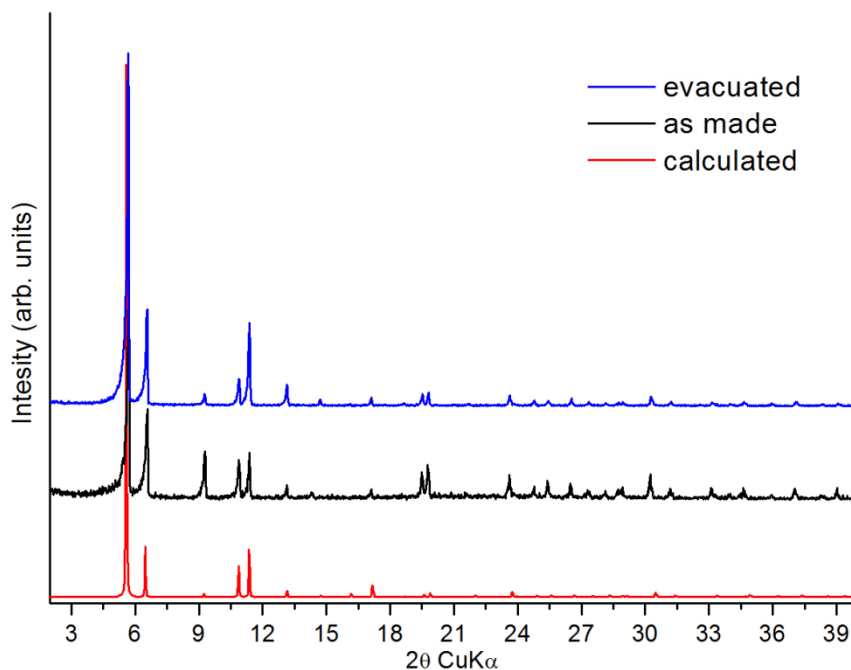
Figure 6.77. Comparison of experimental, calculated and evacuated pxrd patterns for $Zr_6O_4(OH)_4(BPDC-OCH_3)_{4.85}(CH_3COO)_{2.3}$.
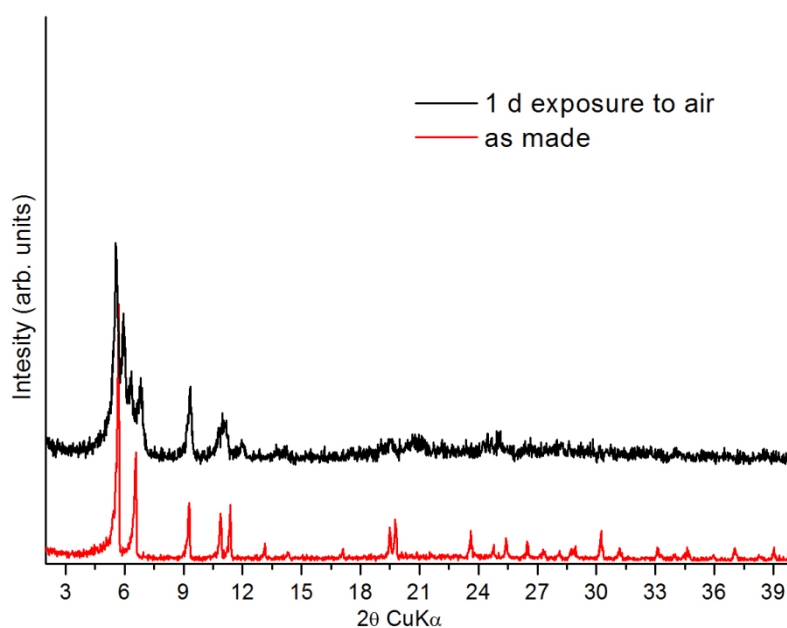
Figure 6.78. Comparison of experimental and after 1 day exposure to air pxrd patterns for $Zr_6O_4(OH)_4(BPDC-OCH_3)_{4.85}(CH_3COO)_{2.3}$.
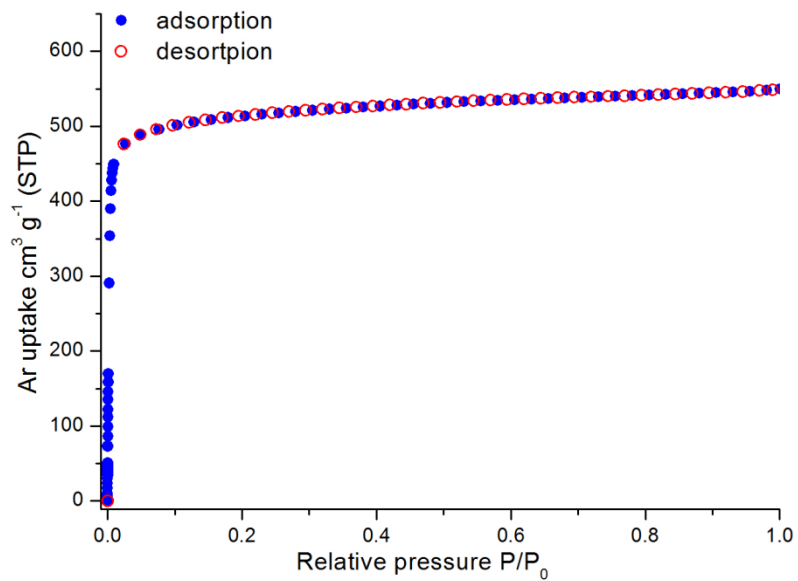
Figure 6.79. Argon sorption isotherm of $Zr_6O_4(OH)_4(BPDC-OCH_3)_{4.85}(CH_3COO)_{2.3}$ at 87 K.
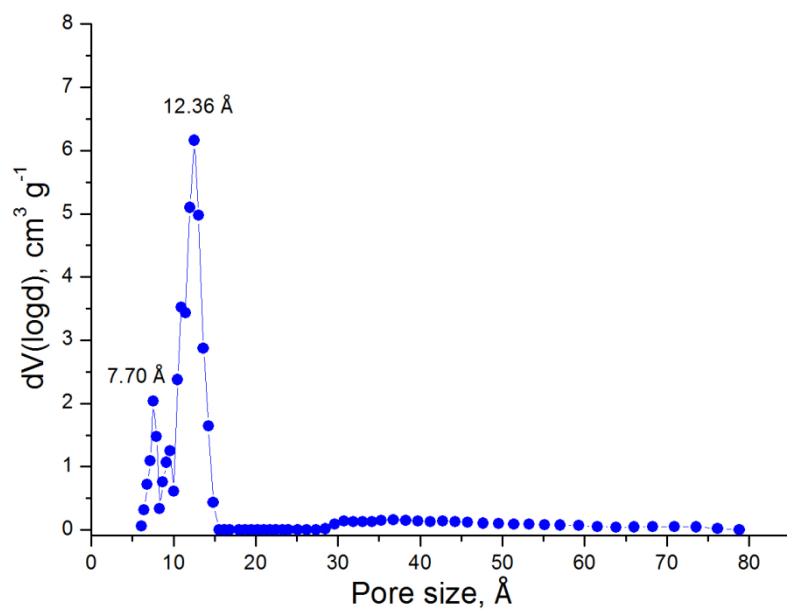
Figure 6.80. Pore size distribution in $Zr_6O_4(OH)_4(BPDC-OCH_3)_{4.85}(CH_3COO)_{2.3}$ calculated from NLDFT analysis.
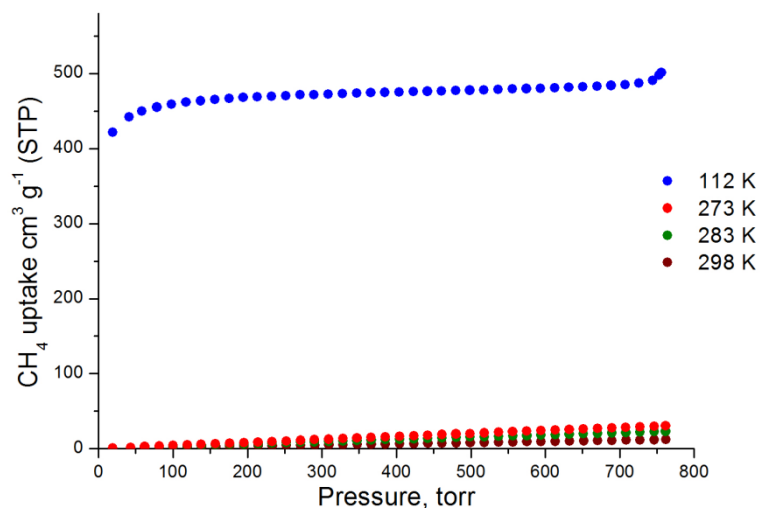
Figure 6.81. CH_4 adsorption isotherms of $Zr_6O_4(OH)_4(BPDC\text{-}OCH_3)_{4.85}(CH_3COO)_{2.3}$ at 112 K, 273 K, 283 K and 298 K.
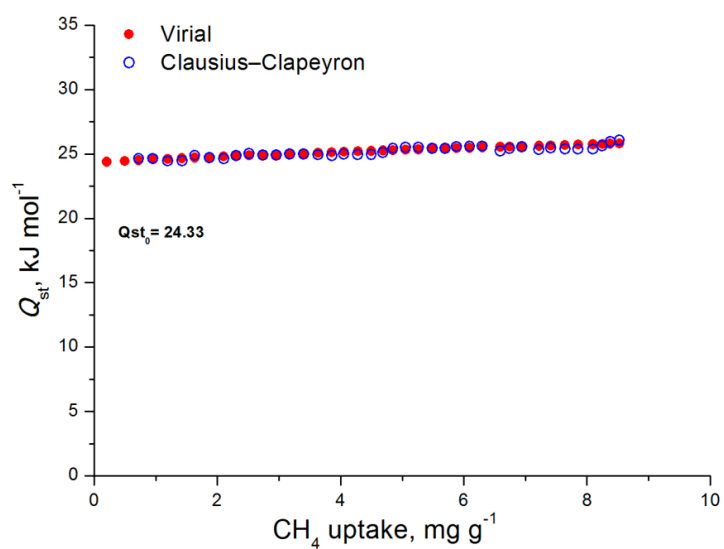
Figure 6.82. CH_4 isosteric heat of adsorption in $Zr_6O_4(OH)_4(BPDC\text{-}OCH_3)_{4.85}(CH_3COO)_{2.3}$ as a function of surface coverage.
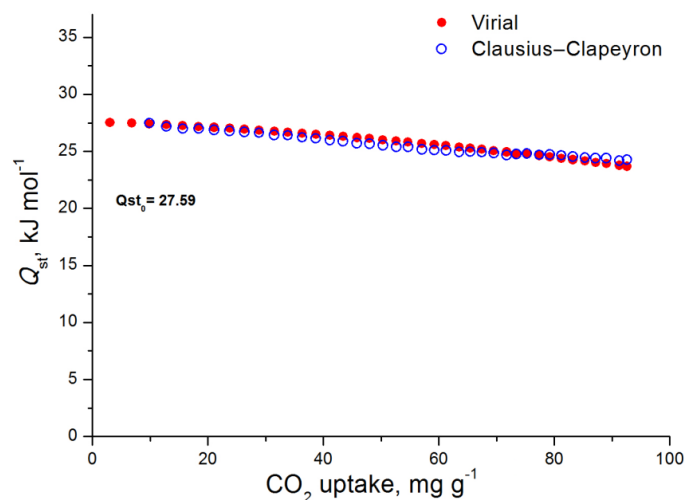
Figure 6.83. CO_2 isosteric heat of adsorption in $Zr_6O_4(OH)_4(BPDC\text{-}OCH_3)_{4.85}(CH_3COO)_{2.3}$ as a function of surface coverage.

187
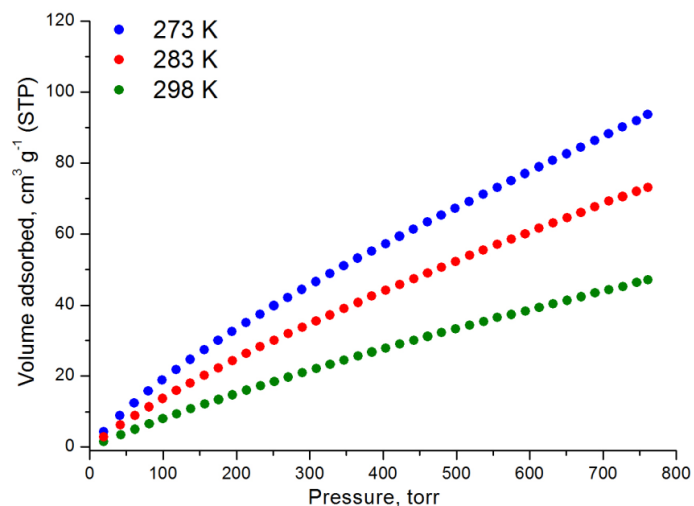
Figure 6.84. CO_2 adsorption isotherms of $Zr_6O_4(OH)_4(BPDC-OCH_3)_{4.85}(CH_3COO)_{2.3}$ at 273 K, 283 K and 298 K.
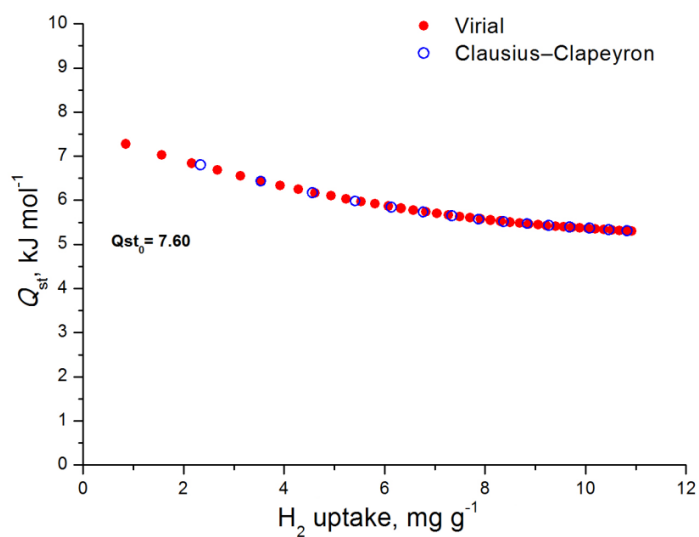
Figure 6.85. H_2 isosteric heat of adsorption in $Zr_6O_4(OH)_4(BPDC-OCH_3)_{4.85}(CH_3COO)_{2.3}$ as a function of surface coverage.
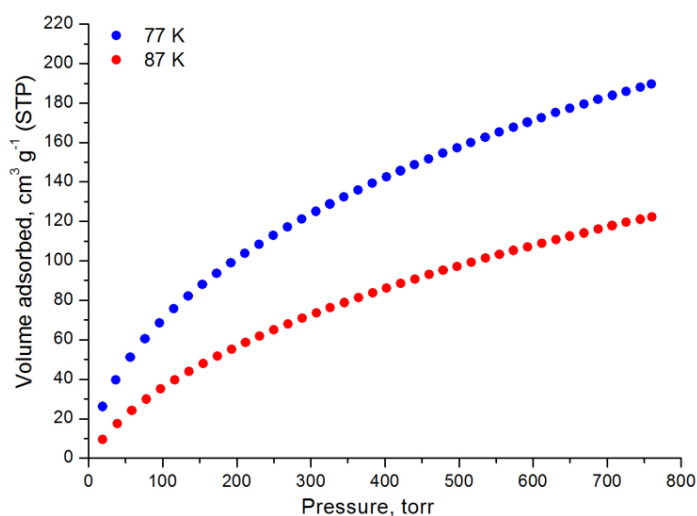
Figure 6.86. Hydrogen adsorption isotherms of $Zr_6O_4(OH)_4(BPDC-OCH_3)_{4.85}(CH_3COO)_{2.3}$ at 77 K and 87 K.
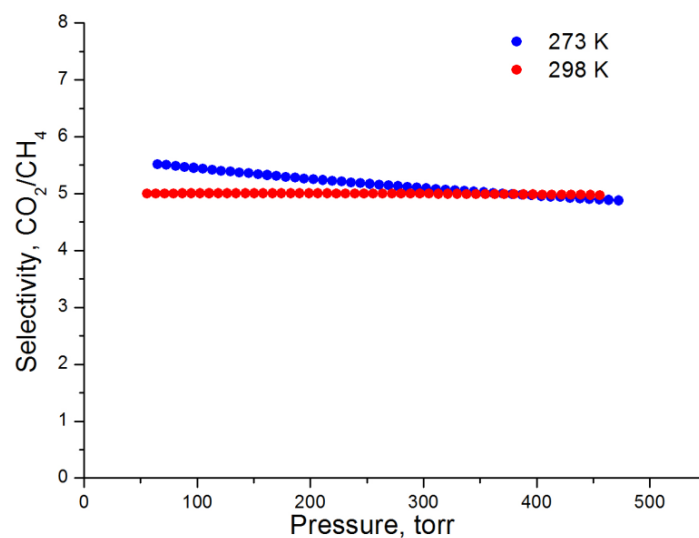
Figure 6.87. Selectivities of CO_2 over CH_4 at 298 K and 273 K for $Zr_6O_4(OH)_4(BPDC-OCH_3)_{4.85}(CH_3COO)_{2.3}$ as predicted by IAST for a 5/95 CO_2/CH_4 molar mixture.

6.9 Zr-MOF synthesis based on organic linker 17
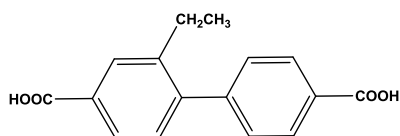
6.9.1 Synthesis of compound $Zr_6O_4(OH)_4(BPDC-OEt)_{4.3}(CH_3COO)_{3.4}$

An amount of 0.030 g (0.11 mmol) of H_2BPDC-OEt and 0.025 g (0.11 mmol) of $ZrCl_4$ were dissolved in a 20 mL glass scintillation vial containing 10 mL DMF and 1 mL of glacial acetic acid. The vial was placed in an oven, heated up to 120 ^{0}C with 0.06 ^{0}C/ min and then held at 120 ^{0}C for 24 h. After that time a white powder was deposited. Yield: 10 % based on H_2BPDC-OEt.
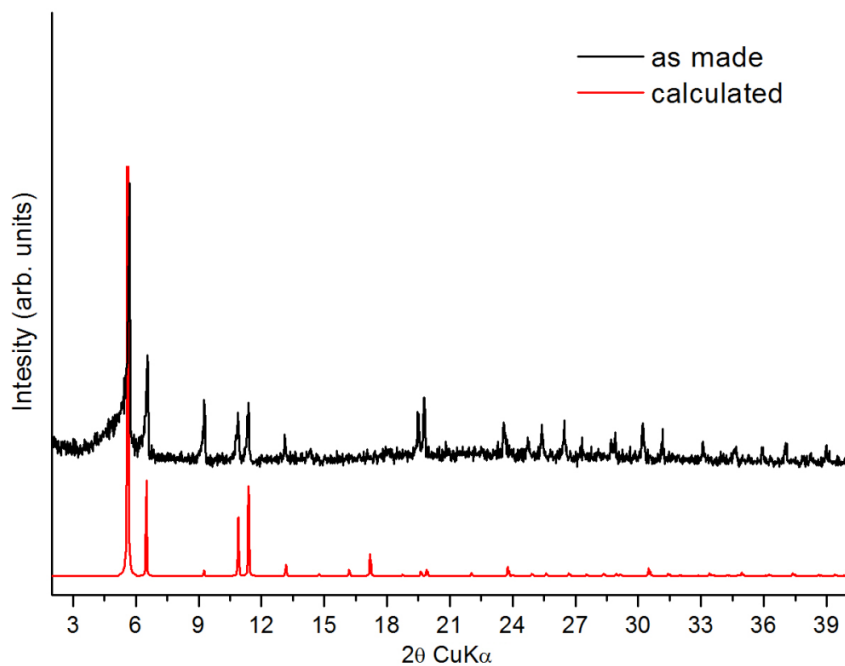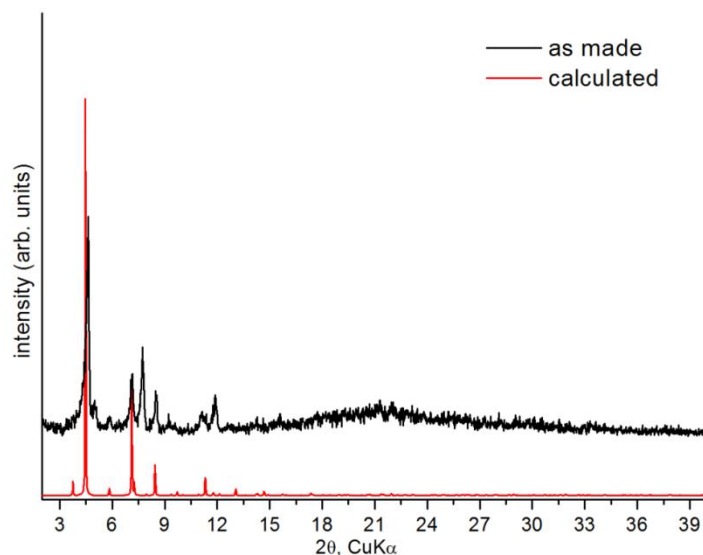
Figure 6.88. Comparison of experimental and calculated pxrd patterns for $Zr_6O_4(OH)_4(BPDC-OEt)_{4.3}(CH_3COO)_{3.4}$.
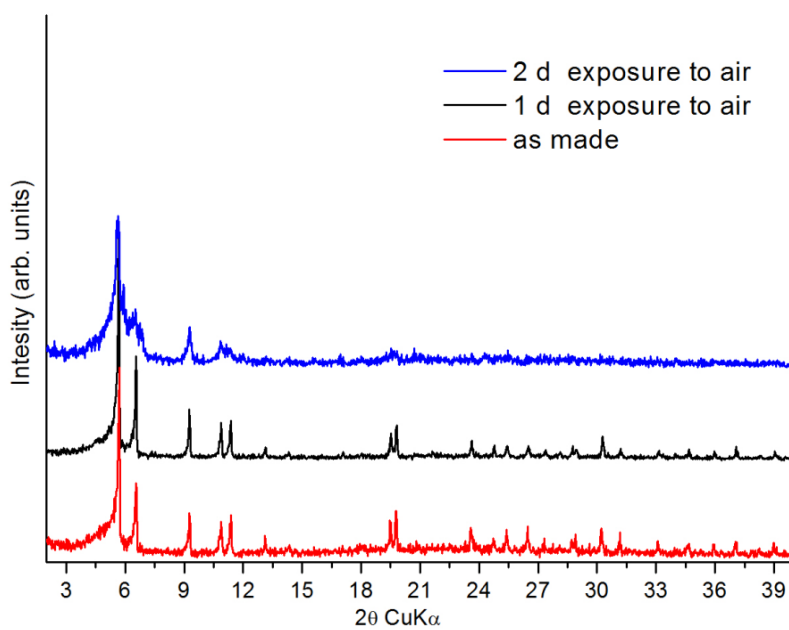
Figure 6.89. Comparison of experimental and after 1 and 2 days exposure to air pxrd patterns for $Zr_6O_4(OH)_4(BPDC-OEt)_{4.3}(CH_3COO)_{3.4}$.

6.10 Zr-MOF synthesis based on organic linker 18
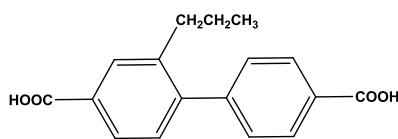
6.10.1 Synthesis of compound $Zr_6O_4(OH)_4(BPDC\text{-}OPr)_6$

An amount of 0.030 g (0.10 mmol) of $H_2BPDC\text{-}OPr$ and 0.024 g (0.10 mmol) of $ZrCl_4$ were dissolved in a 20 mL glass scintillation vial containing 10 mL DMF and 1 mL of glacial acetic acid. The vial was placed in an oven, heated up to 120 ^{0}C with 0.06 ^{0}C/ min and then held at 120 ^{0}C for 24 h. After that time a white powder was deposited. Yield: 11 % based on $H_2BPDC\text{-}OPr$.

After the efficient characterization of the material the evaluation of its gas sorption properties took place. Successful activation was possible as follows: as-made sample was washed with DMF four times per day for 2 days and then the sample was soaked in acetone over a period of 4 days, replenishing the acetone 4 times per day. The sample was transferred to a pre weighted sample cell and acetone was removed under reduced pressure. Finally, the sample was activated under dynamic vacuum at 120 °C for 12 hours and until the outgas rate was less than 2 mTorr/min.
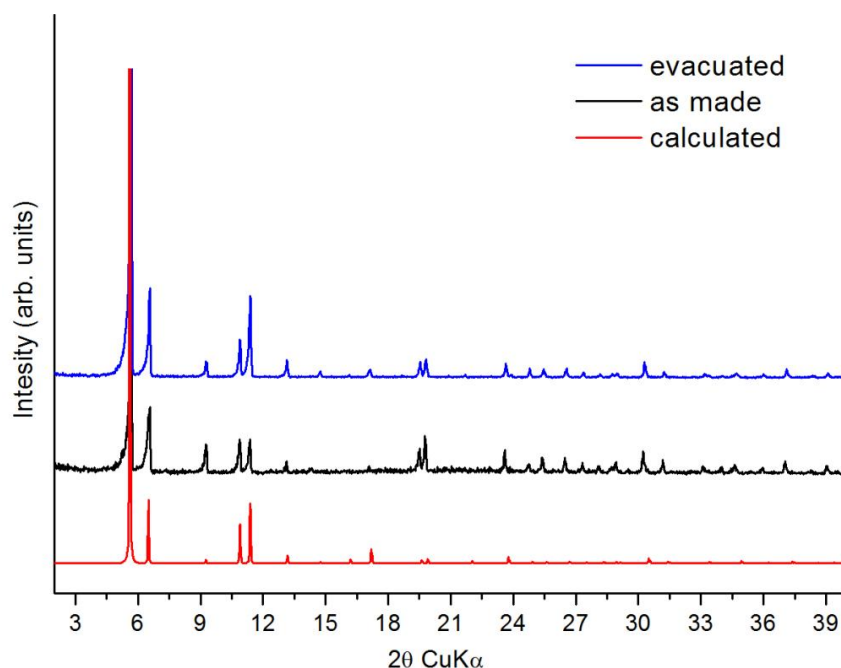
Figure 6.90. Comparison of experimental, calculated and evacuated pxrd patterns for $Zr_6O_4(OH)_4(BPDC\text{-}OPr)_6$.
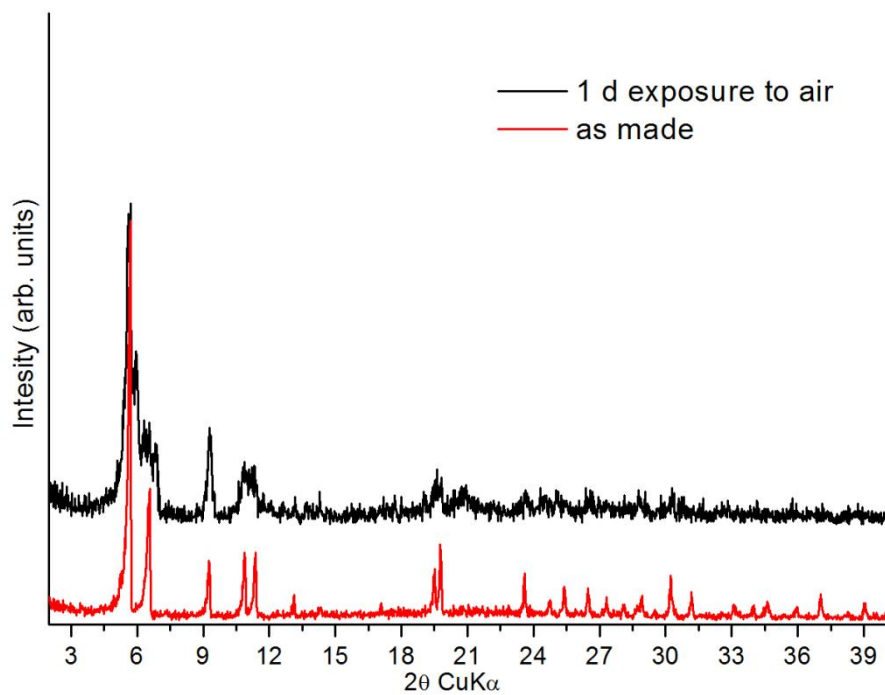
Figure 6.91. Comparison of experimental and after 1 day exposure to air pxrd patterns for $Zr_6O_4(OH)_4(BPDC-OPr)_6$.
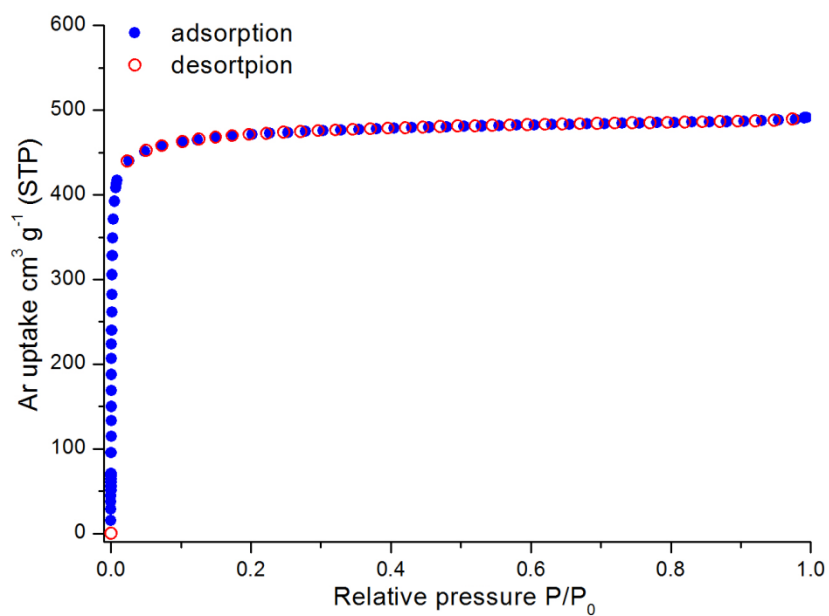
Figure 6.92. Argon sorption isotherm of $Zr_6O_4(OH)_4(BPDC-OPr)_6$ at 87 K.
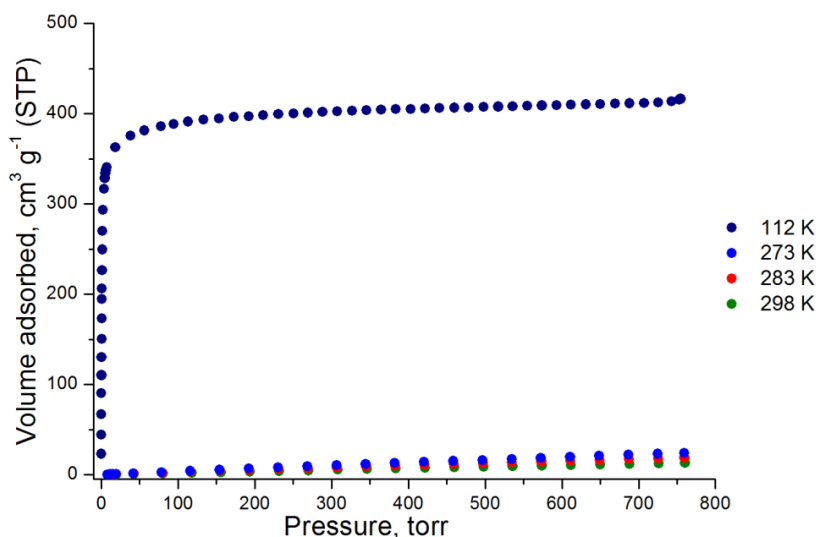
Figure 6.93. CH_4 adsorption isotherms of $Zr_6O_4(OH)_4(BPDC\text{-}OPr)_6$ at 112 K, 273 K, 283 K and 298 K.
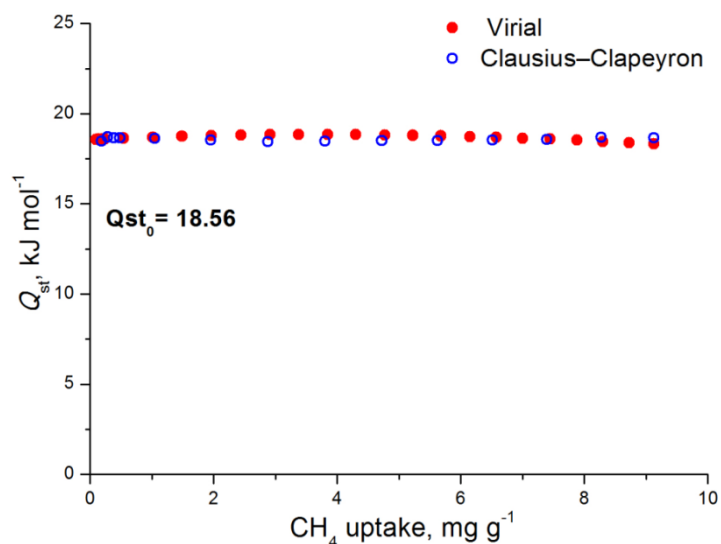
Figure 6.94. CH_4 isosteric heat of adsorption in $Zr_6O_4(OH)_4(BPDC\text{-}OPr)_6$ as a function of surface coverage.
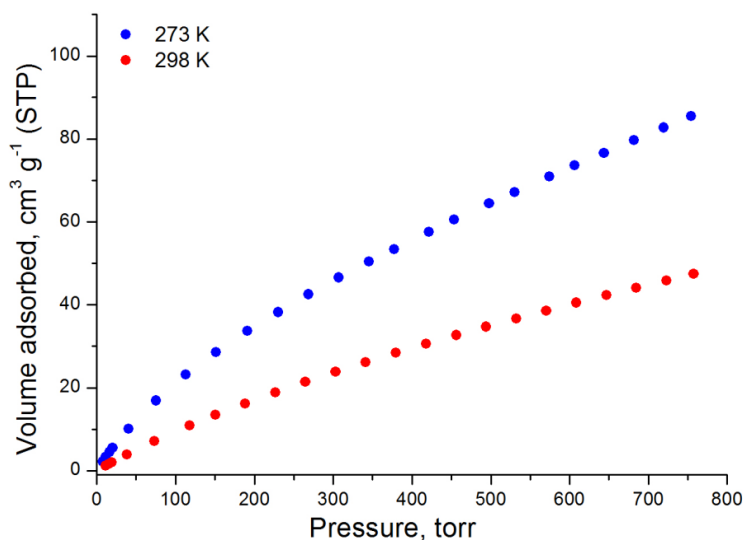
Figure 6.95. CO_2 adsorption isotherms of $Zr_6O_4(OH)_4(BPDC\text{-}OPr)_6$ at 273 K and 298 K.
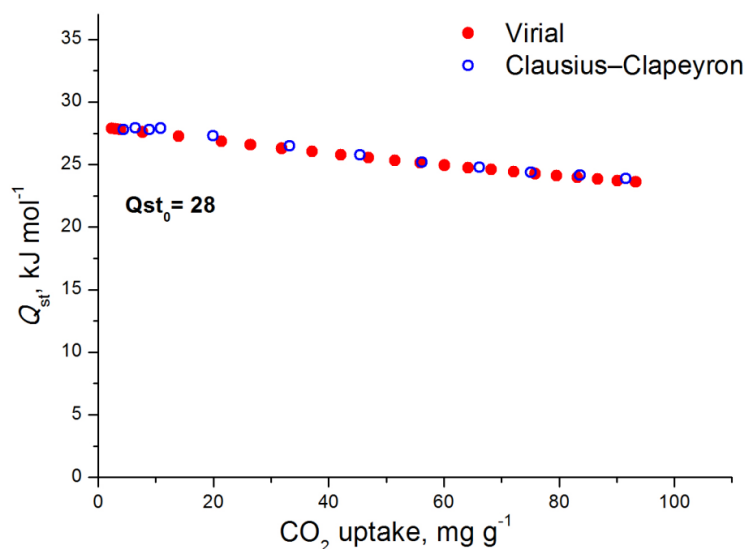
Figure 6.96. CO_2 isosteric heat of adsorption in $Zr_6O_4(OH)_4(BPDC-OPr)_6$ as a function of surface coverage.
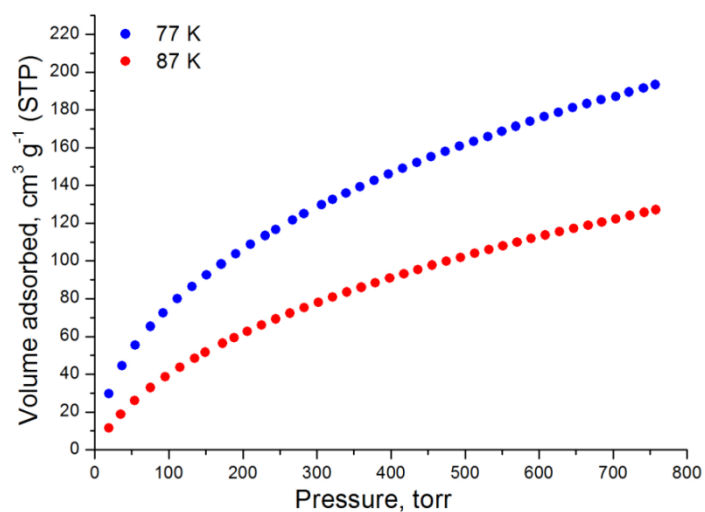
Figure 6.97. Hydrogen adsorption isotherms of $Zr_6O_4(OH)_4(BPDC-OPr)_6$ at 77 K and 87 K.
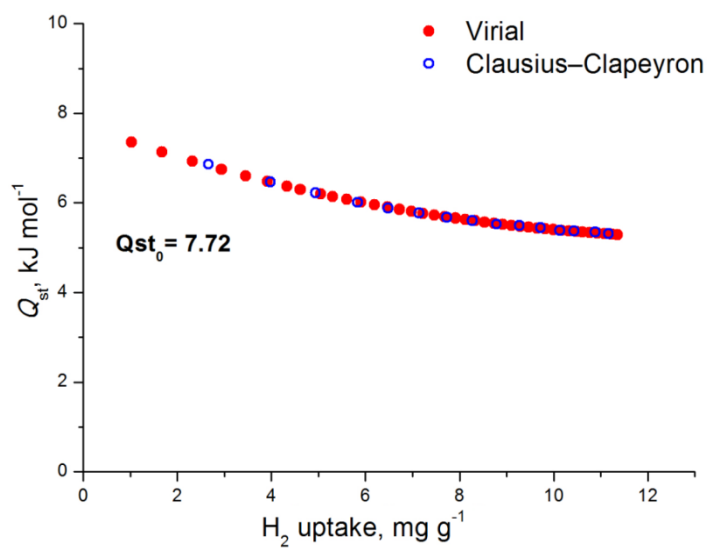
Figure 6.98. H_2 isosteric heat of adsorption in $Zr_6O_4(OH)_4(BPDC-OPr)_6$ as a function of surface coverage.
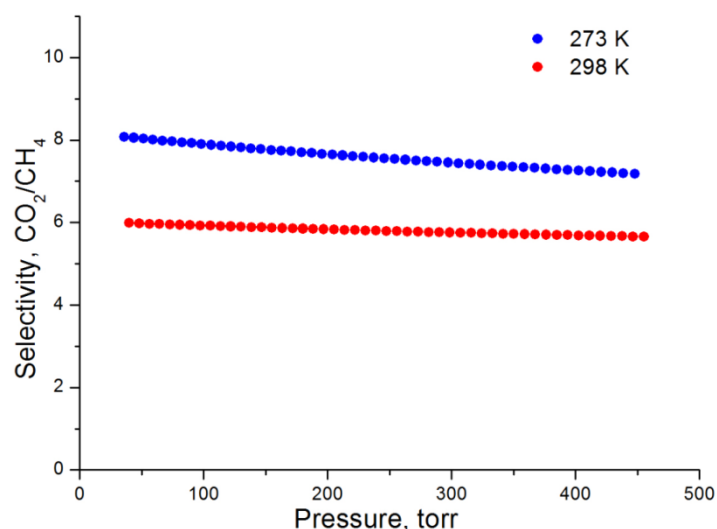
<u>Figure 6.99.</u> Selectivities of CO_2 over CH_4 at 298 K and 273 K for $Zr_6O_4(OH)_4(BPDC\text{-}OPr)_6$ as predicted by IAST for a 5/95 CO_2/CH_4 molar mixture.

6.11 Zr-MOF synthesis based on organic linker 19
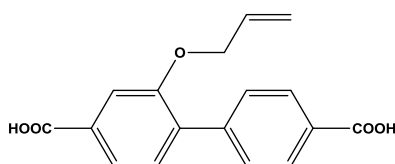
6.11.1 Synthesis of compound $Zr_6O_4(OH)_4(BPDC\text{-}OAllyl)_5(CH_3COO)_2$

An amount of 0.030 g (0.10 mmol) of $H_2BPDC\text{-}OAllyl$ and 0.024 g (0.10 mmol) of $ZrCl_4$ were dissolved in a 20 mL glass scintillation vial containing 10 mL DMF and 1 mL of glacial acetic acid. The vial was placed in an oven, heated up to 120 ^{0}C with 0.06 ^{0}C/ min and then held at 120 ^{0}C for 24 h. After that time a white powder was deposited. Yield: 10 % based on $H_2BPDC\text{-}OAllyl$.

After the efficient characterization of the material the evaluation of its gas sorption properties took place. Successful activation was possible as follows: as-made sample was washed with DMF four times per day for 2 days and then the sample was soaked in acetone over a period of 4 days, replenishing the acetone 4 times per day. The sample was transferred to a pre weighted sample cell and acetone was removed under reduced pressure. Finally, the sample was activated under dynamic vacuum at 120 °C for 12 hours and until the outgas rate was less than 2 mTorr/min.
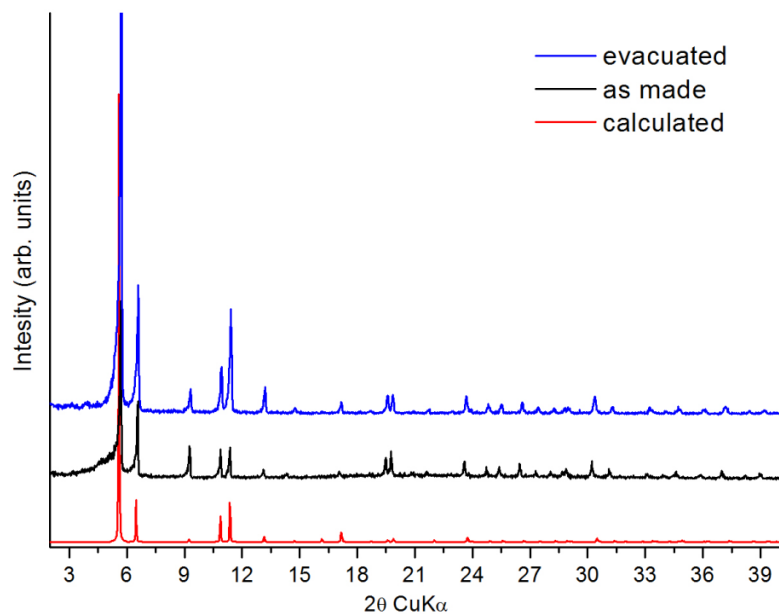
Figure 6.100. Comparison of experimental, calculated and evacuated pxrd patterns for $Zr_6O_4(OH)_4(BPDC-OAllyl)_5(CH_3COO)_2$.
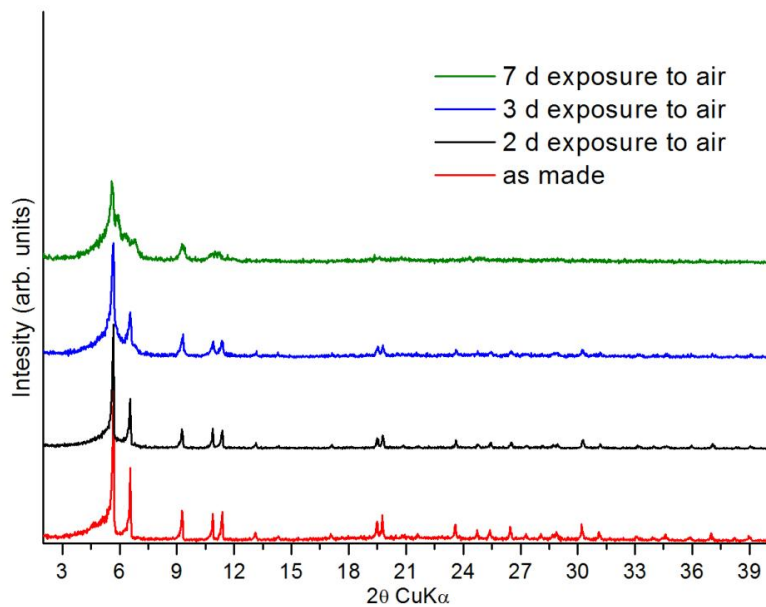
Figure 6.101. Comparison of experimental and after 2, 3 and 7 days exposure to air pxrd patterns for $Zr_6O_4(OH)_4(BPDC-OAllyl)_5(CH_3COO)_2$.
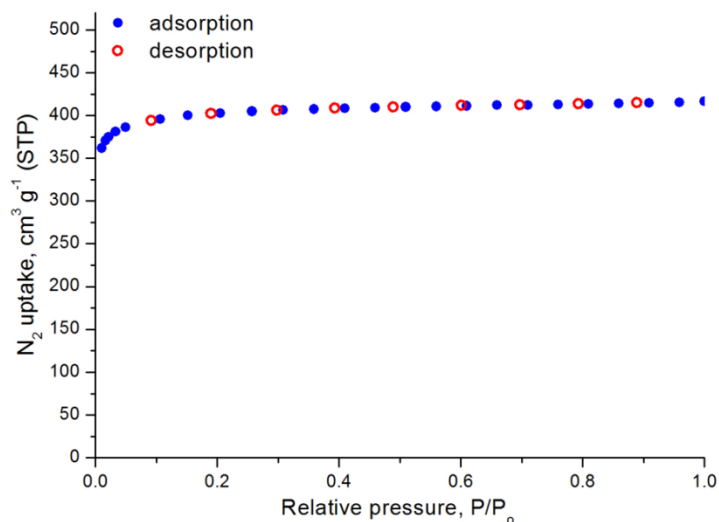
Figure 6.102. Nitrogen sorption isotherm of $Zr_6O_4(OH)_4(BPDC\text{-}OAllyl)_5(CH_3COO)_2$ at 77 K.
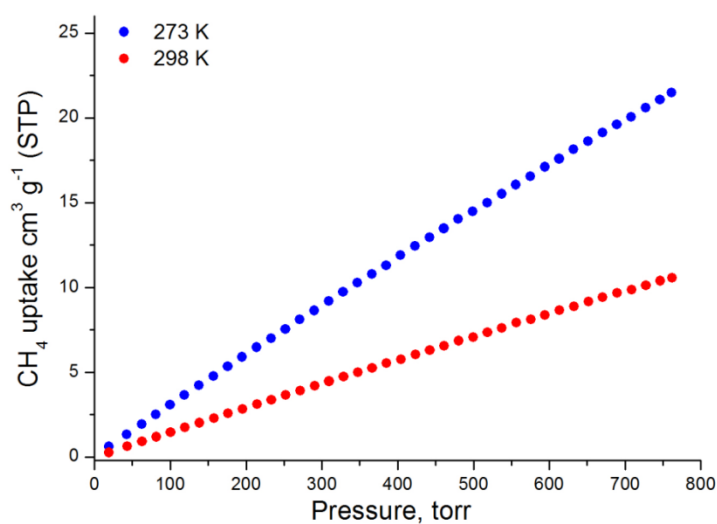
Figure 6.103. CH$_4$ adsorption isotherms of $Zr_6O_4(OH)_4(BPDC\text{-}OAllyl)_5(CH_3COO)_2$ at 273 K and 298 K.
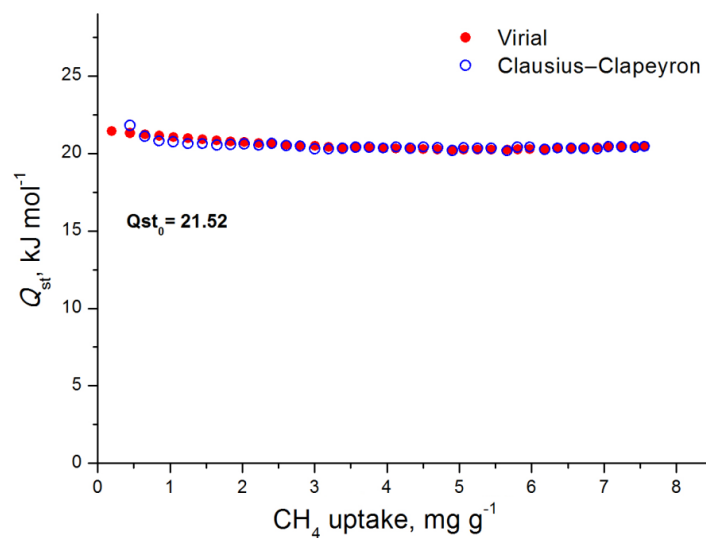
Figure 6.104. CH$_4$ isosteric heat of adsorption in $Zr_6O_4(OH)_4(BPDC\text{-}OAllyl)_5(CH_3COO)_2$ as a function of surface coverage.
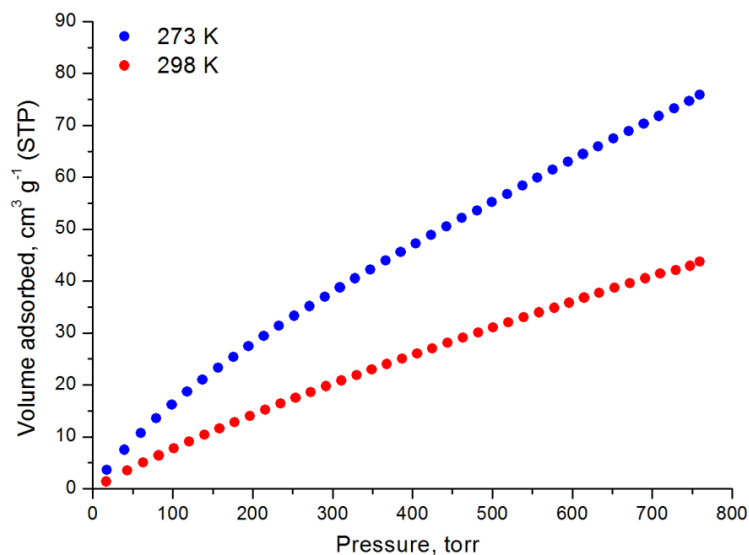
Figure 6.105. CO_2 adsorption isotherms of $Zr_6O_4(OH)_4(BPDC-OAllyl)_5(CH_3COO)_2$ at 273 K and 298 K.
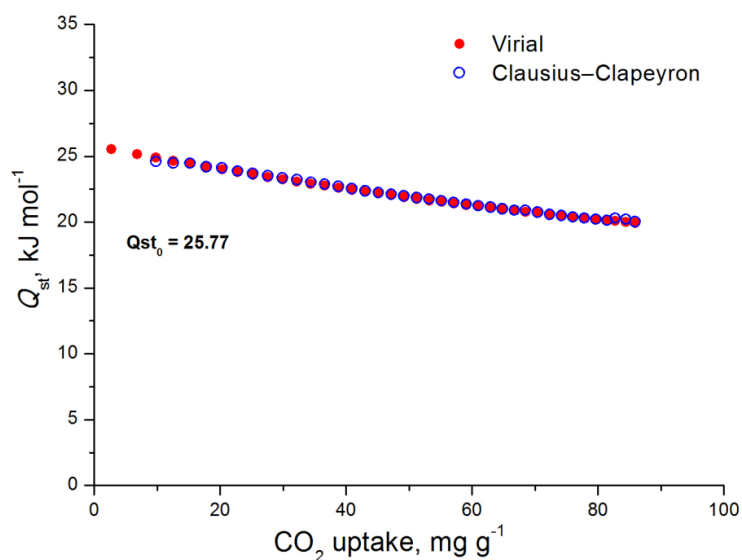
Figure 6.106. CO_2 isoteric heat of adsorption as a function of surface coverage.
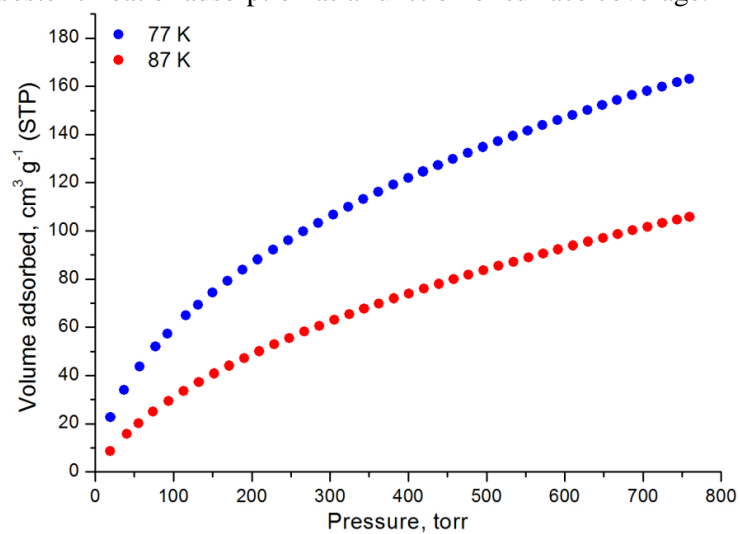
Figure 6.107. Hydrogen adsorption isotherms of $Zr_6O_4(OH)_4(BPDC-OAllyl)_5(CH_3COO)_2$ at 77 K and 87 K.
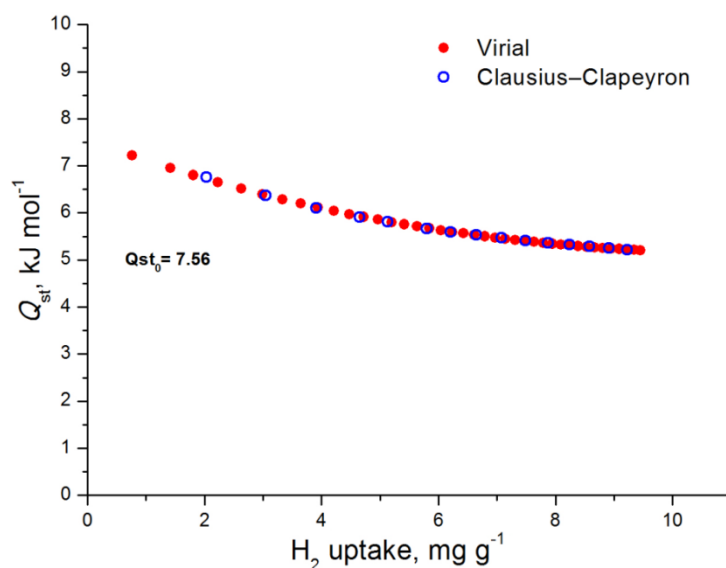
Figure 6.108. H_2 isosteric heat of adsorption in $Zr_6O_4(OH)_4(BPDC-OAllyl)_5(CH_3COO)_2$ as a function of surface coverage.
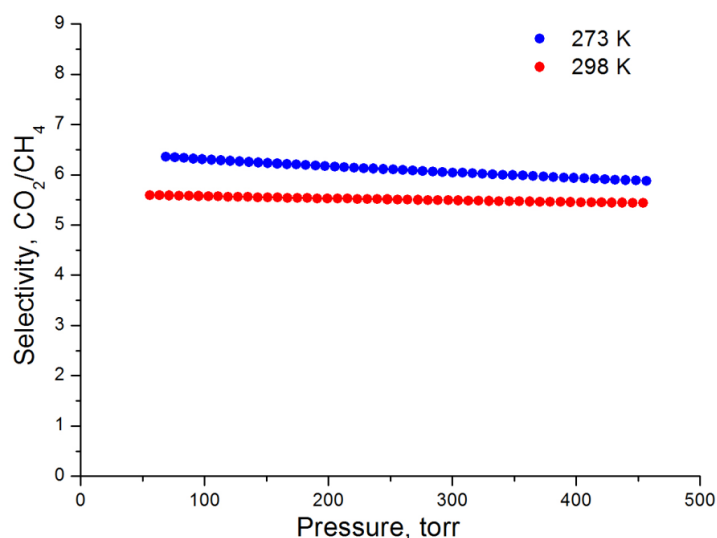
Figure 6.109. Selectivities of CO_2 over CH_4 at 298 K and 273 K for $Zr_6O_4(OH)_4(BPDC-OAllyl)_5(CH_3COO)_2$ as predicted by IAST for a 5/95 CO_2/CH_4 molar mixture.

6.12 Zr-MOF synthesis based on organic linker 20
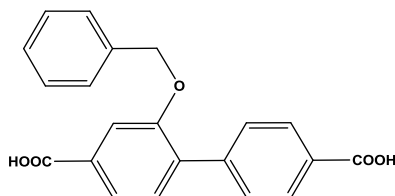
6.12.1 Synthesis of compound $Zr_6O_4(OH)_4(BPDC-OPh)_{5.5}(CH_3COO)_{0.9}$

An amount of 0.030 g (0.09 mmol) of $H_2BPDC-OPh$ and 0.020 g (0.09 mmol) of $ZrCl_4$ were dissolved in a 20 mL glass scintillation vial containing 10 mL DMF and 1 mL of glacial acetic acid. The vial was placed in an oven, heated up to 120 ^0C with 0.06 ^0C/ min and then held at 120 ^0C for 24 h. After that time a white powder was deposited. Yield: 10 % based on $H_2BPDC-OPh$.

199

After the efficient characterization of the material the evaluation of its gas sorption properties took place. Successful activation was possible as follows: as-made sample was washed with DMF four times per day for 2 days and then the sample was soaked in acetone over a period of 4 days, replenishing the acetone 4 times per day. The sample was transferred to a pre weighted sample cell and acetone was removed under reduced pressure. Finally, the sample was activated under dynamic vacuum at 120 °C for 12 hours and until the outgas rate was less than 2 mTorr/min.

Figure 6.110. Comparison of experimental, calculated and evacuated pxrd patterns for $Zr_6O_4(OH)_4(BPDC\text{-}OPh)_{5.5}(CH_3COO)_{0.9}$.
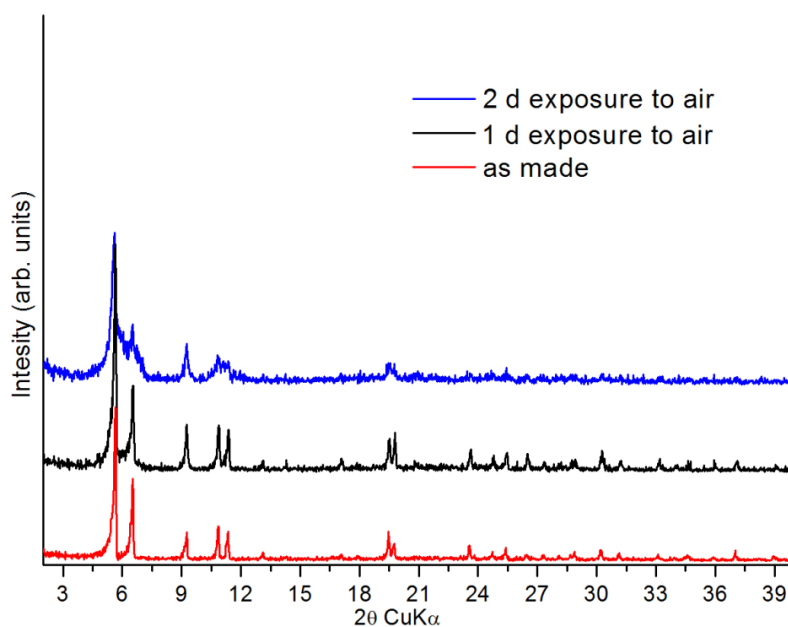
Figure 6.111. Comparison of experimental and after 1 and 2 days exposure to air pxrd patterns for $Zr_6O_4(OH)_4(BPDC\text{-}OPh)_{5.5}(CH_3COO)_{0.9}$.
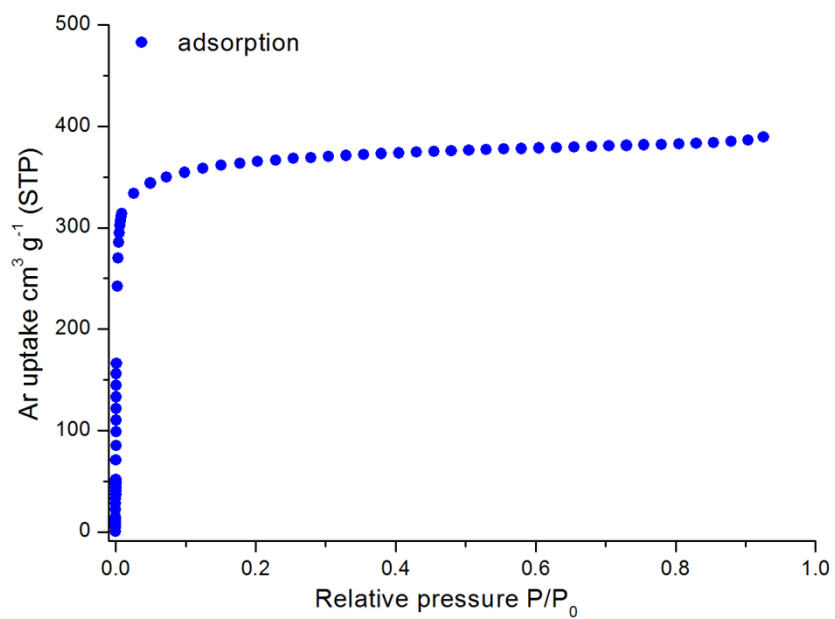
Figure 6.112. Argon sorption isotherm of $Zr_6O_4(OH)_4(BPDC\text{-}OPh)_{5.5}(CH_3COO)_{0.9}$ at 87 K.
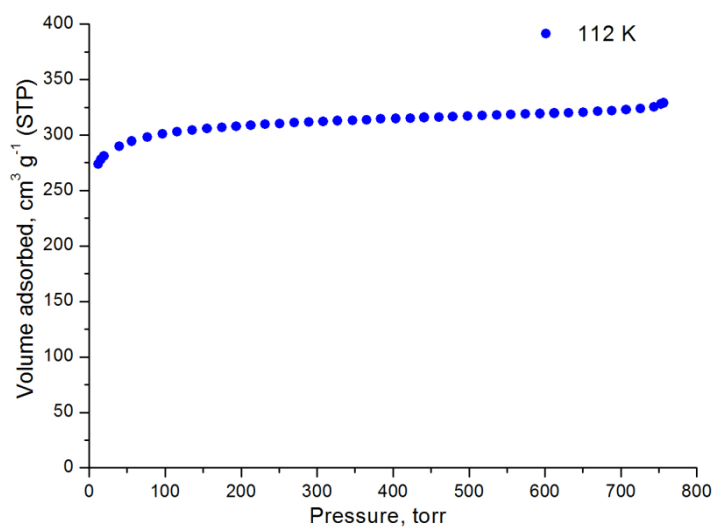
Figure 6.113. CH_4 adsorption isotherm of $Zr_6O_4(OH)_4(BPDC\text{-}OPh)_{5.5}(CH_3COO)_{0.9}$ at 112 K.
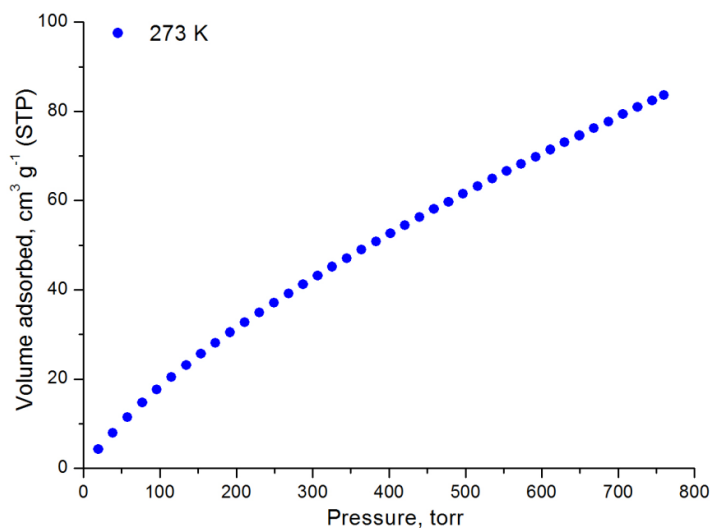
Figure 6.114. CO$_2$ adsorption isotherm of Zr$_6$O$_4$(OH)$_4$(BPDC-OPh)$_{5.5}$(CH$_3$COO)$_{0.9}$ at 273 K.
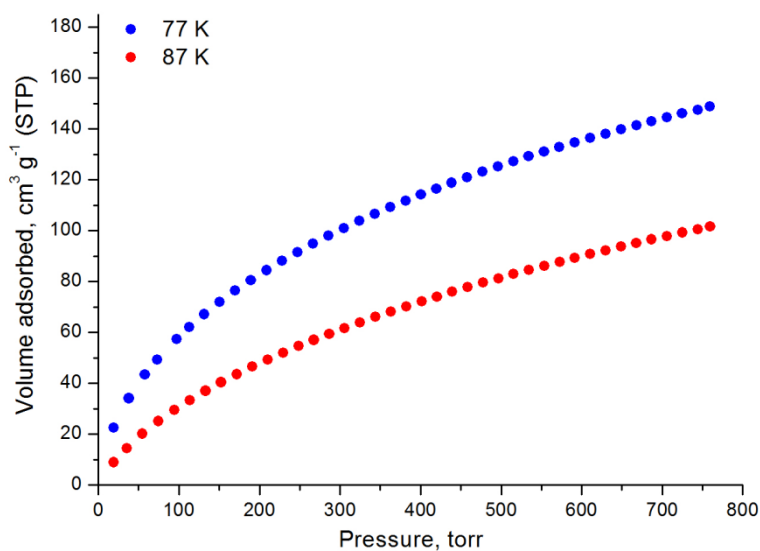
Figure 6.115. Hydrogen adsorption isotherms of Zr$_6$O$_4$(OH)$_4$(BPDC-OPh)$_{5.5}$(CH$_3$COO)$_{0.9}$ at 77 K and 87 K.
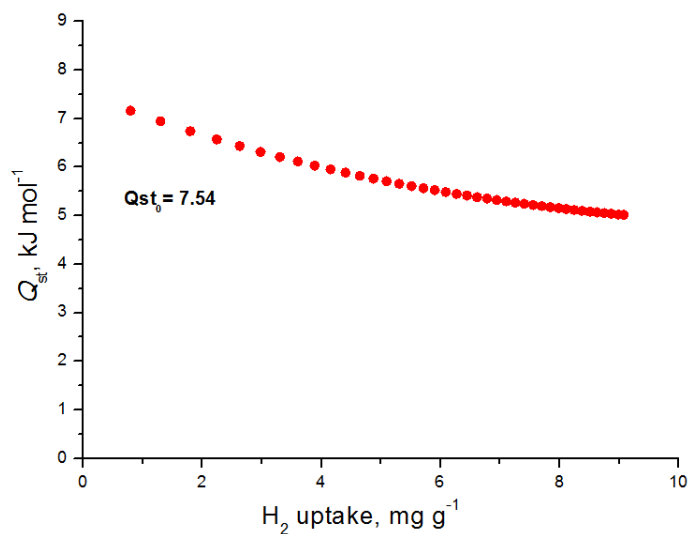
Figure 6.116. H$_2$ isosteric heat of adsorption in Zr$_6$O$_4$(OH)$_4$(BPDC-OPh)$_{5.5}$(CH$_3$COO)$_{0.9}$ as a function of surface coverage.

6.13 Zr-MOF synthesis based on organic linker 21
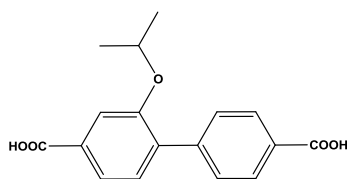
6.13.1 Synthesis of compound $Zr_6O_4(OH)_4(BPDC-OisoPr)_{5.4}(CH_3COO)_{1.2}$

An amount of 0.030 g (0.10 mmol) of $H_2BPDC-OisoPr$ and 0.024 g (0.10 mmol) of $ZrCl_4$ were dissolved in a 20 mL glass scintillation vial containing 10 mL DMF and 1 mL of glacial acetic acid. The vial was placed in an oven, heated up to 120 ^0C with 0.06 ^0C/ min and then held at 120 ^0C for 24 h. After that time a white powder was deposited. Yield: 10 % based on $H_2BPDC-OisoPr$.

After the efficient characterization of the material the evaluation of its gas sorption properties took place. Successful activation was possible as follows: as-made sample was washed with DMF four times per day for 2 days and then the sample was soaked in acetone over a period of 4 days, replenishing the acetone 4 times per day. The sample was transferred to a pre weighted sample cell and acetone was removed under reduced pressure. Finally, the sample was activated under dynamic vacuum at 120 °C for 12 hours and until the outgas rate was less than 2 mTorr/min.
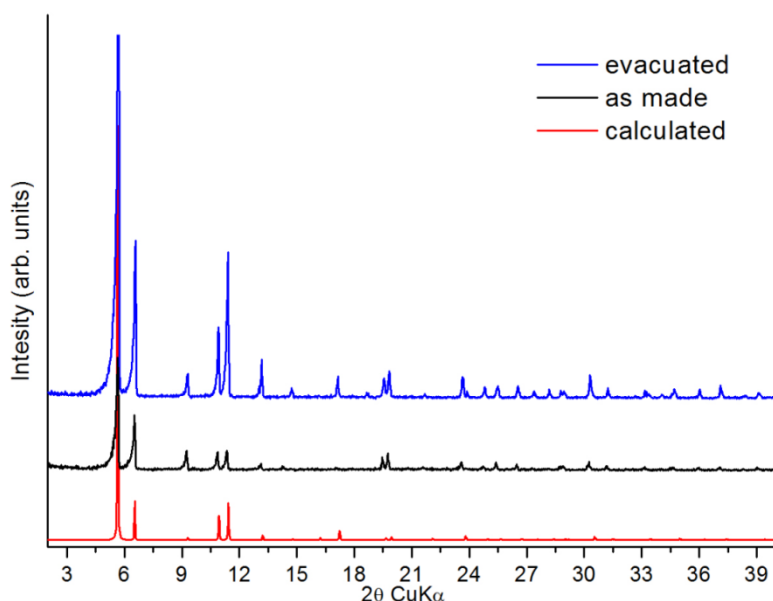
Figure 6.117. Comparison of experimental, calculated and evacuated pxrd patterns for $Zr_6O_4(OH)_4(BPDC-OisoPr)_{5.4}(CH_3COO)_{1.2}$.
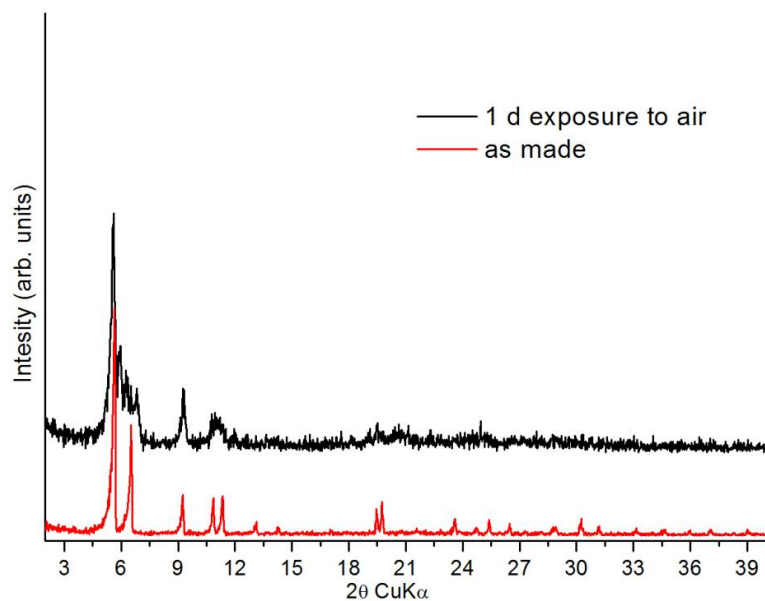
<u>Figure 6.118.</u> Comparison of experimental and after 1 day exposure to air pxrd patterns for $Zr_6O_4(OH)_4(BPDC\text{-}OisoPr)_{5.4}(CH_3COO)_{1.2}$.
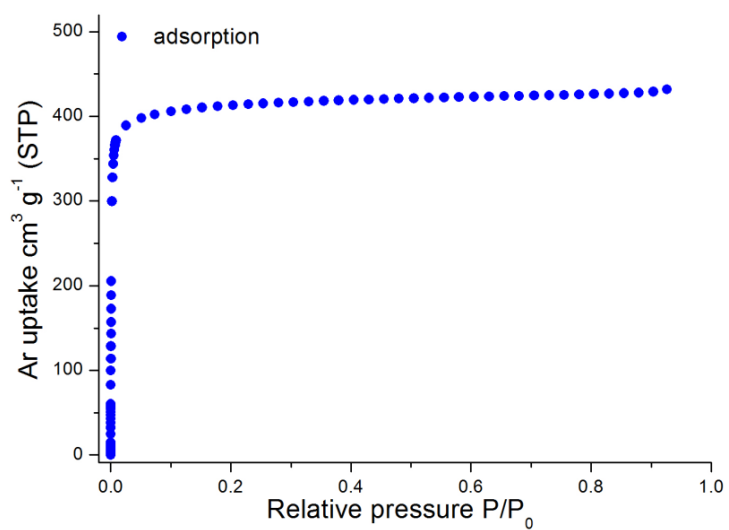
<u>Figure 6.119.</u> Argon sorption isotherm of $Zr_6O_4(OH)_4(BPDC\text{-}OisoPr)_{5.4}(CH_3COO)_{1.2}$ at 87 K.
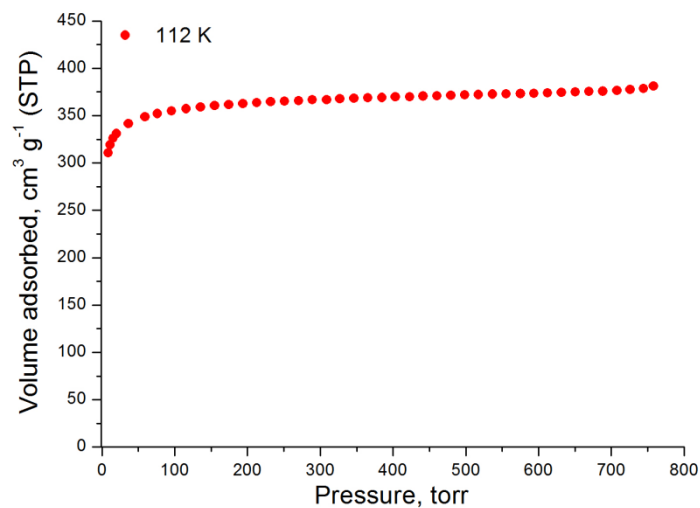
Figure 6.120. CH_4 adsorption isotherm of $Zr_6O_4(OH)_4(BPDC\text{-}OisoPr)_{5.4}(CH_3COO)_{1.2}$ at 112 K.
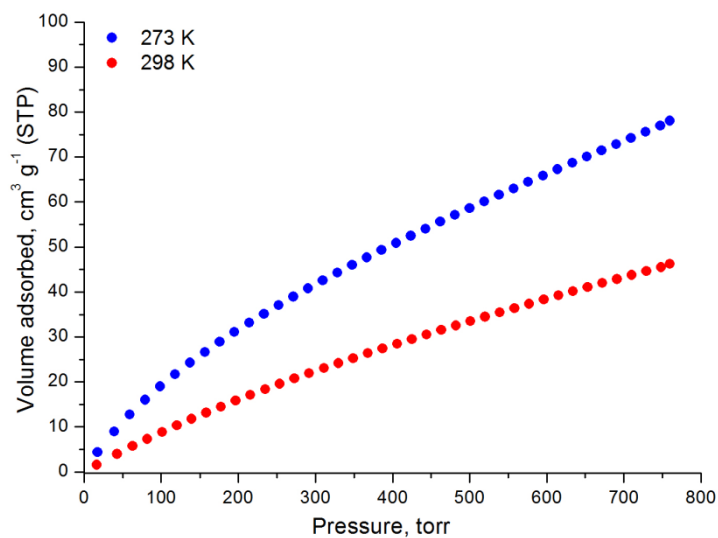
Figure 6.121. CO_2 adsorption isotherms of $Zr_6O_4(OH)_4(BPDC\text{-}OisoPr)_{5.4}(CH_3COO)_{1.2}$ at 273 K and 298 K.
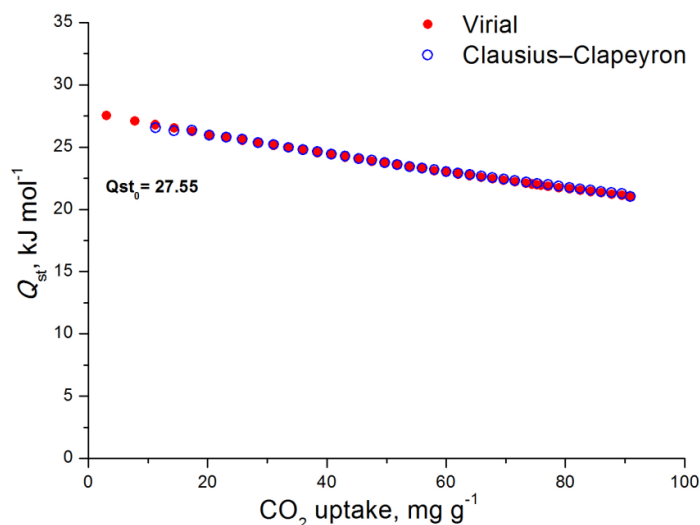
Figure 6.122. CO_2 isosteric heat of adsorption in $Zr_6O_4(OH)_4(BPDC\text{-}OisoPr)_{5.4}(CH_3COO)_{1.2}$ as a function of surface coverage.
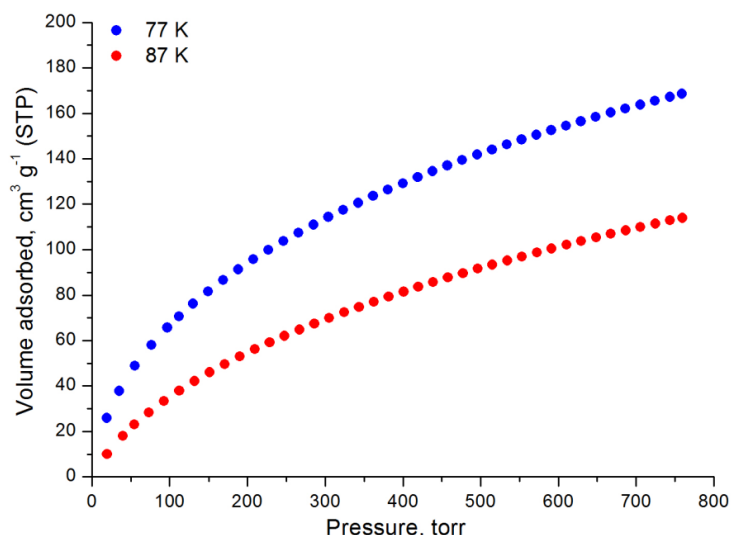
Figure 6.123. Hydrogen adsorption isotherms of $Zr_6O_4(OH)_4(BPDC\text{-}OisoPr)_{5.4}(CH_3COO)_{1.2}$ at 77 K and 87 K.
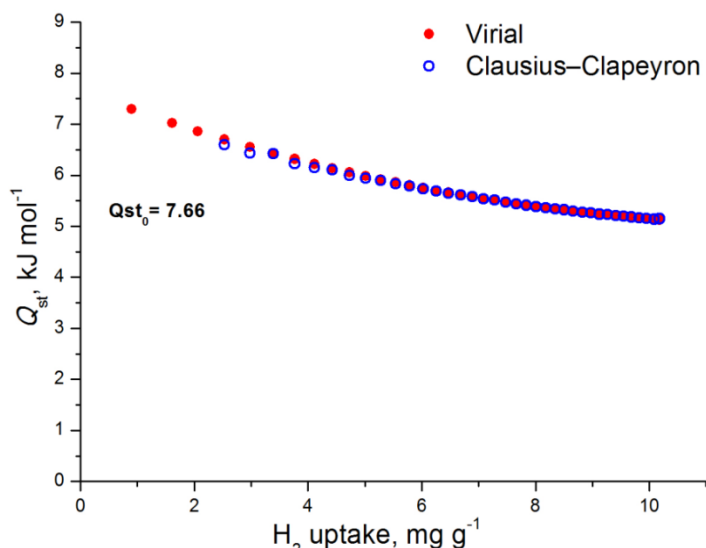
Figure 6.124. H_2 isosteric heat of adsorption in $Zr_6O_4(OH)_4(BPDC\text{-}OisoPr)_{5.4}(CH_3COO)_{1.2}$ as a function of surface coverage.

6.14 Zr-MOF synthesis based on organic linker 22
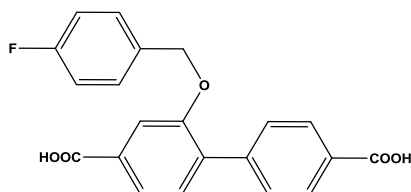
6.14.1 Synthesis of compound $Zr_6O_4(OH)_4(BPDC\text{-}Obenzyl\text{-}F)_{4.3}(CH_3COO)_{3.4}$

An amount of 0.035 g (0.10 mmol) of H_2BPDC-Obenzyl-F and 0.023 g (0.10 mmol) of $ZrCl_4$ were dissolved in a 20 mL glass scintillation vial containing 10 mL DMF and 0.75 mL of glacial acetic acid. The vial was placed in an oven, heated up to 120 ^{0}C with 0.06 ^{0}C/ min and then held at 120 ^{0}C for 24 h. After that time a white powder was deposited. Yield: 10 % based on H_2BPDC-Obenzyl-F.

After the efficient characterization of the material the evaluation of its gas sorption properties took place. Successful activation was possible as follows: as-made sample was washed with DMF four times per day for 2 days and then the sample was soaked in acetone over a period of 4 days, replenishing the acetone 4 times per day. The sample was transferred to a pre weighted sample cell and acetone was removed under reduced pressure. Finally, the sample was activated under dynamic vacuum at 120 °C for 12 hours and until the outgas rate was less than 2 mTorr/min.
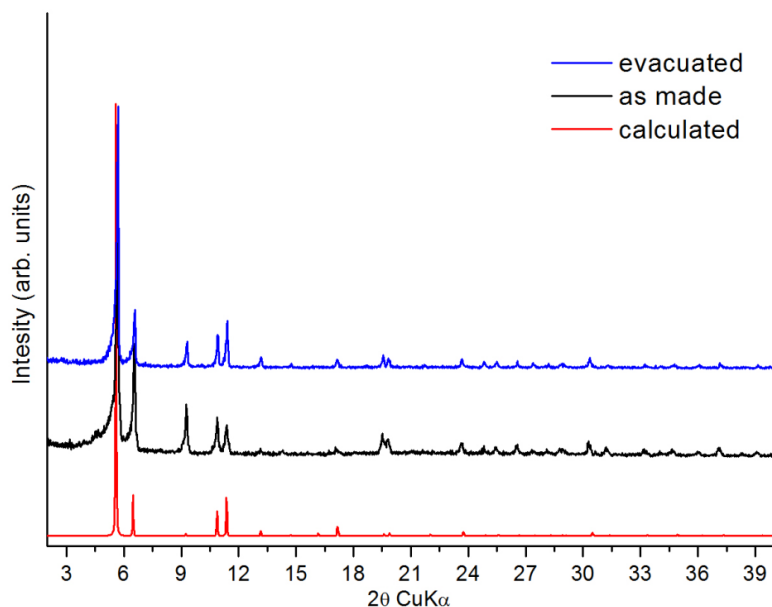
Figure 6.125. Comparison of experimental, calculated and evacuated pxrd patterns for $Zr_6O_4(OH)_4(BPDC-Obenzyl-F)_{4.3}(CH_3COO)_{3.4}$.
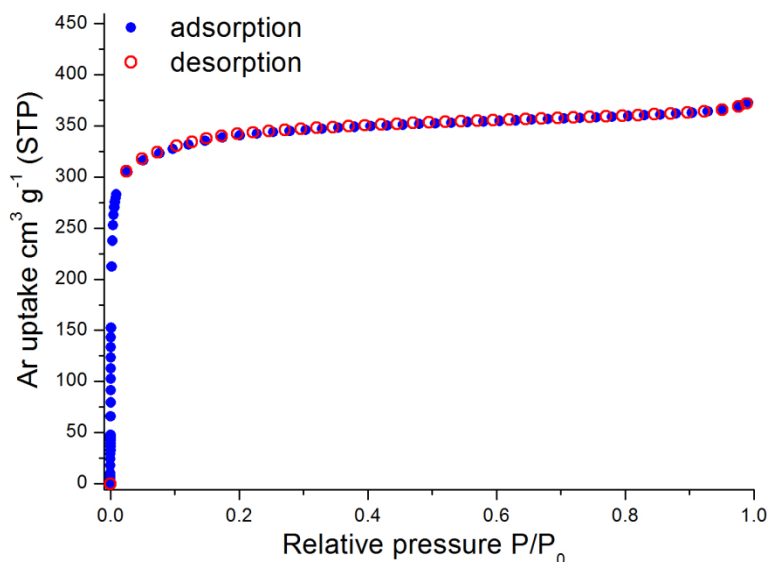
Figure 6.126. Argon sorption isotherm of $Zr_6O_4(OH)_4(BPDC-Obenzyl-F)_{4.3}(CH_3COO)_{3.4}$ at 87 K.
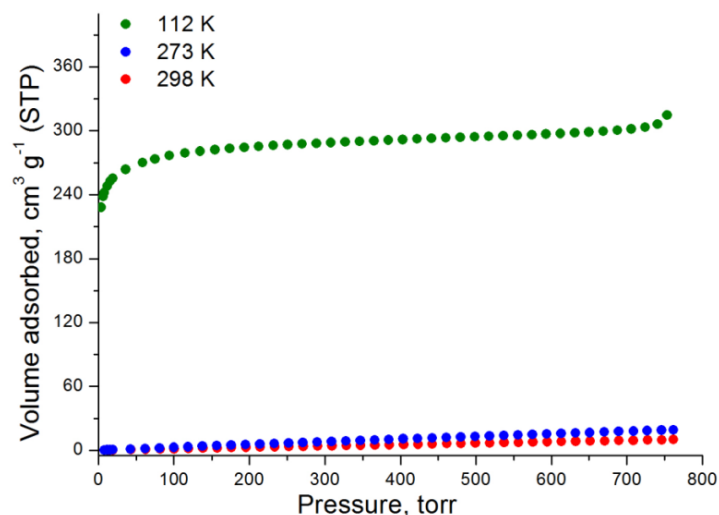
Figure 6.127. CH$_4$ adsorption isotherms of Zr$_6$O$_4$(OH)$_4$(BPDC-Obenzyl-F)$_{4.3}$(CH$_3$COO)$_{3.4}$ at 112 K, 273 K, and 298 K.
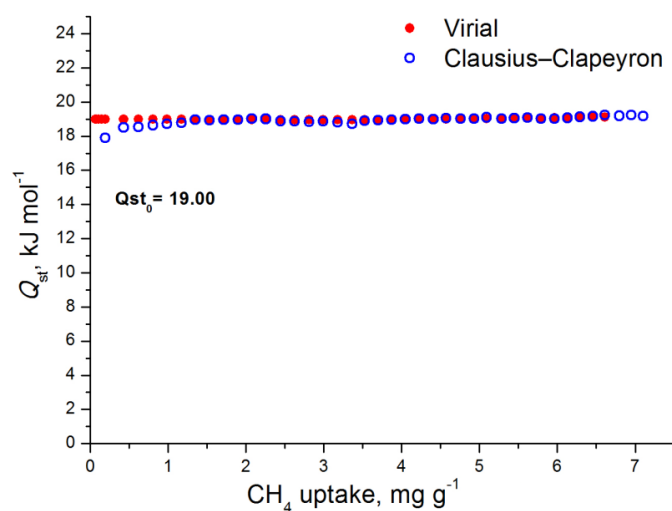
Figure 6.128. CH$_4$ isosteric heat of adsorption in Zr$_6$O$_4$(OH)$_4$(BPDC-Obenzyl-F)$_{4.3}$(CH$_3$COO)$_{3.4}$ as a function of surface coverage.
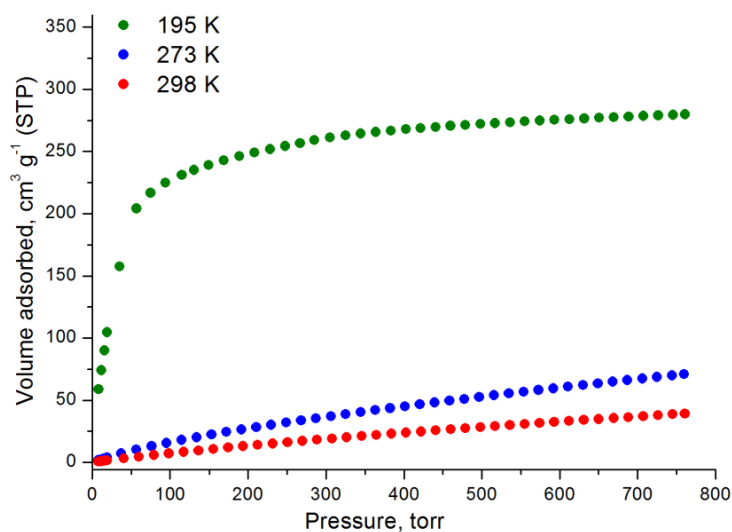
Figure 6.129. CO$_2$ adsorption isotherms of Zr$_6$O$_4$(OH)$_4$(BPDC-Obenzyl-F)$_{4.3}$(CH$_3$COO)$_{3.4}$ at 195 K, 273 K and 298 K.
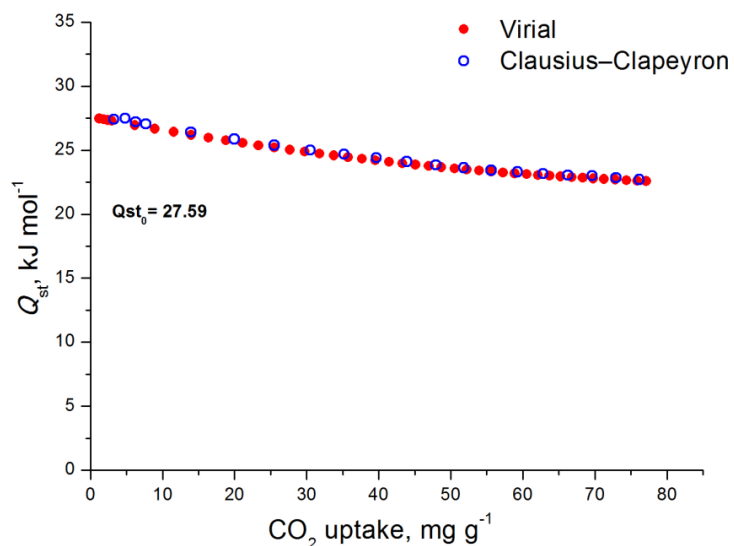
Figure 6.130. CO_2 isosteric heat of adsorption in $Zr_6O_4(OH)_4(BPDC-Obenzyl-F)_{4.3}(CH_3COO)_{3.4}$ as a function of surface coverage.
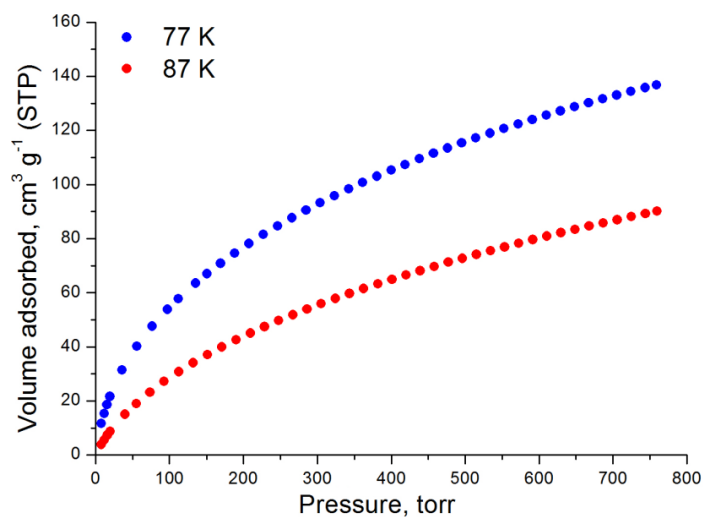
Figure 6.131. Hydrogen adsorption isotherms of $Zr_6O_4(OH)_4(BPDC-Obenzyl-F)_{4.3}(CH_3COO)_{3.4}$ at 77 K and 87 K.
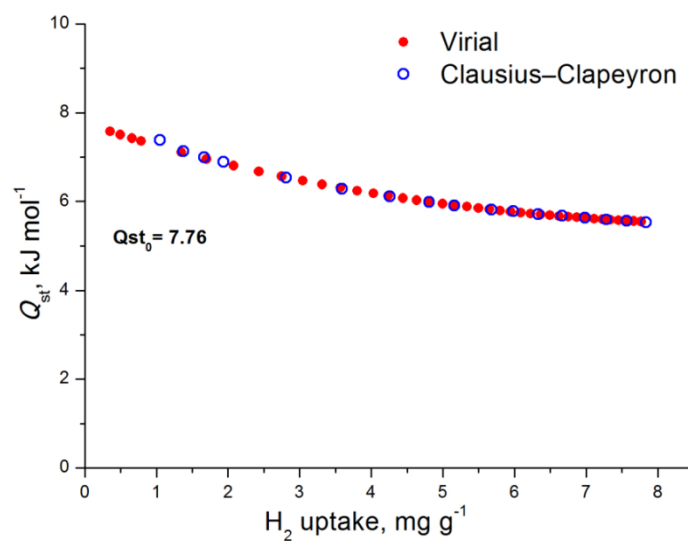
Figure 6.132. H_2 isosteric heat of adsorption in $Zr_6O_4(OH)_4(BPDC-Obenzyl-F)_{4.3}(CH_3COO)_{3.4}$ as a function of surface coverage.
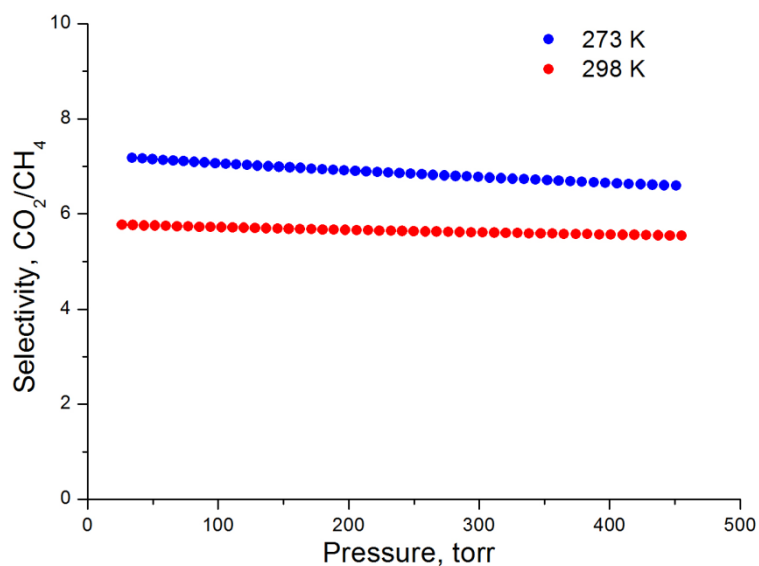
Figure 6.133. Selectivities of CO_2 over CH_4 at 298 K and 273 K for $Zr_6O_4(OH)_4(BPDC-Obenzyl-F)_{4.3}(CH_3COO)_{3.4}$ as predicted by IAST for a 5/95 CO_2/CH_4 molar mixture.

6.15 Zr-MOF synthesis based on organic linker 24
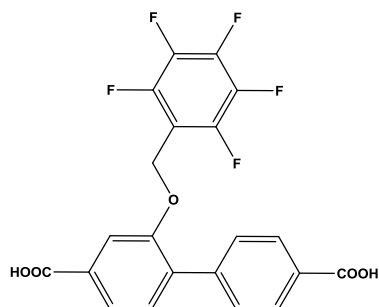
6.15.1 Synthesis of compound $Zr_6O_4(OH)_4(BPDC-Obenzyl-5F)_6$

An amount of 0.030 g (0.07 mmol) of H_2BPDC-Obenzyl-5F and 0.016 g (0.0.07 mmol) of $ZrCl_4$ were dissolved in a 20 mL glass scintillation vial containing 10 mL DMF and 0.75 mL of glacial acetic acid. The vial was placed in an oven, heated up to 120 ^{0}C with 0.06 ^{0}C/ min and then held at 120 ^{0}C for 24 h. After that time a white powder was deposited. Yield: 10 % based on H_2BPDC-Obenzyl-5F.
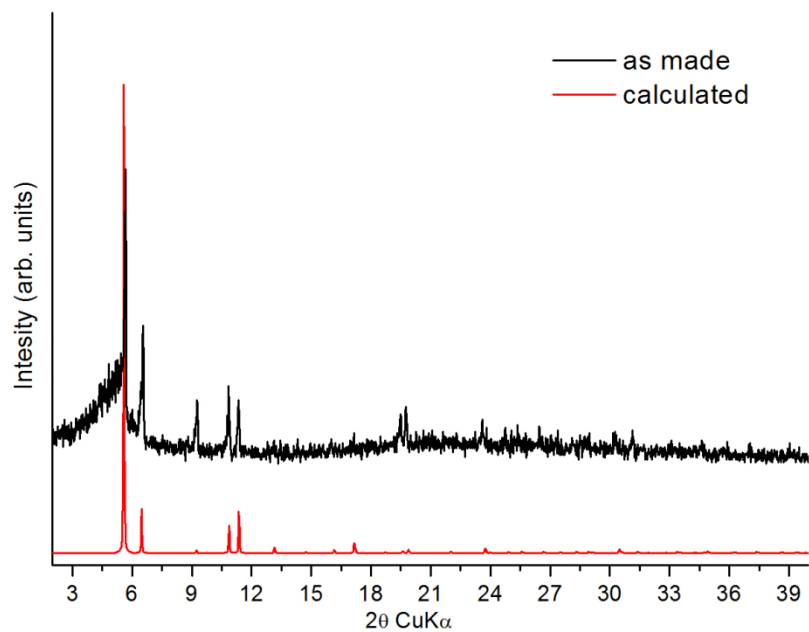
Figure 6.134. Comparison of experimental and calculated pxrd patterns for $Zr_6O_4(OH)_4(BPDC-Obenzyl-5F)_6$.

Comparison of UiO-67 materials 6.7.1- 6.14.1
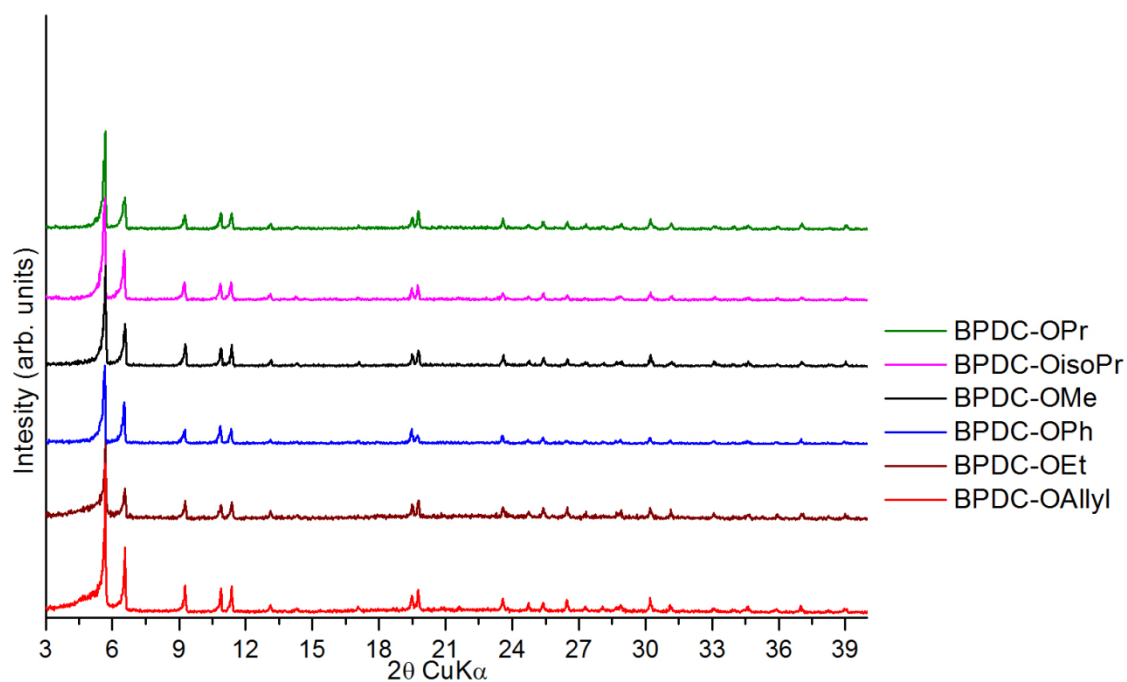
Figure 6.135. Comparison of experimental pxrd patterns for six functionalized UiO-67 analogues.
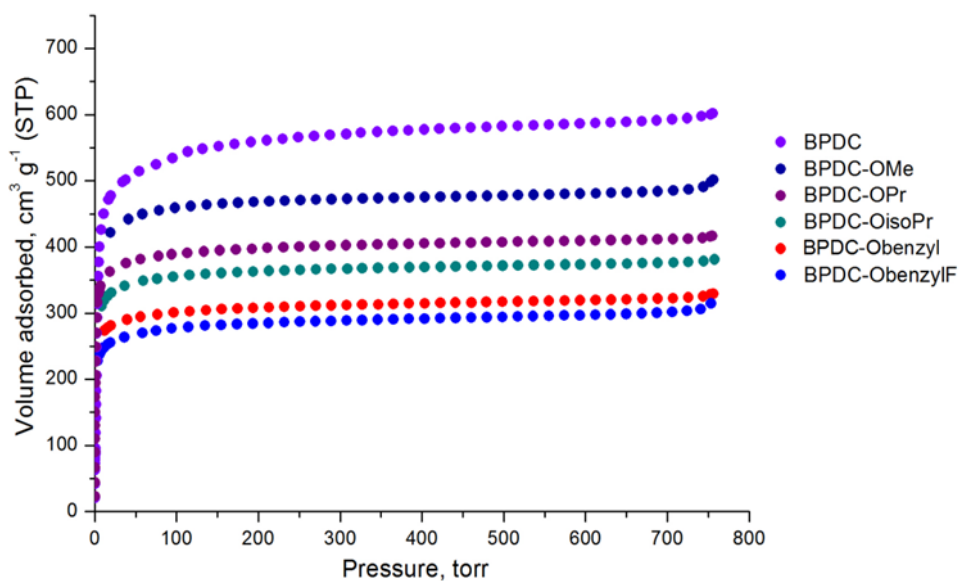
Figure 6.136. CH$_4$ adsorption isotherms recorded at 112 K and 1 bar.
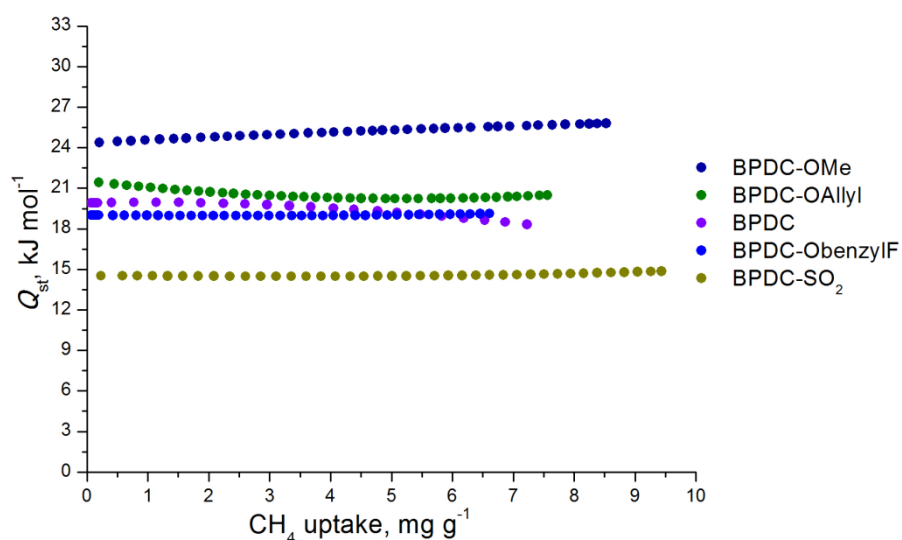
Figure 6.137. CH$_4$ isosteric heats of adsorption as a function of surface coverage.
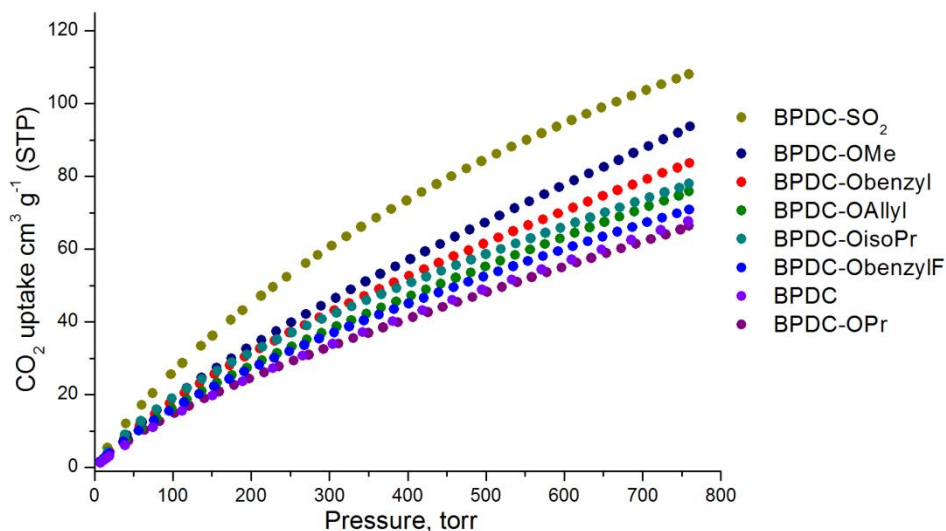
Figure 6.138. CO_2 adsorption isotherms recorded at 273 K and 1 bar.
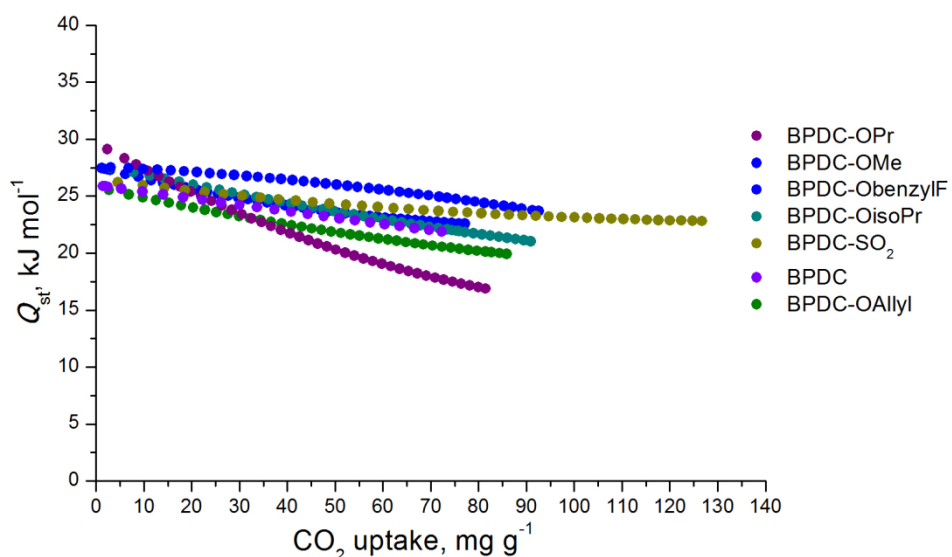
Figure 6.139. CO_2 isosteric heats of adsorption as a function of surface coverage.
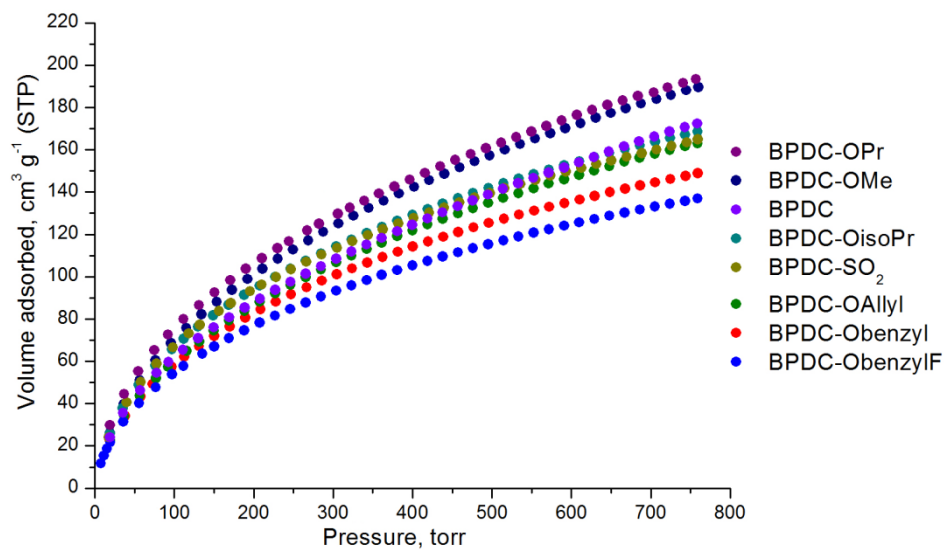
Figure 6.140. Hydrogen adsorption isotherms recorded at 77 K and 1 bar.
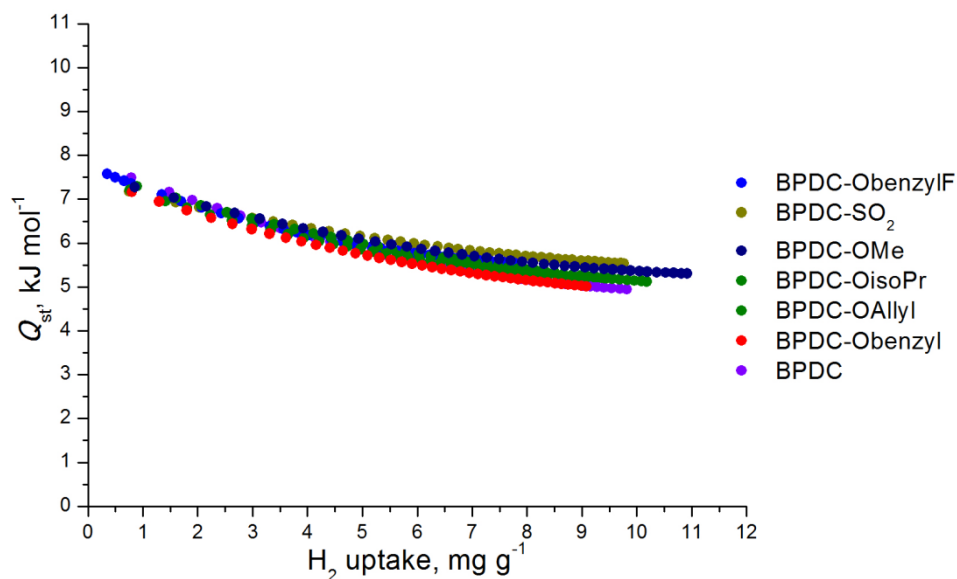
Figure 6.141. H$_2$ isosteric heats of adsorption as a function of surface coverage.

6.16 Zr-MOF synthesis based on organic linker 27
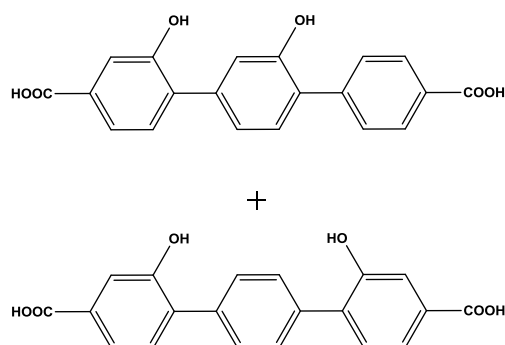
6.16.1 Synthesis of compound Zr$_6$O$_4$(OH)$_4$(TPDC-2OH)$_6$

An amount of 0.040 g (0.11 mmol) of H$_2$TPDC-2OH and 0.059 g (0.22 mmol) of ZrCl$_4$ were dissolved in a 20 mL glass scintillation vial containing 5 mL DMF and 0.5 mL of glacial acetic acid. The vial was placed in an oven, heated up to 120 ^{0}C with 0.06 ^{0}C/min and then held at 120 ^{0}C for 24 h. Yield: 20 % based on H$_2$TPDC-2OH.
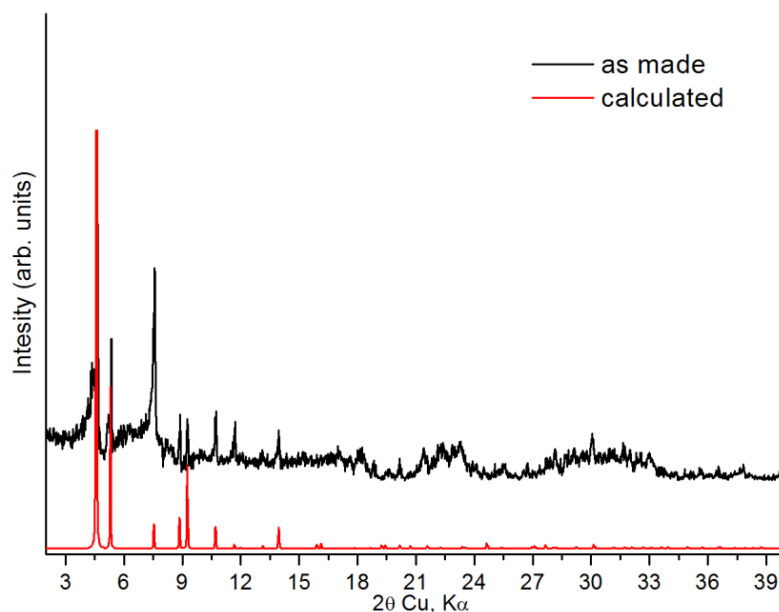
Figure 6.142. Comparison of experimental and calculated pxrd patterns for the compound $Zr_6O_4(OH)_4(TPDC-2OH)_6.$

6.17 Zr-MOF synthesis based on organic linker 31
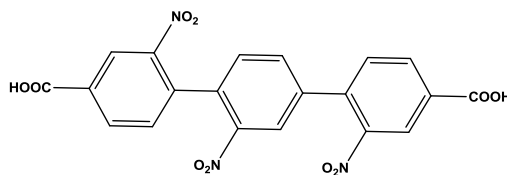
6.17.1 Synthesis of compound $Zr_6O_4(OH)_4(TPDC-3NO_2)_6$

An amount of 0.030 g (0.06 mmol) of $H_2TPDC-3NO_2$ and 0.015 g (0.06 mmol) of $ZrCl_4$ were dissolved in a 20 mL glass scintillation vial containing 10 mL DMF and 0.5 mL of glacial acetic acid. The vial was placed in an oven, heated up to 120 ^{0}C with 0.06 ^{0}C/min and then held at 120 ^{0}C for 24 h. Yield: 48 % based on $H_2TPDC-3NO_2$.

After the efficient characterization of the material the evaluation of its gas sorption properties took place. Successful activation was possible as follows: as-made sample was washed with DMF four times per day for 2 days and then the sample was soaked in acetone over a period of 4 days, replenishing the acetone 4 times per day. The sample was transferred to a pre weighted sample cell and acetone was removed under reduced pressure. Finally, the sample was activated under dynamic vacuum at 100 °C for 12 hours and until the outgas rate was less than 2 mTorr/min.

Figure 6.143. Comparison of experimental, calculated and evacuated pxrd patterns for the compound $Zr_6O_4(OH)_4(TPDC-3NO_2)_6$.
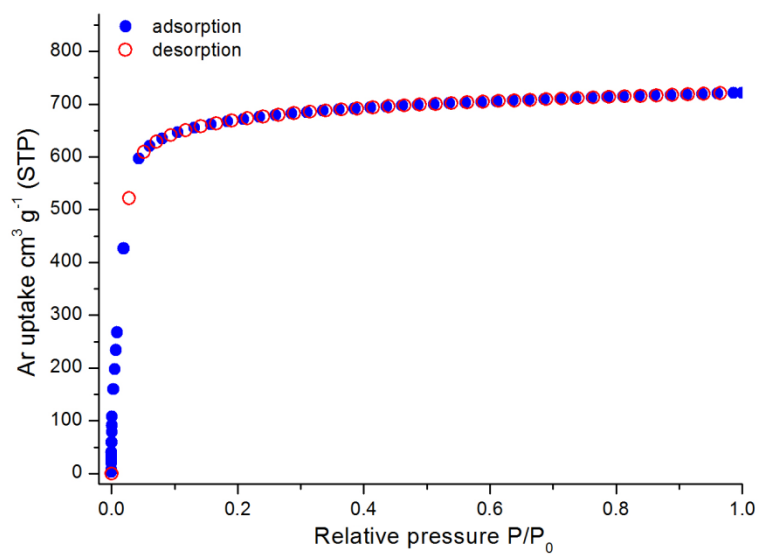
Figure 6.144. Argon sorption isotherm of $Zr_6O_4(OH)_4(TPDC-3NO_2)_6$ at 87 K.
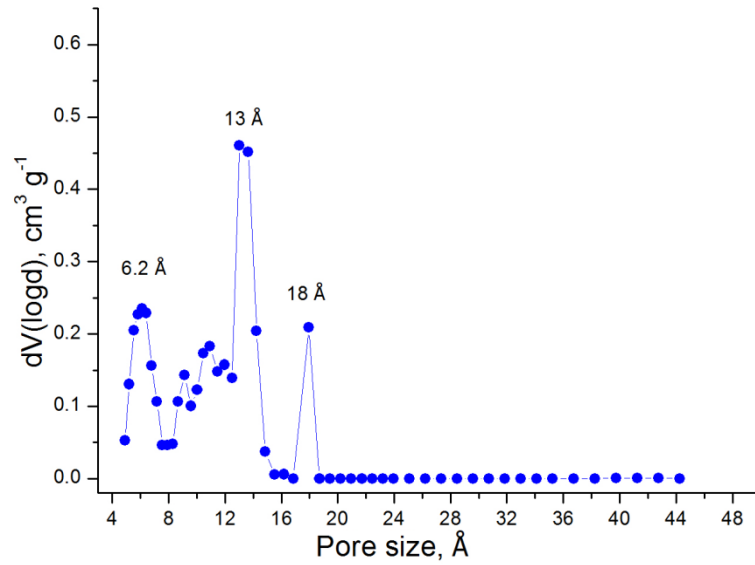
Figure 6.145. Pore size distribution in $Zr_6O_4(OH)_4(TPDC-3NO_2)_6$ calculated from NLDFT analysis.
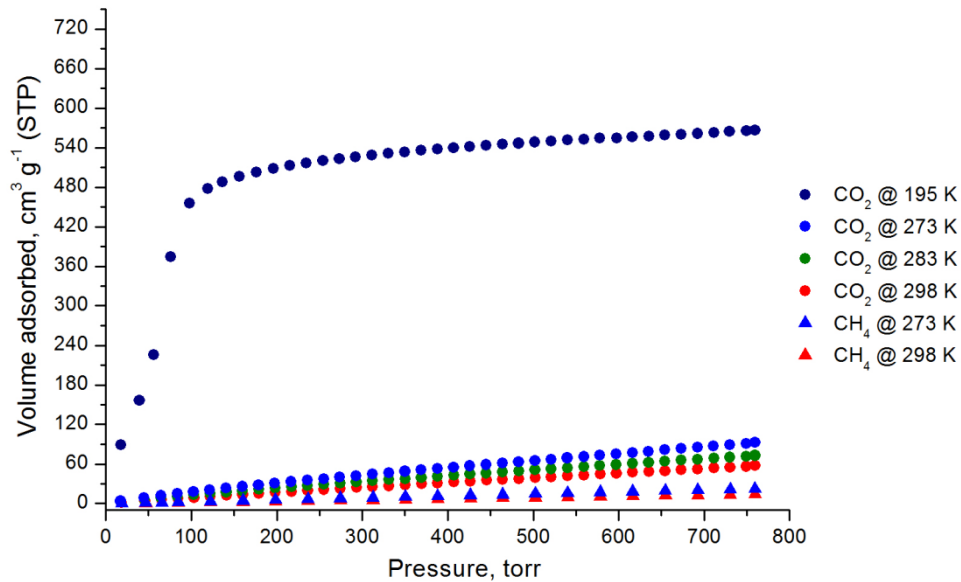
Figure 6.146. CO_2 adsorption isotherms of $Zr_6O_4(OH)_4(TPDC-3NO_2)_6$ at 195 K, 273 K, 283 K and 298 K and CH_4 adsorption isotherms at 273 K and 298 K.
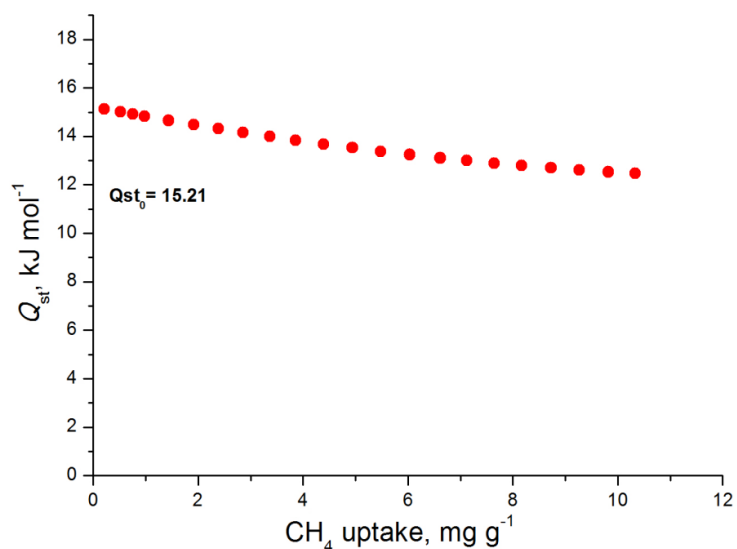
Figure 6.147. CH_4 isosteric heat of adsorption in $Zr_6O_4(OH)_4(TPDC\text{-}3NO_2)_6$ as a function of surface coverage.
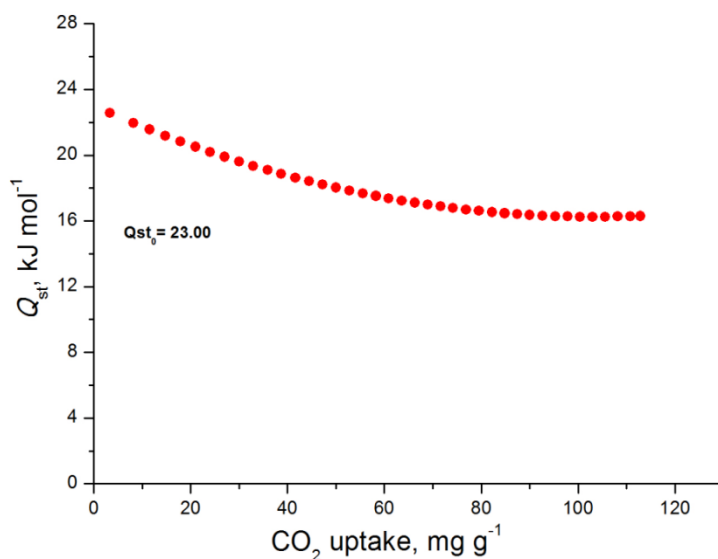
Figure 6.148. CO_2 isosteric heat of adsorption in $Zr_6O_4(OH)_4(TPDC\text{-}3NO_2)_6$ as a function of surface coverage.
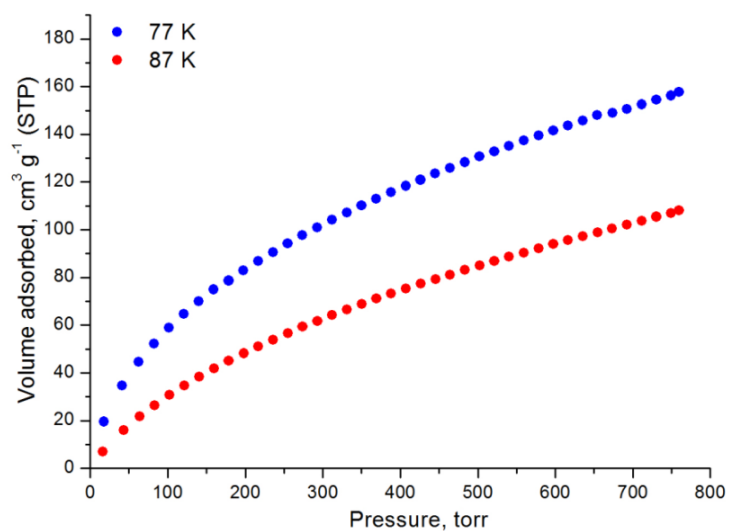
Figure 6.149. Hydrogen adsorption isotherms of $Zr_6O_4(OH)_4(TPDC\text{-}3NO_2)_6$ at 77 K and 87 K.

218
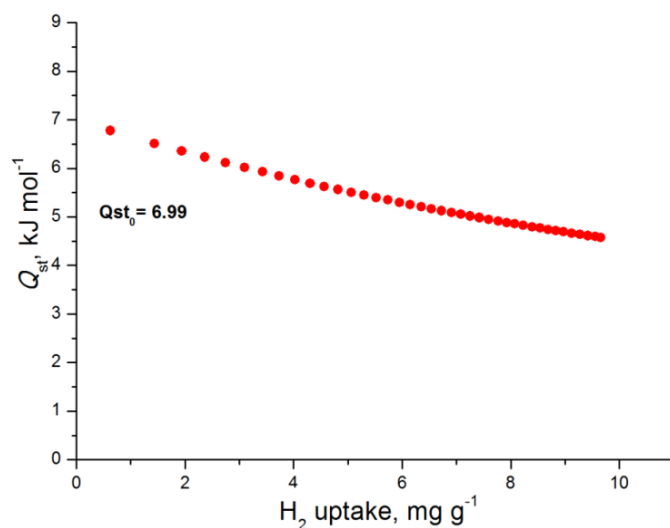
Figure 6.150. H_2 isosteric heat of adsorption in $Zr_6O_4(OH)_4(TPDC-3NO_2)_6$ as a function of surface coverage.
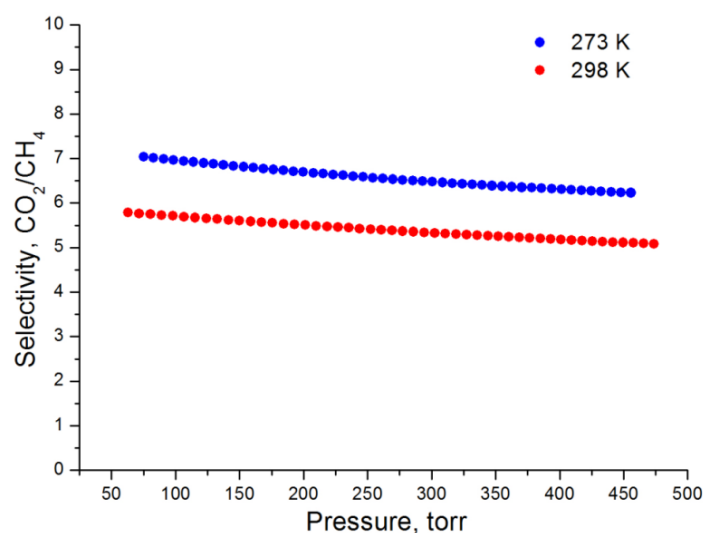
Figure 6.151. Selectivities of CO_2 over CH_4 at 298 K and 273 K for $Zr_6O_4(OH)_4(TPDC-3NO_2)_6$ as predicted by IAST for a 5/95 CO_2/CH_4 molar mixture.

6.18 Zr-MOF synthesis based on organic linker 66
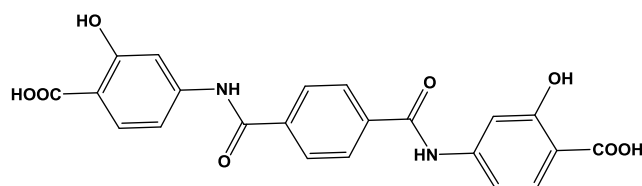
6.18.1 Synthesis of compound $Zr_6O_4(OH)_4(L)_6$

An amount of 0.030 g (0.07 mmol) of H$_2$L and 0.016 g (0.07 mmol) of ZrCl$_4$ were dissolved in a 20 mL glass scintillation vial containing 10 mL DMF and 0.3 mL of glacial acetic acid. The vial was placed in an oven, heated up to 120 ^{0}C with 0.06 ^{0}C/min and then held at 120 ^{0}C for 24 h. After that time an orange powder was deposited. Yield: 40 % based on H$_2$L.
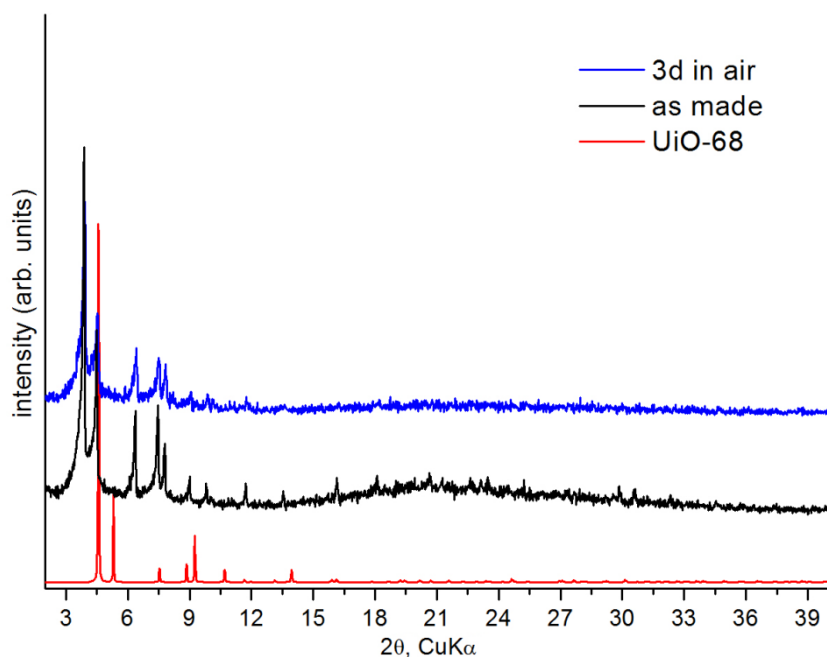
Figure 6.152. Experimental and 3 days in air pxrd patterns for the compound Zr$_6$O$_4$(OH)$_4$(L)$_6$ compared to the calculated UiO-68 pxrd pattern.

6.19 Zr-MOF synthesis based on organic linker 67
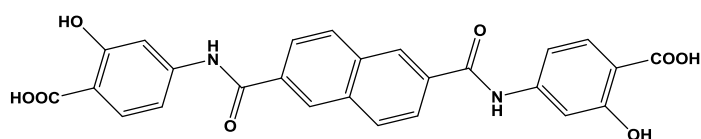
6.19.1 Synthesis of compound Zr$_6$O$_4$(OH)$_4$(L)$_6$

An amount of 0.030 g (0.06 mmol) of H$_2$L and 0.014 g (0.06 mmol) of ZrCl$_4$ were dissolved in a 20 mL glass scintillation vial containing 10 mL DMF and 0.5 mL of glacial acetic acid. The vial was placed in an oven, heated up to 120 ^{0}C with 0.06 ^{0}C/min and then held at 120 ^{0}C for 24 h. After that time an orange powder was deposited. Yield: 30 % based on H$_2$L.
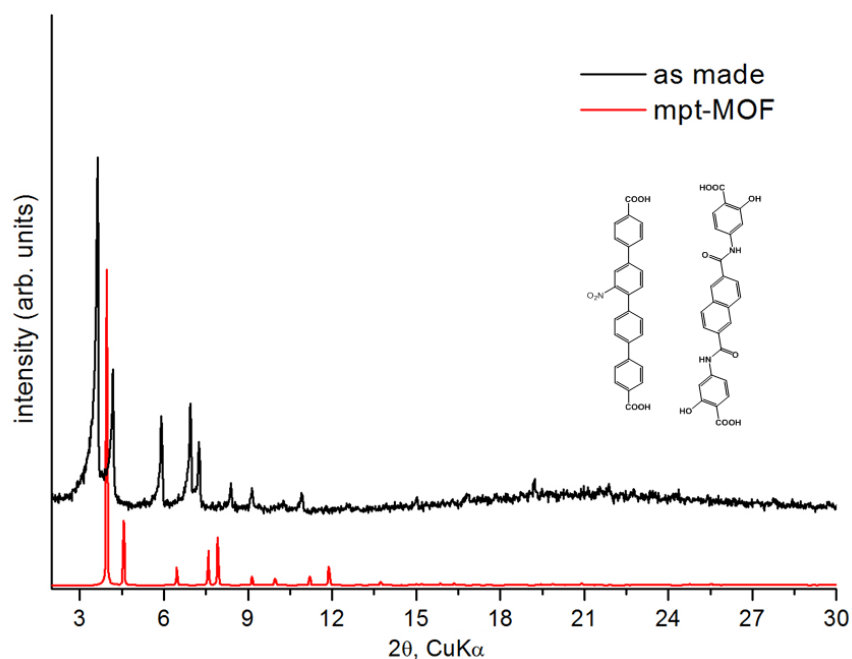
Figure 6.153. Experimental pxrd pattern for the compound $Zr_6O_4(OH)_4(L)_6$ compared to the calculated mpt-MOF pxrd pattern. Inset figure shows the two organic linkers, to the right is our amide functionalized and to the left the linker of the mpt-MOF compound.

6.20 Zr-MOF synthesis based on organic linker 26
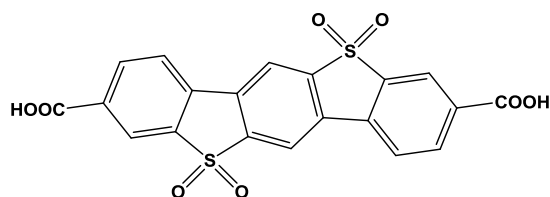
6.20.1 Reaction of linker 26 with ZrCl₄

An amount of 0.030 g (0.065 mmol) of $H_2TPDC-2SO_2$ and 0.015 g (0.065 mmol) of $ZrCl_4$ were dissolved in a 20 mL glass scintillation vial containing 10 mL DMF and 3 mL of glacial acetic acid. The vial was placed in an oven, heated up to 120 ^{0}C with 0.06 ^{0}C/ min and then held at 120 ^{0}C for 24 h. After that time small plate colorless crystals were deposited.

221
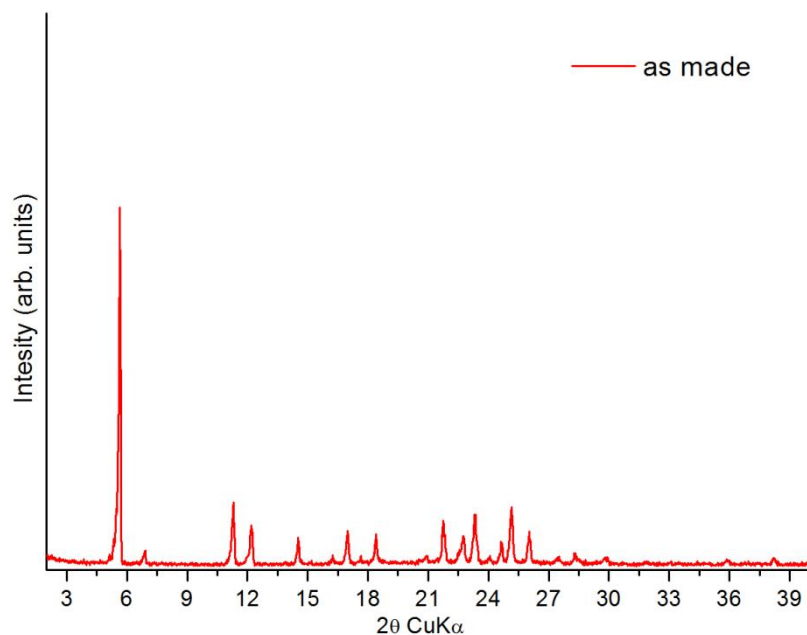
Figure 6.154. Experimental pxrd pattern for material 6.20.1.

6.21 Zr-MOF synthesis based on organic linker 32
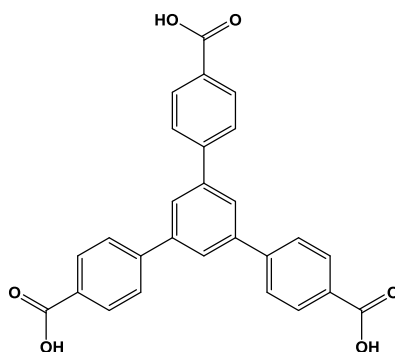
6.21.1 Reaction of linker 32 with ZrCl$_4$

An amount of 0.025 g (0.06 mmol) of H$_3$BTB and 0.013 g (0.06 mmol) of ZrCl$_4$ were dissolved in a 20 mL glass scintillation vial containing 10 mL DMF and 4 mL glacial acetic acid. The vial was placed in an oven, heated up to 120 ^{0}C with 0.06 ^{0}C/min and then held at 120 ^{0}C for 24 h. After that time a white powder was deposited. Yield: 50 % based on H$_3$BTB.
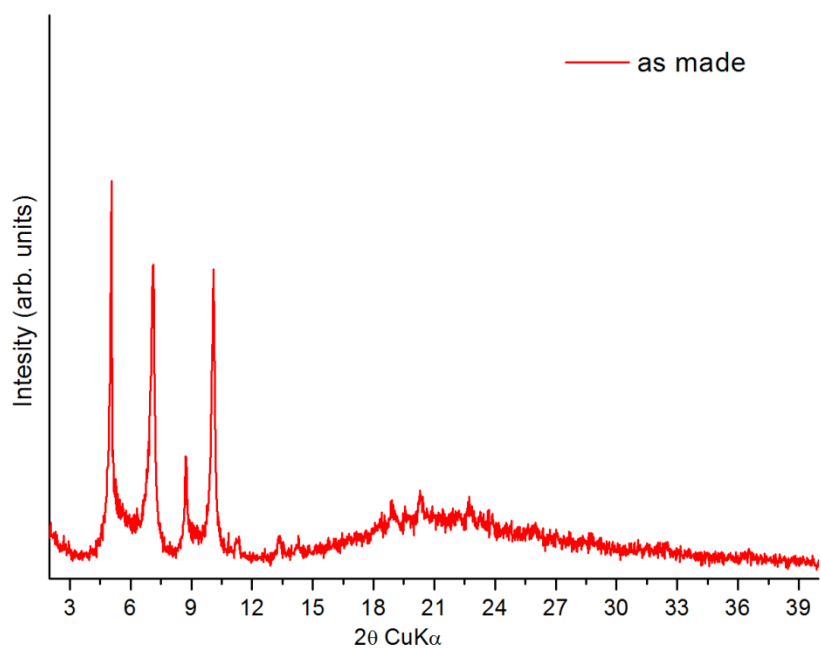
Figure 6.156. Experimental pxrd pattern for compound 6.21.1.
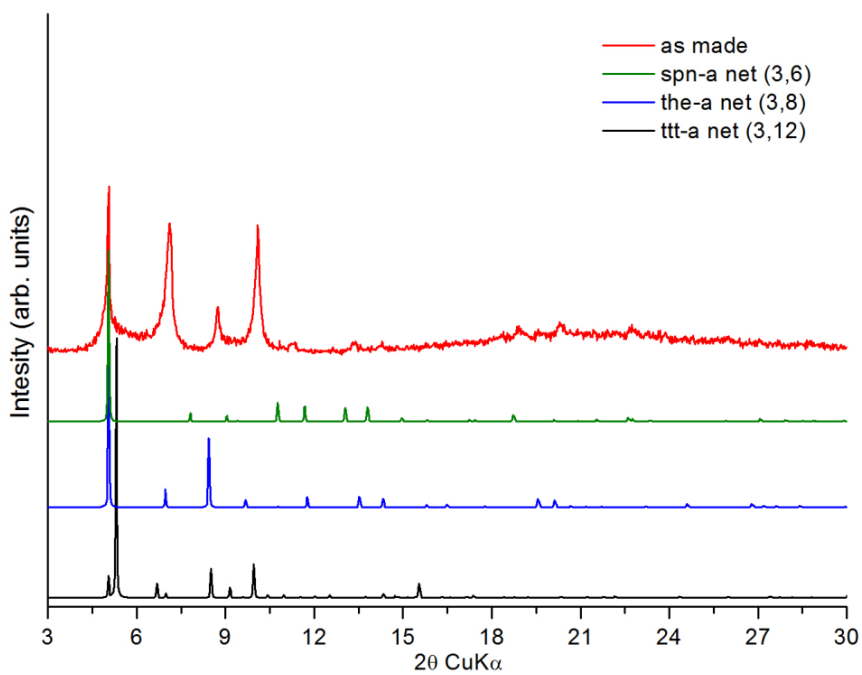
Figure 6.157. Comparison of experimental pxrd pattern for compound 6.21.1, and calculated patterns of compounds with the-a, spn-a and ttt-a net topology.
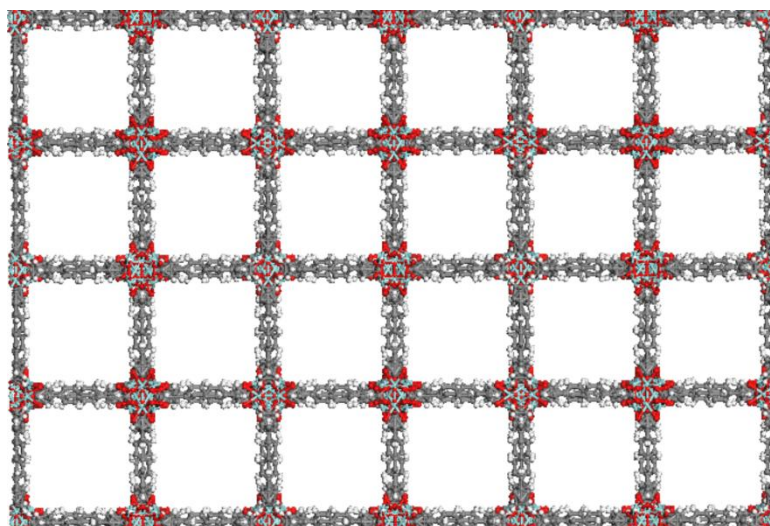
<u>Figure 6.158.</u> Part of the 3-D crystal structure looking down the c axis. The one 2-D net is vertical and the other identical 2-D net is horizontal. Turquoise spheres: Zr, gray: C, red: O, white: H.
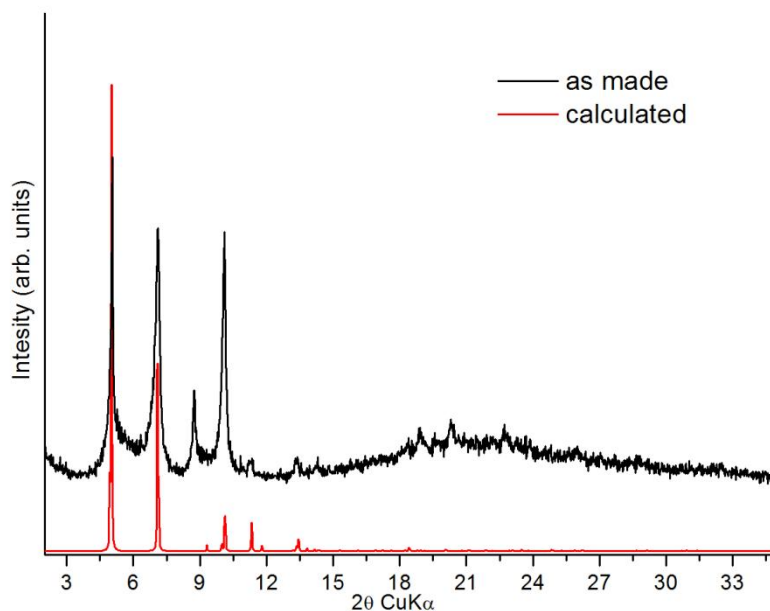
<u>Figure 6.159.</u> Comparison of experimental pxrd pattern for compound 6.21.1 and calculated pattern of compound $Zr_6(\mu_3\text{-}O)_4(\mu_3\text{-}OH)_4(OH)_6(H_2O)_6(BTB)_2$. The experimental peak at $2\theta = 8.77^0$ is expected from the crystal structure.

6.22 Zr-MOF synthesis based on organic linker 36
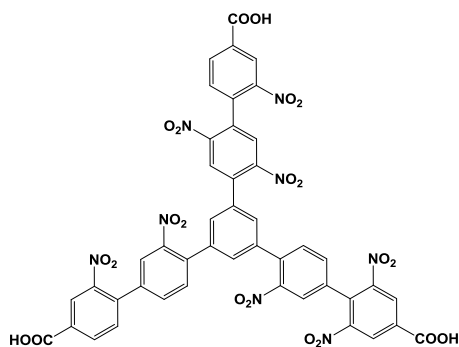
6.22.1 Reaction of linker 36 with ZrCl$_4$

An amount of 0.040 g (0.04 mmol) of H$_3$L and 0.010 g (0.04 mmol) of ZrCl$_4$ were dissolved in a 20 mL glass scintillation vial containing 10 mL DMF and 3 mL glacial acetic acid. The vial was placed in an oven, heated up to 120 ^{0}C with 0.06 ^{0}C/min and then held at 120 ^{0}C for 24 h. After that time an orange solid was deposited.
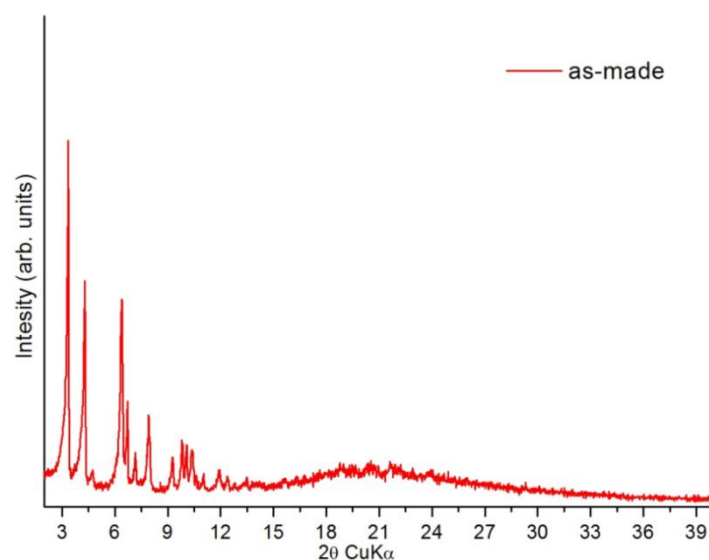
Figure 6.160. Experimental pxrd pattern for compound 6.22.1.
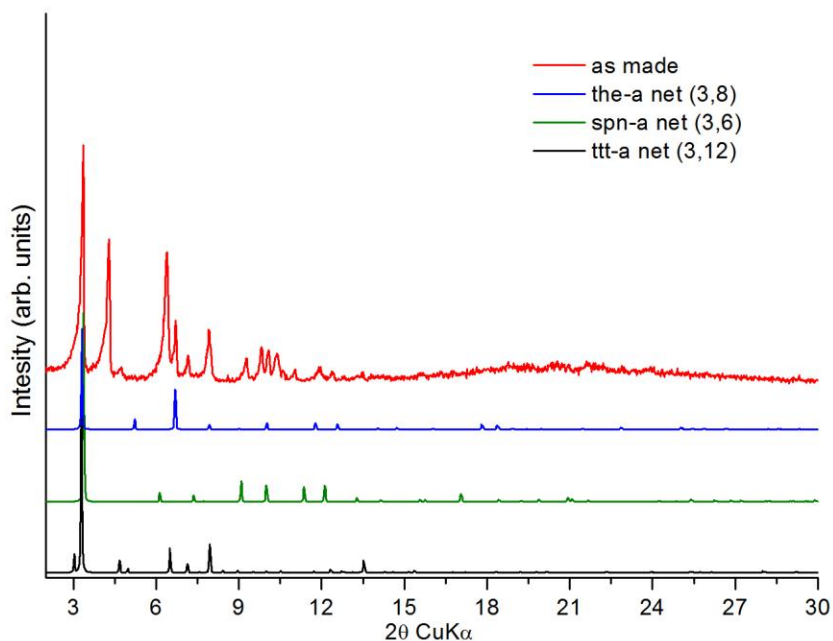
Figure 6.161. Comparison of experimental pxrd pattern for compound 6.22.1, and calculated patterns of compounds with the-a, spn-a and ttt-a net topology.

6.23 Zr-MOF synthesis based on organic linker 39
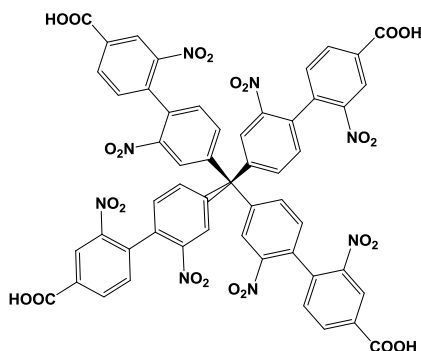
6.23.1 Synthesis of compound $Zr_6(\mu_3\text{-OH})_8(OH)_8)L_2$

An amount of 0.060 g (0.06 mmol) of H_4L, 1500 mg (12.3 mmol) of benzoic acid and 0.060 g (0.26 mmol) of $ZrCl_4$ were dissolved in a 20 mL glass scintillation vial containing 8.5 mL DEF. The vial was placed in an isothermal oven at 120 ^{0}C for 24 h. After that time small yellow crystals were deposited. Yield: 15 % based on H_4L.
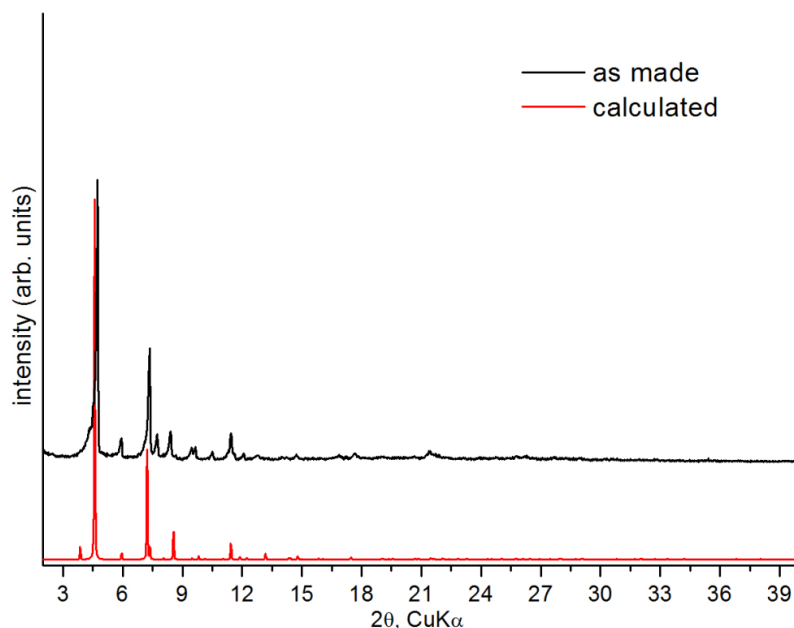
<u>Figure 6.163.</u> Comparison of experimental and calculated pxrd patterns for compound $Zr_6(\mu_3\text{-}OH)_8(OH)_8)L_2$.

6.24 Zr-MOF synthesis based on organic linker 40
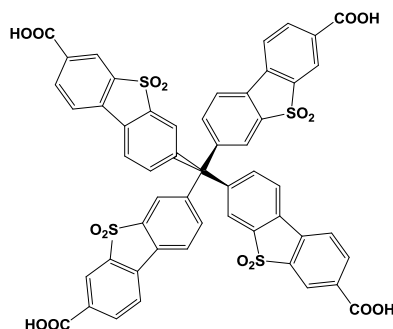
6.24.1 Synthesis of compound $Zr_6(\mu_3\text{-}OH)_8(OH)_8)L_2$

This compound was synthesized using two different synthetic methodologies:

a) An amount of 0.040 g (0.04 mmol) of H_4L, 700 mg (5.70 mmol) of benzoic acid and 0.035 g (0.15 mmol) of $ZrCl_4$ were dissolved in a 20 mL glass scintillation vial containing 9 mL DEF. The vial was placed in an oven, heated up to 120 ^{0}C with 0.06 ^{0}C/ min and then held at 120 ^{0}C for 24 h. After that time a beige solid was deposited. Yield: 15 % based on H_4L.

b) An amount of 0.040 g (0.04 mmol) of H_4L and 0.026 g (0.11 mmol) of $ZrCl_4$ were dissolved in a 20 mL glass scintillation vial containing 10 mL DMF and 2 mL of glacial acetic acid. The vial was placed in an oven, heated up to 120 ^{0}C with 0.06 ^{0}C/ min and then held at 120 ^{0}C for 24 h. After that time a beige solid was deposited. Yield: 15 % based on H_4L.

<u>Figure 6.164.</u> Comparison of experimental and calculated pxrd patterns for compound $Zr_6(\mu_3\text{-}OH)_8(OH)_8)L_2$.

6.25 Zr-MOF synthesis based on organic linker 43
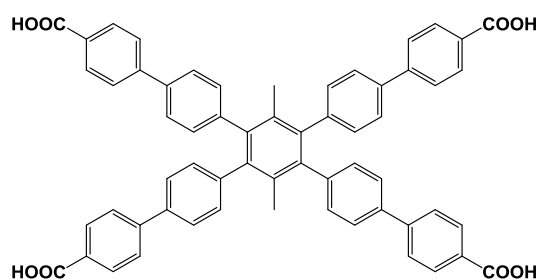
6.25.1 Reaction of linker 43 with $ZrCl_4$

  An amount of 0.035 g (0.04 mmol) of H_4L and 0.030 g (0.13 mmol) of $ZrCl_4$ were dissolved in a 20 mL glass scintillation vial containing 13 mL DMF and 2 mL of glacial acetic acid. The vial was placed in an oven, heated up to 120 ^{0}C with 0.06 ^{0}C/min and then held at 120 ^{0}C for 24 h. After that time small colourless cubic crystals were formed. Yield: 20 % based on H_4L.
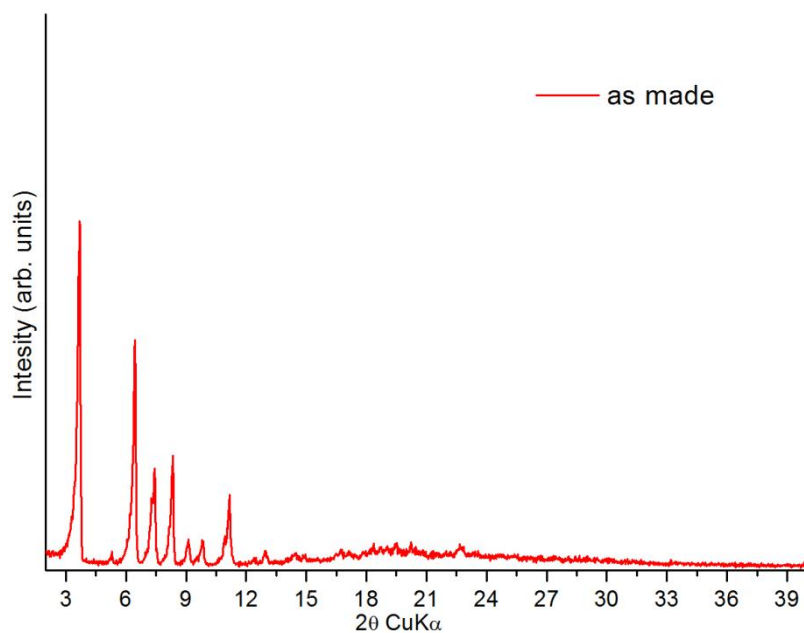
Figure 6.167. Experimental pxrd pattern of compound 6.25.1.
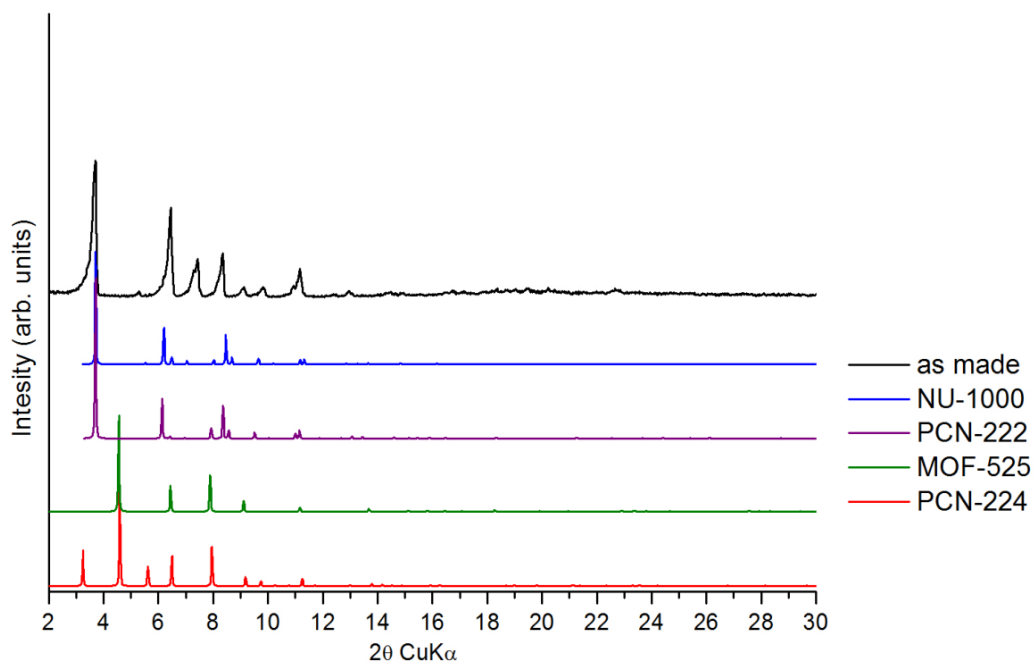
Figure 6.168. Comparison of experimental pxrd pattern of compounds 6.25.1 and calculated patterns of compounds NU-1000, PCN-222, MOF-525 and PCN-224.

6.26 Zr-MOF synthesis based on organic linker 51
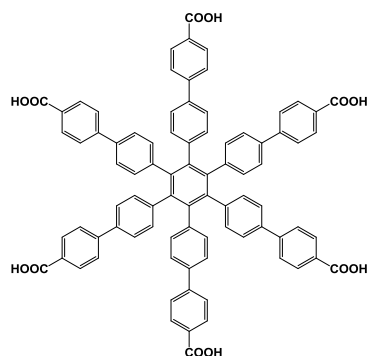
6.26.1 Reaction of linker 51 with $ZrCl_4$

An amount of 0.040 g (0.03 mmol) of linker 51 and 0.031 g (0.13 mmol) of $ZrCl_4$ were dissolved in a 20 mL glass scintillation vial containing 13 mL DMF and 2 mL of glacial acetic acid. The vial was placed in an oven, heated up to 120 ^{0}C with 0.06 ^{0}C/min and then held at 120 ^{0}C for 24 h. After that time small colourless cubic crystals were formed.
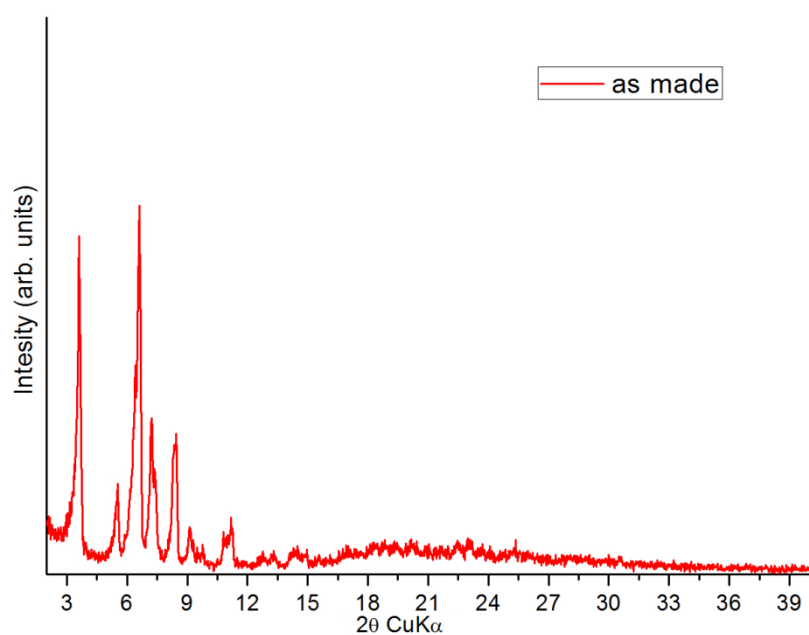
Figure 6.171. Experimental pxrd pattern for the compound 6.26.1.
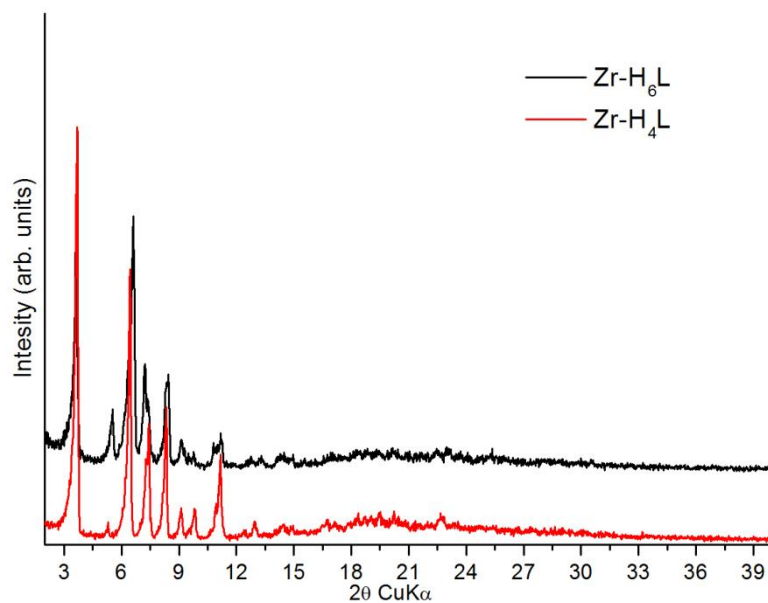
<u>Figure 6.172.</u> Comparison of experimental pxrd patterns for compounds 6.26.1 (Zr-H$_6$L) and 6.25.1 (Zr-H$_4$L).

6.27 IRMOF synthesis based on organic linker 2
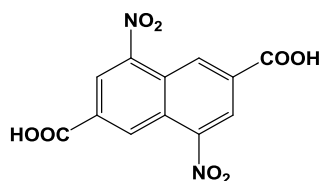
6.27.1 Synthesis of compound IRMOF-8-2NO$_2$ (interpenetrated)

An amount of 0.020 g (0.06 mmol) of 4,8-dinitro-2,6-naphthalene dicarboxylic acid (H$_2$(NDC-2NO$_2$)) and 0.058 g (0.19 mmol) of Zn(NO$_3$)$_2$·6H$_2$O were dissolved in a 20 mL glass scintillation vial containing 10 mL DMF. The vial was heated at 120 ^{0}C for 3 d where dark red cubic crystals were formed. Yield: 30 % based on H$_2$(NDC-2NO$_2$).
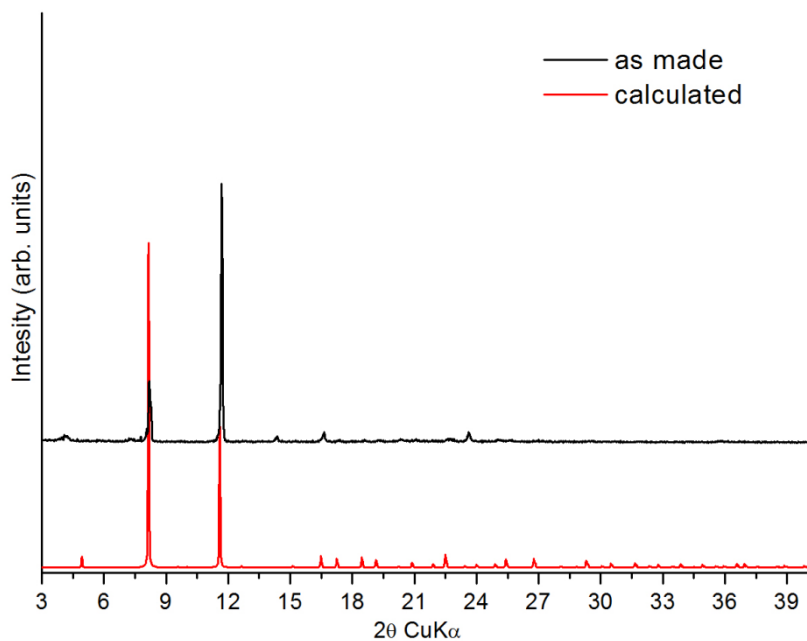
Figure 6.174. Comparison of experimental and calculated pxrd patterns for interpenetrated IRMOF-8-2NO$_2$.

6.28 IRMOF synthesis based on organic linker 3
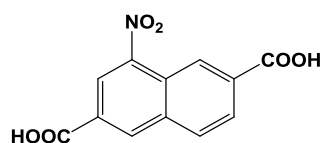
6.28.1 Synthesis of compound IRMOF-8-NO$_2$

An amount of 0.020 g (0.08 mmol) of 4-nitro-2,6-naphthalene dicarboxylic acid (H$_2$(NDC-NO$_2$)) and 0.070 g (0.25 mmol) of Zn(NO$_3$)$_2$·6H$_2$O were dissolved in a 20 mL glass scintillation vial containing 10 mL DMF. The vial was heated at 85 ^{0}C for 3 d where small yellow cubic crystals were formed. Yield: 41 % based on H$_2$(NDC-NO$_2$).
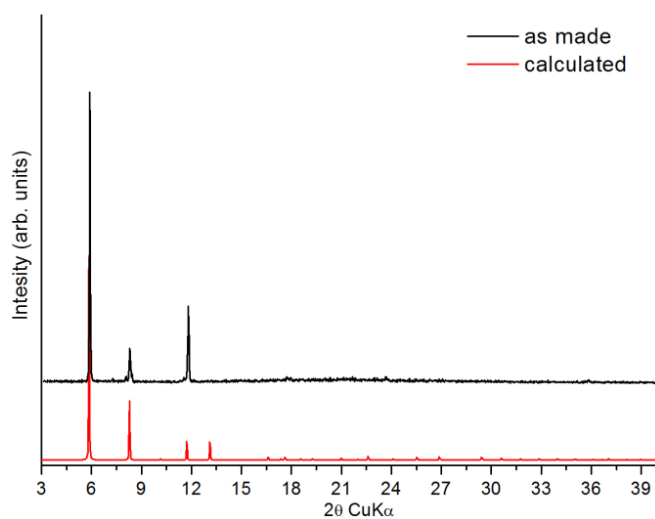
Figure 6.175. Comparison of experimental and calculated pxrd patterns for IRMOF-8-NO$_2$.

6.29 IRMOF synthesis based on organic linker 5
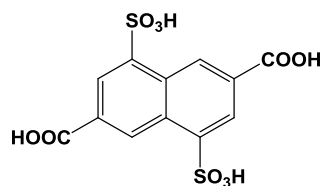
$$SO_3H$$
$$COOH$$
$$HOOC$$
$$SO_3H$$

6.29.1 Synthesis of compound IRMOF-8-2SO$_3$H

The IRMOF-8-SO$_3$H analogue was successfully synthesized using three different synthetic methods:

a) An amount of 0.030 g (0.08 mmol) of 4,8-disulfonyl-2,6-naphthalene dicarboxylic acid (H$_2$(NDC-2SO$_3$H)) and 0.072 g (0.25 mmol) of Zn(NO$_3$)$_2$·6H$_2$O were dissolved in a 20 mL glass scintillation vial containing 6 mL DMF and 4 mL methanol. The vial was heated at 85 ^{0}C for 6 d where small colourless cubic crystals were formed. Yield: 41 % based on H$_2$(NDC-2SO$_3$H).

b) An amount of 0.030 g (0.08 mmol) of 4,8-disulfonyl-2,6-naphthalene dicarboxylic acid (H$_2$(NDC-2SO$_3$H)) and 0.072 g (0.25 mmol) of Zn(NO$_3$)$_2$·6H$_2$O were dissolved in a 20 mL glass scintillation vial containing 6 mL DMF and 4 mL 2-propanol. The vial was heated at 85 ^{0}C for 6 d where small colourless cubic crystals were formed. Yield: 40 % based on H$_2$(NDC-2SO$_3$H).

c) An amount of 0.030 g (0.08 mmol) of 4,8-disulfonyl-2,6-naphthalene dicarboxylic acid (H$_2$(NDC-2SO$_3$H)) and 0.072 g (0.25 mmol) of Zn(NO$_3$)$_2$·6H$_2$O were dissolved in a 20 mL glass scintillation vial containing 6 mL DMF and 4 mL acetonitrile. The vial was heated at 85 ^{0}C for 6 d where small colourless cubic crystals were formed. Yield: 42 % based on H$_2$(NDC-2SO$_3$H).
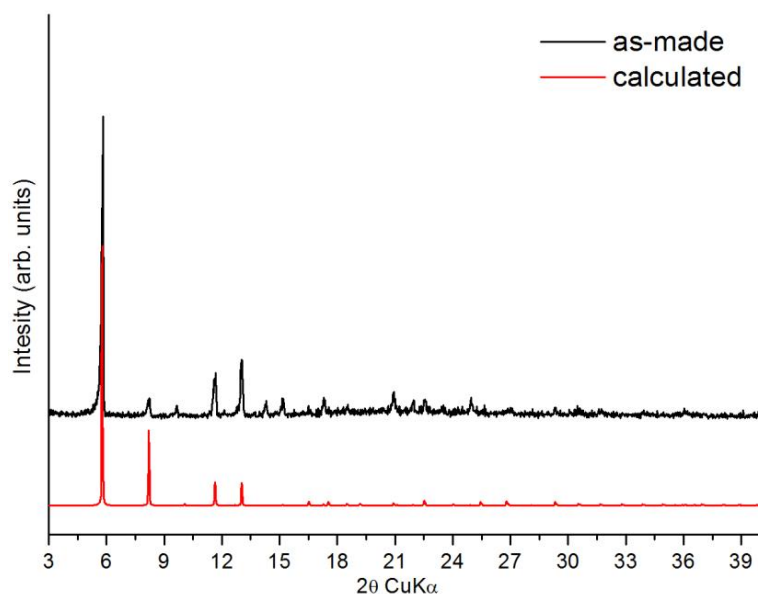
Figure 6.176. Comparison of experimental and calculated pxrd patterns for IRMOF-8-SO$_3$H. All the peaks that are observed to the as made pxrd pattern are predicted from the crystal structure.

6.30 IRMOF syntheses based on organic linker 6
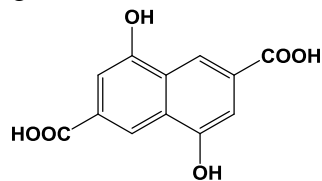
6.30.1 Synthesis of compound IRMOF-8-2OH (Zn)

New synthetic methodologies were developed for the synthesis of an IRMOF:

a) An amount of 0.020 g (0.08 mmol) of 4,8-dihydroxynaphthalene-2,6-dicarboxylic acid (H_2(NDC-2OH)) and 0.079 g (0.25 mmol) of $Zn(NO_3)_2 \cdot 6H_2O$ were dissolved in a 20 mL glass scintillation vial containing 6 mL DMF and 4 mL ethanol. The vial was heated at 85 ^{0}C for 6 h where large, dark orange cubic crystals were formed. Yield: 37 % based on H_2(NDC-2OH).

b) An amount of 0.020 g (0.08 mmol) of 4,8-dihydroxynaphthalene-2,6-dicarboxylic acid (H_2(NDC-2OH)) and 0.079 g (0.25 mmol) of $Zn(NO_3)_2 \cdot 6H_2O$ were dissolved in a 20 mL glass scintillation vial containing 10 mL DMF, 1 mL 2-propanol and 1 mL water. The vial was heated at 70 ^{0}C for 40 h where large, dark orange crystals were formed. Yield: 44 % based on H_2(NDC-2OH).

After the characterization of the MOF, the evaluation of its gas sorption properties took place. The best activation method was found to be the CO_2 supercritical point drying. Prior to analysis, as-made samples were soaked in absolute ethanol at room temperature for three (4) days during of which the supernatant solution was replaced six (8) times. The ethanol suspended samples were transferred inside the chamber of a supercritical CO_2 dryer (Bal-Tec CPD 030) and ethanol was exchanged with liquid CO_2 over a period of 5 hours at 8 ^{o}C. During this period, liquid CO_2 was vented under positive pressure every 3 minutes. The rate of CO_2 venting was always kept below the rate of filling so as to maintain full drying conditions inside the chamber. Following venting, the temperature was raised to 40 ºC (above the critical temperature of CO_2), kept there for 1 hour and then slowly vented over the period of 2 hours. The dried sample was transferred immediately inside a pre-weighted, Argon filled 9 mm cell and closed using CellSeal[TM] provided by Quantachrome to prevent intrusion of oxygen and atmospheric moisture during transfers and weighing.
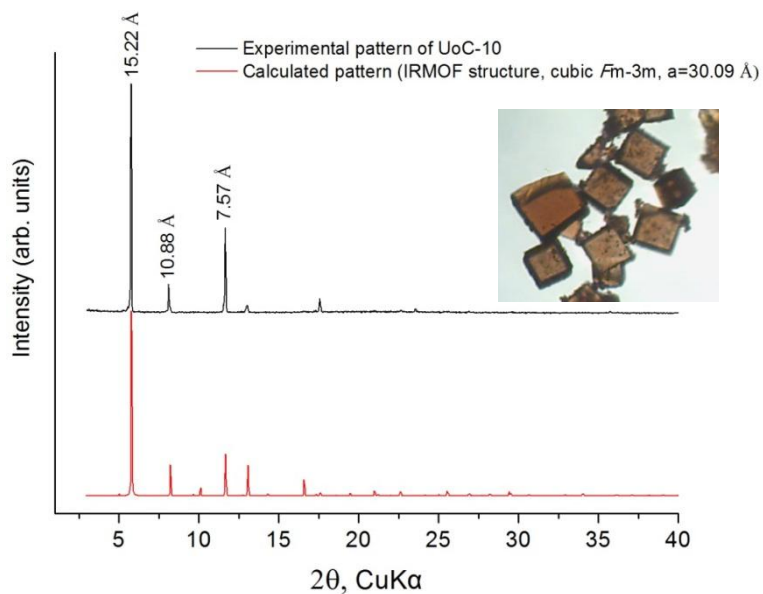
Figure 6.178. Comparison of experimental and calculated pxrd patterns for IRMOF-8-2OH. Inset picture shows the brown crystals of IRMOF-8-2OH.
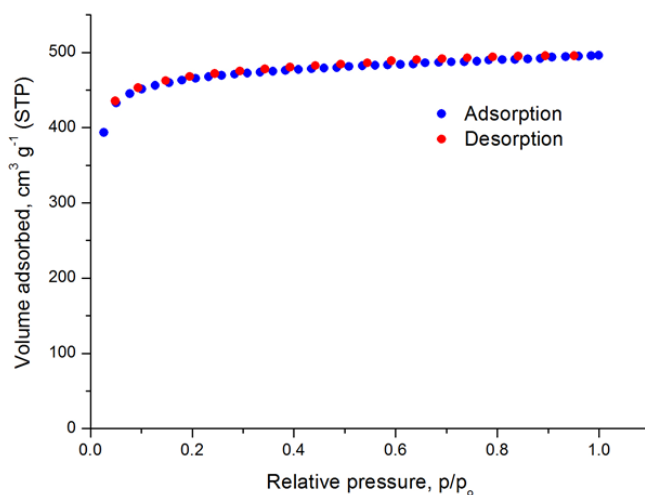
Figure 6.179. Nitrogen sorption isotherm of IRMOF-8-2OH at 77 K.
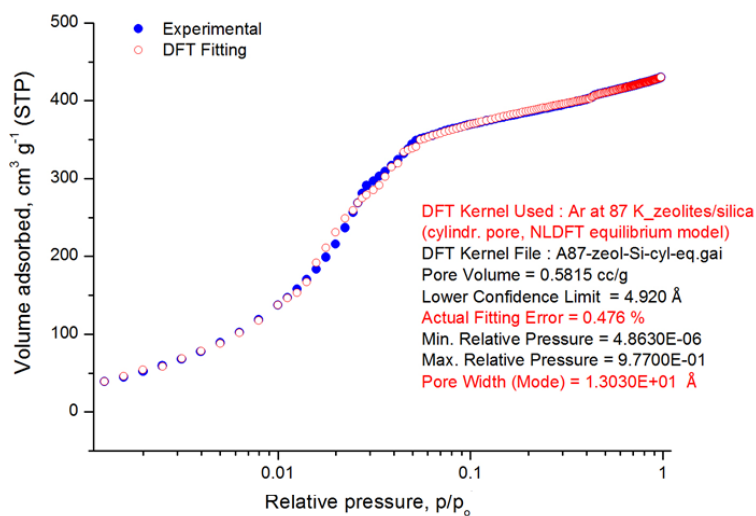
Figure 6.180. Argon sorption isotherm of IRMOF-8-2OH at 87 K and the corresponding NLDFT fitting.
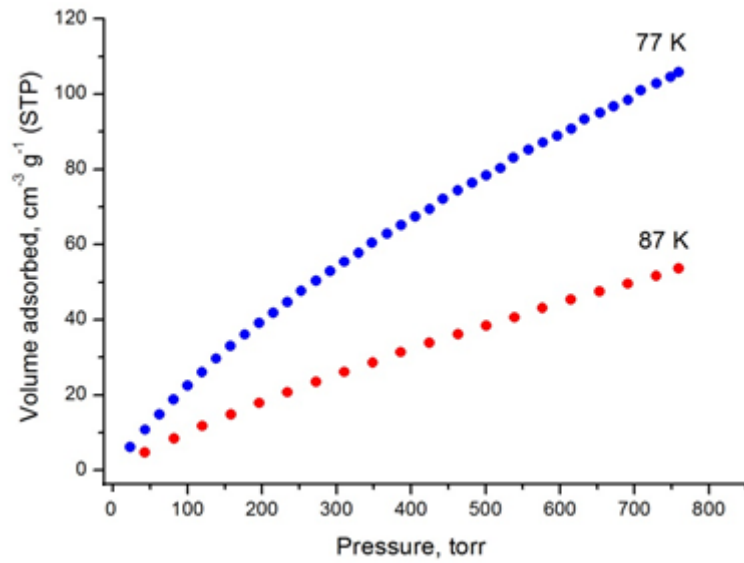
Figure 6.181. Hydrogen adsorption isotherms of IRMOF-8-2OH at 77 K and 87 K.
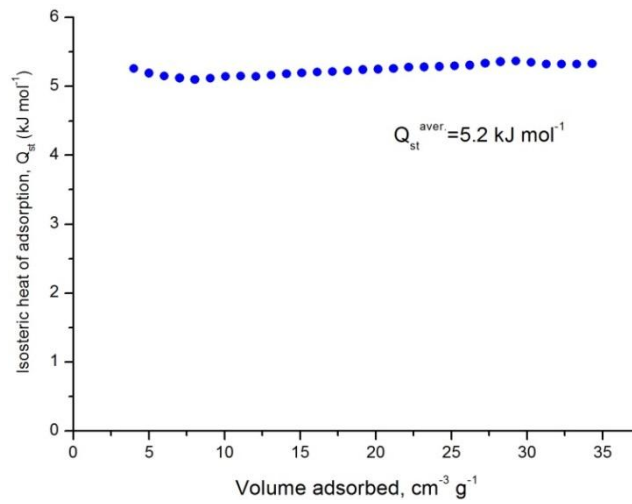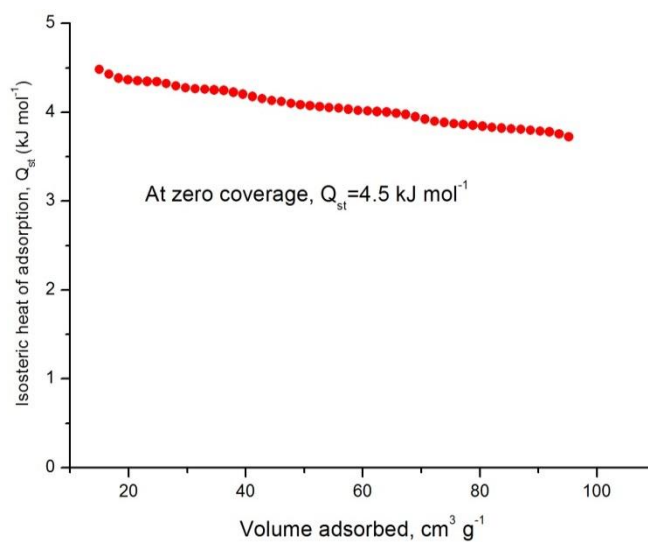

Figure 6.182. H$_2$ isosteric heat of adsorption in IRMOF-8-2OH as a function of surface coverage.
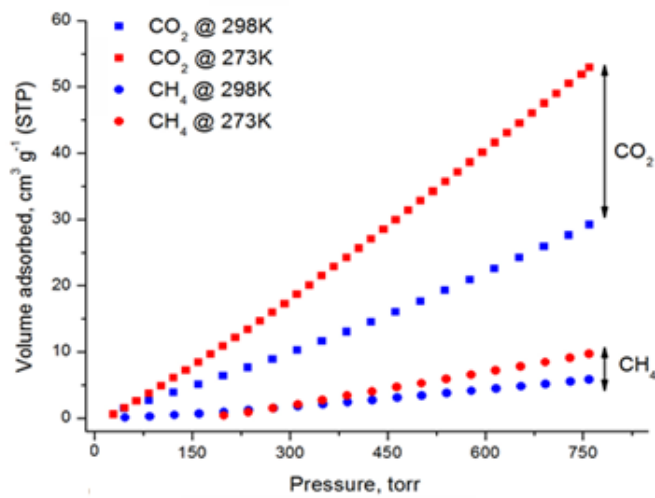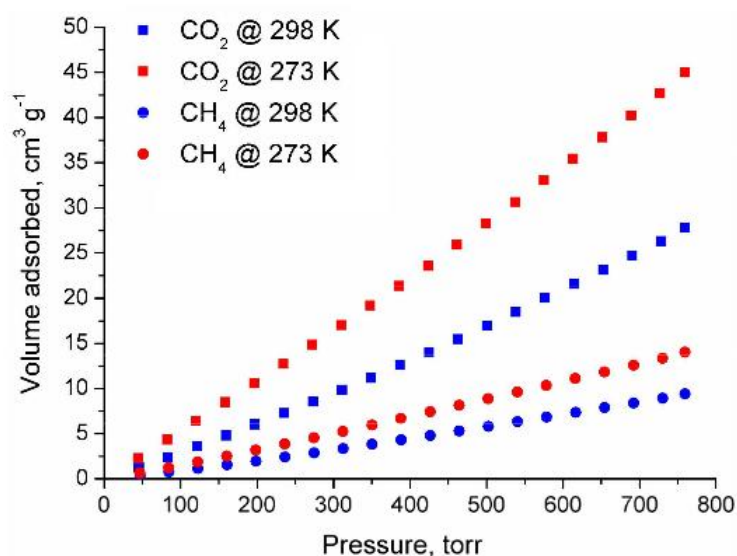

Figure 6.183. CO$_2$ and CH$_4$ adsorption isotherms of IRMOF-8-2OH at 273 K and 298 K.
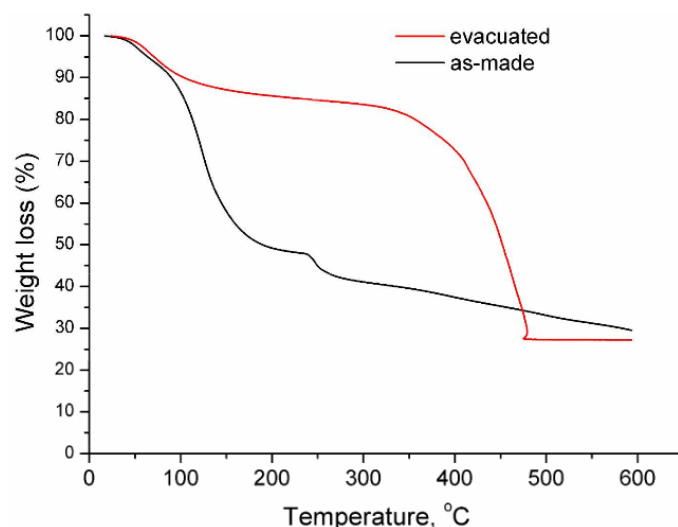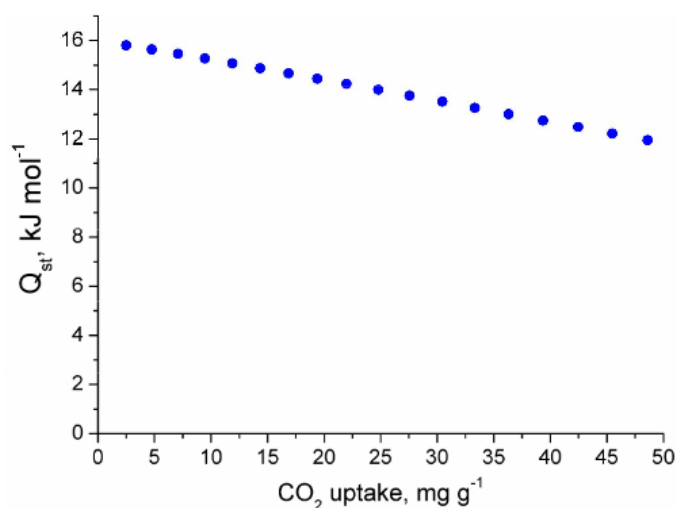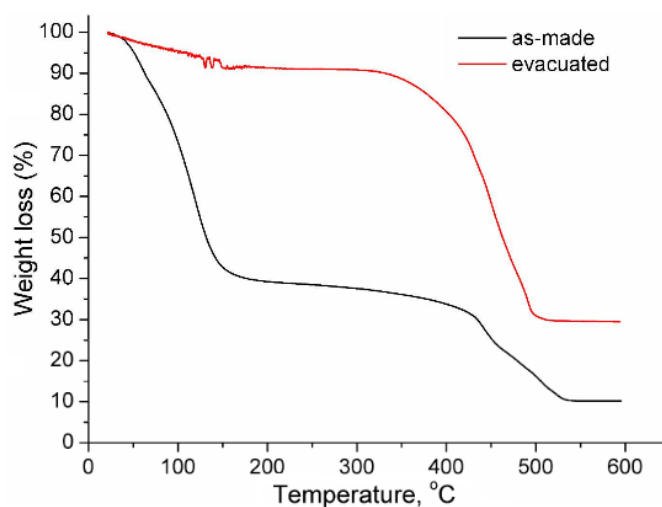
Figure 6.184. TGA curve for the as made IRMOF-8-2OH and the corresponding evacuated solid obtained after CO_2 SCD process, recorded under Ar flow with a heating rate of 5 deg/min.

6.30.2 Synthesis of compound IRMOF-8-2OH (Co)

An amount of 0.025 g (0.10 mmol) of 4,8-dihydroxynaphthalene-2,6-dicarboxylic acid (H$_2$(NDC-2OH)) and 0.057 g (0.24 mmol) of CoCl$_2$·6H$_2$O were dissolved in a 20 mL glass scintillation vial containing 6 mL DMF and 4 mL ethanol. The vial was heated at 85 ^{0}C for 15 h where large, dark blue truncated cubic crystals were formed. Yield: 40 % based on H$_2$(NDC-2OH).
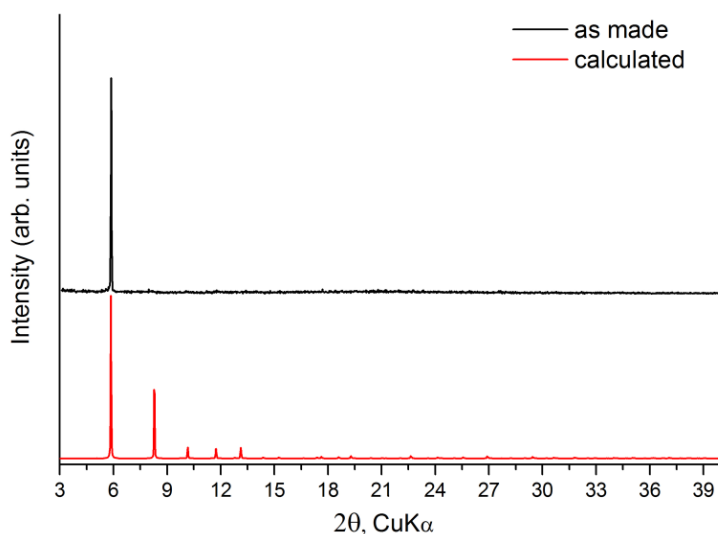
Figure 6.186. Comparison of experimental and calculated pxrd patterns for IRMOF-8-2OH (Co).
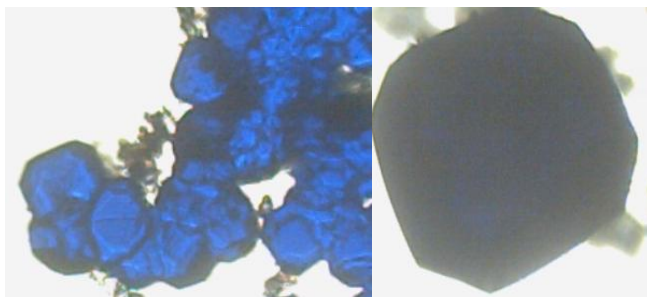
Figure 6.187. Uniform blue single crystals of IRMOF-8-2OH (Co).
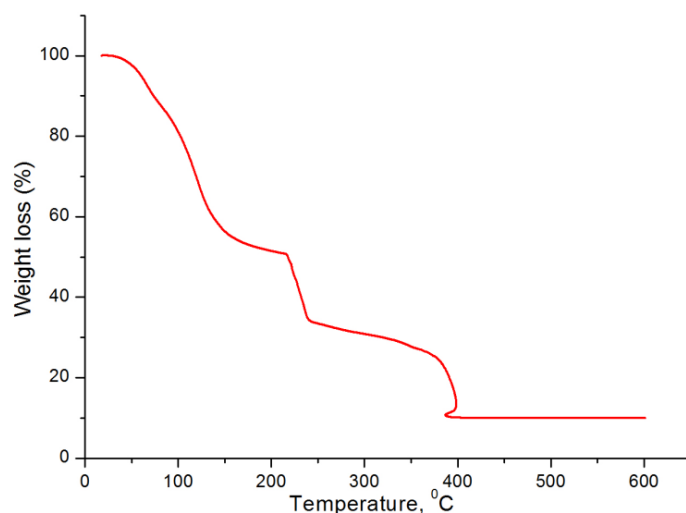
Figure 6.188. TGA curve for the as made IRMOF-8-2OH (Co) recorded under Ar flow with a heating rate of 5 deg/min.

6.30.3 Syntheses of mix-metal compounds IRMOF-8-2OH (Zn: Mg, Mn, Co, Ni, Cd)

Zn-Co: An amount of 0.020 g (0.08 mmol) of 4,8-dihydroxynaphthalene-2,6-dicarboxylic acid (H$_2$(NDC-2OH)), 0.041 g (0.13 mmol) of Zn(NO$_3$)$_2$·6H$_2$O and 0.086 g (0.26 mmol) of Co(NO$_3$)$_2$·6H$_2$O were dissolved in a 20 mL glass scintillation vial containing 10 mL DMF, 1 mL 2-propanol and 1 mL water. The vial was heated at 70 ^{0}C for 40 h where large, dark orange crystals were formed. Yield: 37 % based on H$_2$(NDC-2OH).

Zn-Ni: An amount of 0.020 g (0.08 mmol) of 4,8-dihydroxynaphthalene-2,6-dicarboxylic acid (H$_2$(NDC-2OH)), 0.041 g (0.13 mmol) of Zn(NO$_3$)$_2$·6H$_2$O and 0.086 g (0.26 mmol) of Ni(NO$_3$)$_2$·6H$_2$O were dissolved in a 20 mL glass scintillation vial containing 10 mL DMF, 1 mL 2-propanol and 1 mL water. The vial was heated at 70 ^{0}C for 40 h where large, dark orange crystals were formed. Yield: 37 % based on H$_2$(NDC-2OH).

Zn-Mn: An amount of 0.020 g (0.08 mmol) of 4,8-dihydroxynaphthalene-2,6-dicarboxylic acid (H$_2$(NDC-2OH)), 0.041 g (0.13 mmol) of Zn(NO$_3$)$_2$·6H$_2$O and 0.061 g (0.24 mmol) of Mn(NO$_3$)$_2$·4H$_2$O were dissolved in a 20 mL glass scintillation vial containing 10 mL DMF, 1 mL 2-propanol and 1 mL water. The vial was heated at 70 ^{0}C for 40 h where large, dark orange crystals were formed. Yield: 37 % based on H$_2$(NDC-2OH).

Zn-Cd: An amount of 0.020 g (0.08 mmol) of 4,8-dihydroxynaphthalene-2,6-dicarboxylic acid (H$_2$(NDC-2OH)), 0.041 g (0.13 mmol) of Zn(NO$_3$)$_2$·6H$_2$O and 0.075 g (0.24 mmol) of Cd(NO$_3$)$_2$·4H$_2$O were dissolved in a 20 mL glass scintillation vial containing 10 mL DMF, 1 mL 2-propanol and 1 mL water. The vial was heated at 70 ^{0}C for 40 h where large, dark orange crystals were formed. Yield: 37 % based on H$_2$(NDC-2OH).

Zn-Mg: An amount of 0.020 g (0.08 mmol) of 4,8-dihydroxynaphthalene-2,6-dicarboxylic acid (H$_2$(NDC-2OH)), 0.041 g (0.13 mmol) of Zn(NO$_3$)$_2$·6H$_2$O and 0.066 g (0.26 mmol) of

$Mg(NO_3)_2 \cdot 6H_2O$ were dissolved in a 20 mL glass scintillation vial containing 10 mL DMF, 1 mL 2-propanol and 1 mL water. The vial was heated at 70 ^{0}C for 40 h where large, dark orange crystals were formed. Yield: 37 % based on $H_2(NDC-2OH)$.
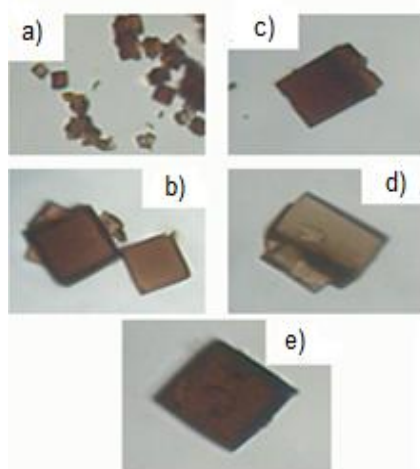
Figure 6.189. Optical microscope pictures of the acquired single crystals for the mix-metal IRMOF-8-2OH analogues: a) Zn-Mg, b) Zn-Mn, c) Zn-Co, d) Zn-Ni, e) Zn-Cd.
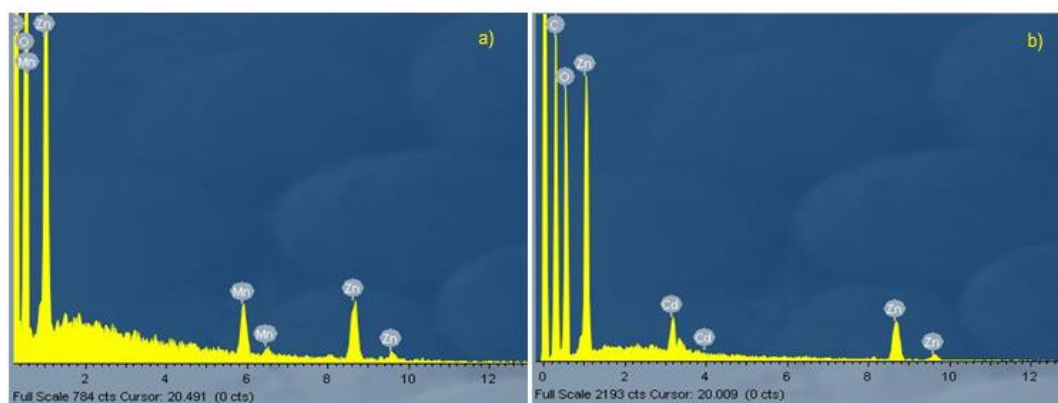
Figure 6.190. The EDS measurements for the mix-metal IRMOF-8-2OH analogues: a) Zn-Mn and b) Zn-Cd.
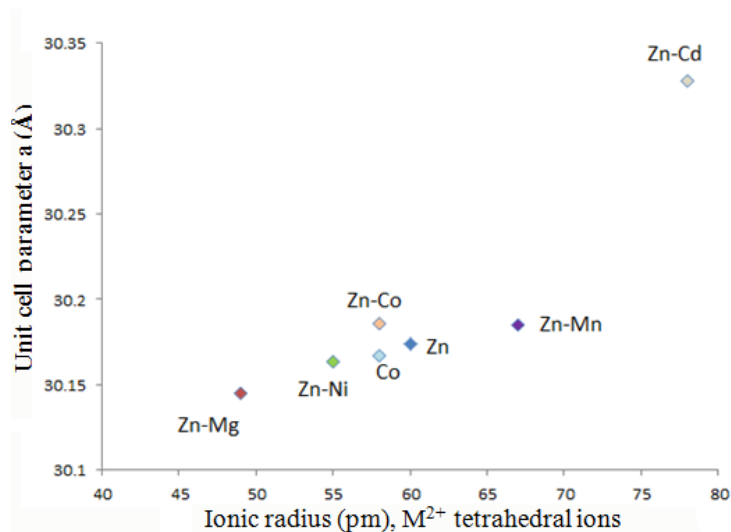
Figure 6.191. This graph shows the relationship between the ionic radius of the metal ions and the unit cell parameter a. The material containing the metal ion with the smaller ionic radius exhibits a lower unit cell parameter in comparison to the material containing larger metal ions.[1]
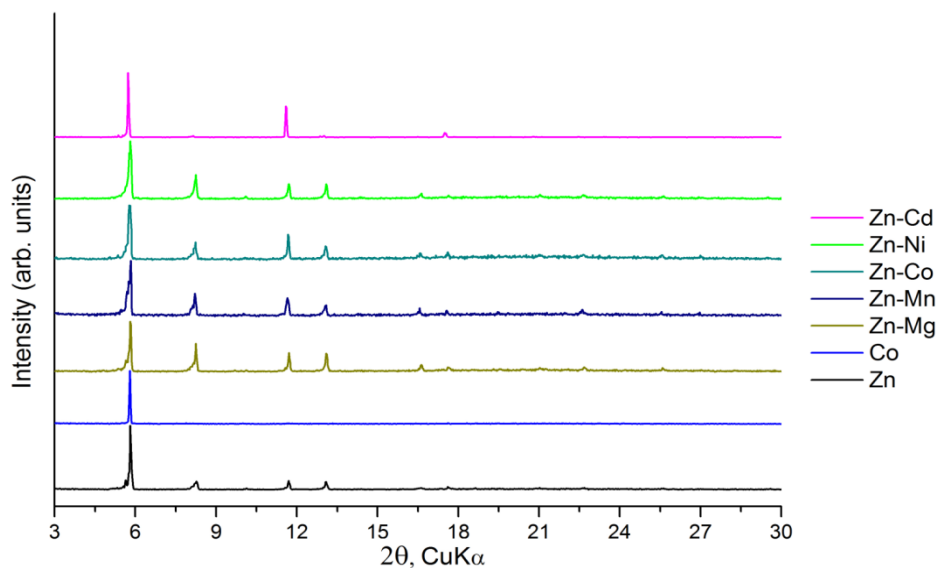
Figure 6.192. Comparison of experimental pxrd patterns for all mix metal IRMOF-8-2OH analogues, including the zinc and cobalt parent materials.
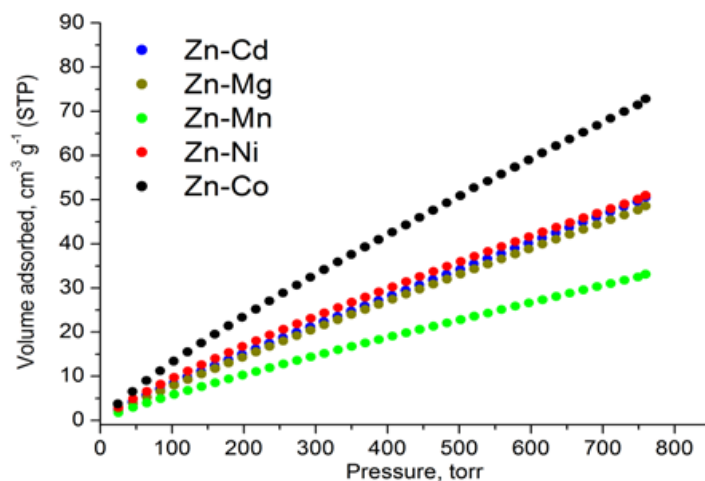
Figure 6.193. CO_2 adsorption isotherms for all samples recorded at 273 K.
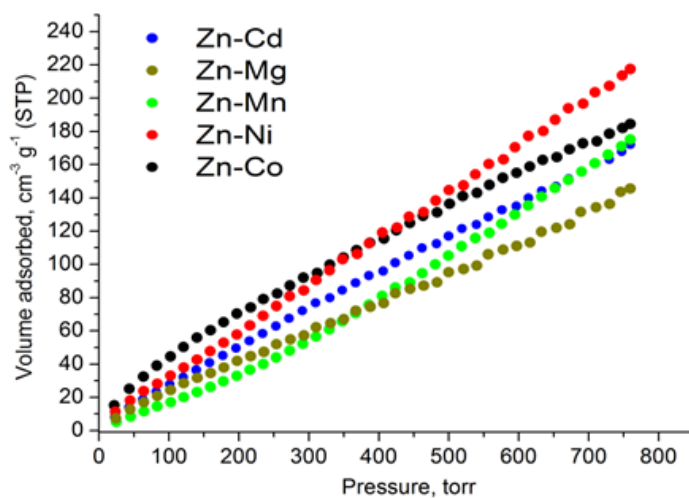
Figure 6.194. H_2 adsorption isotherms for all samples at recorded at 77 K.

Table 6.4. Gas sorption data for all samples including the parent analogue containing only Zn^{2+}.

	S.A BET $(m^2 g^{-1})$	CO_2 uptake 195 K $(mmol\ g^{-1})$	CO_2 uptake 273 K $(mmol\ g^{-1})$	CO_2 uptake 298 K $(mmol\ g^{-1})$	CH_4 uptake 273 K $(mmol\ g^{-1})$	CH_4 uptake 298 K $(mmol\ g^{-1})$	H_2 uptake 77 K $(mmol\ g^{-1})$	H_2 uptake 87 K $(mmol\ g^{-1})$
Zn-Co	1472	13.82	**3.25**	**1.93**	**0.83**	0.25	8.24	**6.93**
Zn-Ni	1032	12.16	2.28	1.41	0.53	0.004	**9.72**	4.71
Zn-Mg	1548	11.29	2.17	1.41	0.55	0.19	6.5	4.99
Zn-Mn	770	9.47	1.48	0.99	0.4	0.12	7.83	4.07
Zn-Cd	**1897**	**14.18**	2.26	1.36	0.55	**0.26**	7.69	4.73
Zn	1927	14.56	2.41	1.34	0.45	0.27	4.7	2.59

Table 6.5. Isoteric heat of adsorption for H_2, CO_2 and selectivity values calculated at 273 K for all samples including the parent analogue containing only Zn^{2+}.

	H_2 Q_{st} $(kJ\ mol^{-1})$	CO_2 Q_{st} $(kJ\ mol^{-1})$	Selectivity CO_2/CH_4 273 K
Zn-Co	5.65	24.97	6.96
Zn-Ni	5.78	**25.77**	10.62
Zn-Mg	**5.95**	21.66	6.78
Zn-Mn	3.14	25.46	7.05
Zn-Cd	3.53	22.99	6.38
Zn	5.2	12.5	**13.6**
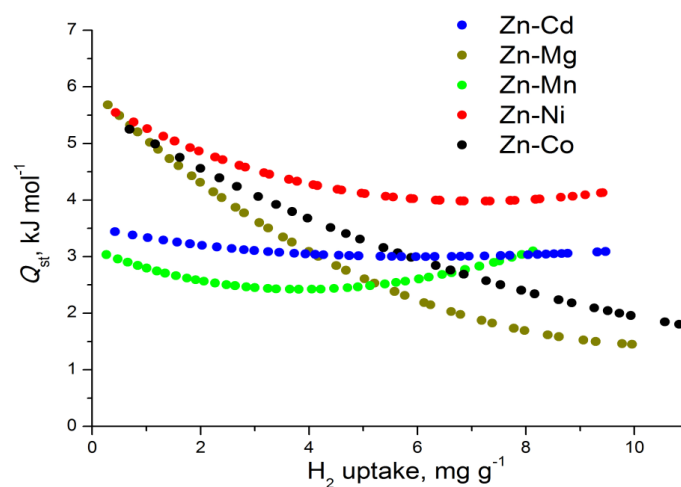
Figure 6.195. H_2 isosteric heat of adsorption for all samples as a function of surface coverage.
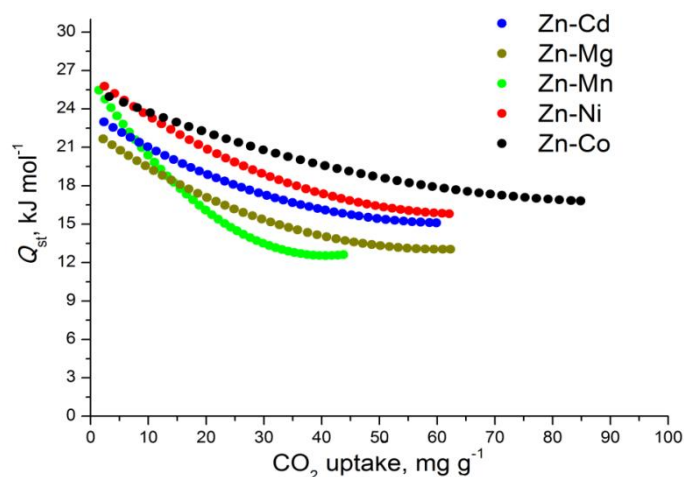
Figure 6.196. CO$_2$ isosteric heat of adsorption for all samples as a function of surface coverage.

6.31 IRMOF synthesis based on organic linker 16
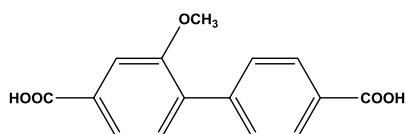
6.31.1 Synthesis of compound IRMOF-10-OCH$_3$

An amount of 0.020 g (0.07 mmol) of H$_2$BPDC-OCH$_3$ and 0.065 g (0.22 mmol) of Zn(NO$_3$)$_2$·6H$_2$O were dissolved in a 20 mL glass scintillation vial containing 6 mL DMF and 4 mL ethanol. The vial was heated at 85 ^{0}C for 48 h where small, colourless cubic crystals were formed. Yield: 30 % based on H$_2$BPDC-OCH$_3$.
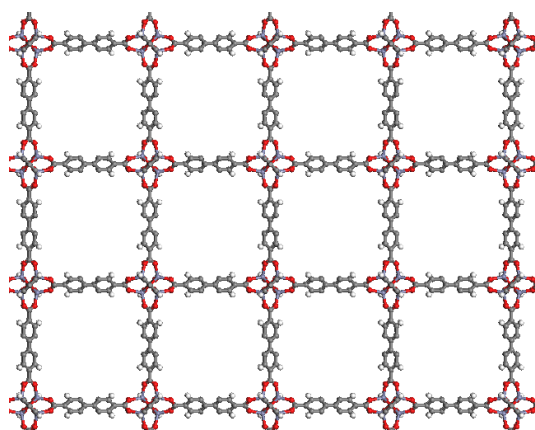
Figure 6.197. Part of the 3-D structure of compound IRMOF-10. Purple spheres: Zn, gray: C, red: O, white: H. Solvent molecules are omitted for clarity.
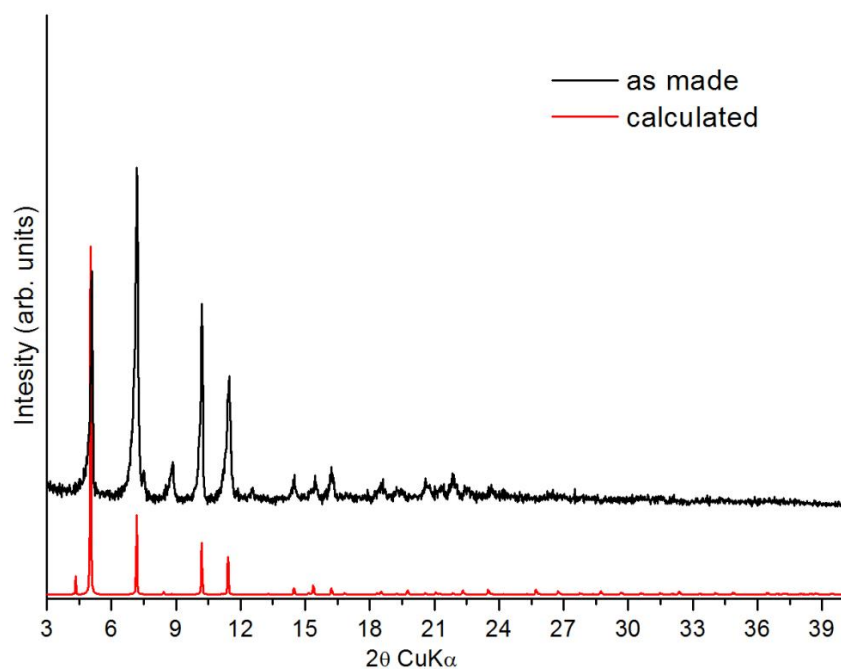
Figure 6.198. Comparison of experimental and calculated pxrd patterns for IRMOF-10-OCH$_3$.

6.32 IRMOF synthesis based on organic linker 23
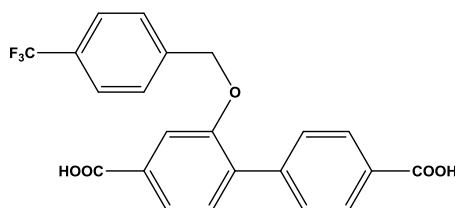
6.32.1 Synthesis of compound IRMOF-10-OBenzyl-CF$_3$

An amount of 0.020 g (0.05 mmol) of H$_2$BPDC-OBenzyl-CF$_3$ and 0.043 g (0.14 mmol) of Zn(NO$_3$)$_2$·6H$_2$O were dissolved in a 20 mL glass scintillation vial containing 6 mL DMF and 4 mL ethanol. The vial was heated at 85 ^{0}C for 24 h where small, colourless cubic crystals were formed. Yield: 30 % based on H$_2$BPDC-OBenzyl-CF$_3$.
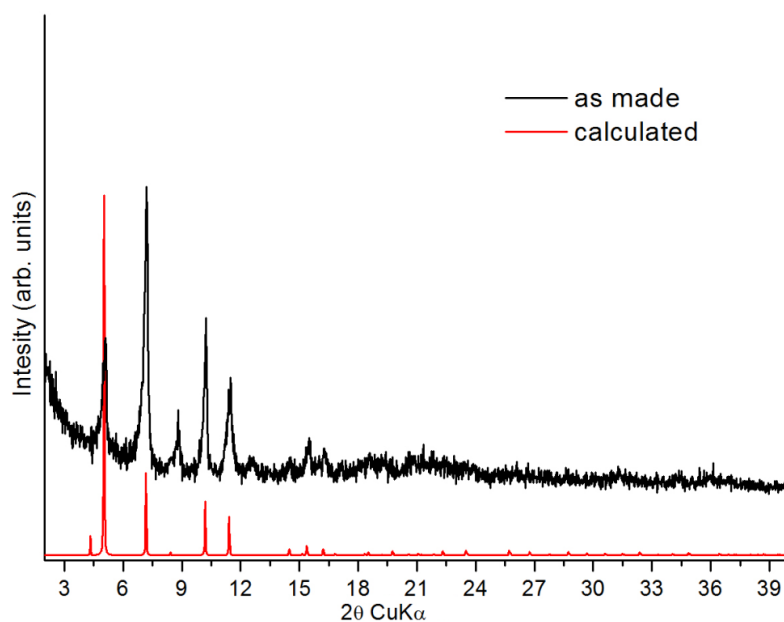
Figure 6.199. Comparison of experimental and calculated pxrd patterns for IRMOF-10-OBenzyl-CF$_3$.

6.33 IRMOF synthesis based on organic linker 20
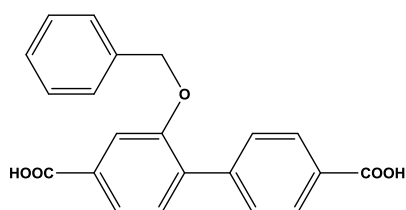
6.33.1 Synthesis of compound IRMOF-10-OPh

An amount of 0.020 g (0.06 mmol) of H$_2$BPDC-OPh and 0.051 g (0.17 mmol) of Zn(NO$_3$)$_2$·6H$_2$O were dissolved in a 20 mL glass scintillation vial containing 6 mL DMF and 4 mL ethanol. The vial was heated at 85 ^{0}C for 48 h where small, colourless cubic crystals were formed. Yield: 30 % based on H$_2$BPDC-OPh.

244
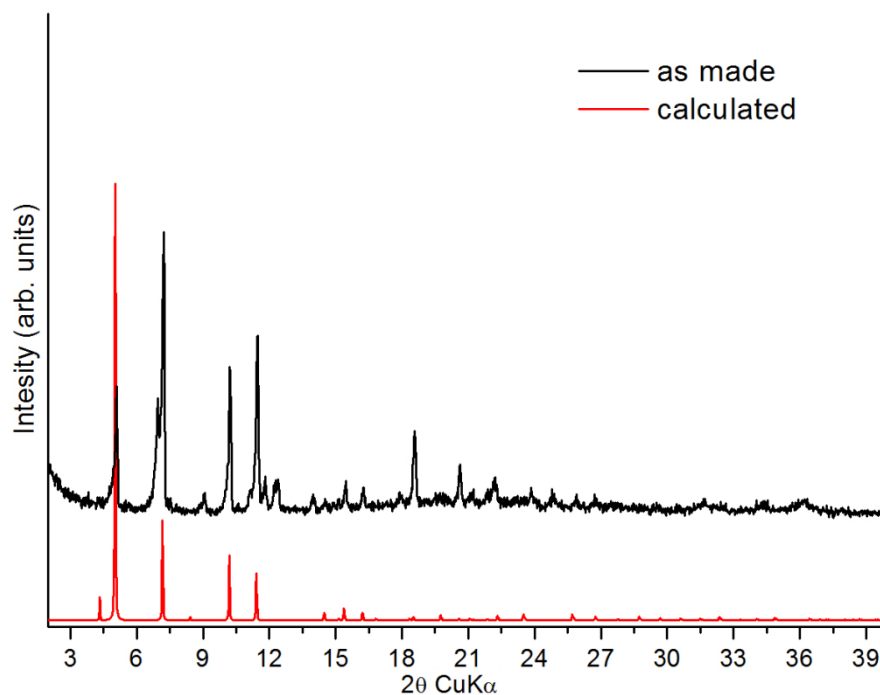
Figure 6.200. Comparison of experimental and calculated pxrd patterns for IRMOF-10-OPh.

6.34 IRMOF synthesis based on organic linker 17
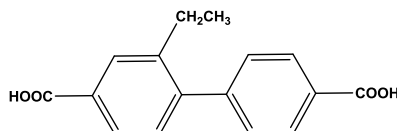
6.34.1 Synthesis of compound IRMOF-10-OEt

An amount of 0.020 g (0.07 mmol) of H_2BPDC-OEt and 0.021 g (0.07 mmol) of $Zn(NO_3)_2 \cdot 6H_2O$ were dissolved in a 20 mL glass scintillation vial containing 6 mL DMF and 4 mL ethanol. The vial was heated at 70 ^{0}C for 48 h where small, colourless cubic crystals were formed. Yield: 30 % based on H_2BPDC-OEt.
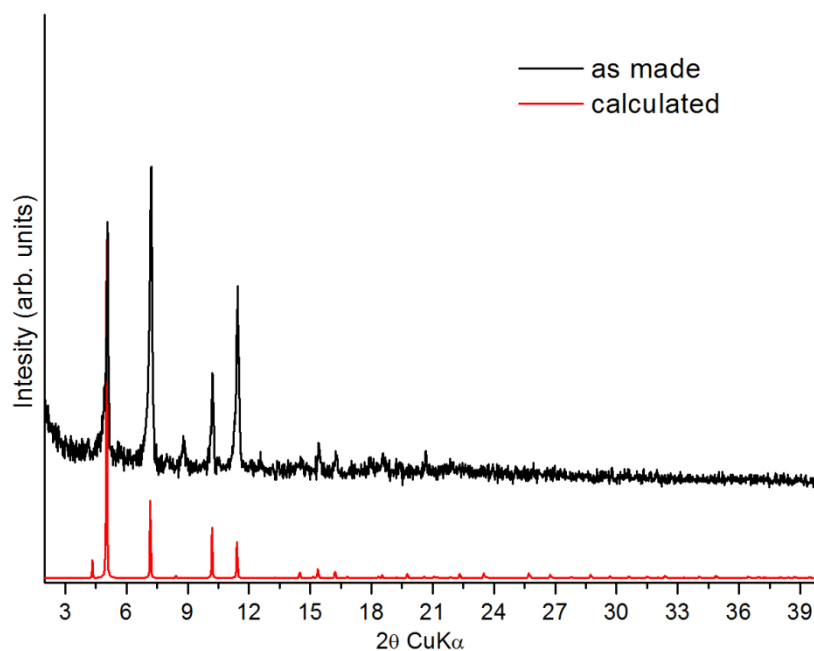
Figure 6.201. Comparison of experimental and calculated pxrd patterns for IRMOF-10-OEt.

6.35 MOF synthesis based on organic linker 5
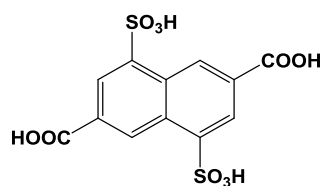
6.35.1 Synthesis of compound In(NDC-2SO$_3$H)$_2$(Me$_2$NH$_2$)

An amount of 0.030 g (0.08 mmol) of 4,8-disulfonyl-2,6-naphthalene dicarboxylic acid (H$_2$(NDC-2SO$_3$H)) and 0.077 g (0.25 mmol) of In(NO$_3$)$_3$xH$_2$O were dissolved in a 20 mL glass scintillation vial containing 6 mL DMF, 4 mL ethanol and 3 drops of c.HCl. The vial was heated at 85 ^{0}C for 2 d where large, orange cubic crystals were formed. Yield: 40 % based on H$_2$(NDC-2SO$_3$H).
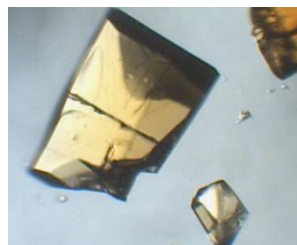
Figure 6.203. Optical microscope picture of In(NDC-2SO$_3$H)$_2$(Me$_2$NH$_2$) crystals.
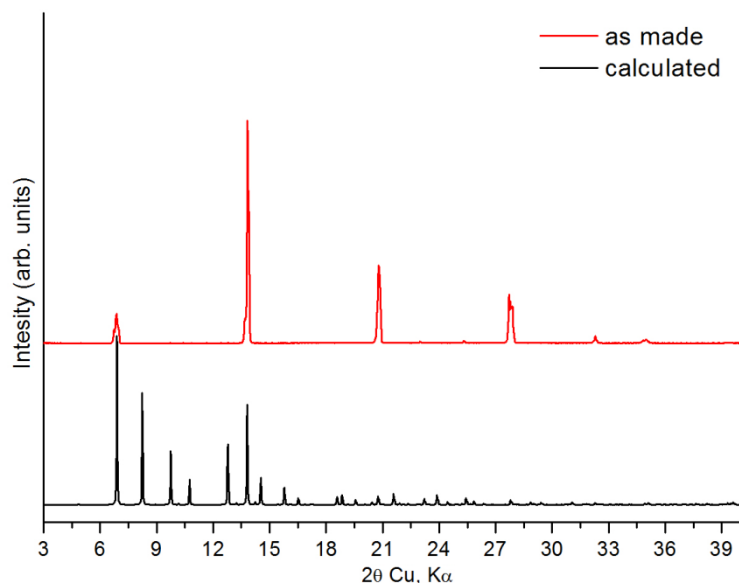
Figure 6.204. Comparison of experimental and calculated pxrd patterns for In(NDC-2SO$_3$H)$_2$(Me$_2$NH$_2$). The differences of the two patterns are attributed to preferred orientation.

6.36 MOF syntheses based on organic linker 6
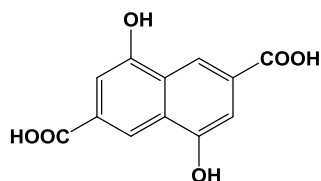
6.36.1 Synthesis of compound Co(NDC-2OH)(DMF)$_2$

An amount of 0.030 g (0.12 mmol) of 4,8-dihydroxynaphthalene-2,6-dicarboxylic acid (H$_2$(NDC-2OH)), 0.110 g (0.37 mmol) of Co(NO$_3$)$_2$·6H$_2$O were dissolved in a 20 mL glass scintillation vial containing 7 mL DMF and 3 mL ethanol. The vial was heated at 85 ^{0}C for 10 h where large, pink crystals were formed. Yield: 36 % based on H$_2$(NDC-2OH).

6.36.2 Synthesis of compound Pr(NDC-2OH)(Cl)(DMF)$_6$

An amount of 0.020 g (0.08 mmol) of 4,8-dihydroxynaphthalene-2,6-dicarboxylic acid (H$_2$(NDC-2OH)), 0.090 g (0.3 mmol) of PrCl$_3$xH$_2$O were dissolved in a 20 mL glass scintillation vial containing 6 mL DMF and 4 mL ethanol. The vial was heated at 85 ^{0}C for 10 h where pale green plate crystals were formed. Yield: 33 % based on H$_2$(NDC-2OH).

247
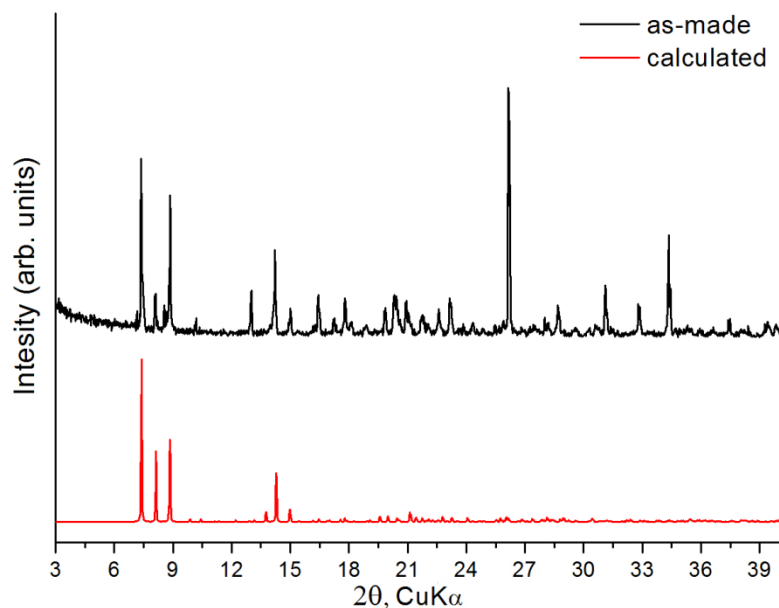
Figure 6.208. Comparison of experimental and calculated pxrd patterns for Pr(NDC-2OH)(Cl)(DMF)$_6$.

6.36.3 Synthesis of compound Eu(NDC-2OH)(Cl)(DMF)$_2$

An amount of 0.020 g (0.08 mmol) of 4,8-dihydroxynaphthalene-2,6-dicarboxylic acid (H$_2$(NDC-2OH)), 0.093 g (0.25 mmol) of EuCl$_3$·6H$_2$O were dissolved in a 20 mL glass scintillation vial containing 6 mL DMF and 4 mL ethanol. The vial was heated at 85 ^{0}C for 10 h where plate crystals were formed. Yield: 30 % based on H$_2$(NDC-2OH).
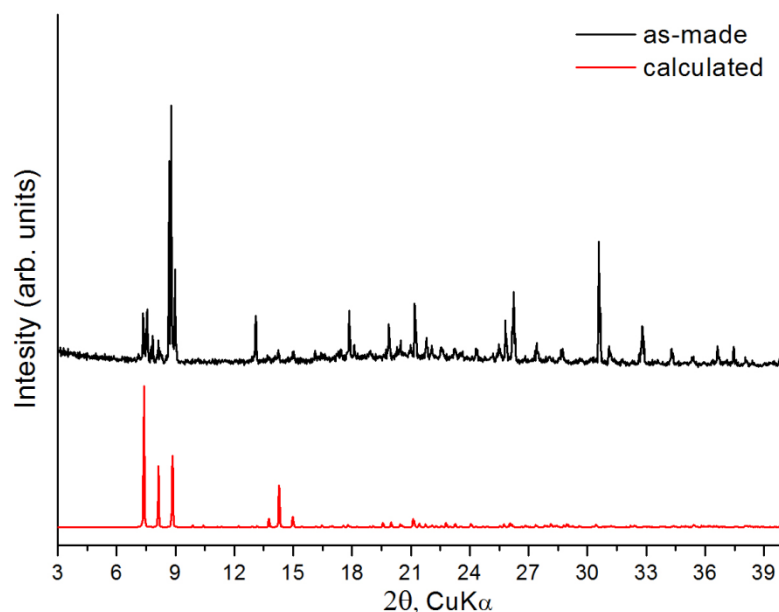
Figure 6.210. Comparison of experimental and calculated pxrd patterns for Eu(NDC-2OH)(Cl)(DMF)$_6$.

6.36.4 Synthesis of compound Sm(NDC-2OH)(Cl)(DMF)$_2$

An amount of 0.020 g (0.08 mmol) of 4,8-dihydroxynaphthalene-2,6-dicarboxylic acid (H$_2$(NDC-2OH)), 0.095 g (0.26 mmol) of SmCl$_3$·6H$_2$O were dissolved in a 20 mL glass scintillation vial containing 6 mL DMF and 4 mL ethanol. The vial was heated at 85 ^{0}C for 10 h where plate crystals were formed. Yield: 30 % based on H$_2$(NDC-2OH).
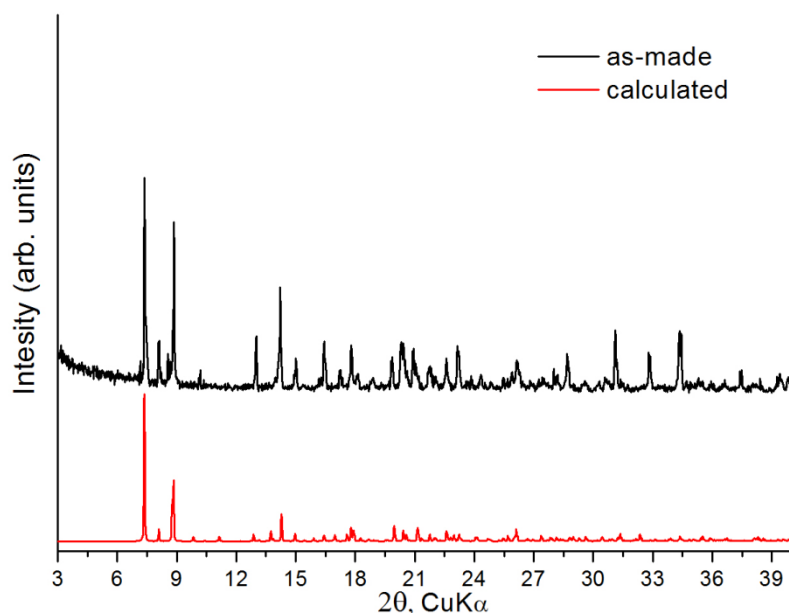
Figure 6.212. Comparison of experimental and calculated pxrd patterns for Sm(NDC-2OH)(Cl)(DMF)$_6$.

6.36.5 Synthesis of compound Tb(NDC-2OH)(DMF)$_2$

An amount of 0.020 g (0.08 mmol) of 4,8-dihydroxynaphthalene-2,6-dicarboxylic acid (H$_2$(NDC-2OH)), 0.096 g (0.26 mmol) of TbCl$_3$·6H$_2$O were dissolved in a 20 mL glass scintillation vial containing 6 mL DMF and 4 mL ethanol. The vial was heated at 85 ^{0}C for 10 h where plate crystals were formed. Yield: 31 % based on H$_2$(NDC-2OH).
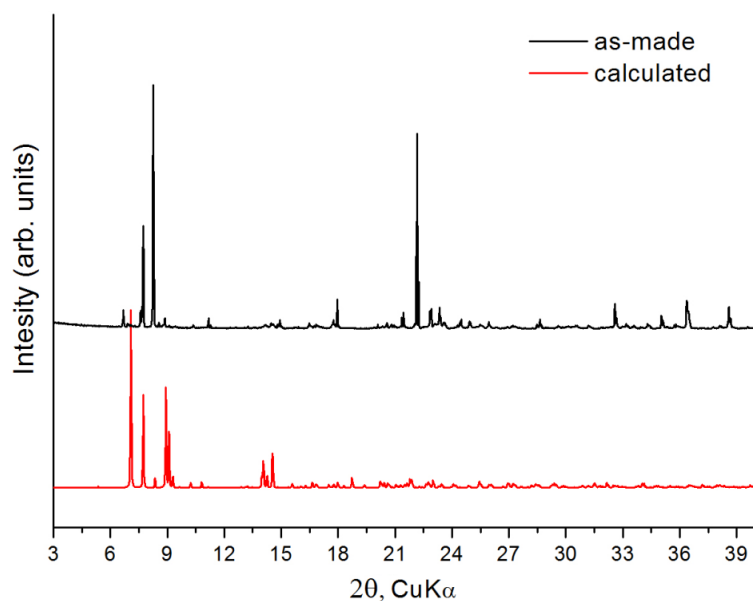
Figure 6.214. Comparison of experimental and calculated pxrd patterns for Tb(NDC-2OH)(Cl)(DMF)$_6$.

6.36.6 Synthesis of compound Zn(NDC-2OH)(DMF)$_2$

An amount of 0.020 g (0.08 mmol) of 4,8-dihydroxynaphthalene-2,6-dicarboxylic acid (H$_2$(NDC-2OH)), 0.072 g (0.24 mmol) of Zn(NO$_3$)$_2$·6H$_2$O were dissolved in a 20 mL glass scintillation vial containing 5 mL DMA and 5 mL ethanol. The vial was heated at 90 ^{0}C for 2 days where large, dark orange crystals were formed. Yield: 35 % based on H$_2$(NDC-2OH).

clarity.
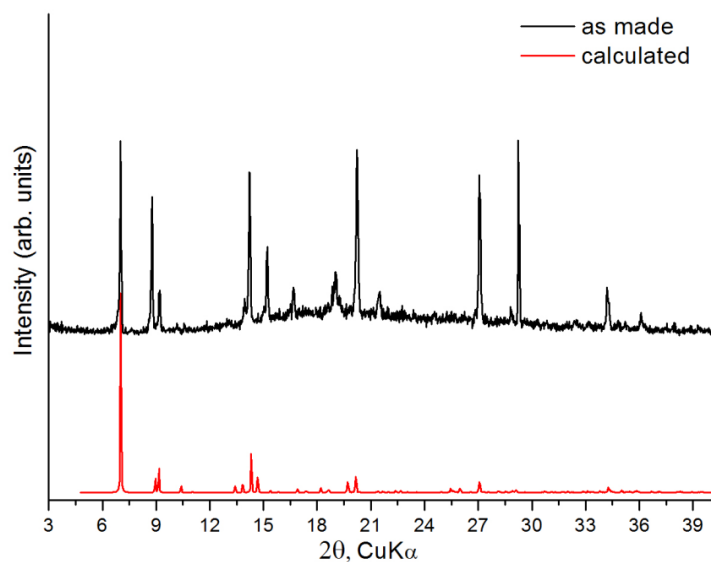
Figure 6.216. Comparison of experimental and calculated pxrd patterns for Zn(NDC-2OH)(DMF)$_2$.

6.36.7 Synthesis of compound Zn$_2$(NDC-2OH)(NO$_3$)$_2$(bis-pyr)(DMF)$_3$

An amount of 0.020 g (0.08 mmol) of 4,8-dihydroxynaphthalene-2,6-dicarboxylic acid (H$_2$(NDC-2OH)), 0.080 g (0.27 mmol) of Zn(NO$_3$)$_2$·6H$_2$O and 0.010 g (0.05 mmol) of 1,2-bis(4-pyridyl)ethane were dissolved in a 20 mL glass scintillation vial containing 6 mL DMF, and 4 mL ethanol. The vial

250

was heated at 85 ^{0}C for 14 h where large orange crystals were formed. Yield: 37 % based on H$_2$(NDC-2OH).
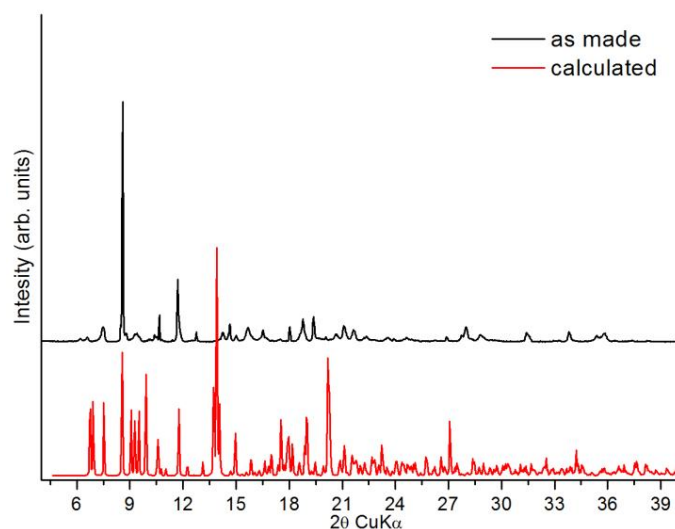
<u>Figure 6.218.</u> Comparison of experimental and calculated pxrd patterns for Zn$_2$(NDC-2OH)(NO$_3$)$_2$(bis-pyr)(DMF)$_3$. The differences of the two patterns are attributed to preferred orientation.

6.37 MOF syntheses based on organic linker 7
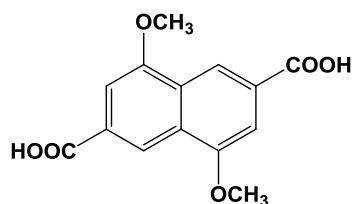
6.37.1 Synthesis of compound Zn(NDC-2OMe)

An amount of 0.020 g (0.07 mmol) of H$_2$(NDC-2OMe) and 0.065 g (0.22 mmol) of Zn(NO$_3$)$_2$·6H$_2$O were dissolved in a 20 mL glass scintillation vial containing 10 mL DMF, 4 mL ethanol and 1 drop of c.HNO$_3$. The vial was heated at 85 ^{0}C for 18 h where large, yellow cubic crystals were formed. Yield: 37 % based on H$_2$(NDC-2OMe).

251
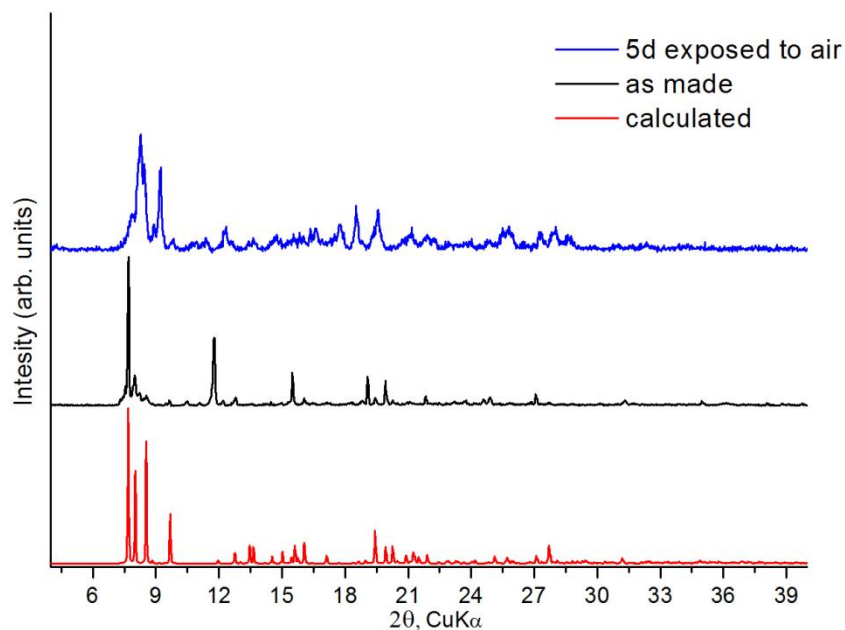
<u>Figure 6.220.</u> Comparison of experimental, calculated and 5 days exposed to air pxrd patterns for Zn(NDC-2OMe). The differences of the as made and calculated patterns are attributed to preferred orientation.

6.38 MOF syntheses based on organic linker 8
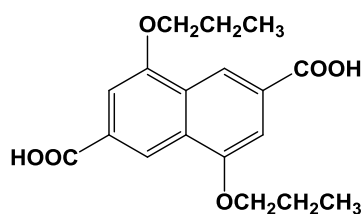
6.38.1 Synthesis of compound Zn(NDC-2OPr)

An amount of 0.020 g (0.06 mmol) of H_2(NDC-2OPr) and 0.054 g (0.18 mmol) of $Zn(NO_3)_2 \cdot 6H_2O$ were dissolved in a 20 mL glass scintillation vial containing 10 mL DMF, 1 mL 2-propanol and 1 mL water. The vial was heated at 70 ^{0}C for 24 h where large, colourless crystals were formed. Yield: 30 % based on H_2(NDC-2Pr).
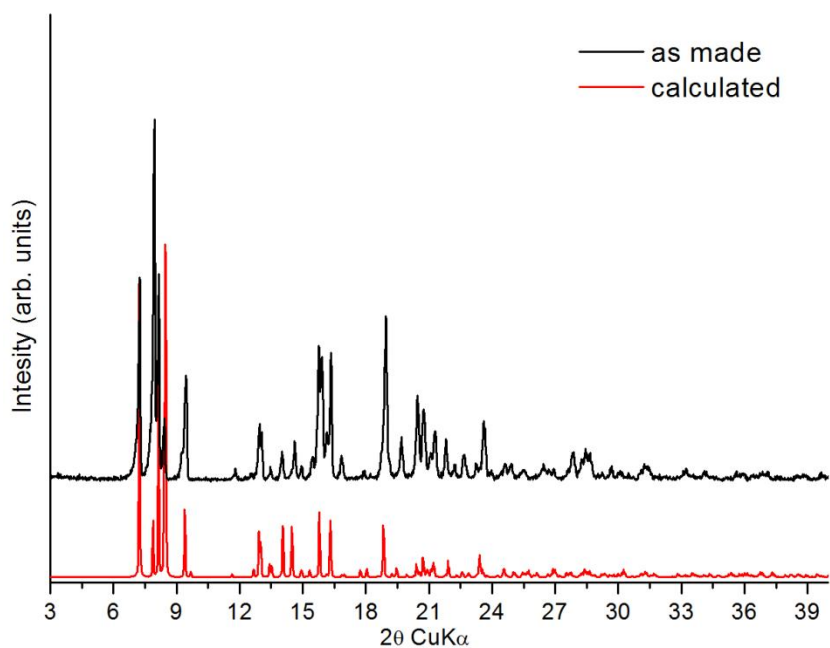
Figure 6.221. Comparison of experimental and calculated pxrd patterns for Zn(NDC-2OPr).

6.38.2 Synthesis of compound Mn(NDC-2OPr)

An amount of 0.020 g (0.06 mmol) of H_2(NDC-2OPr) and 0.046 g (0.18 mmol) of $Mn(NO_3)_2 \cdot 4H_2O$ were dissolved in a 20 mL glass scintillation vial containing 10 mL DMF, 1 mL 2-propanol and 1 mL water. The vial was heated at 70 ^{0}C for 24 h where large, colourless crystals were formed. Yield: 25 % based on H_2(NDC-2Pr).
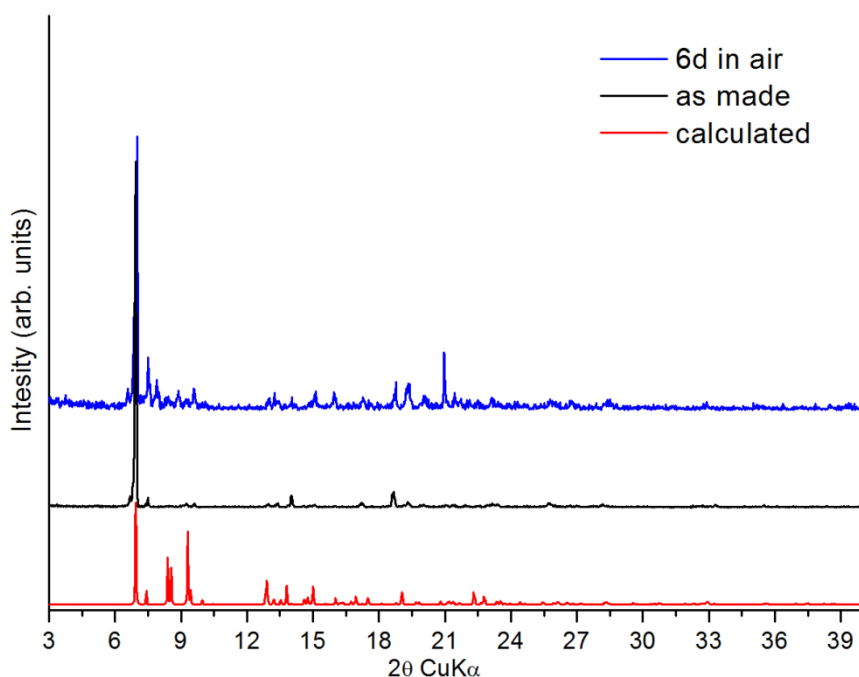
Figure 6.223. Comparison of experimental and calculated pxrd patterns for Mn(NDC-2OPr). The differences of the as made and calculated patterns are attributed to preferred orientation.

6.39 MOF synthesis based on organic linker 12

$$OCH_2CH_3$$

(chemical structure of H₂(NDC-2OEt): a naphthalene ring bearing two COOH groups and two OCH₂CH₃ groups)
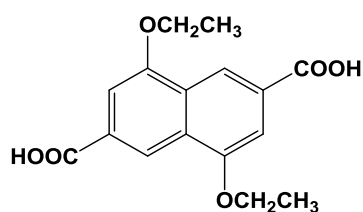
6.39.1 Synthesis of compound Zn(NDC-2OEt)

An amount of 0.020 g (0.065 mmol) of H$_2$(NDC-2OEt) and 0.059 g (0.20 mmol) of Zn(NO$_3$)$_2$·6H$_2$O were dissolved in a 20 mL glass scintillation vial containing 10 mL DMF, 4 mL ethanol and 1 drop of c.HNO$_3$. The vial was heated at 85 ^{0}C for 18 h where large, colourless crystals were formed. Yield: 29 % based on H$_2$(NDC-2OEt).
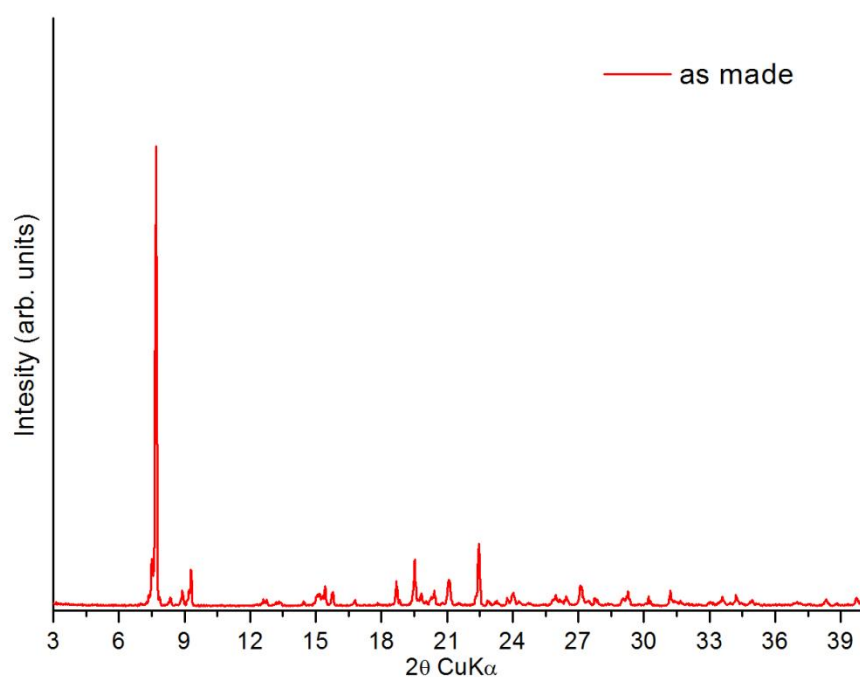
Figure 6.224. Experimental pxrd pattern for Zn(NDC-2OEt).

6.40 Mix linker MOF synthesis based on organic linker 6

(chemical structure: a naphthalene ring bearing two COOH groups and two OH groups)
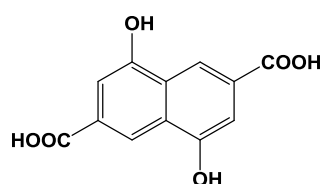
6.40.1 Synthesis of compound MOF-205-2OH

An amount of 0.020 g (0.08 mmol) of 4,8-dihydroxynaphthalene-2,6-dicarboxylic acid (H$_2$(NDC-2OH)), 0.030 g (0.07 mmol) of 4,4′,4″-benzene-1,3,5-triyltribenzoic acid (H$_3$BTB) and 0.079 g (0.25 mmol) of Zn(NO$_3$)$_2$·6H$_2$O were dissolved in a 20 mL glass scintillation vial containing 6 mL DMF and 4 mL ethanol. The vial was heated at 85 ^{0}C for 10 h where large, dark orange truncated-octahedral crystals were formed. Yield: 36 % based on H$_2$(NDC-2OH).

Activation of this material was possible through exchange with absolute ethanol for 4 days, 4 times per day, followed by exchange with supercritical CO$_2$.
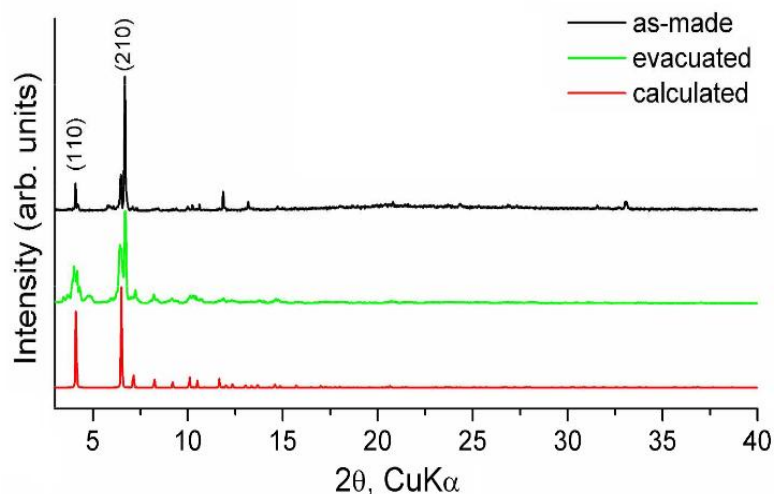
Figure 6.226. Comparison of experimental, calculated and activated pxrd patterns for MOF-205-2OH.
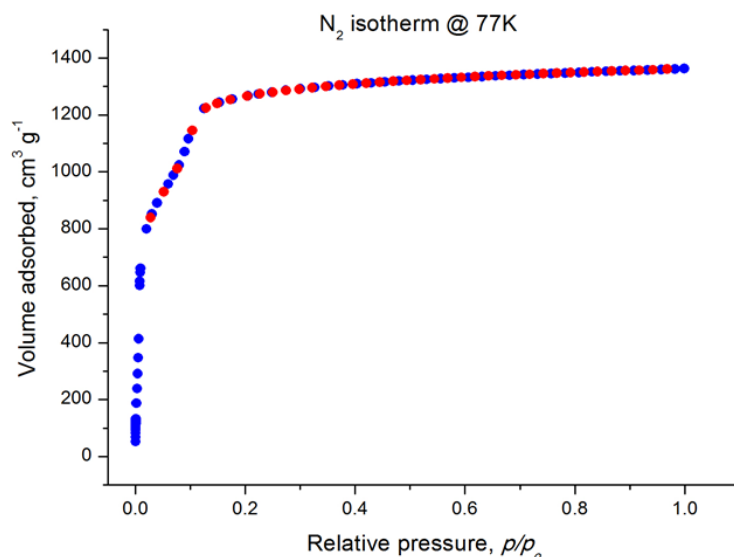
Figure 6.227. Nitrogen sorption isotherm of MOF-205-2OH at 77 K.
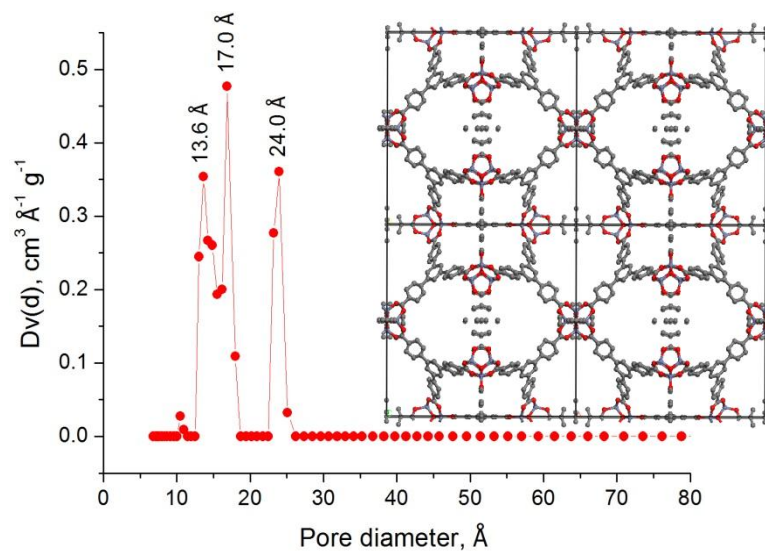
Figure 6.228. Pore size distribution in MOF-205-2OH calculated from NLDFT analysis.
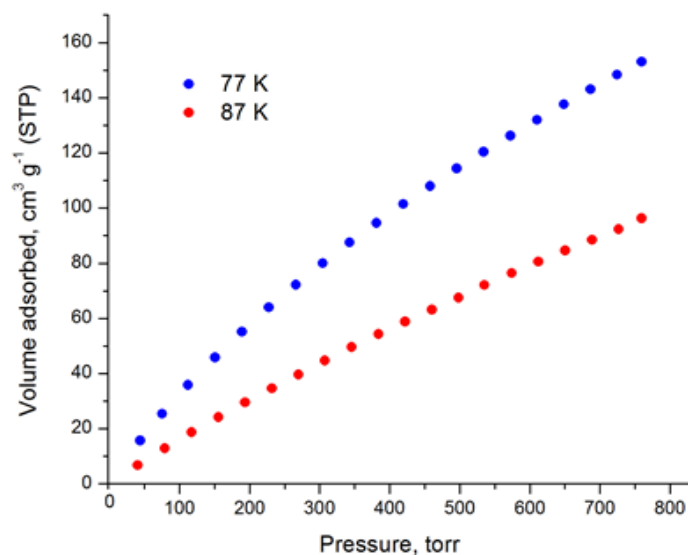
Figure 6.229. Hydrogen adsorption isotherms of MOF-205-2OH at 77 K and 87 K.

At zero coverage, Q_{st}=4.5 kJ mol^{-1}

Figure 6.230. H$_2$ isosteric heat of adsorption in MOF-205-2OH as a function of surface coverage.

Figure 6.231. CO_2 and CH_4 adsorption isotherms of MOF-205-2OH at 273 K and 298 K.

Figure 6.232. CO_2 isosteric heat of adsorption in MOF-205-2OH as a function of surface coverage.

Figure 6.233. TGA curve for the as made MOF-205-2OH and the corresponding evacuated solid obtained after CO_2 SCD process, recorded under Ar flow with a heating rate of 5 deg/min.

6.41 Mix linker MOF syntheses based on organic linker 33
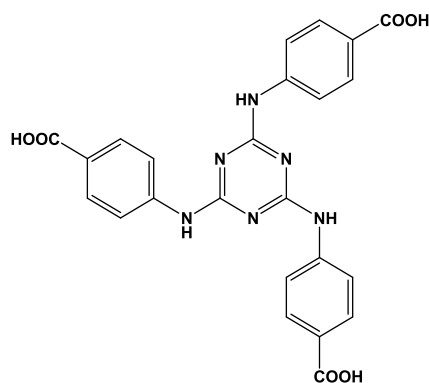
6.41.1 Synthesis of compound Zn$_4$O(BDC)(TATAB)$_{4/3}$

An amount of 0.020 g (0.04 mmol) of H$_3$TATAB, 0.014 g (0.08 mmol) of H$_2$BDC and 0.049 g (0.16 mmol) of Zn(NO$_3$)$_2$·6H$_2$O were dissolved in a 20 mL glass scintillation vial containing 6 mL DMF, 4 mL ethanol and 2 drops of water. The vial was heated at 85 ^{0}C for 24 h where colourless block crystals were formed. Yield: 33 % based on H$_3$TATAB.
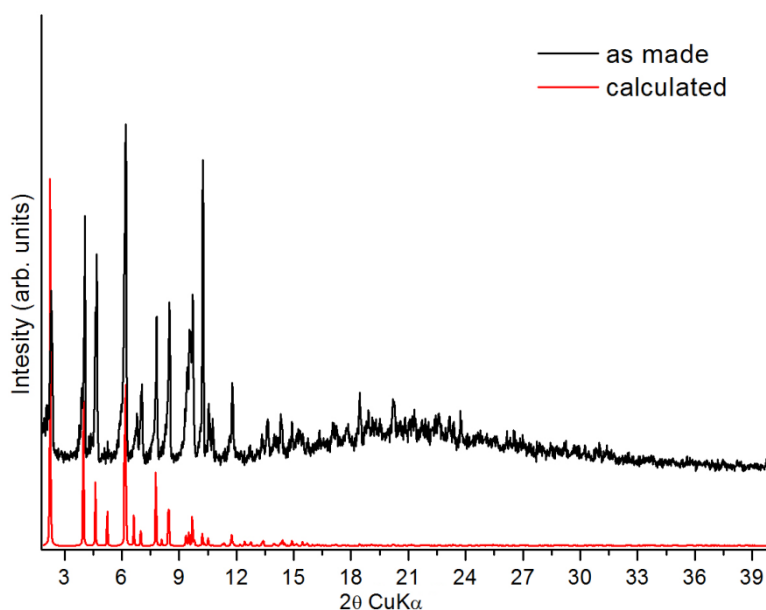
<u>Figure 6.236.</u> Comparison of experimental and calculated pxrd patterns for the compound Zn$_4$O(BDC)(TATAB)$_{4/3}$.

After the efficient characterization of the material the evaluation of its gas sorption properties took place. Successful activation was possible as follows: as-made sample was washed with DMF four times per day for 2 days and then the sample was soaked in CH$_2$Cl$_2$ over a period of 4 days, replenishing the CH$_2$Cl$_2$ 4 times per day. The dichloromethane suspended sample was transferred inside the chamber of a supercritical CO$_2$ dryer (Bal-Tec CPD 030) and CH$_2$Cl$_2$ was exchanged with liquid CO$_2$ over a period of 5 hours at 8 ^{o}C. During this period, liquid CO$_2$ was vented under positive

pressure every 5 minutes. The rate of CO_2 venting was always kept below the rate of filling so as to maintain full drying conditions inside the chamber. Following venting, the temperature was raised to 40 ºC (above the critical temperature of CO_2), kept there for 1.5 hour and then slowly vented over the period of 2 hours. The dried sample was transferred immediately inside a pre-weighted, Argon filled cell provided by Quantachrome to prevent intrusion of oxygen and atmospheric moisture during transfers and weighing. Finally, the sample was activated under dynamic vacuum at room temperature for 12 hours and until the outgas rate was less than 2 mTorr/min. The activated material is highly air sensitive and the pxrd pattern of the evacuated material showed complete loss of crystallinity.
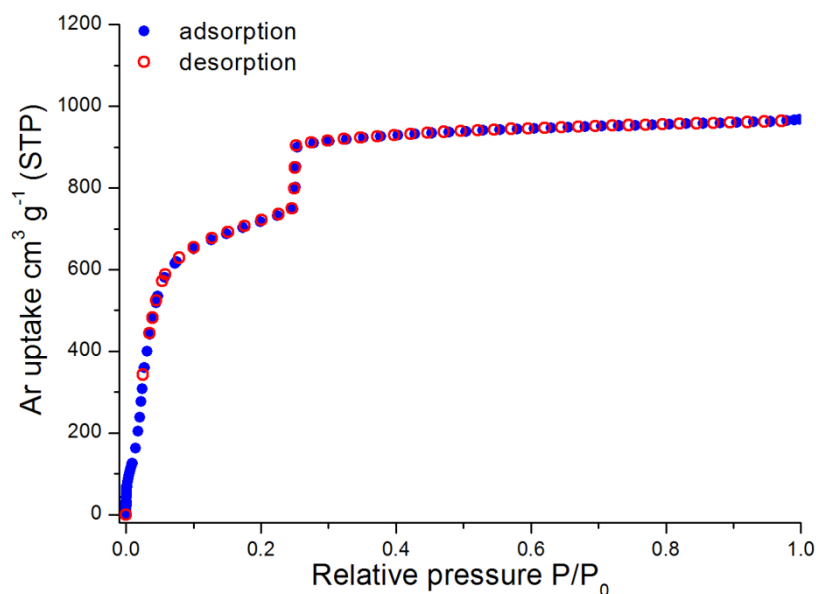
Figure 6.237. Argon sorption isotherm of $Zn_4O(BDC)(TATAB)_{4/3}$ at 87 K.
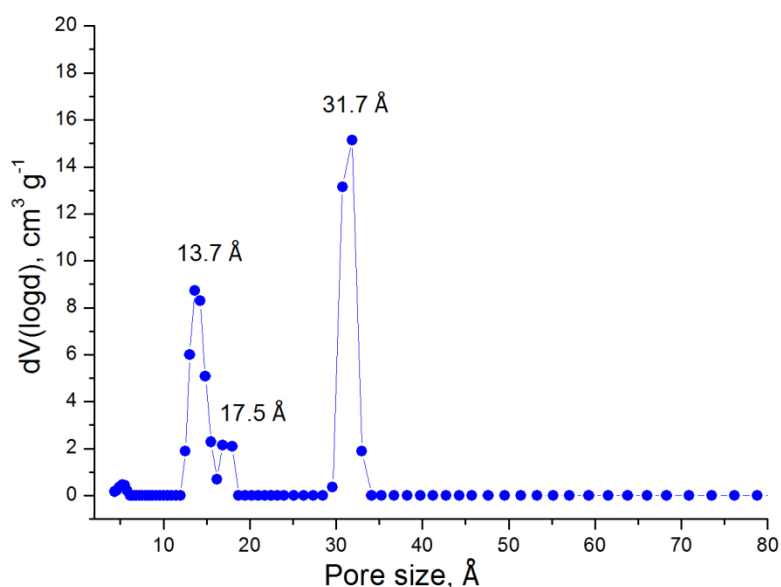
Figure 6.238. Pore size distribution in $Zn_4O(BDC)(TATAB)_{4/3}$ calculated from NLDFT analysis.

259
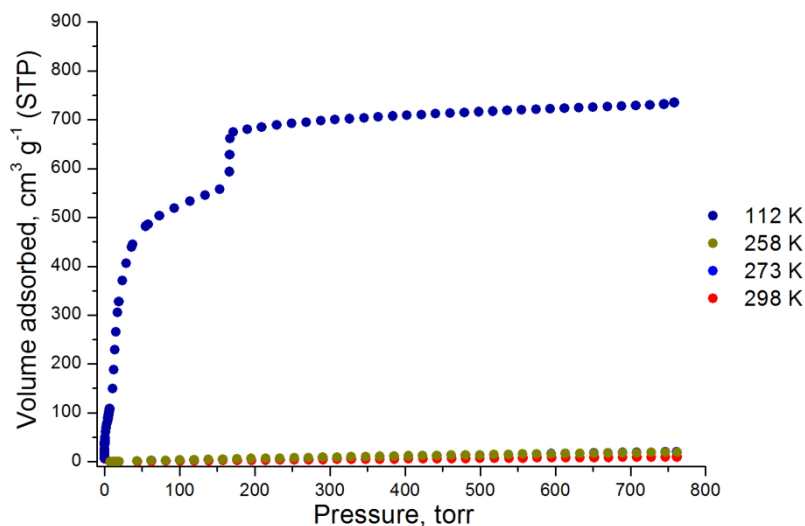
Figure 6.239. CH$_4$ adsorption isotherms of Zn$_4$O(BDC)(TATAB)$_{4/3}$ at 112 K, 258 K, 273 K, and 298 K.
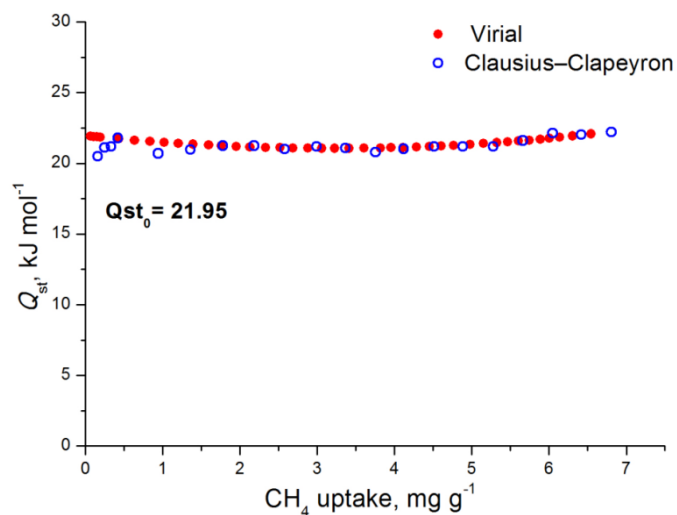
Figure 6.240. CH$_4$ isosteric heat of adsorption in Zn$_4$O(BDC)(TATAB)$_{4/3}$ as a function of surface coverage.
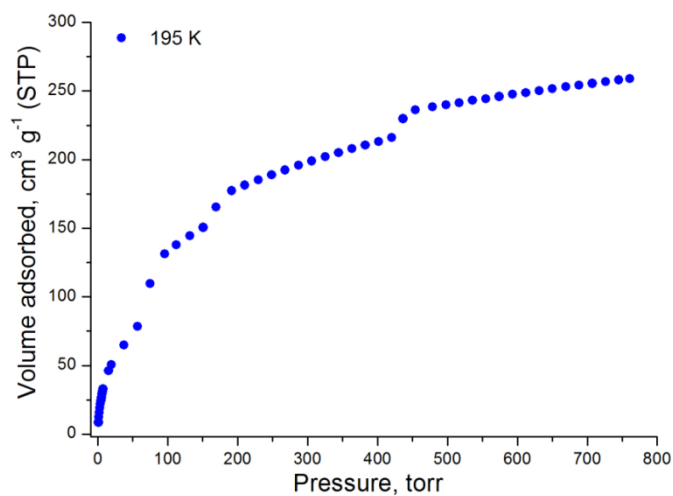
Figure 6.241. CO$_2$ adsorption isotherm of Zn$_4$O(BDC)(TATAB)$_{4/3}$ at 195 K.

6.41.2 Synthesis of compound Zn$_4$O(NDC-2NO$_2$)(TATAB)$_{4/3}$

An amount of 0.030 g (0.06 mmol) of H_3TATAB, 0.023 g (0.07 mmol) of $H_2NDC-2NO_2$ and 0.055 g (0.18 mmol) of $Zn(NO_3)_2 \cdot 6H_2O$ were dissolved in a 20 mL glass scintillation vial containing 9 mL DMF, 1 mL ethanol and 2 drops of water. The vial was heated at 85 ^0C for 24 h where large yellow crystals were formed. Yield: 30 % based on H_3TATAB.
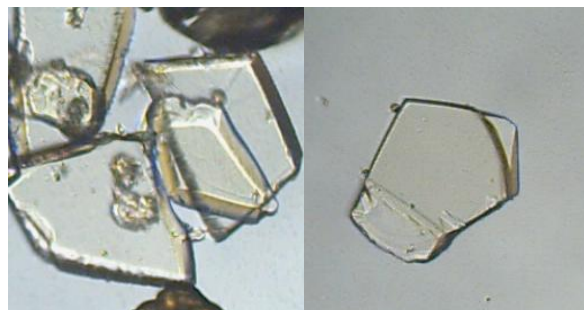
Figure 6.242. Optical microscope pictures of $Zn_4O(NDC-2NO_2)(TATAB)_{4/3}$ crystals.
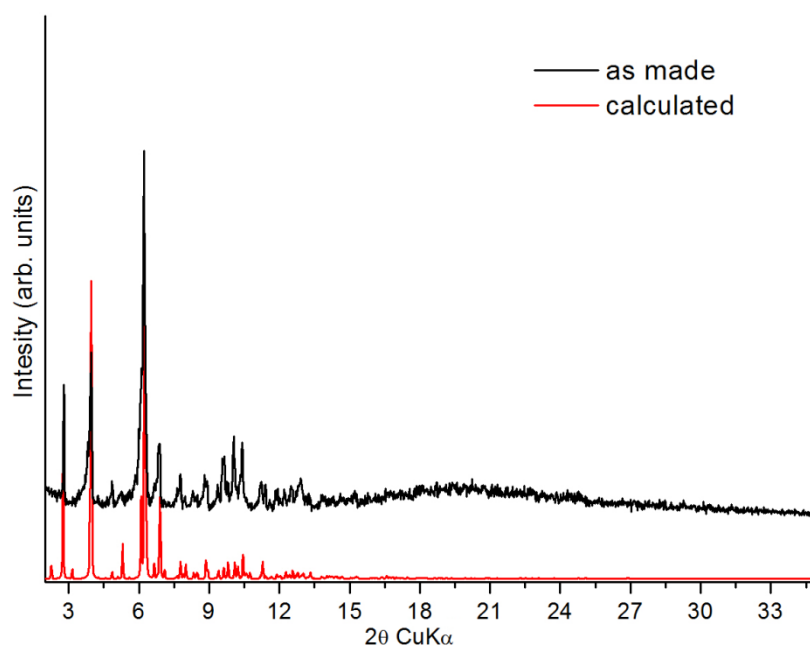
Figure 6.245. Comparison of experimental and calculated pxrd patterns for the compound $Zn_4O(NDC-2NO_2)(TATAB)_{4/3}$.

6.41.3 Synthesis of compound $Zn_4O(NDC-2OPr)(TATAB)_{4/3}$

An amount of 0.020 g (0.04 mmol) of H_3TATAB, 0.014 g (0.04 mmol) of $H_2NDC-2OPr$ and 0.049 g (0.16 mmol) of $Zn(NO_3)_2 \cdot 6H_2O$ were dissolved in a 20 mL glass scintillation vial containing 6 mL DMF, 4 mL ethanol and 2 drops of water. The vial was heated at 85 ^0C for 48 h where crystals were formed. Yield: 30 % based on H_3TATAB.
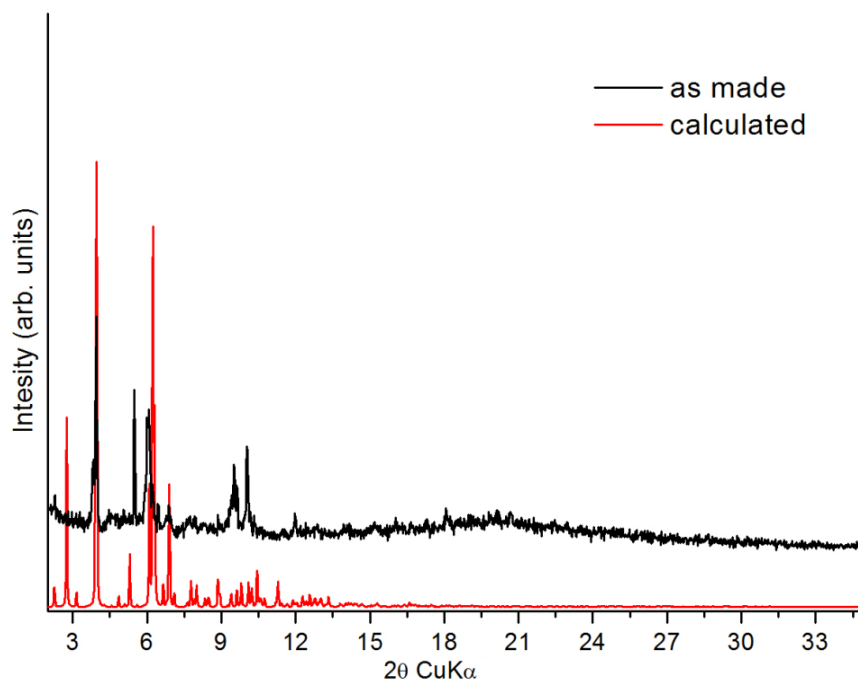
Figure 6.246. Comparison of experimental and calculated pxrd patterns for the compound $Zn_4O(NDC-2OPr)(TATAB)_{4/3}$. All the peaks of the as made pxrd pattern are predicted from the calculated pattern.

6.41.4 Synthesis of compound $Zn_4O(NDC-2OAllyl)(TATAB)_{4/3}$

An amount of 0.020 g (0.04 mmol) of H_3TATAB, 0.014 g (0.04 mmol) of $H_2NDC-2OAllyl$ and 0.049 g (0.16 mmol) of $Zn(NO_3)_2 \cdot 6H_2O$ were dissolved in a 20 mL glass scintillation vial containing 6 mL DMF, 4 mL ethanol and 2 drops of water. The vial was heated at 85 ^{0}C for 48 h where orange crystals were formed. Yield: 30 % based on H_3TATAB.
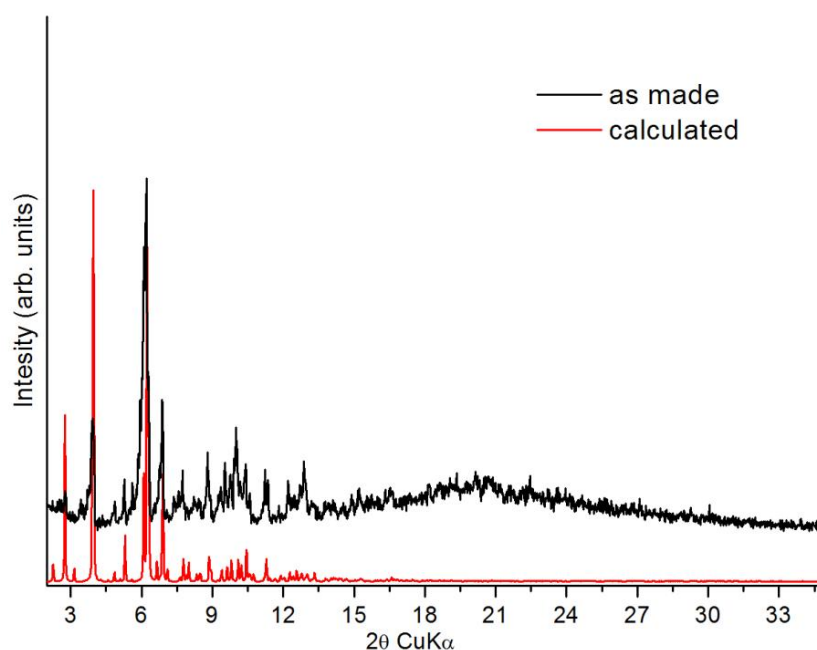
Figure 6.247. Comparison of experimental and calculated pxrd patterns for the compound $Zn_4O(NDC-2OAllyl)(TATAB)_{4/3}$.

6.41.5 Synthesis of compound Zn$_4$O(NDC-2OPh)(TATAB)$_{4/3}$

An amount of 0.020 g (0.04 mmol) of H$_3$TATAB, 0.016 g (0.04 mmol) of H$_2$NDC-2OPh and 0.049 g (0.16 mmol) of Zn(NO$_3$)$_2$·6H$_2$O were dissolved in a 20 mL glass scintillation vial containing 6 mL DMF, 4 mL ethanol and 2 drops of water. The vial was heated at 85 ^{0}C for 48 h where big crystals were formed. Yield: 30 % based on H$_3$TATAB.
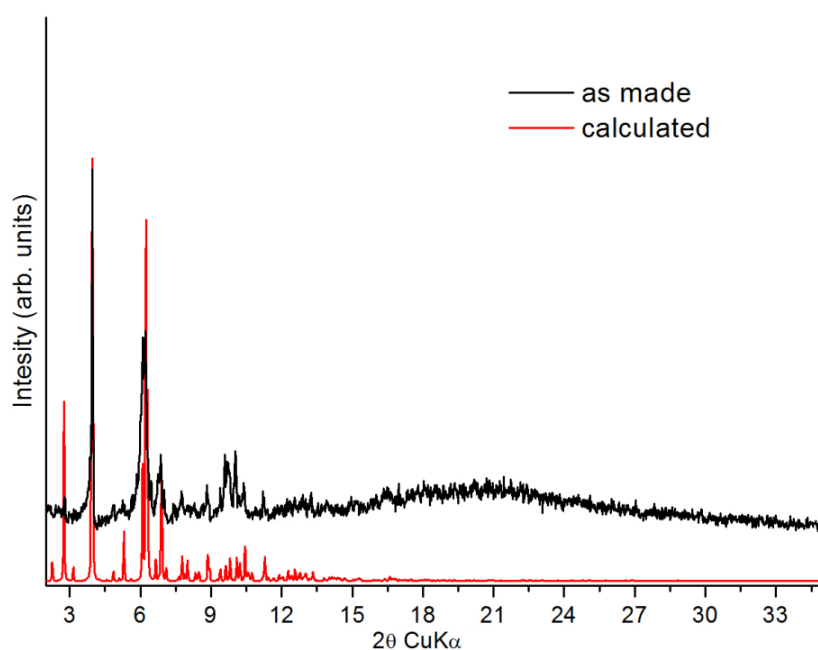
Figure 6.248. Comparison of experimental and calculated pxrd patterns for the compound Zn$_4$O(NDC-2OPh)(TATAB)$_{4/3}$.

6.42 MOF synthesis based on organic linker 39
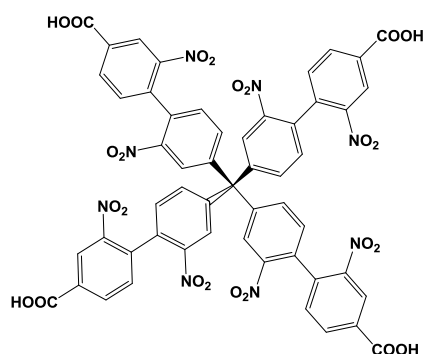
6.42.1 Synthesis of compound Cu$_2$L

A solution of 3 mL DMF, 1 mL EtOH, 3 drops c.HNO$_3$, 0.040 g (0.04 mmol) of H$_4$L and 0.019 g (0.08 mmol) of Cu(NO$_3$)$_2$·3H$_2$O was placed in a 20 mL glass scintillation vial. The vial was sealed and

placed in an isothermal oven at 85 °C for 16 hours. During this period, big dark green crystals were deposited (44 % yield based on H_4L).
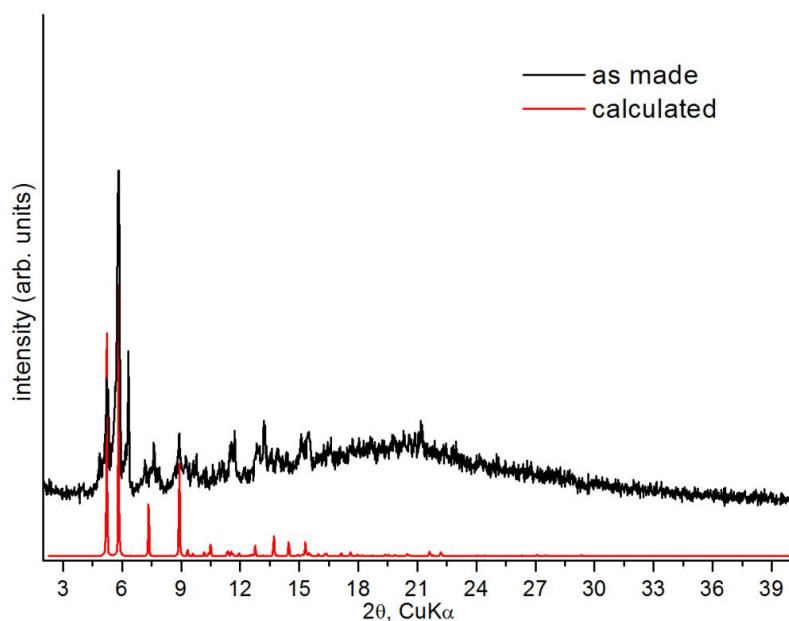
Figure 6.250. Comparison of experimental and calculated pxrd patterns for compound Cu_2L. The peak at $2\theta = 6.37^0$ is expected from the crystal structure.

6.42.2 Reaction of linker 39 with $Co(NO_3)_2 \cdot 6H_2O$

A solution of 3 mL DMF, 1 mL EtOH, 3 drops c.HNO_3, 0.040 g (0.04 mmol) of H_4L and 0.024 g (0.08 mmol) of $Co(NO_3)_2 \cdot 6H_2O$ was placed in a 20 mL glass scintillation vial. The vial was sealed and placed in an isothermal oven at 85 °C for 4 days. During this period red spheres were deposited.
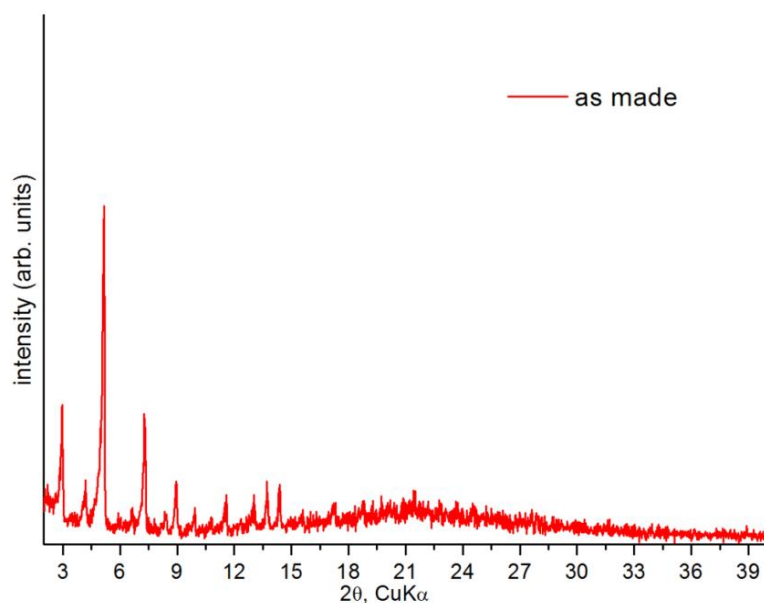
Figure 6.251. Experimental pxrd pattern for material 6.42.2.

6.43 MOF syntheses based on organic linker 40
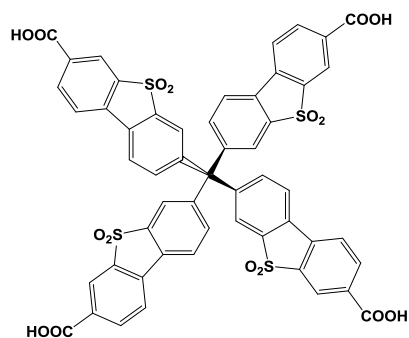
6.43.1 Synthesis of compound Cu₂L

A solution of 3 mL DMF, 1 mL EtOH, 3 drops c.HNO$_3$, 0.040 g (0.04 mmol) of H$_4$L and 0.019 g (0.08 mmol) of Cu(NO$_3$)$_2$·3H$_2$O was placed in a 20 mL glass scintillation vial. The vial was sealed and placed in an isothermal oven at 85 °C for 16 hours. During this period, big dark green crystals were deposited (44 % yield based on H$_4$L).
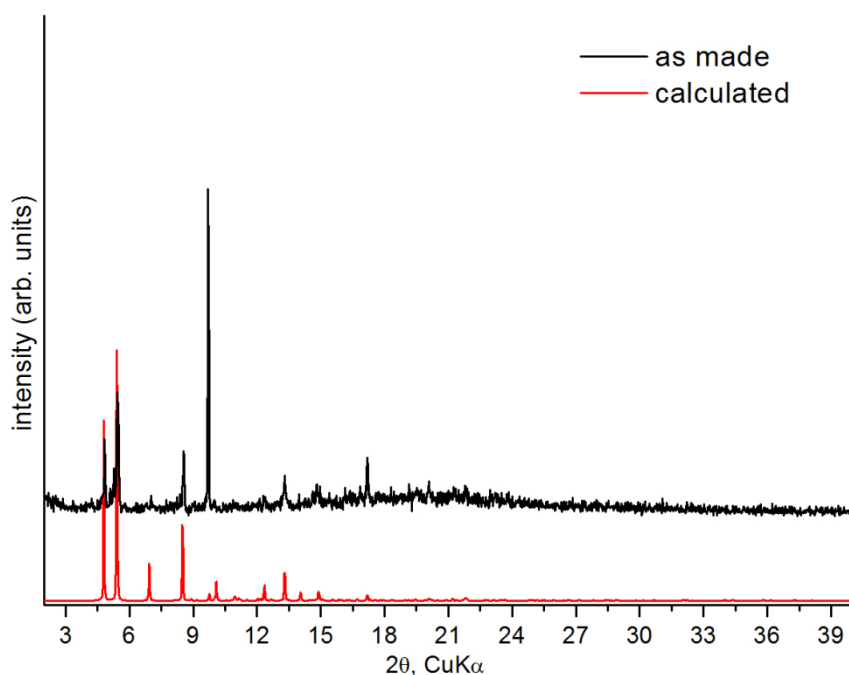
Figure 6.253. Comparison of experimental and calculated pxrd patterns for compound Cu$_2$L.

6.43.2 Synthesis of compound Mg₃O₂L₂(Me₂NH₂)₂

A solution of 2 mL DMF, 3 drops c.HNO$_3$, 0.040 g (0.04 mmol) of H$_4$L and 0.020 g (0.08 mmol) of Mg(NO$_3$)$_2$·6H$_2$O was placed in a 20 mL glass scintillation vial. The vial was sealed and placed in an

isothermal oven at 70 °C for 7 days and at 85 °C for another 7 days. During this period, big colorless crystals were deposited (40 % yield based on H$_4$L).
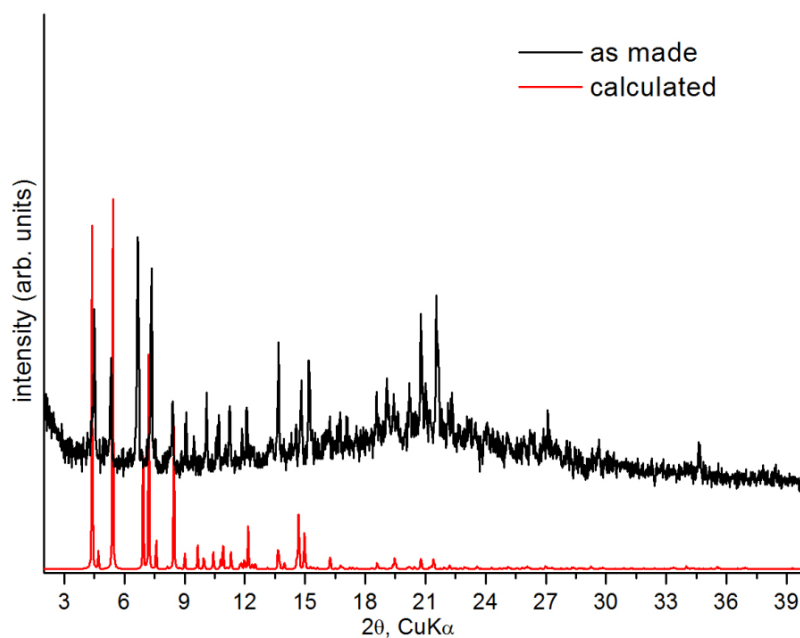
Figure 6.255. Comparison of experimental and calculated pxrd patterns for compound Mg$_3$O$_2$L$_2$(Me$_2$NH$_2$)$_2$. Slight differences of the two patterns can be attributed to preferred orientation.

6.44 MOF syntheses based on organic linker 43
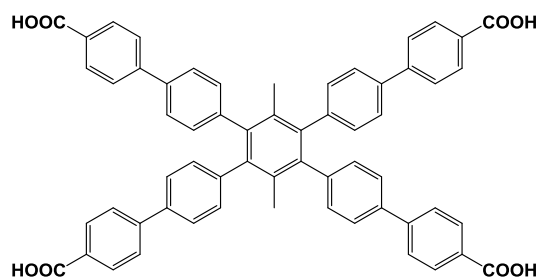
6.44.1 Reaction of linker 43 with CoCl$_2$·6H$_2$O

An amount of 0.037 g (0.04 mmol) of H$_4$L and 0.040 g (0.17 mmol) of CoCl$_2$·6H$_2$O were dissolved in a 20 mL glass scintillation vial containing 6 mL DMF, 4 mL ethanol and 2 drops of c.HCl. The vial was heated at 85 ^{0}C for 18 h where small pink cubic crystals were formed.

266
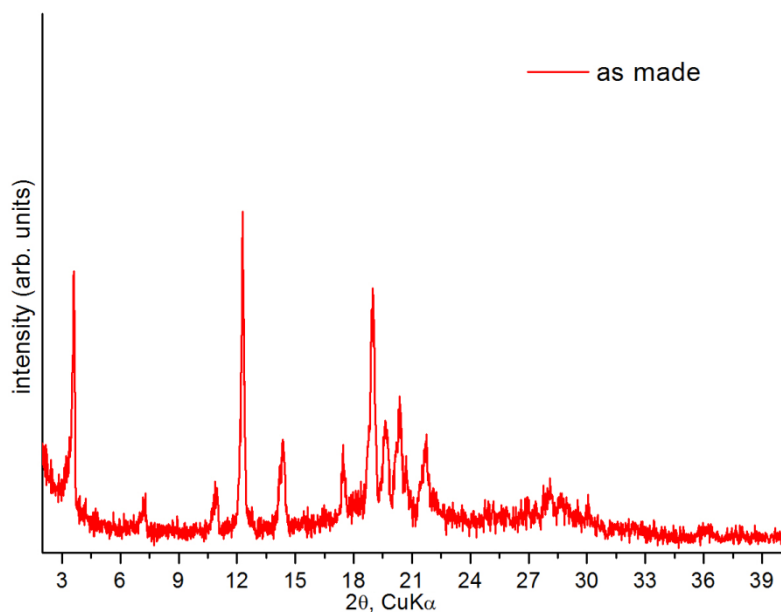
Figure 6.257. Experimental pxrd pattern of compound 6.44.1.
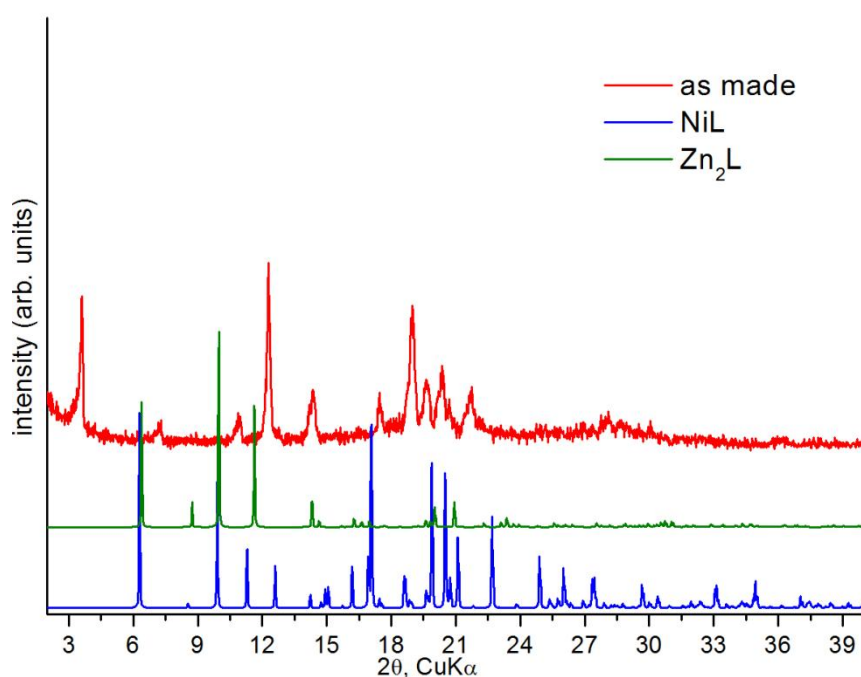
Figure 6.258. Comparison of experimental pxrd pattern of compound 6.44.1 and calculated pxrd patterns for compounds NiL, Zn$_2$L.

6.44.2 Reaction of linker 43 with Zn(NO$_3$)$_2$·6H$_2$O

An amount of 0.037 g (0.04 mmol) of H$_4$L and 0.049 g (0.16 mmol) of Zn(NO$_3$)$_2$·6H$_2$O were dissolved in a 20 mL glass scintillation vial containing 6 mL DMF, 4 mL ethanol and 2 drops of c.HCl. The vial was heated at 85 ^{0}C for 18 h where small colourless crystals were formed.
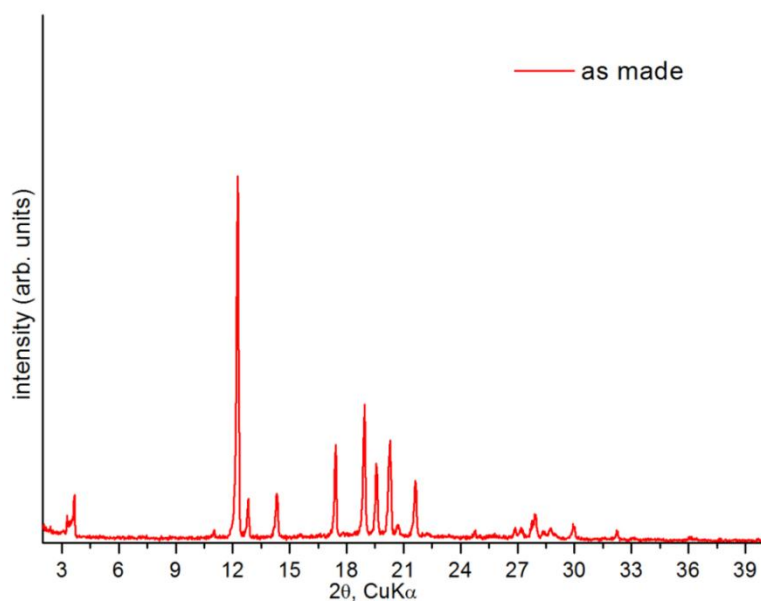
Figure 6.259. Experimental pxrd pattern of compound 6.44.2.

6.44.3 Reaction of linker 43 with $Mg(NO_3)_2 \cdot 6H_2O$

An amount of 0.037 g (0.04 mmol) of H_4L and 0.040 g (0.16 mmol) of $Mg(NO_3)_2 \cdot 6H_2O$ were dissolved in a 20 mL glass scintillation vial containing 6 mL DMF, 4 mL ethanol and 2 drops of c.HCl. The vial was heated at 85 ^{0}C for 18 h where small colourless prismatic crystals were formed.
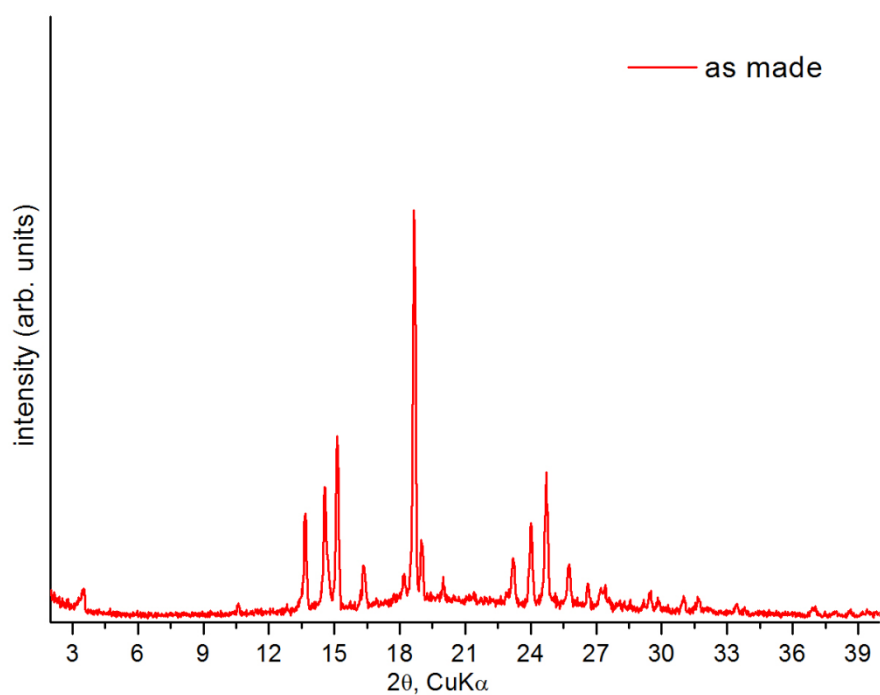
Figure 6.260. Experimental pxrd pattern of compound 6.44.3.

6.44.4 Reaction of linker 43 with $Cu(NO_3)_2 \cdot 3H_2O$

An amount of 0.037 g (0.04 mmol) of H_4L and 0.040 g (0.16 mmol) of $Cu(NO_3)_2 \cdot 3H_2O$ were dissolved in a 20 mL glass scintillation vial containing 6 mL DMF, 4 mL ethanol and 2 drops of c.HCl. The vial was heated at 85 ^{0}C for 3 d where small light blue cubic crystals were formed.
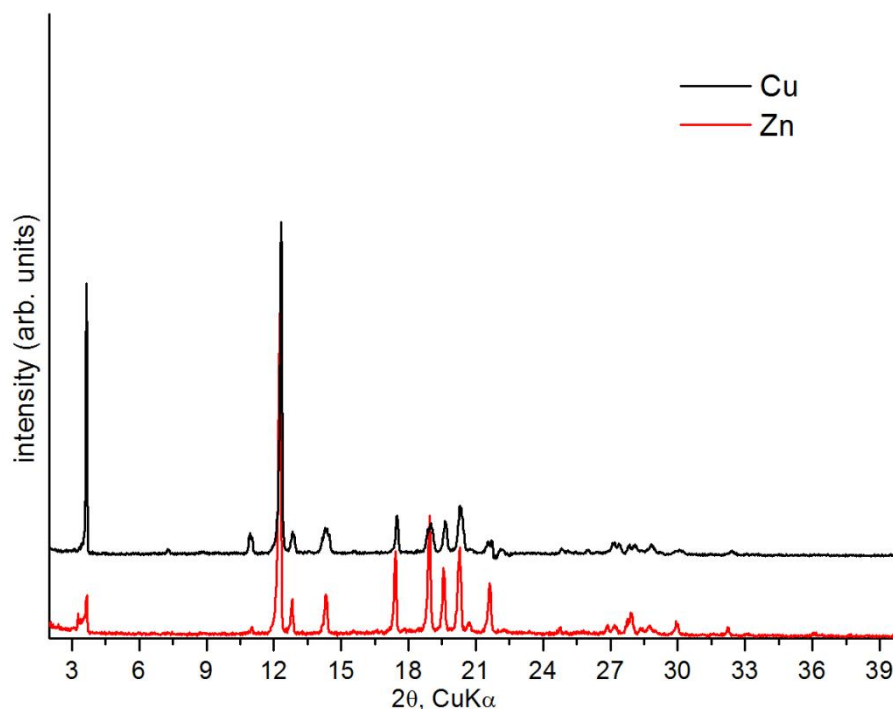
Figure 6.261. Comparison of experimental pxrd patterns of compounds 6.44.2 (Zn) and 6.44.4 (Cu).

6.44.5 Reaction of linker 43 with $Al(NO_3)_3 \cdot 9H_2O$

An amount of 0.037 g (0.04 mmol) of H_4L and 0.058 g (0.16 mmol) of $Al(NO_3)_3 \cdot 9H_2O$ were dissolved in a 20 mL glass scintillation vial containing 5 mL DMF and 12 drops of glacial acetic acid. The vial was heated at 120 ^{0}C for 18 h where a grey powder was deposited.

269
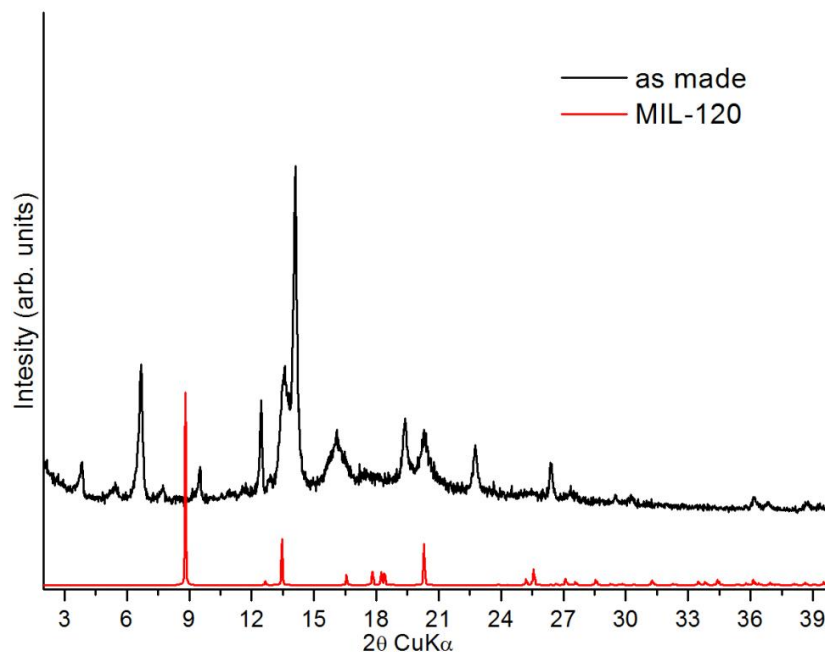
Figure 6.263. Comparison of calculated pxrd pattern of MIL-120 and experimental pxrd pattern of compound 6.44.5 (Al).

6.44.6 Reaction of linker 43 with In(NO$_3$)$_3$xH$_2$O

An amount of 0.037 g (0.04 mmol) of H$_4$L and 0.015 g (0.04 mmol) of In(NO$_3$)$_3$xH$_2$O were dissolved in a 20 mL glass scintillation vial containing 2 mL DMF, 1 mL ACN and 2 drops of c.HNO$_3$. The vial was heated at 85 ^{0}C for 18 h where small colourless block crystals were formed.
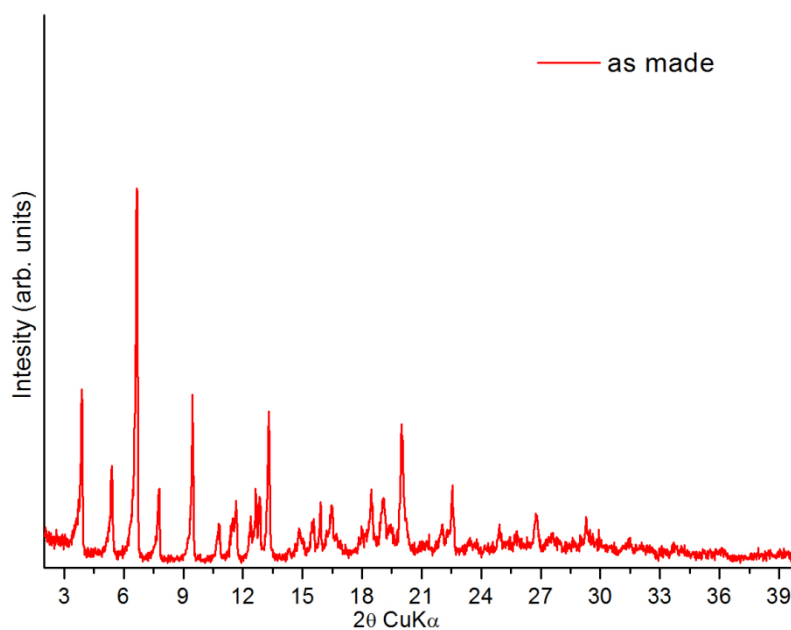
Figure 6.264. Experimental pxrd pattern of compound 6.44.6.

6.44.7 Reaction of linker 43 with $PrCl_3xH_2O$

An amount of 0.034 g (0.04 mmol) of H_4L and 0.013 g (0.04 mmol) of $PrCl_3xH_2O$ were dissolved in a 20 mL glass scintillation vial containing 3 mL DMF, 1 mL ACN and 4 drops of c.HNO_3. The vial was heated at 85 ^{0}C for 48 h where small light green spheres were formed.
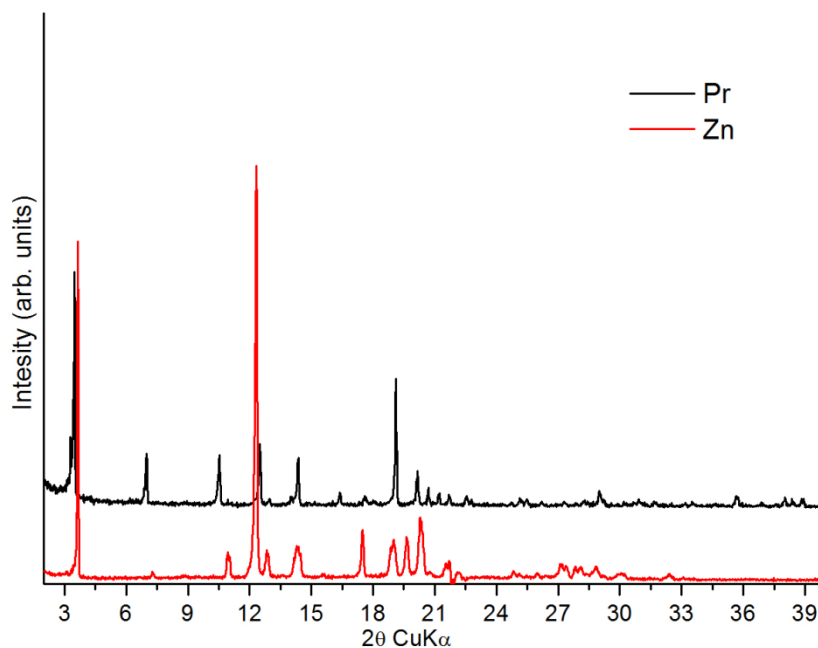
Figure 6.265. Comparison of experimental pxrd patterns of compounds 6.44.2 (Zn) and 6.44.7 (Pr).

6.44.8 Reaction of linker 43 with $La(NO_3)_3\cdot6H_2O$

An amount of 0.034 g (0.04 mmol) of H_4L and 0.016 g (0.04 mmol) of $La(NO_3)_3\cdot6H_2O$ were dissolved in a 20 mL glass scintillation vial containing 5 mL DMF, 1 mL ACN and 4 drops of c.HNO_3. The vial was heated at 85 ^{0}C for 3 d where a white solid was deposited.
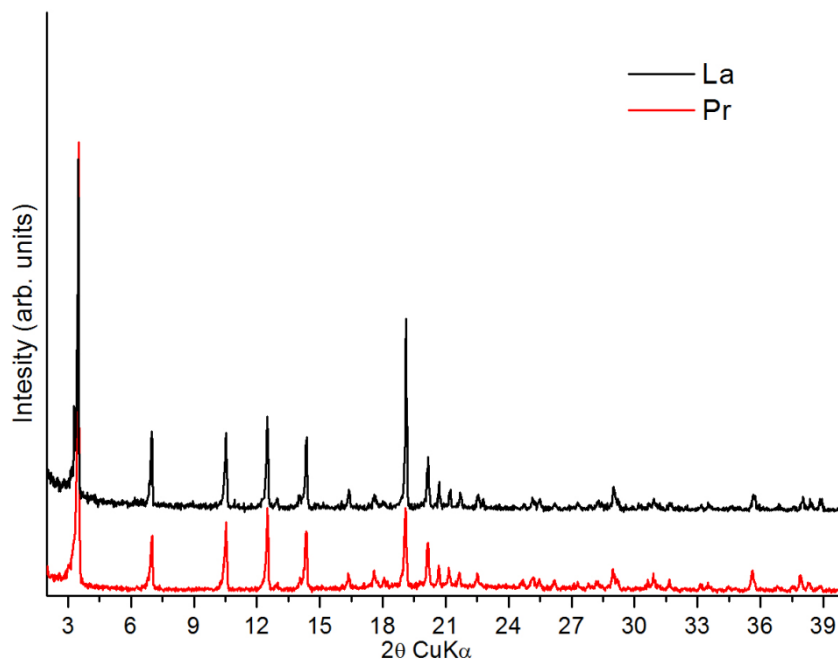
Figure 6.266. Comparison of experimental pxrd patterns of compounds 6.44.8 (La) and 6.44.7 (Pr).

6.45 MOF syntheses based on organic linker 47
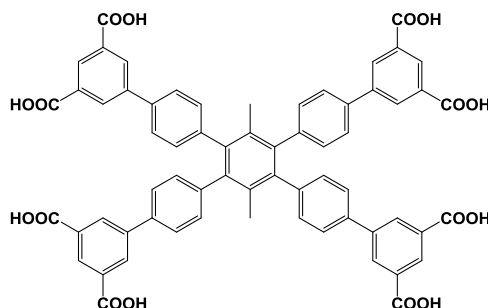
6.45.1 Syntheses of tbo-compounds [Cu$_4$L], [Zn$_4$L], [Co$_4$L].

[Zn$_4$L], Zn-tbo: A solution of 3 mL DMF, 1 mL EtOH, 2 drops c.HNO$_3$, 0.040 g of H$_8$L and 0.022 g of Zn(NO$_3$)$_2$·6H$_2$O was placed in a 20 mL glass scintillation vial. The vial was sealed and placed in an isothermal oven at 85 °C for 18 hours. During this period, big pale brownish crystals were deposited (40% yield based on H$_8$L).

[Co$_4$L], Co-tbo: A solution of 3 mL DMF, 1 mL EtOH, 2 drops c.HNO$_3$, 0.035 g of H$_8$L and 0.022 g of Co(NO$_3$)$_2$·6H$_2$O was placed in a 20 mL glass scintillation vial. The vial was sealed and placed in an isothermal oven at 85 °C for 18 hours. During this period, small brownish block crystals were deposited (44% yield based on H$_8$L).

[Cu$_4$L], Cu-tbo: A solution of 3 mL DMF, 1 mL EtOH, 3 drops c.HNO$_3$, 0.035 g of H$_8$L and 0.017 g of Cu(NO$_3$)$_2$·3H$_2$O was placed in a 20 mL glass scintillation vial. The vial was sealed and placed in an

isothermal oven at 85 °C for 18 hours. During this period, small light blue crystals were deposited (35% yield based on H_8L).
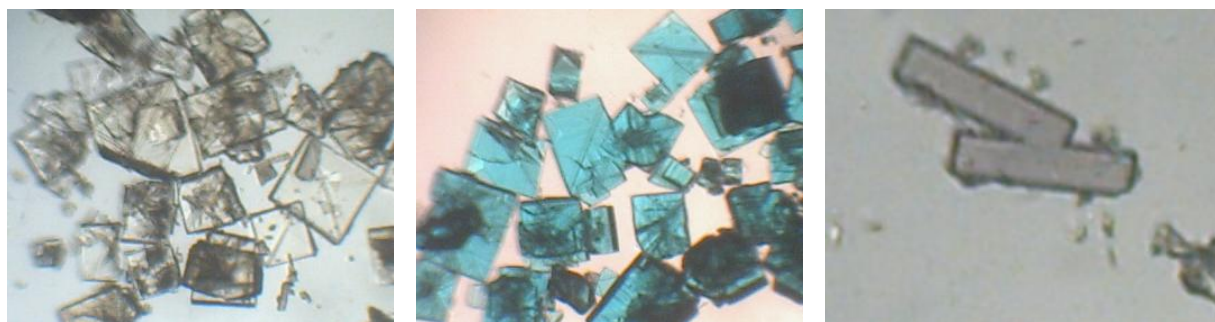
Figure 6.267. Optical microscope pictures of Zn-tbo (left), Cu-tbo (middle) and Co-tbo (right) single crystals.
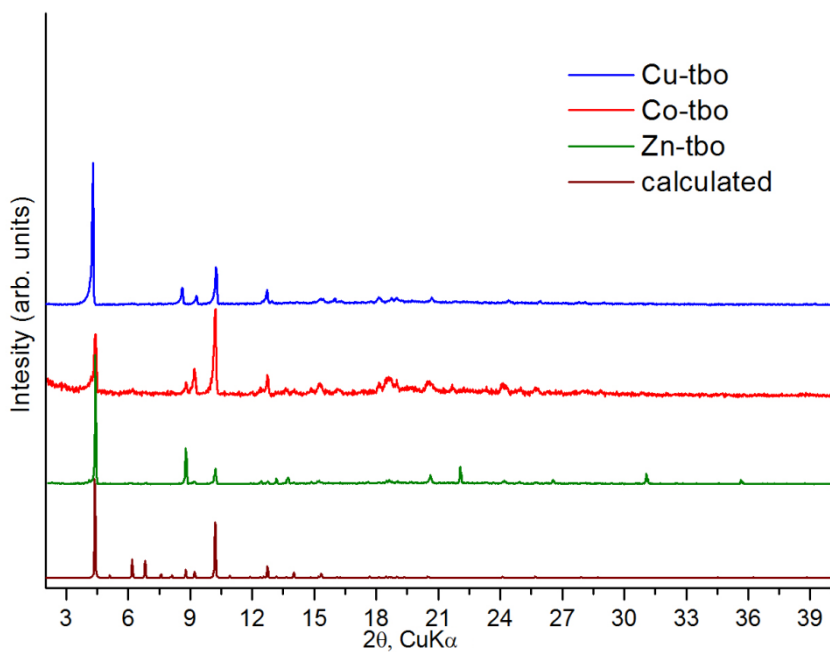
Figure 6.269. Experimental powder X-ray diffraction patterns of the indicated, as-made solids, along with the calculated one from the crystal structure of Zn-tbo.
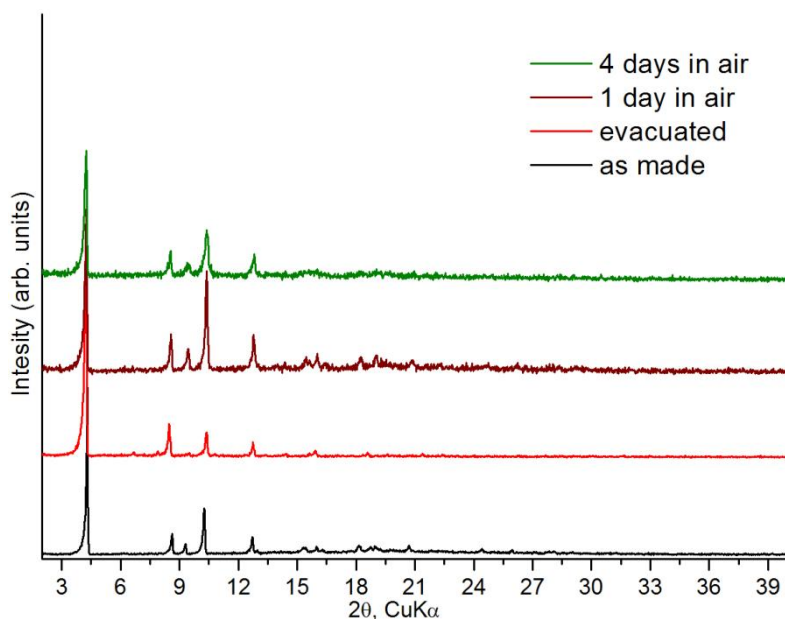
<u>Figure 6.270.</u> Experimental powder X-ray diffraction pattern of as-made**,** evacuated, after 1 and 4 days, exposure in air of Cu-tbo.

Activation of the MOF took place as follows: Prior to analysis, as-made sample was washed with DMF four times per day for 2 days and then the sample was soaked in acetone over a period of 4 days, replenishing the acetone 4 times per day. Afterwards the acetone was exchanged with CH_2Cl_2, 2 times per day for 2 days. Finally, the sample was activated under dynamic vacuum at 60 °C for 12 hours and until the outgas rate was less than 2 mTorr/min. The color of the material changed from light blue to deep purple.
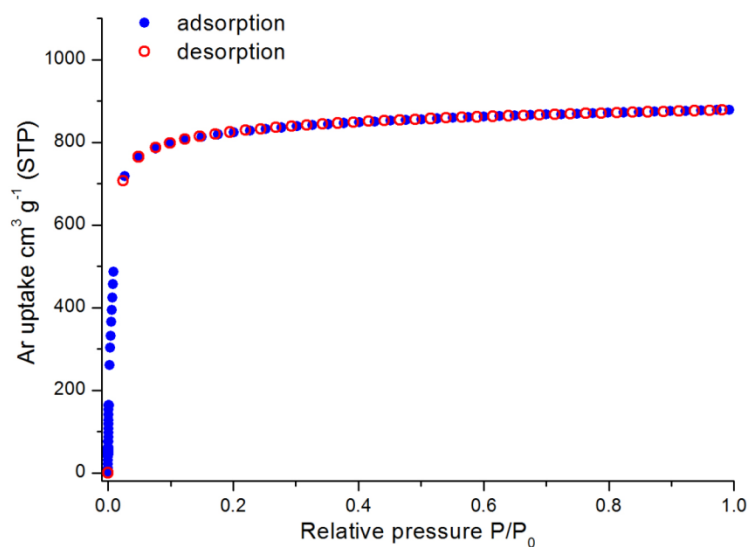
<u>Figure 6.271.</u> Argon adsorption isotherm of Cu-tbo recorded at 87 K.

274
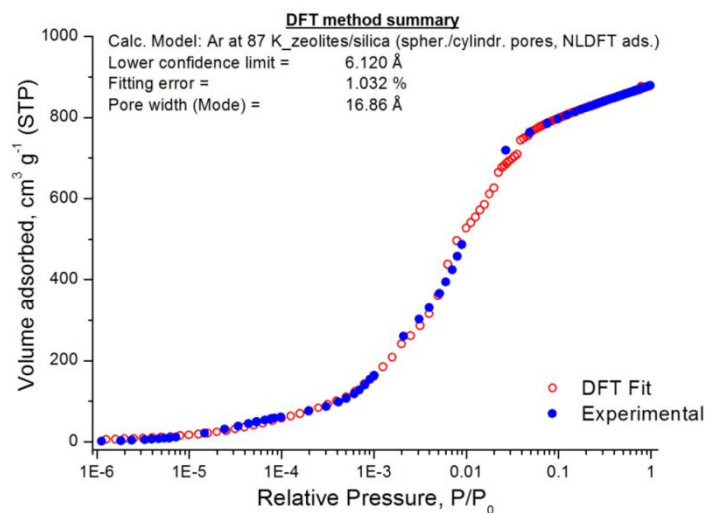
Figure 6.272. Argon adsorption isotherm of Cu-tbo recorded at 87 K and the corresponding NLDFT fitting.
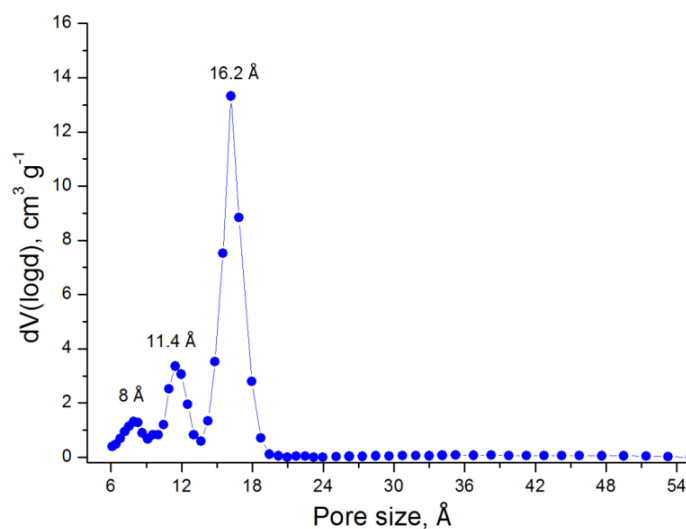
Figure 6.273. Pore size distribution in Cu-tbo calculated from NLDFT analysis.
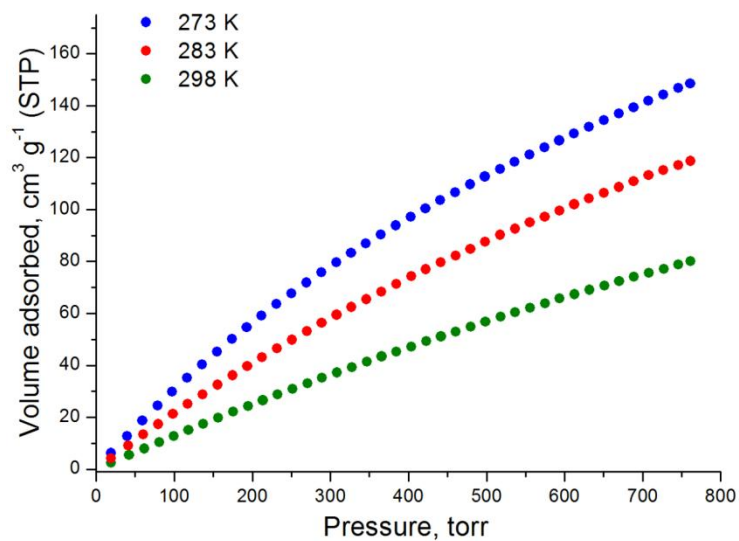
Figure 6.274. CO_2 adsorption isotherms of Cu-tbo at 273 K, 283 K and 298 K.
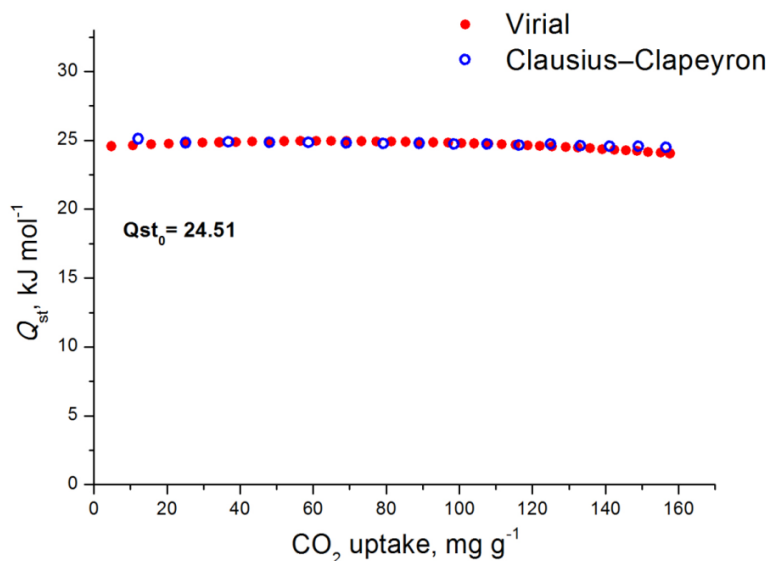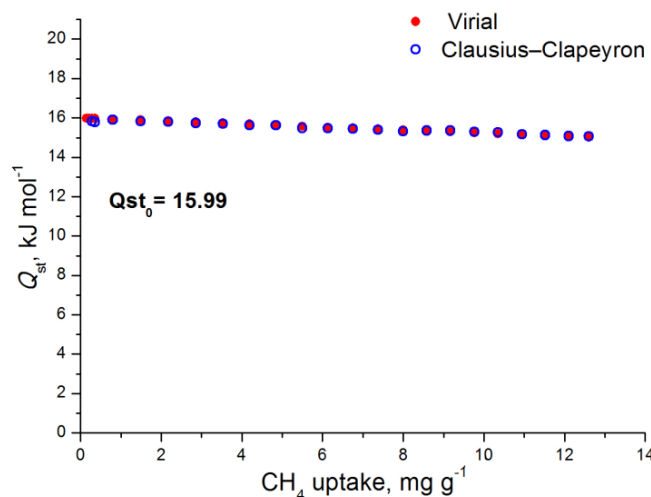
Figure 6.275. CO_2 isosteric heat of adsorption in Cu-tbo as a function of surface coverage.
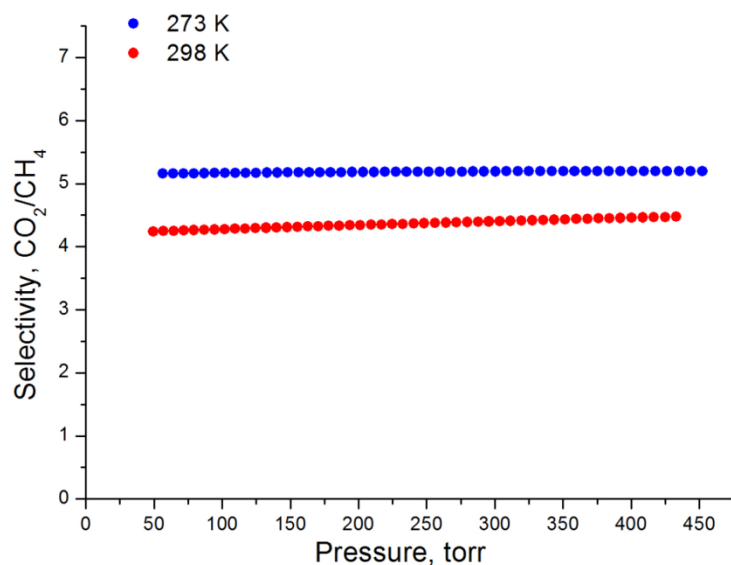
Figure 6.276. Selectivities of CO_2 over CH_4 at 298 K and 273 K for Cu-tbo as predicted by IAST for a 5/95 CO_2/CH_4 molar mixture.
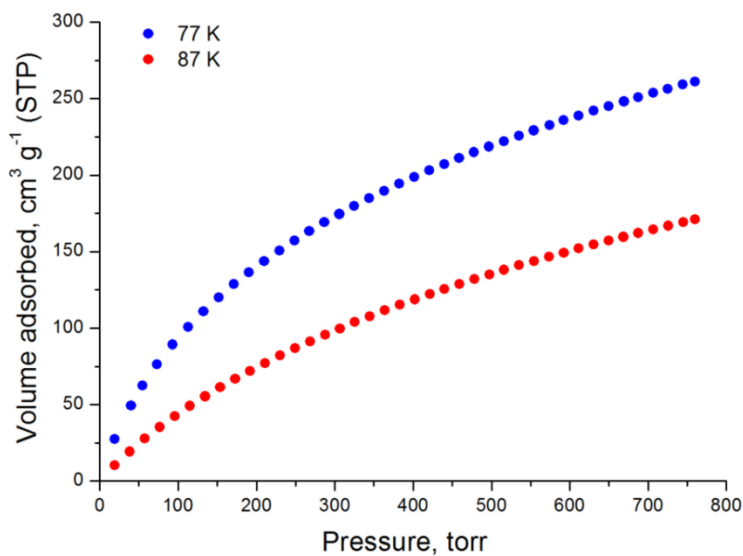
Figure 6.277. Hydrogen adsorption isotherms of Cu-tbo at 77 K and 87 K.
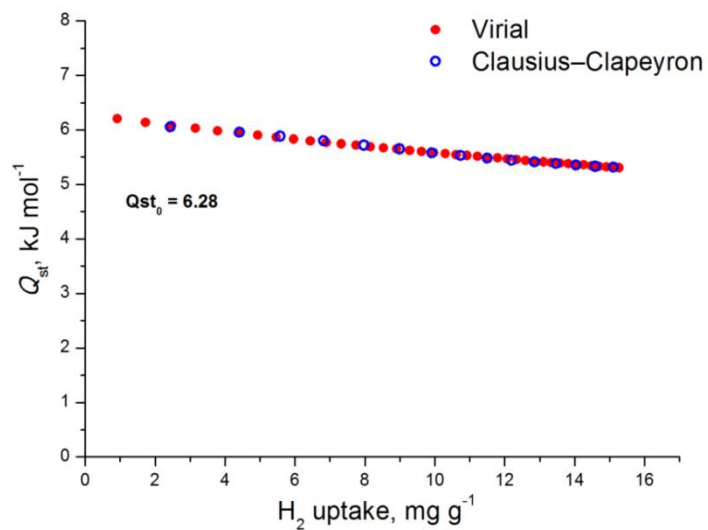
Figure 6.278. H$_2$ isosteric heat of adsorption in Cu-tbo as a function of surface coverage.
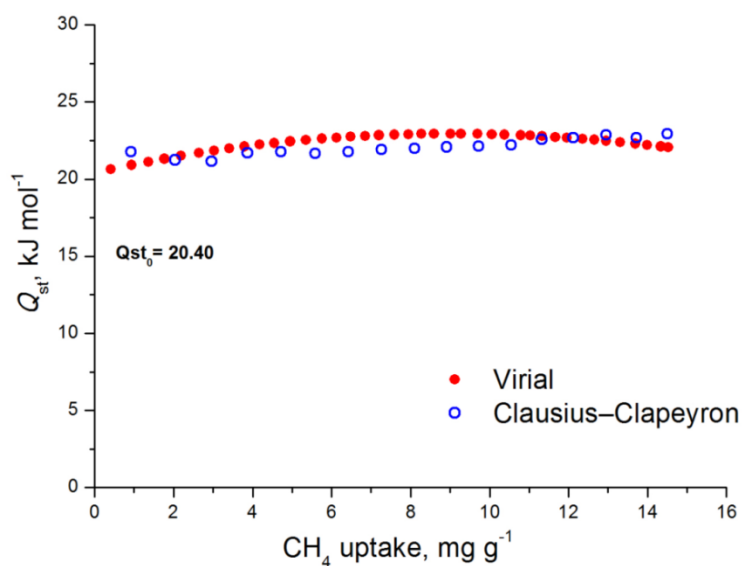
Figure 6.279. CH$_4$ isosteric heat of adsorption in Cu-tbo as a function of surface coverage.
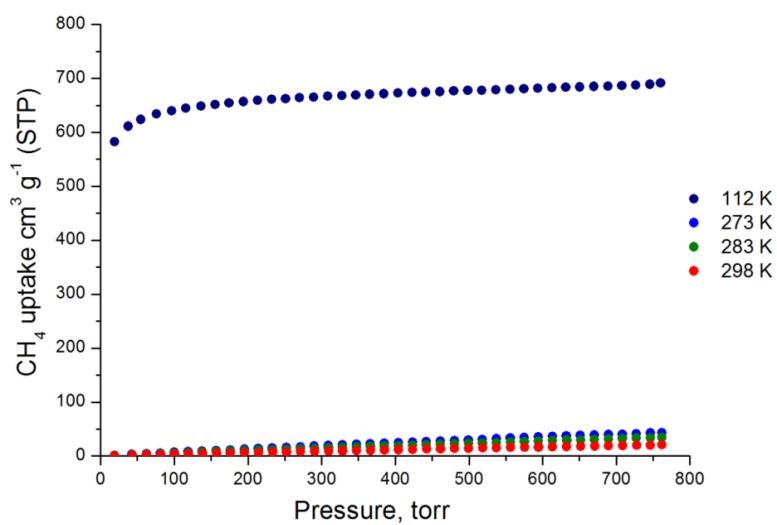
Figure 6.280. CH$_4$ adsorption isotherms of Cu-tbo at 112 K, 273 K, 283 K and 298 K.
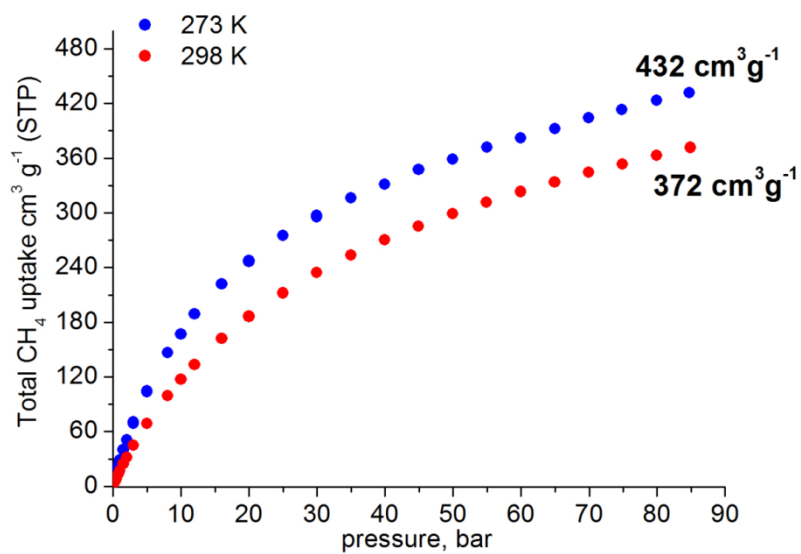
Figure 6.281. Total gravimetric CH$_4$ adsorption isotherms of Cu-tbo at 273 K and 298 K.
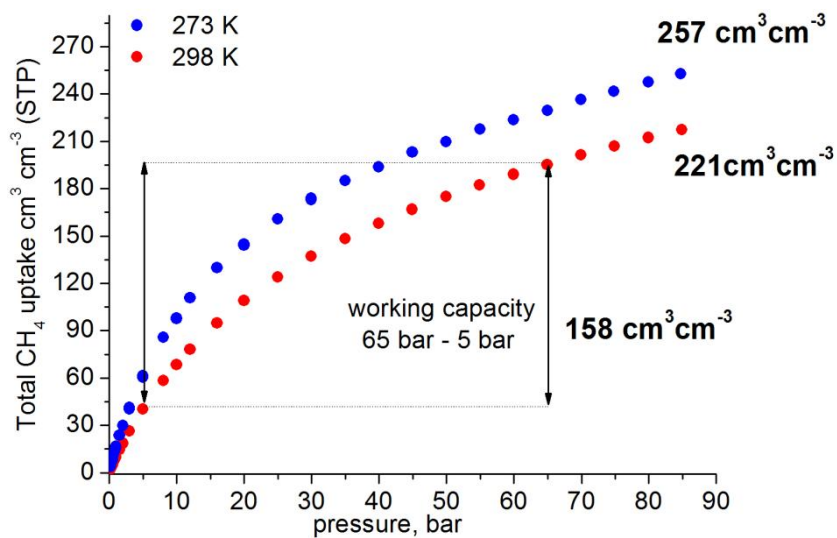
Figure 6.282. Total volumetric CH$_4$ adsorption isotherms of Cu-tbo at 273 K and 298 K, the black arrows indicate the working capacity (65 bar – 5 bar) at 298 K.
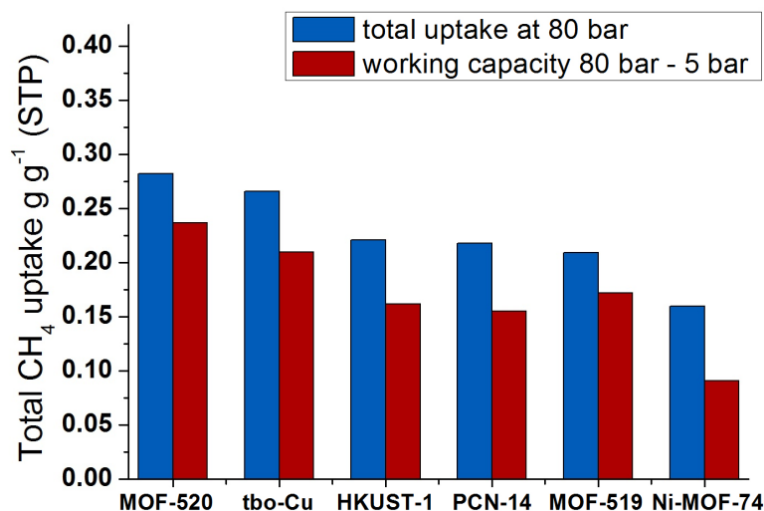
Figure 6.283. Comparison of Cu-tbo with some of the best methane storage candidates in terms of total gravimetric CH_4 uptake at 80 bar and 298 K and gravimetric working capacity between 80 bar and 5 bar at 298 K.
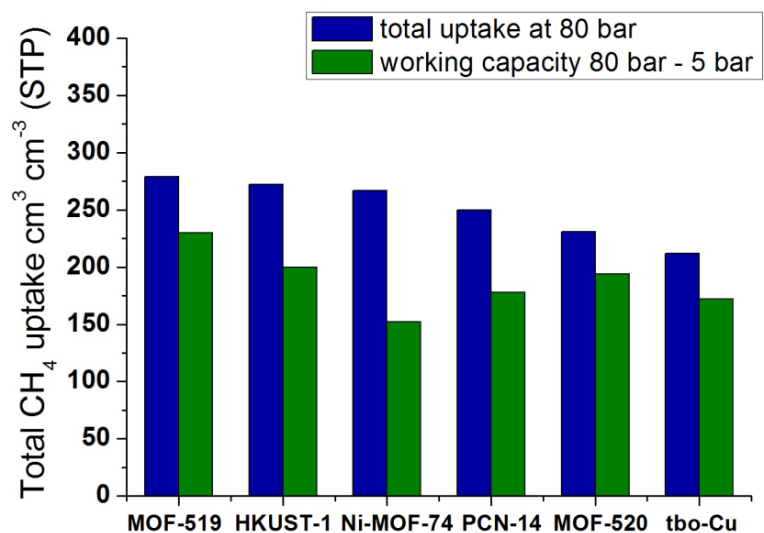
Figure 6.284. Comparison of Cu-tbo with some of the best methane storage candidates in terms of total volumetric CH_4 uptake at 80 bar and 298 K and volumetric working capacity between 80 bar and 5 bar at 298 K.

Table 6.6. Comparison of Cu-tbo with selected MOFs in terms of Total Methane Uptake, Working Capacity (Desorption at 5 bar) at 65 bar at 298 K and isosteric heat of adsorption.

Material	Surface area, m^2 g^{-1}		Density, g cm^{-3}	Total uptake at 65 bar, g g^{-1}	Total uptake at 65 bar, cm^3 cm^{-3}	Working capacity at 65 bar, g g^{-1}	Working capacity at 65 bar, cm^3 cm^{-3}	Q_{st}^0 KJ mol^{-1}
	BET	Langmuir						
Cu-tbo	3971	4123	0.595	0.238	199	0.189	158	20.4
Ni-MOF-74[2]	1350	-	1.195	0.148	251	0.077	129	**21.4**
HKUST-1[107]	1850	-	0.881	0.216	**267**	0.154	190	17
PCN-14[107]	2000	-	0.819	0.197	230	0.136	157	18.7
UTSA-76[3]	2820	-	0.699	0.263	257	0.201	**197**	15.4
NU-111[4]	4930	-	0.409	**0.360**	205	**0.313**	177	14.2
NU-1100[74]	4020	-	0.467	0.270	180	0.24	160	13.7

Table 6.7. Comparison of Cu-tbo with selected MOFs in terms of Total Methane Uptake, Working Capacity (Desorption at 5 bar) at 35 and 80 bar at 298 K.[5]

Material	Surface area, m^2 g^{-1}		Density, g cm^{-3}	Total uptake at 35 bar, cm^3 cm^{-3}	Total uptake at 80 bar, cm^3 cm^{-3}	Total uptake at 80 bar, g g^{-1}	Working capacity at 35 bar, cm^3 cm^{-3}	Working capacity at 80 bar, cm^3 cm^{-3}	Working capacity at 80 bar, g g^{-1}
	BET	Langmuir							
Cu-tbo	3971	4123	0.595	151	216	0.260	110	175	0.210
MOF-519	2400	2660	0.953	200	**279**	0.209	151	**230**	0.172
MOF-520	3290	3930	0.586	162	231	0.282	125	194	0.237
Ni-MOF-74	-	1438	1.195	**230**	267	0.160	115	152	0.091
HKUST-1	-	1977	0.881	225	272	0.221	**153**	200	0.162
PCN-14	-	2360	0.819	200	250	0.218	128	178	0.155
AX-21	-	4880	0.487	153	222	**0.326**	103	172	**0.252**
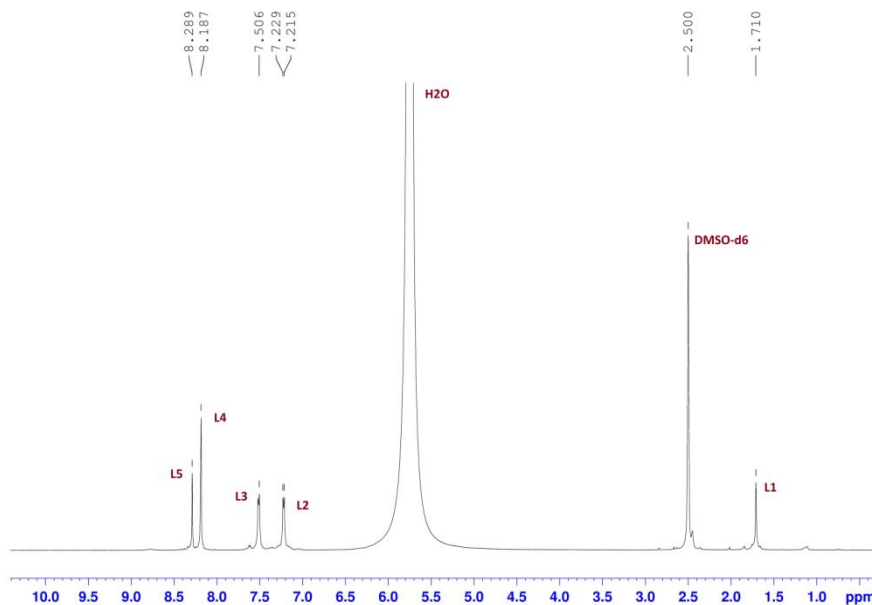
Figure 6.285. ^{1}H NMR spectrum of evacuated Cu-tbo after digesting the sample in HCl/DMSO-d_6 solution.
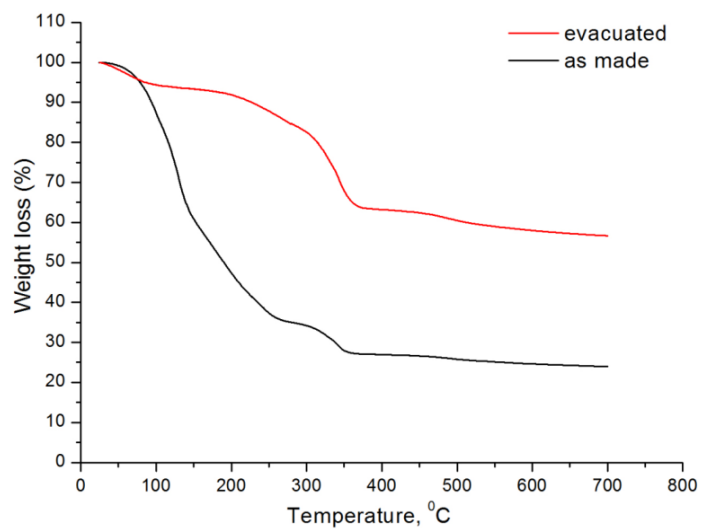
Figure 6.286. TGA curve for the as-made Cu-tbo and the corresponding evacuated solid, recorded under nitrogen flow with a heating rate of 5 deg/min.

6.46 MOF synthesis based on organic linker 48
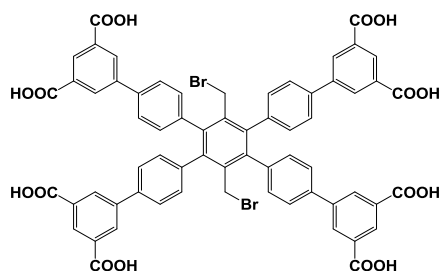
6.46.1 Synthesis of tbo-compound [Cu$_4$L](Cu-tbo-Br).

A solution of 3 mL DMF, 1 mL EtOH, 3 drops c.HNO$_3$, 0.035 g (0.03 mmol) of H$_8$L and 0.014 g (0.06 mmol) of Cu(NO$_3$)$_2$·3H$_2$O was placed in a 20 mL glass scintillation vial. The vial was sealed and placed in an isothermal oven at 85 °C for 18 hours. During this period, small blue crystals were deposited (54% yield based on H$_8$L).

After the efficient characterization of the material the evaluation of its gas sorption properties took place. Successful activation was possible as follows: as-made sample was washed with DMF four times per day for 2 days and then the sample was soaked in acetone over a period of 4 days, replenishing the acetone 4 times per day. Afterwards the acetone was exchanged with CH$_2$Cl$_2$, 2 times per day for 2 days. Finally, the sample was activated under dynamic vacuum at 60 °C for 12 hours and until the outgas rate was less than 2 mTorr/min. The color of the material changed from light blue to deep purple.
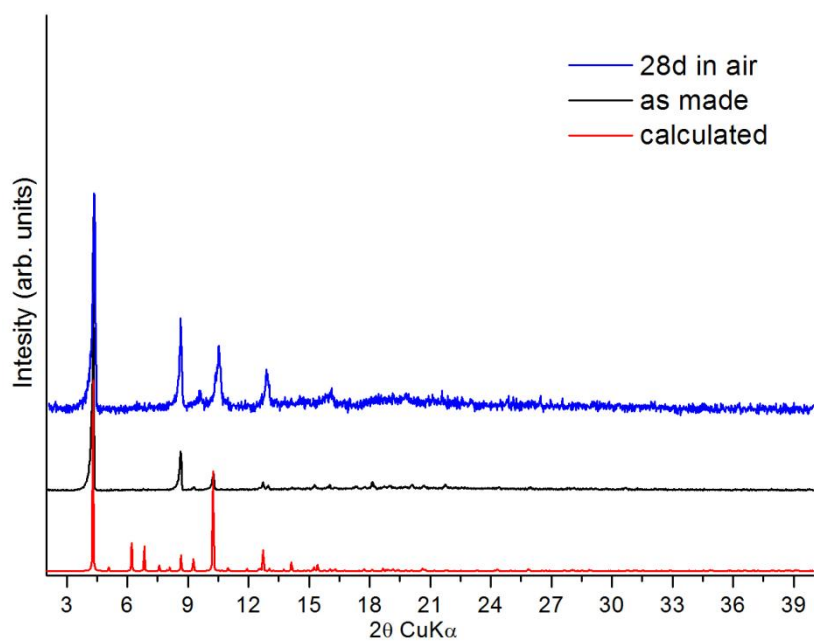
Figure 6.287. Comparison of experimental, calculated and 28 days in air pxrd patterns for the compound Cu-tbo-Br.
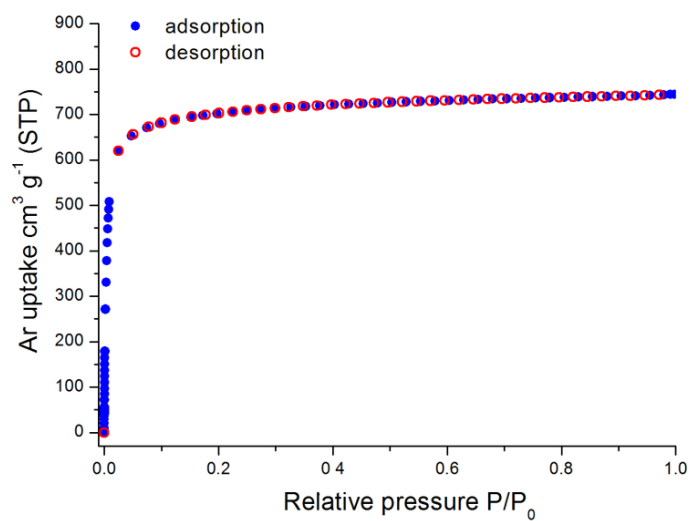
Figure 6.288. Argon adsorption isotherm of Cu-tbo-Br recorded at 87 K.
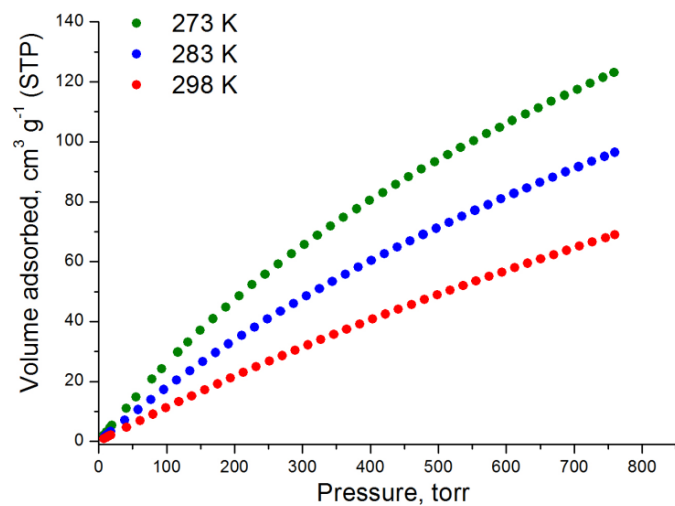
Figure 6.289. CO_2 adsorption isotherms of Cu-tbo-Br at 273 K, 283 K and 298 K.
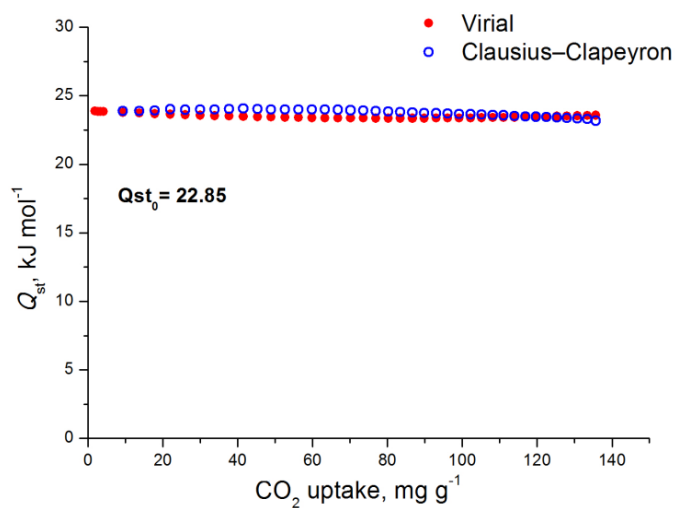
Figure 6.290. CO_2 isoteric heat of adsorption in Cu-tbo-Br as a function of surface coverage.
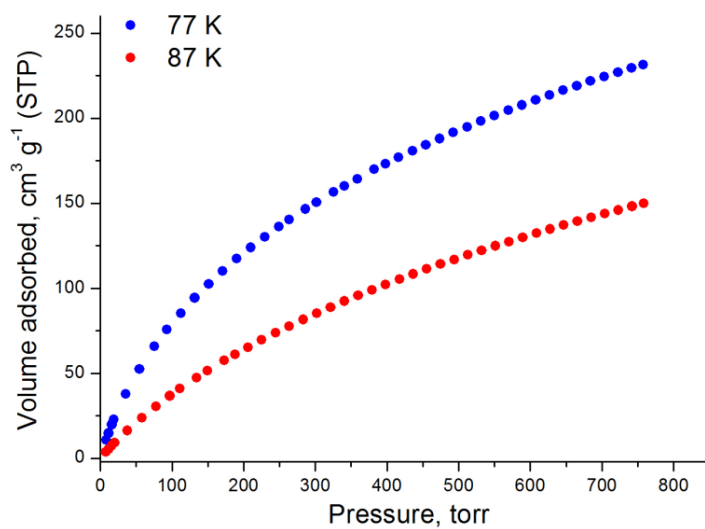
Figure 6.291. Hydrogen adsorption isotherms of Cu-tbo-Br at 77 K and 87 K.
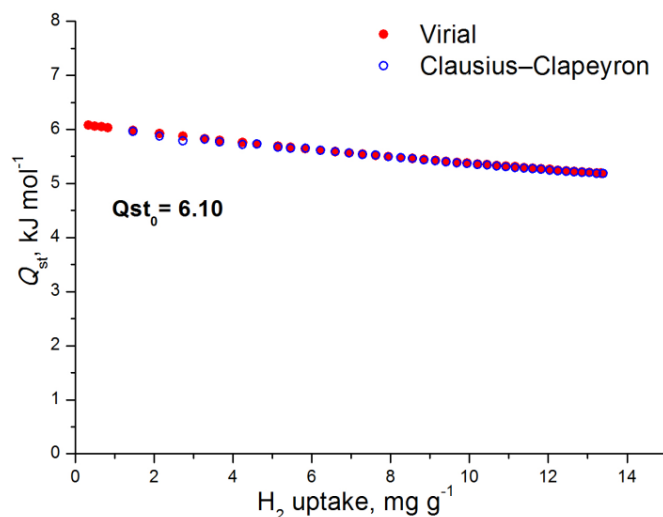
Figure 6.292. H_2 isosteric heat of adsorption in Cu-tbo-Br as a function of surface coverage.
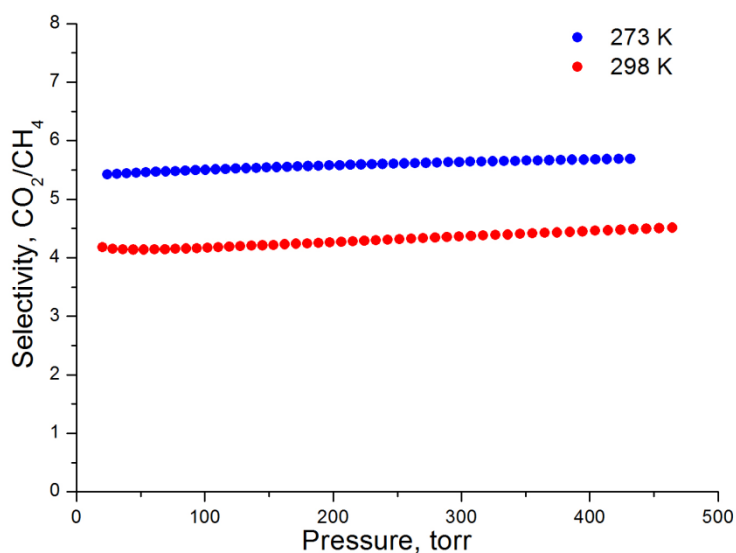
Figure 6.293. Selectivities of CO_2 over CH_4 at 298 K and 273 K for Cu-tbo-Br as predicted by IAST for a 5/95 CO_2/CH_4 molar mixture.
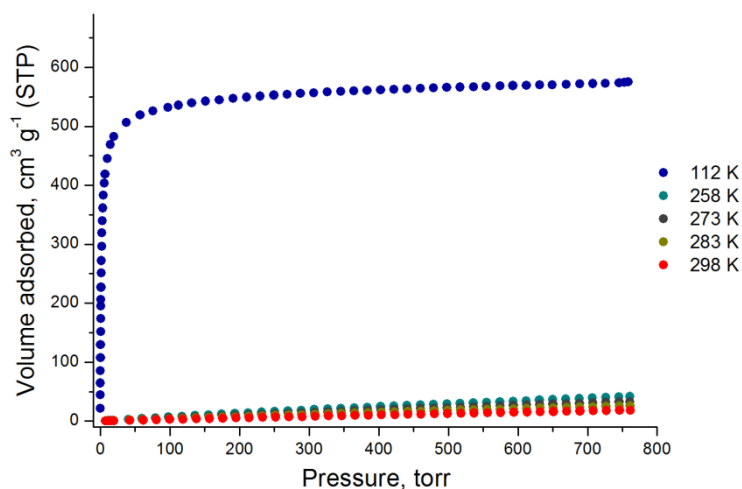
Figure 6.294. CH_4 adsorption isotherms of Cu-tbo-Br at 112 K, 258 K, 273 K, 283 K and 298 K.
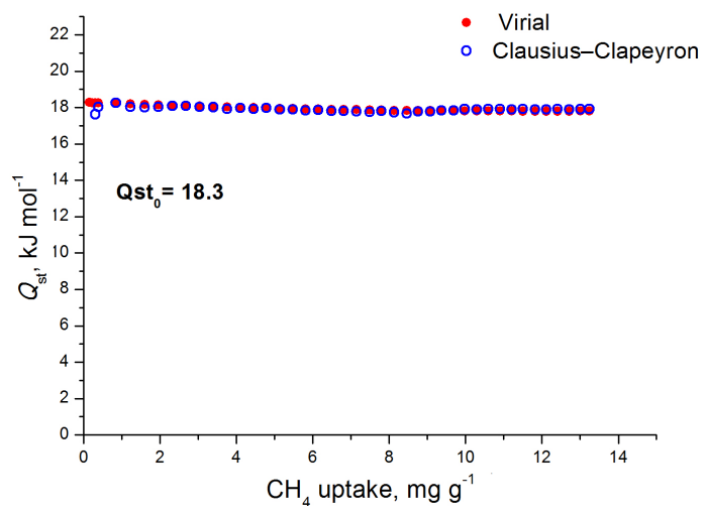
Figure 6.295. CH_4 isosteric heat of adsorption in Cu-tbo-Br as a function of surface coverage.
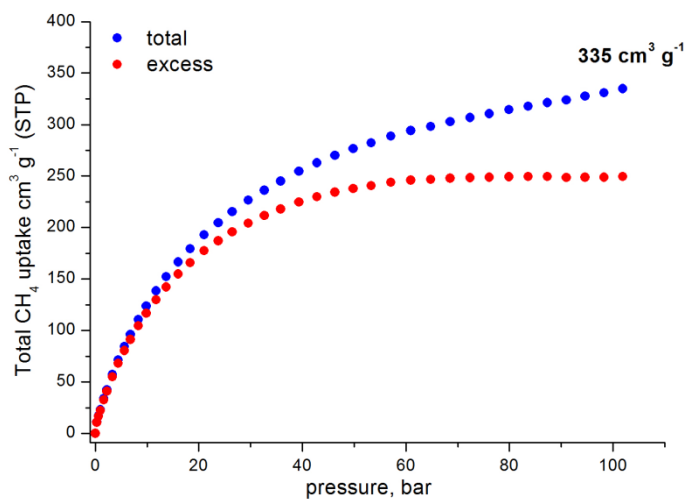
Figure 6.296. Total and excess gravimetric CH_4 adsorption isotherms of Cu-tbo-Br at 298 K.
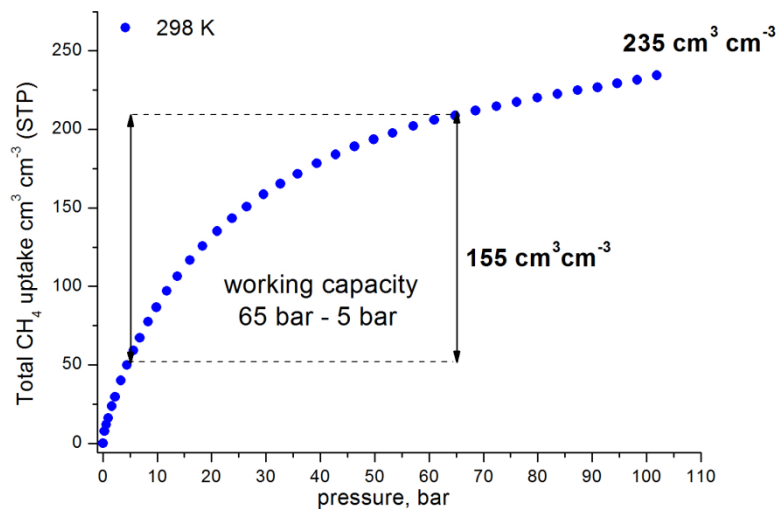
Figure 6.297. Total volumetric CH_4 adsorption isotherm of Cu-tbo-Br at 298 K, the black arrows indicate the working capacity (65 bar – 5 bar).
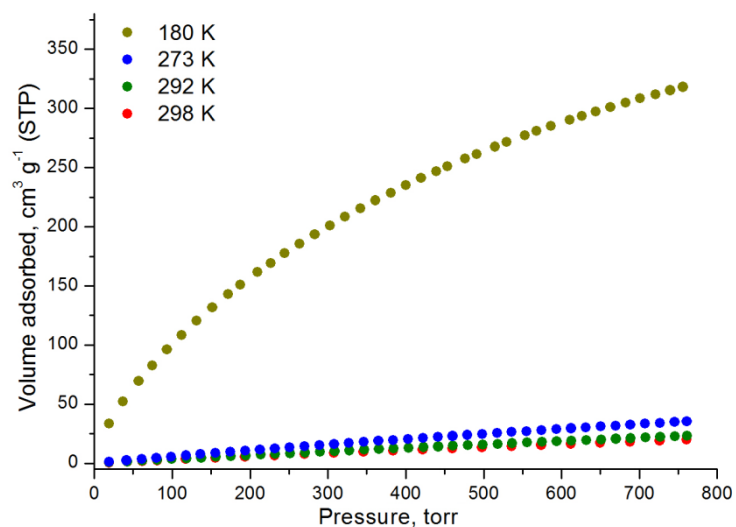
Figure 6.298. Kr adsorption isotherms of Cu-tbo-Br at 180 K, 273 K, 292 K and 298 K.
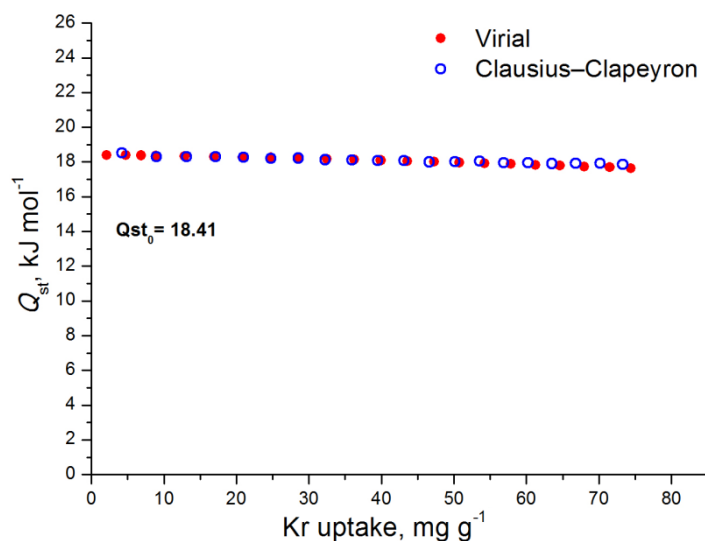
Figure 6.299. Kr isosteric heat of adsorption as a function of surface coverage.
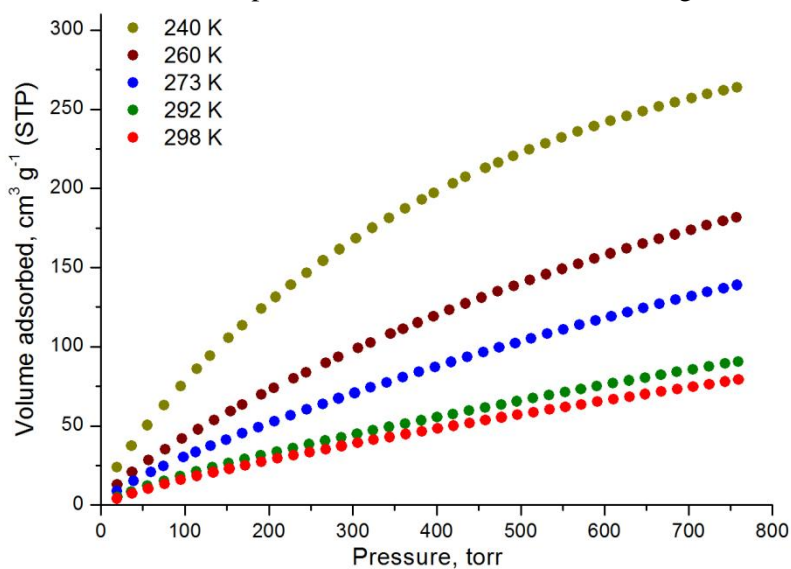
Figure 6.300. Xe adsorption isotherms of Cu-tbo-Br at 240 K, 260 K, 273 K, 292 K and 298 K.

287
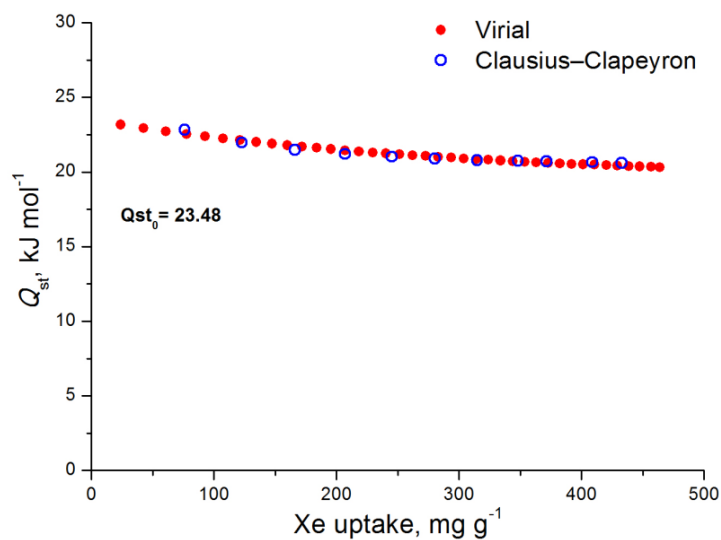
Figure 6.301. Xe isosteric heat of adsorption as a function of surface coverage.
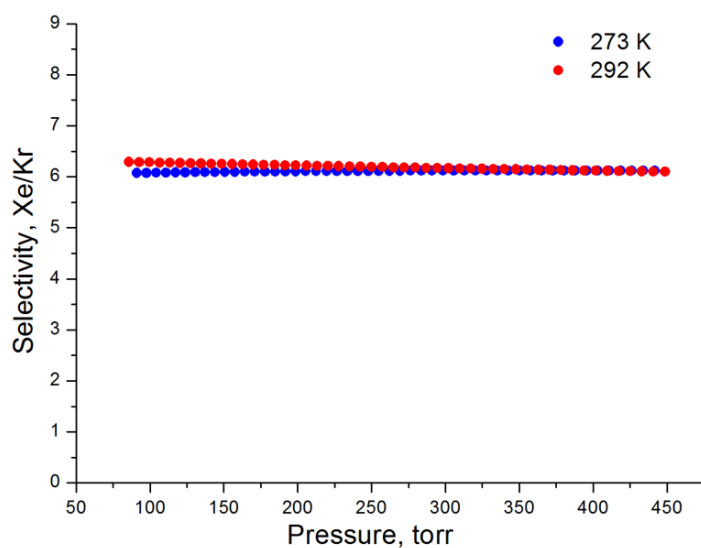
Figure 6.302. Selectivities of Xe over Kr at 292 K and 273 K for Cu-tbo-Br as predicted by IAST for a 5/95 Xe/Kr molar mixture.

6.47 MOF synthesis based on organic linker 49
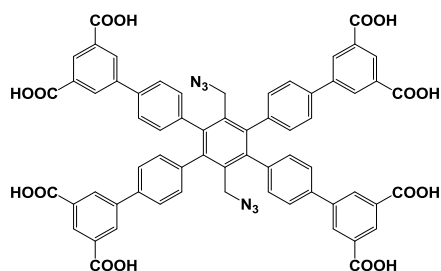
6.47.1 Synthesis of tbo-compound [Cu$_4$L](Cu-tbo-N$_{3)}$.

A solution of 3 mL DMF, 1 mL EtOH, 3 drops c.HNO$_3$, 0.035 g (0.03 mmol) of H$_8$L and 0.018 g (0.07 mmol) of Cu(NO$_3$)$_2$·3H$_2$O was placed in a 20 mL glass scintillation vial. The vial was sealed and placed in an isothermal oven at 85 °C for 18 hours. During this period, small blue crystals were deposited (55% yield based on H$_8$L).

After the efficient characterization of the material the evaluation of its gas sorption properties took place. Successful activation was possible as follows: as-made sample was washed with DMF four times per day for 2 days and then the sample was soaked in acetone over a period of 4 days, replenishing the acetone 4 times per day. Afterwards the acetone was exchanged with CH$_2$Cl$_2$, 2 times per day for 2 days. Finally, the sample was activated under dynamic vacuum at 60 °C for 12 hours and until the outgas rate was less than 2 mTorr/min. The color of the material changed from light blue to deep purple.

Figure 6.303. Comparison of experimental, calculated and 18 days in air pxrd patterns for the compound Cu-tbo-N$_3$.
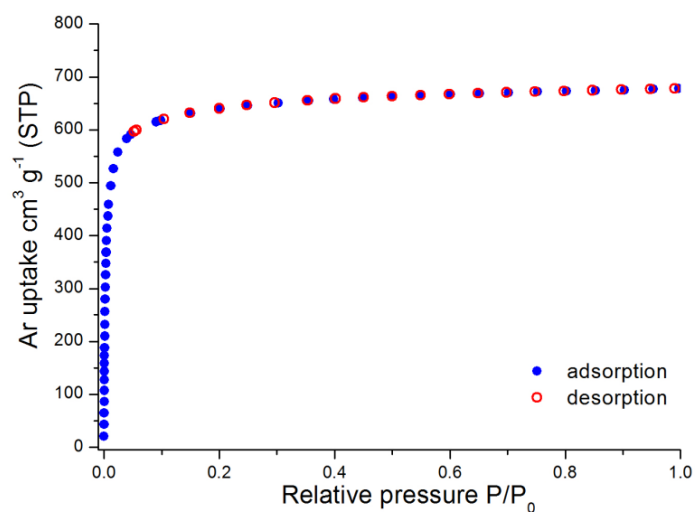
Figure 6.304. Argon adsorption isotherm of Cu-tbo-N_3 recorded at 87 K.
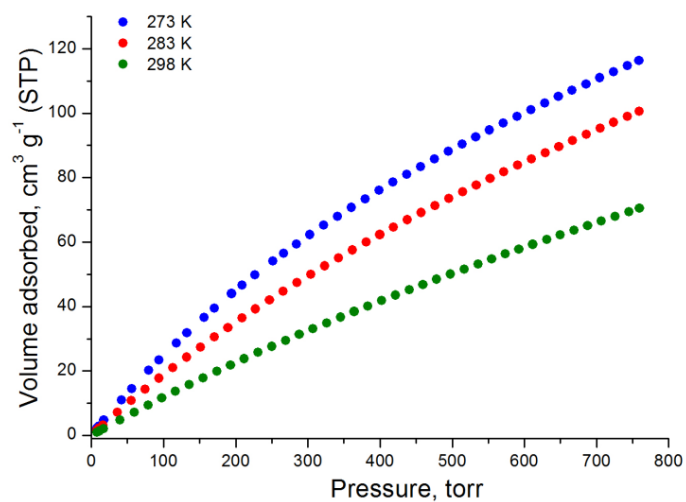
Figure 6.305. CO_2 adsorption isotherms of Cu-tbo-N_3 at 273 K, 283 K and 298 K.
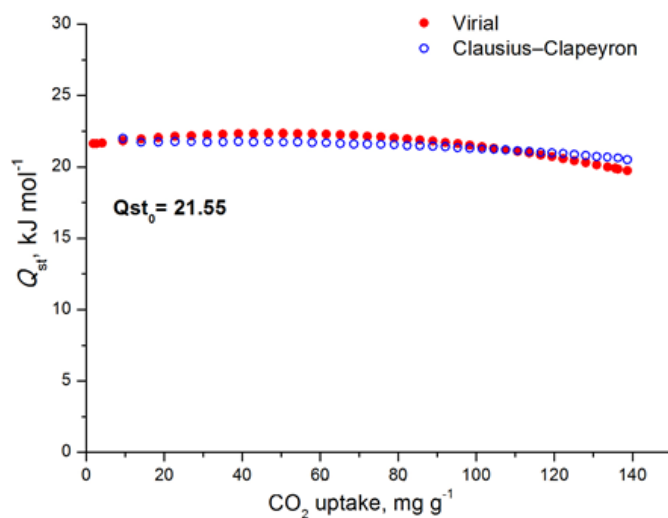
Figure 6.306. CO_2 isosteric heat of adsorption in Cu-tbo-N_3 as a function of surface coverage.
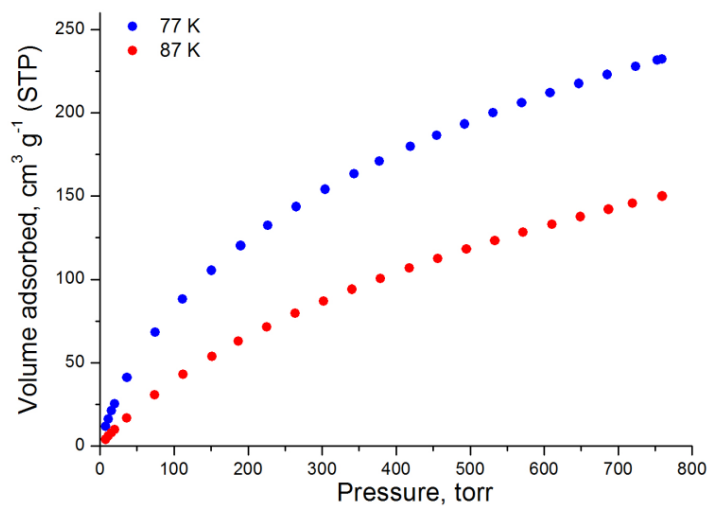
Figure 6.307. Hydrogen adsorption isotherms of Cu-tbo-N_3 at 77 K and 87 K.
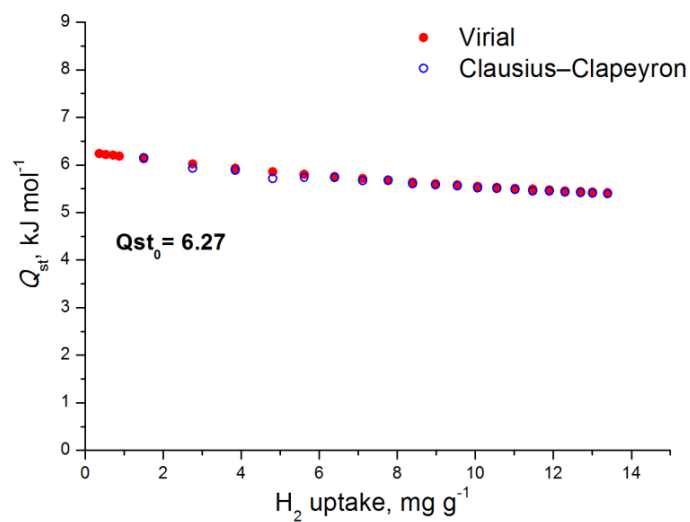
Figure 6.308. H_2 isosteric heat of adsorption in Cu-tbo-N_3 as a function of surface coverage.
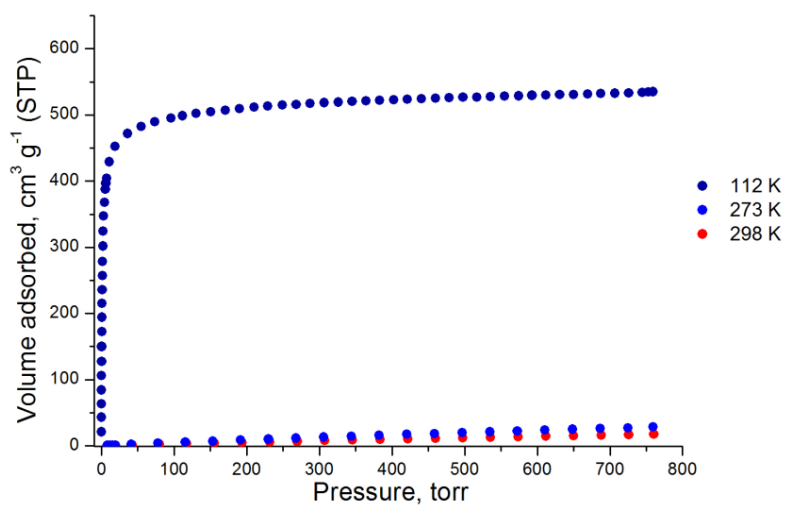
Figure 6.309. CH_4 adsorption isotherms of Cu-tbo-N_3 at 112 K, 273 K, and 298 K.

Figure 6.310. CH$_4$ isosteric heat of adsorption in Cu-tbo-N$_3$ as a function of surface coverage.
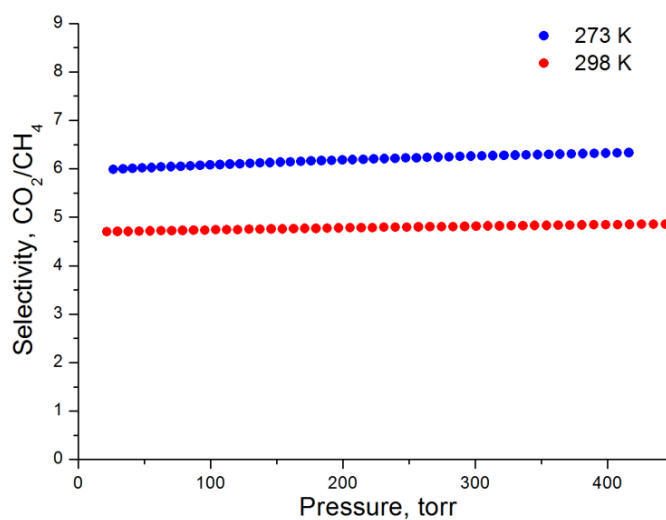
Figure 6.311. Selectivities of CO$_2$ over CH$_4$ at 298 K and 273 K for Cu-tbo-N$_3$ as predicted by IAST for a 5/95 CO$_2$/CH$_4$ molar mixture.

6.48 MOF synthesis based on organic linker 50
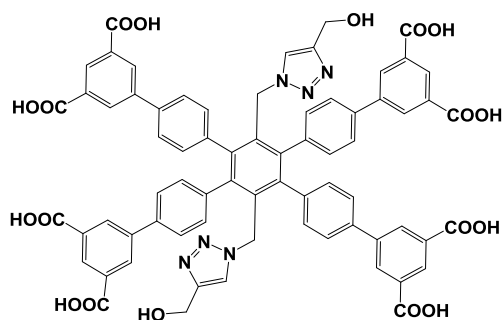
6.48.1 Synthesis of tbo-compound [Cu$_4$L](Cu-tbo-triazole).

A solution of 3 mL DMF, 1 mL EtOH, 3 drops c.HNO$_3$, 0.035 g (0.03 mmol) of H$_8$L and 0.013 g (0.05 mmol) of Cu(NO$_3$)$_2$·3H$_2$O was placed in a 20 mL glass scintillation vial. The vial was sealed and placed in an isothermal oven at 85 °C for 18 hours. During this period, small blue crystals were deposited (55% yield based on H$_8$L).
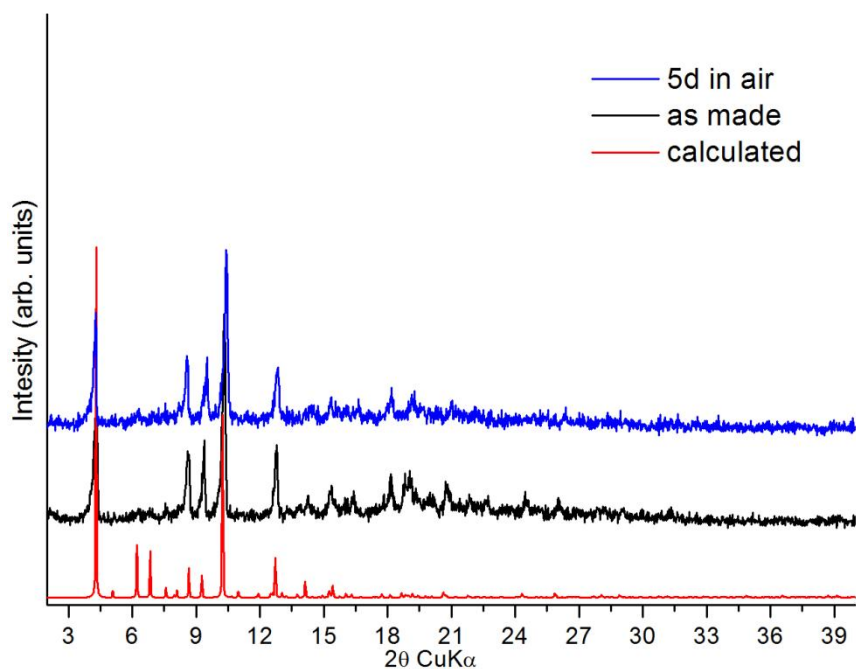
Figure 6.312. Comparison of experimental, calculated and 5 days exposure in air pxrd patterns for the compound Cu-tbo-triazole.
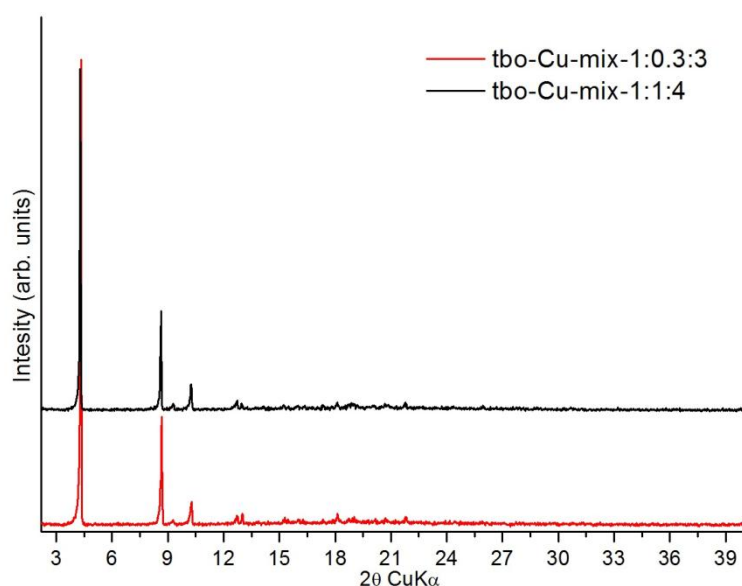
Figure 6.313. Comparison of experimental pxrd patterns for mixed linker Cu-tbo compounds.

6.49 MOF syntheses based on organic linker 51
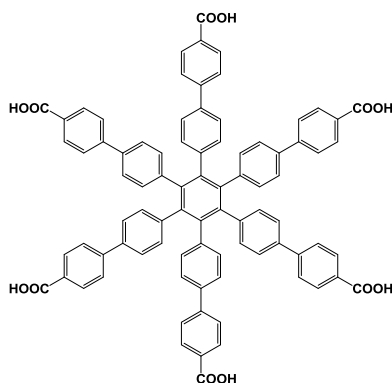
6.49.1 Synthesis of compound $Co_4(L)Cl_2(DMF)_3$

An amount of 0.050 g (0.04 mmol) of linker 51 (H_6L) and 0.035 g (0.28 mmol) of $CoCl_2 \cdot 6H_2O$ were dissolved in a 20 mL glass scintillation vial containing 3 mL DMF, 7 mL ethanol and one drop of c.HCl. The vial was heated at 85 ^{0}C for 16 h where uniform, blue plate like crystals were formed. Yield: 40 % based on linker H_6L.
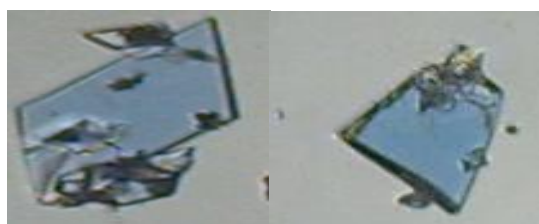
<u>Figure 6.314.</u> Optical microscope pictures of $Co_4(L)Cl_2(DMF)_3$ crystals.
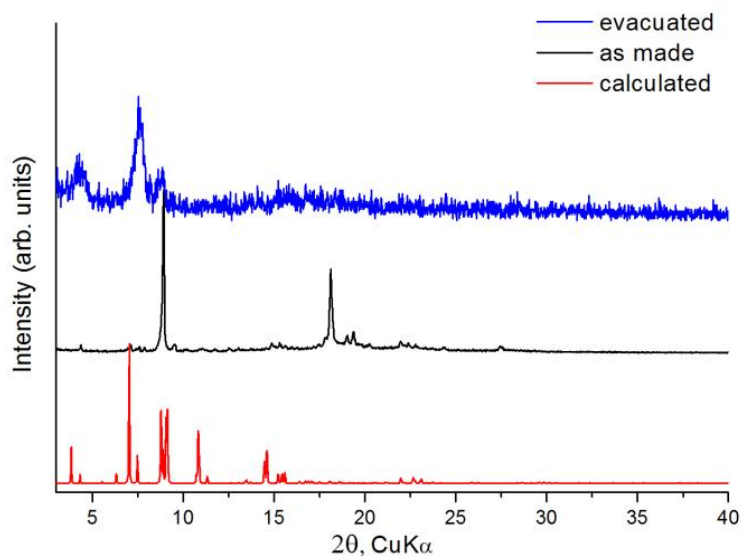
<u>Figure 6.317.</u> Comparison of experimental, calculated and evacuated pxrd patterns for $Co_4(L)Cl_2(DMF)_3$. The differences between the calculated and as made one are attributed to preferred orientation.

Prior to analysis, as-made sample was soaked in absolute ethanol at room temperature for three (3) days during of which the supernatant solution was replaced six (6) times. The ethanol suspended samples were transferred inside the chamber of a supercritical CO_2 dryer (Bal-Tec CPD 030) and ethanol was exchanged with liquid CO_2 over a period of 5 hours at 8 ^{o}C. During this period, liquid CO_2 was vented under positive pressure every 2 minutes. The rate of CO_2 venting was always kept below the rate of filling so as to maintain full drying conditions inside the chamber. Following venting, the temperature was raised to 40 ºC (above the critical temperature of CO_2), kept there for 1 hour and then slowly vented over the period of 2 hours. The dried sample was transferred immediately inside a pre-weighted, Argon filled 9 mm cell and closed using CellSealTM provided by Quantachrome to prevent intrusion of oxygen and atmospheric moisture during transfers and weighing. The cell was then transferred to the outgassing station were the sample was evacuated under dynamic vacuum at room temperature until the outgas rate was less than 2 mTorr/min. After evacuation, the sample and cell were re-weighed to obtain the precise mass of the evacuated sample. Finally, the tube was transferred to the analysis port of the gas adsorption instrument.
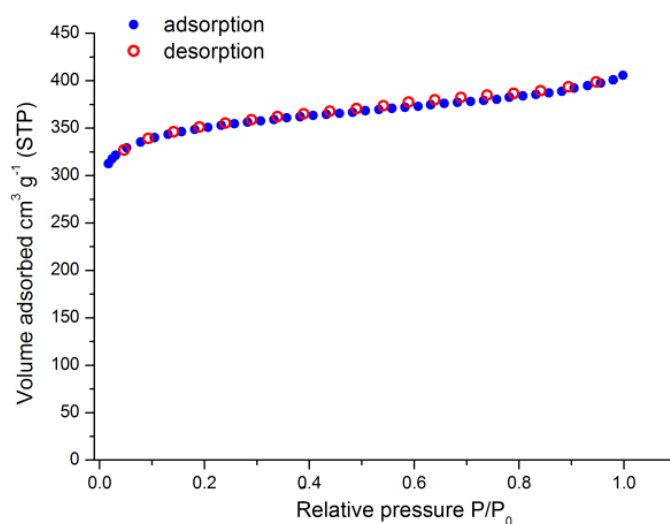
Figure 6.318. Nitrogen adsorption isotherm of $Co_4(L)Cl_2(DMF)_3$ recorded at 77 K.
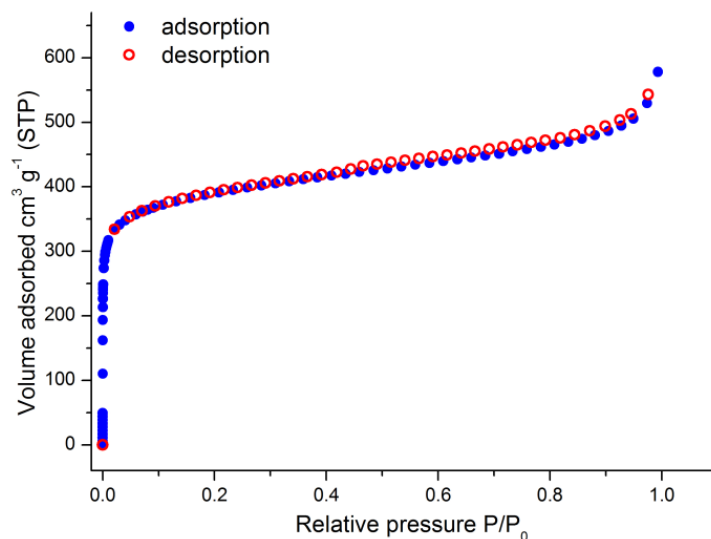
Figure 6.319. Argon adsorption isotherm of $Co_4(L)Cl_2(DMF)_3$ recorded at 87 K.

Slope =	1.646
Intercept =	1.463e-03
Correlation coefficient, r =	0.999998
C constant=	1126.008
Surface Area =	**1299.435 m²/g**
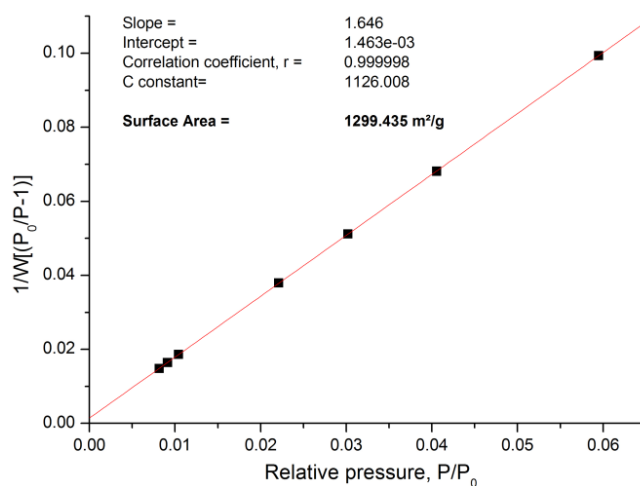
Figure 6.320. BET plot for $Co_4(L)Cl_2(DMF)_3$ from Ar adsorption isotherm.

Slope =	1.58680
Intercept =	0.00185
Correlation coefficient, r =	1.000
Surface Area =	**1349.012 m²/g**
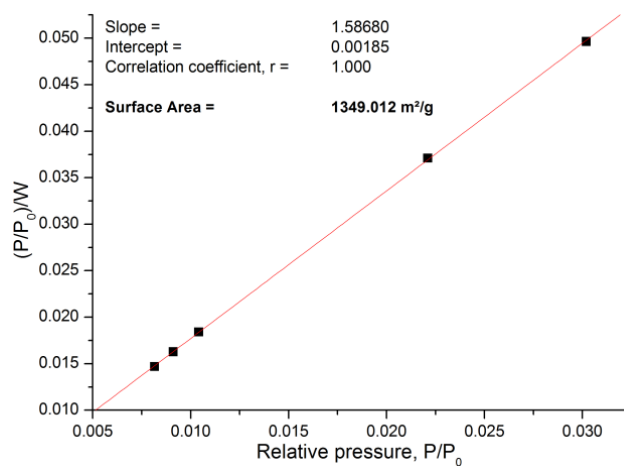
Figure 6.321. Langmuir plot for $Co_4(L)Cl_2(DMF)_3$ from Ar adsorption isotherm.

DFT method summary
Calc. Model: Ar at 87 K_zeolites/silica (spher./cylindr. pores, NLDFT ads.)
Lower confidence limit =   6.800 Å
Fitting error =   0.118 %
Pore width (Mode) =   10.030 Å
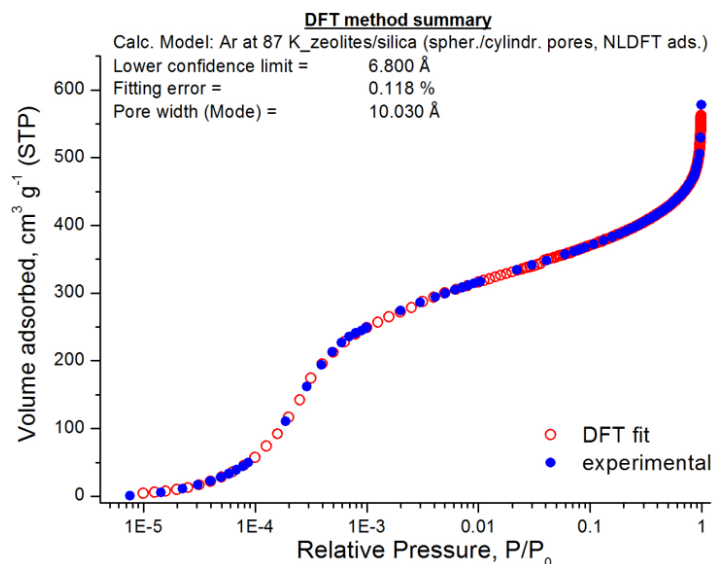
Figure 6.322. Argon adsorption isotherm of $Co_4(L)Cl_2(DMF)_3$ recorded at 87 K and the corresponding NLDFT fitting.
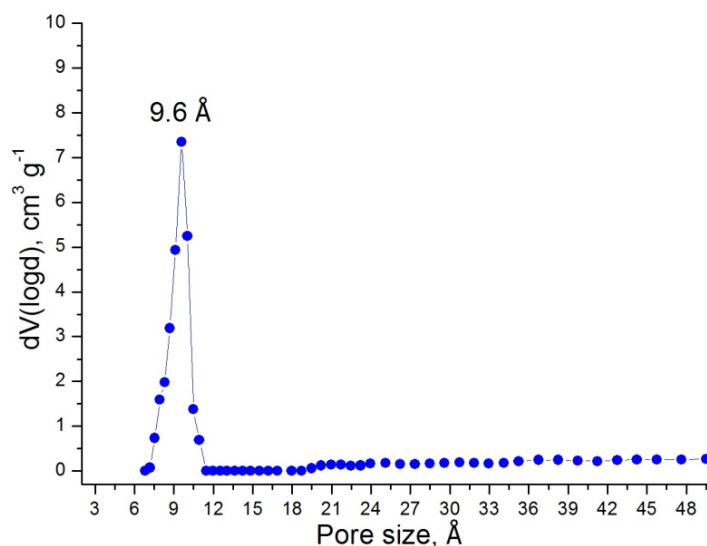
Figure 6.323. Pore size distribution in $Co_4(L)Cl_2(DMF)_3$ calculated from NLDFT analysis.
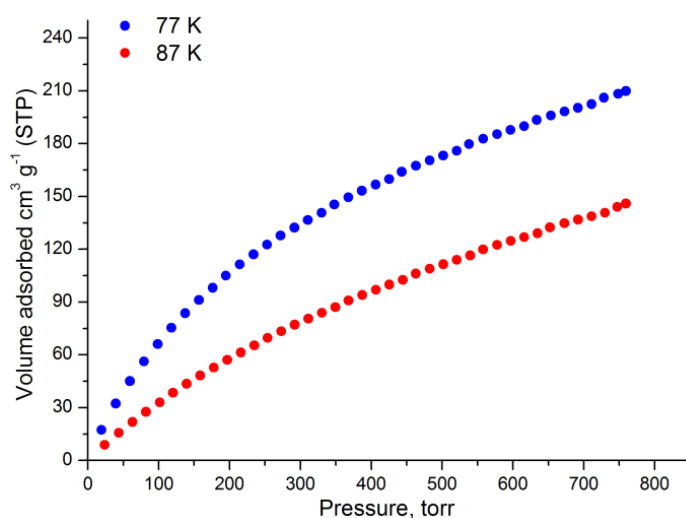
Figure 6.324. Hydrogen adsorption isotherms of $Co_4(L)Cl_2(DMF)_3$ at 77 K and 87 K.
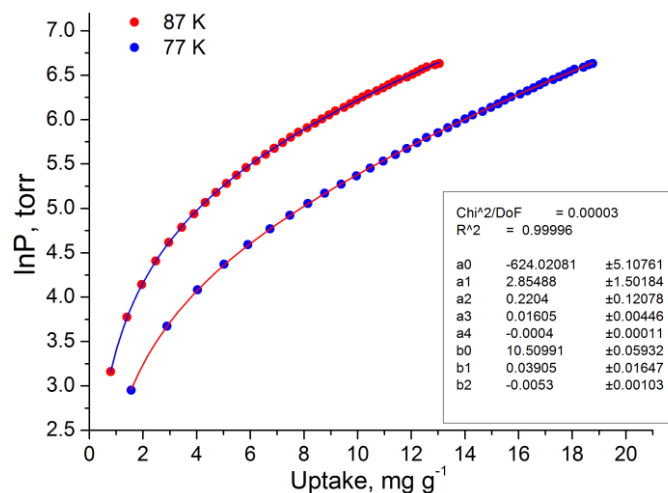
Figure 6.325. Virial type fitting of H_2 adsorption isotherms of $Co_4(L)Cl_2(DMF)_3$ at 77 K and 87 K.
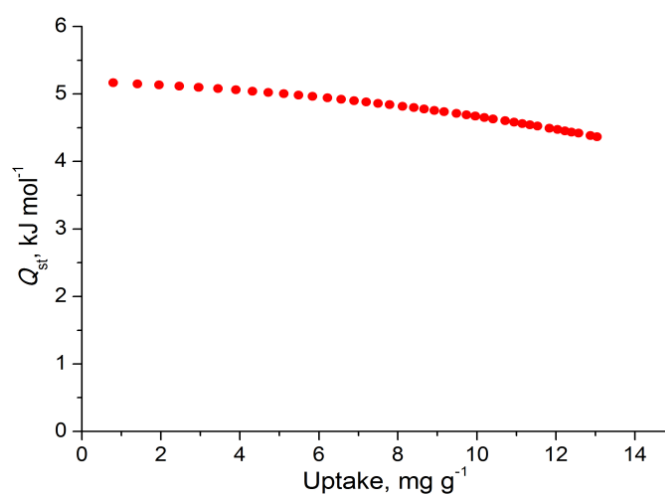
Figure 6.326. H_2 isosteric heat of adsorption in $Co_4(L)Cl_2(DMF)_3$ as a function of surface coverage.
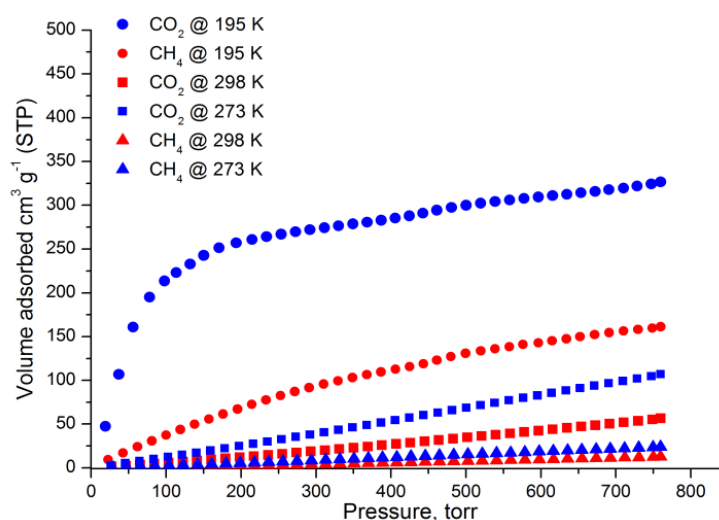
Figure 6.327. CO_2 and CH_4 adsorption isotherms of $Co_4(L)Cl_2(DMF)_3$ at 195 K, 273 K and 298 K.
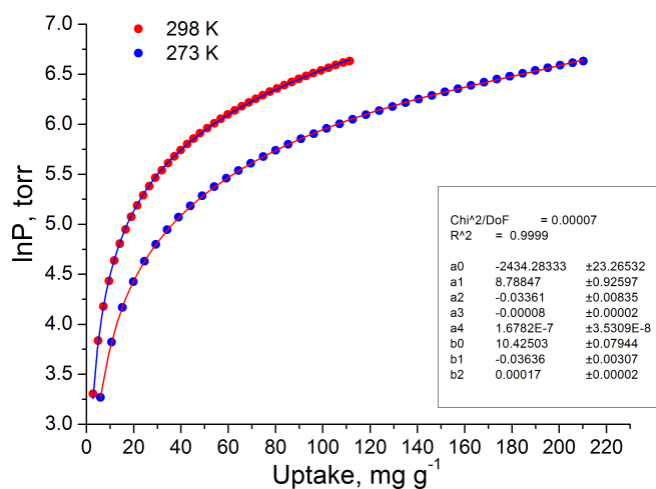
Figure 6.328. Virial type fitting of CO_2 adsorption isotherms of $Co_4(L)Cl_2(DMF)_3$ at 273 K and 298 K.
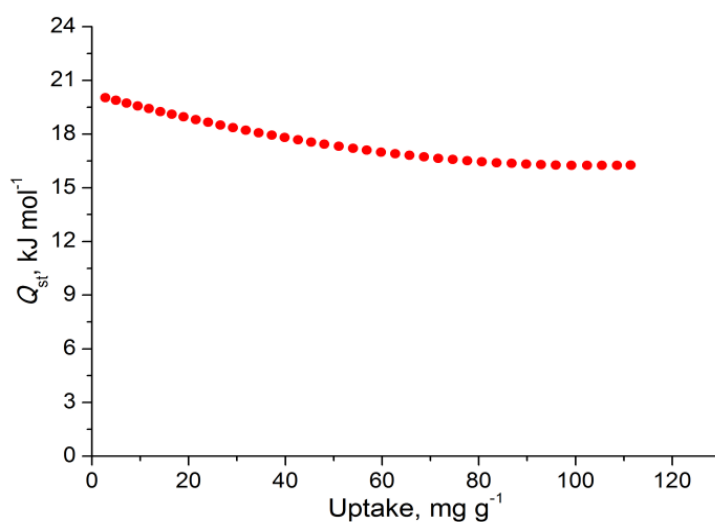
Figure 6.329. CO_2 isosteric heat of adsorption in $Co_4(L)Cl_2(DMF)_3$ as a function of surface coverage.
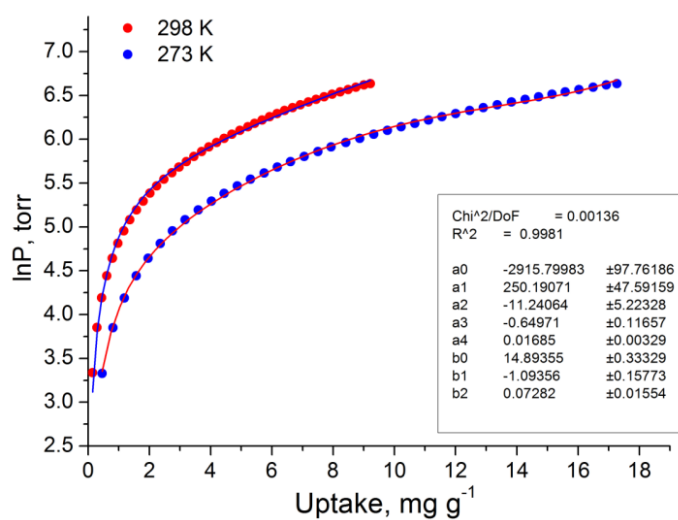
Figure 6.330. Virial type fitting of CH_4 adsorption isotherms of $Co_4(L)Cl_2(DMF)_3$ at 273 K and 298 K.

299
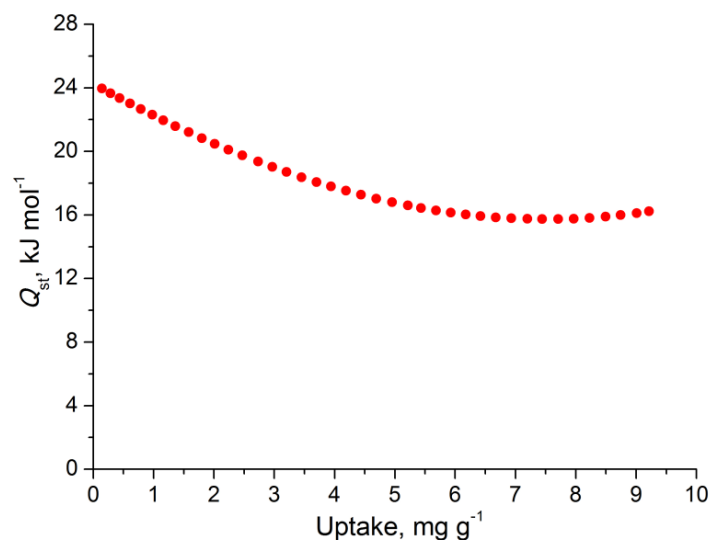
Figure 6.331. CH_4 isosteric heat of adsorption in $Co_4(L)Cl_2(DMF)_3$ as a function of surface coverage.
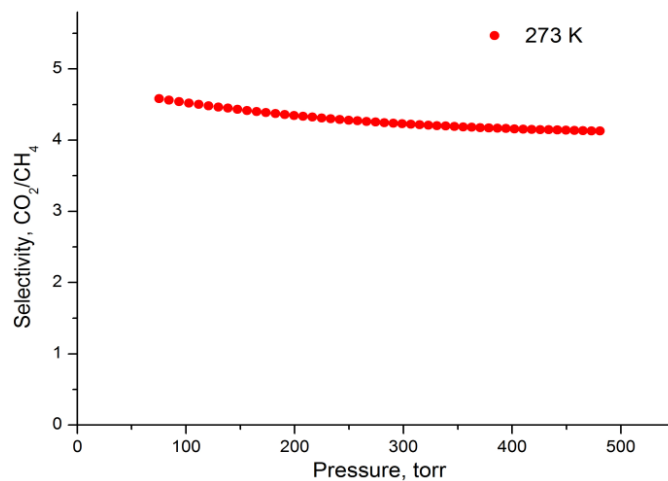
Figure 6.332. Selectivity of CO_2 over CH_4 at 273 K for $Co_4(L)Cl_2(DMF)_3$ as predicted by IAST for a 5/95 CO_2/CH_4 molar mixture.
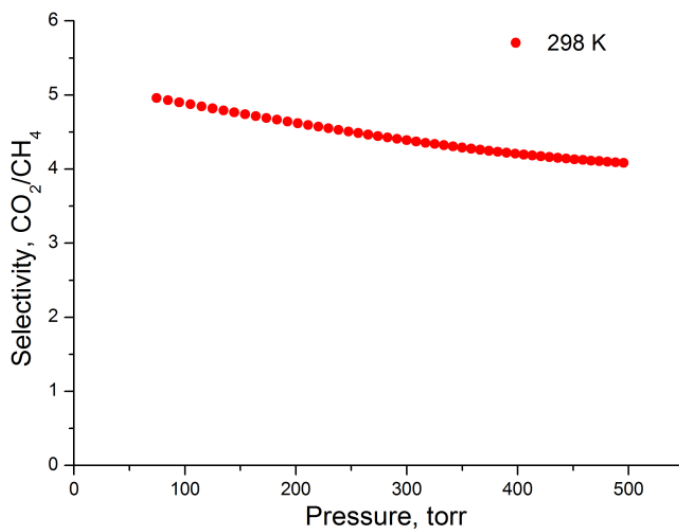
Figure 6.333. Selectivity of CO_2 over CH_4 at 298 K for $Co_4(L)Cl_2(DMF)_3$ as predicted by IAST for a 5/95 CO_2/CH_4 molar mixture.
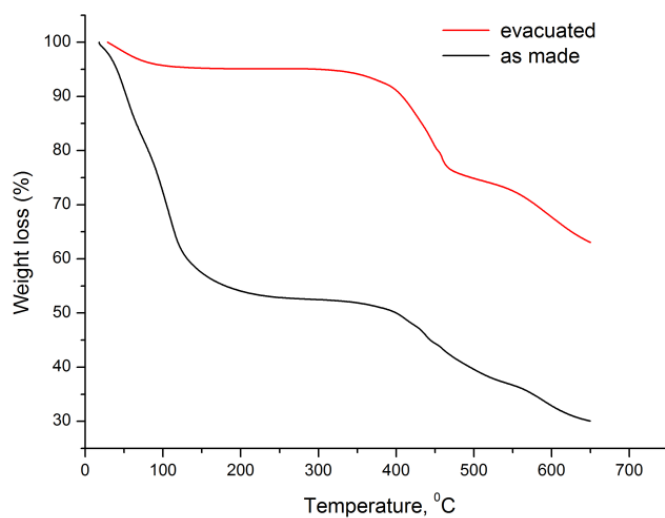
Figure 6.334. TGA curve for the as-made $Co_4(L)Cl_2(DMF)_3$ and the corresponding evacuated solid obtained after CO_2 SCD process, recorded under N_2 flow with a heating rate of 5 deg/min.
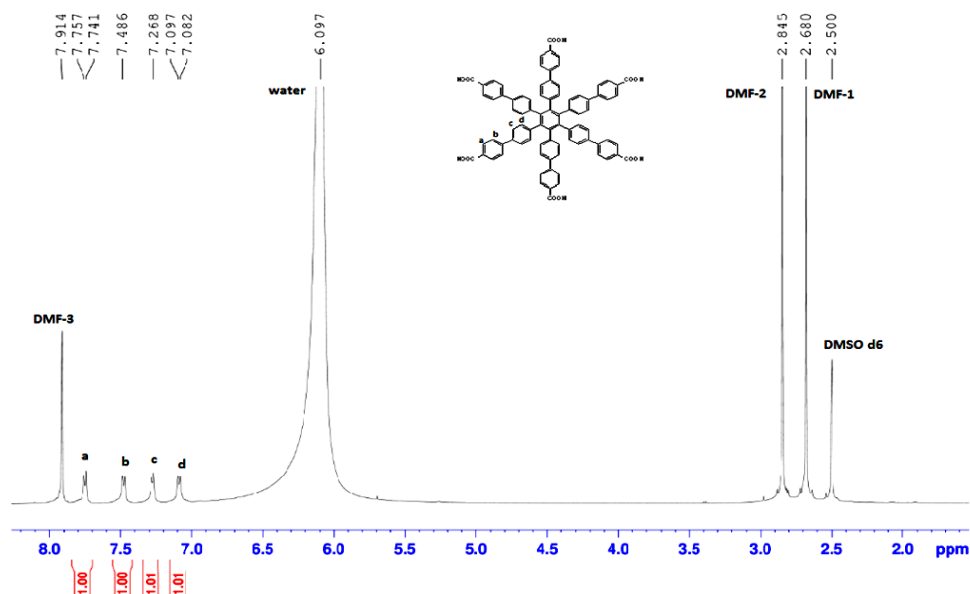
Figure 6.335. ^1H NMR spectrum of as-made $Co_4(L)Cl_2(DMF)_3$ after digesting the sample in HCl/DMSO-d6 solution.
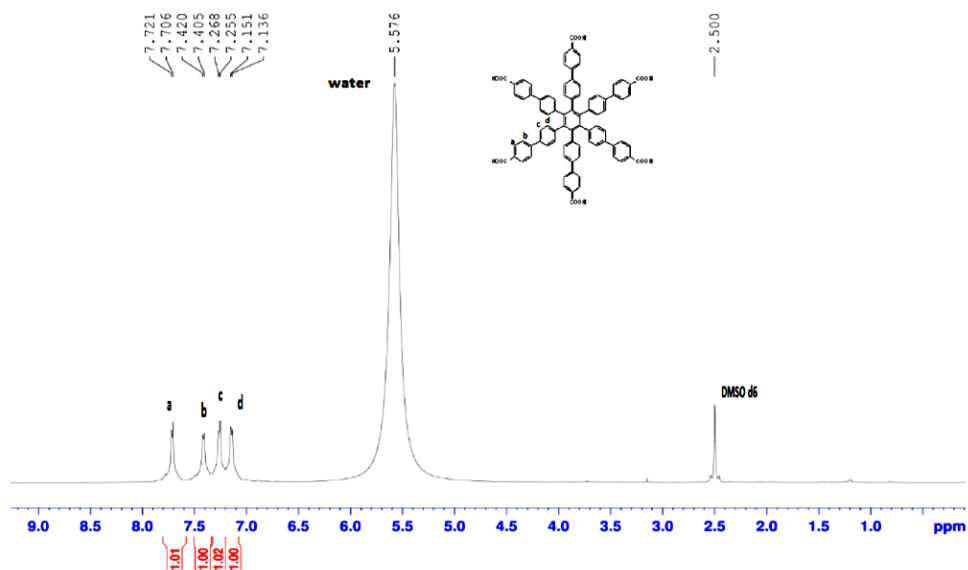
Figure 6.336. ^{1}H NMR spectrum of $Co_4(L)Cl_2(DMF)_3$ after CO_2 supercritical drying and digesting the sample in HCl/DMSO-d6 solution. There are no residual solvents.

6.49.2 Synthesis of compound $[In_2(L)(CH_3COO)_2]((CH_3)_2NH_2)_2$

   An amount of 0.035 g (0.03 mmol) of linker 51 (H_6L) and 0.057 g (0.18 mmol) of $In(NO_3)_3xH_2O$ were dissolved in a 20 mL glass scintillation vial containing 6 mL DMA, 4 mL ethanol and 3 drops of c.HCl. The vial was heated at 85 ^{0}C for 9 days where large brown crystals were formed. Yield: 20 % based on linker H_6L.
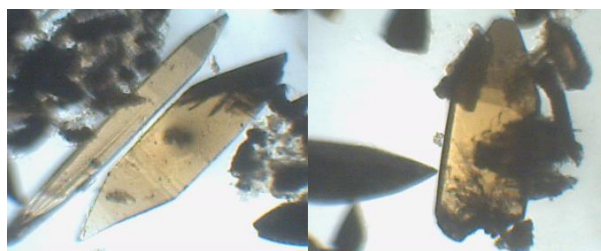
Figure 6.337. Optical microscope pictures of $[In_2(L)(CH_3COO)_2]((CH_3)_2NH_2)_2$ crystals.
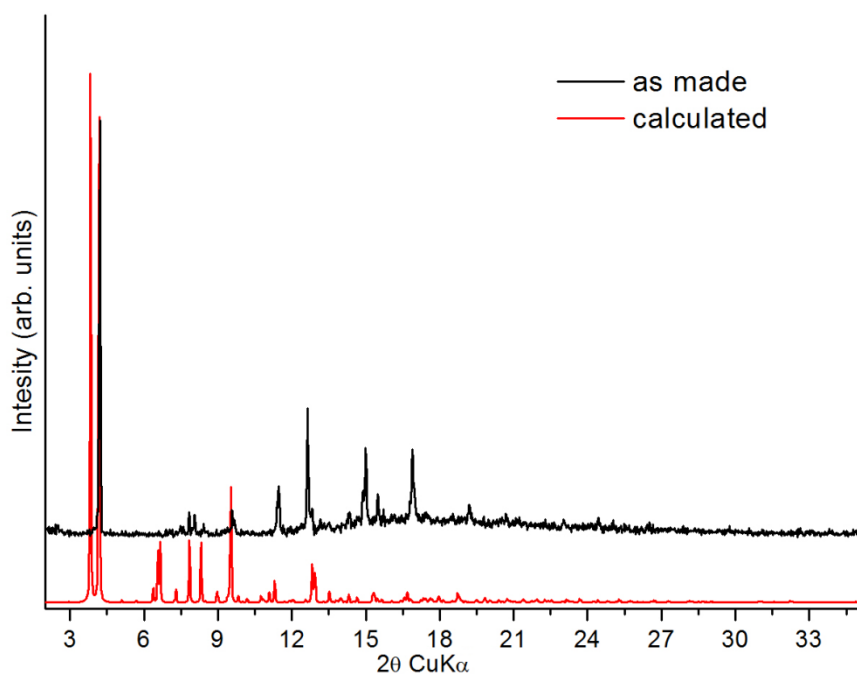
Figure 6.339. Comparison of experimental and calculated pxrd patterns for compound [In$_2$(L)(CH$_3$COO)$_2$]((CH$_3$)$_2$NH$_2$)$_2$.

6.49.3 Reaction of linker 51 with Al(NO$_3$)$_3$·9H$_2$O

An amount of 0.035 g (0.03 mmol) of linker 51 and 0.033 g (0.09 mmol) of Al(NO$_3$)$_3$·9H$_2$O were dissolved in a 20 mL glass scintillation vial containing 5 mL DMF and 2.5 mL of glacial acetic acid. The vial was placed in an oven, heated up to 120 ^{0}C with 0.06 ^{0}C/min and then held at 120 ^{0}C for 24 h. After that time a grey material was deposited.
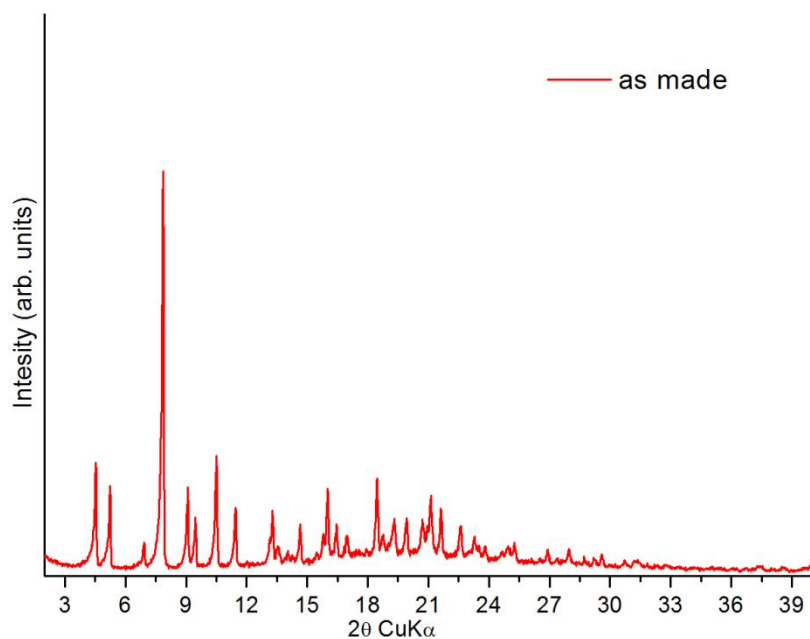
Figure 6.340. Experimental pxrd pattern for the compound 6.49.3.

6.50 MOF synthesis based on organic linker 52
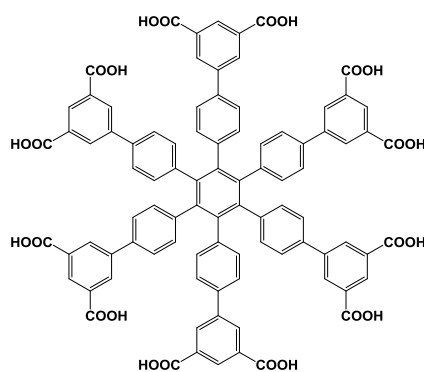
6.50.1 Reaction of linker 52 with $Zn(NO_3)_2 \cdot 6H_2O$

An amount of 0.012 g (0.008 mmol) of linker 52 ($H_{12}L$) and 0.030 g (0.10 mmol) of $Zn(NO_3)_2 \cdot 6H_2O$ were dissolved in a 20 mL glass scintillation vial containing 4 mL DMF, 1 mL water, and 0.1 mL of c.HNO_3. The solution was heated at 85 ^{0}C for 3 d where colourless crystals were formed.
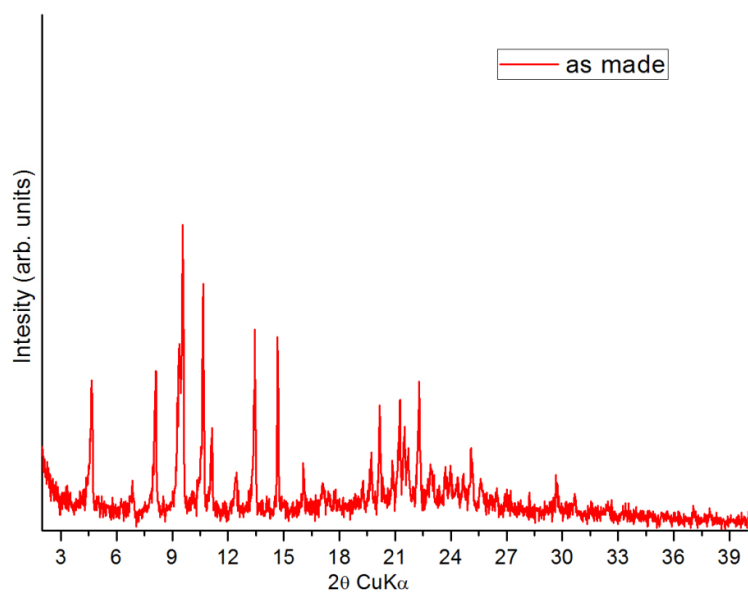
Figure 6.342. Experimental pxrd pattern for the compound 6.50.1.
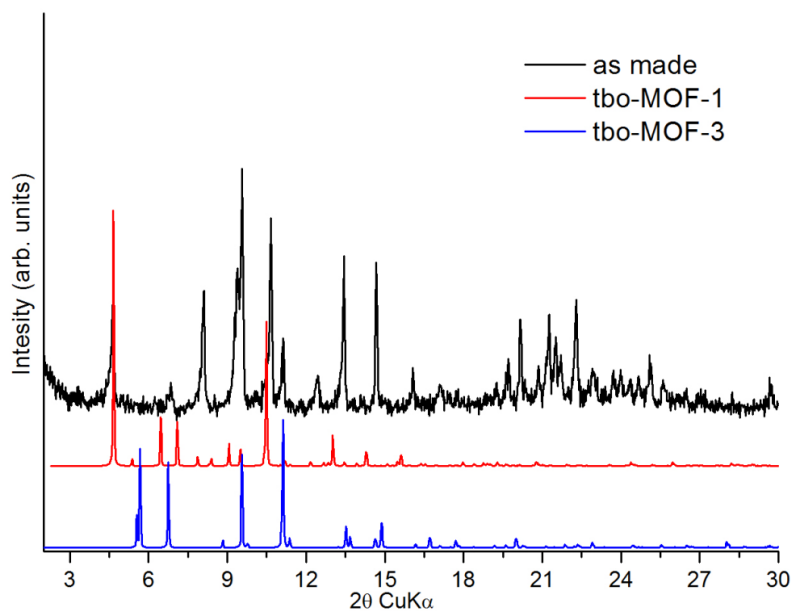
Figure 6.343. Experimental pxrd pattern for the compound 6.50.1 compared to the calculated pxrd patterns of tbo-MOF-1 (compound 6.48.1) and tbo-MOF-3 (based on linker $H_{12}L_2$).

6.51 MOF syntheses based on organic linker 73
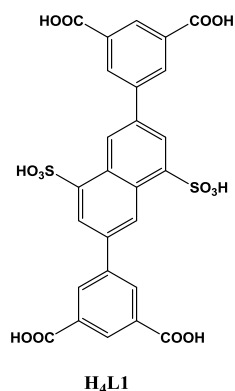
H₄L1

6.51.1 Synthesis of compound Cu₂L1

A solution of 3 mL DMF, 1 mL EtOH, 4 drops c.HNO₃, 0.035 g (0.057 mmol) of H₄L1, and 0.027 g (0.112 mmol) of Cu(NO₃)₂·3H₂O was placed in a 20 mL glass scintillation vial. The vial was sealed and placed in an isothermal oven at 85 °C for 18 hours. During this period, small green crystals were deposited (45% yield based on H₄L1).
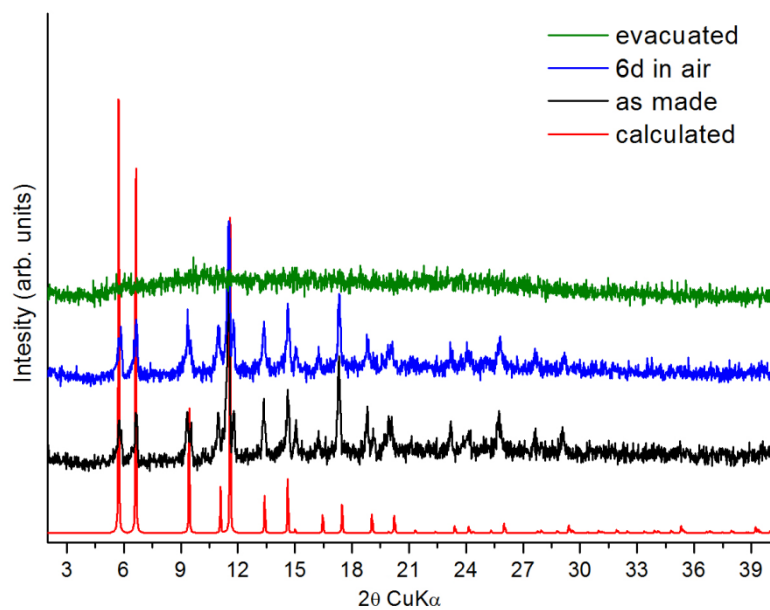
Figure 6.345. Comparison of experimental, 6 days exposure in air, calculated and evacuated pxrd patterns for the compound Cu₂L1.

6.51.2 Synthesis of compound $Cu_2L1_{0.4}L2_{0.6}$
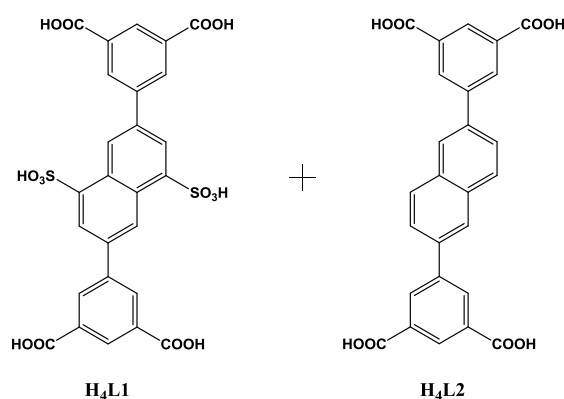
A solution of 3 mL DMF, 1 mL EtOH, 4 drops c.HNO_3, 0.015 g (0.024 mmol) of H_4L1, 0.022 g (0.048 mmol) of H_4L2, and 0.023 g (0.095 mmol) of $Cu(NO_3)_2 \cdot 3H_2O$ was placed in a 20 mL glass scintillation vial. The vial was sealed and placed in an isothermal oven at 85 °C for 18 hours. During this period, small green crystals were deposited (50% yield based on H_4L1+ H_4L2).

Successful activation of the material was possible as follows: as-made sample was washed with DMF four times per day for 2 days and then the sample was soaked in acetone over a period of 4 days, replenishing the acetone 4 times per day. Finally, the sample was activated under dynamic vacuum at 50 °C for 12 hours and until the outgas rate was less than 2 mTorr/min.
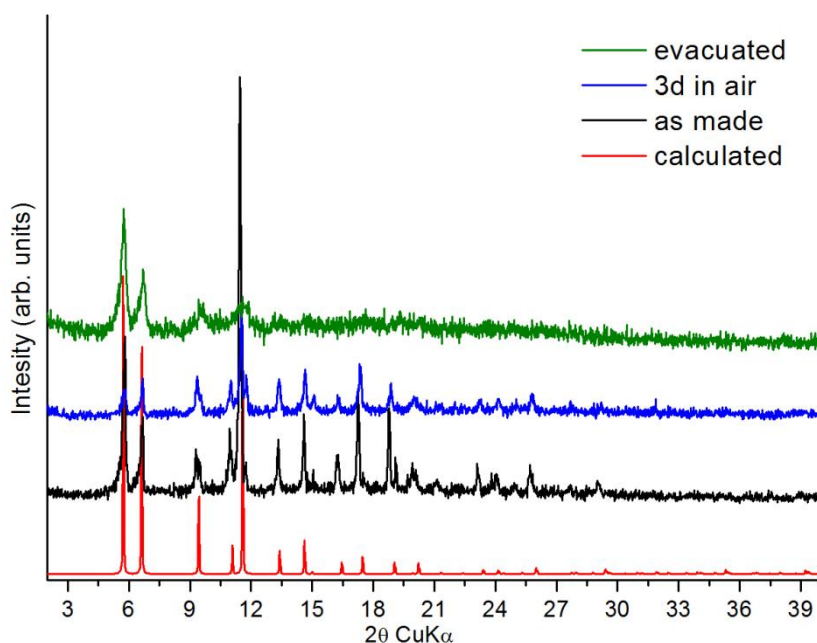
<u>Figure 6.346.</u> Comparison of experimental, 3 days exposure in air, calculated and evacuated pxrd patterns for the compound $Cu_2L1_{0.4}L2_{0.6}$.
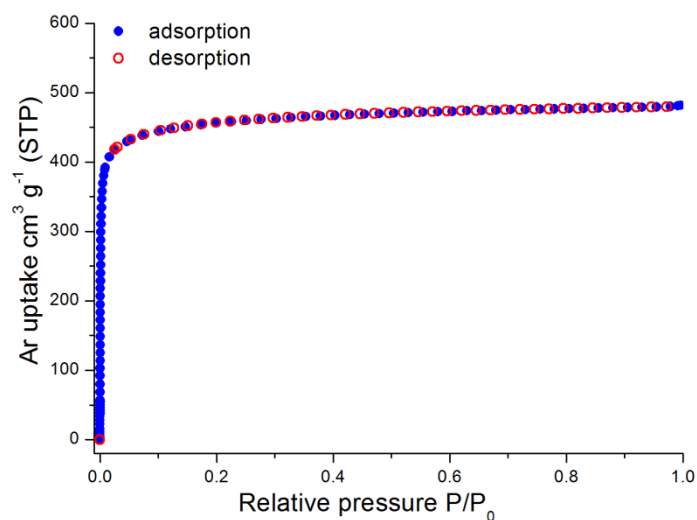
Figure 6.347. Ar sorption isotherm of $Cu_2L1_{0.4}L2_{0.6}$ at 87 K.
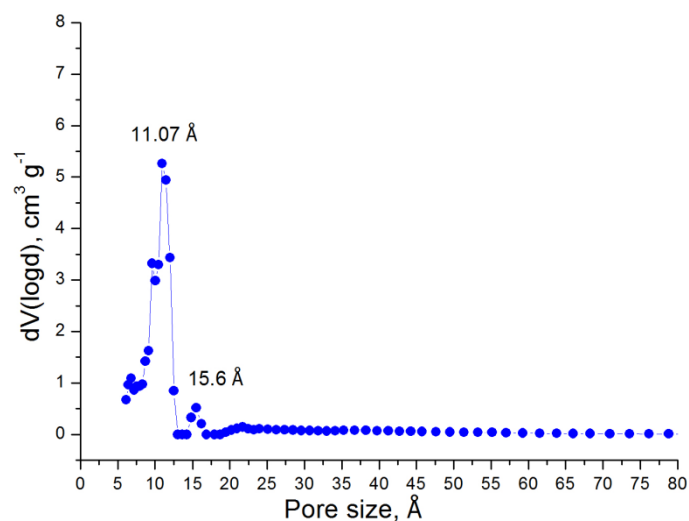
Figure 6.348. Pore size distribution in $Cu_2L1_{0.4}L2_{0.6}$ calculated from NLDFT analysis.
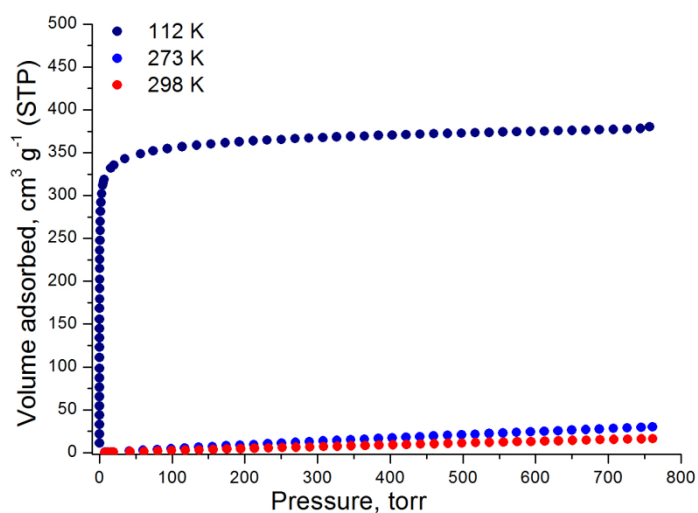
Figure 6.349. CH_4 adsorption isotherms of $Cu_2L1_{0.4}L2_{0.6}$ recorded at at 112 K, 273 K and 298 K.
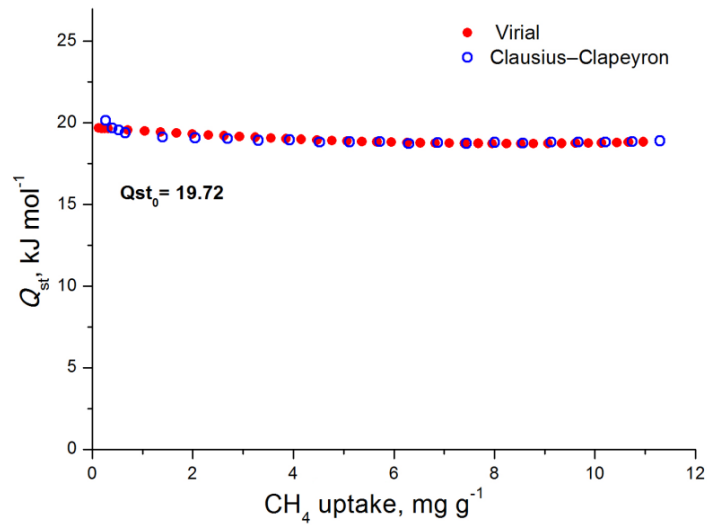
Figure 6.350. CH$_4$ isosteric heat of adsorption in Cu$_2$L1$_{0.4}$L2$_{0.6}$ as a function of surface coverage.
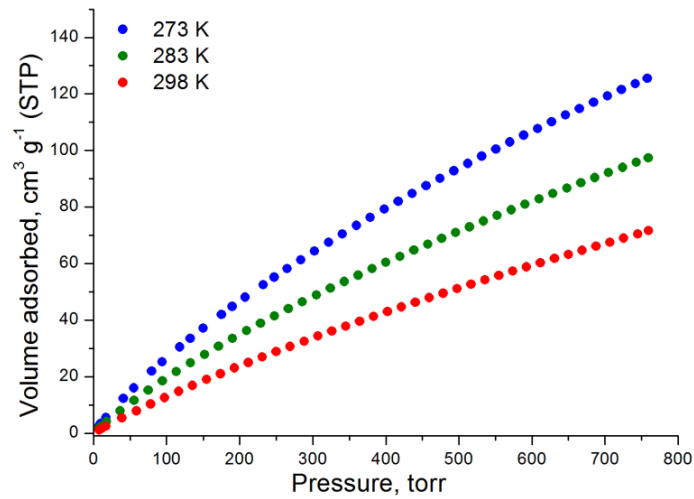
Figure 6.351. CO$_2$ adsorption isotherms of Cu$_2$L1$_{0.4}$L2$_{0.6}$ at 273 K, 288 K, 293 K and 298 K.
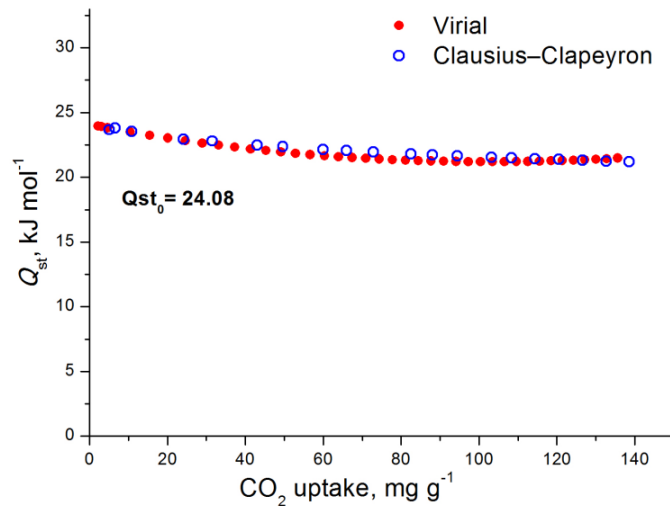
Figure 6.352. CO$_2$ isosteric heat of adsorption in Cu$_2$L1$_{0.4}$L2$_{0.6}$ as a function of surface coverage.
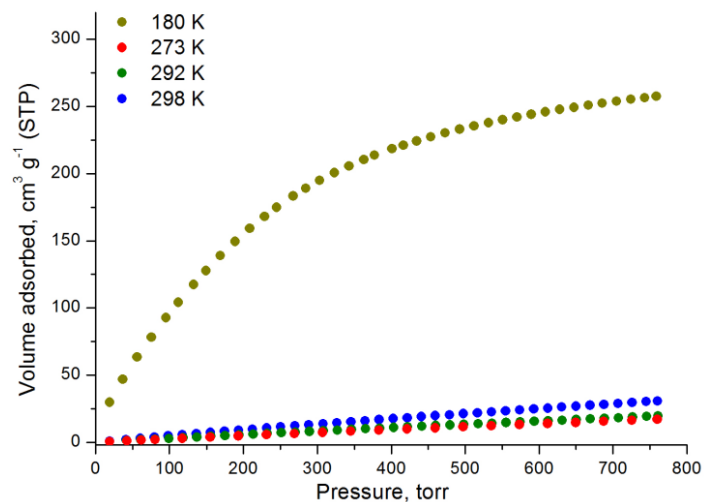
Figure 6.353. Kr adsorption isotherms of $Cu_2L1_{0.4}L2_{0.6}$ at 180 K, 273 K, 292 K and 298 K.
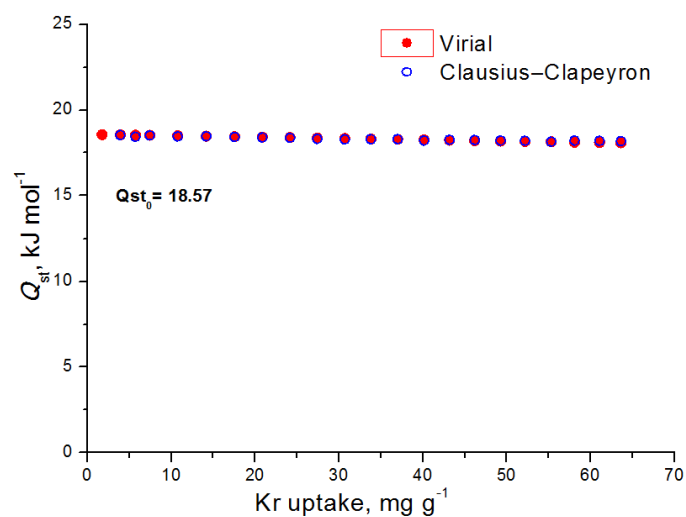
Figure 6.354. Kr isosteric heat of adsorption as a function of surface coverage.
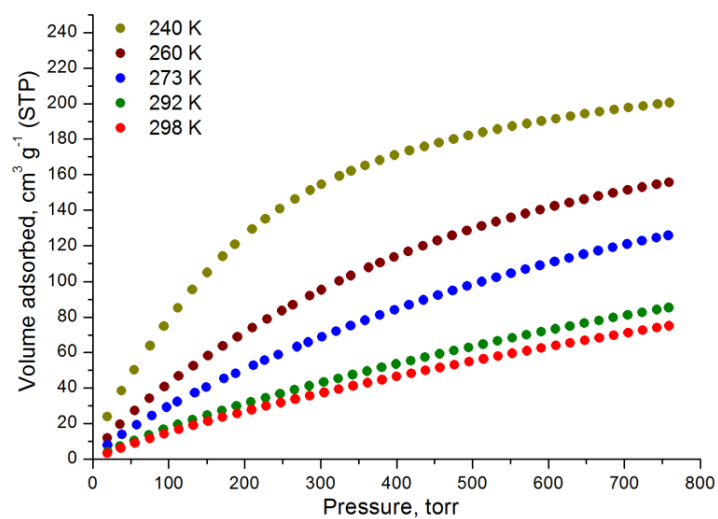
Figure 6.355. Xe adsorption isotherms of $Cu_2L1_{0.4}L2_{0.6}$ at 240 K, 260 K, 273 K, 292 K and 298 K.
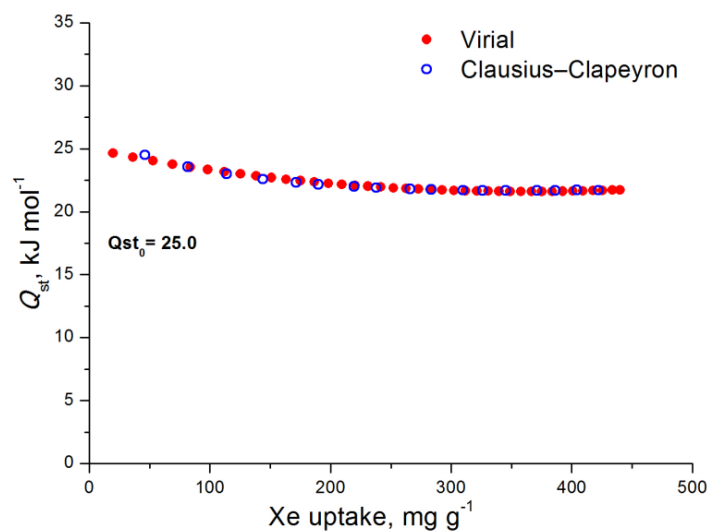
Figure 6.356. Xe isosteric heat of adsorption as a function of surface coverage.
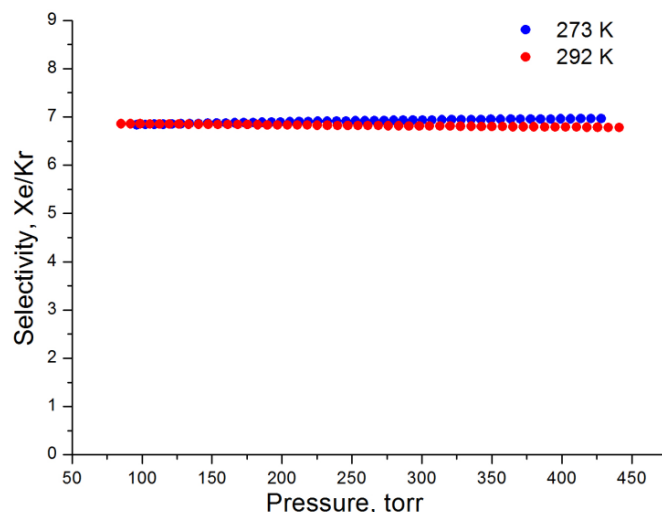
Figure 6.357. Selectivities of Xe over Kr at 292 K and 273 K for $Cu_2L1_{0.4}L2_{0.6}$ as predicted by IAST for a 5/95 Xe/Kr molar mixture.

6.52 MOF synthesis based on organic linker 57
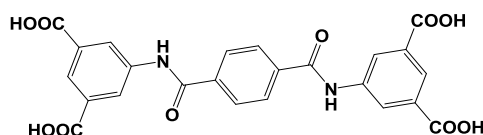
6.52.1 Synthesis of compound Cu_2L

An amount of 0.030 g (0.06 mmol) of linker 57 (H_4L) and 0.059 g (0.25 mmol) of $Cu(NO_3)_2 \cdot 3H_2O$ were dissolved in a 20 mL glass scintillation vial containing 6 mL DMF, 1 mL water and 2 drops of c.HCl. The solution was heated at 85 ^0C for 16 h where big light blue crystals were formed. Yield: 30 % based on linker H_4L.
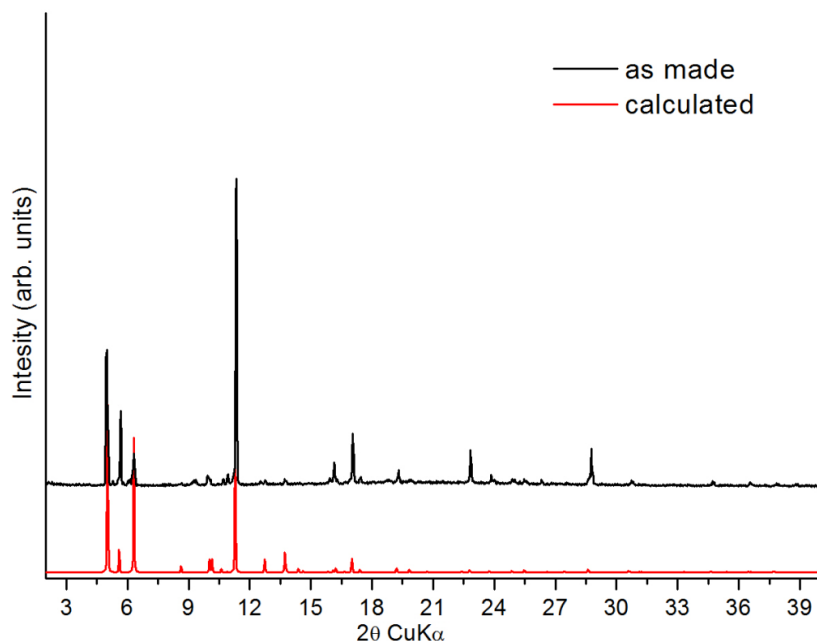
Figure 6.359. Comparison of experimental and calculated pxrd pattern for compound Cu_2L.

6.53 MOF synthesis based on organic linker 56
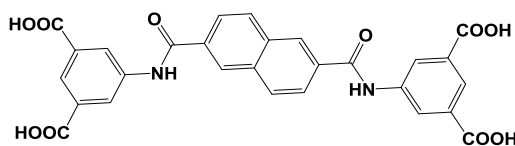
6.53.1 Synthesis of compound Cu_2L

An amount of 0.030 g (0.05 mmol) of linker 56 (H_4L) and 0.054 g (0.22 mmol) of $Cu(NO_3)_2 \cdot 3H_2O$ were dissolved in a 20 mL glass scintillation vial containing 6 mL DMF, 3 mL DMA, 1 mL water and 5 drops of c.HNO_3. The solution was heated at 85 ^{0}C for 1 d where big light blue crystals were formed. Yield: 30 % based on linker H_4L.

Figure 6.360. Optical microscope pictures of Cu_2L crystals.

312
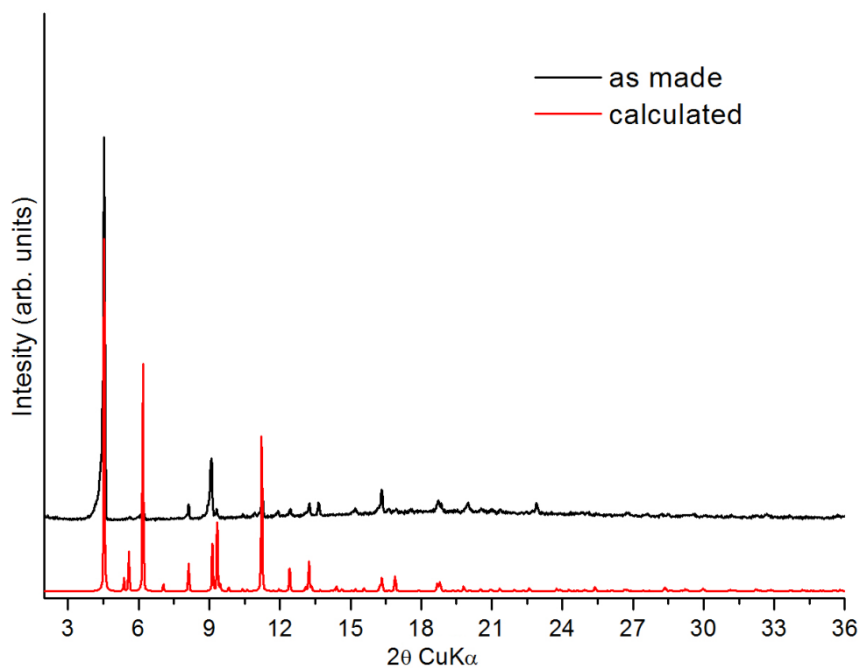
Figure 6.361. Comparison of experimental and calculated pxrd pattern for compound Cu_2L.

6.54 MOF syntheses based on organic linker 55
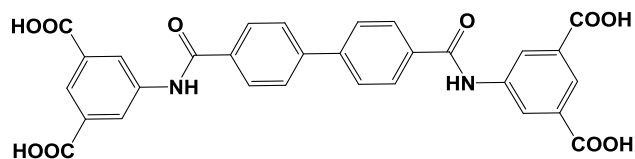
6.54.1 Synthesis of compound Cu_2L

An amount of 0.035 g (0.06 mmol) of linker 55 (H_4L) and 0.060 g (0.25 mmol) of $Cu(NO_3)_2 \cdot 3H_2O$ were dissolved in a 20 mL glass scintillation vial containing 6 mL DMF, 3 mL DMA, 1 mL water and 2 drops of c.HCl. The solution was heated at 85 ^0C for 1 d where big light blue crystals were formed. Yield: 30 % based on linker H_4L.
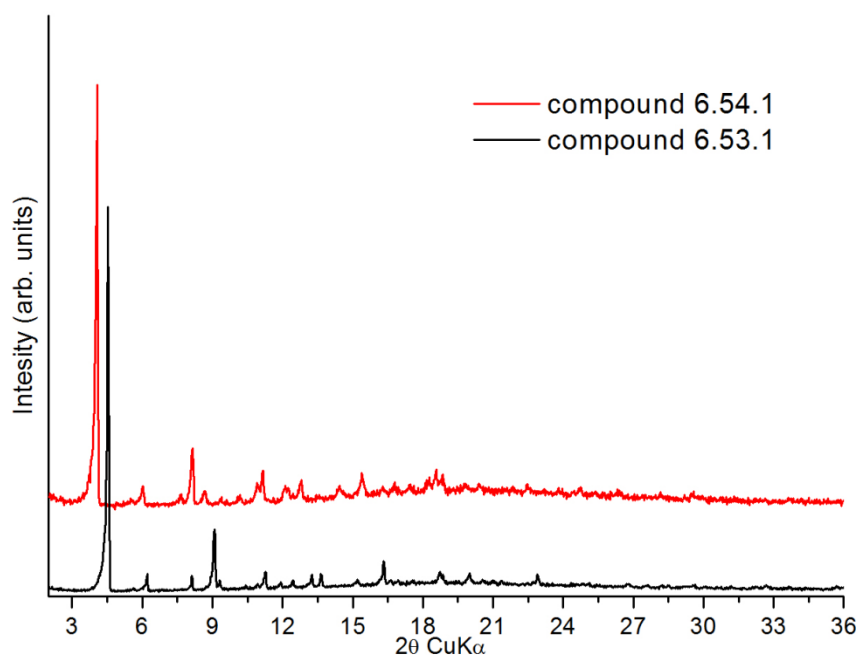
Figure 6.362. Comparison of experimental pxrd patterns of compounds 6.53.1 and 6.54.1.

6.54.2 Reaction of linker 55 with $In(NO_3)_3xH_2O$

An amount of 0.030 g (0.05 mmol) of linker 55 (H_4L) and 0.018 g (0.05 mmol) of $In(NO_3)_3xH_2O$ were dissolved in a 20 mL glass scintillation vial containing 2 mL DMF, 1 mL ACN and 2 drops of c.HNO_3. The solution was heated at 85 ^{0}C for 2 d where small colourless crystals were formed.
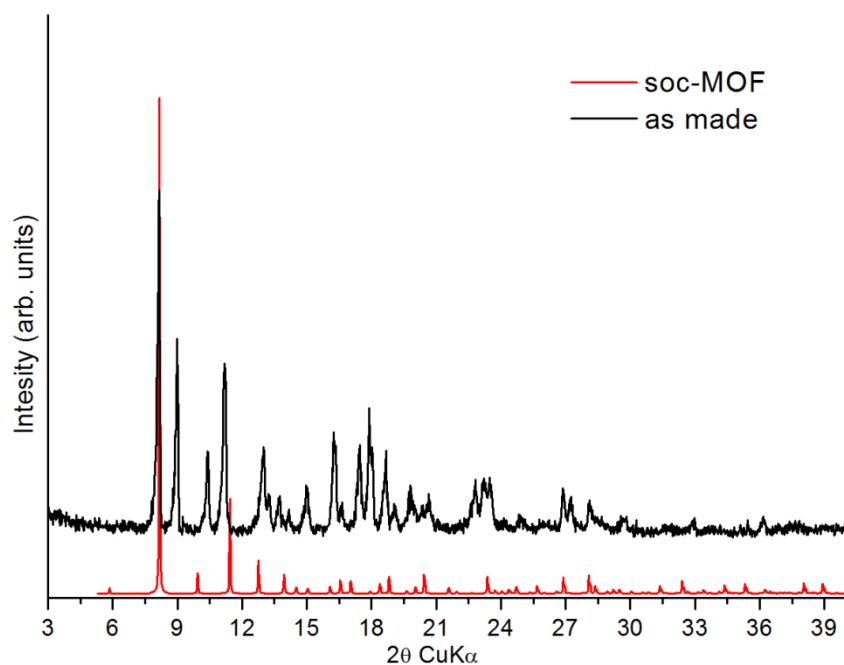
Figure 6.363. Experimental pxrd pattern for the compound 6.54.2 compared to the calculated soc-MOF pxrd pattern.

314

6.55 MOF synthesis based on organic linker 71

HOOC   COOH

$$Cl$$
HOOC—N—Pd—N—COOH
$$Cl$$

HOOC   COOH
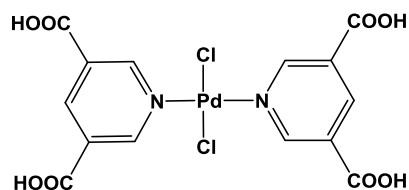
6.55.1 Synthesis of compound $Cu_2[Pd(PDC)Cl_2]$

A solution of 10 mL DMF, 0.025 g (0.048 mmol) of $Pd(PDC)Cl_2$ and 0.025 g (0.015 mmol) of $CuCl_2 \cdot 2H_2O$ was placed in a 20 mL glass scintillation vial. The vial was sealed and placed in an isothermal oven at 85 °C for 48 hours. During this period, small light blue cubic crystals of $Cu_2[Pd(PDC)Cl_2]$ were deposited. (40% yield based on $Pd(PDC)Cl_2$).

Therefore the as made material was washed with DMF four times per day for 2 days and then the sample was soaked in methanol over a period of 4 days, replenishing the methanol 4 times per day. The methanol suspended sample was transferred inside a pre-weighted sample cell and the methanol was removed under reduced pressure. Finally, the sample was activated under dynamic vacuum at 60 °C for 12 hours and until the outgas rate was less than 2 mTorr/min.
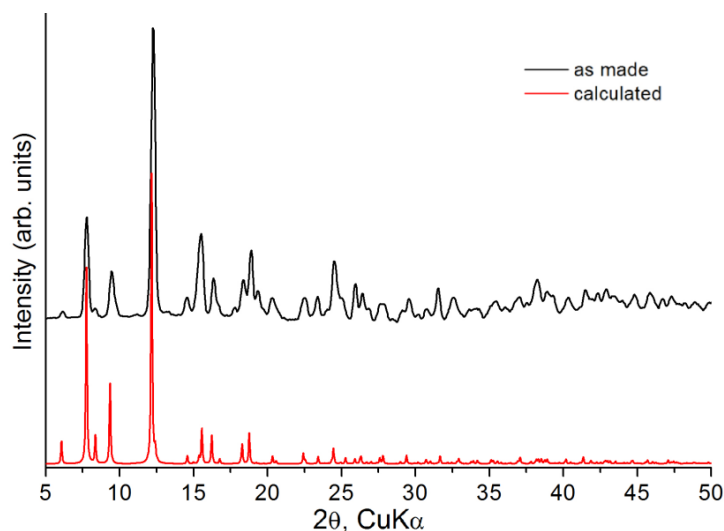
Figure 6.366. Experimental powder X-ray diffraction patterns of the as-made solid $Cu_2[Pd(PDC)Cl_2]$ along with the calculated one from the crystal structure.
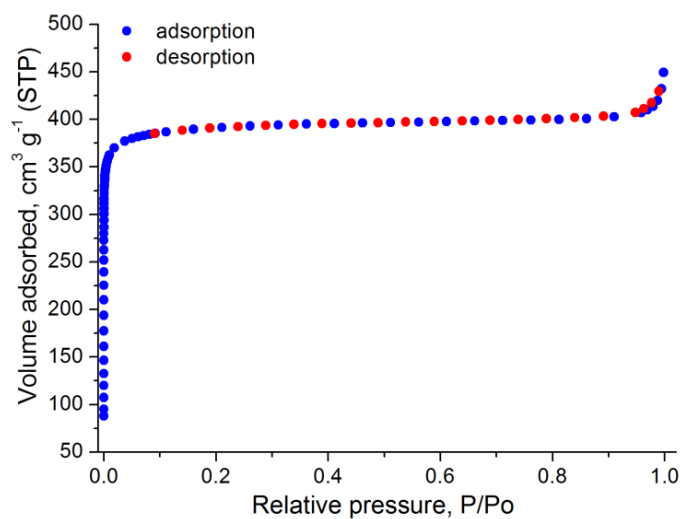
Figure 6.367. Nitrogen sorption isotherm of $Cu_2[Pd(PDC)Cl_2]$ at 77 K.
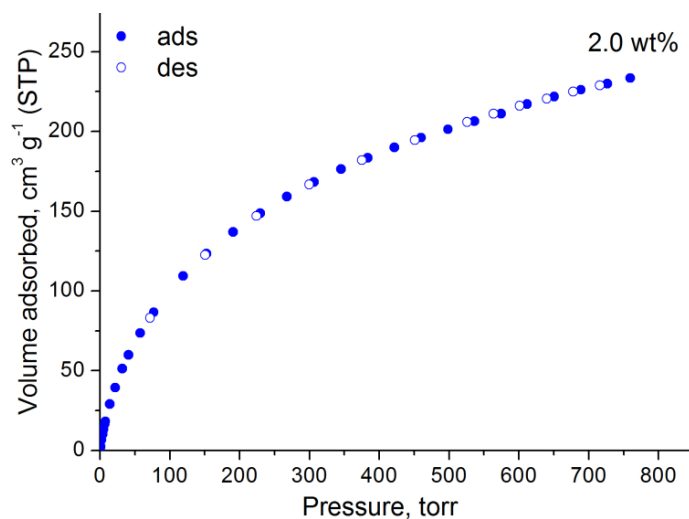
Figure 6.368. Hydrogen adsorption isotherm of $Cu_2[Pd(PDC)Cl_2]$ at 77 K.
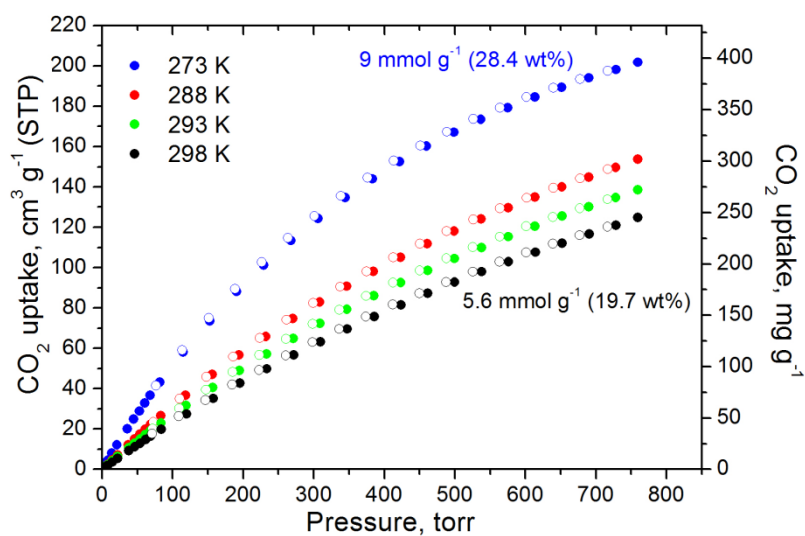
Figure 6.369. CO_2 adsorption isotherms of $Cu_2[Pd(PDC)Cl_2]$ at 273 K, 288 K, 293 K and 298 K.
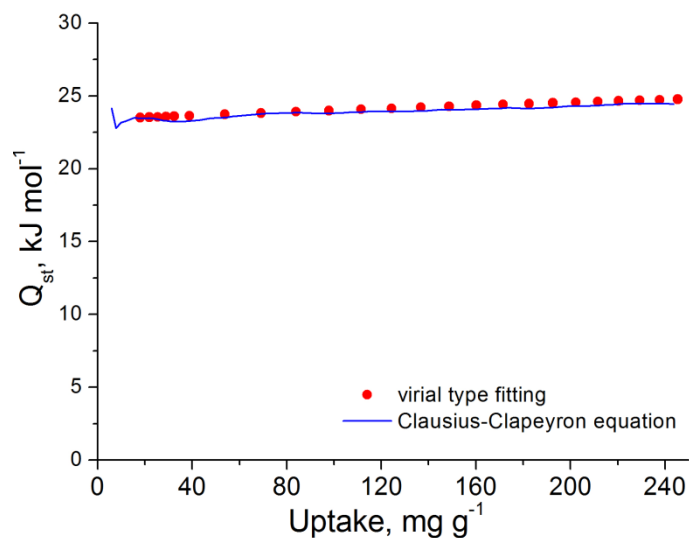
Figure 6.370. CO_2 isosteric heat of adsorption in $Cu_2[Pd(PDC)Cl_2]$ as a function of surface coverage.
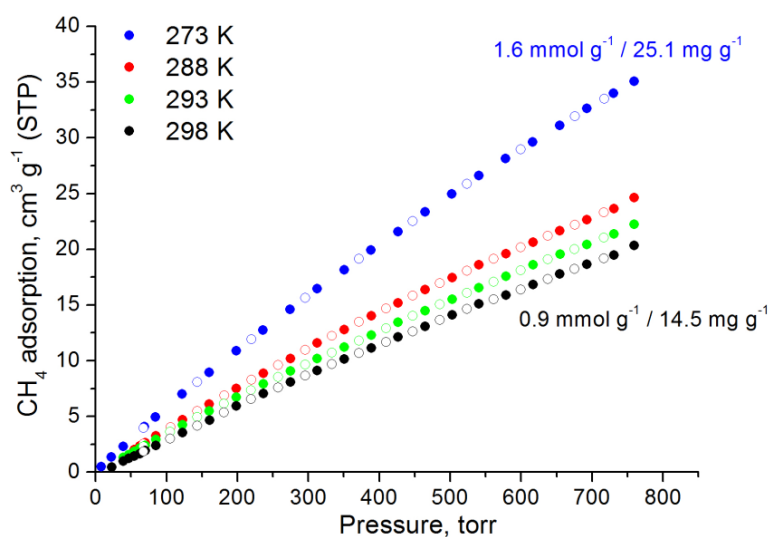
Figure 6.371. CH_4 adsorption isotherms of $Cu_2[Pd(PDC)Cl_2]$ recorded at at 273 K, 288 K, 293 K and 298 K.
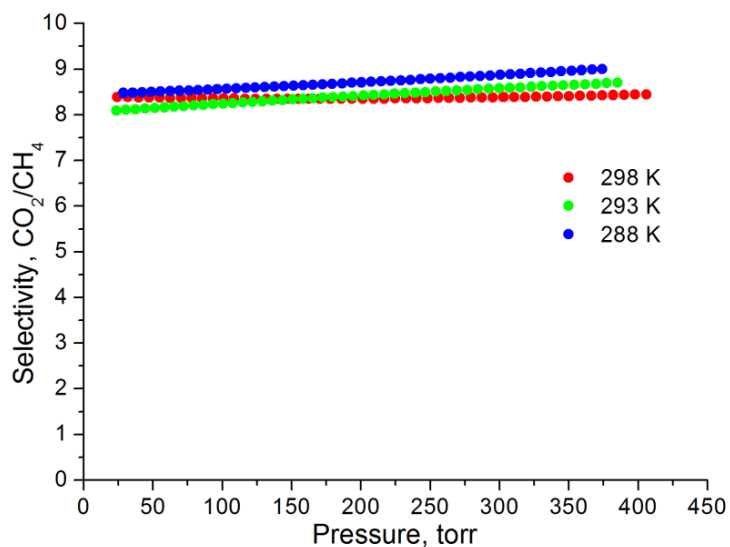
Figure 6.372. Selectivities of CO_2 over CH_4 at 298 K, 293 K and 288 K for $Cu_2[Pd(PDC)Cl_2]$ as predicted by IAST for a 5/95 CO_2/CH_4 molar mixture.
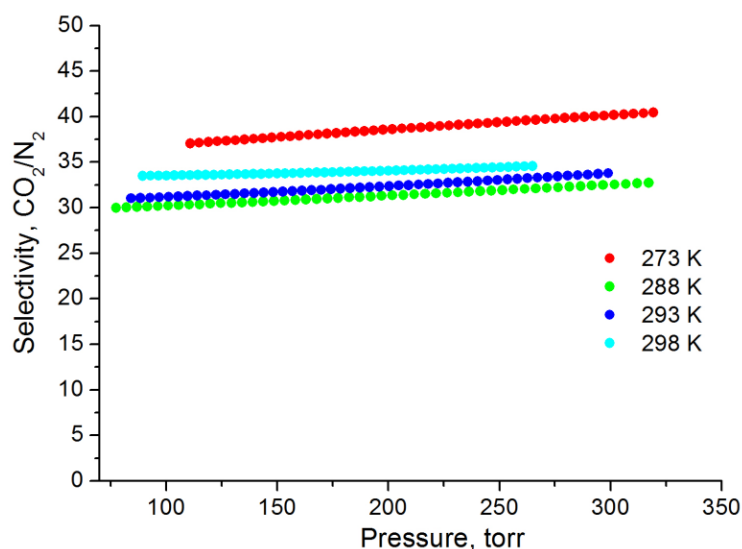
Figure 6.373. Selectivities of CO_2 over N_2 at 298 K, 293 K, 288 K and 273 K for $Cu_2[Pd(PDC)Cl_2]$ as predicted by IAST for a 5/95 CO_2/N_2 molar mixture.

6.56 MOF synthesis based on organic linker 58
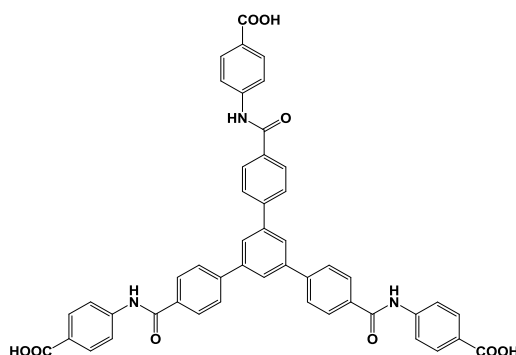
6.56.1 Synthesis of compound Al(L)

An amount of 0.035 g (0.05 mmol) of linker 58 (H_3L), 0.005 g (0.04 mmol) of benzoic acid and 0.017 g (0.045 mmol) of $Al(NO_3)_3 \cdot 9H_2O$ were dissolved in a 20 mL glass scintillation vial containing 1 mL DMF. The solution was transferred in a 20 mL teflon Parr bomb reactor and it was heated at 180 ^{0}C for 2 d where white microcrystalline solid was formed. Yield: 30 % based on linker 58.

The resulting material was characterized using pxrd measurements. This synthetic procedure revealed a highly crystalline material. The lack of single crystals prompted us to construct the crystal structure using molecular simulations.

The construction of the theoretical periodic model was based on the periodic model of the CAU-4 structure.[6] At first, the molecular model of the proposed organic linker was optimized by performing first principles calculations. The prediction of the geometry was based on the Density Functional Theory (DFT) method and the RI-PBE/def2-TZVP[7] computational model was used during

318

calculations. Very tight convergence criteria were used for both the self consistent field procedure (10^{-8} au) and the gradient (10^{-4} au). The corresponding auxiliary basis sets were used for the Resolution of Identity (RI) [8]approximation. During the optimization of the geometry, symmetry restrictions were applied in order to keep the carboxylate groups which are connected to the Al atoms in a geometry similar with that in CAU-4. The calculation was performed with the Turbomole[9] quantum chemistry package. Afterwards, the periodic model of the new Al-MOF was constructed. In order to build it, we removed the organic linkers of the CAU-4 and we replaced them with the new organic linker. At the same time, we altered the dimensions of the a, b, c axes (the angles of the cell were kept fixed) and the positions of the Al and O atoms in order to achieve that the new organic linker will fit in the position of the replaced organic linker of the CAU-4. Then, we performed a molecular mechanics calculation for the periodic cell in order to equilibrate the position of the atoms and the dimensions of the periodic cell. The symmetry of the periodic cell was P1 during the calculation. The calculation was performed with a modified version of the UFF[10] forcefield especially for MOF structures, as implemented in the GULP[11] program.
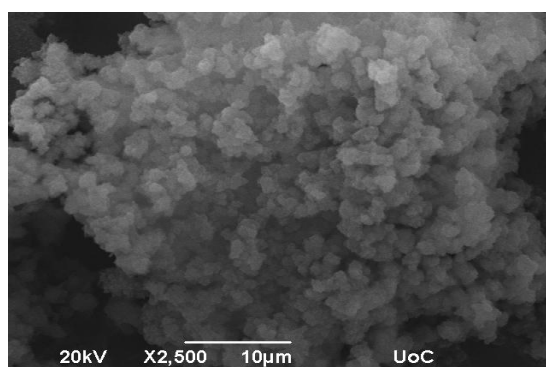
Figure 6.376. A representative SEM image of as made Al(L).
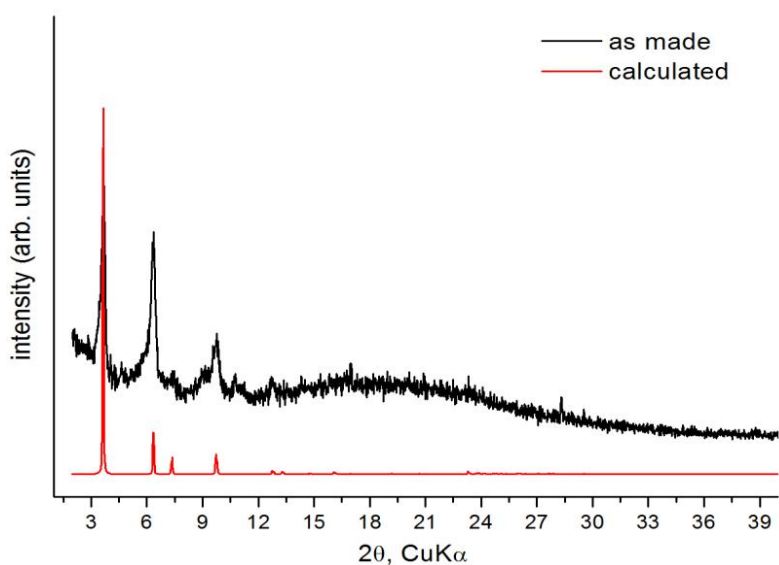
Figure 6.377. Experimental powder X-ray diffraction patterns of the as-made solid Al(L) along with the calculated one from the crystal structure.

After the successful characterization of the material a suitable activation procedure would allow the evaluation of its gas sorption properties. Therefore the as made material was washed with DMF four times per day for 2 days and then the sample was soaked in acetone over a period of 4 days, replenishing the acetone 4 times per day. Afterwards the acetone was exchanged with CH_2Cl_2, 2 times per day for 2 days. The CH_2Cl_2 suspended sample was transferred inside the chamber of a supercritical CO_2 dryer (Bal-Tec CPD 030) and CH_2Cl_2 was exchanged with liquid CO_2 over a period of 5 hours at 8 °C. During this period, liquid CO_2 was vented under positive pressure every 5 minutes. The rate of CO_2 venting was always kept below the rate of filling so as to maintain full drying conditions inside the chamber. Following venting, the temperature was raised to 40 ºC (above the critical temperature of CO_2), kept there for 1 hour and then slowly vented over the period of 2 hours. Finally, the sample was activated under dynamic vacuum at 60 °C for 12 hours and until the outgas rate was less than 2 mTorr/min.
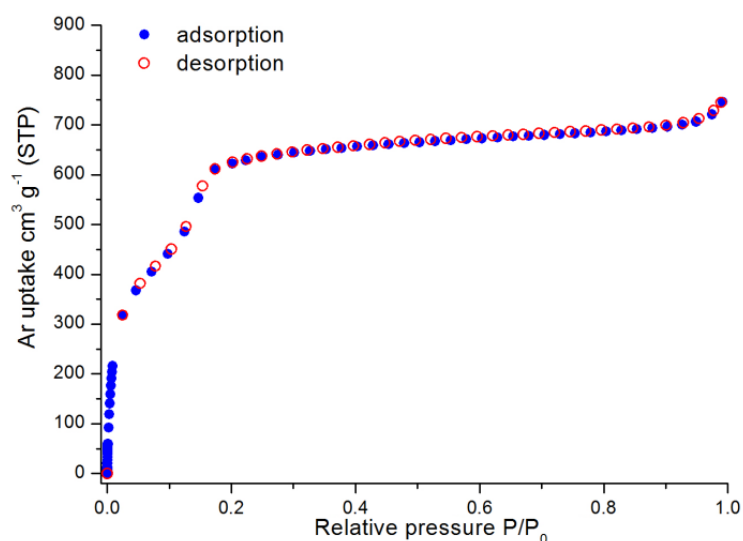
Figure 6.378. Ar sorption isotherm of Al(L) at 87 K.
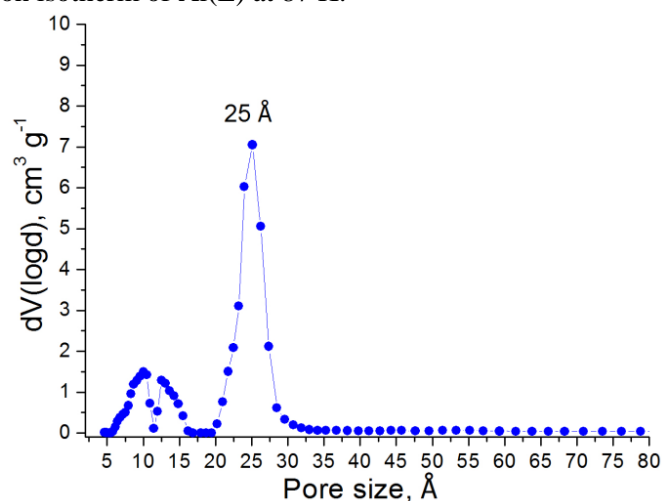
Figure 6.379. Pore size distribution in Al(L) calculated from NLDFT analysis.
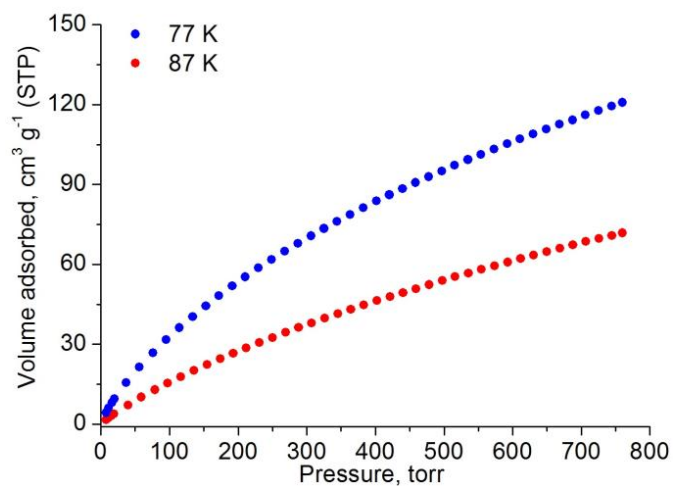
Figure 6.380. Hydrogen adsorption isotherms of Al(L) at 77 K and 87 K.
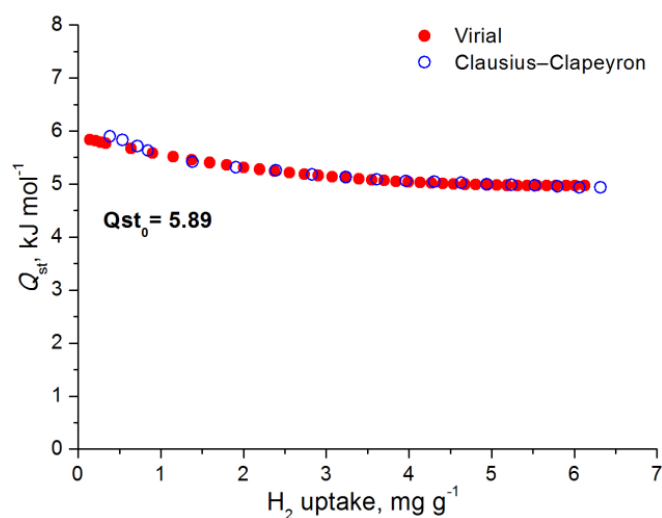
Figure 6.381. H_2 isosteric heat of adsorption in Al(L) as a function of surface coverage.
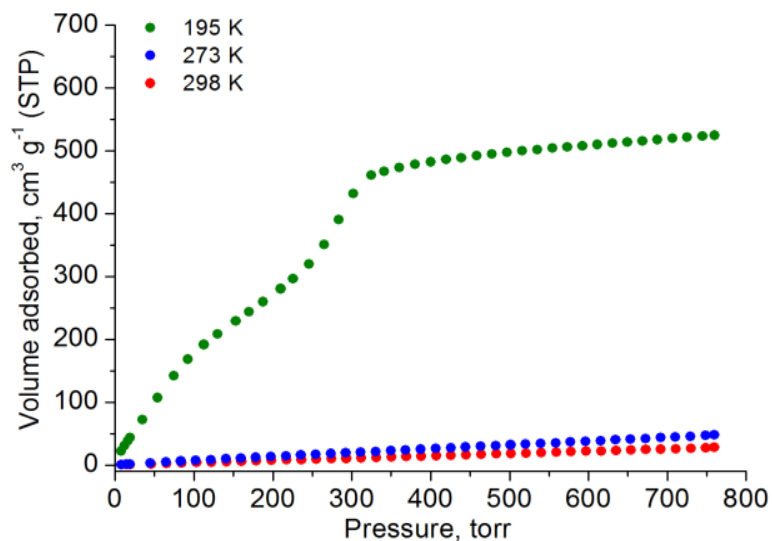

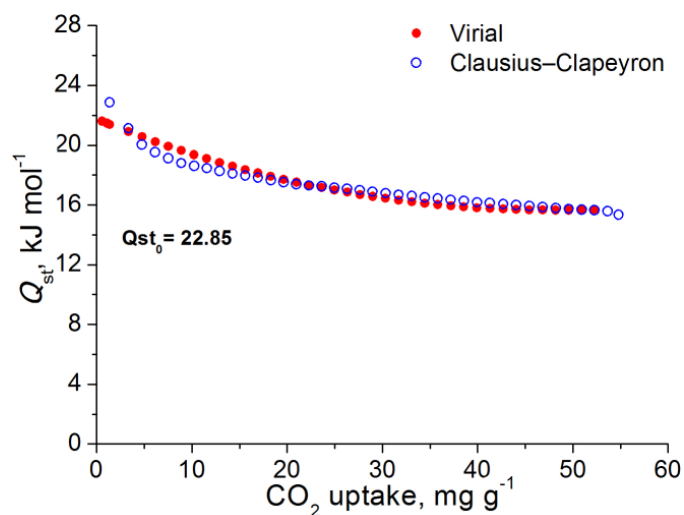Figure 6.382. CO_2 adsorption isotherms of Al(L) at 195 K, 273 K and 298 K.

Figure 6.383. CO_2 isosteric heat of adsorption in Al(L) as a function of surface coverage.
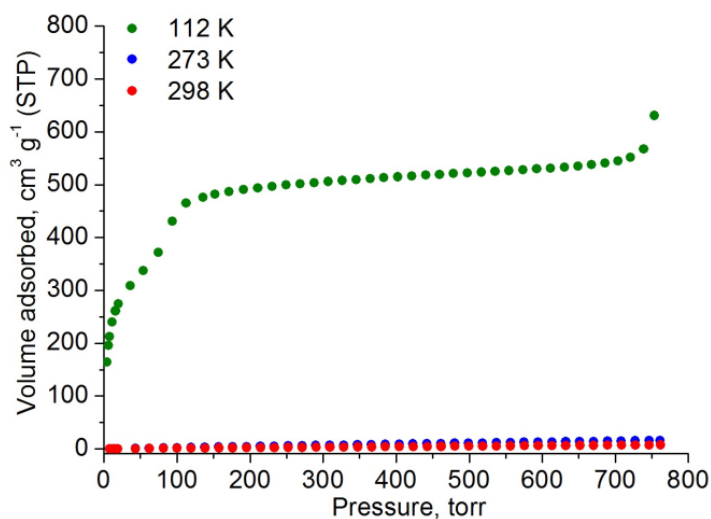

Figure 6.384. CH_4 adsorption isotherms of Al(L) recorded at at 112 K, 273 K and 298 K.
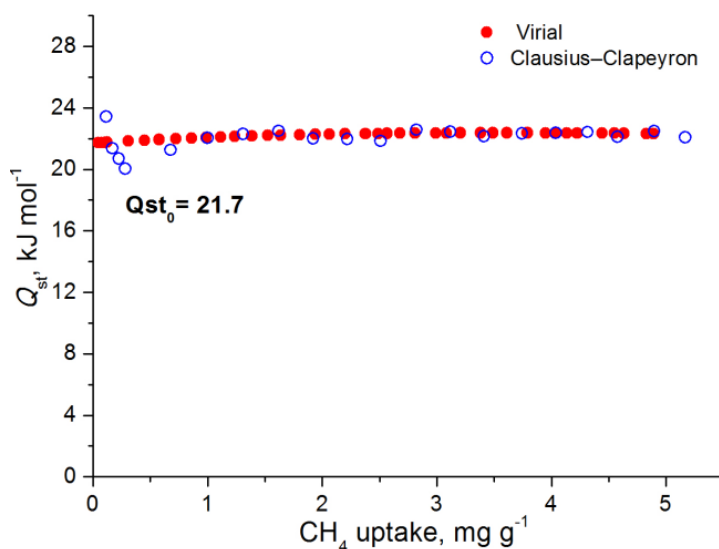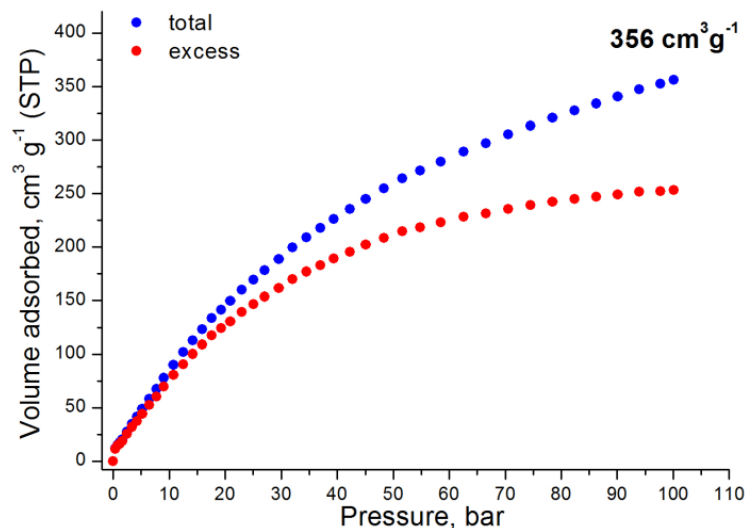

Figure 6.385. CH_4 isosteric heat of adsorption in Al(L) as a function of surface coverage.

Figure 6.386. High pressure total and excess gravimetric CH_4 adsorption isotherms of Al(L) at 298 K.
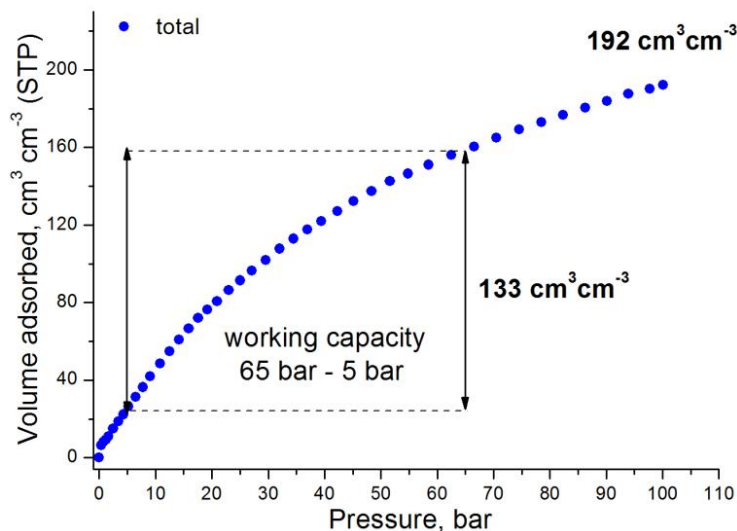
Figure 6.387. High pressure total volumetric CH_4 adsorption isotherm of Al(L) at 298 K. The black arrows indicate the working capacity (65 bar – 5 bar).
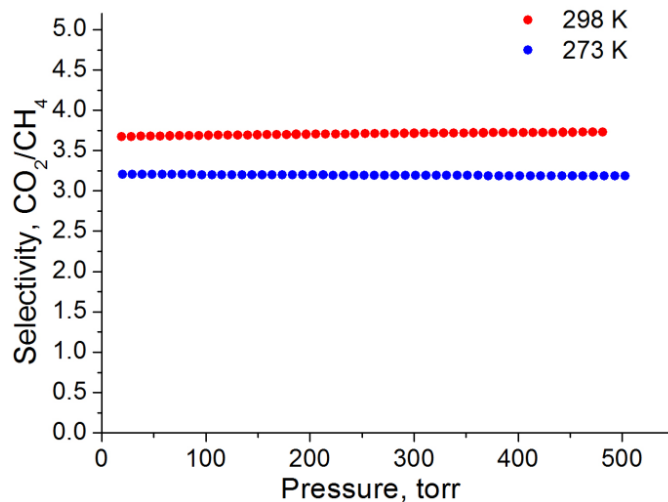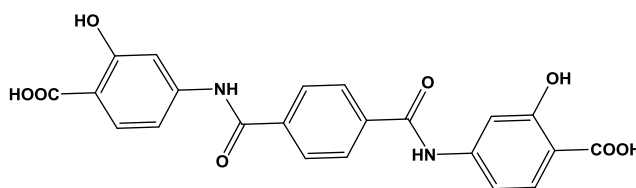

Figure 6.388. Selectivities of CO_2 over CH_4 at 298 K and 273 K for Al(L) as predicted by IAST for a 5/95 CO_2/CH_4 molar mixture.

6.57 MOF syntheses based on organic linker 66

6.57.1 Synthesis of compound Zn$_2$L

An amount of 0.035 g (0.08 mmol) of linker 66 (H$_4$L) and 0.095 g (0.32 mmol) of Zn(NO$_3$)$_2$·6H$_2$O were dissolved in a 20 mL glass scintillation vial containing 4 mL DMF and 1 mL EtOH. The solution was heated at 120 ^{0}C for 48 h where a beige solid was deposited. Yield: 20 % based on linker H$_4$L.
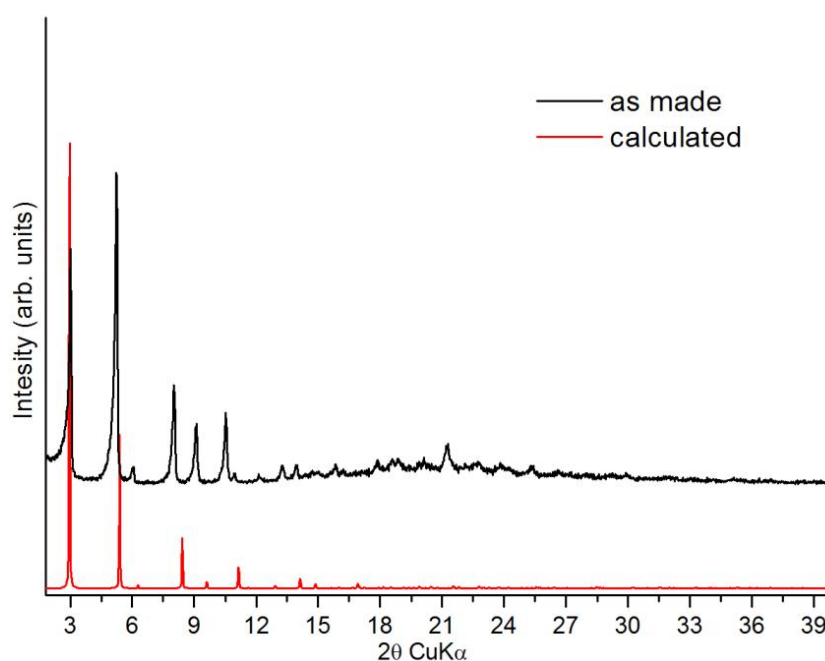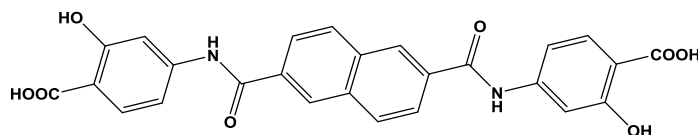

Figure 6.391. Comparison of experimental and calculated pxrd patterns of compound 6.57.1.

6.58 MOF syntheses based on organic linker 67

6.58.1 Synthesis of compound Zn$_2$L

An amount of 0.035 g (0.07 mmol) of linker 67 (H$_4$L) and 0.085 g (0.29 mmol) of Zn(NO$_3$)$_2$·6H$_2$O were dissolved in a 20 mL glass scintillation vial containing 7 mL DMF and 1 mL EtOH. The solution was heated at 120 ^{0}C for 48 h where a beige solid was deposited. Yield: 20 % based on linker H$_4$L.
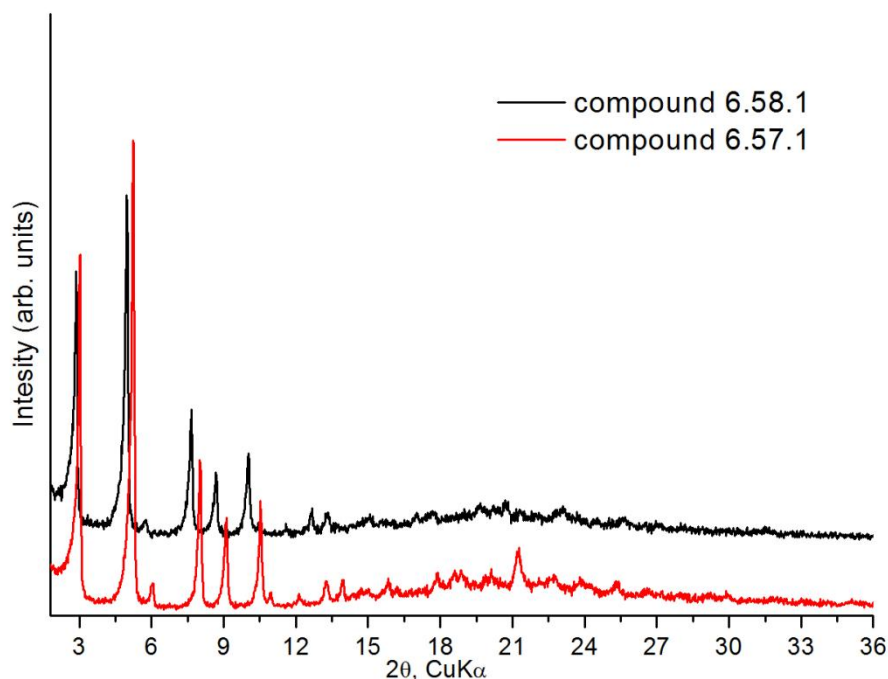
Figure 6.392. Comparison of experimental pxrd patterns of compounds 6.57.1 and 6.58.1.

6.58.2 Synthesis of compound Mg_2L

An amount of 0.030 g (0.06 mmol) of linker 67 (H_4L) and 0.063 g (0.25 mmol) of $Mg(NO_3)_2 \cdot 6H_2O$ were dissolved in a 20 mL glass scintillation vial containing 7 mL DMF, 3 mL EtOH, 1 mL water and 2 drops of triethylamine 99%. The solution was heated at 130 ^{0}C for 48 h where an off white solid was deposited. Yield: 20 % based on linker H_4L.
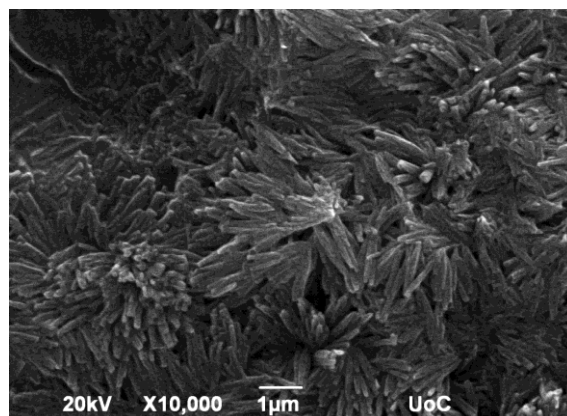

Figure 6.393. Representative SEM image of the as synthesized Mg_2L material.
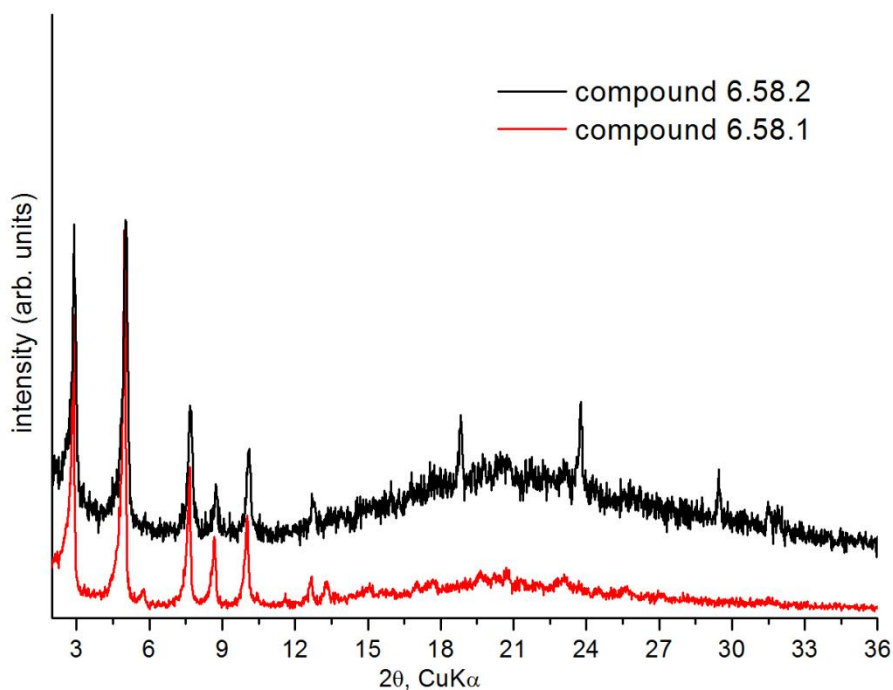
Figure 6.394. Comparison of experimental pxrd patterns of compounds 6.58.2 and 6.58.1.

6.58.3 Synthesis of compound Mn$_2$L

An amount of 0.035 g (0.07 mmol) of linker 67 (H$_4$L) and 0.072 g (0.29 mmol) of Mn(NO$_3$)$_2$·4H$_2$O were dissolved in a 20 mL glass scintillation vial containing 7 mL DMF, 3 mL EtOH, 1 mL water and 1 drop of triethylamine 99%. The solution was heated at 130 ^{0}C for 48 h where a white solid was deposited. Yield: 20 % based on linker H$_4$L.
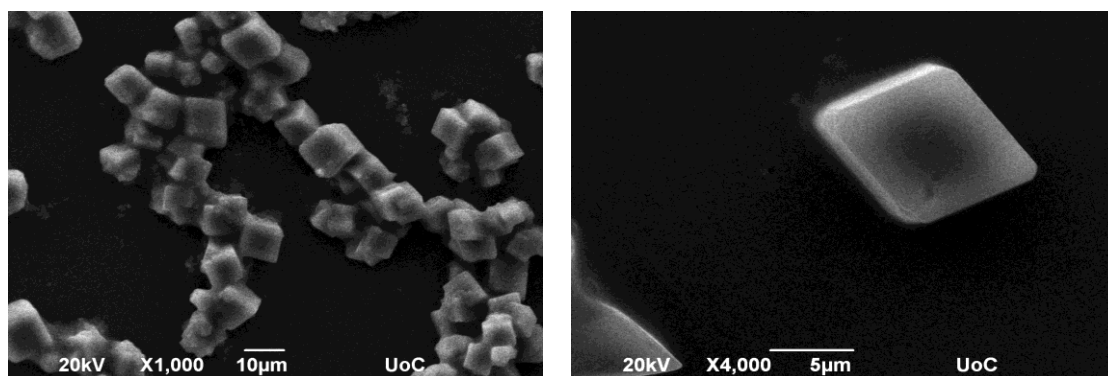

Figure 6.395. Representative SEM images of the as synthesized Mn$_2$L material. The material consists of very small crystal cubes.
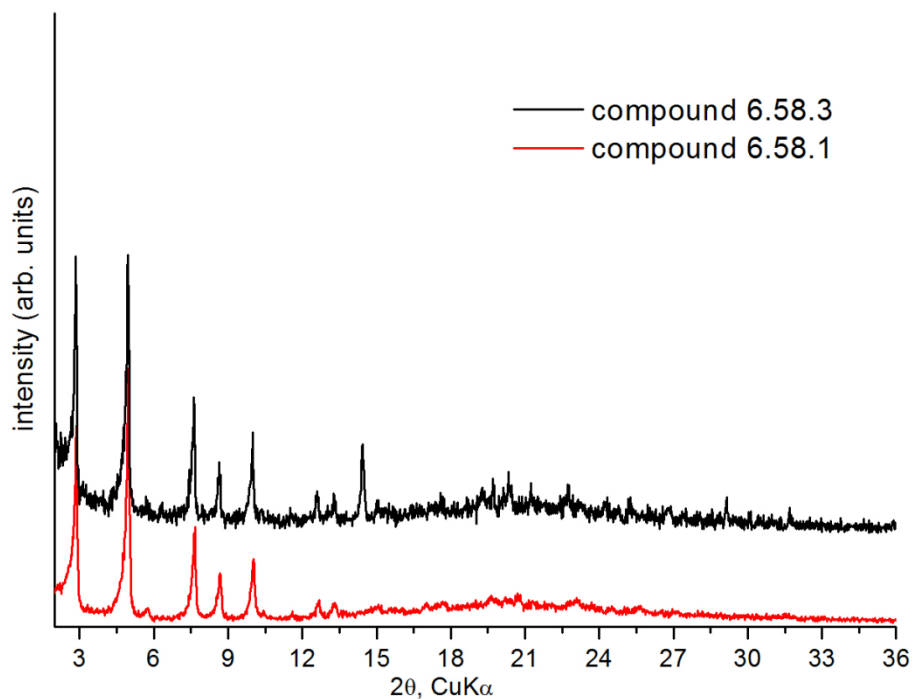
Figure 6.396. Comparison of experimental pxrd patterns of compounds 6.58.1 (Zn) and 6.58.3 (Mn).

6.58.4 Synthesis of compound Co_2L

An amount of 0.035 g (0.07 mmol) of linker 67 (H$_4$L) and 0.085 g (0.29 mmol) of Co(NO$_3$)$_2$·6H$_2$O were dissolved in a 20 mL glass scintillation vial containing 7 mL DMF, 3 mL EtOH, 1 mL water and 1 drop of triethylamine 99%. The solution was heated at 130 ^{0}C for 48 h where a white solid was deposited. Yield: 20 % based on linker H$_4$L.
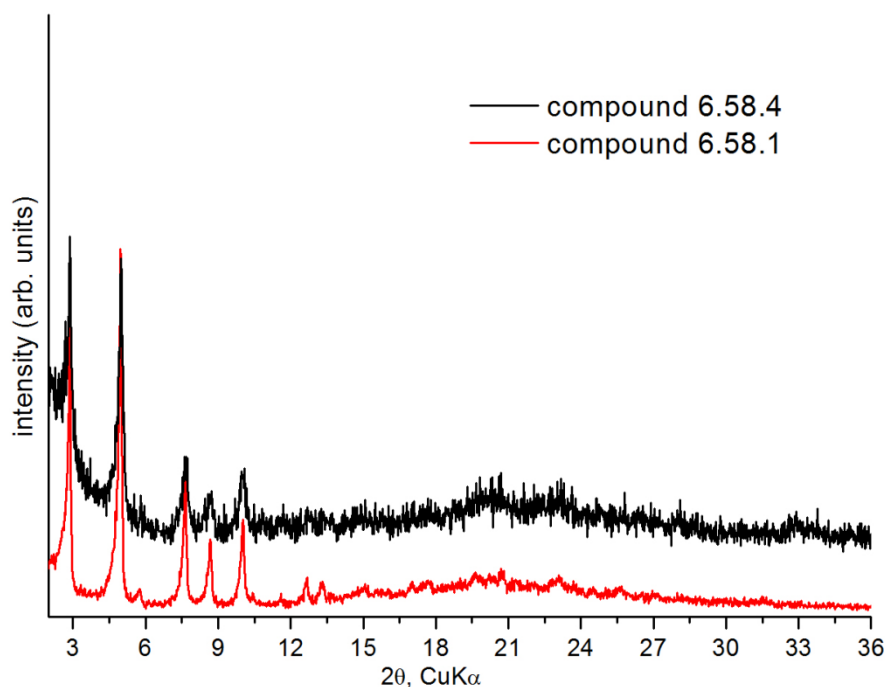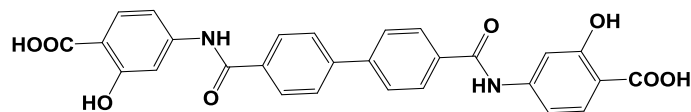

Figure 6.397. Comparison of experimental pxrd patterns of compounds 6.58.1 (Zn) and 6.58.4 (Co).

6.59 MOF syntheses based on organic linker 68

6.59.1 Synthesis of compound Zn₂L

An amount of 0.035 g (0.07 mmol) of linker 68 (H$_4$L) and 0.081 g (0.27 mmol) of Zn(NO$_3$)$_2$·6H$_2$O were dissolved in a 20 mL glass scintillation vial containing 7 mL DMF and 1 mL EtOH. The solution was heated at 120 ^{0}C for 48 h where a beige solid was deposited. Yield: 20 % based on linker H$_4$L.
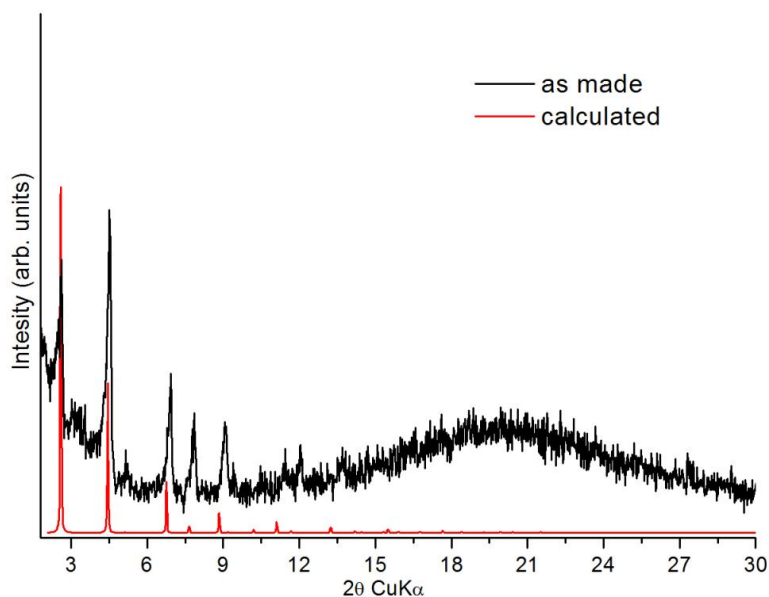

Figure 6.400. Comparison of experimental and calculated pxrd patterns of compound 6.59.1.

6.59.2 Synthesis of compound Mg₂L

An amount of 0.035 g (0.07 mmol) of linker 68 (H$_4$L) and 0.052 g (0.20 mmol) of Mg(NO$_3$)$_2$·6H$_2$O were dissolved in a 20 mL glass scintillation vial containing 7 mL DMF, 3 mL EtOH, 1 mL water and 2 drops of triethylamine 99%. The solution was transferred into a 25 mL Teflon Parr bomb reactor. The bomb was heated at 130 ^{0}C for 48 h where an off white solid was deposited. Yield: 20 % based on linker H$_4$L.
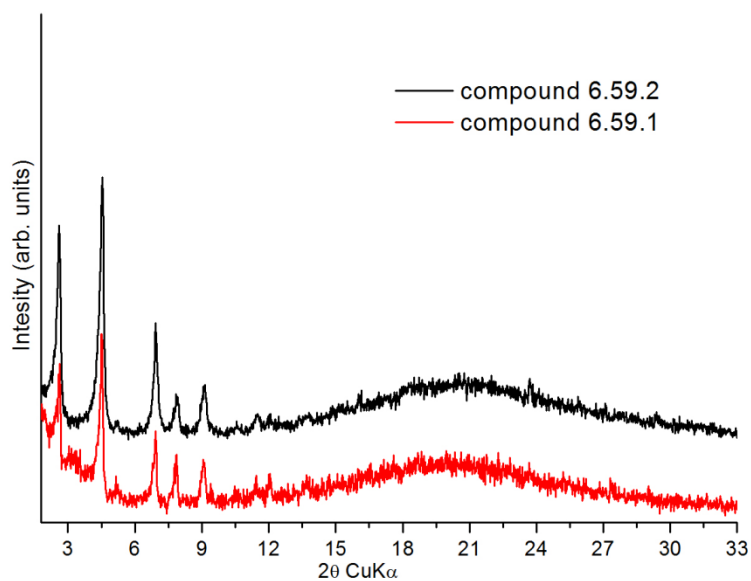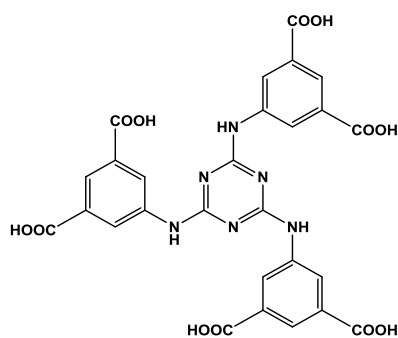
<u>Figure 6.401.</u> Comparison of experimental pxrd patterns of compounds 6.59.2 (Mg) and 6.59.1 (Zn).

6.60 MOF syntheses based on organic linker 72

6.60.1 Synthesis of compound Co_3L

A solution of 5 mL DMF, 3 drops of water, 2 drops of c.HCl, 0.040 g (0.06 mmol) of H_6L and 0.080 g (0.27 mmol) of $CoCl_2·6H_2O$ was placed in a 20 mL glass scintillation vial. The vial was sealed and placed in an isothermal oven at 85 °C for 5 days. During this period, big blue cubic crystals were deposited (30 % yield based on H_6L).
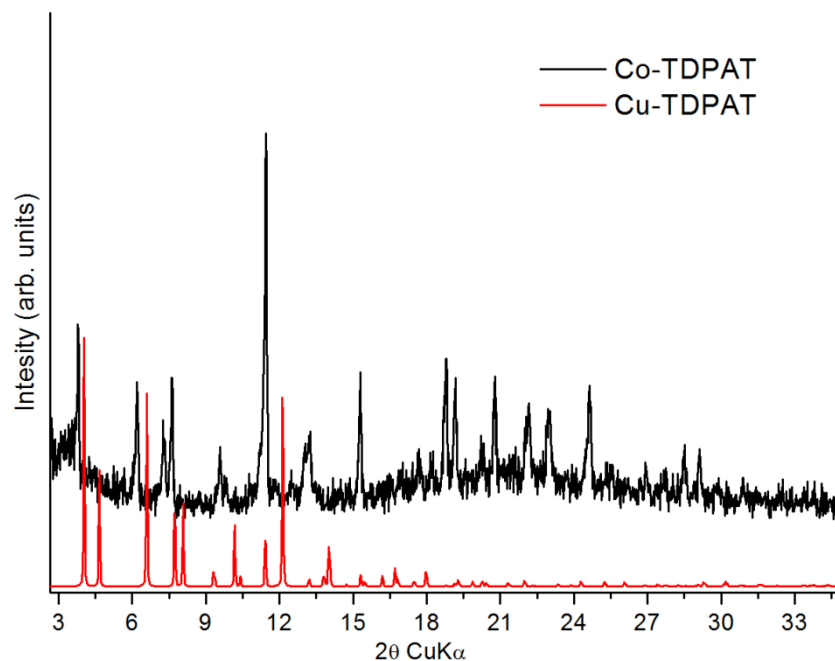
Figure 6.403. Comparison of experimental pxrd pattern of compound Co-TDPAT and calculated pattern of compound Cu-TDPAT.

6.60.2 Synthesis of compound Mg₃L₂

A solution of 5 mL DMF, 3 drops of water, 2 drops of c.HCl, 0.040 g (0.06 mmol) of H_6L and 0.079 g (0.30 mmol) of $Mg(NO_3)_2 \cdot 6H_2O$ was placed in a 20 mL glass scintillation vial. The vial was sealed and placed in an isothermal oven at 85 °C for 5 days. During this period, small colorless crystals were deposited (30 % yield based on H_6L).
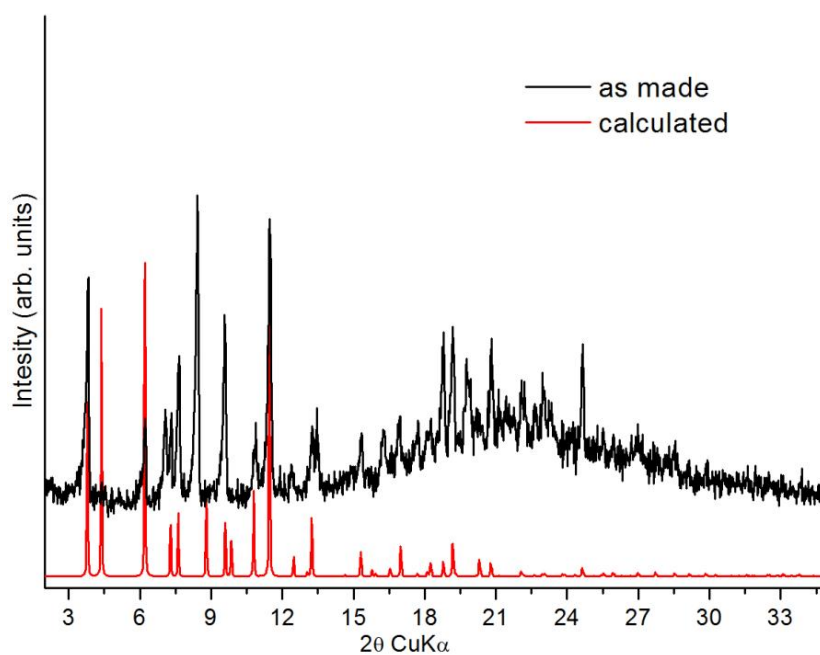

Figure 6.405. Comparison of experimental and calculated pxrd patterns of compound Mg_3L_2.

6.61 MOF synthesis based on organic linker 75

6.61.1 Synthesis of compound $Mg_{4.5}(H_2O)_3OL_{1.5}(Me_2NH_2)$

A solution of 3 mL DMF, 1 mL EtOH, 1 drop c.HNO$_3$, 0.035 g (0.07 mmol) of H$_4$L, and 0.051 g (0.20 mmol) of Mg(NO$_3$)$_2$·6H$_2$O was placed in a 20 mL glass scintillation vial. The vial was sealed and placed in an isothermal oven at 85 °C for 7days. During this period, small yellow crystals were deposited (30% yield based on H$_4$L).
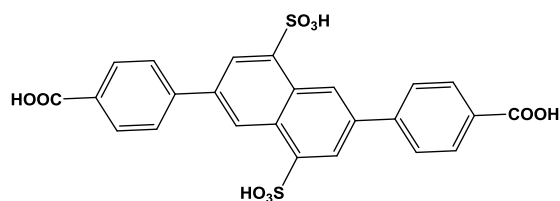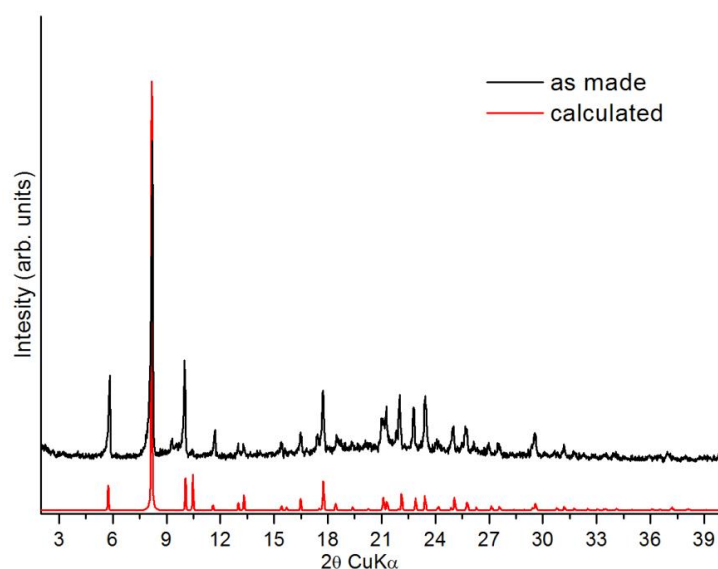

Figure 6.408. Comparison of experimental and calculated pxrd patterns of compound $Mg_{4.5}(H_2O)_3OL_{1.5}(Me_2NH_2)$.

APPENDIX B

Instrumentation

- ^1H and ^{13}C NMR measurements were recorded on 300 MHz and 500 MHz Bruker-AMX instruments.

- Sonic-spray ionization (SSI) mass spectrometry (MS) measurements were recorded on a Thermo LCQ mass spectrometer.

- Powder X-ray diffraction (PXRD) measurements were recorded on a Panalytical X'pert Pro MPD system (CuKα radiation) operated at 45 kV and 40 mA.

- Single-crystal X-ray diffraction data were collected at 250 K on:
  - STOE IPDS II diffractometer operated at 2000 W power (50 kV, 40 mA) with graphite monochromatized MoKα (λ= 0.71073 Å) radiation
  - Diamond Light Source beamline I19, Didcot, UK using a wavelength λ = 1.0402 Å
  - BESSY II MX beamline 14.3 at Helmholtz-Zentrum Berlin using a wavelength λ = 0.91841 Å
  - Elettra XRD1 beamline at Trieste, Italy.

- Thermogravimetric analyses (TGA) were performed using Shimadzu TA-50 and TA SDT Q 600 instruments.

- Scanning Electron Microscopy (SEM) and Energy-dispersive X-ray spectroscopy (EDS) measurements were recorded on a Jeol JSM 6390LV instrument.

- A supercritical CO_2 dryer (Bal-Tec CPD 030) and a custom made dryer, using flow of supercritical CO_2, was used for the activation of some samples.

- Low-pressure nitrogen, argon, hydrogen, carbon dioxide and methane sorption measurements were carried at different temperatures using Autosorb 1-MP and Autosorb-iQ$_2$ instruments from Quantachrome equipped with a cryocooler system. High pressure gas sorption studies were performed on a magnetic suspension balance marketed by Rubotherm, and on a volumetric Hy-Energy PCTPro-2000 (SETARAM) instrument. Ultra-high purity grade N_2 (99.999%), Ar (99.999%), He (99.999%), H_2 (99.999%), CO_2 (99.9995%), CH_4 (99.9995%), NH_3 (99.999%), Kr (99.99%) and Xe (99.99%) were used for all adsorption measurements.

APPENDIX C

Determination of heat of adsorption and selectivity values

Heat of adsorption. To calculate the heat of adsorption, the corresponding adsorption isotherms at two different temperatures (77 K / 87 K for H_2 and 273 K / 293 K for CO_2 and CH_4) were simultaneously fitted using the virial type Equation 1:

$$\ln P = \ln N + \frac{1}{T}\sum_{i=0}^{m} a_i N^i + \sum_{i=0}^{n} b_i N^i \qquad (1)$$

The heat of adsorption at zero coverage was calculated from Equation 2, where as a function of surface coverage, from Equation 3:

$$Q_{st} = -Ra_o \qquad (2)$$

$$Q_{st}(N) = -R\sum_{i=0}^{m} a_i N^i \qquad (3)$$

For the determination of the isosteric heat of adsorption using the Clausius Clapeyron equation a commercially available software, ASiQwin (version 3.01) purchased from Quantachrome, was used.

Gas selectivity using IAST. The corresponding calculations were performed according to an established procedure. Specifically, the single-component adsorption isotherms were described by fitting the data with the following virial-type equation:

$$p = \frac{n}{K}\exp\left(c_1 1n + c_2 n^2 + c_3 n^3 + c_4 n^4\right) \qquad (4)$$

where p is the pressure in Torr, n is the adsorbed amount in mmol g^{-1}, K is the Henry constant in mmol g^{-1} Torr^{-1} and c_i are the constants of the virial equation.

The free energy of desorption at a given temperature and pressure of the gas is obtained from the analytical integration of eq. (4):

$$G(T,p) = RT \int_0^p \frac{n}{p}\,dp = RT\left(n + \frac{1}{2}c_1 n^2 + \frac{2}{3}c_2 n^3 + \frac{3}{4}c_3 n^4 + \frac{4}{5}c_4 n^5\right) \qquad (5)$$

The free energy of desorption is a function of temperature and pressure $G(T,p)$ and describes the minimum work (Gibbs free energy) required to completely degas the adsorbent surface.

For a binary mixture of component i and j eq. (5) yields the individual pure loadings n_i^0 and n_j^0 at the same free energy of desorption:

$$G_i^0(n_i^0) = G_j^0(n_j^0) \qquad (6)$$

The partial pressure of component i and j in an ideal adsorption mixture is given by the following equations:

$$py_i = p_i^0(n_i^0)x_i \qquad (7)$$
$$py_j = p_j^0(n_j^0)x_j \qquad (8)$$

where y_i $(=1-y_j)$ and x_i $(=1-x_j)$ is the molar fraction of component i in the gas phase and the adsorbed phase respectively and p_i^0, p_j^0 is the pure component pressure of i and j respectively. From eq. (6)-(8) and (3), the selectivity for the adsorbates i and j ($S_{i,j}$) and the total pressure (p) of the gas mixture were calculated from eq. (9) and eq. (10), respectively.

$$S_{ij} = \frac{x_i/y_i}{x_j/y_j} = \frac{p_j^0}{p_i^o} \qquad (9)$$

$$p = \Sigma_i^j(p_i^o\, x_i) \qquad (10)$$

APPENDIX D

Synthesis and Characterization of organic linkers

Details about synthesis and characterization of the organic linkers are available upon request. Please contact Dr. Ioannis Spanopoulos (ioaspan@chemistry.uoc.gr) and Professor Pantelis N. Trikalitis (ptrikal@uoc.gr).

References

[1] Shannon R. D., *Acta Cryst.,* **1976**, A32, 751-767.

[2] Peng Y., Krungleviciute V., Eryazici I., Hupp J. T., Farha O. K., Yildirim T., *J. Am. Chem. Soc.*, 135, **2013**, 11887-11894.

[3] Li B., Wen H., Wang H., Wu H., Tyagi M., Yildirim T., Zhou W., Chen B., *J. Am. Chem. Soc.*, **2014**, 136, 6207-6210.

[4] Peng Y., Srinivas G., Wilmer C. E., Eryazici I., Snurr R. Q., Hupp J. T., Yildirim T., Farha O. K., *Chem. Commun.*, **2013**, 49, 2992-2994.

[5] Gándara F., Furukawa H., Lee S., Yaghi O. M, *J. Am. Chem. Soc.,* **2014**, 136, 5271-5274.

[6] Reinsch H., Krüger M., Wack J., Senker J., Salles F., Maurin G., Stock N., *Micropor. Mesopor. Mater.*, **2012**, 157, 50-55.

[7] Weigend F., Ahlrichs R., *Phys. Chem. Chem. Phys.*, **2005**, 7, 3297-3305.

[8] Weigend F., Häser M., *Theor. Chem. Acc.,* **1997**, 97, 331-340.

[9] Ahlrichs R., Bar M., Haser M., Horn H., Kolmel C., *Chem. Phys. Lett.,* **1989**, 162, 165-169.

[10] Rappe A. K., Casewit C. J., Colwell K. S., Goddard W. A., Skiff W. M., *J. Am. Chem. Soc.,* **1992**, 114, 10024-10035.

[11] Gale J. D., *JCS Faraday Trans.,* **1997**, **93**, 629-637.